Mathematical Problems in Engineering

Computational Intelligence Techniques for Realization of Power Electronic Converters for Next Generation Grids

Lead Guest Editor: Ravi Samikannu
Guest Editors: Abu Zaharin Ahmad and Albert Alexander Stonier

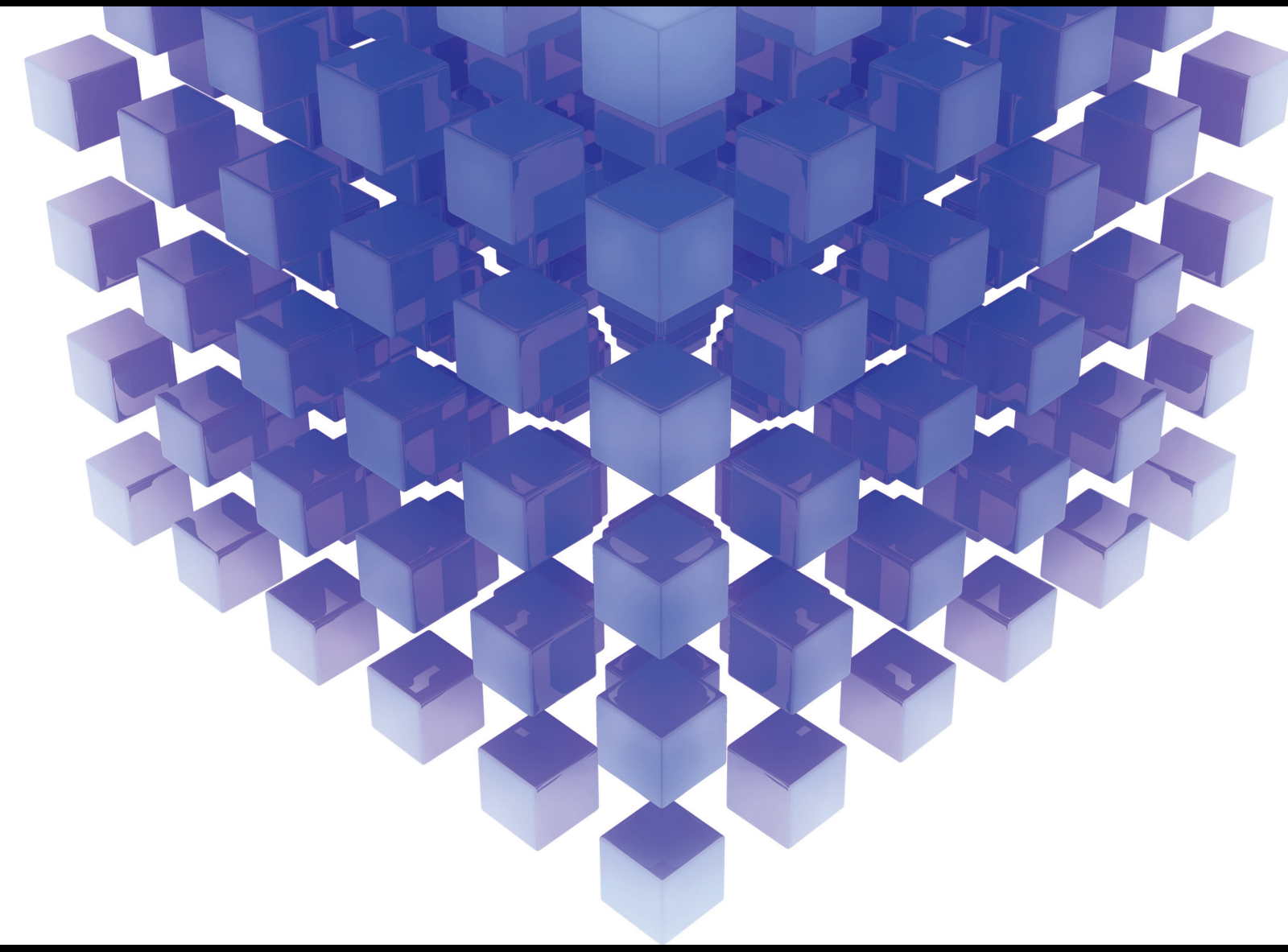

Computational Intelligence Techniques for Realization of Power Electronic Converters for Next Generation Grids

Mathematical Problems in Engineering

Computational Intelligence Techniques for Realization of Power Electronic Converters for Next Generation Grids

Lead Guest Editor: Ravi Samikannu
Guest Editors: Abu Zaharin Ahmad and Albert Alexander Stonier

Contents

Erratum to "Dynamic Equivalent Modeling of Wind Farm Based on Dominant Variable Hierarchical Clustering Algorithm"
Wenbo Jiang and Mingyue Zhong
Erratum (1 page), Article ID 9797619, Volume 2024 (2024)

Modified High Gain DC-DC Converter with APICs for Microgrid
G. Amritha, G. Kanimozhi, K. Mohana Sundaram, L. Natrayan, and Kiran Ramaswamy
Research Article (9 pages), Article ID 7582036, Volume 2022 (2022)

Mathematical Modeling of Real-Time Systems Using Heun and Piecewise Methods
Urfa Malik Gul, Anand Paul, and K.-W.-A. Chee
Research Article (6 pages), Article ID 4651084, Volume 2022 (2022)

Optimization and Design of a Sustainable Industrial Grid System
Samat Iderus, Geno Peter, K. Praghash, and Aruna Rai Vadde
Research Article (12 pages), Article ID 4418329, Volume 2022 (2022)

Mathematical Model for Energy and Exergy-Based Simulation of Triangular Solar Energy Extractor for Air Heating Applications
C. Ramesh, M. Vijayakumar, L. Jeyanthi, P. L. Rupesh, A. Kanchana, P. R. Jyothi Sankar, V. S. Sajith, Neha Munjal, and Habtewolde Ababu Birhanu
Research Article (14 pages), Article ID 7157334, Volume 2022 (2022)

An Improved Power Quality Disturbance Detection Using Deep Learning Approach
Kavaskar Sekar, Karthick Kanagarathinam, Sendilkumar Subramanian, Ellappan Venugopal, and C. Udayakumar
Research Article (12 pages), Article ID 7020979, Volume 2022 (2022)

Power-Sharing Analysis of Hybrid Microgrid Using Iterative Learning Controller (ILC) considering Source and Load Variation
S. Angalaeswari, K. Jamuna, K. Mohana sundaram, L. Natrayan, L. Ramesh, and Kiran Ramaswamy
Research Article (6 pages), Article ID 7403691, Volume 2022 (2022)

Performance Enhancement of a Three Phase Boost-Cascaded Fifteen Level Inverter Using the PI Controller
S. Sathish Kumar, R. Ramkumar, S. Sivarajeswari, D. Ramya, T. Subburaj, and Martin Sankoh
Research Article (17 pages), Article ID 3888571, Volume 2022 (2022)

A Bridgeless LUO Converter with Glowworm Swarm Optimized Tuned PI Controller for Electrical Applications
M. Sivaramkrishnan, M. Siva Ramkumar, Siva Subramanian S, and Nyagong Santino David Ladu
Review Article (8 pages), Article ID 2401261, Volume 2022 (2022)

Equivalent Circuit Analysis of Linear Phase-Shifting Transformer with End Effect
Mei Wu, Jinghong Zhao, Guoqiang Guo, and Yiyong Xiong
Research Article (15 pages), Article ID 1984595, Volume 2022 (2022)

Low Voltage Ride through Enhancement Using Grey Wolf Optimizer to Reduce Overshoot Current in the Grid-Connected PV System
N. Jaalam, A.Z. Ahmad, A. M. A. Khalid, R. Abdullah, N. M. Saad, S. A. Ghani, and L. N. Muhammad
Research Article (12 pages), Article ID 3917775, Volume 2022 (2022)

An Efficient Energy Management Scheme for an Islanded DC Microgrid with Hybrid VRFB System
S. Hameed, I. Prabhakar Reddy, V Ganesh, and Aruna rai Vadde
Research Article (13 pages), Article ID 9083307, Volume 2022 (2022)

Tournament Selected Glowworm Swarm Optimization Based Measurement of Selective Harmonic Elimination in Multilevel Inverter for Enhancing Output Voltage and Current
Udayakumar Chandran, Sathiyasekar Kumarasamy, Ravi Samikannu, Rajamani M. P. E., Vinoth Krishnamoorthy, and Srinivasan Murugesan
Research Article (11 pages), Article ID 5845249, Volume 2022 (2022)

Elderly People Activity Recognition in Smart Grid Monitoring Environment
Anusha Ganesan, Anand Paul, and HyunCheol Seo
Research Article (12 pages), Article ID 9540033, Volume 2022 (2022)

Electric Vehicle Usage Pattern Analysis Using Nonnegative Matrix Factorization in Renewable EV-Smart Charging Grid Environment
Anandkumar Balasubramaniam, Thirunavukarasu Balasubramaniam, Anand Paul, and HyunCheol Seo
Research Article (9 pages), Article ID 9365214, Volume 2022 (2022)

Multithreaded Multiswarm Model for Intelligent Economic Prosumer Load Dispatch for Battery Supported DC Microgrid
C. R. Sarin, Geetha Mani, Albert Alexander Stonier, M. Arivarasu, Ravi Samikannu, and Srinivasan Murugesan
Research Article (13 pages), Article ID 7739945, Volume 2022 (2022)

A Combined PWM and AEM-Based AC Voltage Controller for Resistive Loads
Geno Peter, K. Praghash, Anli Sherine, and Vivekananda Ganji
Research Article (11 pages), Article ID 9246050, Volume 2022 (2022)

Design and Implementation of Automatic Water Spraying System for Solar Photovoltaic Module
L. Ashok Kumar, V. Indragandhi, Yuvaraja Teekaraman, Ramya Kuppusamy, and Arun Radhakrishnan
Research Article (11 pages), Article ID 7129610, Volume 2022 (2022)

Contents

SSNN-Based Energy Management Strategy in Grid Connected System for Load Scheduling and Load Sharing
Yuvaraja Teekaraman, K. A. Ramesh Kumar, Ramya Kuppusamy, and Amruth Ramesh Thelkar
Research Article (9 pages), Article ID 2447299, Volume 2022 (2022)

Dynamic Equivalent Modeling of Wind Farm Based on Dominant Variable Hierarchical Clustering Algorithm
Wenbo Jiang and Mingyue Zhong
Research Article (10 pages), Article ID 7629414, Volume 2021 (2021)

Hindawi
Mathematical Problems in Engineering
Volume 2024, Article ID 9797619, 1 page
https://doi.org/10.1155/2024/9797619

Erratum

Erratum to "Dynamic Equivalent Modeling of Wind Farm Based on Dominant Variable Hierarchical Clustering Algorithm"

Wenbo Jiang[1,2] **and Mingyue Zhong**[1,2]

[1]*School of Electrical Engineering and Electronic Information, Xihua University, Chengdu 610039, China*
[2]*Sichuan Provincial Key Laboratory of Signal and Information Processing, Xihua University, Chengdu 610039, China*

Correspondence should be addressed to Wenbo Jiang; caswenbojiang@gmail.com

Received 4 December 2023; Accepted 4 December 2023; Published 30 January 2024

In the article titled "Dynamic Equivalent Modeling of Wind Farm Based on Dominant Variable Hierarchical Clustering Algorithm" [1], a reference citation was error. The reference is shown below:

D. C. Fabrizio, V. Alfredo, and V. Domenico, "Adaptive wind generation modeling by fuzzy clustering of experimental data," Electronics, vol. 7, no. 4, pp. 1–16, 2018.

This should appear as the following sentences in the text [2]:

F. De Caro, A. Vaccaro, and D. Villacci, "Adaptive wind generation modeling by fuzzy clustering of experimental data," Electronics, vol. 7, no. 4, pp. 1–16, 2018.

The error was introduced during the production process of the article, and Hindawi apologies for causing this error in the article.

References

[1] W. Jiang and M. Zhong, "Dynamic Equivalent Modeling of Wind Farm Based on Dominant Variable Hierarchical Clustering Algorithm," *Mathematical Problems in Engineering*, vol. 2021, Article ID 7629414, 10 pages, 2021.

[2] F. De Caro, A. Vaccaro, and D. Villacci, "Adaptive wind generation modeling by fuzzy clustering of experimental data," *Electronics*, vol. 7, no. 4, pp. 1–16, 2018.

Hindawi
Mathematical Problems in Engineering
Volume 2022, Article ID 7582036, 9 pages
https://doi.org/10.1155/2022/7582036

Research Article

Modified High Gain DC-DC Converter with APICs for Microgrid

G. Amritha,[1] G. Kanimozhi,[2] K. Mohana Sundaram,[3] L. Natrayan,[4] and Kiran Ramaswamy[5]

[1]*School of Electrical Engineering, Vellore Institute of Technology, Chennai, Tamil Nadu, India*
[2]*Centre for Smart Grid Technologies, School of Electrical Engineering, Vellore Institute of Technology, Chennai, Tamil Nadu, India*
[3]*Department of Electrical and Electronics Engineering, Centre for Energy Sciences and Engineering, KPR Institute of Engineering and Technology, Arasur, Coimbatore, India*
[4]*Department of Mechanical Engineering, Saveetha School of Engineering, SIMATS, Chennai, Tamil Nadu, India*
[5]*Department of Electrical Engineering, Ambo University, Ambo, Ethiopia*

Correspondence should be addressed to G. Kanimozhi; kanimozhi.g@vit.ac.in, L. Natrayan; natrayan07@gmail.com, and Kiran Ramaswamy; kiran.ramaswamy@ambou.edu.et

Received 8 March 2022; Revised 8 June 2022; Accepted 14 June 2022; Published 5 October 2022

Academic Editor: Ravi Samikannu

This paper proposes a nonisolated high voltage gain DC-DC converter. The active–passive inductor cells (APICs) makes the converter topology expandable, and it also helps in providing a high gain quality at lower duty cycles. The proposed converter is suitable for high gain applications mainly necessitating microgrid as well as integration of renewable energy sources into the existing grid infrastructure. The merits of the converter can be attributed to the ability to achieve high gain and low current stress and switching losses on power electronic switches. The proposed converter is analyzed in both continuous and discontinuous modes of operation, the efficiency is calculated and simulation results substantiate the operation of the converter.

1. Introduction

tIntegration of renewable energy sources into the grid infrastructure and expanding focus on microgrids and their economic as well as environmental significance have compelled a demand for new topologies in converters for high gain applications. This is mainly caused by the low-output voltage derived from these sources, which have always stood as the foremost limitation in their utilization. An extendable converter using APICs is presented [1]. The DC-DC converter introduced is based on the technique that uses three states of switching [2]. The converter is analyzed theoretically and is also verified experimentally through a laboratory prototype. Several other topologies are reviewed to understand their limitations and also to prove the advantages of the proposed topology.

The conventional boost converters do not have the ability to provide high gains owing to the design structure with power switches, diodes, the presence of inductors, and capacitors [3]. The proposed structure is based on parallel charging of inductors during switch ON period and series discharging during switch OFF period. The converter provides high step-up voltage within a shorter range of duty ratio. The converter is based on active switched inductors and passive switched capacitors. Apart from the ability to achieve high gain the topology also achieves high efficiency and reduces voltage stress along with the number of elements in the circuit [4]. The family of transformerless active switched inductor and switched capacitor Cuk converter with high gain ability provides low voltage and current stress. Semiconductor devices with low voltage ratings are used to curtail the conduction losses [5]. Applications like grid-connected PV systems require high step-up voltage. The employment of traditional boost converters in such scenarios are limited. The paper introduces hybrid switched inductor converters to achieve high gain conversion [6].

A hybrid transformerless converter designed with two inductor boost converter consisting of a voltage multiplier and switched capacitor cells is proposed by Andrade et al.

[7]. Improved voltage gain and efficiency, low current and voltage stress, and the ease of operation are some of the key features of the structure. In the two inductor high gain converter topology the difference between two inductor current can be compensated by increasing the inductor current of the corresponding path. This is obtained through increasing the turn-on time. The suggested method has no effect on voltage transfer gain of the converter [8]. Switching structures designed with two capacitors and two-three diodes or two inductors and two-three diodes are described. These can be classified into ldquostep-downrdquo or ldquostep-up.rdquo. These structures when combined with converters such as buck, boost, buck-boost, Cuk, zeta, and sepic converters give a step up function. These converters can increase or decrease the gain more than the classical converters [9].

High gain DC-DC converter integrates voltage RE-Lift, and Super RE-Lift Luo converters have provided sufficient solar energy to the grids. High voltage gain and high power efficiency are benefits of the topology alongside high efficiency. The output voltage is increased in geometric progression. The voltage gain produced by most of the converter structures is narrowed down by the losses [10]. This possesses a limitation in the integration of renewable energy sources using these converters. Melo de Andrade et al. targets series connection of DC-DC converters to prepare an assessment based on Cuk and SEPIC converter topologies [11]. Das and Agarwal studied an expandable high gain converter for microgrid applications. High gain quality is obtained at lower duty cycles themselves. High efficiency, low stress on switches, and minimum output voltage ripple (MOVR) are other benefits [12].

A new series DC-DC converters "XL converters" are suggested by Sayed et al. The main application is renewable energy conversion. The topology is implemented using two buck-boost converters combined with different switched reactive networks [13]. This converter structure offers the feature of high negative voltage at moderate duty ratios. It does not include a transformer and has only a single power control switch. Bidirectional DC-DC converters play a vital role in applications involving increased voltage gain ratios. Asha et al. presented a nonextendable bidirectional buck-boost converter. This topology does not require coupled inductors [14]. The topology has stages of operation and the voltage gain can be derived for n times. Kanimozhi et al. proposed a boost converter based on a new coupled inductor. The structure can be realized for battery charging in photovoltaic systems fed PMDC motor. The closed-loop control is also achieved and maximum possible energy from the PV panels is extorted through the method of single-stage conversion [15].

Improving the output voltage level obtained from various distributed energy sources is very crucial to determine a common voltage throughout the DC link of a particular microgrid. Mahajan et al. intended to eliminate the limitation of the conventional boost converters for this function. The recommended topology provides a quadratic voltage gain. The converter has been validated through comparison with existing topologies and also through loss analysis [16]. The converter proposed by Hossein Hosseini et al. is appropriate for applications involving hybrid electric vehicles. The exceptional aspects include reduction in voltage stress, switching, and conduction losses [17]. The method adopted is that of bipolar switching, to benefit from decreased losses. The converter discussed in Sundaram et al. is nonisolated and maintains a high gain [18]. Low input current ripple makes it a good choice for realizing MPPT in photovoltaic systems. Further assessment of the converter is aided with steady-state analysis, which also justifies the efficacy of the converter.

A DC-DC converter with high gain and without isolation is established on dual coupled inductors by Ahmad et al. achieves high gain via the dual coupled inductors. The topology is consistent with applications involving distributed energy resources. A regenerative snubber circuit is combined to recycle the energy leaked. This converter is promising in transformerless grid-connected PV systems [19]. A magnetically coupled single switch converter implemented by Kanimozhi et al. [20] attains a high voltage ratios on the basis of the inverse operating principle. The applications of the converter are renewable-based energy systems. To prevent core saturation a regenerative circuit is added to the topology [21] that examines a bidirectional DC-DC converter. It consists of coupled inductor and a voltage doubler cell. Extended output voltage is received through a dual active half-bridge circuit. ZVS is utilized for lowering the switching losses. The losses in the semiconductor devices are calculated to compute the losses in the converter. The conduction losses are calculated by multiplying the voltage and current values across individual devices, measured through voltage and current measurement units from the simulation of the converter.

Forouzesh et al. proposed a modular switched capacitor converter topology. The topology is modified from the original Dickson converter. To achieve dynamic variation in gain, two different methods are carried out [22]. The prototype and the equivalent circuits are analyzed with experimental results. The converter design is convenient for green energy-related applications. The structure has been analyzed and the results are presented. Furthermore, the power conversion efficiency has a scope of improvement [23]. A large gain step-up converter is achieved with an asymmetric voltage multiplier network. The converter is designed to mitigate the problem of reverse recovery in the diode of the leakage inductor [24].

2. Proposed Converter

The topology of the proposed converter is depicted in Figure 1. For the analysis, all the inductors are given the same inductance values. The converter is analyzed in both continuous conduction mode (CCM) and discontinuous conduction mode (DCM) of operation.

The circuit diagram of the converter for $n = 1$ is given in Figure 2. The theoretical waveforms for CCM and DCM operation are given in Figure 3. Figure 4 represents the operational modes of the structure and the corresponding circuit diagrams.

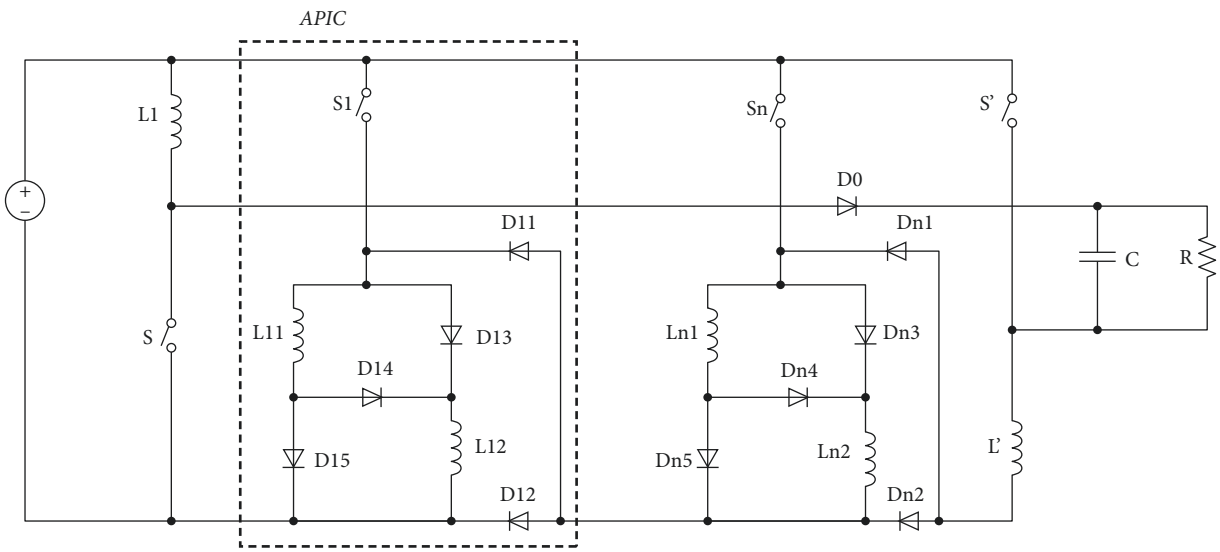

Figure 1: Proposed converter for n APICs.

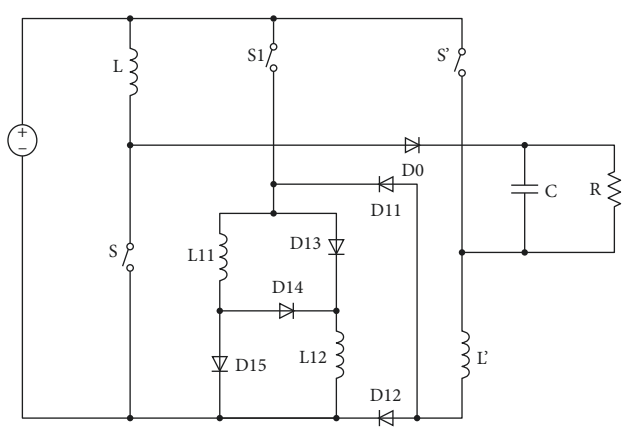

Figure 2: Circuit diagram of the converter for $n = 1$.

3. Analysis of the Converter

3.1. Analysis of the Converter in CCM

3.1.1. Time Interval of T_{ON}. All the switches are turned ON. The voltage across the inductor during this period is given by the following equation:

$$VL = Vi. \tag{1}$$

The inductor current is as follows:

$$i_L = \frac{Vi}{L}t + I_{LV}. \tag{2}$$

In this interval, the inductors get charged therefore the inductor current increases and reaches its maximum value at $t = DT$. Applying $t = DT$ in equation (2) the maximum inductor current can be derived as follows:

$$ILP = \frac{ViDT}{L} + I_{LV}. \tag{3}$$

The capacitor is discharged by the interval end, and the capacitor voltage decreases to V_{CV}.

3.1.2. Time Interval of T_{OFF}. All the switches are OFF. The voltage across the inductor can be given as follows:

$$VL = \frac{Vi - Vo}{2n + 2}. \tag{4}$$

n is the number of APICs. For this interval the current across the inductors is as follows:

$$i_L = \frac{Vi - Vo}{(2n + 2)L}t + I_{LP}. \tag{5}$$

At the end of this interval, the inductor current will be equal to I_{LV}, since the current decreases as a result of the inductor discharging. Applying $t = (1 - D)T$ in equation (4), the minimum inductor current is as follows:

$$i_L = \frac{(Vi - Vo)(1 - D)T}{(2n + 2)L} + I_{LP}. \tag{6}$$

As the current across inductors and the capacitor decreases at this interval, inductor provides the load current along with charging the capacitor.

3.1.3. Voltage Gain Calculation. Considering equations (1) and (3), the voltage gain can be derived as follows:

$$\frac{Vo}{Vi} = \frac{1 + D(2n + 1)}{(1 - D)}. \tag{7}$$

The converter is designed considering minimum output voltage ripple. Least OVR is obtained in CCM operation. The value of the inductor is calculated as given in Table 1. The voltage gain as well as the output ripple of the converter is independent of the inductance value.

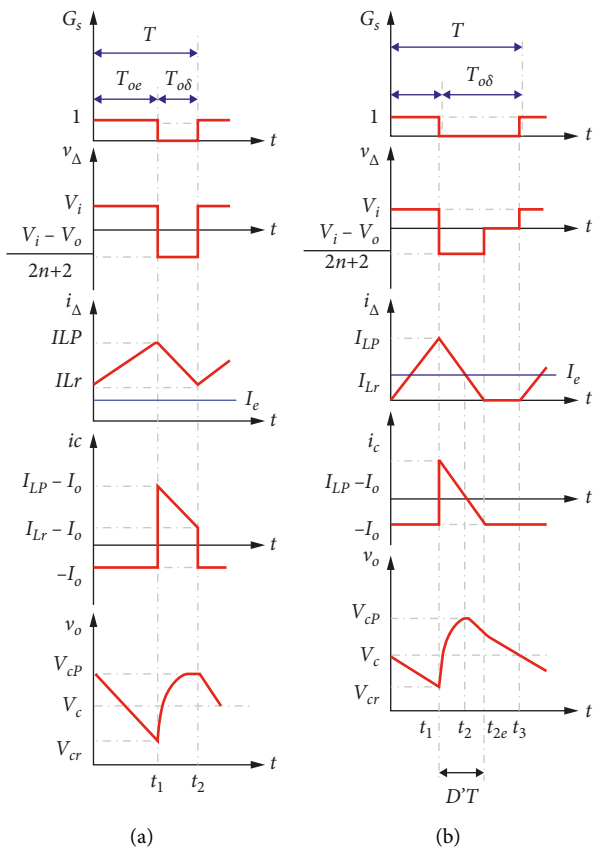

Figure 3: Theoretical waveforms. (a) CCM. (b) DCM.

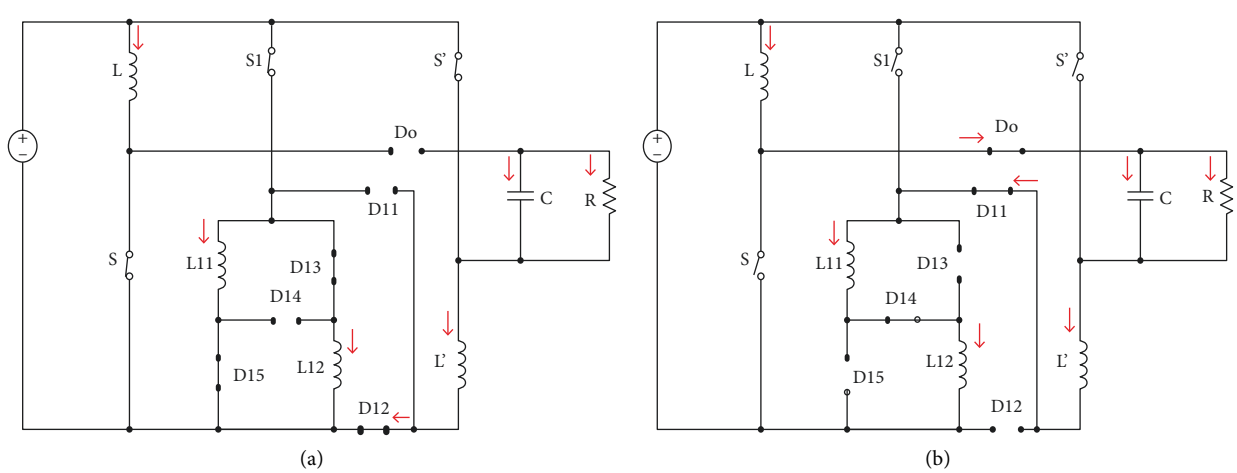

Figure 4: Operation modes diagram of the converter for $n = 1$. (a) T_{ON}. (b) T_{OFF}.

Table 1: Different operational modes in the converter versus inductance values.

Inductance values	Operational mode
$L > L_C$	CCM
$L < L_C$	DCM

3.1.4. Voltage Stress and Current Stress. The voltage stress across the switches and the diodes depends upon the voltage gain and the number of APICs and can be formulated as a function of the same. Since the ripple factor of the converter is considerably low (~2%), the voltage and current stress of the converter are reduced.

Table 2: Simulation parameters.

Simulation parameter	Value
Output voltage, (V_0)	400 V
Switching frequency, (F)	50 kHz
Load resistance, (R)	50–100 Ω
Capacitance, (C)	200 mF
Output power, (P_0)	2 kW
Input voltage (V_i)	20 V–40 V
Inductance, (L_c)	11.3 μH

3.2. Analysis of the Converter in DCM

3.2.1. Time Interval of T_{ON}. At this time interval, the analysis is the same as that of CCM, therefore the maximum current through the inductor is given as follows:

$$i_{LP} = \frac{Vi\ DT}{L}. \tag{8}$$

3.2.2. Time Interval of T_{OFF}. At this time interval, the capacitor current equals the load current. The capacitor voltage decreases as the capacitor discharges. The maximum inductor current is as follows:

$$I_{LP} = \frac{(Vo - Vi)DT}{(2n+2)L}. \tag{9}$$

3.3. Critical Inductance. The minimum inductor current is given as follows:

$$I_{LV} = Io\left(\frac{1}{1-D} - \frac{R\ D}{2Lf}\frac{(1-D)}{[1+(2n+1)D]}\right). \tag{10}$$

Applying $I_{LV} = 0$ (10), the critical inductance between CCM and DCM can be obtained as follows:

$$L_c = \frac{R\ D(1-D)}{2f}\frac{Vi}{Vo}. \tag{11}$$

4. Design Considerations

The converter components are designed to obtain suitable operation with less output voltage ripple. The critical inductance is derived as a function of V_i and R. For a particular value of inductance the converter can operate in either CCM or DCM mode, as given in Table 1. The output voltage of the converter is less in CCM operation than that of DCM [25]. The converter is specified for renewable energy integration with the grid in microgrids. In these cases the quality of the waveform is crucial. Therefore maintaining MOVR is a very important condition considering these aspects. The converter is suitable for such applications.

5. Simulation Results

The simulation results are discussed to validate the converter topology. The converter parameters are verified for $n = 1$. The converter parameters are consolidated in Table 2. The critical inductance value obtained is $L_C = 11.3\ \mu$H. The simulation is implemented in both modes of operation. The CCM analysis is performed for $L = 20\ \mu$H and DCM analysis is performed for $L = 5\ \mu$H. Figures 5 and 6 show the output waveforms attained for CCM. The output waveforms obtained for DCM are presented in Figures 7 and 8. It can be inferred from the waveforms that voltage stress is highest in the diode at the output side. An output voltage ripple (OVR) of 2% is produced. The MOVR does not depend upon inductance value.

For further analysis, the theoretical and simulation results are compared. The efficiency as well as the voltage gain of the topology are improved with the increase in n (number of APICs). The efficiency reduces with an increase in the number of passive elements.

The capacitive filter of the converter is calculated based on minimum output voltage ripple. The ripple factor is considered to be 2% and the C value is calculated from the following equation:

$$C = \frac{D}{\text{Rrf}}. \tag{12}$$

where C is the capacitance in farad, R is resistance, r is the ripple factor, and f is the switching frequency.

6. Comparison

A conventional boost converter and an extendable high gain converter is used for comparing the topology. The comparison among different parameters of the same is given in Table 3. The output voltage and the corresponding voltage gain increases with an increase in 'n' APICs. This converter is appropriate for application in microgrids for integrating renewable energy systems into the grid. Reasonably high values of voltage gain can be obtained at lower values of duty ratios. The number of inductors and passive elements in the topology is lesser than other extendable topologies. Considering the overall losses contributed by the semiconductor devices, major proportion (approximately 98%) is contributed by the total diodes used in the design. But with respect to the topology used for comparison, the losses are further reduced since the number of diodes in the design are less by a number of 5 and the inductors by a number of 2. Therefore the losses are reduced. Small inductance values are sufficient.

All the inductors in the topology are considered to be of the same value to make the analysis of the converter simpler. Voltage gain of the converter depends upon the number of

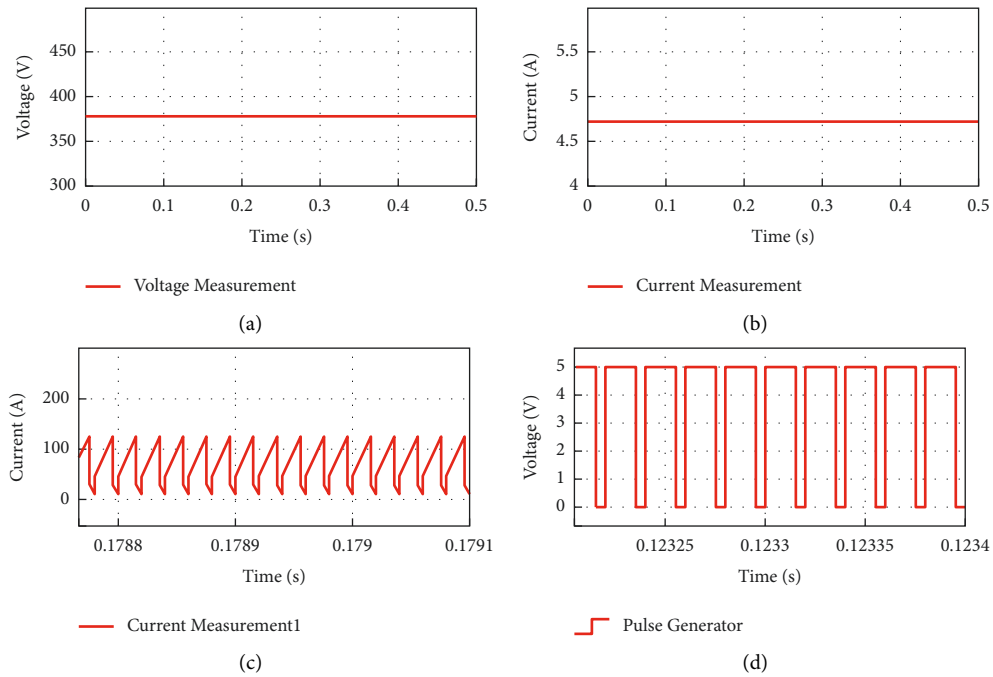

Figure 5: Simulation results in CCM. (a) Output voltage. (b) Output current. (c) Inductor current. (d) Switching pulse.

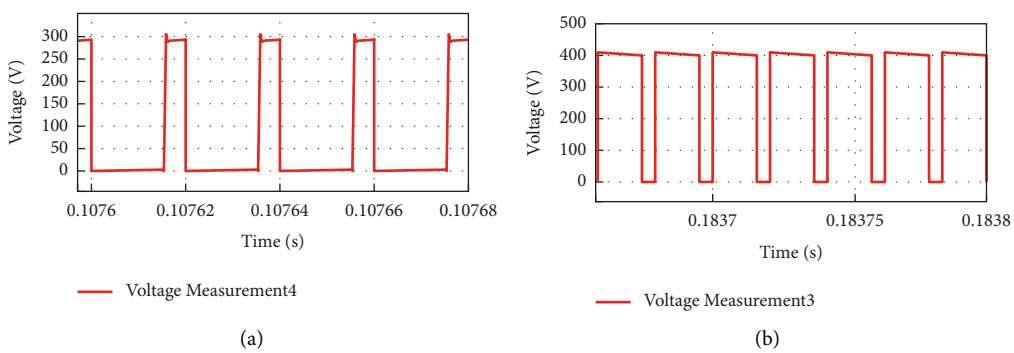

Figure 6: (a) Voltage stress across switches S' in CCM. (b) Voltage stress across diode Do in CCM.

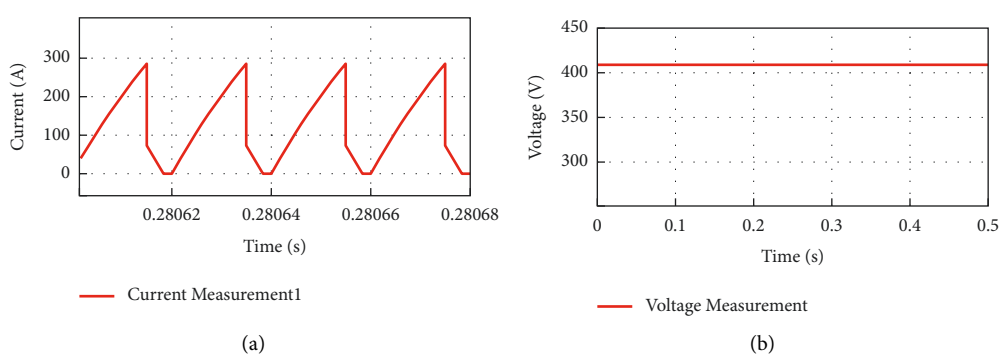

Figure 7: Continued.

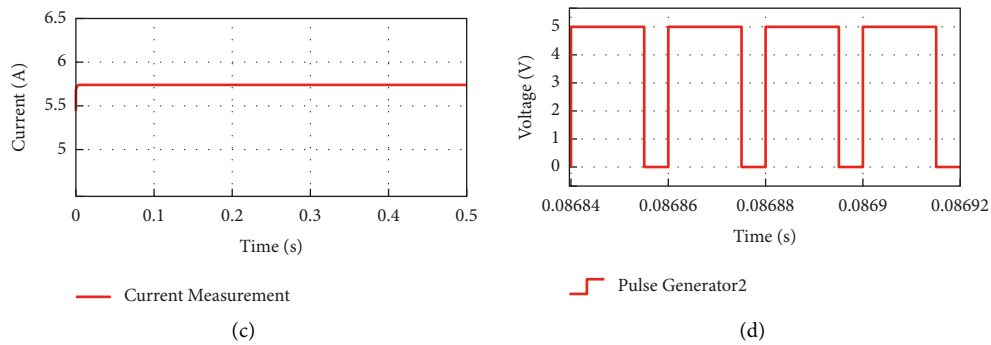

(c) (d)

Figure 7: Simulation results in DCM. (a) Output voltage. (b) Output current. (c) Inductor current. (d) Switching pulse.

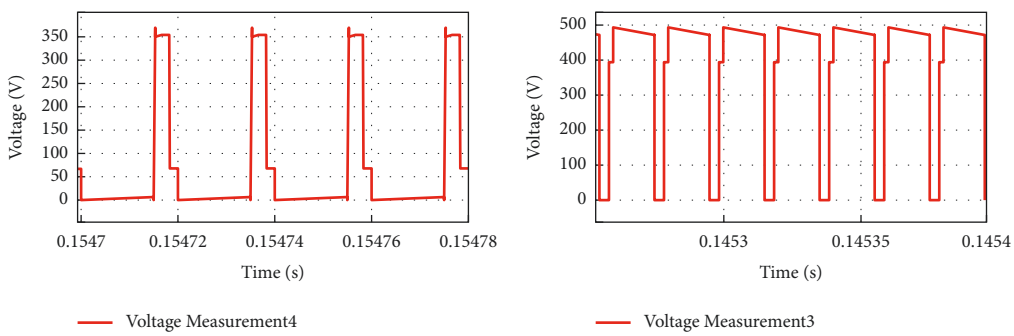

(a) (b)

Figure 8: (a) Voltage stress across switches S' in DCM. (b) Voltage stress across diode Do in DCM.

Table 3: Results comparison.

Elements	Boost converter	Extendable nonisolated converter	Proposed converter
Diodes	1	$5n+6$	$5n+1$
Switches	1	$n+2$	$n+2$
Inductors	1	$2n+4$	$2n+2$
Voltage gain	$1/1-D$	$1+(2n+3)D/1-D$	$1+(2n+1)D/1-D$
Efficiency	98.33%	95.6%	96.6%

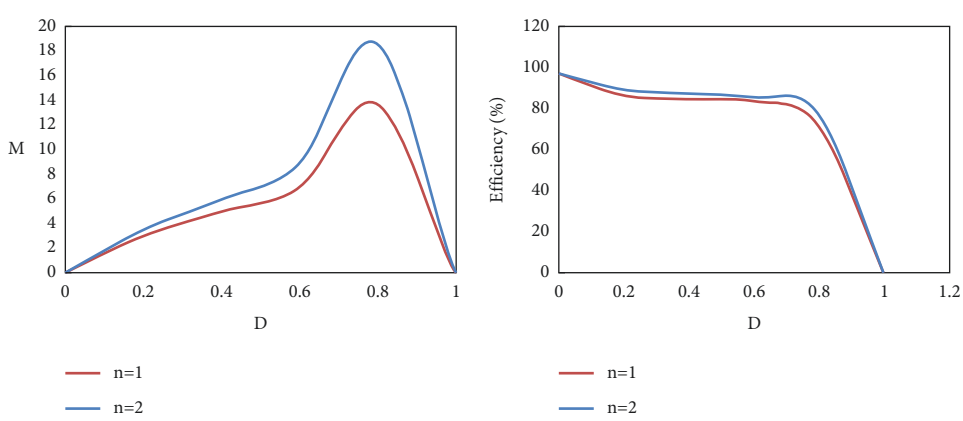

(a) (b)

Figure 9: (a) Voltage gain versus duty cycle. (b) Efficiency versus duty cycle.

inductors in the circuit, which is derived assuming same inductors. If the inductors of different inductance values are considered, then analysis of the converter will be different. But even in such cases the final result of the main parameters will be similar. The proposed converter efficiency all though higher than the topology used for comparison is less than that of the conventional boost converter. However the comparison of efficiency is not approved due to certain factors of consideration. Furthermore, the variation in voltage gain and the efficiency with respect to duty cycle that are plotted and compared for $n = 1$ and $n = 2$ are shown in Figure 9. From the plot of efficiency versus duty cycle it can be validated that for a typical value of duty cycle the efficiency of the converter is improved with the increase in n.

7. Conclusion

An extendable high gain DC-DC converter has been proposed for microgrid applications. Since the topology involves active–passive inductor cells the topology can be extended to provide improved voltage gain. The voltage stress on semiconductor devices is low, thereby reducing the losses. The inductors required are of small size. The proposed topology can achieve high gains at lower values of the duty cycle, which is difficult to accomplish from conventional boost converters. The topology is compared with conferred literature structures and the conventional boost converter. The converter elements are designed based on MOVR. The simulation results validate the merits of the proposed converter.

Data Availability

The data used to support the findings of this study are included in the article. However, the reader may contact the corresponding author for more details on the data.

Conflicts of Interest

The authors declare that there are no conflicts of interest regarding the publication of this paper.

Acknowledgments

The authors thank Vellore Institute of Technology, Chennai, for the technical assistance. The authors appreciate the supports from Ambo University, Ethiopia.

References

[1] E. Babaei, H. Mashinchi, M. Sabahi, and S. H. Hosseini, "Extendable non-isolated high gain DC-DC converter based on active- passive inductor cells," *IEEE Transactions on Industrial Electronics*, vol. 65, no. 12, pp. 9478–9487, 2018.

[2] F. L. Tofoli, D. de Souza Oliveira, R. P. Torrico-Bascopé, and Y. J. A. Alcazar, "Novel nonisolated high-voltage gain DC–DC converters based on 3SSC and VMC," *IEEE Transactions on Power Electronics*, vol. 27, no. 9, pp. 3897–3907, 2012) Novel.

[3] Y. Sheng, T. Juu, and J. F. Chen, "Lung "Transformerless dc-dc converters with high step-up voltage gain," *IEEE Transactions on Industrial Electronics*, vol. 56, no. 8, pp. 3144–3152, 2009.

[4] M. A. Salvador, J. M. de Andrade, T. B. Lazzarin, and R. F. Coelho, "Nonisolated high-step-up dc-dc converter derived from switched-inductors and switched-capacitors," *IEEE Transactions on Industrial Electronics*, vol. 67, no. 10, pp. 8506–8516, 2020.

[5] A. M. S. S. Andrade, T. M. K. Faistel, A. Toebe, and R. A Guisso, "Family of transformerless active switched inductor and switched capacitor cuk DC–DC converter for high voltage gain applications," *IEEE Journal of Emerging and Selected Topics in Industrial Electronics*, vol. 2, no. 4, pp. 390–398, 2021.

[6] yu Tang, D. Fu, T. Wang, and Z. Xu, "Hybrid switched-inductor converters for high step-up conversion," *IEEE Transactions on Industrial Electronics*, vol. 62, no. 3, pp. 1480–1490, 2015.

[7] A. Andrade, T. Faistel, R. Guisso, and A. Toebe, "Hybrid high voltage gain transformerless DC–DC converter," *IEEE Transactions on Industrial Electronics*, vol. 69, no. 3, pp. 2470–2479.

[8] Z. Y. Chen, Z. D. Lu, Y. Chen, and Y. Wu, "Two-inductor high-voltage-gain converter with turn-off delay controlled current-sharing method," *Electronics Letters*, vol. 56, pp. 508–510, 2020.

[9] B. Axelrod, Y. Berkovich, and A Ioinovici, "Switched-capacitor/switched-inductor structures for getting transformerless hybrid DC–DC PWM converters," *IEEE Transactions on Circuits and Systems I: Regular Papers*, vol. 55, no. 2, pp. 687–696, 2008.

[10] H. Gholizadeh, S. Aboufazeli, Z. Rafiee, E. Afjei, and M. Hamzeh, "A Non-isolated High Gain DC-DC Converters with Positive Output Voltage and Reduced Current Stresses," in *Proceedings of the 11th Power Electronics, Drive Systems, and Technologies Conference (PEDSTC)*, Tehran, Iran, February 2020.

[11] J. Melo de Andrade, M. A. Salvador, R. F. Coelho, and T. B. Lazzarin, "General method for synthesizing high gain step-up DC–DC converters based on differential connections," in *Proceedings of the IEEE Transactions on Power Electronics*, vol. 35, no. 12, December 2020.

[12] M. Das and V. Agarwal, "Generalized Small Signal Modeling of Coupled-Inductor-Based High-Gain High-Efficiency DC–DC Converters," in *Proceedings of the IEEE Transactions on Industry Applications*, June 2017.

[13] S. S. Sayed, ElM. Mena, M. Elmenshawy, L. Ben-Brahim, and M. Ahmed, "Design and Analysis of High-Gain Medium-Voltage DC-DC Converters for High-Power PV Applications," in *Proceedings of the 2018 IEEE 12th International Conference on Compatibility, Power Electronics and Power Engineering (CPE-POWERENG 2018)*.

[14] P. Asha, L. Natrayan, B. T. Geetha et al., "IoT enabled environmental toxicology for air pollution monitoring using AI techniques," *Environmental research*, vol. 205, Article ID 112574, 2022.

[15] G. Kanimozhi, O. V. Gnana Swathika, K. Logavani, and A. Ambikapathy, "High gain DC-DC converter with extendable APIC's," *Materials Today Proceedings*, 2020.

[16] S. Mahajan, S. Padmanaban, and J. K. Pedersen, "Jens Bo Holm-Nielsen, Zbigniew Leonowicz," XL Converters- New Series of High Gain DC-DC Converters for Renewable Energy Conversion"" in *Proceedings of the IEEE International Conference on Environment and Electrical Engineering*, Genova, Italy, June 2019.

[17] S. Hossein Hosseini, R. Ghazi, S. Farzamkia, and M. Bahari, "A Novel High Gain Extendable DC-DC Bidirectional Boost-

Buck Converter," in *Proceedings of the 11th Power Electronics, Drive Systems, and Technologies Conference*, Tehran, Iran, February 2020.

[18] M. SundaramK, P. Prakash, S. Angalaeswari, T. Deepa, L. Natrayan, and P. Paramasivam, "Influence of process parameter on carbon nanotube field effect transistor using response surface methodology," *Journal of Nanomaterials*, vol. 2021, p. 1, 2021 7739359.

[19] J. Ahmad, M. Zaid, A. Sarwar et al., "A new high-gain DC-DC converter with continuous input current for DC microgrid applications," *Energies*, vol. 14, no. 9, p. 2629.

[20] G. Kanimozhi, C. Umayal, and S. Dhanasekar, "FPGA based Hybrid Resonant Switching DC/DC converter for Electric Vehicles," *International Journal of Innovative Technology and Exploring Engineering (IJITEE) ISSN: 2278-3075*, vol. 89 pages, July 2019.

[21] H. Ardi, A. Ajami, and M. Sabahi, "A novel high step-up dc-dc converter with continuous input current integrating coupled inductor for renewable energy applications," *IEEE Transactions on Industrial Electronics*, In press, 2017.

[22] M. Forouzesh, Y. Shen, K. Yari, Y. P. Siwakoti, and F. Blaabjerg, "High-efficiency high step-up dc-dc converter with dual coupled inductors for grid-connected photovoltaic Systems," *IEEE Transactions on Industrial Electronics*, In press, 2017.

[23] Y. P. Siwkoti, F. Blaabjerg, and P. C. Loh, "High step-up trans inverse dc-dc converter for the distributed generation system," *IEEE Transactions on Industrial Electronics*, vol. 63, no. 7, pp. 316–322, 2016.

[24] H. Wu, K. Sun, L. Chen, L. Zhu, and Y. Xing, "High step-up/stepdown soft-switching bidirectional dc-dc converter with coupled inductor and voltage matching control for energy storage systems," *IEEE Transactions on Industrial Electronics*, vol. 63, no. 5, pp. 2892–2903.

[25] D. K. Jain, S. K. S. Tyagi, S. Neelakandan, M. Prakash, and L. Natrayan, "Metaheuristic optimization-based resource allocation technique for cybertwin-driven 6G on IoE environment," *IEEE Transactions on Industrial Informatics*, vol. 18, no. 7, pp. 4884–4892, 2022.

Hindawi
Mathematical Problems in Engineering
Volume 2022, Article ID 4651084, 6 pages
https://doi.org/10.1155/2022/4651084

Research Article

Mathematical Modeling of Real-Time Systems Using Heun and Piecewise Methods

Urfa Malik Gul,[1] Anand Paul,[1] and K.-W.-A. Chee[2,3]

[1]*The School of Computer Science and Engineering, Kyungpook National University, Daegu, Republic of Korea*
[2]*School of Electronic and Electrical Engineering, Kyungpook National University, Daegu 41566, Republic of Korea*
[3]*School of Electronics Engineering, College of IT Engineering, Kyungpook National University, Daegu 41566, Republic of Korea*

Correspondence should be addressed to K.-W.-A. Chee; kwac2@cantab.net

Received 28 January 2022; Revised 8 March 2022; Accepted 15 June 2022; Published 21 August 2022

Academic Editor: Ravi Samikannu

It is often said that mathematical modeling is an implementation of mathematics in real-world problems with the aim of better understanding them, so we can say that mathematical modeling is linked to the solution of problems. Some of the essential principles and procedures of mathematical modeling are discussed using formulas and equations. We investigate the stability and convergence characteristics and demonstrate the suitability of different mathematical methods in a set of numerical examples. The described methods in our paper are the best choices for the simulation of linear phenomena and are more efficient for use with high-order spatial discretization. We emphasized the importance of mathematical modeling technologies used in computational tools. Our study shows that these new methods are more stable with lower errors.

1. Introduction

Various numerical methods are used to obtain the initial value solution, and studies show great development on this topic in this century. Other factors also amount to the reason for the implementation of mathematical methods like electronic computers needing efficient numerical algorithms in mathematical modeling. Many complex methods that are driven by partial differential equations (PDE) evolve [1–3], which requires the search for the appropriate numerical solution to a system of ordinary differential equations (ODEs) in a wide range of situations [4–6]. The differential equations contain derivatives, either ordinary or partial derivatives, and along with an initial condition that determines the value of the unknown function at a certain point, make up the initial value problem (IVP). These equations are also used in semiconductor engineering, biology, chemistry, physics, and economics to solve various problems in research. There are several analytical approaches for determining the solution of differential equations [7, 8]. On the other hand, analytical methods cannot always solve complex differential equations. Therefore, it is important to make numerical approximations.

The advanced differential equation is solved by using numerical techniques for which computer programming is a very powerful tool. The well-known Runge–Kutta (RK) analysis is the most often used technique for integrating these technologies of ODEs in real time [7–10]. RK methods can be classified in a variety of ways, such as the structure of implicit or explicit, by convergence order, or the number of steps [1]. The complexity of the equation that must be solved determines the numerical stability of various numerical methods.

Figure 1 summarizes the flow of ordinary equations used to model real-time systems and the application of analytical and numerical methods to solve these equations. An example here is encapsulating the physical characteristics of a parachutist descending, where g is gravitational constant, m is mass, c is drag coefficient, and $\mathrm{d}v/\mathrm{d}t$ is an unknown function/differential equation (rate equation).

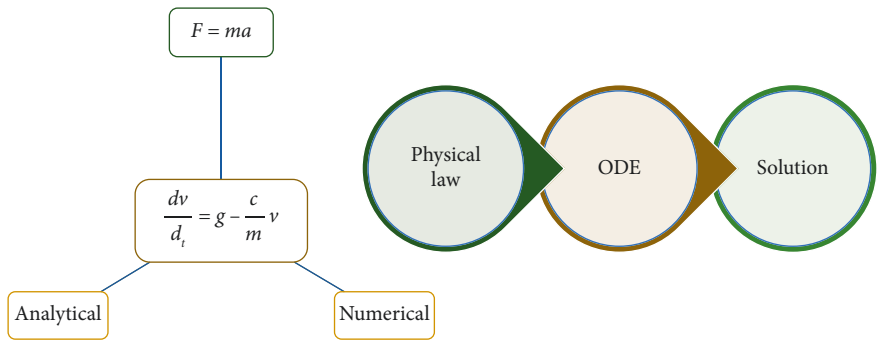

Figure 1: The summary of steps in the application of ODEs to engineering problem solving, such as a parachutist descending.

In the RK family, the most well-known member is the classic Runge–Kutta method (RK4), and (1) presents the initial problem as follows:

$$\frac{\mathrm{d}y}{\mathrm{d}t} = f(t, y), y(t_0) = y_0. \tag{1}$$

In the above equation (1), y can be a scalar or vector function that is not known at time t that we want to estimate. $\mathrm{d}y/\mathrm{d}t$ is the time rate at which y changes and t_0 is the initial time; hence, the corresponding y value is y_0.

$$\begin{aligned} y_{n+1} &= y_n + \frac{1}{2}h(k_1 + 2k_2), \\ t_{n+1} &= t_n + h, \\ k_1 &= f(t_n, y_n), \\ k_2 &= f\left(t_n + \frac{h}{2}, y_n + h\frac{k_1}{2}\right), \\ k_2 &= f(t_n + h, y_n + hk_1). \end{aligned} \tag{2}$$

The k_1 and k_2 are known as stages of the RK method which are shown in (2) and (3). They relate to various estimations of solutions for the slope. We note here that $y_n + hk_1$ is the Euler step from (t_n, y_n) with stepsize h. Now, the following equation shows an explicit second-order RK method by supposing

$$\begin{aligned} y(t+h) &= y(t) + h\left[b_1\tilde{k} + b_2\tilde{k}_2\right] + O\left(h^3\right), \\ \tilde{k}_1 &= f(t, y), \\ \tilde{k}_2 &= f\left(t + c_2h, y + ha_{21}\tilde{k}_1\right). \end{aligned} \tag{3}$$

Therefore, the second-order RK supposition becomes

$$\begin{aligned} f\left(t + c_2h, y + ha_{21}\tilde{k}_1\right) &= f(t, y)c_2hf_t(t, y) + ha_{21}f_y(t, y)\tilde{k}_1 + O\left(h^2\right), \\ &\cdot f(t, y)c_2hf_t(t, y) + ha_{21}f_y(t, y)\tilde{k}_1 f(t, y) + O\left(h^2\right), \\ y(t+h) &= y(t) + h\left[b_1 f(t, y) + b_2\left\{f_t\left(t, y\right) + c_2hf_t(t, y)ha_{21}f_y\left(t, y\right)f(t, y)\right\}\right] + O\left(h^3\right), \\ &\cdot y(t) + (b_1 + b_2)hf\left(t, y\right) + b_2h^2\left[c_2hf_t(t, y) + a_{21}f_y\left(t, y\right)f(t, y)\right] + O\left(h^3\right). \end{aligned} \tag{4}$$

Therefore, for four unknowns, we have three nonlinear equations which lead to Euler's method (first-order method). Euler's method is commonly used to build more complicated approaches like the predictor/corrector method and is sometimes also called the midpoint rule as follows:

$$\begin{aligned} y_{n+1} &= y_n + hk_2, \\ k_1 &= f(t_n, y_n), \\ k_2 &= f\left(t_n + \frac{h}{2}, y_n + \frac{h}{2}k_1\right). \end{aligned} \tag{5}$$

As we know, the RK methods are a set of implicit and explicit optimization methods in numerical analysis, including the well-known Euler's method, which is usually used in temporal discretization for approximate solutions of ODEs [1, 11]. Here, the differential equation is considered as a formula that can be used to compute the slope of the tangent line to the curve at any point once we determined the location of that point. The solution to the ODE at a time t_n: $y_n \approx y(t_n)$ is approximated by the value of y_n. The explicit Euler's method shows that the solution y_{n+1} is an explicit function of y_i for $i \leq n$. We must mention here that there is no assurance about any curves' concavity that will

remain consistent. It may shift from concave-up to concave-down. Because the real solution curve goes up and down, there is no approximate way to estimate whether our next point will be an over- or underestimate. To overcome this deficiency, we have a clever Heun's method to use.

2. Heun's Method

Heun's method is the improved (or modified) Euler method and the second order of the RK method. The modified Euler method allows us to find a clear expression for y given a finite number of elementary functions, x. It is possible to solve the ODE for y and x given their initial values.

The Euler's method algorithm is as follows:

(1) Start
(2) Define function
(3) Determine $x0$, $y0$, h, and xn (here $x0$ and $y0$ are initial conditions while h is interval and xn is required value)
(4) $n = (xn - x0/h + 1)$
(5) From $i = 1$ ton start looping
(6) $y = y0 + h \times f\,(x0,\ y0)$, $x = x + h$
(7) Print the $y0$ and $x0$ values
(8) If $x < xn$, assign $x0 = x$ and $y0 = y$
If no, go to 9
(9) Loop i end
(10) Stop

We can use the algorithm and flowchart in a high-level programming language to construct a program for Euler's method though this approach is not one of the best techniques to solve ODEs.

Heun's formula is used to solve the ODE which is given in the initial state [10, 12]. Euler's method is the foundation of Heun's method. As we discussed earlier, Euler's method fails to converge in the case of a concave-up curve because it overestimates the next point. Heun's method solves this solution problem by taking two tangents on each side of the curve. One tangent underestimates and the other overestimates, and then, Heun's method estimates the next point from both tangents using Euler's method. Using (6), we can determine the numerical solution to the problem of initial values using the following method:

$$\begin{aligned} y_{(i+1)} &= y_i + \frac{(k_1 + k_2)(h)}{2}, \\ k_1 &= f(x_i, y_i), \\ k_2 &= f(x_i + h, y_i + k_1 h). \end{aligned} \tag{6}$$

where k_1 and k_2 are under- and overestimates. The step size is denoted by h, and initial conditions are x_i and y_i. The accuracy of Euler's method improves linearly as step size decreases but the accuracy of Heun's method improves quadratically [10, 12–15].

3. Derivations

While using the elementary idea that the line's slope equals its rise over run, the parameters at the endpoint can be calculated using the following symbolic development:

$$\begin{aligned} \text{slope}_{\text{left}} &= f(x_i, y_i), \\ \text{slope}_{\text{right}} &= f(x_i + h, y_i + hf(x_i, y_i)), \\ \text{slope}_{\text{ideal}} &= \frac{\Delta y}{h}, \\ \text{slope}_{\text{ideal}} &= \frac{1}{2}\left(\text{slope}_{\text{left}} + \text{slope}_{\text{right}}\right), \\ \Delta y &= h\left(\text{slope}_{\text{ideal}}\right), \\ x_{i+1} &= x_i + h,\ y_{i+1} = y_i + \Delta y, \\ y_{i+1} &= y_i + h\text{slope}_{\text{ideal}}, \\ y_{i+1} &= y_i + \frac{1}{2h}\left(\text{slope}_{\text{left}} + \text{slope}_{\text{right}}\right), \\ y_{i+1} &= y_i + \frac{h}{2}\left(f(x_i, y_i) + f(x_i + h, y_i + hf(x_i, y_i))\right). \end{aligned} \tag{7}$$

Using Euler's method, the next point in the numerical solution is estimated roughly, and the initial estimation could be predicted or corrected using this information. Therefore, we can calculate the slope of the prediction line by taking the average of the slopes of the left and right tangent lines, at either end of the interval. The values of the $f\ (x, y)$ on the right-hand side of Equation (7) can be determined [16]. Following a rough estimate of the location of the next solution point from Euler's method, the coordinates may be used to determine the slope of the tangent line at the right end of the interval.

3.1. Modified Algorithm. The initial or boundary conditions must be given for both the algorithm and the flowchart, as follows:

(1) Start
(2) Define function for slope calculation $f\,(x, y)$
(3) State variables
(4) Input value
(5) Find slope while using initial value
(6) Find new y, $y = y0 + m0 \times h$
(7) Increase value of x, which is $x1 = x0 + h$
(8) Find new slope using $x1$ and y
(9) Calculate the mean of $m0$ and m
10) (Find y new and assign y new with y again
(11) From step 6, repeat until two consecutive y are equal
(12) Repeat step 5 until $x = xn$
(13) Print x and y corresponding
(14) Stop

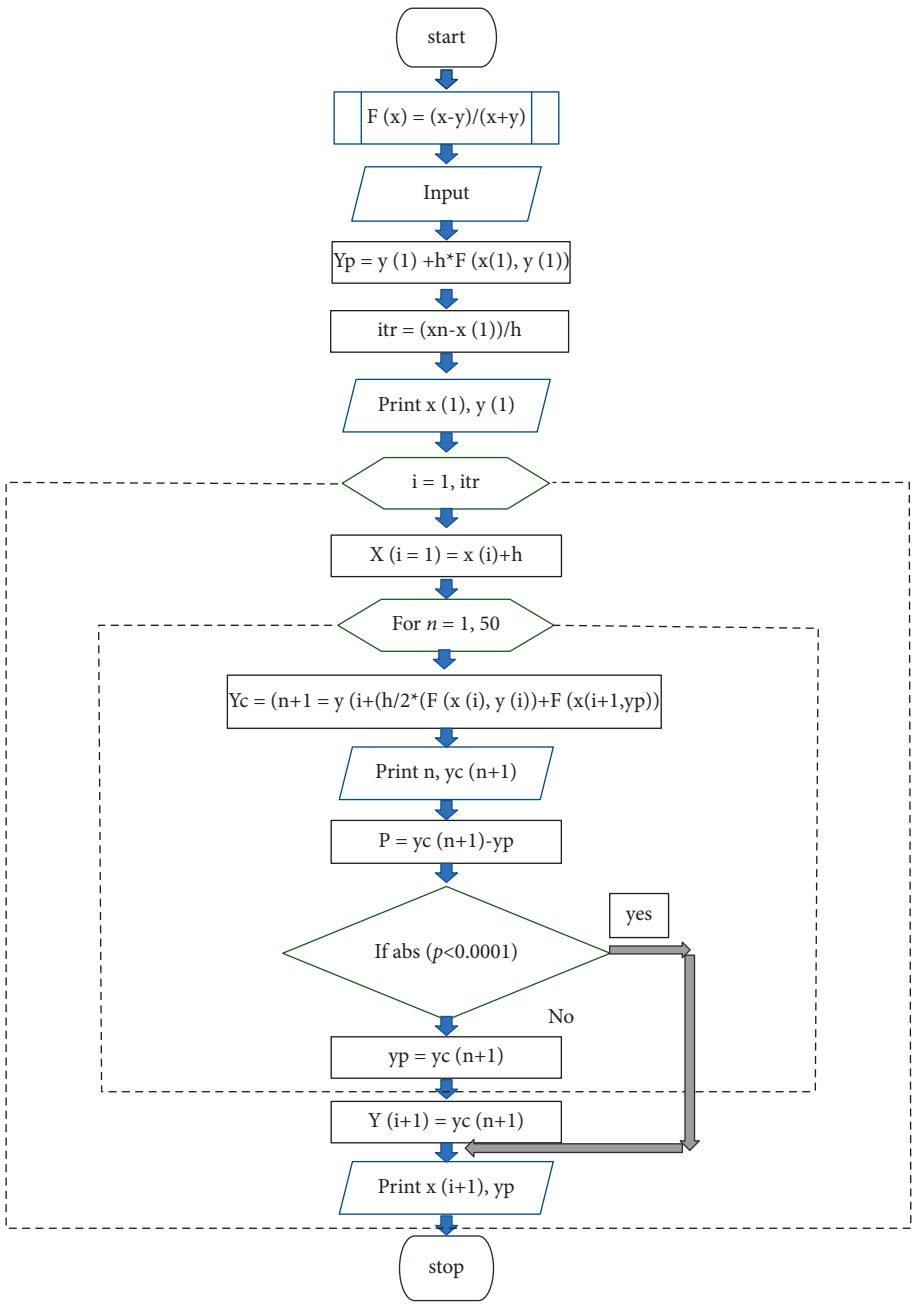

Figure 2: Modified Euler's method flowchart.

3.2. Flowchart. The numerical solution of ODEs with Heun's method is simple from both the numerical and programming points of view as compared to analytical techniques. The updated Euler's method algorithm and flowchart are described in Figure 2. They may be used to produce source code in any high-level programming language.

In the case of complex problems, analytical methods frequently fail; however, Heun's method does not fail but provides better solution accuracy and high speed. It also improves Euler's technique with a lengthy code where we can pick a lower number of h to get high accuracy.

4. Piecewise Method

Nonlinear programming is used to solve a variety of optimization issues in science and technology. Piecewise linearization methods are used in recent years to turn nonlinear programming into linear programming or a mixed convex programming problem to get the desired solution [16–19]. The piecewise function is a hybrid function that is defined by numerous subfunctions and each corresponding to a different interval of the main function domain or a subdomain. Piecewise can describe the nature of the function rather than

just be a way of expressing it. In addition, the term piecewise can also refer to any piecewise-defined function that applies to each piece but may not be applicable for the whole function. The piecewise or continuous differentiable behavior of a function is that each piece is differentiable within its domain, regardless of whether the whole function is differentiable at the intersection. When functions are analyzed convexly, the notation of a derivative can be replaced by that of the subderivative [17]. A function can indeed be described as "piecewise linear" or "piecewise continuous" or "piecewise differentiable" even if the pieces are not intervals. Equation (8) shows a piecewise notation that expresses the absolute value function as follows:

$$|x| = \begin{cases} -x, & if\, x < 0, \\ +x, & if\, x \geq 0. \end{cases} \tag{8}$$

To turn negative values into positive, the first function -x is used for all x values, and this invalidates the sign of the input value. The second function x is applied for all x values which could be larger than or equal to zero.

4.1. Linear Piecewise. The piecewise linear function is a collection of quadratic functions, each defined on a set of intervals of real numbers. A finite collection of such intervals must exist if the domain of the function will either need to be finite or be locally finite [20–23].

There are several contexts in which piecewise linear functions are relevant. In general, the piecewise linear function can be defined on any vector space or affine space and simplicial complexes [18, 19, 24]. A linear function is not simply a linear transformation, but in these contexts, it is an affine linear function. There are two major subclasses of a piecewise linear function, called continuous and convex. As we can see from (9), every n-dimensional continuous function, in general, will have the following formulas:

$$\begin{aligned} &\%\Pi \int P\left(P\left(\mathbb{R}^{n+1}\right)\right), \\ fl_x = &\min_{\sum \int \%\Pi\ (a,b)} \max_{\int \%\Sigma} \vec{a} \cdot \vec{x} + b, \\ &\Sigma \int P\left(\mathbb{R}^{n+1}\right), \\ &f(\vec{x}) = \max \vec{a} \cdot \vec{x} + b \\ &(\vec{a}, b) \int \%\Sigma \end{aligned} \tag{9}$$

5. Conclusion

We provided a class of numerical approaches for approximating the solutions of differential equations in this study which are based on a modified version. When applied to ODEs, these approaches yield a continuous approximate solution that is accurate to order $2n$ at the nodes and to order $n+1$ evenly over the interval. To extend the approaches to delay differential equations, some a posteriori tweaks boost the uniform accuracy to order $2n$. Real-world issues are subjected to numerical testing and compared with other methodologies. Four methods have been presented for linear system integration of ODEs, and those methods require less memory and less computational effort than the low storage methods. The notations and formulations have been studied in such a way that subsequent development of the theory of differential equations will follow the structure of ODEs. We also presented that when a nonstandard piecewise function is used correctly, it produces fractional-order differential equations that converge to the original equation as the parameter leads to zero. Even though it was not developed from quadrature, the method has been demonstrated to be equivalent to quadrated-based methods. Nonuniform time steps can be used to accomplish the approach. The difference equation may appropriately describe the dynamics of the underlying fractional differential equation, as demonstrated in the formulas.

Data Availability

Data will be shared on request.

Conflicts of Interest

The authors declare that they have no conflicts of interest.

Acknowledgments

This research was carried out with the support of the Dongil Cultural Scholarship Foundation for academic research in 2022, the Kyungpook National University Research Fund, 2021, the Kyungpook National University Excellent New Research Fund, and the Brain Korea (BK) 21 four project funded by the Ministry of Korea (4199990113966) and the National Research Foundation of Korea.

References

[1] J. A. D. Sandretto and A. Chapoutot, "Validated explicit and implicit Runge-Kutta methods. Reliable computing electronic edition," 2016, https://hal.archives-ouvertes.fr/hal-01243053/.

[2] N. C. Nguyen, ""A multiscale reduced-basis method for parametrized elliptic partial differential equations with multiple scales"," *Journal of Computational Physics*, vol. 227, no. 23, pp. 9807–9822, 2008.

[3] P. Colella, J. Bell, N. Keen, T. Ligocki, M. Lijewski, and B. V. Straalen, "Performance and scaling of locally-structured grid methods for partial differential equations," *J. Phys. Conf. Ser.*,vol. 78, no. 1, Article ID 012013, 2007.

[4] A. Slavík, "Dynamic equations on time scales and generalized ordinary differential equations," *Journal of Mathematical Analysis and Applications*, vol. 385, no. 1, pp. 534–550, 2012.

[5] O. Guner and A. Bekir, "A novel method for nonlinear fractional differential equations using symbolic computation," *Waves in Random and Complex Media*, vol. 27, no. 1, pp. 1–8, 2016.

[6] M. Rodríguez, F. Blesa, and R. Barrio, "OpenCL parallel integration of ordinary differential equations: applications in computational dynamics," *Computer Physics Communications*, vol. 192,pp. 228–236, Jul, 2015.

[7] H. Cao, L. Kang, Y. Chen, and J. Yu, "Evolutionary modeling of systems of ordinary differential equations with genetic programming," *Genetic Programming and Evolvable Machines*, vol. 1, no. 4, pp. 309–337, 2000.

[8] P. E. Kloeden and E. Platen, "Time discrete approximation of deterministic differential equations," *Numerical Solution of Stochastic Differential Equations*, pp. 277–303, 1992.

[9] H. Zhang, J. Yan, X. Qian, and S. Song, "Numerical analysis and applications of explicit high order maximum principle preserving integrating factor Runge-Kutta schemes for Allen-Cahn equation," *Applied Numerical Mathematics*, vol. 161, pp. 372–390, Mar. 2021.

[10] M. Molavi-Arabshahi and O. Nikan, "Solving some ordinary differential equations in mechanical engineering using Runge Kutta and Heun's methods," *Proc. 2nd Int. Conf. Comb. Cryptogr. Comput.*,vol. 7, no. 1, 2006.

[11] N. Ahmady, T. Allahviranloo, and E. Ahmady, "A modified Euler method for solving fuzzy differential equations under generalized differentiability," *Computational and Applied Mathematics*, vol. 39, no. 2, pp. 104–121, May 2020.

[12] W. Lay, S. Y. Slavyanov, T. Wiseman, W. Lay, and S. Y. Slavyanov, "The central two-point connection problem for the Heun class of ODEs," *Journal of Physics A: Mathematical and General*, vol. 31, no. 18, pp. 4249–4261, 1998.

[13] M. Hortaçsu, "Heun functions and some of their applications in physics," *Advances in High Energy Physics*, vol. 2018, Article ID 8621573, 14 pages, 2018.

[14] P. P. Fiziev, "The Heun functions as a modern powerful tool for research in different scientific domains," 2015, https://arxiv.org/abs/1512.04025v1.

[15] O. V. Motygin, "On numerical evaluation of the Heun functions," *2015 Days on Diffraction (DD)*, vol. 2015, Article ID 7354864, 227 pages, 2015.

[16] P. P. Fiziev, H. Zhong, M. T. Batchelor, and P. P. Fiziev, "Novel relations and new properties of confluent Heun's functions and their derivatives of arbitrary order," *Journal of Physics A: Mathematical and Theoretical*, vol. 43, no. 3, Article ID 035203, 2009.

[17] A. Magnani and S. P. Boyd, "Convex piecewise-linear fitting," *Optimization and Engineering*, vol. 10, no. 1, pp. 1–17, 2008.

[18] J. Pittman and C. A. Murthy, "Fitting optimal piecewise linear functions using genetic algorithms," *IEEE Transactions on Pattern Analysis and Machine Intelligence*, vol. 22, no. 7, pp. 701–718, 2000.

[19] M. H. Lin, J. G. Carlsson, D. Ge, J. Shi, and J. F. Tsai, "A review of piecewise linearization methods," *Mathematical Problems in Engineering*, vol. 2013, Article ID 101376, 8 pages, 2013.

[20] A. Atangana and S. İğret Araz, "New concept in calculus: piecewise differential and integral operators," *Chaos, Solitons & Fractals*, vol. 145, Article ID 110638, 2021.

[21] A. Rantzer and M. Johansson, "Piecewise linear quadratic optimal control," *IEEE Transactions on Automatic Control*, vol. 45, no. 4, pp. 629–637, 2000.

[22] R. Ambrosino, E. Garone, M. Ariola, and F. Amato, "Piecewise quadratic functions for finite-time stability analysis," in *Proceedings of the 2012 IEEE 51st IEEE Conference on Decision and Control (CDC)*, pp. 6535–6540, Maui, HI, USA, December 2012.

[23] J. Puerto, A. M. Rodríguez-Chía, and A. Tamir, "On the planar piecewise quadratic 1-center problem," *Algorithmica*, vol. 57, no. 2, pp. 252–283, 2008.

[24] L. Rodrigues, J. P. How, and L. Rodrigues, "Observer-based control of piecewise-affine systems," *International Journal of Control*, vol. 76, no. 5, pp. 459–477, 2003.

Hindawi
Mathematical Problems in Engineering
Volume 2022, Article ID 4418329, 12 pages
https://doi.org/10.1155/2022/4418329

Research Article

Optimization and Design of a Sustainable Industrial Grid System

Samat Iderus,[1] **Geno Peter**,[1] **K. Praghash**,[2] **and Aruna Rai Vadde**[3]

[1]*CRISD, School of Engineering and Technology, University of Technology Sarawak, Sarawak, Malaysia*
[2]*Department of Electronics and Communication Engineering, Christ University, Bengaluru, India*
[3]*Department of Electrical and Computer Engineering, Debre Tabor University, Debra Tabor, Ethiopia*

Correspondence should be addressed to Aruna Rai Vadde; dr.rai@dtu.edu.et

Received 2 February 2022; Accepted 30 May 2022; Published 8 July 2022

Academic Editor: Ravi Samikannu

Electricity is a multifaceted form of energy and is used globally, with a continuously growing demand. Electrical power grids are there for more than 150 years. The generated electrical power is delivered to different industrial, commercial, and residential sectors, thereby fulfilling the ever-growing demand. In this research paper, the design and optimization of an industrial grid for various electrical loads is discussed. The electrical grid ensures a stable power supply to the loads by providing quality power with the minimum total harmonic distortion (THD) possible. A complete study of the short circuit current has been done in two different electrical grid systems, as it is seen that the short circuit current depends on the impedance of the transformer which feeds the load. These two designs of a single diagram will be simulated by using a power system analyzer, the Electrical Transient Analyzer Program (ETAP) software. The different electrical parameters, like choosing the optimised rated generator, cables, and transformers, are done. Load flow analysis is performed on both the design to evaluate the THD, short circuit fault, as well as to choose the right protection circuit for the system.

1. Introduction

Energy use in industrial plants has long been a significant financial consideration. Due to price fluctuation related to utility deregulation and system stability, energy cost control is critical to profitability. There are plentiful opportunities to expand power usage, reliability, and quality in an industrial environment. The power system plays a vital role in a process plant. A plant's operations and production depend on a safe and reliable power system. Each plant power system design, whether new or an expansion to an existing system, must be analysed to ensure that it is safe, is reliable, meets the present objective, and permits expansion for future needs [1]. At the planning and design stage of an industrial power system, the following considerations must be made: the electrical system must be designed cost-effectively for continuous and reliable service, people and equipment safety, ease of maintenance and operation, minimal power losses, mechanical equipment protection, interchangeability, and load addition [2, 3]. A major study based on many theories and actual experiences would be required to accomplish the above goals and obtain the expected results. Loads are constantly being eliminated in modest increments in many process facilities. The net effort is also not visible until a component of the system is overloaded or has other issues. Many times, circuits are added without the required reforms to the upstream circuit breakers' usual settings. The one-line diagram serves as a road map for optimal equipment design, redundancy, and protection. The goal of this study is to come up with solutions for categorising electrical loads in the energy industry and providing stable electricity to these loads using ETAP. The aforementioned study is to come up with answers on how diverse electrical loads should be classified in the energy business as well as how to supply these loads with reliable power sources. In addition, the critical role of the transformers' short-circuit impedance in regulating the short-circuit current will be addressed. The techniques for selecting electrical equipment and accessories, such as cables, transformers, and circuit breakers, are also provided. Basic design and detailed design are the two significant stages of the analysis. The location and process of the refinery are investigated in the basic design stage, and a preliminary estimate of the types of load and demand is obtained as a result. The best option is chosen for the next stage, and basic calculations, drawings, and specifications are

Table 1: Summary of the voltage drop from IEE Wiring Regulation.

Voltage drop points	Lighting (%)	Other uses (%)
1. Public low voltage distribution system supplying LV load	3	5
2. Private low voltage distribution system supplying LV load	6	8

Table 2: Percentage of allowable voltage drop by IEC 60364 : 2001.

Voltage drop points	Lighting (%)	Other uses (%)
1. Public low voltage distribution system supplying LV distribution systems	3	5
2. Private low voltage distribution system supplying LV distribution systems	6	8

*When the main wiring systems of the installation are longer than 100 m, these voltage drops may be increased by 0.005% per meter of wiring system beyond 100 m, without this supplement being greater than 0.5%.

produced as a result. We expect to publish detailed drawings in the detailed design, which will reflect our preference for enhanced power distribution with minimal power losses. As a result, all engineering-related details should be accomplished in this step. It is essential to recognize that all of the detailed documentation must meet the specifications.

2. Literature Review

2.1. Voltage Drop. Voltage drops on an electrical power distribution system are mainly caused by cables, transformers, and motors. Voltage drop describes how the supplied energy of a voltage source is reduced as electric current moves through the passive elements (elements that do not supply voltage) of an electrical circuit. Voltage drop happens when load current (I_b) flows through a conductor or transformer having a finite impedance. Severe voltage drops will result in motor failures, dimming of lamps, and CPU shutdown [4]. Voltage drop calculation is important to the system for maintaining the nominal voltage at service sides. Tables 1 and 2 depict the summary of the voltage drop from the IEE Wiring Regulation (BS7671 : 2008) and IEC60343 : 2001.

Voltage drop is determined from the current-using equipment, applying diversity factors where applicable, or from the value of the design current of the circuits.

The voltage drop can be determined by the following formula:

(i) Approximation method

$$\%V_d \approx \frac{\sqrt{3}|I_b| \times [R_L \times \cos\theta - X_L \times \sin\theta]}{V_S}, \quad (1)$$

where V_d is the voltage drop, V_s is the system voltage, R_L is the circuit resistance in Ohms, X_L is the circuit reactance in Ohms, I_b is the design current/line current, and θ is the phase angle of line current.

(ii) Tabulated method

$$V_{\text{drop}} = \frac{\text{tabulated}\,(\text{mV/A/m}) \times I_b \times l}{1000}\,\text{volts}, \quad (2)$$

where V_d is the voltage drop, mV/A/m is the tabulated cable value in milli volt per ampere per meter, I_b is the design current/line current, l is the length of the cable, large voltage drop can be caused by a variety of factors, including the following:

(i) Incorrect conductor size (undersized).

(ii) Incorrect conductor diameter and length.

(iii) Improper cable conducting material.

(iv) The actual load current exceeds the design circuit current.

2.2. Short Circuit Fault. A fault in an electrical power system is a failure which interferes with the normal flow of current. Faults occur when two or more conductors that normally operate with different potentials come into contact with each other. When fault occurs in a system, it induces a large current flow and this will cause damage to the equipment [5]. During fault occurrence in a network, it will have an effect on the generator due to the short circuit at the point of the generator. Short-circuit current exceeds locked-rotor current and can reach thousands of amperes [6]. The maximum short circuit current occurs at the time of fault occurrence only, which is when the system is at fault. Short-circuit current can also lead to arcing or flashing, which may cause severe damage to the power system. The severance effect of short circuit current is seen in a bolted fault more than in an arcing fault [7]. The short circuit current may be classified into "symmetrical" and "asymmetrical" terms, which are terms used to describe the symmetry of the short-circuit current waveform around the zero axis. A "fault" is another term for a short circuit. It is a particular type of current that injects a lot of energy into a power system. It can take the form of either heat or magnetic force. In essence, it is a low-resistance energy channel that bypasses part of a circuit and causes the bypassed circuit to stop operating. The reliability and safety of electric power distribution systems depend on accurate and thorough knowledge of short-circuit fault currents that can be present and on the ability of protective devices to satisfactorily interrupt these currents [8].

Figure 1 describes the typical short circuit current waveform. The symmetrical short circuit current contains only the pure alternating current component within its sinusoidal waveform [9]. It is applicable only to balanced three-phase power systems and can be calculated as the total line-to-neutral voltage over the total impedances of the power system. The reliability of power electronic converters

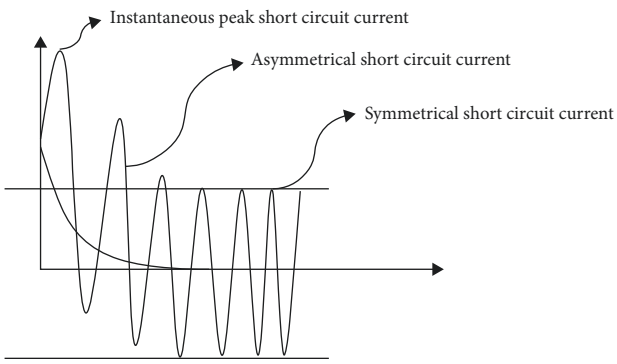

Figure 1: Short current waveform.

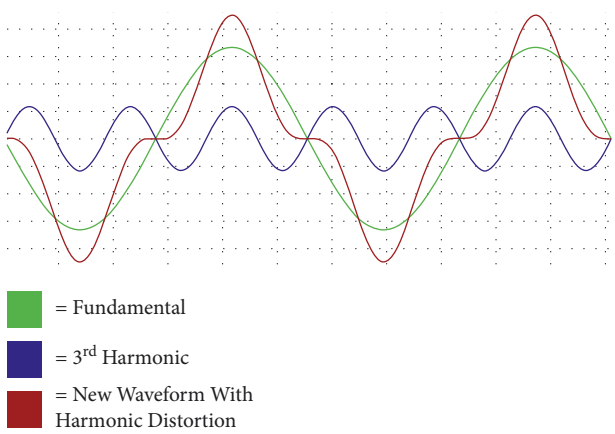

Figure 2: Harmonic distortion waveform.

used in a power system is very important for improving the overall power system design [10].

The asymmetrical short circuit current is the actual current that flows during a fault condition. It consists of direct current (DC) and alternating current (AC) components that contribute to a certain amount of "DC offset" in the waveform immediately after the initiation of the fault. The amount of "DC offset," or asymmetry, depends on the point where the fault occurs. The instantaneous peak short circuit current is the maximum peak instantaneous fault current on the asymmetrical short circuit current waveform [11].

2.3. Harmonics in Power System. A "sinusoidal component of a periodic wave or quantity with a frequency that is an integral multiple of the fundamental frequency" is how a harmonic is defined. As a result, harmonics can be defined as voltages and/or currents in an electrical system that are a multiple of the fundamental frequency as shown in Figure 2. The fifth (300 Hz), seventh (420 Hz), and eleventh harmonics are typical for a 60-Hz system (660 Hz) [12].

The direct outcome of harmonics might be power system problems such as communication disruptions, heating, and defects in the solid-state equipment. The following categorization and list of these problems are given with a short explanation or an approach to understand each of the reasons [13]. The most important issue related to power quality is harmonics [14]. The so-called "communication interference" can be caused by magnetic couplings between electric circuits and communications systems. The current flow of the power system results in the generation of a magnetic field, which induces a current in the surrounding communication connectors. The level of interference will depend on the magnetic coupling magnitude of the induced current, frequency, and efficiency [3, 7]. The other effects include the following:

(i) Induced line noise

(ii) Power line carrier system interference

(iii) Relay malfunction.

(iv) Solid-state Device Malfunctions

If the equipment is susceptible to null passages, harmonics may cause solid-state devices to fail. Resonance can cause zero crossings to occur more than once every half cycle in the current waveform [13]. This mode is usually exemplified by the diode. Since a device's operational parameters are usually defined in terms of user convenience root mean square (RMS), in the presence of harmonics, it may not function effectively since it senses a pinnacle value that does not directly match the RMS value of the wave shape [3, 4, 11]. Other defects in the stability system include the following.

(i) Mistakes in measuring equipment

(ii) Molestation in the operation of relays and breakers

(iii) Unstable interference with the engine controls of the zero voltage crossing

2.4. Previous Work. Arizaldi et al. [15] used ETAP software in conducting case studies for calculations of short circuit disturbances. The author of this paper attempts to determine the safety capacity that is capable of protecting the electrical system, and the same is functioning well in the electrical system of Lhokseumawe [15]. Riaz et al. [16] proposed a harmonic analysis in industry using a Fluke Energy Analyzer. The measured THD percent values for the voltage and current were utilised to model and analyse global harmonics in the Textile Plant's complete three-phase distribution system via simulation utilising ETAP software. Using the Fluke Energy Analyzer to take measurements, it was determined that the 5th and 7th harmonic orders are the most dominant in magnitude and are responsible for increased THD levels. ETAP utilised the Fluke Energy Analyzer results to perform a harmonic analysis of the entire plant. A resonance phenomenon was identified as a result of the conventional capacitor bank used to improve the power factor. Consequently, a single tuned filter was created, and the power factor improvement bank was replaced with a single tuned filter. The harmonic filter not only reduced the level of harmonic distortion but also improved the power factor [16]. ETAP software was used to analyse power system harmonics and discuss the full approach in detail by Azim Bhuiyan [17]. In order to inject harmonic current into the power network, a general load was simulated as a harmonic source. A harmonic load flow analysis was then performed to

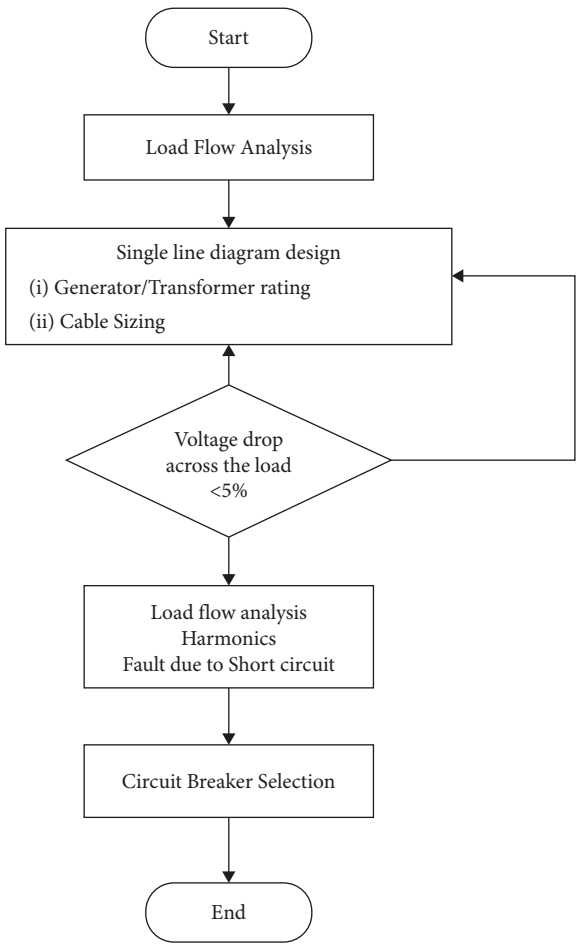

Figure 3: Flow chart of the research.

determine the impact of harmonic current, and harmonic distortion was detected [17].

3. Methodology

ETAP software is used in implementing the one-line diagram. Figure 3 describes the method used in completing the research. In this research, there are two designs for one-line diagrams proposed by using the ETAP software, which are Design A and Design B. Then, to meet the requirements of the design power system industry, analyse the technical report from ETAP software, which includes short circuit, THD, and voltage drop.

3.1. Load Analysis. Load analysis would be the first step before designing the whole distribution system. This is important in determining the incoming supply for each load and the total power that is needed for the whole system. From the analysis, two levels of incoming supply are needed for the loads, which are the 6.6 kV for process compressors A, B, and C and 415 V for the rest of the loads. The longer the transition detection time is, the more dangerous power electronic equipment operation is [18].

A feasibility study on the given industrial loads in Table 3 was performed in this power demand estimation. This study has focused on the proposal of divisions of the installation area/section, the total estimated power demand (P and Q for continuous, intermittent, and standby), and the overall power factor of the industrial installation. The estimated power demand is analysed into three categories:

(i) Operating load.

(ii) Peak load (C + I + S).

(iii) Design load (Peak load + 10% operating load).

Table 4 shows the total estimated power demand for different types of operating loads.

3.2. Cable Sizing. In designing the cable sizing of Design A and Design B, the cable sizing compiles or refers to the standards of BS 7671 : 2008, IEE Wiring Regulations 17th Edition, and IEC 60364 : 2001. In the ETAP software, the cable sizing follows the standard from the IEC. In order to select the cable size, the properties or steps are as follows:

(i) Based on the current, the size of the required cable is calculated.

(ii) Based on the Voltage drop, the size of the cable may increase.

(iii) Based on the short circuit current, the size of the cable may increase.

Both cable size and length have an impact on both current and voltage. Its impact on the voltage is much greater than that on the current. Various lengths of feeder cable were selected for this research in order to compare which design follows the limitation design from the theory. The various lengths of cable are investigated with the help of the ETAP software.

3.3. Transformer Sizing. A "transformer is the heart of an AC system." The transformer is the most important unit in an electrical distribution network. A transformer is a passive electrical device that transfers electrical energy from one electrical circuit to one or more other circuits. A transformer can be loaded up to 110% of the rated voltage, provided the cooling unit is healthy. There are many factors that need to be considered when choosing the right sizing of the transformer. The factors are as follows:

(1) Size of transformer to be powered.

(2) Machines and appliances to be installed.

(3) Location.

(4) Personnel capacity of building or structure.

The designs mostly follow the voltage distribution levels (33 kV, 22 kV, 6.6 kV, and 0.415 kV) and the classification of load types. Two designs are being prepared for comparison purposes. For the designs, the loading section will have the same topology and the only part that differs is the head (transformer and voltage distribution) for investigation purposes. Figures 4 and 5 show the one-line diagram for both designs. For this research, a standard frequency of 50 Hz was chosen, and the IEC standard is used in doing ETAP work.

Table 3: List of industrial loading.

Load description	Real power (P) KW	Reactive power (Q) KVAR	Power factor	Apparent power (S) KVA	Voltage (V)	Current (I) KA	Duty (%)	Estimate power demand (PD) KW
Split unit air conditional	50.00	30.99	0.85	58.82	415.00	0.08	100	50.00
General lighting distribution board (DB)	5.56	2.69	0.90	6.17	415.00	0.01	100	5.55
General power sockets	33.33	20.66	0.85	39.22	415.00	0.05	100	33.33
Fire water pump A	85.23	50.57	0.86	99.10	415.00	0.14	10	8.52
Fire water pump B	85.23	50.57	0.86	99.10	415.00	0.14	10	8.52
Fire water pump C	85.23	50.57	0.86	99.10	415.00	0.14	10	8.52
UPS system	88.89	55.09	0.85	104.58	415.00	0.15	100	88.88
Process compressor A	842.11	477.24	0.87	967.94	6600.00	0.08	100	842.10
Process compressor B	842.11	477.24	0.87	967.94	6600.00	0.08	10	84.21
Process compressor C	842.11	477.24	0.87	967.94	6600.00	0.08	100	842.10
Recirculation pump A	46.51	31.26	0.83	56.04	415.00	0.08	100	46.51
Recirculation pump B	46.51	31.26	0.83	56.04	415.00	0.08	10	4.65
Recirculation pump C	46.51	31.26	0.83	56.04	415.00	0.08	100	46.51
Conveyor motor A	33.33	25.00	0.80	41.67	415.00	0.06	100	33.33
Conveyor motor B	33.33	25.00	0.80	41.67	415.00	0.06	100	33.33
Conveyor motor C	33.33	25.00	0.80	41.67	415.00	0.06	100	33.33
Welding system A	13.64	6.60	0.90	15.15	415.00	0.02	50	6.82
Welding system B	13.64	6.60	0.90	15.15	415.00	0.02	50	6.82
Welding system C	13.64	6.60	0.90	15.15	415.00	0.02	50	6.82
HVAC	100.00	61.97	0.85	117.65	415.00	0.16	100	100.00
Lighting DB A	22.22	13.19	0.86	25.84	415.00	0.04	100	22.22
Lighting DB B	22.22	13.19	0.86	25.84	415.00	0.04	10	2.22
Lighting DB C	22.22	13.19	0.86	25.84	415.00	0.04	100	22.22
Lift	11.76	8.21	0.82	14.35	415.00	0.02	50	5.88
Total (P, Q, S, I & PD)	3418.65	1991.19		3957.99		1.72		2342.41

Table 4: Total analysed estimation power demand.

Types of load	Total power (kW)
i. Operating load	2166.12
ii. Peak load	2342.44
iii. Peak load + 10% of (i)	2559.06

4. Result and Analysis

Using ETAP the optimization analysis is done between the two simulated one-line diagram designed and the best out of it chosen. The analysis is based on the below mentioned:

(i) Design of one-line diagram
(ii) Voltage drop
(iii) Short circuit analysis
(iv) Harmonics

4.1. Design of One-Line Diagram (Design A and Design B). Figures 4 and 5 illustrates the one-line diagram for Design A and Design B, respectively. Figure 4 illustrates Design A; a 33 kV (100 MVAsc) of incoming power supply from the utility is stepped down to 6.6 kV by a 33 kV/6.6 kV (20 MVA) step down transformer. The voltage is then further stepped down to 415 V by a 6.6 kV/415 V (5 MVA) step down transformer. In Design B as shown in Figure 5, the incoming 33 kV of power supply is stepped down to 6.6 k by a 33 kV/6.6 kV (10 MVA) step down transformer at one end and is stepped down to 11 kV by a 33 kV/11 kV (4 MVA) transformer at the other end. A 11 kV/415 V (1 MVA) is used to reduce the voltage from 11 kV to 415 V. From incoming voltage for both designs, six groups of load are divided each consisting of the following loads:

(i) Process Compressor
(ii) Conveyer motor and lift
(iii) Welding system
(iv) Firewater pumps
(v) General lightings
(vi) Air conditioner, UPS, HVAC, and sockets

The comprehensive load modelling is performed in the ETAP based upon original system data. Different design between Design A and Design B are summarised as in Table 5 below.

In Design B, instead of using a single 33 kV/415 step down transformer, a 33 kV/11 kV step down transformer and a 11 kV/415 V transformer is used to step down the voltage from 33 kV to 415 V. It is not advisable to step down directly for following reasons. The transmission of electrical energy will experience losses if the system is directly stepped down from 33 kV to 415 V.

4.2. Voltage Drop Analysis (Design A and Design B). The ETAP software calculates the voltage drop for each bus as shown below in Figures 6 and 7. The voltage drop (V_d) is

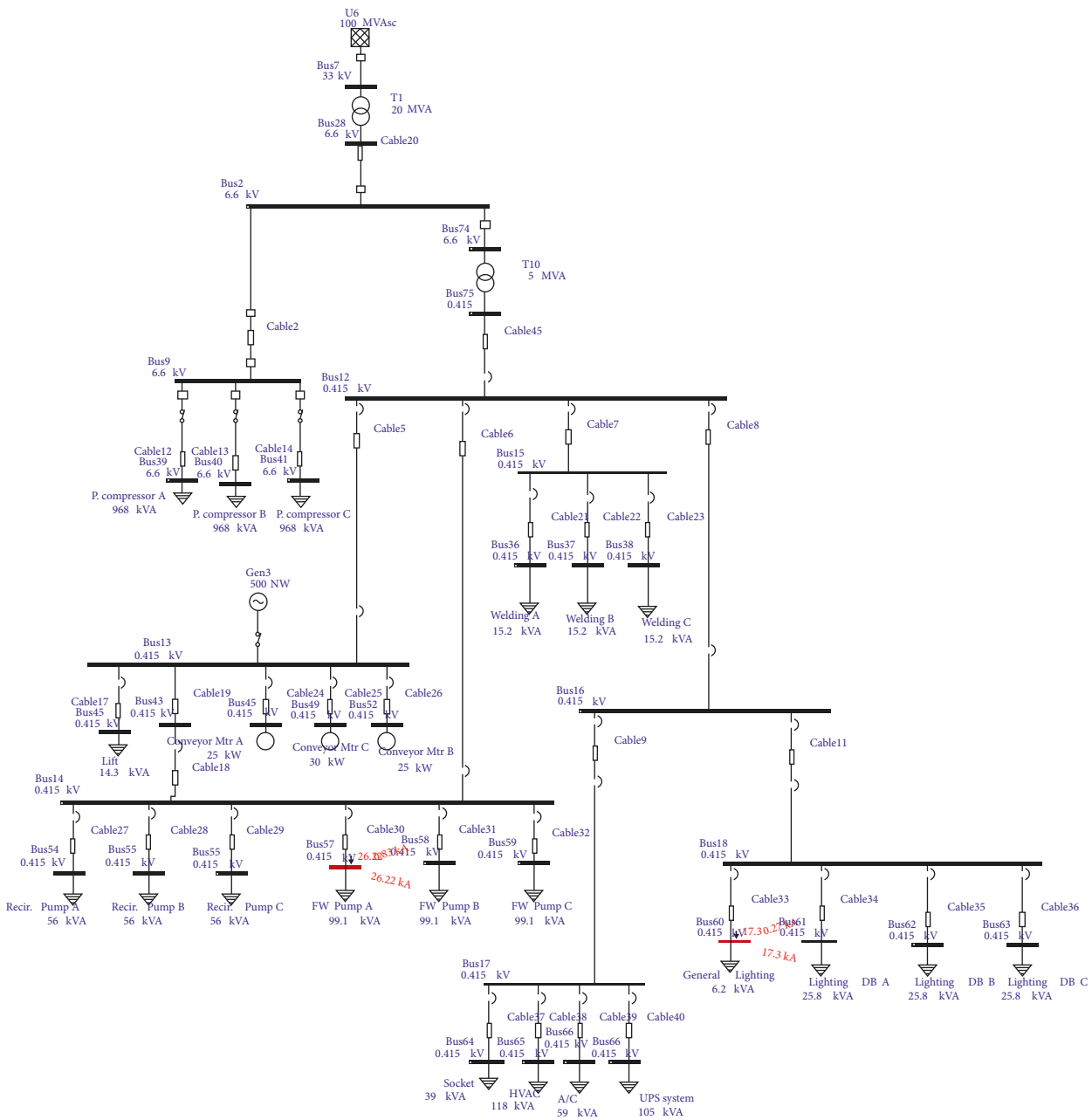

Figure 4: Single Line diagram-Design A.

measured after voltage has flowed through the bus line as well as the loading on the bus, such as transformer, cable, and other loads. Then the voltage loss is computed and displayed. According to the results achieved in Design A, the highest voltage drop is observed at cable 8 with a V_d value of 0.64 percent, while the lowest voltage drop is observed with a Vd value of 0 percent. Because the percentage of voltage drop is less than the allowable voltage drop, which is less than 5%, this design may be considered acceptable. In Design B, it demonstrates that the highest voltage drop is measured at transformer 10, which has a 0.34% V_d. The lowest voltage drop is measured to be 0.0%. The difference in reading the voltage drop is due to the distance between the cable and the impedance of the cable. Also, the voltage drop in the transformer is due to the sizing of the transformer. The arrangement of the transformer also plays a main role in the voltage drop. In Design B, the number of transformers used is three, and there is utilisation of the tap changer transformer. The purpose of the tap changer transformer is to supply a desired voltage to the load, to counter the voltage drops due to loads, and to counter the input supply voltage changes on load. The voltage control is done by changing the turn ratio. This is done by the provision of taps in the winding. Design B can

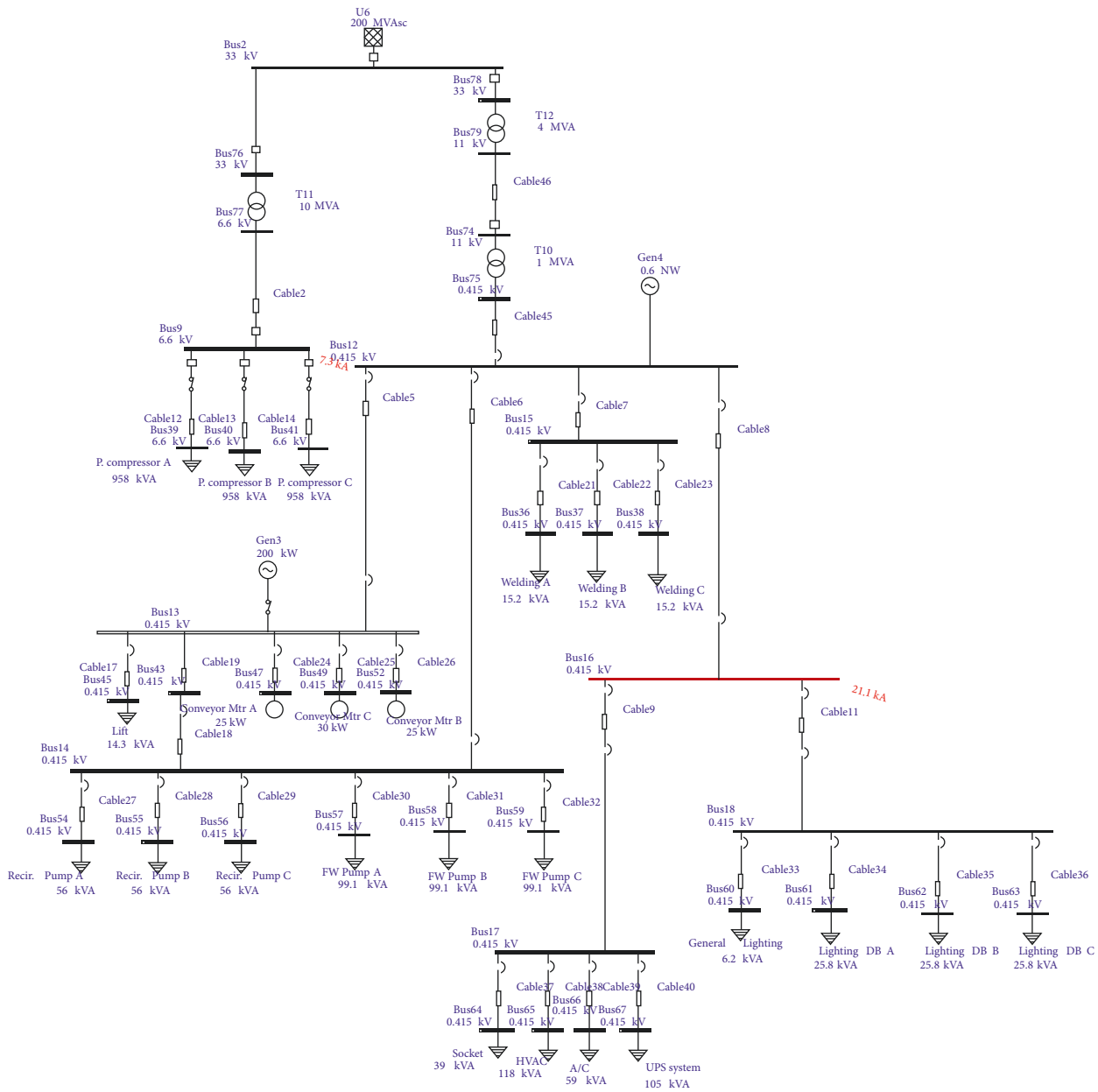

Figure 5: Single Line diagram-Design B.

Table 5: Comparison load modelling for Design A and B.

No	Design A	Design B
1	Step down voltage rating 33 kV ⟶ 6.6 kV ⟶ 415 V	Step down voltage rating 33 kV ⟶ 11 kV ⟶ 415 V
2	Two transformers	Three transformers
3	One emergency generator set	Two emergency generator set
4	Same sub load	Same sub load
5	Different design in supplying power	Different design in supplying power
6	100 MVA supplying power	200 MVA supplying power

also be said to be a good design because the percentage of the voltage drop is less than the acceptable voltage drop, which is 5%. The report generated by ETAP for the voltage drop is shown in Figures 6–8 from the branch losses summary report.

Table 6 summarises the report's findings for both case studies in relation to the IEE Wiring Regulation (BS7671 : 2008) and IEC60343 : 2001. According to the data, Design B is a better design to Design A in terms of voltage drop percent.

CKT / Branch	From-To Bus Flow		To-From Bus Flow		Losses		% Bus Voltage		Vd % Drop in Vmag
ID	MW	Mvar	MW	Mvar	kW	kvar	From	To	
Cable 2	1.752	0.993	-1.752	-0.993	0.1	0.1	99.6	99.5	0.01
Cable 20	-2.288	-1.344	2.288	1.344	0.3	0.4	99.6	99.6	0.02
Cable 7	0.020	0.010	-0.020	-0.010	0.0	0.0	98.4	98.4	0.02
Cable 8	0.311	0.192	-0.310	-0.191	1.6	2.0	98.4	97.8	0.64

Figure 6: Report list for voltage drop percent at cable 8 in Design A.

CKT / Branch	From-To Bus Flow		To-From Bus Flow		Losses		% Bus Voltage		Vd % Drop in Vmag
ID	MW	Mvar	MW	Mvar	kW	kvar	From	To	
T10	0.083	0.395	-0.082	-0.387	1.4	8.0	100.0	100.3	0.34
T11	1.766	1.033	-1.764	-1.000	2.2	33.4	100.0	99.9	0.11
T12	0.084	0.398	-0.083	-0.395	0.3	2.9	100.0	100.0	0.01
					6.7	48.0			

Figure 7: Report list for voltage drop percent at transformer 10 in Design B.

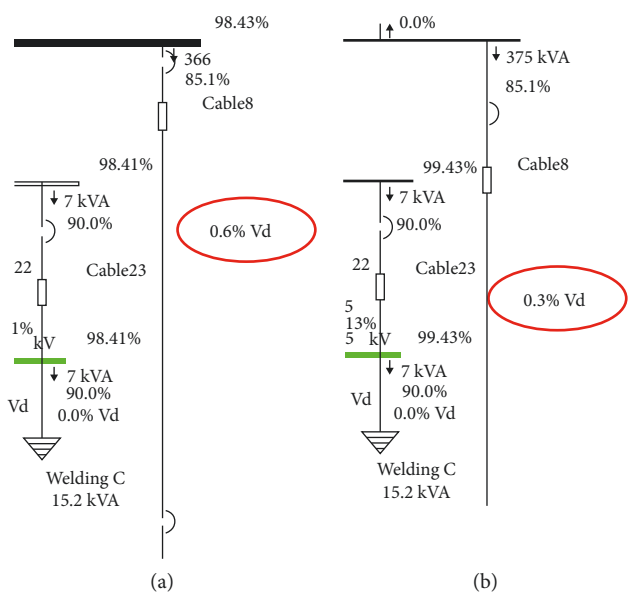

Figure 8: Branch summary report. (a) Design A–V_d at cable 8. (b) Design B–V_d at transformer 10.

Table 6: Summarised report of Voltage drop between Design A and Design B.

Type of supply	BS7671 : 2008 (%)	IEC60343 : 2001 (%)	Design A	Design B
Public low voltage distribution system supplying LV load	5	5	Cable 6 = 0.65% Cable 8 = 0.64% Cable 9 = 0.27% Cable 38 = 0.10% Cable 45 = 0.56% Transformer 1 = 0.43%	Cable 6 = 0.12% Cable 8 = 0.33% Cable 9 = 0.28% Cable 45 = 0.32% Transformer 10 = 0.34%

Table 7: Summaries of fault current between Design A and B.

No	Design A	Design B
1	Fault current at bus 57 = 26.44 kA	Fault current at bus 9 = 7.3 kA
2	Fault current at bus 60 = 17.3 kA	Fault current at bus 16 = 21.1 kA

Table 8: Comparison of %THD for Design A and Design B.

No	Industrial load	%THD	
		Design A	Design B
1	Process compressor	1.92	1.40
2	Conveyer motor	2.11	1.50
3	Lift	2.11	1.51
4	Welding system	2.12	1.51
5	Firewater Pumps	2.13	1.53
6	General lightings	2.25	1.59
7	UPS and HVAC	2.31	1.65
8	Air cond and sockets	2.30	1.64

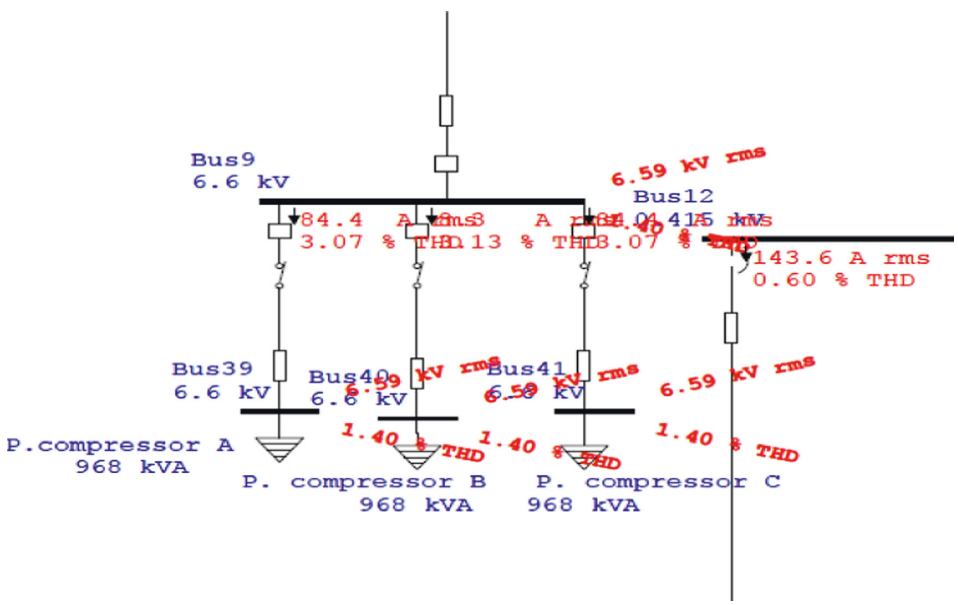

Figure 9: Value of %THD for load process compressor.

4.3. Short Circuit Analysis (Design A and B). In Design A the fault is located at the bus 57 and bus 60. When the fault occurs, the current value at the bus 57 increased up until 26.44 kA and the current value at bus 60 rise to 17.3 kA. While for the Design B, the fault is located at the bus 9 and bus 16. Table 6 summarises the fault current for both of design.

The current on bus 9 climbed to 7.3 kA during the fault, whereas the current on bus 16 jumped to 21.1 kA as shown in Table 7. The current value becomes extremely high because the impedance to current flow is extremely low. The fault current generated during a short circuit has a tendency to take the small impedance path and always reaches the ground. The evaluation of the earth faults and localization is very important for an industrial grid [10]. The closer the power sources are, the more they contribute to the fault current. Currents from the separate power sources concentrate near the fault, resulting in a total fault current that can be hundreds of times larger than usual. Design B is determined to be better than Design A in terms of fault current since the magnitude of the fault current is substantially reduced compared to Design A.

4.4. Harmonics. Total harmonic distortion is measured in percentage. From Table 8, all loads in Design B shows the lower value of THD compared to Design A which indicates the higher value of THD.

Design B demonstrates that lower percentages indicate significantly smaller THD. The difference between these two designs can be seen in the waveforms and spectrums. The overall harmonic current and voltage restrictions for this

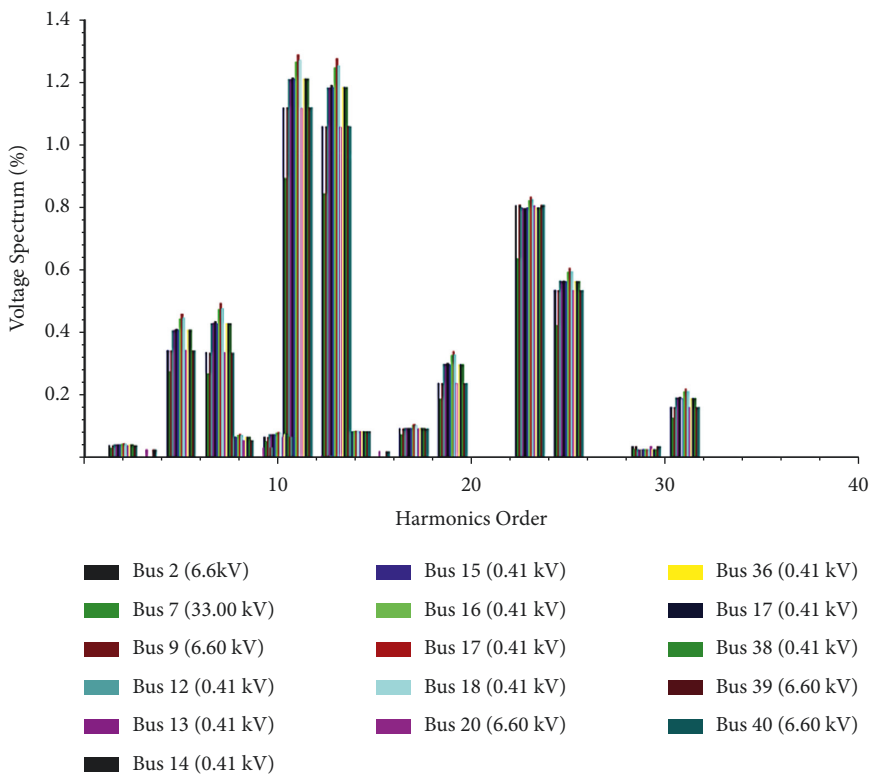

Figure 10: Harmonic diagram bus Design A–Spectrum.

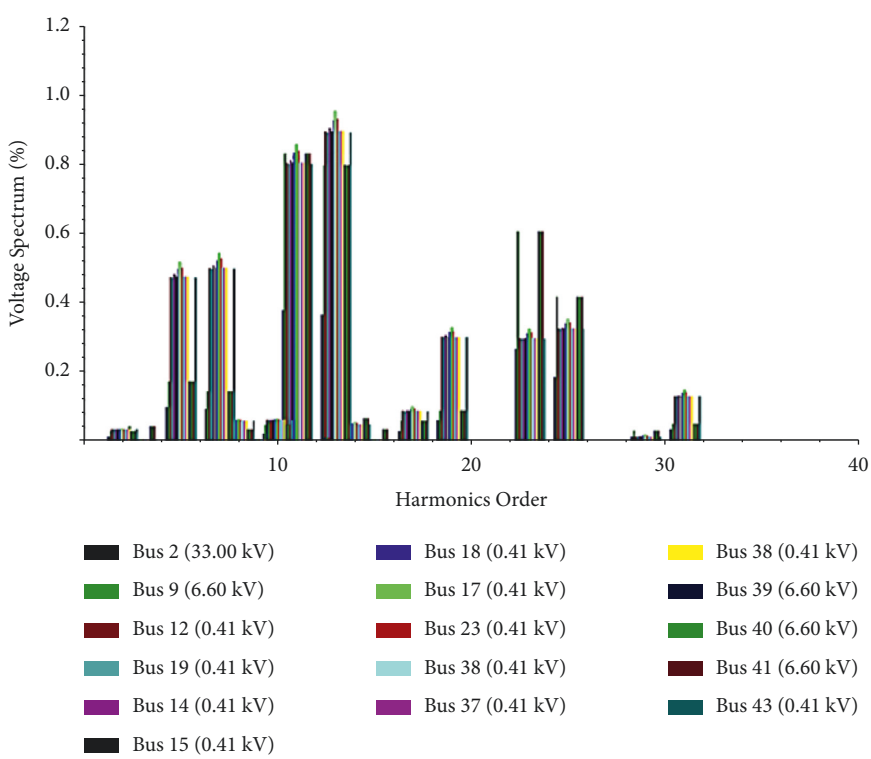

Figure 11: Harmonic diagram bus Design B–Spectrum.

power system will be set at 8% and 5%, respectively, by the IEEE519-92 standard. The objectives of the current limits are to limit the maximum individual frequency voltage harmonics to 3% of the fundamental and the voltage THD to 5% for systems. The results obtained show the circuit succeeds in achieving THD of less than 5%. Figure 9 shows the

THD for the process compressor under design B. Figures 10 and 11 show the harmonic spectrum for designs A and B, respectively.

5. Conclusion

The goal of this research is to design a long-term industrial power system in a practical situation. Two separate power systems of one-line diagram have been built with both systems in reference to the environment and sustainability issues, safety of personnel and equipment, minimum power losses, harmonic analysis, and addition of the load using the ETAP software. Before designing the one-line diagram, effective load planning and total power demand estimation must be established, and the loads must also be classified according to their rating and powered by a reliable power source. The precise load list in terms of required power, load factors, load types, and relevant feeding types assures a reliable system. During the designing of the one-line diagram, selection procedures of the electrical equipment and accessories, including cables, transformers, and circuit breakers, are presented with the following factors: the size of equipment, voltage drops, losses, and THD will be checked by the load flow study and according to the standards.

Cable sizing, for example, is vital in many aspects, such as cost, voltage drop, and reactive power losses. Improper cable sizing could have a severe impact on the system, resulting in faulty conditions. After finalising the power system design, the two designs are analysed by applying energy efficiency considerations to specific loadings such as voltage drop analysis, fault current analysis, and THD analysis. According to the results of the analysis, Design B is significantly better than Design A. Upon completing this research, it is evident that designing an electrical system is not a straightforward process, and there are numerous factors that should be carefully examined, either on the estimating or analysis side.

Data Availability

The data can be obtained from the corresponding author upon request.

Conflicts of Interest

The authors declare that they have no conflicts of interest.

Acknowledgments

There is no funding for this research. Editing and writing was supported by Debre Tabor University, Ethiopia

References

[1] G. Peter, K. Praghash, A. Sherine, and V. Ganji, "A combined PWM and AEM-based AC voltage controller for resistive loads," *Mathematical Problems in Engineering*, vol. 2022, Article ID 9246050, 1-11 pages, 2022.

[2] K. Handono, T. Tukiman, I. M. Putra, and L. Subekti, "Short circuit analysis on electrical power supply building # 71 BATAN for case reliability study of nuclear power plant electrical protection system," in *Proceedings of the AIP Conference Proceedings*, Padang, Indonesia, December 2019.

[3] J. S. Subjak and J. S. McQuilkin, "Harmonics-causes, effects, measurements, and analysis: an update," *IEEE Transactions on Industry Applications*, vol. 26, no. 6, pp. 1034–1042, 1990.

[4] G. Peter and A. Sherine, "Induced over voltage test on transformers using enhanced Z-source inverter based circuit," *Journal of Electrical Engineering*, vol. 68, no. 5, pp. 378–383, 2017.

[5] S. Liling, L. Heming, and X. Boqiang, "Analysis on the transient of stator-rotor-hybrid fault in squirrel cage induction motors," in *Proceedings of the 2005 International Conference on Electrical Machines and Systems*, pp. 1939–1944, Nanjing, China, September 2005.

[6] G. Peter, A. Sherine, and S. B. Iderus, "Enhanced Z-source inverter-based voltage frequency generator to conduct induced over voltage test on power transformers," *International Journal of Power Electronics*, vol. 12, no. 4, p. 493, 2020.

[7] P. P. Khera, "Application of zigzag transformers for reducing harmonics in the neutral conductor of low voltage distribution system," in *Proceedings of the Conference Record of the 1990 IEEE Industry Applications Society Annual Meeting*, p. 1092, IEEE, Seattle, WA, U.S.A, October 1990.

[8] K. Handono, E. Sumarno, K. Kiswanta, and K. Indrakoesoema, "Short circuit analysis on HPS electrical system," *Journal of Physics: Conference Series*, vol. 1198, no. 2, Article ID 022001, 2019.

[9] A. Blaszczyk and A. Uhl, "A contribution to industrial grid computing," in *Recent Advances in Parallel Virtual Machine and Message Passing Interface*, D. Kranzlmüller, J. Volkert, P. Kacsuk, and J. Dongarra, Eds., pp. 70–77, Springer, Berlin, Germany, , 2002.

[10] T. Kamel, Y. Biletskiy, and L. Chang, "Fault diagnoses for industrial grid-connected converters in the power distribution systems," *IEEE Transactions on Industrial Electronics*, vol. 62, no. 10, pp. 6496–6507, 2015.

[11] K. W. Klontz, T. J. E. Miller, M. I. McGilp, H. Karmaker, and P. Zhong, "Short-circuit analysis of permanent-magnet generators," *IEEE Transactions on Industry Applications*, vol. 47, no. 4, pp. 1670–1680, 2011.

[12] F. Erata, A. Goknil, E. Yıldız et al., "ETAP: Energy-Aware Timing Analysis of Intermittent Programs," 2022, https://arxiv.org/abs/2201.11433.

[13] G. P. Kornilov, I. R. Abdulveleev, R. R. Khramshin, and O. V. Gazizova, "The system for stabilizing voltage for essential consumers in industrial grids," in *Proceedings of the 2021 International Conference on Industrial Engineering, Applications and Manufacturing (ICIEAM)*, pp. 209–213, IEEE, Sochi, Russia, May 2021.

[14] B. M. A. Kadhimi, "Analysis for industrial grid containing nonlinear loads," *Wasit Journal of Engineering Sciences*, vol. 5, no. 1, pp. 35–58, 2018.

[15] A. Arizaldi, S. Salahuddin, M. Muhammad, V. Jain, G. P. Pandey, and M. J. Watane, "Short circuit analysis on distribution network 20 kV using etap software," *Journal of Renewable Energy, Electrical, and Computer Engineering*, vol. 1, no. 2, 2021.

[16] M. T. Riaz, M. M. Afzal, S. M. Aaqib, and H. Ali, "Analysis and evaluating the effect of harmonic distortion levels in industry," in *Proceedings of the 2021 4th International Conference on*

Energy Conservation and Efficiency (ICECE), Lahore, Pakistan, March 2021.

[17] N. A. Bhuiyan, "Power system harmonic analysis using ETAP," *School of Engineering & Design Electronic & Computer Engineering MSc Sustainable Electrical Power*, Brunel University, England, UK, 2017.

[18] S. Li, X. Du, and L. Wang, "A grid voltage synchronization method based on decoupled multiple synchronous reference frame," *Transactions of China Electrotechnical Society*, vol. 26, no. 12, pp. 183–189, 2011.

Hindawi
Mathematical Problems in Engineering
Volume 2022, Article ID 7157334, 14 pages
https://doi.org/10.1155/2022/7157334

Research Article

Mathematical Model for Energy and Exergy-Based Simulation of Triangular Solar Energy Extractor for Air Heating Applications

C. Ramesh,[1] M. Vijayakumar,[2] L. Jeyanthi,[3] P. L. Rupesh,[4] A. Kanchana,[5] P. R. Jyothi Sankar,[6] V. S. Sajith,[7] Neha Munjal,[8] and Habtewolde Ababu Birhanu[9]

[1]*Department of Mechanical Engineering, KIT-KalaignarKarunanidhi Institute of Technology, Coimbatore 641402, Tamilnadu, India*
[2]*Department of Mechanical Engineering, PSN College of Engineering and Technology, Tirunelveli 627152, Tamilnadu, India*
[3]*Department of Mathematics, Panimalar Engineering College, Chennai 600123, Tamilnadu, India*
[4]*Department of Mechanical Engineering, Vel Tech Rangarajan Dr Sagunthala R&D Institute of Science and Technology, Chennai 600062, Tamilnadu, India*
[5]*Department of Mathematics, Rajalakshmi Institute of Technology, Chennai 600124, Tamilnadu, India*
[6]*Department of Mechanical Engineering, NSS College of Engineering, Palakkad 678008, Kerala, India*
[7]*Department of Mathematics, NSS College of Engineering, Palakkad 678008, Kerala, India*
[8]*Department of Physics, Lovely Professional University, Phagwara 144411, Punjab, India*
[9]*Faculty of Mechanical Engineering, Arba Minch Institute of Technology, Arba Minch University, P.O. Box 21, Arba Minch, Ethiopia*

Correspondence should be addressed to Habtewolde Ababu Birhanu; habtewold.ababu@amu.edu.et

Received 24 March 2022; Revised 9 April 2022; Accepted 13 April 2022; Published 7 June 2022

Academic Editor: Ravi Samikannu

In the present work, the thermal and exergy efficiency of the equilateral triangular duct solar air heater is analytically investigated and its performance is improved by attaching an inclined wire rib over the absorber surface. Using triangular ducts improves the operating flow conditions up to the Reynolds number of 35000. The thermal model of solar air heater is solved by using an iterative procedure by code developed in MATLAB. The analysis considers the roughness parameters that roughness pitch (P)-to-height (e) ratio (P/e) of 4 to 16, roughness height (e)-to-hydraulic diameter (D_h) ratio (e/D_h) of 0.021 to 0.043, and rib inclination angle (α) of 30 to 75°. While increasing the Reynolds number from 2000 to 35000, the inclined rib roughened triangular duct solar air heater thermal performance is increased and attains the maximum value of 83.61% and the effective thermal efficiency of 80.26%. The maximum exergy efficiency of 2.62% is obtained at the Reynolds number value of 1864. It improves the thermal performance by 14.2% as compared with the rectangular rib roughened triangular duct solar air heater. The optimum value of roughness parameters is P/e of 12, e/D of 0.042, and α of 75°. The air heater is useable to attain the temperature rise parameter ranges from 0.001 to 0.03 K·m^2/W.

1. Introduction

Industries in developing countries are unsustainable because of the rapid escalation in the emission of greenhouse gases [1]. Therefore they are formulating their new energy policy to encourage eco-friendly energy usage for sustainable development. The researchers and economists identified the potential of solar thermal technologies specifically for industries for sustainable operations and production of low carbon emissions [2]. Among the industrial solar heat production devices, the flat plate solar air heaters are applicable for low temperature heating processes with an operating temperature range of 60 to 85°C [3].

The thermal performance improvement in rectangular duct solar air heaters is achieved by incorporating the techniques like artificial roughness, jet impingement, fins, and baffles [4]. The thermal performance enhancement techniques raise fluid friction and improve the pumping

power consumption. The researchers also utilized novel roughness shapes such as winglike tabulators [5], trapezoidal louvered winglets with wavy grooves [6], and double pass [7] arrangements to maximize the thermos hydraulic performance of rectangular duct solar air heater. These techniques effectively improve the heat transfer rate with a penalty of higher consumption in pumping power. Then it is identified that usage of triangular flow passages lowers the pressure drop and minimizes the consumption of pumping power [8]. The triangular ducts can integrate with artificial roughness and can produce a better performance as compared with conventional ducts. The influence of apex angle and dimple roughness on heat transfer and frictional characteristics of triangular air heater was experimentally investigated by Goel et al. and revealed that an apex angle of 60° makes the system more efficient [9]. Kumar et al. improved the thermohydraulic features of triangular duct channels by incorporating semicircular ribs and concluded that lower pitch distance and higher roughness height values improved the system performance by 2.2 times as compared with conventional system [10]. The provision of the rounded corner and straight ribs on triangular channels are investigated by Kumar et al. who observed the performance augmentation by 2.48 times at the Reynold number of 18000 and the relative roughness pitch value of 12 [11]. The researchers also investigated the aspect ratio of straight ribs suitable for triangular channels and concluded that providing the aspect ratio rib roughness values of 4.0 improves the hydraulic performance parameter by 1.89 times as compared with earlier studies [12].

Bharadwaj et al. [13] experimentally analyzed the heated triangular duct by using inclined rib roughness and suggested formulating a correlation between energy transfer and frictional factors as a function of inclined rib roughness parameters. Singh [14] uses recycling and discrete V ribs on TDSAH and concluded that the maximum thermohydraulic performance of the system was 71% at the hydraulic diameter of 0.06 m with a temperature rise parameter of 0.004 kW/m^2. Kumar et al. [15] also investigated the roughened triangular airflow channels by using CFD analysis for the roughness profiles of elliptical, rectangular, and circular ribs. While comparing the results, it is concluded that the rectangular ribs have superior performance that yields around 1.89 times improvement in thermohydraulic performance [16]. Kumar et al. [17] further carried out a thermal performance investigation in this field by varying the radius of curvature (R_c) of the duct and identified that R_c of 0.33 h provides the enhancement by 21 to 25%. Jain et al. [18] incorporated broken inclined ribs on equilateral triangular ducts and carried out the numerical analysis and revealed that relative gap positions with a value of 0.25 provide the thermohydraulic performance parameter of 2 for the Reynolds number ranging from 4000 to 8000.

Nidhul et al. [19] carried out an exegetic performance of TDSAH with the integration of V-shaped rib roughness for the Reynolds number ranges from 5000 to 20000 and concluded that an effective rib angle of 45° yields the maximum exergetic performance of the collector of 2.3%. Misra et al. [20] modified this V shape design with multiple gaps and carried out the investigation numerically for roughness pitch and angle of attack varies from 8 to 14 and 45 to 60°, respectively. Among these conditions, roughness pitch of 10 and angle of attack of 45 formulate better turbulence with a minimum formulation of eddy viscosity. Nidul et al. [21] carried out exergetic performance using an analytical model for straight rectangular ribs and concluded that the enhancement in thermal and exergy efficiency by 36 and 17% for the rib aspect ratio of 4. Kumar et al. [22] compared the exergetic performance of semicircular and square straight ribs and resulted that semicircular ribs enhance the performance by 26%.

The analytical and experimental investigations available in triangular duct solar air heaters have been summarized in Table 1. However, it was noted that heat transfer and friction factor analysis were considered for the analysis of artificially roughened TDSAH and less work is conveyed on the first law, effective thermal and exergy based analysis. From the table, it was noticed that exergy based performance analysis was considered for the roughness shaped of straight rectangular, semicircular, and V ribs. These designs result in lower enhancements of thermal performance on SAH.

The literature studies also recognized that the influence of artificial roughness with inclined circular ribs is not investigated based on its thermohydraulic and exergetic performance. There is very lesser analysis carried out for triangular air heaters to evaluate its realistic performance on exergy basis. The objective of this work is to improve the performance of solar air heater and investigate the effective thermal and exergetic performance by using inclined circular ribs on triangular duct solar air heaters. The configuration is stated as an inclined rib roughened triangular duct solar air heater (IRTDSAH). During this analysis, the influence of roughness pitch (P) to height (e) ratio (P/e), roughness height (e) to hydraulic diameter (D_h) ratio (e/D_h), and rib inclination angle (α) on effective thermal and exergy efficiency is investigated to identify its optimum values.

2. Theoretical Analysis

The inclined rib roughened triangular duct solar air heater is illustrated in Figure 1(a). Three identical size plates that are to be considered backplates and absorber plates create the airflow path for the air heater. The triangular channel is covered by insulation at the bottom and sides and a transparent glass cover at the top to minimize heat losses. The inclined wire ribs are attached at the bottom of the absorber plate to act as a tabulator for improving the convection current. The details of the inclined wire ribs and the operating parameters are described in Figure 1(b). The inclined rib attached over the absorber plate breaks the sublayer formulation, and the pitch between the plates and its inclination angle supports flow separation in upstream and flow reattachment in downstream conditions.

3. Energy-Based Performance of IRTDSAH

3.1. Thermal Efficiency. The real usability of IRTDSAH is calculated by considering the quantity of thermal energy

Table 1: Particulars of reported research on artificially roughened triangular duct solar air heater.

Roughness design	Heat transfer and friction factor analysis	First law based energy and effective thermal performance	Second law based exergy analysis
Dimple shape	Goel et al. [9]	×	×
Straight semi-circular rib	Kumar et al. [10]	Kumar et al. [22]	Kumar et al. [22]
Straight circular rib	Kumar et al. [11]	×	×
Straight rectangular rib	Kumar et al. [12]	×	Nidhul et al. [21]
Inclined circular rib	Bharadwaj et al. [13]	×	×
Inclined broken square rib	Jain et al. [18]	×	×
V rib	Nidhul et al. [19]	×	Nidhul et al. [19]
V rib with multiple gap	Misra et al. [20]	×	×

flowing inwards to the system through the glass cover and the amount of heat that bring back to the ambient.

It is evaluated by considering the assumption that the roughened absorber plate is working at a mean temperature of T_{wf} and a surrounding temperature of T_{as} [23].

$$Q_{u1} = F_R A_C \left[I(\alpha\tau) - U_L \left(T_{wf} - T_{as} \right) \right]. \quad (1)$$

In the above equation, T_f is given by the following:

$$T_{wf} = \frac{T_{wfi} + T_{wfo}}{2}. \quad (2)$$

The rise in enthalpy of outlet air describes the energy gained by the working fluid evaluated using the relation as follows:

$$Qu_1 = m_{wf} C_{pf} \left(T_{wfo} - T_{wfi} \right). \quad (3)$$

Heat removal factor F_R from the roughened absorber plate is stated as follows [21]:

$$F_R = \frac{m_{wf} C_{pf} \left(T_{wfo} - T_{wfi} \right)}{A_C \left[I(\tau\alpha) - U_L \left(T_{wf} - T_{as} \right) \right]}. \quad (4)$$

The thermal performance of IRTDSAH can be calculated by using the equation stated by Hottel-Whiler-Bliss by using the parameters that cumulative heat loss coefficient U_L and heat removal factor F_R. It is stated as follows [24]:

$$\eta_{th} = \frac{Q_{u_1}}{IA_C} = F_R \left[I(\tau\alpha) - U_L \left(\frac{T_{wf} - T_{sa}}{I} \right) \right]. \quad (5)$$

Heat removal factor F_R in terms of collector efficiency factor is stated as follows:

$$F_R = \frac{mC_p}{U_L A_c} \left[1 - \exp\left(\frac{U_L A_p F'}{mC_p} \right) \right]. \quad (6)$$

3.2. Effective Thermal Efficiency. The effective thermal efficiency indicates the performance of IRTDSAH by considering the pumping power losses consumed by the system. It is evaluated by using the equation (7), which consists of efficiency of blower (η_B), efficiency of motor (η_m), efficiency of transmission (η_T), and power plant (η_P) [25].

$$\eta_{EE} = \frac{Q_{u1}}{IA_C} - \frac{P_m}{IA_C \left(\eta_B \eta_m \eta_T \eta_P \right)}. \quad (7)$$

3.3. Exergy Analysis. Exergy refers to the conversion of available energy into useful energy or work, and so exemplifies the compactness of the solar air heater. Exergy efficiency can also be stated as useful work that a system may produce with respect to the ambient, and it is defined as follows [26]:

$$\eta_{ex} = \frac{E_u}{E_{sun}}, \quad (8)$$

where E_u represents useful exergy output from RTDSAH and E_{sun} exergy input to the system from the Sun. It can be evaluated using the relation as follows [26]:

$$\dot{E}_{sun} = A_c I \left(1 - \frac{4}{3} \left(\frac{T_{fo}}{T_{sun}} \right) + \frac{1}{3} \left(\frac{T_{fo}}{T_{sun}} \right)^4 \right). \quad (9)$$

Equation (10) evaluates the irreversibility produced by loss of pressure and energy transfer to the air in the system. It is evaluated as follows:

$$\dot{E}_u = \dot{Q}_{u1} - \dot{m}\, C_p T_o . \ln\left(\frac{T_{fo}}{T_{fi}} \right) - \dot{m} T_o \frac{\Delta P}{\rho_f T_{fi}}, \quad (10)$$

where ΔP is the pressure drop that happens across the solar air heater path.

The entropy values describe the energy destruction from the solar air heater that is not able to convert as useful heat with respect to corresponding operating conditions and ambient temperature. It is evaluated using the following equation:

$$\text{Entropy} = \frac{E_{sun} - E_u}{T_a}. \quad (11)$$

3.4. Analytical Procedure. The energy and exergy analysis of IRTDSAH was evaluated by considering assumptions as follows [27].

(1) The energy and exergy investigations are carried out at the 1D-steady state model.

(2) There is a negligible temperature drop that happens across the components of IRTDSAH.

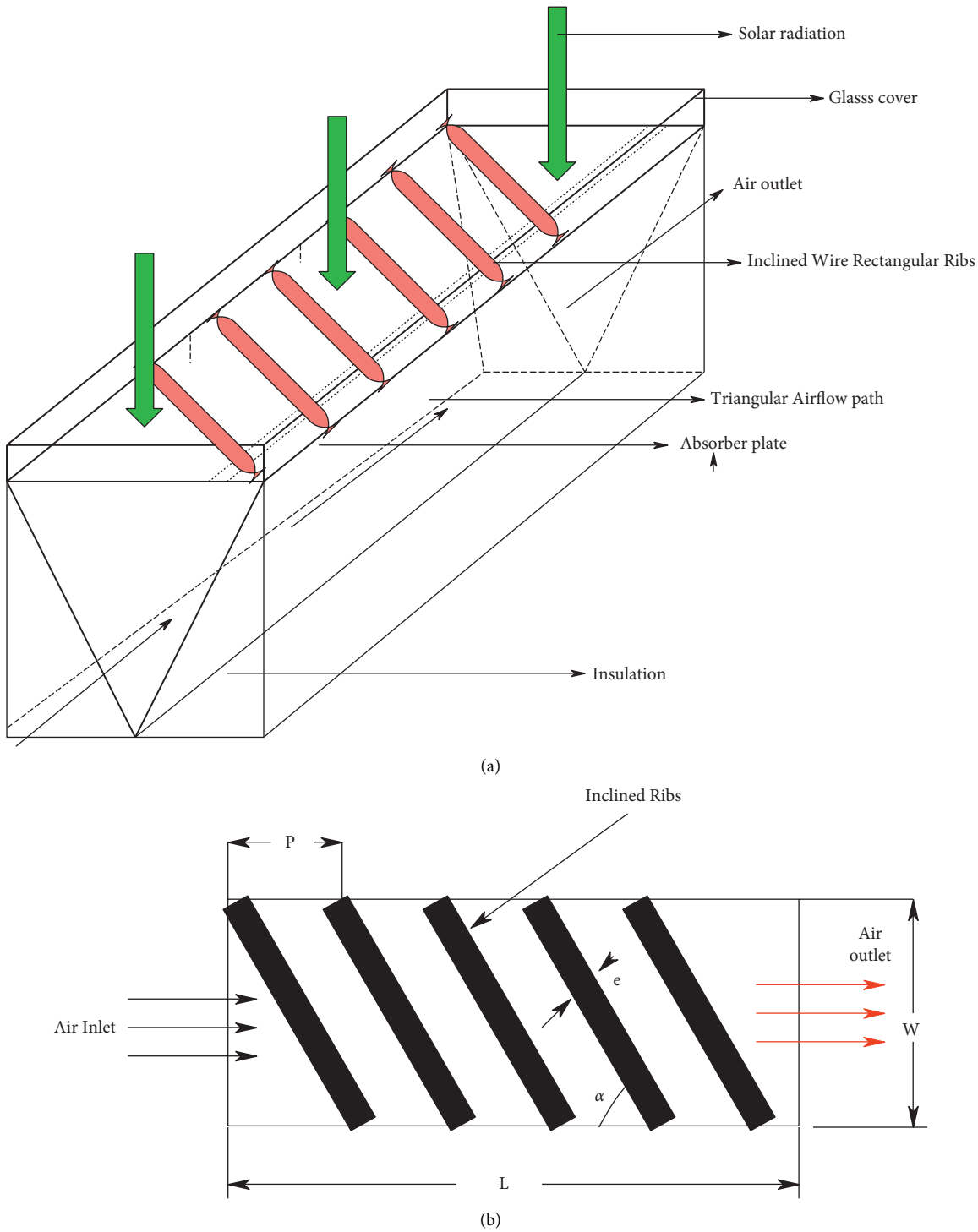

Figure 1: (a) Inclined rib roughened triangular duct solar air heater. (b) Roughness details.

(3) The joints of the air heater are leak-proof.

(4) The variation in convective heat transfer is coefficient across the length of the collector or negligible.

(5) Energy transfer that happens in the axial direction of the collector is only considered for evaluate the outlet temperature of air.

The thermal modeling procedure to evaluate the energy and exergetic performance of IRTDSAH is described below.

Step 1: The design parameters of inclined wire roughness and surrounding and operating conditions of SAH are taken from Table 2.

Table 2: Typical value of design and operating conditions.

Design and operating parameters	Value
Length (L) and width (W) of the duct	1.5 m
Thickness (δ_i) of insulation	0.06 m
Glass transparent cover thickness (t_g)	0.004 m
Thermal conductivity value of insulation (k_i)	0.04 W/mK
Thermal conductivity value of glass cover (k_g)	0.75 W/mK
Radiation of intensity (I)	1000 W/m^2
Atmospheric temperature (T_a)	300 K
Temperature rise parameter ($\Delta T/I$)	0.002–0.03 K·m^2/W
Reynolds number (Re)	2000–35000
Relative roughness height (e/D_h)	0.021–0.043
Relative roughness pitch (P/e)	4–16
Inclination angle of arc (α)	30–75°

Step 2: It is assumed that the air sucked from the surroundings to the inlet of the SAH is in thermal equilibrium with ambient air temperature. Therefore, the rise in temperature at the outlet (T_{fo}) of the air is evaluated by the following:

$$T_{fo} = T_{fi} + \Delta T. \tag{12}$$

Here ΔT represents the rise in temperature of air from the absorber surface. It is used to evaluate the rise in temperature ($\Delta T/I$) [18, 19, 28].

$$\Delta T = \frac{\Delta T}{I} \times I. \tag{13}$$

Step 3: Then equations (10)–(12) are used to evaluate the thermophysical properties of air [25].

$$\mu = 0.181 \times 10^{-4} \left(\frac{T_{wf}}{293}\right)^{0.735}, \tag{14}$$

$$C_p = 0.1006 \times 10^{4} \left(\frac{T_{wf}}{293}\right)^{0.0155}, \tag{15}$$

$$k = 0.275 \times 10^{-3} \left(\frac{T_{wf}}{293}\right)^{0.086}. \tag{16}$$

Step 4: The mean temperature of the absorber surface is estimated by using the equation as follows [26]:

$$T_{ap} = \frac{T_{fo} + T_{fi}}{2} + 10. \tag{17}$$

Step 5: The wasted heat losses through the top cover, back insulations, and side cover of the IRTDSAH due to convection are named as overall heat loss that is evaluated by using the relation [18, 19].

$$U_l = U_t + U_b + U_e. \tag{18}$$

In the above relation (18), U_b, Ut and U_e represent bottom, top, and side losses that happen in the SAH. The top loss of the SAH is influenced by the parameters of wind velocity, glass, and absorber plate temperature. Akhtar and Mullick correlation describes the top loss as follows [22]:

$$U_t = \left[\frac{\sigma\left(T_{ap}{}^2 + T_{gc}{}^2\right)\left(T_{ap} + T_{gc}\right)}{\left(1/\varepsilon_{ap}\right) + \left(1/\varepsilon_{gc}\right) - 1} + \left(\frac{kNu_l}{L_1}\right)\right] + \left[\sigma\varepsilon_g\left(T_{ap}{}^2 + T_{gc}{}^2\right)\left(T_{gc} + T_a\right) + h_w\right]^{-1} + \frac{t_{gc}}{k_{gc}}. \tag{19}$$

The terms in equation (16) are evaluated using the relations as follows:

$$\begin{aligned}
T_{gc} &= \left[\frac{F_l T_{ap} + cT_{as}}{1 + F_l}\right] \\
Nu_l &= 1 + 1.44\left[1 - \frac{1708}{Ra\cos\beta}\right] + \left[1 - \frac{1708(\sin 1.8\,\beta)^{1.6}}{Ra\cos\beta}\right] + \left[\left(\frac{Ra\cos\beta}{5830}\right)^{0.33} - 1\right] \\
F_l &= \frac{\left[12 \times 10^{-8}\left(T_{as} + 0.2T_{ap}\right)^3 + h_w\right]^{-1} + 0.3L_g}{\left[6 \times 10^{-8}\left(\varepsilon_{ap} + 0.028\right) \times \left(T_{ap} + 0.5T_{as}\right)^3 + 0.6L_1{}^{-0.2}\left\{\left(T_{ap} - T_{as}\right)\cos\beta\right\}^{0.25}\right]^{-1}} \\
c &= \left[\frac{\left(T_{sky}/T_{as}\right) + \left(h_w/3.5\right)}{1 + \left(h_w/3.5\right)}\right] \\
T_s &= 0.0522 \times \left(T_a\right)^{1.5}.
\end{aligned} \tag{20}$$

The edge and bottom losses from the system are evaluated using the relation as follows [21]:

$$U_b = \frac{k_i}{\delta_i},$$
$$U_e = \frac{t_e ki}{\delta_i} \times \left[\frac{3a}{(1/2) \times aH}\right]. \tag{21}$$

Step 6: The useful energy gain from the IRTDSAH is given by the following:

$$Q_{u1} = A_c\left[I(\tau\alpha) - U_L\left(T_{ap} - T_{as}\right)\right]. \tag{22}$$

Step 7: The mass flow rate that happens in the IRTDSAH is evaluated by the following equations [21]:

$$\dot{m} = \frac{Q_{u_1}}{C_p \Delta T}, \tag{23}$$

$$\mathrm{Re} = \frac{\dot{m} D_h}{\mu A_{cs}}. \tag{24}$$

Step 8: Then the convective heat transfer coefficient of IRTDSAH is calculated based on the Nusselt number correlation that incorporates the relation between the nondimensional inclined wire roughness design parameters is as follows [13]:

$$Nu = 0.0031\left[\mathrm{Re}^{1.0972}\left(\frac{P}{e}\right)^{1.0832}\left(\frac{\alpha}{60}\right)^{0.0792}\left(\frac{e}{D_h}\right)^{0.3585}\right.$$
$$\left.\times \exp\left\{-0.1908\left(\ln\left(\frac{\alpha}{60}\right)\right)^2\right\}\times\right]\exp\left\{-0.246\left(\ln\left(\frac{P}{e}\right)\right)^2\right\},$$
$$h_c = \frac{Nuk_a}{D_h}. \tag{25}$$

Step 9: The plate efficiency factor F′ is calculated by using the value of convective heat transfer coefficient value h_c and the heat loss coefficient value of UL by using the relation shown below [21]:

$$F' = \frac{h_c}{h_c + U_L}. \tag{26}$$

Step 10: The outlet temperature based heat gain value (Qu_2) is calculated using the equation as mentioned below [21, 22]:

$$Q_{u2} = F_R A_c\left[I(\tau\alpha) - U_L\left(T_{fo} - T_{fi}\right)\right]. \tag{27}$$

Step 11: Then, the deviation between Q_{u2} and Q_{u1} is evaluated. If the difference between the heat gain values is more than 0.01%, then the mean plate temperature of the IRTDSAH is recalculated and resubstituted by equations (22) and (28). The procedure is repeated from the sequence of steps 4 to Step 10 up to the attainment of convergence [26].

$$T_{ap} = T_{as} + \frac{\left[I(\alpha\tau) - \left[Q_{u2}/A_C\right]\right]}{U_L}. \tag{28}$$

Once the convergence is achieved, then the energy efficiency of the SAH is evaluated using equation (5).

Step 12: The frictional flow resistance occurred by the inclined rob roughness is evaluated by using the correlations, and the pump power requirement for propelling the air is given by the following [13]:

$$fr = 11.845\left[\mathrm{Re}^{-0.693}\left(\frac{P}{e}\right)^{1.1389}\left(\frac{\alpha}{60}\right)^{0.0418}\left(\frac{e}{D_h}\right)^{0.3365}\right.$$
$$\left.\times \exp\left\{-0.1686\left(\ln\left(\frac{\alpha}{60}\right)\right)^2\right\}\times\right]\exp\left\{-0.2644\left(\ln\left(\frac{P}{e}\right)\right)^2\right\}. \tag{29}$$

Step 13: The evaluated friction factor from equation (29) is substituted in equation (30) to estimate the pressure drop (ΔP) and loss of pumping power (P_m) that occurs in IRTDSAH [27].

$$\Delta P = \frac{4frLv^2\rho}{2D_h}, \tag{30}$$

$$P_m = \frac{m\Delta P}{\rho}. \tag{31}$$

The effective thermal efficiency based performance of the IRTDSAH is evaluated by using the relation stated in equation (7).

4. Results and Discussion

The inclined rib roughened triangular duct solar air heater is analytically investigated and the influence of roughness pitch (P) to height (e) ratio (P/e), roughness height (e) to hydraulic diameter (D_h) ratio (e/D_h), and rib inclination angle (α) on thermal, effective and exergy efficiency of the IRTDSAH are presented in following sections.

4.1. Effect of Rib Roughness Angle (α) on Thermal Performance of IRTDSAH. The wire ribs are mounted on the IRTDSAH absorber plate with the inclination of angle α varies from 30° to 75°, and its effects on the thermal effective thermal and exergy efficiency are shown in Figures 2–7.

Figure 2 reveals the impact of rib roughness angle (α) ranges from 30 to 75° on the thermal efficiency of IRTDSAH, while flowing of air at the Reynolds number from 2000 to 35000, and maintaining other roughness parameters are constant, i.e., $e/D_h = 0.043$ and $P/e = 12$. While increasing the Reynolds number from 2000 to 35000, the thermal efficiency of IRTDSAH improved by a maximum of 52.8% to 83.8% for the rib inclination angle (α) value of 75°. While decreasing the value of α decreases the thermal performance of IRTDSAH due to the production of thermally dead zones.

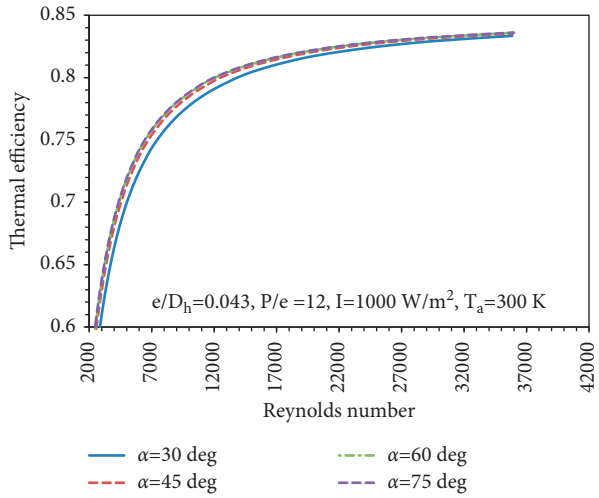

Figure 2: Impact of rib roughness angle (α) and Reynolds number on the thermal efficiency of IRTDSAH.

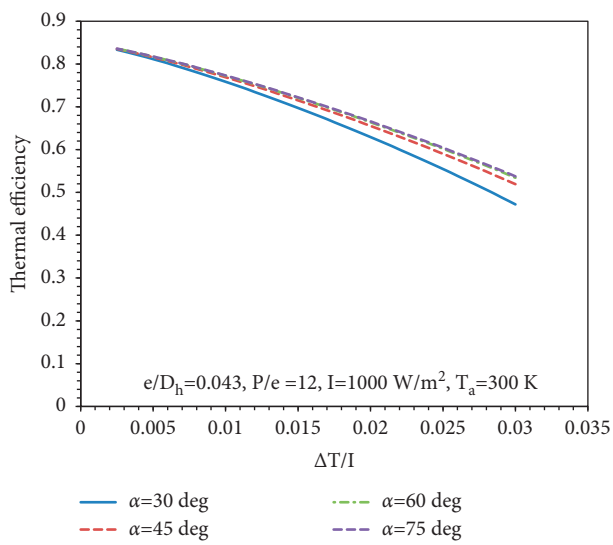

Figure 3: Impact of rib roughness angle (α) and rise in temperature parameter on thermal efficiency of IRTDSAH.

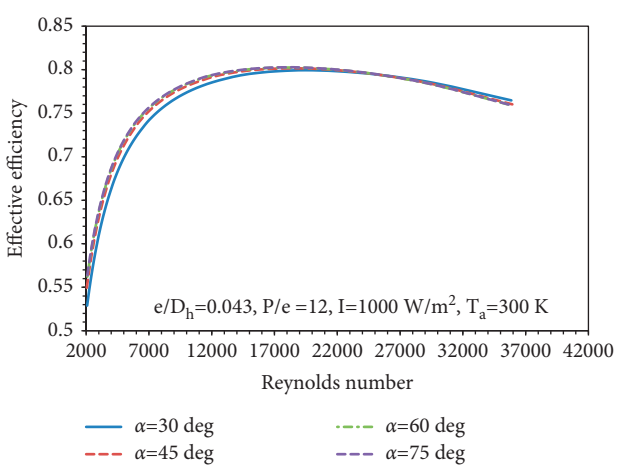

Figure 4: Impact of rib roughness angle (α) and Reynolds number on the effective thermal efficiency of IRTDSAH.

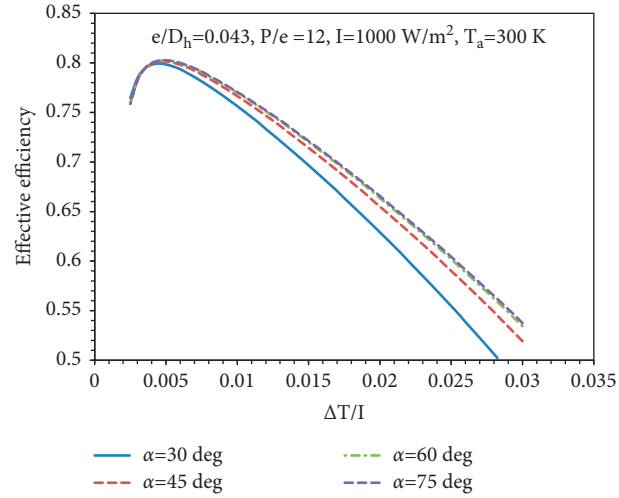

Figure 5: Impact of rib roughness angle (α) and rise in temperature parameter on the effective thermal efficiency of IRTDSAH.

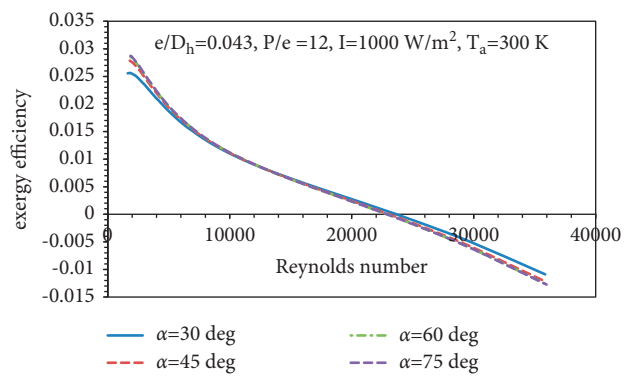

Figure 6: Impact of rib roughness angle (α) and reynolds number on exergy efficiency of IRTDSAH.

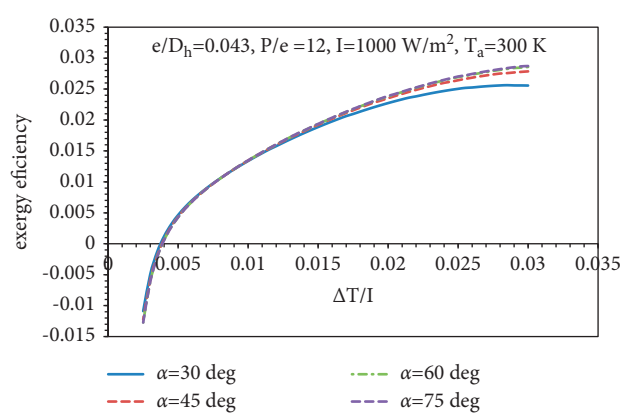

Figure 7: Impact of rib roughness angle (α) and rise in temperature parameter on exergy efficiency of IRTDSAH.

Figure 3 reveals the impact of rib roughness angle (α) ranging from 30 to 75° on the thermal efficiency of IRTDSAH while producing hot air with a rise in temperature parameter value ranging from 0.001 to 0.03 K·m^2/W and maintaining other roughness parameters are constant, i.e., *e*/

$D_h = 0.043$ and $P/e = 12$. The thermal efficiency values were found to increase with the increase in α. The maximum thermal efficiency value found in the analysis is 83.61% at $\alpha = 75^\circ$. Comparatively at a higher angle of attack, the thermal efficiency is higher because of effective flow reattachment in the boundary layer.

Figure 4 reveals the impact of rib roughness angle (α) ranges from 30 to 75° on the effective thermal efficiency of IRTDSAH, while flowing of air at the Reynolds number from 2000 to 35000, and maintaining other roughness parameters are constant, i.e., $e/D_h = 0.043$ and $P/e = 12$. The effective efficiency values found increases up to the critical Reynolds Number as shown in Table 3. The maximum effective efficiency value found in the analysis is 80.26% in $\alpha = 75^\circ$ at 17534 Reynolds number. For the same Reynolds number with $\alpha = 30^\circ$ the effective efficiency is 79.94%, while the trend gets reversed at higher Reynolds numbers (>25000) that $\alpha = 30^\circ$ yields better performance due to offering lesser flow resistance and consumption of lower pumping power. At a higher Reynolds Number, the pressure drop increases due to the turbulent flow nature of the air. Due to this reason, there is a dip in effective efficiency after the 17528 Reynolds Number. Comparatively, at a higher angle of attack, the effective efficiency is higher, which is evident.

Figure 5 reveals the impact of rib roughness angle (α) ranging from 30 to 75° on the effective thermal efficiency of IRTDSAH while producing hot air with a rise in temperature parameter value ranging from 0.001 to 0.03 K·m^2/W and maintaining other roughness parameters are constant, i.e., $e/D_h = 0.043$ and $P/e = 12$. The effective efficiency values found increase up to the critical value of rising in temperature parameter as shown in Table 4. The maximum effective efficiency value found in the analysis is 80.26% at $\alpha = 75^\circ$. Comparatively, at a higher angle of attack, the effective efficiency is higher.

Figure 6 reveals the impact of rib roughness angle (α) ranges from 30 to 75° on exergy efficiency of IRTDSAH, while flowing of air at the Reynolds number from 2000 to 35000, and maintaining other roughness parameters are constant, i.e., $e/D_h = 0.043$ and $P/e = 12$.

The exergy efficiency values were found to increase up to the critical value of the Reynolds number, as shown in Table 5. The maximum exergy efficiency value found in the analysis is 2.87% at $\alpha = 75^\circ$ at Re of 1864, and a further rise in Re > 1864 reduces the exergy efficiency. Comparatively, at operating the air heater lower angle of attack declines the second law efficiency of the system due to higher exergy losses and destructions at a lower Reynolds number. At the system operated at a Reynolds number >20000, it produces a negative value of exergy efficiency for all the values of α due to the rise in internal exergy destruction parameter such as fluid friction occurring between absorber plate and working fluid.

Figure 7 reveals the impact of rib roughness angle (α) ranges from 30 to 75° on exergy efficiency of IRTDSAH while producing hot air with a rise in temperature parameter value ranging from 0.001 to 0.03 K·m^2/W, and maintaining other roughness parameters are constant, i.e., $e/D_h = 0.043$ and $P/e = 12$. The exergy efficiency values were found to increase with the increase in $\Delta T/I$ and α till $\Delta T/I = 0.03$ K·m^2/W. The maximum exergy efficiency value found in the analysis is 2.87% at $\alpha = 75^\circ$. Comparatively, at a higher angle of attack, the exergy efficiency is higher. It is observed that at higher $\Delta T/I$, the exergy efficiency value increases.

Table 3: Critical Reynolds number based on different values of α.

S. no	α (°)	Maximum effective efficiency (%)	Reynolds number
1	30	79.94	19469
2	45	80.13	19551
3	60	80.24	17528
4	75	80.26	17534

Table 4: Influence of α on the rise in temperature parameter.

S. n	α (°)	$\Delta T/I$ for maximum effective efficiency	Maximum effective efficiency (%)
1	30	0.0045	79.94
2	45	0.005	80.13
3	60	0.005	80.24
4	75	0.005	80.26

Table 5: Critical reynolds number based on different values of α.

S. n	α (°)	Maximum exergy efficiency (%)	Reynolds number
1	30	2.56	1821
2	45	2.78	1801
3	60	2.85	1853
4	75	2.87	1864

4.2. Effect of Roughness Height (e)-to-Hydraulic Diameter (D_h) Ratio (e/D_h) on Thermal Performance of IRTDSAH. The wire ribs are mounted on the IRTDSAH absorber plate with roughness height to diameter ratio (e/D_h) varying from 0.021 to 0.042, and its effects on the thermal effective thermal and exergy efficiency are shown in Figures 8–14.

Figure 8 reveals the rib roughness height (e) to hydraulic diameter (D_h) ratio ranging from 0.021 to 0.043 on the thermal efficiency of IRTDSAH, while flowing of air at the Reynolds number from 2000 to 35000, and maintaining other roughness parameters are constant, i.e., $\alpha = 0.75^\circ$ and $P/e = 12$.

The maximum thermal efficiency value found in the analysis is 83.8% at $e/D_h = 0.043$. While increasing the Reynolds number from 2000 to 35000, the thermal efficiency of IRTDSAH improved by a maximum of 53.1% to 83.8% for the rib roughness height (e) to hydraulic diameter (D_h) ratio (e/D_h) value of 0.043. While decreasing the value of e/D_h decreases the thermal performance of IRTDSAH due to the poor formulation, secondary flow reattachment points at the downward part of IRTDSAH.

Figure 9 reveals the impact of rib roughness height (e) to hydraulic diameter (D_h) ratio from 0.021 to 0.043 on the thermal efficiency of IRTDSAH while producing hot air with a rise in temperature parameter value ranging from 0.001 to 0.03 K·m^2/W, and maintaining other roughness parameters are constant, i.e., $\alpha = 75^\circ$ and $P/e = 12$. The thermal efficiency

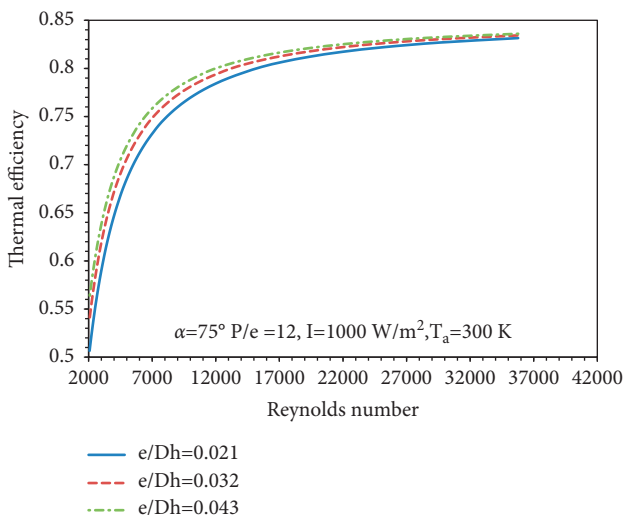

Figure 8: Impact of rib roughness height (e) to hydraulic diameter (D_h) ratio (e/D_h) and Reynolds number on the thermal efficiency of IRTDSAH.

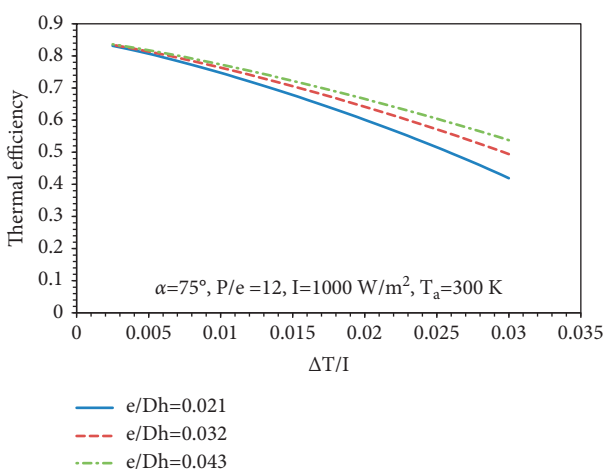

Figure 9: Impact of rib roughness height (e) to hydraulic diameter (D_h) ratio (e/D_h) and rise in temperature parameter on thermal efficiency.

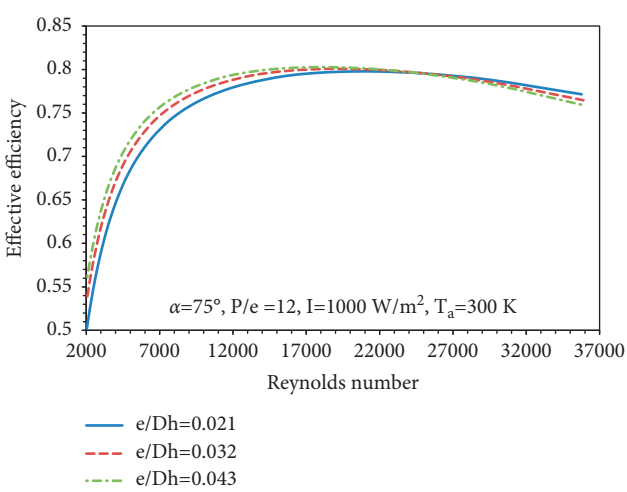

Figure 10: Impact of rib roughness height (e) to hydraulic diameter (D_h) ratio (e/D_h) on effective thermal efficiency of IRTDSAH.

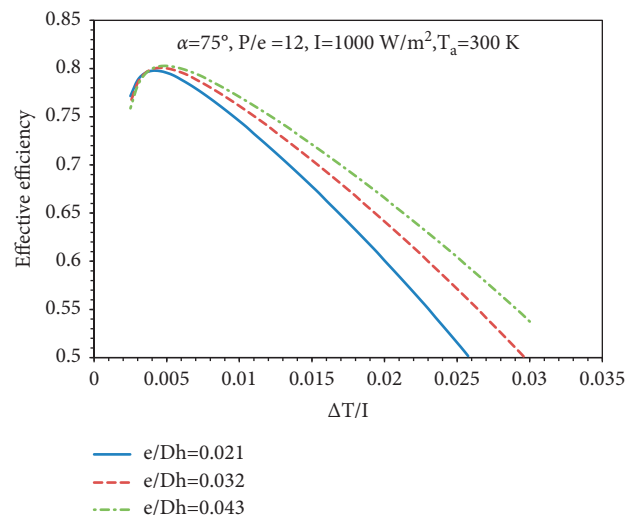

Figure 11: Impact of rib roughness height (e) to hydraulic diameter (D_h) ratio (e/D_h) and rise in temperature parameter on the effective thermal efficiency of IRTDSAH.

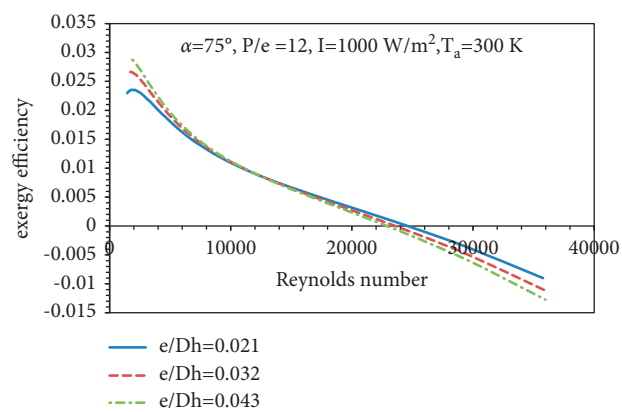

Figure 12: Impact of rib roughness height (e) to hydraulic diameter (D_h) ratio (e/D_h) on the effective thermal efficiency of IRTDSAH.

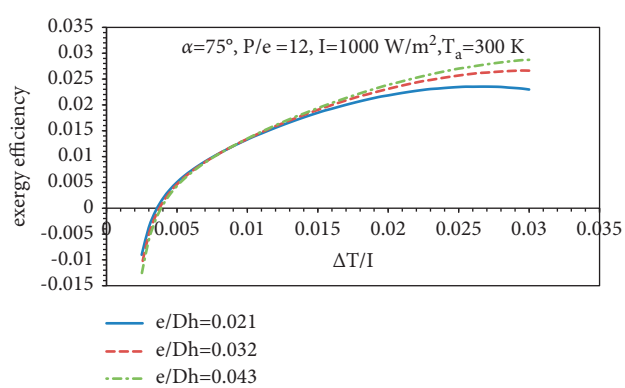

Figure 13: Impact of rib roughness height (e) to hydraulic diameter (D_h) ratio (e/D_h) on exergy thermal efficiency of IRTDSAH.

values were found to increase with the increase in e/D_h. The maximum thermal efficiency value found in the analysis is 83.61% at $e/D_h = 0.043$. Comparatively, at higher relative roughness height, the thermal efficiency is higher because of

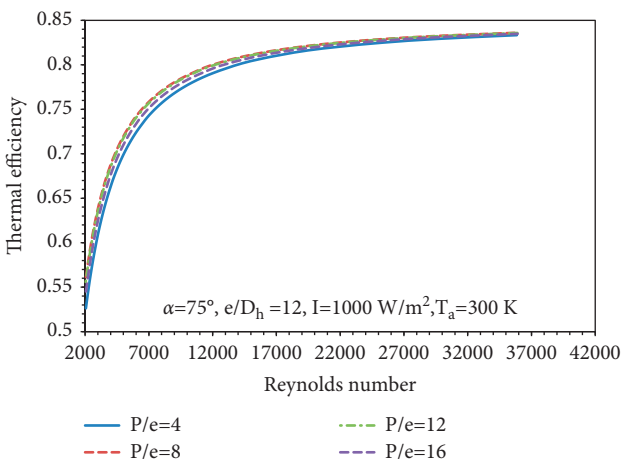

Figure 14: Impact of roughness pitch (p) to height (e) ratio (p/e) and Reynolds number on the thermal efficiency of IRTDSAH.

the effective breaking of thermal barrier formulated in fluid boundaries.

Figure 10 reveals the impact of rib roughness height (e) to hydraulic diameter (D_h) ratio (e/D_h) ranges from 0.021 to 0.043 on effective thermal efficiency of IRTDSAH, while flowing of air at the Reynolds number from 2000 to 35000, and maintaining other roughness parameters are constant, i.e., $\alpha = 75^\circ$ and $P/e = 12$. The effective efficiency values found increase up to the critical Reynolds Number, as shown in Table 6. The maximum effective efficiency value found in the analysis is 80.26% in $e/D_h = 0.043$ at 17534 Reynolds number. For the same Reynolds number with $e/D_h = 0.021$, the effective efficiency is 79.76%, while the trend gets reversed at higher Reynolds numbers (>25000) that $e/D_h = 0.021$ yield better performance due to offering lesser flow resistance and consumption lower pumping power. At a higher Reynolds number, the pressure drop increases due to the increment in roughness size increasing the pressure drop. Due to this reason, there is a dip in effective efficiency after the 17534 Reynolds Number. Comparatively, at higher relative roughness height, the effective efficiency is higher, which is evident.

Figure 11 reveals the impact of rib roughness height (e) to hydraulic diameter (Dh) ratio (e/D_h) ranging from 0.021 to 0.043 on the effective thermal efficiency of IRTDSAH while producing hot air with a rise in temperature parameter value ranging from 0.001 to 0.03 K·m^2/W, and maintaining other roughness parameters are constant, i.e., $\alpha = 75^\circ$ and $P/e = 12$. The effective efficiency values found increase up to the critical value of rising in temperature parameter as shown in Table 7. The maximum effective efficiency value found in the analysis is 80.26% at $e/D_h = 0.043$. Comparatively, at higher roughness height, the effective efficiency is higher.

Figure 12 reveals the impact of rib roughness height (e) to hydraulic diameter (D_h) ratio (e/D_h) on the exergy efficiency of IRTDSAH while flowing air at the Reynolds number from 2000 to 35000 and maintaining other roughness parameters that are constant, i.e., $\alpha = 75^\circ$ and $P/e = 12$. The exergy efficiency values found to increase up to the critical value of the Reynolds number, as shown in

Table 6: Critical Reynolds number based on different values of e/D_h.

S. n	e/D_h	Maximum effective efficiency (%)	Reynolds number
1	0.021	79.76	21937
2	0.032	80.07	19503
3	0.043	80.26	17534

Table 7: Influence of e/D_h on temperature parameter.

S. n	e/D_h	$\Delta T/I$ for maximum effective efficiency	Reynolds number
1	0.021	0.004	21937
2	0.032	0.0045	19503
3	0.043	0.005	17534

Table 8: Critical Reynolds number based on different values of e/D_h.

S. n	e/D_h	Maximum exergy efficiency (%)	Reynolds number
1	0.021	2.35	1850
2	0.032	2.66	1774
3	0.043	2.87	1864

Table 8. The maximum exergy efficiency value found in the analysis is 2.87% at $e/D_h = 0.043$ and at Re of 1864, and a further rise in Re > 1864 reduces the exergy efficiency. Comparatively, at operating the air heater lower rib roughness height (e) to hydraulic diameter (D_h) ratio declines the second law efficiency of the system due to higher exergy losses and destructions at a lower Reynolds number. At the system operated at a Reynolds number >20000, it produces a negative value of exergy efficiency for all the values of e/D_h due to the rise in internal exergy destruction parameters such as fluid friction occurs between absorber plate and working fluid.

Figure 13 reveals the impact of rib roughness height (e) to hydraulic diameter (D_h) ratio (e/D_h) ranging from 0.021 to 0.043 on exergy efficiency of IRTDSAH, while producing hot air with a rise in temperature parameter value ranges from 0.001 to 0.03 K·m^2/W, and maintaining other roughness parameters are constant, i.e., $\alpha = 75^\circ$ and $P/e = 12$. The exergy efficiency values were found to increase with the increase in $\Delta T/I$ and α till $\Delta T/I$ 0.03 K·m^2/W. The maximum exergy efficiency value found in the analysis is 2.87% at $e/D_h = 0.043$. Comparatively, at higher e/D_h the exergy efficiency is higher. It is observed that at higher $\Delta T/I$ the exergy efficiency value increases.

4.3. Effect of Roughness Pitch (P)-to-Height (e) Ratio (p/e) on Thermal Performance of IRTDSAH. The wire ribs are mounted on the IRTDSAH absorber plate with roughness pitch (p) to height (e) ratio (p/e) varies from 4 to 16, and its effects on the thermal effective thermal and exergy efficiency are shown in Figures 13–17.

Figure 14 reveals the impact of rib roughness pitch (p) to height (e) ratio (p/e) ranging from 4 to 16 on the thermal

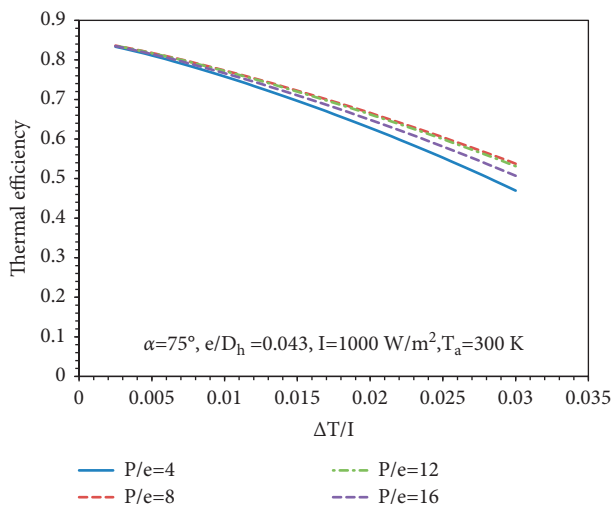

Figure 15: Impact of roughness pitch (p) to height (e) ratio (p/e) and rise in temperature parameter on the thermal efficiency of IRTDSAH.

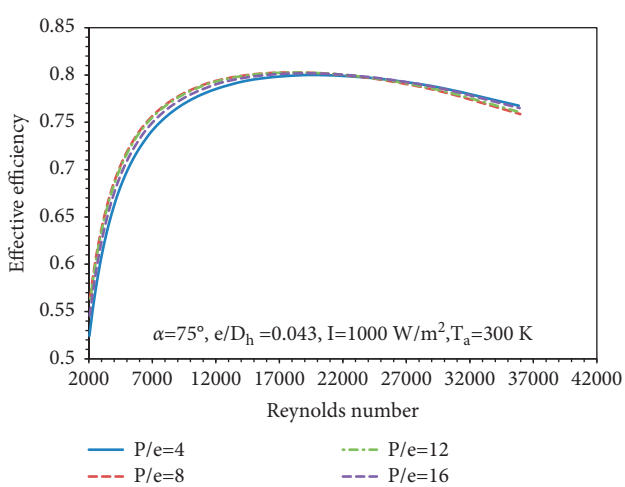

Figure 16: Impact of rib roughness pitch (p) to height (e) ratio (p/e) and Reynolds number on the effective thermal efficiency of IRTDSAH.

efficiency of IRTDSAH while flowing of air at the Reynolds number from 2000 to 35000 and maintaining other roughness parameters are constant, i.e., $e/D_h = 0.043$ and $\alpha = 75^\circ$. While increasing the Reynolds number from 2000 to 35000, the thermal efficiency of IRTDSAH improved by a maximum of 53.1% to 83.8% for the rib roughness pitch (p) to height (e) ratio (p/e) value of 12. While increasing or decreasing the value of P/e value of 12 decreases the thermal performance of IRTDSAH due to the formulation of sluggish boundary layers.

Figure 15 exemplifies the impact of roughness pitch (p) to height (e) ratio (p/e) on the thermal efficiency of IRTDSAH while producing hot air with a rise in temperature parameter value ranging from 0.001 to 0.03 K·m^2/W and maintaining other roughness parameters are constant, i.e., $e/D_h = 0.043$ and $\alpha = 75^\circ$. The thermal efficiency values were found to increase with the increase in p/e value up to 12 and

Table 9: Critical Reynolds number based on different values of P/e.

S. n	P/e	Maximum effective efficiency (%)	Reynolds number
1	4	80	19469
2	8	80.1	17522
3	12	80.22	17534
4	16	80.17	19527

achieving the maximum thermal efficiency value of 83.61%. Comparatively providing the p/e of 12 improves the thermal efficiency because of the increase in reattachment points in the boundary layer and enriching the local heat transfer coefficients.

Figure 16 rib roughness pitch (p) to height (e) ratio (p/e) ranges from 4 to 16 on the effective thermal efficiency of IRTDSAH, while flowing of air at the Reynolds number from 2000 to 35000, and maintaining other roughness parameters are constant, i.e., $\alpha = 75^\circ$ and $e/D_h = 0.043$. The effective efficiency values found increase up to the critical Reynolds Number, as shown in Table 9. The maximum effective efficiency value found in the analysis is 80.26% in $P/e = 12$ at the Reynolds number of 17534.

For the same Reynolds number with $P/e = 4$, the effective efficiency is 80%, while the trend gets reversed at higher Reynolds numbers (>25000) that $P/e = 4$ yield better performance due to offering of lesser flow resistance and consumption of lower pumping power. At a higher Reynolds number, the frictional resistance increases due to the increment in the number of elements, increasing the pressure drop. Due to this reason, there is a dip in effective efficiency after the 17534 Reynolds Number.

Figure 17 reveals the impact rib roughness pitch (p) to height (e) ratio (p/e) ranges from 4 to 16 on the effective thermal efficiency of IRTDSAH, while producing hot air with a rise in temperature parameter value ranges from 0.001 to 0.03 K·m^2/W, and maintaining other roughness parameters are constant, i.e., $\alpha = 75^\circ$ and $e/D = 0.043$. The effective efficiency values found increase up to the critical value of rise in temperature parameter as shown in Table 10. The maximum effective efficiency value found in the analysis is 80.26% at $P/e = 12$.

Figure 18 reveals the impact of rib roughness pitch (p) to height (e) ratio (p/e) on the exergy efficiency of IRTDSAH while flowing of air at the Reynolds number from 2000 to 35000, and maintaining other roughness parameters are constant, i.e., $\alpha = 75^\circ$ and $e/D_h = 0.042$. The exergy efficiency values were found to increase up to the critical value of the Reynolds number, as shown in Table 11. The maximum exergy efficiency value found in the analysis is 2.87% at $P/e = 12$ at the Re of 1864 and a further rise in Re > 1864 reduces the exergy efficiency.

Figure 19 reveals the impact rib roughness pitch (p) to height (e) ratio (p/e) ranging from 4 to 16 on exergy efficiency of IRTDSAH while producing hot air with a rise in temperature parameter value ranging from 0.001 to 0.03 K·m^2/W and maintaining other roughness parameters are constant, i.e., $\alpha = 75^\circ$ and $e/D = 0.043$. The exergy efficiency values were found to increase with the increase in $\Delta T/$

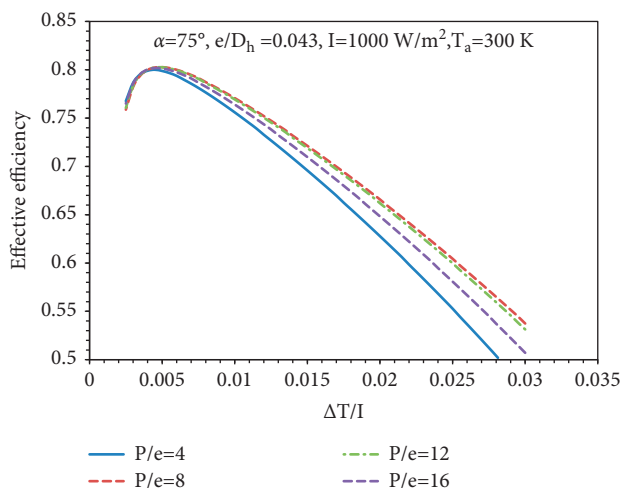

Figure 17: Impact of rib roughness pitch (p) to height (e) ratio (p/e) and rise in temperature parameter on the effective thermal efficiency of IRTDSAH.

Table 10: Influence of P/e on temperature parameter.

S. n	P/e	$\Delta T/I$ for maximum effective efficiency	Reynolds number
1	4	0.0045	19469
2	8	0.005	17522
3	12	0.005	17534
4	16	0.0045	19527

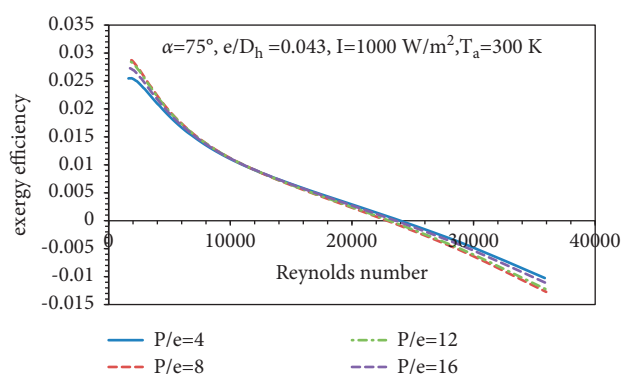

Figure 18: Impact of rib roughness pitch (p) to height (e) ratio (p/e) and Reynolds number on the effective thermal efficiency of IRTDSAH.

Table 11: Critical Reynolds number based on different values of P/e.

S. n	P/e	Maximum exergy efficiency (%)	Reynolds number
1	4	2.54	1878
2	8	2.63	1864
3	12	2.87	1843
4	16	2.72	1759

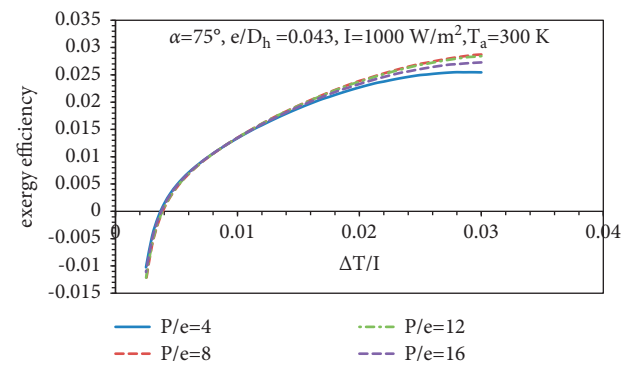

Figure 19: Influence of rib roughness pitch (p) to height (e) ratio (p/e) on the rise in temperature parameter on exergy thermal efficiency of IRTDSAH.

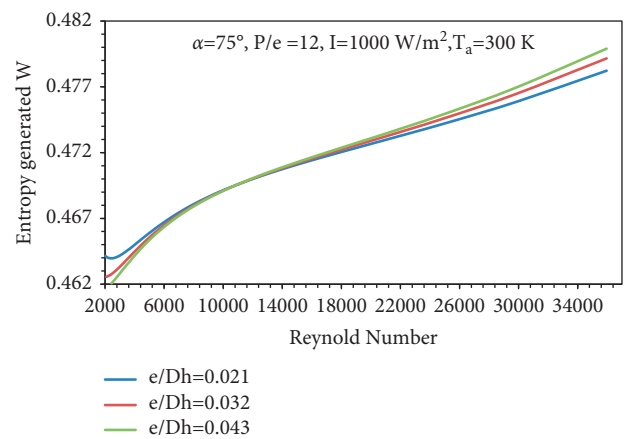

Figure 20: Influence of rib roughness height (e) ratio to hydraulic diameter (e/D_h) and Reynolds number on entropy generation of IRTDSAH.

I and α till $\Delta T/I$ 0.03 K·m^2/W. The maximum exergy efficiency value found in the analysis is 2.87% at $e/D_h = 0.043$. Comparatively, at higher p/e up to 12, the exergy efficiency is higher.

4.4. Entropy Generation. The influence of e/D_h value on entropy generation is described in Figure 20. From the figure, it is observed that the e/D_h value of 0.043 produces a lower value of entropy for the Re ranging from 2000 to 6000. Then increase in flow rate rise value of entropy generation and the maximum value destruction occurs during the operating condition that consists of the e/D_h value of 0.021.

5. Conclusion

In the present work, circular wire ribs attached over an absorber plate in an inclined manner act as an artificial roughness for a triangular duct solar air heater. The analytical model is used to evaluate the optimum dimensions of the roughness dimensions relative roughness height of 0.021–0.043, relative roughness pitch of 4–16 and inclination angle of the arc of 30 to 75°. From the analytical results, it is concluded that

(i) While increasing the roughness pitch (P) to height (e) ratio (P/e), roughness height (e) to hydraulic diameter (D_h) ratio (e/D_h), rib inclination angle (α), and mass flow rate improve the thermal performance of the system. It is also noticed that the exergy performance of IRTDSAH decreases with the increase in Reynolds number > 1864

(ii) The maximum thermal efficiency of 83.61% is obtained at P/e of 12, e/D of 0.042, and α of 75°. It is founded that the thermal efficiency is increased with the rise in all these parameters and obtains its maximum value at Re of 35000

(iii) The effective thermal efficiency attains its maximum value of 80.26% at the Re of 17543 with the roughness parameters ranges of P/e of 12, e/D of 0.042, and α of 75°

(iv) The maximum exergy efficiency of 2.62% is attained at the Re of 1864 at the optimized operating conditions. The air heater can produce a rise in temperature value 0.005 to 0.03 K·m^2/W as compared with other systems. The exergy based parameter optimization yields more accurate results to fix the roughness parameters

Nomenclature

Ac: Area of the collector
C_{pf}: Specific heat of air (J/kg K)
D_h: Triangular tube hydraulic diameter (m)
F_R: Triangular heater heat removal factor
Fr: Friction at triangular channel
h: Convective heat transfer coefficient (W/m^{2}K)
I: Solar radiation (W/m^2)
k: Thermal conductivity (W/m K)
L: Length of the triangular duct (m)
m: Mass flow rate (kg/s)
Nu: Nusselt number
P_m: Pumping power (W)
Q_u: Useful heat gain (W)
Re: Reynolds number
T: Temperature (K)
tg: Thickness of glass (m)
UL: Overall loss coefficient (W/mK)
W: Width of the duct (9 m)

Greek symbols
μ: Viscosity (Ns m^{-2})
ρ: Density (kg/m^3)
ε: Emissivity
α_τ: Product of transmittance and absorptance
β: Tilt angle (°)
η: Efficiency (%)
δ: Thickness of insulation (m)

Subscripts
a: Ambient air
c: Convection
g: Glass
p: Plate
i: Inlet
o: Outlet

Abbreviations
SAH: Solar air heater
IRTDSAH: Inclined rib roughened triangular duct solar air heater.

Data Availability

The data used to support the findings of this study are included within the article.

Conflicts of Interest

The authors declare that there are no conflicts of interest regarding the publication of this article.

References

[1] S. H. Farjana, N. Huda, M. A. P. Mahmud, and R. Saidur, "Solar process heat in industrial systems - a global review," *Renewable and Sustainable Energy Reviews*, vol. 82, pp. 2270–2286, 2018.

[2] V. Manoj Praveen, R. Vigneshkumar, N. Karthikeyan, A. Gurumoorthi, R. Vijayakumar, and P. Madhu, "Heat transfer enhancement of air-concrete thermal energy storage system - CFD simulation and experimental validation under transient condition," *Proceedings of the Institution of Mechanical Engineers - Part E: Journal of Process Mechanical Engineering*, vol. 235, no. 5, pp. 1304–1314, 2021.

[3] N. S. Suresh and B. S. Rao, "Solar energy for process heating: a case study of select Indian industries," *Journal of Cleaner Production*, vol. 151, pp. 439–451, 2017.

[4] V. Singh Bisht, A. Kumar Patil, and A. Gupta, "Review and performance evaluation of roughened solar air heaters," *Renewable and Sustainable Energy Reviews*, vol. 81, pp. 954–977, 2018.

[5] C.-S. Wang, C.-C. Chen, W.-C. Chang, and T.-M. Liou, "Experimental studies of turbulent pulsating flow and heat transfer in a serpentine channel with winglike turbulators," *International Communications in Heat and Mass Transfer*, vol. 131, Article ID 105837, 2022.

[6] P. Promvonge, P. Promthaisong, and S. Skullong, "Experimental and numerical thermal performance in solar receiver heat exchanger with trapezoidal louvered winglet and wavy groove," *Solar Energy*, vol. 236, pp. 153–174, 2022.

[7] G. Verma, S. Singh, S. Chander, and P. Dhiman, "Numerical investigation on transient thermal performance predictions of phase change material embedded solar air heater," *Journal of Energy Storage*, vol. 47, Article ID 103619, 2022.

[8] R. Kumar, A. Varun, and A. Kumar, "Thermal and fluid dynamic characteristics of flow through triangular cross-sectional duct: a review," *Renewable and Sustainable Energy Reviews*, vol. 61, pp. 123–140, 2016.

[9] V. Goel, P. Guleria, and R. Kumar, "Effect of apex angle variation on thermal and hydraulic performance of roughened triangular duct," *International Communications in Heat and Mass Transfer*, vol. 86, pp. 239–244, 2017.

[10] R. Kumar, A. Kumar, and V. Varun, "Computational fluid dynamics based study for analyzing heat transfer and friction factor in semicircular rib-roughened equilateral triangular duct," *International Journal of Numerical Methods for Heat and Fluid Flow*, vol. 27, no. 4, pp. 941–957, 2017.

[11] R. Kumar, A. Varun, and A. Kumar, "Experimental and computational fluid dynamics study on fluid flow and heat transfer in triangular passage solar air heater of different configurations," *Journal of Solar Energy Engineering*, vol. 139, no. 4, Article ID 041013, 2017.

[12] R. Kumar, A. Kumar, and V. Goel, "A parametric analysis of rectangular rib roughened triangular duct solar air heater using computational fluid dynamics," *Solar Energy*, vol. 157, pp. 1095–1107, 2017.

[13] G. Bharadwaj, R. Varun Kumar, R. Kumar, and A. Sharma, "Heat transfer augmentation and flow characteristics in ribbed triangular duct solar air heater: an experimental analysis," *International Journal of Green Energy*, vol. 14, no. 7, pp. 587–598, 2017.

[14] S. Singh, "Thermal performance analysis of semicircular and triangular cross-sectioned duct solar air heaters under external recycle," *Journal of Energy Storage*, vol. 20, pp. 316–336, 2018.

[15] R. Kumar, V. Goel, A. Kumar, S. Khurana, P. Singh, and S. B. Bopche, "Numerical investigation of heat transfer and friction factor in ribbed triangular duct solar air heater using Computational fluid dynamics (CFD)," *Journal of Mechanical Science and Technology*, vol. 32, no. 1, pp. 399–404, 2018.

[16] R. Kumar, S. Khurana, A. Kumar, and V. Goel, "Effect of dimple intrusions and curvature radius of rounded corner triangular duct on fluid flow and heat transfer," *Journal of Thermal Science and Engineering Applications*, vol. 11, no. 3, Article ID 031001, 2019.

[17] R. Kumar, A. Kumar, and V. Goel, "Effect of rounded corners on heat transfer and fluid flow through triangular duct," *Journal of Heat Transfer*, vol. 140, no. 12, Article ID 121709, 2018.

[18] S. K. Jain, G. D. Agrawal, R. Misra, P. Verma, S. Rathore, and D. K. Jamuwa, "Performance investigation of a triangular solar air heater duct having broken inclined roughness using computational fluid dynamics," *Journal of Solar Energy Engineering*, vol. 141, no. 6, Article ID 061008, 2019.

[19] K. Nidhul, S. Kumar, A. K. Yadav, and S. Anish, "Enhanced thermo-hydraulic performance in a V-ribbed triangular duct solar air heater: CFD and exergy analysis," *Energy*, vol. 200, Article ID 117448, 2020.

[20] R. Misra, J. Singh, S. K. Jain et al., "Prediction of behavior of triangular solar air heater duct using V-down rib with multiple gaps and turbulence promoters as artificial roughness: a CFD analysis," *International Journal of Heat and Mass Transfer*, vol. 162, Article ID 120376, 2020.

[21] K. Nidhul, S. Kumar, A. K. Yadav, and S. Anish, "Influence of rectangular ribs on exergetic performance in a triangular duct solar air heater," *Journal of Thermal Science and Engineering Applications*, vol. 12, no. 5, Article ID 051010, 2020.

[22] S. Kumar, R. Kumar, V. Goel, S. Bhattacharyya, and A. Issakhov, "Exergetic performance estimation for roughened triangular duct used in solar air heaters," *Journal of Thermal Analysis and Calorimetry*, vol. 145, no. 3, pp. 1661–1672, 2021.

[23] M. K. Sahu and R. K. Prasad, "Exergy based performance evaluation of solar air heater with arc-shaped wire roughened absorber plate," *Renewable Energy*, vol. 96, pp. 233–243, 2016.

[24] R. Chauhan and N. S. Thakur, "Investigation of the thermohydraulic performance of impinging jet solar air heater," *Energy*, vol. 68, pp. 255–261, 2014.

[25] M. M. Matheswaran, T. V. Arjunan, and D. Somasundaram, "Analytical investigation of solar air heater with jet impingement using energy and exergy analysis," *Solar Energy*, vol. 161, pp. 25–37, 2018.

[26] M. M. Matheswaran, T. V. Arjunan, and D. Somasundaram, "Energetic, exergetic and enviro-economic analysis of parallel pass jet plate solar air heater with artificial roughness," *Journal of Thermal Analysis and Calorimetry*, vol. 136, no. 1, pp. 5–19, 2019.

[27] M. K. Sahu, M. M. Matheswaran, and P. Bishnoi, "Experimental Investigation of Augmented thermal and performance Characteristics of Solar Air Heater Ducts Due to Varied Orientations of Roughness Geometry on the Absorber Plate," *Archives of Thermodynamics*, vol. 41, pp. 147–182, 2020.

[28] M. Matheswaran, T. Arjunan, and M. K. Sahu, "Influence of twisted tape fins on heat transfer and friction factor characteristics for impinging jet solar air heater," *Proceedings of the Institution of Mechanical Engineers - Part E: Journal of Process Mechanical Engineering*, vol. 235, no. 4, pp. 824–831, 2021.

Hindawi
Mathematical Problems in Engineering
Volume 2022, Article ID 7020979, 12 pages
https://doi.org/10.1155/2022/7020979

Research Article

An Improved Power Quality Disturbance Detection Using Deep Learning Approach

Kavaskar Sekar,[1] Karthick Kanagarathinam,[2] Sendilkumar Subramanian,[3] Ellappan Venugopal,[4] and C. Udayakumar[5]

[1]*Head-Power System Studies, KNR Engineers (INDIA) Private Limited, Chennai, India*
[2]*Department of Electrical and Electronics Engineering, GMR Institute of Technology, Rajam, India*
[3]*Department of Electrical and Electronics Engineering, S. A. Engineering College (Autonomous), Chennai, India*
[4]*Department of Electronics and Communication Engineering, School of Electrical Engineering and Computing, Adama Science and Technology University, Adama, Ethiopia*
[5]*Department of Electrical and Electronics Engineering, JKK Nattraja College of Engineering and Technology, Komarapalayam, India*

Correspondence should be addressed to Ellappan Venugopal; ellappan.venugopal@astu.edu.et

Received 14 November 2021; Accepted 25 April 2022; Published 21 May 2022

Academic Editor: Ravi Samikannu

Recently, the distribution network has been integrated with an increasing number of renewable energy sources (RESs) to create hybrid power systems. Due to the interconnection of RESs, there is an increase in power quality disturbances (PQDs). The aim of this article was to present an innovative method for detecting and classifying PQDs that combines convolutional neural networks (CNNs) and long short-term memory (LSTM). The disturbance signals are fed into a combined CNN and LSTM model, which automatically recognizes and classifies the features associated with power quality disturbances. In comparison with other methods, the proposed method overcomes the limitations associated with conventional signal analysis and feature selection. Additionally, to validate the proposed method's robustness, data samples from a modified IEEE 13-node hybrid system are collected and tested using MATLAB/Simulink. The results are good and encouraging.

1. Introduction

Renewable energy sources (RESs) can provide an efficient solution to increase in demand for electricity and also reduce the risk of pollution or global warming. However, the integration of RESs increases the use of solid-state devices, which overstress power quality disturbances (PQDs) such as harmonics, sag or swell in voltage, flicker, and voltage unbalance. Moreover, RESs have major characteristics of fluctuation and intermittent. The instability of renewable energy (RE) generation is an important cause of power quality disturbance, which guides voltage unbalance or fluctuation [1, 2]. The PQDs lead to a failure of electrical equipment [3]. It is understandable that these disturbances are a threat to grid when connected with multiple energy sources. Hence, there is an essential requirement to detect these PQDs to get better quality of power and keep the equipment away from failures. The identification and classification of PQDs depend mainly on feature extraction [4]. For feature extraction, several methods have been developed to detect and classify PQDs. The Fourier transform (FT) is a frequency-domain analysis and is suitable for stationary signal analysis. However, it is incapable to choose feature information when the signal is nonstationary. The discrete Fourier transform (DFT) and short-time Fourier transform (STFT) overcome the drawback of FT using a time-frequency window to localize transient in a signal proposed in [5]. The transient signals are not effectively designated in the STFT due to a fixed window. The S transform (ST) [6–9] uses a moving window, but the precision becomes lower while examining nonstationary transients.

The authors proposed a Hilbert–Huang transform (HHT)-based method for detecting the single and multiple PQD signals [10–12], but the HHT is unsuccessful to build a frequency spectrum that leads to a loss of frequency components having small energy contents. The DWT [13–19] methods are more suitable in the signal processing for PQDs to overcome the fixed resolution issue of STFT for analyzing the PQDs. The selection of suitable mother wavelets and sampling rate is the main challenge in DWT. Its accuracy relies on proper feature selection and classifier. Besides, all of these approaches are likely to be pretentious by the noise level of the signal and substantial computational work. Consequently, there is a requirement for a novel PQD detection with wide applicability.

Deep learning (DL) is very effective in automatic feature extraction of image and speech analysis. The DL can extract spatial and temporal features from the input without signal transformation [20]. The application of DL in the PQD problem not only improves the accuracy but also simplifies the process by eliminating handcrafted feature extraction. The application of convolutional neural networks (CNNs) in PQD classification is provided in [21], and the CNN combined with a long-short term memory (LSTM) is used for PQD classification in [22], but the training time, the number of parameters, and the performance against noise were not discussed. Besides, both [21, 22] have not considered the overfitting problem, which may extremely decline the accuracy of DNN. The PQDs are assessed based on a deep belief network in [23]. Although these methods are producing acceptable results in PQD detection in single PQDs, they scuffle with multiple PQDs.

The PQD signal is converted to a 2D image, which is input to DCNN for the detection and classification in [24]. The 2D image of the signal is entirely different from the 1D signal data. Moreover, multiple PQDs are not considered in this work. An effective technique is proposed in [25, 26] using DCNN for single and multiple PQD detection and classification. However, these methods need an enhancement. In this study, a PQD detection method based on combined CNN and LSTM is proposed. The contributions of work are enumerated as follows: (1) by analyzing single and multiple PQDs, the combination of CNN and LSTM layers eliminates manual feature extraction and enables automatic feature extraction and classification. (2) Since the computational complication of the CNN is high, the batch normalization (BN) layer is used to speed up the training process, and the reduced number of parameters is fed to LSTM. (3) To investigate the strength of the method, a complete evaluation of training parameters and accuracy with another model is conducted, including DCNN and CNN with the gated recurrent unit (GRU). 4). Further, to analyze the method, the data are collected by simulating a hybrid system with the PQDs and tested. The rest of this article is arranged as follows: Section 2 explains mathematical models of PQD. In Section 3, the construction proposed model is discussed. Section 4 presents the detailed results and comparison. Section 5 infers construction and verification of the proposed method on hybrid system. Section 6 concludes the work.

2. Power Quality Disturbance Data

A total of 16 PQDs are considered in this work, which include 10 single PQDs (normal, sag, swell, harmonics, flicker, interruption, spike, notch, impulsive, and oscillatory transient) and 6 multiple PQDs (sag with harmonics, sag with flicker, flicker with harmonics, interruption with harmonics, swell with harmonics, and swell with flicker). The proposed PQD detection method uses the data set, which is obtained from mathematical models given in Table 1.

The parameters of the mathematical model are varied as per the direction of IEEE 1159 standard [27]. In all the mathematical models of PQDs, the parameter "A" indicates the amplitude of the waveform and is set to 1 per unit. The factor "α" shows the intensity of the disturbances. The step function $u(t)$ of model presents the time span of PQD in a signal. Harmonic disturbance data use the 3rd, 5th, and 7th orders. The flicker frequency ($\propto_f$) varied from 5 to 20 Hz, and the corresponding flicker magnitude varied from 0.1 to 0.2 p.u. During oscillatory transient signal generation, f_n varies from 300 to 900 Hz, time constant (τ) varies from 0.008 to 0.04 s, and impulse magnitude ($\propto_i$) varies from 0 to 0.414 p.u. The notch or spike magnitude (k) varies from 0.1 to 0.4 p.u, and the width varies from 0.01 to 0.05 cycles. The sampling frequency of 3200 Hz is set because electric power signal recording equipment mostly uses the chosen sampling frequency. The generated signal contains 640 sampling points (10 cycles, 0.2 s) with the fundamental frequency of 50 Hz. In each PQD case, 8000 data have been generated by varying parameters, and hence, a total of 1,28,000 (8000×16 PQDs) data instances have been generated, but there is always some noise superimposed in the signal when it is actually collected from the real system through sensors. So, noise is added to the PQD data set with different signal-to-noise ratios (SNRs) of 20 dB to 40 dB, which increases the total data samples to 5,12,000 ($4 \times 1,28,000$). The details of data set used in this study are presented in Table 2. The characteristic PQ signals simulated by mathematical model equations are shown in Figure 1.

3. The Proposed Method

The disadvantages of conventional signal investigation and feature selection can be overwhelmed by DL. A CNN can be used to take widespread feature extraction by convolutional layer and feature dimension reduction by pooling. Hence, the CNN reveals better generalization capability than old-fashioned feature extraction methods. In PQD detection, a 1D convolutional operation is ensuring spatial feature extraction while holding temporal features. The LSTM network shows outstanding temporal feature extraction capability. The PQD detection is a kind of time-series signal data. This needs that the PQD detection model would hold exceptional temporal and spatial feature extraction capabilities. Consequently, 1D CNN and LSTM network are utilized in the PQD detection model. It extracts the spatial features by 1D CNN, and then, it extracts the temporal features by LSTM network. As a result, this model extracts

Table 1: Mathematical model for PQDs.

Label	Event	Mathematical models	Model parameters
C1	Normal	$x(t) = A[1 \pm \propto (u(t-t1) - u(t-t2))]\sin wt$	$\propto \leq 0.1,\ \mathrm{T} \leq t2 - t1 \leq 9T$
C2	Sag	$x(t) = A[1 - \propto (u(t-t1) - u(t-t2))]\sin wt$	$0.1 \leq \propto \leq 0.9,\ \mathrm{T} \leq t2 - t1 \leq 9T$
C3	Swell	$x(t) = A[1 + \propto (u(t-t1) - u(t-t2))]\sin wt$	$0.1 \leq \propto \leq 0.8,\ \mathrm{T} \leq t2 - t1 \leq 9T$
C4	Interruption	$x(t) = A[1 - \propto (u(t-t1) - u(t-t2))]\sin wt$	$0.9 \leq \propto \leq 1,\ \mathrm{T} \leq t2 - t1 \leq 9T$
C5	Harmonics	$x(t) = A[\propto_1 \sin wt + \propto_3 \sin(3wt) + \propto_5 \sin(5wt) + \propto_7 \sin(7wt)$	$0.05 \leq \propto_3, \propto_5, \propto_7 \leq 0.15,\ \sum \propto_i^2 = 1$
C6	Flicker	$x(t) = A[1 + \propto_f \sin(\beta wt)]\sin wt$	$0.1 \leq \propto_f \leq 0.2, 5 \leq \beta \leq 20\mathrm{Hz}$
C7	Oscillatory transient	$x(t) = A[\sin wt + \propto^{-c(t-t_1)/\tau} \sin w_n(t-t_1)(u(t_2) - u(t_1))]$	$0.1 \leq \propto \leq 0.8,\ 0.5T \leq t2 - t1 \leq 3T,$ $8 \leq \tau \leq 40\mathrm{ms}, 300 \leq f_n \leq 900\mathrm{Hz}$
C8	Impulsive transient	$x(t) = A[1 - \propto_i (u(t-t1) - u(t-t2))]\sin wt$	$0 \leq \propto_i \leq 0.414,\ T/20 \leq t2 - t1 \leq T/10$
C9	Notch	$x(t) = \sin(wt) - \mathrm{sign}(\sin(wt)) \times \left\{ \sum_{n=0}^{9} k[u(t - (t_1 - 0.02n)) - u(t - (t_1 - 0.02n))] \right\}$	$0.1 \leq k \leq 0.4,\ 0 \leq t2, t1 \leq 0.5T,\ 0.01T \leq t2 - t1 \leq 0.05T$
C10	Spike	$x(t) = \sin(wt) + \mathrm{sign}(\sin(wt)) \times \left\{ \sum_{n=0}^{9} k[u(t - (t_1 - 0.02n)) - u(t - (t_1 - 0.02n))] \right\}$	$0.1 \leq k \leq 0.4,\ 0 \leq t2, t1 \leq 0.5T,\ 0.01T \leq t2 - t1 \leq 0.05T$
C11	Sag with harmonics	$x(t) = A[1 - \propto (u(t-t1) - u(t-t2))][\propto_1 \sin wt + \propto_3 \sin(3wt) + \propto_5 \sin(5wt)]$	$0.1 \leq \propto \leq 0.9,\ \mathrm{T} \leq t2 - t1 \leq 9T,\ 0.05 \leq \propto_3, \propto_5, \propto_7 \leq 0.15,$ $\sum \propto_i^2 = 1$
C12	Swell with harmonics	$x(t) = A[1 + \propto (u(t-t1) - u(t-t2))][\propto_1 \sin wt + \propto_3 \sin(3wt) + \propto_5 \sin(5wt)]$	$0.1 \leq \propto \leq 0.8,\ \mathrm{T} \leq t2 - t1 \leq 9T,\ 0.05 \leq \propto_3, \propto_5, \propto_7 \leq 0.15,$ $\sum \propto_i^2 = 1$
C13	Flicker with harmonics	$x(t) = A[1 + \propto_f \sin(\beta wt)]\sin wt[\propto_1 \sin wt + \propto_3 \sin(3wt) + \propto_5 \sin(5wt)]$	$0.1 \leq \propto_f \leq 0.2,\ 5 \leq \beta \leq 20\mathrm{Hz},\ 0.05 \leq \propto_3, \propto_5, \propto_7 \leq 0.15,$ $\sum \propto_i^2 = 1$
C14	Interruption with harmonics	$x(t) = A[1 - \propto (u(t-t1) - u(t-t2))[\propto_1 \sin wt + \propto_3 \sin(3wt) + \propto_5 \sin(5wt)]]$	$0.1 \leq \propto \leq 0.9,\ \mathrm{T} \leq t2 - t1 \leq 9T,\ 0.05 \leq \propto_3, \propto_5, \propto_7 \leq 0.15,$ $\sum \propto_i^2 = 1$
C15	Flicker with sag	$x(t) = A[1 + \propto_f \sin(\beta wt)]\sin wt[1 - \propto (u(t-t1) - u(t-t2))]$	$0.1 \leq \propto \leq 0.9,\ \mathrm{T} \leq t2 - t1 \leq 9T,\ 0.1 \leq \propto_f \leq 0.2,\ 5 \leq \beta \leq 20\mathrm{Hz},$
C16	Flicker with swell	$x(t) = A[1 + \propto_f \sin(\beta wt)]\sin wt[1 + \propto (u(t-t1) - u(t-t2))]$	$0.1 \leq \propto \leq 0.8,\ \mathrm{T} \leq t2 - t1 \leq 9T,\ 0.1 \leq \propto_f \leq 0.2, 5 \leq \beta \leq 20\mathrm{Hz},$

Table 2: Data set.

	Samples number	Noise level
Training set	$32000 \times 16 = 512000$	20 dB to 40 dB
Validation set	$512000 \times 0.01 = 5120$	20 dB to 40 dB
Test set	$512000 \times 0.01 = 5120$	20 dB to 40 dB

the features of PQD more completely. The proposed structure of combined CNN and LSTM model is presented in Figure 2, which comprises pair of CNN (two convolutional layers + pooling layers) stacked with three LSTM layers and two fully connected layers at the end.

3.1. Convolutional Layers. The convolutional layer (CL) is the primary layer in CNN. It transfers low-level features into high-level features. The convolutional operator is accomplished on the input with a kernel to create features. The output of CL is given as follows:

$$y = f\left(w^r * x_i + b^r\right), \tag{1}$$

where y is the output of CL. w^r and b^r are the weight and bias of the rth layer, respectively, and $f(x)$ is the activation function. It comprehends the activation of a neuron to output. The rectified linear unit (ReLU) activation function is preferred in deep learning rather than the tanh function.

$$f_{\text{ReLU}} = \max(0, y). \tag{2}$$

3.2. Pooling Layer. A pooling layer is commonly added next to the CL. It is primarily used for downsampling. The pooling layer is used to reduce the dimension of the data after the convolution layer and extract vital information. It may decrease the influence of data fluctuations. For the PQD waveform, max pooling is better than average pooling and is hence used in this work. The mathematical expression for max pooling is given as follows:

$$f(y) = \max_i\left(y_i\right). \tag{3}$$

3.3. BN Layer. BN is a method to increase the speed of neural networks. It is used to normalize the input by means of adjusting and scaling the activations. It allows each network to learn by itself more independently than other layers. Besides, it reduces overfitting efficiently compared with dropout. The input data batch x_i may be normalized using the following formula:

$$y_i = \gamma \times \frac{x_i - \mu_x}{\sqrt{\varepsilon + \sigma_x{}^2}} + \beta, \tag{4}$$

where μ_x is the batch mean and $\sigma_x{}^2$ is the batch variance. The learned scale and shift parameters are given by Υ and β, respectively, ensuring that the input data have the same distribution.

3.4. Fully Connected Layer. It is also called the dense layer, and this layer has learning parameter D. The output of the dense layer is calculated by the following formula:

$$y = f\left(x * D^r + b^r\right). \tag{5}$$

3.5. Softmax Layer. The softmax layer computes the probability distribution of "n" output classes. Hence, the softmax layer is used to foresee the class to which the input data belong. The probability distribution is computed by the following equation:

$$P_i = \frac{e^{x_i}}{\sum e^{x_j}}, \quad j = 0, 1, 2, \ldots\ldots n, \tag{6}$$

where x_i is the input. The output of p lies between 0 and 1, and the sum of all the probabilities will be equal to 1. The softmax layer is used for PQD classification in this work.

3.6. LSTM. LSTM is capable of learning long-term dependencies. A LSTM unit is composed of a cell, input gate, output gate, and forget gate. The cell evokes value over arbitrary time intervals, and the three gates control the flow of information into and out of the cell [28]. The LSTM is well suited for classification problems based on time-series data. Figure 3 demonstrates the construction of LSTM, which comprises input gate, output gate, and forget gate. These gates pick and discard the information passing over the network. Input gate $i(t)$ has an activation function tanh ranging from −1 to 1.

It takes the current input $x(t)$, $C(t-1)$, and $h(t-1)$ parameters for processing. Forget gate $f(t)$ has two activation functions namely sigmoid and tanh. The forget gate chooses exactly how much information is retained from the previous output. The data are to be passed through the network when the value is 1. On the other hand, the data are not to be transformed into the network when the value is 0. The output gate $o(t)$ has an activation function of sigmoid ranging from −1 to 1. The following equations are used to compute $i(t)$, $o(t)$, and $f(t)$ at each and every time step:

$$\begin{aligned} i(t) &= \sigma\left(W^i\left[C^{t-1}h^{t-1} \times x^t\right] + b^i\right), \\ o(t) &= \sigma\left(W^o\left[C^{t-1}h^{t-1} \times x^t\right] + b^i\right), \\ f(t) &= \sigma\left(W^f\left[C^{t-1}h^{t-1} \times x^t\right] + b^i\right). \end{aligned} \tag{7}$$

3.7. GRU. The GRU is also a kind of RNN similar to LSTM with forget gate but has less parameters than LSTM [29]. It is also reducing time consumption in the training process due to lack of output gate. Hence, GRU is used for the PQD classification problem for comparison. A CNN stacked with GRU is used in this study for comparison.

4. Simulation Results

4.1. Metrics for Evaluation. The evaluation parameters of the proposed method are given as follows:

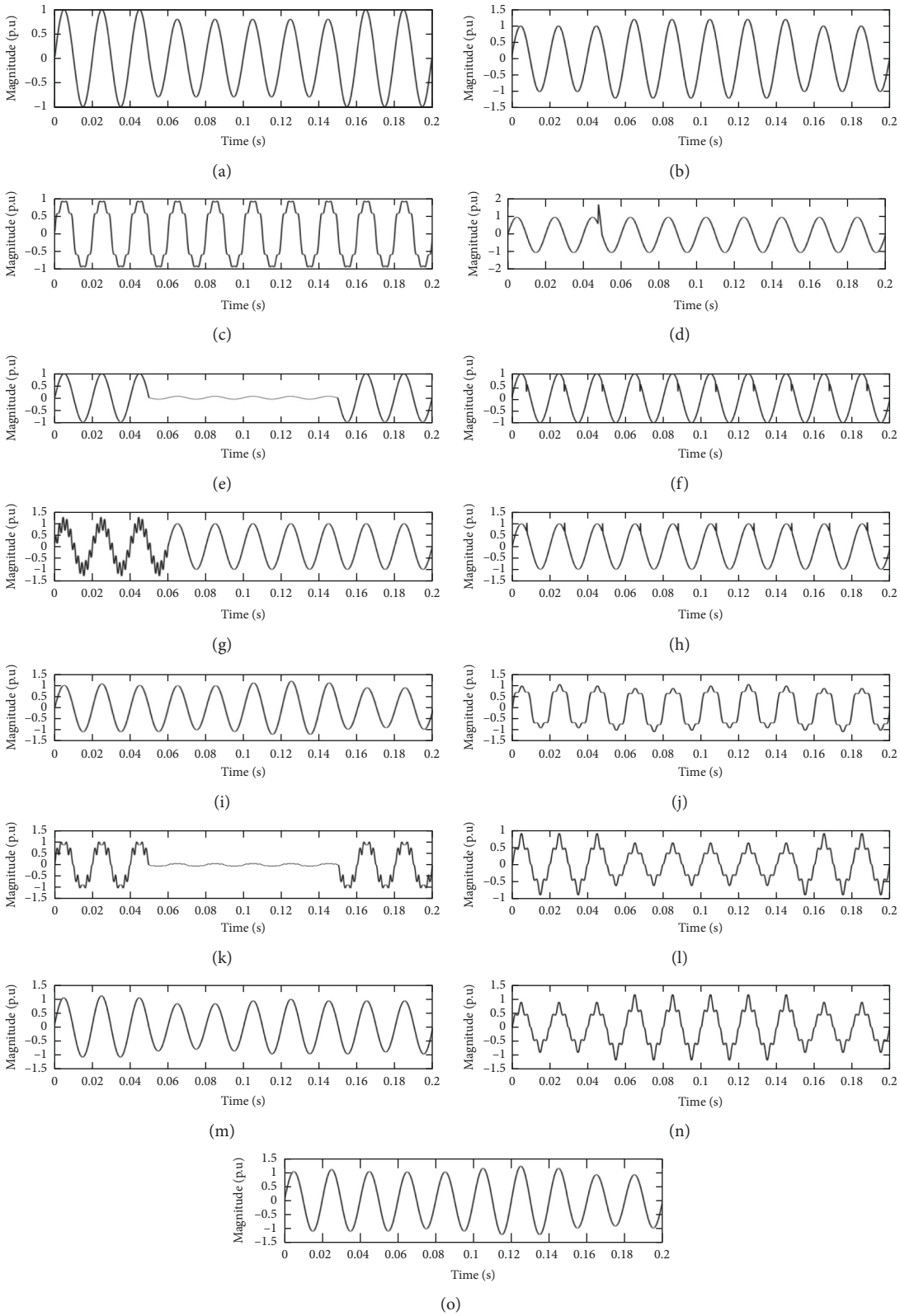

Figure 1: PQ disturbances: (a) sag, (b) swell, (c) harmonics, (d) impulse, (e) interruption, (f) notch, (g) oscillatory, (h) spike, (i) flicker, (j) flicker with harmonics, (k) interruption with harmonics, (l) sag with harmonics, (m) sag with flicker, (n) swell with harmonics, and (o) swell with flicker.

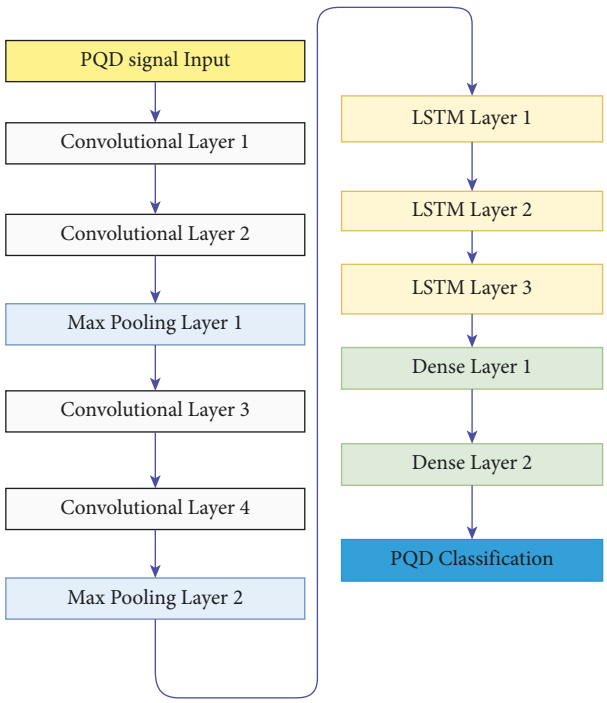

Figure 2: Proposed CNN + LSTM architecture.

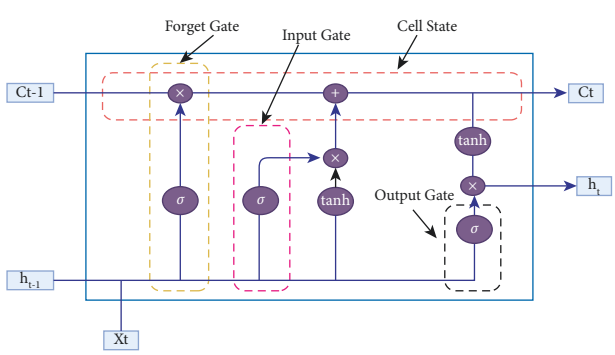

Figure 3: LSTM network.

Confusion Matrix: it is used to assess the classification performance of a model.

Accuracy = (true positive + true negative)/total test cases

Precision = true positive/(true positive + true negative)

Recall = true positive/(true positive + false negative)

F1 Score = 2 ∗ precision ∗ recall/(precision + recall)

4.2. Results and Discussions. Initially, 512000 samples have been produced as described in Section 2. From the total data set, 98% are used for training, 1% for validation, and 1% for testing. Usually, the training procedure is done with a mini-batch in deep learning. The mini-batch size is chosen as 64 for all three models, such that the training time of different methods is computed accurately. A total of 100 epochs are chosen in this work. However, in each epoch, loss during validation was monitored. The validation loss does not drop

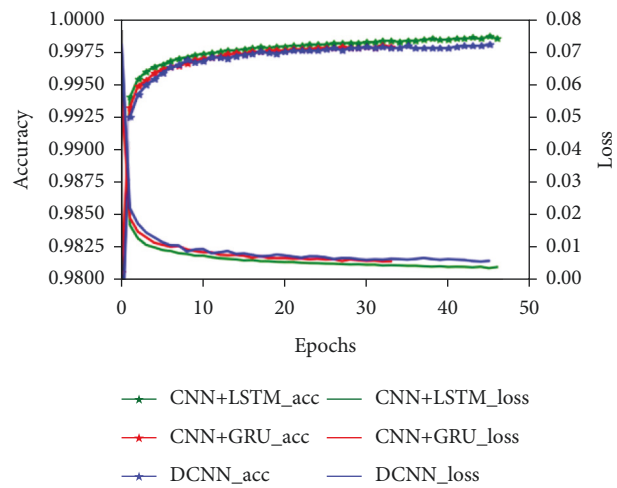

Figure 4: Comparison of training accuracy and loss of different DL models.

for incessant 20 epochs, and the training algorithm would be finished in advance of the scheduled epoch to evade overfitting. Then, the model with the top show in the validation set is chosen as the ultimate model. Moreover, the Python coding for the complete architecture of the proposed CNN + LSTM was carried out in Tesla K80 GPU in this work. During the training, the accuracy and loss values of all models are shown in Figure 4. It is noted that the CNN + LSTM model has better accuracy and less loss during training compared with the other two models.

For all three models, the details of final models and their properties such as parameters, training time, elapsed epochs, accuracy, and loss during validation are presented in Table 3. The combined CNN and LSTM model has less training parameters and produces better classification accuracy during validation. A total of 5120 cases were considered during testing, and the confusion matrices of all three models are shown in Tables 4-6. It was noted that the DCNN model accurately classified 5105 cases and 15 cases are misclassified that produces an accuracy of 99.70%. The combined CNN and GRU has classified 5109 cases correctly and produces the classification accuracy of 99.78%. The proposed method (CNN + LSTM) produces better calcification accuracy of 99.90% with only 5 cases that were misclassified.

Table 7 shows the effectiveness of the combined CNN and LSTM method in terms of precision, recall, andF1 score. The proposed CNN + LSTM model produced 99.90% precision (macro-average), while other deep learning models such as CNN + GRU and DCNN attained 99.79% and 99.71%, respectively. Similarly, F1 score for CNN + LSTM is 99.92%, while CNN + GRU has 99.78% and DCNN has 99.71%. The proposed CNN + LSTM model has the highest precision and F1 score compared with the other DL models. Hence, the proposed CNN + LSTM model outclassed the other models in terms of evaluation parameters.

To test the proposed model under noise grade, 1% of data from each category (both no noise and noise grade) has been randomly selected and the test results are presented in

Table 3: DNN training model performance.

Type of model	Time consumed during each epoch (s)	Total parameters	Best validation loss	Best validation accuracy	Training time (s)	Elapsed epoch
CNN + LSTM	77	95632	0.0032	0.9990	3619	47
CNN + GRU	78	100944	0.0037	0.9978	2652	34
DCNN	97	174820	0.0040	0.9970	4462	46

Table 4: Confusion matrix of combined CNN and LSTM.

Actual	Predicted															
	C1	C2	C3	C4	C5	C6	C7	C8	C9	C10	C11	C12	C13	C14	C15	C16
C1	304	-	-	-	-	-	-	-	-	-	-	-	-	-	-	-
C2	1	319	-	-	-	-	-	1	-	-	-	-	-	-	-	-
C3	3	-	303	-	-	-	-	-	-	-	-	-	-	-	-	-
C4	-	-	-	299	-	-	-	-	-	-	-	-	-	-	-	-
C5	-	-	-	-	287	-	-	-	-	-	-	-	-	-	-	-
C6	-	-	-	-	-	327	-	-	-	-	-	-	-	-	-	-
C7	-	-	-	-	-	-	309	-	-	-	-	-	-	-	-	-
C8	-	-	-	-	-	-	-	345	-	-	-	-	-	-	-	-
C9	-	-	-	-	-	-	-	-	342	-	-	-	-	-	-	-
C10	-	-	-	-	-	-	-	-	-	304	-	-	-	-	-	-
C11	-	-	-	-	-	-	-	-	-	-	307	-	-	-	-	-
C12	-	-	-	-	-	-	-	-	-	-	-	360	-	-	-	-
C13	-	-	-	-	-	-	-	-	-	-	-	-	308	-	-	-
C14	-	-	-	-	-	-	-	-	-	-	-	-	-	311	-	-
C15	-	-	-	-	-	-	-	-	-	-	-	-	-	-	361	-
C16	-	-	-	-	-	-	-	-	-	-	-	-	-	-	-	329

Table 5: Confusion matrix of combined CNN and GRU.

Actual	Predicted															
	C1	C2	C3	C4	C5	C6	C7	C8	C9	C10	C11	C12	C13	C14	C15	C16
C1	300	-	3	-	-	-	-	-	1	-	-	-	-	-	-	-
C2	1	319	-	-	-	-	-	1	-	-	-	-	-	-	-	-
C3	2	-	304	-	-	-	-	-	-	-	-	-	-	-	-	-
C4	-	-	-	299	0	-	-	-	-	-	-	-	-	-	-	-
C5	-	-	-	-	287	-	-	-	-	-	-	-	-	-	-	-
C6	-	-	-	-	-	327	-	-	-	-	-	-	-	-	-	-
C7	-	-	-	-	-	-	309	-	-	-	-	-	-	-	-	-
C8	-	-	-	-	-	-	-	345	-	-	-	-	-	-	-	-
C9	-	-	-	-	-	-	-	-	341	1	-	-	-	-	-	-
C10	-	-	-	-	-	-	-	-	-	304	-	-	-	-	-	-
C11	-	-	-	-	-	-	-	-	-	-	307	-	-	-	-	-
C12	-	-	-	-	-	-	-	-	-	-	-	360	-	-	-	-
C13	-	-	-	-	-	-	-	-	-	-	-	-	308	-	-	-
C14	-	-	-	-	-	-	-	-	-	-	-	-	-	311	-	-
C15	-	-	-	-	-	-	-	-	-	-	-	-	-	2	359	-
C16	-	-	-	-	-	-	-	-	-	-	-	-	-	-	-	329

Table 8. The DCNN has provided good accuracy with pure signal (no noise signal). On the other hand, when the noise grade increases the performance is very poor. It uses 174410 trainable parameters and 410 non-trainable parameters. The LSTM + GRU model has a slight improvement in accuracy in all the categories of noise grade. However, the CNN + LSTM proposed in this work produces 100% classification rate for less noise grade and 99.31% under the worst noise grade of 20 dB as well. It uses 95632 parameters with training time of 95 s per epoch on GPU. This shows that the CNN + LSTM is an effective method to identify comprehensive features of each PQD. The performance of CNN + LSTM is better than CNN + GRU and DCNN under different noise levels.

4.3. Comparison of Computational Time. The DNNs may be performed on GPU to accomplish greater speed. The total number of units in GPU is greater than the CPU processor.

Table 6: Confusion matrix of DCNN.

Actual	Predicted															
	C1	C2	C3	C4	C5	C6	C7	C8	C9	C10	C11	C12	C13	C14	C15	C16
C1	300	-	3	-	-	-	-	-	1	-	-	-	-	-	-	-
C2	1	319	-	-	-	-	-	1	0	-	-	-	-	-	-	-
C3	2	-	304	-	-	-	-	-	-	-	-	-	-	-	-	-
C4	-	-	-	299	-	-	-	-	-	-	-	-	-	-	-	-
C5	-	-	-	-	287	-	-	-	-	-	-	-	-	-	-	-
C6	-	-	-	-	-	-	-	-	-	-	-	-	-	-	-	-
C7	-	-	-	-	-	-	309	-	-	-	-	-	-	-	-	-
C8	-	-	-	-	-	-	-	345	-	-	-	-	-	-	-	-
C9	-	-	-	-	-	-	-	-	341	1	-	-	-	-	-	-
C10	-	-	-	-	-	-	-	-	-	304	-	-	-	-	-	-
C11	-	-	-	-	-	-	-	-	-	0	307	-	-	-	-	-
C12	-	-	-	-	-	-	-	-	-	0	0	360	-	-	-	-
C13	-	-	-	-	-	-	-	-	-	-	-	-	307	-	1	-
C14	-	-	-	-	-	-	-	-	-	-	-	-	-	310	-	1
C15	-	-	-	-	-	-	-	-	-	-	-	-	-	2	359	-
C16	-	-	-	-	-	-	-	-	-	-	-	-	-	-	-	327

Table 7: Evaluation parameters of the three models.

Actual	CNN + LSTM			CNN + GRU			DCNN		
	Precision	Recall	F1 score	Precision	Recall	F1 score	Precision	Recall	F1 score
C1	1.0000	0.9902	0.9951	0.9868	0.9901	0.9885	0.9868	0.9901	0.9885
C2	0.9938	1.0000	0.9969	0.9938	1.0000	0.9969	0.9938	1.0000	0.9969
C3	0.9902	1.0000	0.9951	0.9935	0.9902	0.9918	0.9935	0.9902	0.9918
C4	1.0000	1.0000	1.0000	1.0000	1.0000	1.0000	1.0000	1.0000	1.0000
C5	1.0000	1.0000	1.0000	1.0000	1.0000	1.0000	1.0000	1.0000	1.0000
C6	1.0000	1.0000	1.0000	1.0000	1.0000	1.0000	1.0000	1.0000	1.0000
C7	1.0000	1.0000	1.0000	1.0000	1.0000	1.0000	1.0000	1.0000	1.0000
C8	1.0000	0.9971	0.9986	1.0000	0.9971	0.9986	1.0000	0.9971	0.9986
C9	1.0000	1.0000	1.0000	0.9971	0.9971	0.9971	0.9971	0.9971	0.9971
C10	1.0000	1.0000	1.0000	1.0000	0.9967	0.9984	1.0000	0.9967	0.9984
C11	1.0000	1.0000	1.0000	1.0000	1.0000	1.0000	1.0000	1.0000	1.0000
C12	1.0000	1.0000	1.0000	1.0000	1.0000	1.0000	1.0000	1.0000	1.0000
C13	1.0000	1.0000	1.0000	1.0000	1.0000	1.0000	0.9968	1.0000	0.9984
C14	1.0000	1.0000	1.0000	1.0000	0.9936	0.9968	0.9968	0.9936	0.9952
C15	1.0000	1.0000	1.0000	0.9945	1.0000	0.9972	0.9945	0.9917	0.9931
C16	1.0000	1.0000	1.0000	1.0000	1.0000	1.0000	0.9939	0.9970	0.9954
Average	0.9990	0.9992	0.9991	0.9979	0.9978	0.9978	0.9971	0.9971	0.9971

Hence, the computational speed for DCNN on GPU is very fast. The computational time of DCNN is considerably lesser due to its parallel computation of GPU. The computation time in GPU and CPU is compared for 512000 samples in the DCNN model in Table 9.

4.4. Comparison with Existing Work. To validate the proposed method, the comparison has been done with existing DCNN and the conventional methods. The performance of different methods under complex PQ disturbances is listed in Table 10. This shows that the conventional methods require features from signal transformation before classification. Basically, the variance in the number and type of features produces a difference in the classification rate. For example, the FDST and DT designed with twenty features produced an accuracy of 99.28% [33]. Conversely, the ST and RF attained 99.7% of accuracy with only four features [30]. Hence, the multiple information is captured by CNN + LSTM, which makes it promising for automatic feature extraction. The proposed CNN + LSTM shows the superiority of the model compared with the traditional models. The proposed CNN + LSTM considered sixteen PQDs and produced 100% accuracy for low noise grade and 99.31% under the worst noise grade compared with the other DL models and other traditional methods.

5. Simulation of PQDs in Hybrid System

5.1. Hybrid System Studied. To further analyze the proposed method, a standard IEEE 13-node system [34] is modified to form a hybrid system as shown in Figure 5.

The hybrid system model is generated by incorporating the wind and solar photovoltaic (PV) cells into a standard

Table 8: Performance of DCNN and hybrid CNN.

PQD label	The performance of DL model under noise grade											
	DCNN				CNN + GRU				CNN + LSTM			
	Pure	40 dB	30 dB	20 dB	Pure	40 dB	30 dB	20 dB	Pure	40 dB	30 dB	20 dB
C1	100.00	100.00	98.81	97.62	100.00	100.00	100.00	100.00	100.00	100.00	100.00	100.00
C2	100.00	98.63	98.63	97.26	100.00	98.63	98.63	97.26	100.00	100.00	98.63	98.63
C3	100.00	98.67	98.67	98.67	100.00	100.00	98.67	98.67	100.00	100.00	98.67	97.33
C4	100.00	100.00	100.00	98.63	100.00	100.00	100.00	98.63	100.00	100.00	100.00	100.00
C5	100.00	100.00	100.00	98.73	100.00	100.00	100.00	98.73	100.00	100.00	100.00	100.00
C6	100.00	100.00	100.00	98.65	100.00	100.00	100.00	98.65	100.00	100.00	100.00	100.00
C7	100.00	100.00	100.00	98.73	100.00	100.00	100.00	100.00	100.00	100.00	100.00	100.00
C8	100.00	100.00	98.81	98.81	100.00	100.00	98.81	98.81	100.00	100.00	100.00	100.00
C9	100.00	100.00	100.00	98.78	100.00	100.00	97.56	98.78	100.00	100.00	100.00	100.00
C10	100.00	100.00	100.00	98.90	100.00	100.00	100.00	98.90	100.00	100.00	100.00	100.00
C11	100.00	100.00	98.81	98.81	100.00	100.00	100.00	100.00	100.00	100.00	100.00	100.00
C12	100.00	100.00	98.25	98.28	100.00	100.00	98.25	98.28	100.00	100.00	98.25	96.55
C13	100.00	100.00	100.00	97.78	100.00	100.00	98.89	98.89	100.00	100.00	100.00	100.00
C14	100.00	100.00	98.82	98.82	100.00	100.00	100.00	98.82	100.00	100.00	100.00	100.00
C15	100.00	100.00	97.59	98.80	100.00	100.00	100.00	98.80	100.00	100.00	100.00	97.59
C16	100.00	98.84	98.84	98.84	100.00	98.84	98.84	98.84	100.00	100.00	98.84	98.84
Average	**100.00**	**99.76**	**99.20**	**98.51**	**100.00**	**99.84**	**99.35**	**98.88**	**100.00**	**100.00**	**99.66**	**99.31**

Table 9: Impact of processor on training time.

Processor	Training time (s)	
	For 128000 samples	For 512000 samples
GPU (Tesla K80)	24	95
CPU (Intel i7 Processor)	90	360

Table 10: Comparison with the existing methods.

Methods	Number of features selected	Number of PQDs	Accuracy in %			
			Pure	40 dB	30 dB	20 dB
WPT and GA [18]	15	8	98.33	-	-	-
WT and PSO [19]	11	9	98	96.87	93.625	–
ST and RF [30]	4	15	99.7	99.9	99.7	95.9
FFT and ANNs [31]	–	8	–	93.95	95.65	–
ST and PNN [32]	4	11	97.4	-	-	-
FDST and DT [33]	20	13	99.28	98.8	97.49	–
Deep CNN [24]	AUTO	9	99.67	-	-	-
Deep CNN [25]	AUTO	16	99.96	99.95	99.66	98.13
Deep CNN [26]	AUTO	24	-	-	-	99.26
The proposed CNN + LSTM	**AUTO**	**16**	**100**	**100**	**99.69**	**99.31**

IEEE 13-node test system. In the modified system, a wind energy conversion system (WECS) with doubly fed induction motor (DFIG) rated 1.5 MW, 575 V integrated at bus 680 through the transformer XWG, and an 8 km overhead transmission line. The model parameters of wind energy system have been reported in [35]. Similarly, a PV plant with the capacity of 1 MW is connected to the grid through the transformer XSPV at node 680, and the model parameters of complete PV system have been reported in [36]. Consequently, node 680 is considered as a point of common coupling (PCC). The complete experimental parameters such as load details, transformer data, and feeder details of the proposed system are provided in [37]. A capacitor bank is associated with nodes 611 and 675. The nonlinear load is connected to node 680 in the modified IEEE 13-node test system, and voltage regulator between nodes 632 and 650 is not used.

5.2. Generation of PQDs in Hybrid System. The modified IEEE 13-node system is simulated in MATLAB/Simulink. A normal waveform is produced at standard voltage and frequency. The voltage sag signal may be produced by adding line to ground faults at the generation side, switching huge

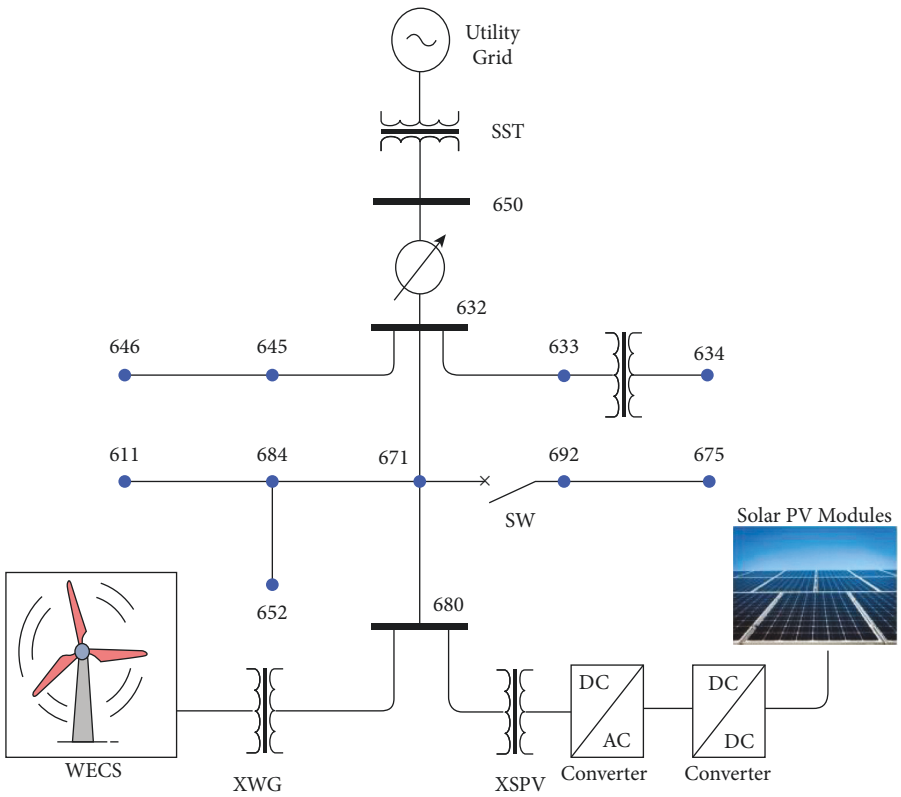

Figure 5: Modified hybrid system.

Table 11: Confusion matrix of hybrid system.

Actual	Predicted												
	C1	C2	C3	C4	C5	C6	C7	C8	C9	C10	Precision	Recall	F1 score
C1	80	0	0	0	0	0	0	0	0	0	100.00	98.77	99.38
C2	0	79	0	0	0	0	0	1	0	0	98.75	100.00	99.37
C3	**1**	0	79	0	0	0	0	0	0	0	98.75	100.00	99.37
C4	0	0	0	80	0	0	0	0	0	0	100.00	100.00	100.00
C5	0	0	0	0	80	0	0	0	0	0	100.00	100.00	100.00
C6	0	0	0	0	0	80	0	0	0	0	100.00	100.00	100.00
C7	0	0	0	0	0	0	80	0	0	0	100.00	100.00	100.00
C8	0	0	0	0	0	0	0	80	0	0	100.00	97.56	98.77
C9	0	0	0	0	0	0	0	1	79	0	98.75	100.00	99.37
C10	0	0	0	0	0	0	0	0	0	80	100.00	100.00	100.00
Average											99.63	99.63	99.63

load at a time, and sudden start-up of wind turbine. Voltage swell signals are generated by removing huge load in the system or by adding line to line faults at the generator end. For the generation of voltage interruption signal, the system is operated in islanding mode with the huge load in DGs that are tripped. Harmonics and notch are generated by connecting nonlinear loads. An oscillatory transient and spike are generated by switching a capacitor bank to the system due to the islanding process. The arc furnace model is connected at the load side to create flickering waveforms [38]. An impulsive transient is generated by connecting the lightning model in the system.

The multiple PQDs may be produced by simultaneous presentations of faults, switching, and mode changing of the grid. Nevertheless, there is less opportunity for multiple PQDs at a time in any system. Therefore, on a hybrid system only single PQDs with 200 cases are generated by changing different combinations of grid operations. These samples are added with noise (40 dB, 30 dB, and 20 dB) such that the total samples are 800 (200×4). All these samples are validated through the proposed CNN + LSTM method, and the test results are presented in Table 11. It is noted that 797 among 800 cases are classified correctly with the classification rate of 99.63%. The evaluation metrics such as precision, recall, and F1 score is the same as accuracy with 99.63%, which infers that the proposed DL model works better even though the test data set is different. These results show that the proposed DL model is a more generalized model for the detection and classification of PQDs.

6. Conclusion

This study proposes an application of combined CNN and LSTM to the PQD classification. The proposed CNN + LSTM comprehends an automatic feature extraction and selection and eliminates conventional ladders to enhance PQD detection. The proposed CNN + LSTM is compared with the other models such as DCNNs and CNN + GRU. The result indicates that the proposed CNN + LSTM method has higher accuracy, while taking less training than the other DL models. Compared with the existing methods, the CNN + LSTM algorithm performs well in noisy environments. The number of the parameters and complexity of the CNN + LSTM model are reduced, and hence, the computation speed is less. The proposed method is validated with a hybrid system and evidenced to achieve PQD classification with high accuracy. The proposed method is comprehended under offline environments. However, the online implementation is considered in future work.

Data Availability

The generated data set is available with this article as a supplementary file.

Conflicts of Interest

The authors have no conflicts of interest to declare.

Supplementary Materials

The generated signal contains 640 sampling points (10 cycles, 0.2 s) with the fundamental frequency of 50 Hz. In each PQD case, 8000 data have been generated by varying parameters, and hence, a total of 1,28,000 (8000×16 PQDs) data have been generated. The noise is superimposed on the signal when it is actually collected from the real system through sensors. So, noise is added to the PQD data set with different signal-to-noise ratios (SNRs) of 20 dB, 30 dB, and 40 dB, which increases the total data samples to 5,12,000 ($4 \times 1{,}28{,}000$). The following is the description of each file: x0db_test.txt: data of 0 dB noise; x20db_test.txt: data of 20 dB noise superimposed on the signal; x30db_test.txt: data of 30 dB noise superimposed on the signal; x40db_test.txt: data of 40 dB noise superimposed on the signal. (*Supplementary Materials*)

References

[1] X. Liang, "Emerging power quality challenges due to integration of renewable energy sources," *IEEE Transactions on Industry Applications*, vol. 53, no. 2, pp. 855–866, 2017.

[2] O. P. Mahela, A. G. Shaik, and N. Gupta, "A critical review of detection and classification of power quality events," *Renewable and Sustainable Energy Reviews*, vol. 41, pp. 495–505, 2015.

[3] R. Ahila, V. Sadasivam, and K. Manimala, "An integrated PSO for parameter determination and feature selection of ELM and its application in classification of power system disturbances," *Applied Soft Computing*, vol. 32, pp. 23–37, 2015.

[4] C.-Y. Lee and Y.-X. Shen, "Optimal feature selection for power-quality disturbances classification," *IEEE Transactions on Power Delivery*, vol. 26, no. 4, pp. 2342–2351, October 2011.

[5] Y. H. Gu and M. H. J. Bollen, "Time-frequency and time-scale domain analysis of voltage disturbances," *IEEE Transactions on Power Delivery*, vol. 15, no. 4, pp. 1279–1284, 2000.

[6] I. W. C. Lee and P. K. Dash, "S-transform-based intelligent system for classification of power quality disturbance signals," *IEEE Transactions on Industrial Electronics*, vol. 50, no. 4, pp. 800–805, 2003.

[7] P. K. Dash, B. K. Panigrahi, and G. Panda, "Power quality analysis using S-transform," *IEEE Transactions on Power Delivery*, vol. 18, no. 2, pp. 406–411, 2003.

[8] H. S. Behera, P. K. Dash, and B. Biswal, "Power quality time series data mining using S-transform and fuzzy expert system," *Applied Soft Computing*, vol. 10, no. 3, pp. 945–955, 2010.

[9] N. Huang, D. Xu, X. Liu, and L. Lin, "Power quality disturbances classification based on S-transform and probabilistic neural network," *Neurocomputing*, vol. 98, pp. 12–23, 2012.

[10] R. Kumar, B. Singh, and D. T. Shahani, "Recognition of single-stage and multiple power quality events using hilbert-huang transform and probabilistic neural network," *Electric Power Components and Systems*, vol. 43, no. 6, pp. 607–619, 2015.

[11] M. J. Afroni, D. Sutanto, and D. Stirling, "Analysis of nonstationary power-quality waveforms using iterative Hilbert Huang transform and SAX algorithm," *IEEE Transactions on Power Delivery*, vol. 28, no. 4, pp. 2134–2144, 2013.

[12] S. Shukla, S. Mishra, and B. Singh, "Empirical-mode decomposition with Hilbert transform for power-quality assessment," *IEEE Transactions on Power Delivery*, vol. 24, no. 4, pp. 2159–2165, 2009.

[13] P. Kanirajan and V. Suresh Kumar, "Power quality disturbance detection and classification using wavelet and RBFNN," *Applied Soft Computing*, vol. 35, pp. 470–481, 2015.

[14] S. Khokhar, A. A. Mohd Zin, A. P. Memon, and A. S. Mokhtar, "A new optimal feature selection algorithm for classification of power quality disturbances using discrete wavelet transform and probabilistic neural network," *Measurement*, vol. 95, pp. 246–259, 2017.

[15] M. A. S. Masoum, S. Jamali, and N. Ghaffarzadeh, "Detection and classification of power quality disturbances using discrete wavelet transform and wavelet networks," *IET Science, Measurement & Technology*, vol. 4, no. 4, pp. 193–205, 2010.

[16] P. K. Ray, S. R. Mohanty, and N. Kishor, "Disturbance detection in grid-connected distributed generation system using wavelet and S-transform," *Electric Power Systems Research*, vol. 81, no. 3, pp. 805–819, 2011.

[17] U. D. Dwivedi and S. N. Singh, "Denoising techniques with change-point Approach for wavelet-based power-quality monitoring," *IEEE Transactions on Power Delivery*, vol. 24, no. 3, pp. 1719–1727, 2009.

[18] K. Manimala, K. Selvi, and R. Ahila, "Optimization techniques for improving power quality data mining using wavelet packet based support vector machine," *Neurocomputing*, vol. 77, no. 1, pp. 36–47, 2012.

[19] R. Hooshmand and A. Enshaee, "Detection and classification of single and combined power quality disturbances using

fuzzy systems oriented by particle swarm optimization algorithm," *Electric Power Systems Research*, vol. 80, no. 12, pp. 1552–1561, 2010.

[20] J. Schmidhuber, "Deep learning in neural networks: an overview," *Neural Networks*, vol. 61, pp. 85–117, 2015.

[21] E. Balouji and O. Salor, "Classification of power quality events using deep learning on event images," in *Proceedings of the 2017 Third International Conference on Pattern Recognition and Image Analysis*, pp. 216–221, IPRIA), Shahrekord, Iran, April 2017.

[22] N. Mohan, K. P. Soman, and R. Vinayakumar, "Deep power: deep learning architectures for power quality disturbances classification," in *Proceedings of the 2017 International Conference on Technological Advancements in Power and Energy*, pp. 1–6, TAP Energy), Kollam, India, December 2017.

[23] C. Li, Z. Li, N. Jia, Z. Qi, and J. Wu, "Classification of power-quality disturbances using deep belief network," in *Proceedings of the 2018 International Conference on Wavelet Analysis and Pattern Recognition*, pp. 231–237, ICWAPR), Chengdu, China, July 2018.

[24] K. Cai, W. Cao, L. Aarniovuori, H. Pang, Y. Lin, and G. Li, "Classification of power quality disturbances using wigner-ville distribution and deep convolutional neural networks," *IEEE Access*, vol. 7, Article ID 119099, 2019.

[25] S. Wang and H. Chen, "A novel deep learning method for the classification of power quality disturbances using deep convolutional neural network," *Applied Energy*, vol. 235, pp. 1126–1140, 2019.

[26] W. Qiu, Q. Tang, J. Liu, and W. Yao, "An automatic identification framework for complex power quality disturbances based on multifusion convolutional neural network," *IEEE Transactions on Industrial Informatics*, vol. 16, no. 5, pp. 3233–3241, 2020.

[27] Ieee Recommended Practice for Monitoring Electric Power Quality, *IEEE Standard 1159–2019*, IEEE, Piscataway, NJ, USA, 2019.

[28] S. Hochreiter and J. Schmidhuber, "Long short-term memory," *Neural Computation*, vol. 9, no. 8, pp. 1735–1780, 1997.

[29] S. Li, W. Li, C. Cook, C. Zhu, and Y. Gao, "Independently recurrent neural network (IndRNN): building A longer and deeper RNN," in *Proceedings of the 2018 IEEE/CVF Conference on Computer Vision and Pattern Recognition*, pp. 5457–5466, Salt Lake City, UT, USA, 2018.

[30] N. Huang, G. Lu, G. Cai et al., "Feature selection of power quality disturbance signals with an entropy-importance-based random forest," *Entropy*, vol. 18, no. 2, pp. 44–65, 2016.

[31] F. A. S. Borges, R. A. S. Fernandes, I. N. Silva, and C. B. S. Silva, "Feature extraction and power quality disturbances classification using smart meters signals," *IEEE Transactions on Industrial Informatics*, vol. 12, no. 2, pp. 824–833, 2016.

[32] S. Mishra, C. N. Bhende, and B. K. Panigrahi, "Detection and classification of power quality disturbances using S-transform and probabilistic neural network," *IEEE Transactions on Power Delivery*, vol. 23, no. 1, pp. 280–287, 2008.

[33] M. Biswal and P. K. Dash, "Detection and characterization of multiple power quality disturbances with a fast S-transform and decision tree based classifier," *Digital Signal Processing*, vol. 23, no. 4, pp. 1071–1083, 2013.

[34] W. H. Kersting, "Radial distribution test feeders," *IEEE Transactions on Power Systems*, vol. 6, no. 3, pp. 975–985, 1991.

[35] O. P. Mahela and A. G. Shaik, "Power quality detection in distribution system with wind energy penetration using discrete wavelet transform," in *Proceedings of the 2015 Second International Conference on Advances in Computing and Communication Engineering*, pp. 328–333, Dehradun, India, May 2015.

[36] O. P. Mahela and A. G. Shaik, "Detection of power quality events associated with grid integration of 100kW solar PV plant," in *Proceedings of the 2015 International Conference on Energy Economics and Environment (ICEEE)*, pp. 1–6, Greater Noida, India, March 2015.

[37] A. G. Shaik and O. P. Mahela, "Power quality assessment and event detection in hybrid power system," *Electric Power Systems Research*, vol. 161, pp. 26–44, 2018.

[38] G. C. Montanari, M. Loggini, A. Cavallini, L. Pitti, and D. Zaninelli, "Arc-furnace model for the study of flicker compensation in electrical networks," *IEEE Transactions on Power Delivery*, vol. 9, no. 4, pp. 2026–2036, 1994.

Hindawi
Mathematical Problems in Engineering
Volume 2022, Article ID 7403691, 6 pages
https://doi.org/10.1155/2022/7403691

Research Article

Power-Sharing Analysis of Hybrid Microgrid Using Iterative Learning Controller (ILC) considering Source and Load Variation

S. Angalaeswari,[1] K. Jamuna,[1] K. Mohana sundaram,[2] L. Natrayan,[3] L. Ramesh,[4] and Kiran Ramaswamy[5]

[1]*School of Electrical Engineeirng, Vellore Institute of Technology, Chennai 600127, TamilNadu, India*
[2]*Department of Electrical and Electronics Engineering, KPR Institute of Engineering and Technology, Arasur, Coimbatore 641407, TamilNadu, India*
[3]*Department of Mechancial Engineering, Saveetha School of Engineering, SIMATS, Chennai, TamilNadu, India*
[4]*Department of Electrical and Electronics Engineering, Dr. M. G. R. Educational and Research Institute, Chennai, TamilNadu, India*
[5]*Department of Electrical and Computer Engineering, Dambi Dollo University, Dambi Dollo, Ethiopia*

Correspondence should be addressed to K. Jamuna; jamuna.k@vit.ac.in and Kiran Ramaswamy; kiran.ramaswamy@ambou.edu.et

Received 8 March 2022; Revised 21 April 2022; Accepted 29 April 2022; Published 20 May 2022

Academic Editor: Ravi Samikannu

In this study, a novel iterative learning controller is proposed to maintain power balance in hybrid microgrid considering source and load variation. A hybrid microgrid comprising of solar, battery, utility grid, and AC and DC loads are developed with ac and dc bus in MATLAB Simulink environment. The primary or local level control is implemented for solar and battery for maintaining stable dc bus voltage. The secondary or system level control is implemented by controlling the interlinking converter placed between ac and dc bus to supply stable voltage along with the smooth grid synchronization and ensuring the proper real power sharing between dc/ac buses. The simulation studies reveal that the proposed iterative controller has efficient and effective control over the voltage and power in hybrid microgrid under various modes of operation such as autonomous and grid connected modes.

1. Introduction

The traditional strategies for generation of electrical energy can cause great negative impacts on the natural fuel sources and have more wastages of energy during power generation and transmission. The distributed energy resources (DER), energy storage systems (ESS), and loads form a microgrid (MG) that acts as single controllable unit from the grid point of view [1]. Microgrid has reduced power loss and improved power quality and reliability. Due to the sporadic environment of renewable energy sources, MG must be linked to the conventional grid for continuous and reliable power supply. When the MGs are operated in the grid connected mode, it facilitates the bidirectional power transfer between the microgrid components and the utility grid (UG).

The most preferable microgrid structure is AC microgrid which could be easily coupled with the UG through point of common coupling (PCC) [2]. However, DC microgrids are developed currently due to solar power generation compatibility, energy storage facility, and increase in DC loads such as electric vehicles, LED lighting, and data centers [3]. Because increase in DC power sources and majority of loads in the utility grid are AC loads, hybrid AC/DC microgrids are emerging recently. To decrease the power conversion phases, to improve the efficiency, and to provide a reliable and quality power supply, AC subgrids and DC subgrids have been developed with their DERs and loads; this in turn forms a hybrid microgrid (HMG) [4].

Both subgrids of AC and DC in an HMG are connected together through an interlinking converter (IC) which enables the power flow in both directions between the grids [5]. Generally, the control techniques for IC control are responsible to sustain bus voltages in HMG. The droop control of ICs for power disbursement among AC and DC subgrids

ends up with frequency deviation and low voltage quality which leads to system instability. Also, achieving both accurate (optimal) power sharing and voltage control is very difficult with the droop control [6].

Most of the literature discussed the energy management strategies used in hybrid microgrid controlled by the system operator. Rather than this centralized system, the authors [7] proposed a management system having distributed nature for finding day-ahead schedules using the information obtained from the energy management solution. The mixed integer quadratic programming has been formulated with the constraints of distributed energy sources, storage system, system operation, and converter operation constraints. The results proved that the proposed algorithm has effective optimal energy management for hybrid microgrid. An optimal energy strategy has been proposed with display in [8] for the grid connected and standalone microgrid having wind, solar, fuel cell, diesel generator, and microturbine as sources and battery energy storage systems. Using mixed integer linear programming with multiobjective solution of demand response program, with these techniques and energy management strategy, the carbon dioxide emission has been reduced almost fifty percentage.

An economic and environmental analysis of a grid tied microgrid is carried out in [9] for the cost saving and reduced CO_2 emission. The battery life and daily operation cost is considered in this work which yields almost 99 percent saving in cost and giving income also with the application of hybrid FMINCON and GA algorithms. Various topology of hybrid energy storage system (HESS) is proposed in [10] having passive, semiactive, and active topologies. The analysis of various systems is carried out taking the parameters of cost, flexibility, efficiency, complexity, and controllability, and the results show that the system with power electronic interference has better performance, and it is sensitive to state of charge level.

The HMG operated in both grid connected and autonomous mode and its transition is controlled by the IC located between AC and DC buses. Even though many controllers have been available for the microgrid application, iterative learning control (ILC) [11] is considered and implemented in this study because of its repetitive nature. The concept of ILC started from robotics engineering for its repetitive movements. ILC has been accepted to be an effective method of the control method to enhance the dynamic response for a set up with repetitive act [12]. In this study, an HMG is modelled in MATLAB/Simulink simulation environment with solar and battery along DC bus side; AC loads and utility grid are connected to AC bus. AC and DC subgrids are interconnected through IC. For efficient power sharing and voltage control, the iterative learning controller with the forgetting factor is implemented for control of IC. The developed microgrid is controlled by IC with the aid of proposed ILC, which utilizes the DC bus voltage as controller input.

The uniqueness of this research work is listed as

(i) Implementation of novel ILC to enrich the output of the controller used for interlinking converter operation for optimizing the power-sharing method, stabilizing voltage and frequency

(ii) Simulation analysis of the hybrid microgrid under various scenarios and its realization

2. Structure of Hybrid Microgrid System and Operation

The presented HMG shown in Figure 1 comprises of separate DC and AC buses which are interconnected to each other through IC. The modelling of solar, battery, and the entire microgrid set up has been referred from [13], and the specification is given in Table 1. Furthermore, AC bus with local loads is linked with the utility grid through the transformer at PCC. Solar photovoltaic (PV) panel is treated as the main source for HMG and the battery is served to be the storage and back up device to satisfy the time-varying loads. The boost converter for DC operation is used to get the maximum power from the PV with maximum power point tracking (MPPT). The function of battery in HMG is used to store the excess energy from the PV source and deliver the power to loads whenever the voltage production from the PV system is less.

Typically, the PV source has variable power output due to variations in its input solar irradiation. Still, the voltage level of the PV source must be the same, irrespective of its input variations. In order to maintain a constant voltage at DC bus, the decentralized fuzzy logic controller is employed for the solar converter. The dc bus voltage is being converted to AC voltage using IC. The IC in an HMG is playing the role of rectifier and an inverter reliant on the power flow direction at every instant. The control and co-ordination of hybrid microgrid with various control approaches are highlighted in [14], and the ICs are deployed as the grid-side converter for the transfer of renewable energy power to the AC grid. Due to the intermittent power output from the renewables, it is necessary to take severe steps to avoid the opposing effects of the renewable sources. Hence, HMG control is more significant to meet out the power balance and the voltage stability by ensuring the good performance as well.

3. Materials and Methods

A method of the repetitive controller called iterative learning controller (ILC) is used for the control of IC in both modes of operation for efficient power management and voltage control of HMG. The concept of ILC and its implementation to meet out the control objectives are referred from [15]. The proposed HMG shown in Figure 1 has been modelled in MATLAB/Simulink. In this research work, the solar PV panel is assumed to be the base source to meet the loads since it is the best clean and environment friendly energy. The various modes of operation, duration of PV source, and grid availability are highlighted in Table 2.

The solar cell control logic and battery control algorithm has been implemented to maintain stable dc voltage at the dc

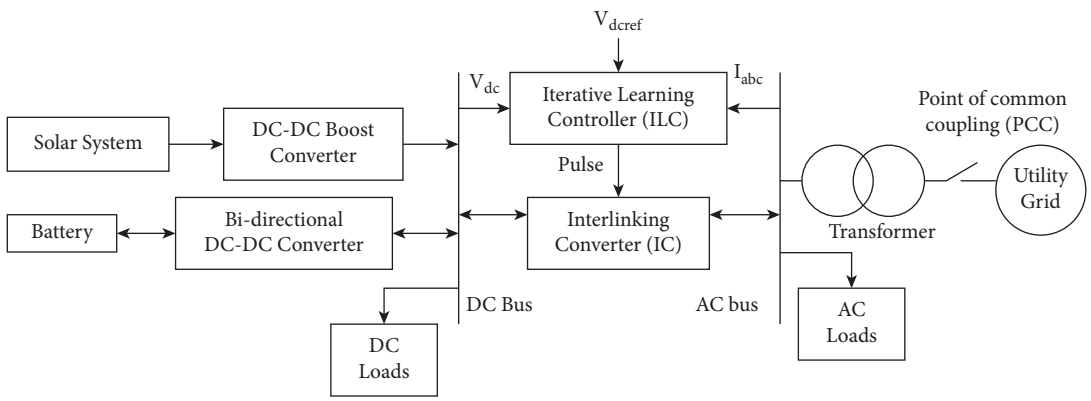

Figure 1: Block diagram of the proposed hybrid microgrid.

Table 1: Specification of HMG setup.

Sl. no.	Parameters	Values
1	Solar power rating	1 kW, 135 V operating voltage
2	DC-DC boost converter	1 kW
3	Battery rating	8 nos of 12 V, 120 Ah
4	Bidirectional converter	1 kW, SKM100GB12T-IGBT
5	DC link capacitor	400 μF
6	DC bus voltage	200 V
7	Transformer	3Φ, 6 A, 415/(0–470 V)

Table 2: Various scenarios under autonomous and grid connected mode of operation for HMG.

Mode of operation	Cases	Description	Interval in sec	Solar panel	Battery
Autonomous mode	Scenario-I (SC-I)	Abundant solar energy + normal loading	0.0–5.0	MPPT	Charging
	Scenario-II (SC-II)	Abundant solar energy + heavy loading	5.0–10.0	MPPT	Discharging
	Scenario-III (SC-III)	Abundant solar energy + light loading	10.0–15.0	Constant power	Charging/idle
	Scenario-IV (SC-IV)	Absence of sunlight + normal loading	15.0–20.0	No power	Discharging
Transition mode	Scenario-V (SC-V)	Mode change	@25s	Mode change from autonomous to grid connected mode	
Grid connected mode	Scenario-VI (SC-VI)	Power import + normal loading	20.0–25.0	No power	Discharging/ idle
	Scenario-VII (SC-VII)	Power export + light loading	25.0–30.0	MPPT	Charging/idle

bus irrespective of the variation in the solar input and load variation. The control diagrams of solar and battery are explained in Figures 2 and 3, respectively.

In the figures, I_{pv} and V_{PV} are the solar output current (A) and voltage (V), respectively, V_{dc} and V_{batt} are the dc bus voltage and battery output voltage, respectively, and I_L and I_o are current (A) from the battery and dc-dc converter currents, respectively. Instead of real power P control, *Vdc* can be employed in the outer control loop particularly for solar applications. The fundamental concept behind this theory is that the capacitor voltage depends on the energy balance between the power received by the VSI and the power delivered by it.

If these two are equal, then the dc-link voltage will remain constant. If power received by VSI is greater than the power delivered by it, then the extra energy will be put into the capacitance which in turn will elevate its voltage. On the contrary, if the power delivered by VSI is greater than the power received, then the additional power is supplied by the capacitor results in the reduction of its voltage. Thus, by monitoring the dc-link voltage, it is possible to deliver a required amount of active power.

The entire simulation is carried out for 30 sec under these operating conditions; the power distribution among the source, battery, and loads is shown in Figure 4.

3.1. Autonomous Mode. In this condition, HMG is isolated from the main grid and operates autonomously. The solar PV panel and energy storage device in the microgrid are alone delivering the power to the loads [16]. To verify the performance of HMG with the proposed ILC controller, four different scenarios are analyzed under solar isolation varying and load fluctuations [17].

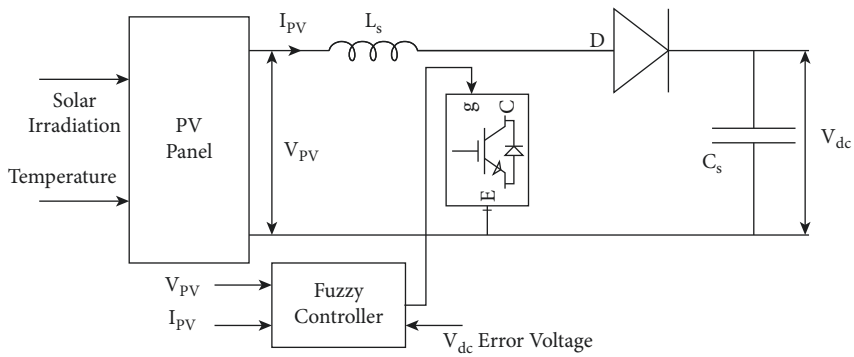

Figure 2: Block diagram of the DC-DC converter for solar cell.

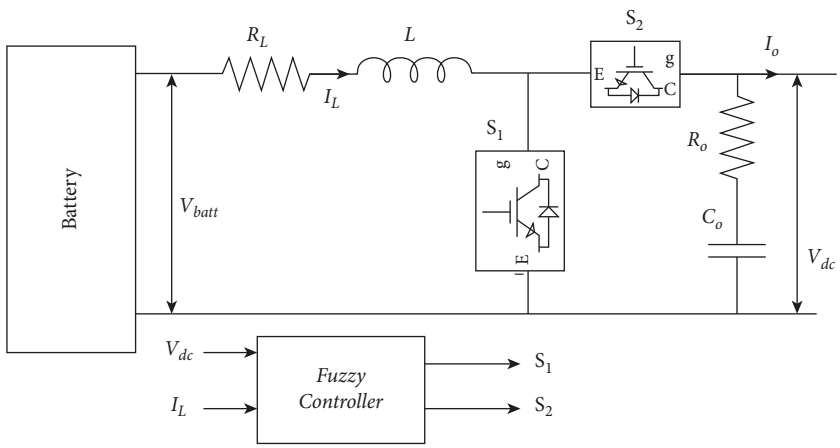

Figure 3: Block diagram of control circuit of battery.

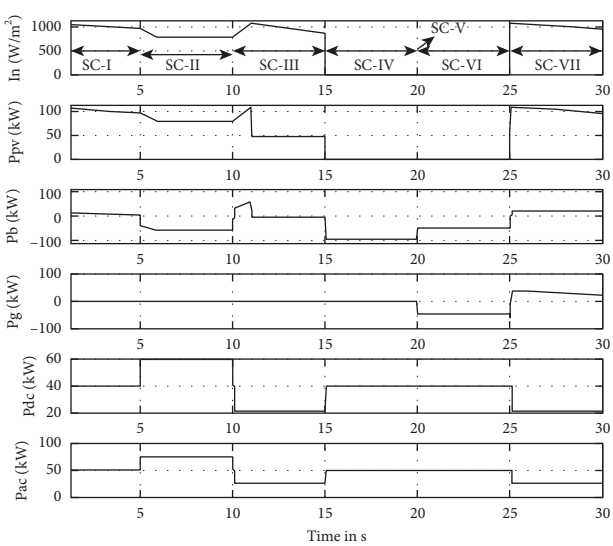

Figure 4: Power distribution among various sources and loads for HMG.

3.1.1. Scenario I: Solar Supplies Power to Loads and Charging Battery. In this scenario, an abundant amount of sunlight is falling on the PV panel, and fixed nominal loads are present at DC and AC subgrids. Under this condition, the DC-DC enhancement converter is operating in MPPT mode to extract the peak power from the solar panel and deliver the maximum power to loads [18]. The surplus power from the solar is charging the battery.

3.1.2. Scenario II: Solar Power Reduces and Battery Discharges for an Increase in Loads. In this scenario, an abundant amount of sunlight is falling on the PV panel, but loads are slightly increased above the nominal ratings. Under this condition, the converter still operates in MPPT mode to get the highest power from the PV panel and delivers a position of power to the loads [19]. To maintain a proper power balance between the sources and loads, the excess power demand by the loads is taken from the energy storage device by discharging it [20].

3.1.3. Scenario III: Solar in Constant Power Mode and Battery Is in Idle Condition. In this scenario, an abundant amount of sunlight is falling on the PV panel, but loads are slightly decreased below the nominal ratings. Under this condition, total load demand can be lesser than the power output from the PV panel when it operates in the MPPT mode [21]. Thus, the DC-DC boost converter is operating in the constant power mode to maintain the proper power distribution among the components to meet the balance. Under this condition, the battery is being charged until SOC upper limit and it becomes idle [22].

3.1.4. Scenario IV: No Solar Power and Battery Discharges for Constant Load. In this scenario, an absence of sunlight or deficit amount of solar energy is falling on the PV panel to generate sufficient power, and nominal loads are connected at the subgrids. Under this condition, there is no power available from the PV panel; hence, the battery is being discharged to satisfy the load demands until it reaches the SOC lower limit [23].

During transition mode from autonomous to grid connection, the breaker at PCC is closed, and the HMG is connected to the utility grid. It is observed that the dc bus voltage has 8.34 percentage deviation for 0.015 s and settles to the desired value [24]. This indicates that the proposed controller operates efficiently and has an ability to maintain the voltage and frequency constant.

3.2. Grid Connected Mode. Once the HMG is coupled to the utility main grid, the HMG functions in either power export mode or power import mode are subject to the presence of solar energy from the sun. These two modes of operation under grid connected condition are discussed as follows.

3.2.1. Scenario V: No Solar Power and Grid Supplies Power to Loads and Charges the Battery. This scenario is considered as HMG power import mode. In absence of sunlight, no power can be extracted from the PV panel. Hence, the energy storage device in the HMG starts to discharge and deliver the power to loads until SOC limits, and it becomes idle [25]. Meanwhile, HMG gets the essential power from the grid to maintain the power balance.

3.2.2. Scenario VI: Solar Power Exports to Grid and Battery Is in Fully Charged. In this scenario, an abundant amount of sunlight is falling on the PV panel, and loads are slightly decreased below the nominal ratings [26]. Under this condition, the DC-DC boost converter operates in the MPPT mode and extracts utmost power from the PV panel. The PV power satisfies the load demands and the residual extra power is utilized for charging the battery. When the battery reaches the SOC upper limit, the HMG starts to export this extra power to the main grid.

4. Conclusion

A hybrid microgrid comprising of solar, battery, and loads has been considered for the simulation analysis. Individual decentralized fuzzy-based controllers have been implemented for the solar and battery to provide fixed dc voltage irrespective of its input variation. Novel iterative learning controller has been implemented for the control of the interlinking converter to ensure the constant bus voltages and frequency under various modes and scenarios for varying generation and loading conditions. The controller is also responsible for the power management among the source and the loads. The simulation results reveal that the power sharing among the source and loads under variable conditions is enhanced with ILC. In future, the hardware implementation of the proposed hybrid microgrid will be carried out for power export and import operation. In the future work, the voltage and frequency stabilization and current measurement with additional loads will be considered. The optimization algorithms for the parameter improvement will also be implemented in the research work in future.

Data Availability

The data used to support the findings of this study are included within the article. For further data or information, these are available from the corresponding author upon request.

Conflicts of Interest

The authors declare that there are no conflicts of interest regarding the publication of this paper.

Acknowledgments

The authors thank Vellore Institute of Technology, Chennai, for the technical assistance.

References

[1] D. T. Ton and M. A. Smith, "The U.S. Department of energy's microgrid initiative," *The Electricity Journal*, vol. 25, no. 8, pp. 84–94, 2012.

[2] J. M. Guerrero, J. C. Vasquez, J. Matas, L. G. de Vicuna, and M. Castilla, "Hierarchical control of droop-controlled AC and DC microgrids-A general approach toward standardization," *IEEE Transactions on Industrial Electronics*, vol. 58, no. 1, pp. 158–172, 2011.

[3] B. T. Patterson, "DC, come home: DC microgrids and the birth of the "enernet"," *IEEE Power and Energy Magazine*, vol. 10, no. 6, pp. 60–69, 2012.

[4] A. Gupta, S. Doolla, and K. Chatterjee, "Hybrid AC-DC microgrid: systematic evaluation of control strategies," *IEEE Transactions on Smart Grid*, vol. 9, no. 4, pp. 3830–3843, 2018.

[5] H. Xiao, A. Luo, Z. Shuai, G. Jin, and Y. Huang, "An improved control method for multiple bidirectional power converters in hybrid AC/DC microgrid," *IEEE Transactions on Smart Grid*, vol. 7, no. 1, pp. 340–347, 2016.

[6] A. A. A. Radwan and Y. A.-R. I. Mohamed, "Networked control and power management of AC/DC hybrid microgrids," *IEEE Systems Journal*, vol. 11, no. 3, pp. 1662–1673, 2017.

[7] Y. Chen, L. Hao, and G. Yin, "Distributed energy management of the hybrid AC/DC microgrid with high penetration of distributed energy resources based on ADMM," *Complexity*, vol. 2021, no. 9, pp. 1–9, Article ID 1863855, 2021.

[8] V. V. S. N. Murty and A. Kumar, "Retracted article: multi-objective energy management in microgrids with hybrid energy sources and battery energy storage systems," *Protection and Control of Modern Power Systems*, vol. 5, no. 1, p. 2, 2020.

[9] M. Azaroual, M. Ouassaid, and M. Maaroufi, "Optimum energy flow management of a grid-tied photovoltaic-wind-battery system considering cost, reliability, and CO2 emission," *International Journal of Photoenergy*, vol. 2021, pp. 1–20, Article ID 5591456, 2021.

[10] T. M. Amirthalakshmi, S. Ramesh, R. T. Prabu et al., "A novel approach in hybrid energy storage system for maximizing solar PV energy penetration in microgrid," *International Journal of Photoenergy*, vol. 2022, pp. 1–7, Article ID 3559837, 2022.

[11] D. Huang, J. Xu, Y. Jian, and D. Min, "Precision motion tracking of piezoelectric actuator using sampled-data iterative learning control," *Precision Motion Systems*, pp. 57–80, 2019.

[12] B. Ufnalski, L. M. Grzesiak, A. Kaszewski, and A. Galecki, "On the similarity and challenges of multiresonant and iterative learning current controllers for grid converters and why the disturbance feedforward matters," *Przeglad Elektrotechniczny*, vol. 1, no. 5, pp. 40–48, 2018.

[13] S. Angalaeswari and K. Jamuna, "Design and implementation of a robust iterative learning controller for voltage and frequency stabilization of hybrid microgrids," *Computers & Electrical Engineering*, vol. 84, Article ID 106631, 2020.

[14] N. Sahoo, M. R. Kar, and R. Pravat Kumar, "Evaluating Odisha's COVID-19 response: from quiet confidence to a slippery road," *Journal of Social and Economic Development*, vol. 23, no. S2, pp. 373–387, 2020.

[15] H. Deng, R. Oruganti, and D. Srinivasan, "Analysis and design of iterative learning control strategies for UPS inverters," *IEEE Transactions on Industrial Electronics*, vol. 54, no. 3, pp. 1739–1751, 2007.

[16] S. K. Jha and D. Kumar, "Demand side management for stand-alone microgrid using coordinated control of battery energy storage system and hybrid renewable energy sources," *Electric Power Components and Systems*, vol. 47, no. 14-15, pp. 14-15, 2019.

[17] D. Emara, M. Ezzat, A. Y. Abdelaziz, K. Mahmoud, M. Lehtonen, and M. M. F. Darwish, "Novel control strategy for enhancing microgrid operation connected to photovoltaic generation and energy storage systems," *Electronics*, vol. 10, no. 11, p. 1261, 2021.

[18] P. Asha and L. B. T. J. R. R. G. S. Natrayan, "IoT enabled environmental toxicology for air pollution monitoring using AI techniques," *Environmental Research*, vol. 205, Article ID 112574, 2022.

[19] D. Leskarac, M. Moghimi, J. Liu, W. Water, J. Lu, and S. Stegen, "Hybrid AC/DC Microgrid testing facility for energy management in commercial buildings," *Energy and Buildings*, vol. 174, pp. 563–578, 2018.

[20] B. Mohandes, S. Acharya, M. S. E. El Moursi, A. S. Al-Sumaiti, H. Doukas, and S. Sgouridis, "Optimal design of an islanded microgrid with load shifting mechanism between electrical and thermal energy storage systems," *IEEE Transactions on Power Systems*, vol. 35, no. 4, pp. 2642–2657, 2020.

[21] S. Batiyah, R. Sharma, S. Abdelwahed, and N. Zohrabi, "An MPC-based power management of standalone DC microgrid with energy storage," *International Journal of Electrical Power & Energy Systems*, vol. 120, Article ID 105949, 2020.

[22] M. SundaramK, P. Prakash, S. Angalaeswari, T. Deepa, L. Natrayan, and P. Paramasivam, "Influence of process parameter on carbon nanotube field effect transistor using response surface methodology," *Journal of Nanomaterials*, vol. 2021, pp. 1–9, Article ID 7739359, 2021.

[23] P. Singh and J. S. Lather, "Power management and control of a grid-independent DC microgrid with hybrid energy storage system," *Sustainable Energy Technologies and Assessments*, vol. 43, no. 2021, Article ID 100924, 2021.

[24] M. Chankaya, I. Hussain, and A. Ahmad, "Seamless control of grid-tied PV-hybrid energy storage system," *International Journal of Emerging Electric Power Systems*, vol. 22, no. 5, pp. 569–582, 2021.

[25] D. K. Jain, S. K. S. Tyagi, S. Neelakandan, M. Prakash, and L. Natrayan, "Metaheuristic optimization-based resource allocation technique for cybertwin-driven 6G on IoE environment," *IEEE Transactions on Industrial Informatics*, vol. 18, no. 7, pp. 4884–4892, July 2022.

[26] K. Dhingra and M. Singh, "Frequency support in a micro-grid using virtual synchronous generator based charging station," *IET Renewable Power Generation*, vol. 12, no. 9, pp. 1034–1044, 2018.

Hindawi
Mathematical Problems in Engineering
Volume 2022, Article ID 3888571, 17 pages
https://doi.org/10.1155/2022/3888571

Research Article

Performance Enhancement of a Three Phase Boost-Cascaded Fifteen Level Inverter Using the PI Controller

S. Sathish Kumar,[1] **R. Ramkumar**,[2] **S. Sivarajeswari**,[3] **D. Ramya**,[4] **T. Subburaj**,[5] **and Martin Sankoh**[6]

[1]*Department of Electrical and Electronics Engineering, M.Kumarasamy College of Engineering, Karur, Tamilnadu, India*
[2]*Department of Electrical and Electronics Engineering, Dhanalakshmi Srinivasan University, Trichy, Tamilnadu, India*
[3]*Department of Electrical and Electronics Engineering, Sri Sai Ram Institute of Technology, Chennai, Tamilnadu, India*
[4]*Department of Electrical and Electronics Engineering, Sathyabama Institute of Science and Technology, Chennai, Tamilnadu, India*
[5]*Department of Master of Computer Applications, Rajarajeswari College of Engineering, Bangalore, India*
[6]*Department of Mechanical and Maintenance Engineering, Fauroh Bay College, University of Sierra Leone, Fairtown, Sierra Leone*

Correspondence should be addressed to S. Sathish Kumar; sathishphd2k17@gmail.com and Martin Sankoh; sankohmartinsidi@gmail.com

Received 24 March 2022; Revised 17 April 2022; Accepted 20 April 2022; Published 19 May 2022

Academic Editor: Dragan Z. Marinkovic

Photovoltaic power generation is a potential alternative energy source that offers several benefits over other alternative energy sources such as wind, sun, ocean, biomass, geothermal, and so on. Multilevel inverters are essential for power conversion in solar power generation. These multilevel inverters employ three distinct topologies: diode-clamped (neutral-point clamped) inverter, capacitor-clamped (flying capacitor) inverter, and cascaded H-bridge multilevel inverter. The cascaded H-bridge multilevel inverter is more appropriate for photovoltaic applications than the other two topologies. The proposed system asymmetrical cascaded multilevel inverter (ACMLI) is energized using a photovoltaic system (PV). A three-phase cascaded H-bridge fifteen-level inverter for grid-connected solar systems is given in this study utilizing a proportional integral controller. The harmonic distortion was removed using a multicarrier pulse width modulation method. The MATLAB/Simulink is used to simulate the performance of a three-phase cascaded H-bridge fifteen-level inverter in terms of harmonic content and number of switches. To test the performance of the designed system, a hardware prototype was created. From the obtained results, the proposed method reduces the switch count, harmonic distortion, and rejects the external disturbances of input and output variables.

1. Introduction

Automatic regulation is a configuration and research method for a self-regulating device. This automated control technique can be used in a number of applications, such as manufacturing processes and chemical industry. By minimizing the objective function, the automated control deals with the creation of an optimized controller for both offline and online industrial applications, thus satisfying other constraints such as interruption and robustness. PID controllers are most commonly used in many manufacturing applications and process control industries to control the system with the desired fixed point due to flexibility and ease of tuning. The PID controller algorithm is then clarified by three functions, such as proportional gain (K_p), integral gain (K_i), and derivative gain (K_d). In order to get the best plant output, these three parameters are modified. [1–4].

The controller comprises of a fractional derivative, and relative to traditional PID controllers, the integral could achieve improved efficiency and robustness. The fractional controls are calibrated for the satisfactory efficiency of the plant. Controller tuning is the method of getting the

parameters of the controller to match the output requirements that are specified. This work proposed tuning of H controllers for the fractional SISO method [5–10].

The tuning technique of these controllers is based on previous understanding of the regulation of fractional and integer order. The suggested linear input-output mapping of the rule base has been shown to be used. [11] By rendering the fuzzy fractional controller nonlinear by applying saturation with squared membership function, the stability of the fractional controller was checked. The fuzzy fractional order PID controller is then designed for better device dynamic control.

The proportional integral controller is designed for a class of fractional systems. From the simulation and experimental performance, both the fractional PI controller designed and the standard integer order designed for the same set of tuning constraints applied were designed. [7, 12–16] This will guarantee the optimal control quality and robustness to the loop gain variants of the built controllers. In this process, with enhanced efficiency, the two built fractional order controllers function effectively. As compared to the stabilizing integer order PID controller, the built FOPI and FO (PI) controllers will increase the control efficiency for the fractional order systems.

The open-loop transfer functions of many practical systems are highly unstable, making it challenging for the closed-loop system to maintain acceptable stability margins and control efficiency. As a result, a single fixed controller is included in the "robust control" family of such systems. Quantitative feedback theory (QFT) is a method for designing a reliable feedback control system. Horowitz (Horowitz, 1991) and Horowitz, 1992) established an approach that allows for the direct design of closed-loop resilient output and stability criteria. The following is a simple description of the QFT controller design approach: Before designing the QFT in parametric uncertain systems, we must first create plant models (at a fixed frequency; the plant frequency response set is called a template). [17, 18] The nominal open-loop function is then tuned to satisfy its restrictions while still maintaining nominal closed-loop stability. The nonlinear plant is turned into a family of linear and unknown processes in the QFT system. The QFT literature provides a variety of methods for this purpose (Horowitz, 1991), (Horowitz, 1992), Gharib et al. (2010), Gharib et al. (2011), Gharib and Moavenian (2012), including linear time-invariant equivalent (LTIE) of nonlinear plants and nonlinear equivalent disturbance attenuation (NLEDA) techniques (Horowitz, 1991).

A class of nonlinear control approaches relies on feedback linearization under the assumption of measured states [12, 19, 20]. The basic idea is to convert a nonlinear system into a linear system by adding a component to the control force that cancels out the nonlinear dynamics. When this is accomplished, the state equation becomes linear, allowing for the use of traditional control methods. This method is used in this study, with the linear quadratic regulator (LQR) as the control tool; this is a popular choice for vibration reduction. [18].

For industrial use, the fractional controller is used to increase the efficiency of machine operation. The architecture of the FOPID controller not only provides the need for benefit design but also for derivative and integral design instructions. There are two new variables for FOC to tune. This extension will offer even more consistency in the design of PID control. Superior efficiency and robustness can be obtained relative to conventional fractional controllers. [21].

2. Proposed Three Phase Fifteen Level ACMLI

Three single phase H-bridge connections are used to create a three-phase fifteen-level asymmetrical cascaded multilevel inverter arrangement. In a half bridge construction, each cell is produced using independent dc sources. This is linked to the load, which might be linear or nonlinear, balanced or unbalanced. In a single-phase arrangement, each cell's output is linked in series with the next cell. [4].

The three-phase asymmetrical fifteen-level output multilevel inverter setup with the nonlinear or unbalanced load is shown in Figure 1.

The single-phase configuration contains three times the number of switches, input dc sources, power diodes, and gate driver circuit components.

2.1. Multicarrier Pulse Width Modulation. Only by employing the correct pulse with modulation approach can the fifteen-level output voltage be achieved. The gating pulses are generated using a multicarrier pulse width modulation method. Only the suggested multilayer inverter may use the thirteen-level output. The fifteen-level output voltage waveform is created by comparing the sinusoidal 180° displaced reference signal with triangular carrier signals. [13, 22–24].

The suggested inverter is a multilayer inverter, which means it has multiple switching components. As a result, the signals carried by multilayer inverters are based on the number of levels. The suggested multilayer inverter's number of carrier signals (Nc) is calculated using (n-1)/2, where n is the number of output levels. The number carrier signal, for example, is (15–1)/2, which equals seven (7). Because of this, the suggested fifteen-level inverter is seven levels positive (+7Vdc) and seven levels negative (+7Vdc). The phase shifted disposition method is used to arrange the carrier signals, which are then compared to the sinusoidal reference signal to create the gating signals for power switches. The amplitude, frequency, and phase of the carrier signals are all the same. The multicarrier signal is compared to the reference in Figure 2. [4].

The ratio of the reference signal to the carrier signal determines the modulation index (MI) for this amplitude method. Similarly, the frequency ratio is computed by dividing the carrier frequency by the frequency of the reference signal.

$$N_C = \frac{n-1}{2},$$
$$MI_a = \frac{A_r}{A_c(n-1)}, \tag{1}$$
$$MI_a = \frac{f_r}{f_c},$$

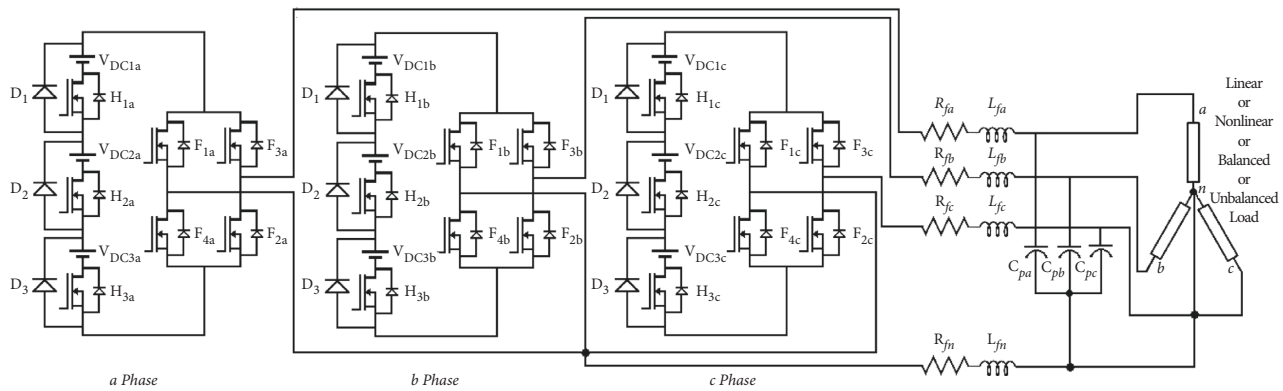

Figure 1: Three-phase fifteen-level asymmetrical cascaded multilevel inverter.

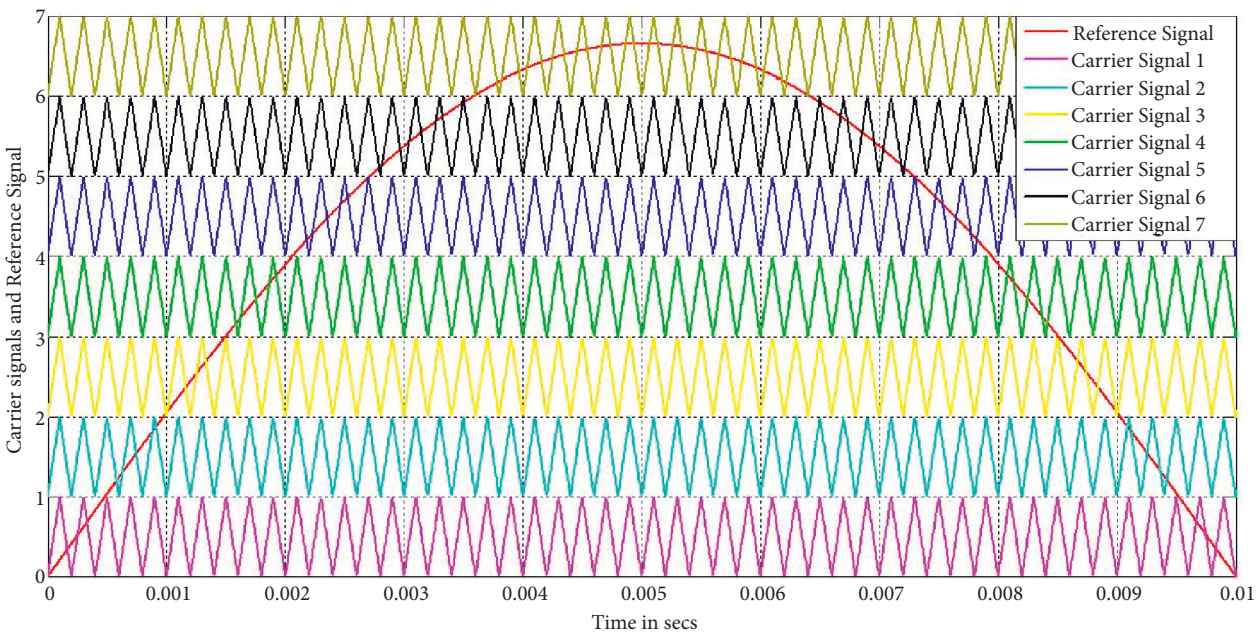

Figure 2: Multicarrier signal compared with the reference signal.

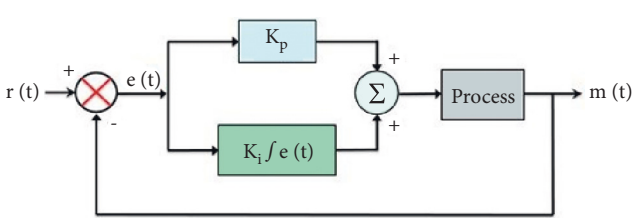

Figure 3: Block diagram of the PI controller.

Table 1: Comparison of P, PI, and PID controllers.

Parameter	Speed of response	Stability	Accuracy
Climbing K	Raise	Decays	Enhances
Climbing K_i	Drop	Decays	Enhances
Climbing K_d	Raise	Enhances	Ineffective

Table 2: Comparison of parameters with various controllers.

Parameter	P controller	PI controller	PID controller
Rise time	Drop	Drop	Minor drop
Overshoot	Raise	Raise	Minor drop
Settling time	Small difference	Raise	Minor drop
Steady state error	Drop	Dramatic change	No change
Stability	Poor	Poor	If K_d little better.

where A_r is the amplitude of the reference signal, A_c is the amplitude of the carrier signal, N is the number of levels, f_r is the frequency of the reference signal, and f_c is the frequency of the carrier signal.

2.2. Proportional Integral (PI) Controller. Because of its simple form, ease of design, and low cost, the PI controller is currently the most extensively used in industrial

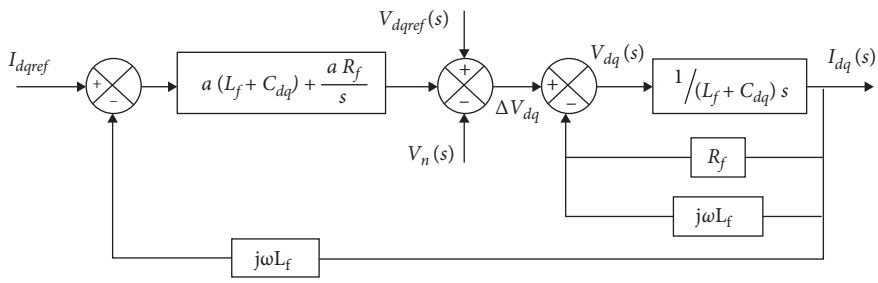

Figure 4: PI controller feedback mechanism.

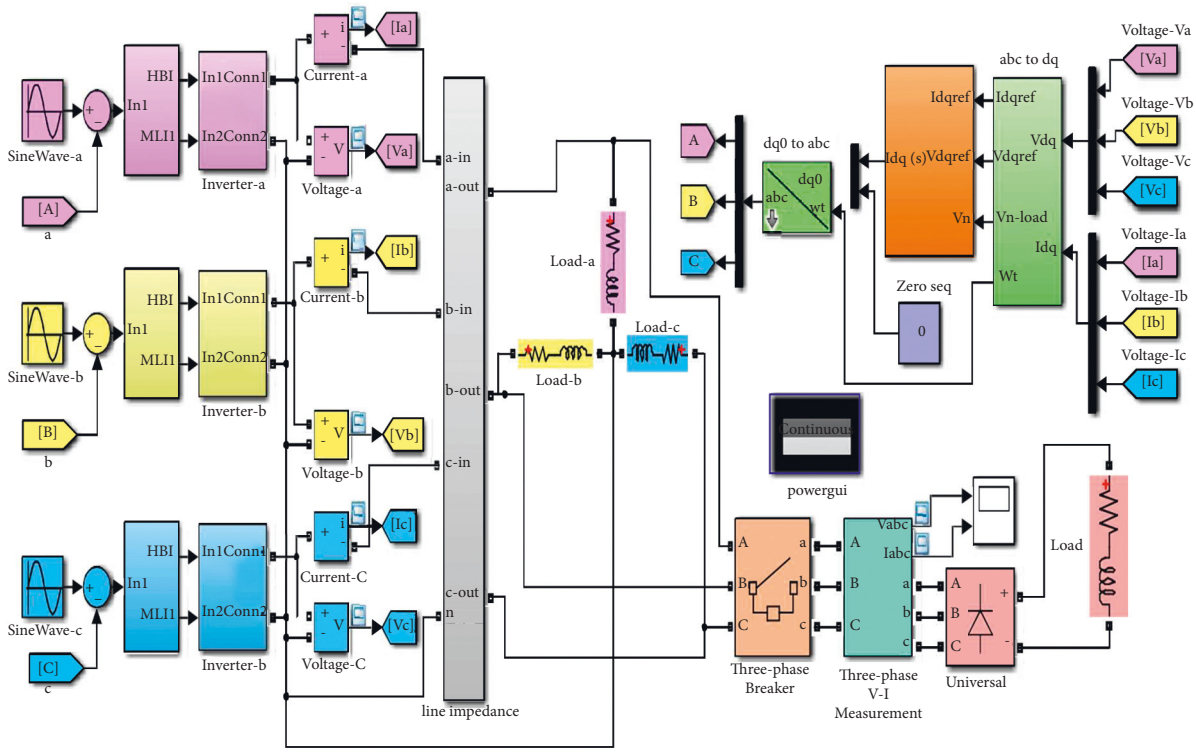

Figure 5: Simulink framework of the three phase fifteen-level cascaded boost multilevel inverter.

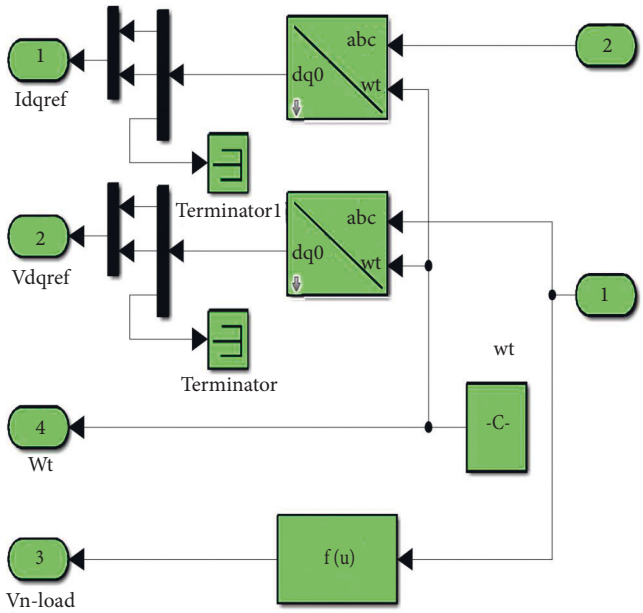

Figure 6: abc to dq transition current and voltage.

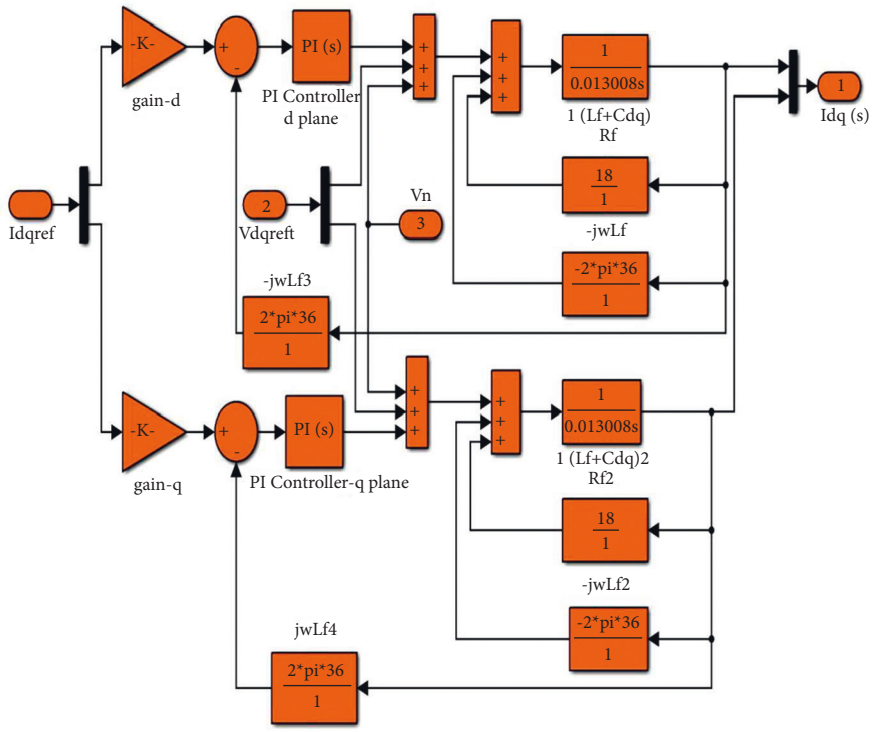

Figure 7: Frame work of PI controller feedback.

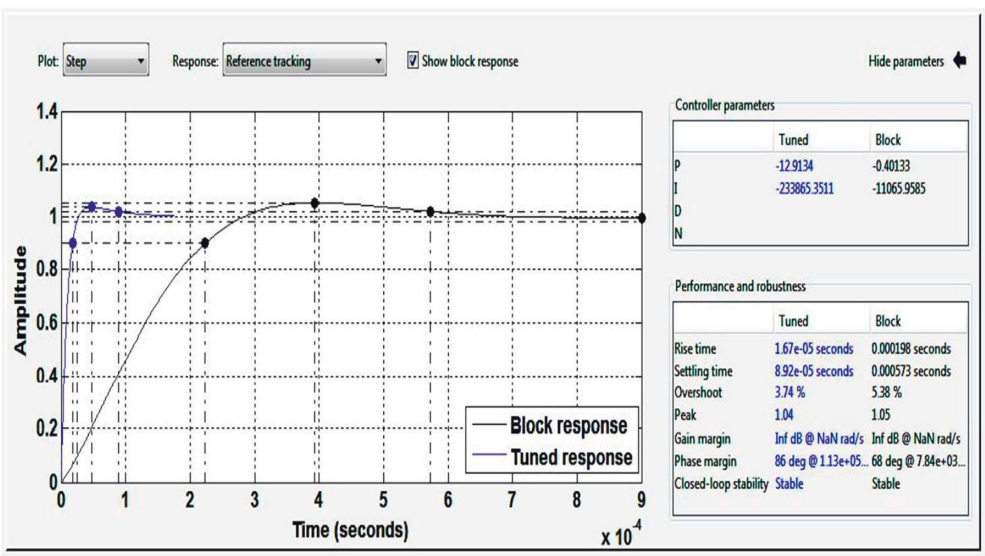

Figure 8: Tracking of reference based on Kp = −12.9134 and Ki = −23 variables.

applications. Despite these benefits, when the controlled object is highly nonlinear and uncertain, the PI controller fails. The PI controller will minimize forced oscillations and steady state errors, allowing on-off and P controllers to function properly. Integral mode, on the other hand, has a negative impact on the system's response time and overall stability. As a result, the PI controller will not increase the reaction time. It is to be expected, given that the PI controller has no way of knowing what will happen with the error in the near future. This difficulty can be overcome by using the derivative mode, which can predict what will happen with the error in the near future, reducing the controller's reaction time. In the industry, PI controllers are frequently employed, especially when response time is not a concern. [17]. where K_p is the proportional gain and K_i is the integral gain.

Figure 3 shows a block diagram of the PI controller. The output response of a PI controller, which uses an integral

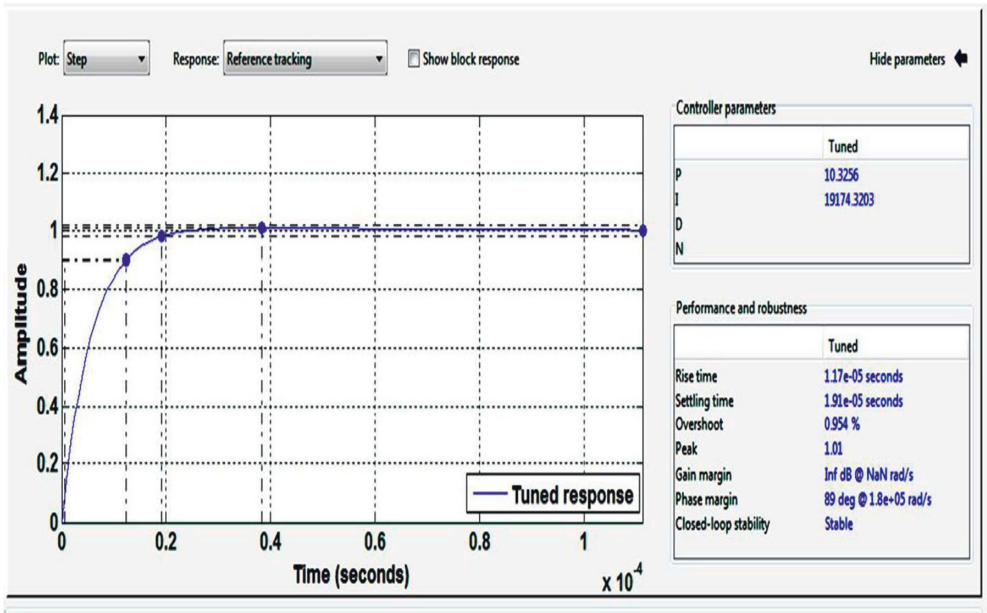

Figure 9: Tracking response of final step Kp = 10.3256 and Ki = 19174.3203.

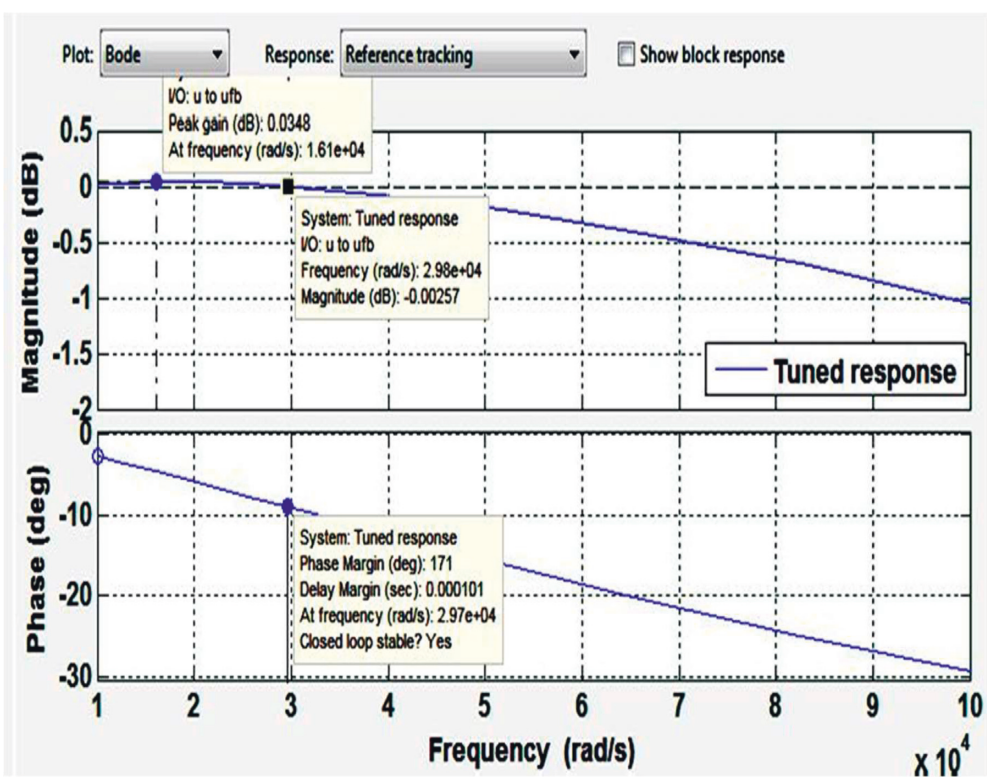

Figure 10: Response of the Bode plot at Kp = 10.3 and Ki = 19174.

error compensation system, is dependent on the integral of the actuating signal in some way. This sort of compensation is achieved by utilizing a controller that generates an output signal with two terms, one proportional to the actuating signal and the other proportional to the integral of the signal. Proportional plus integral controllers, or PI controllers, are examples of such controllers. [18].

$$u(t) = Kp.e(t) + Ki \int e(t)dt, \tag{2}$$

Tables 1 and 2 show the effects of changing the coefficients and control parameters, respectively. The rising time, overshoot, and settling times have all decreased, yet the steady state error has remained the same. The PID controller

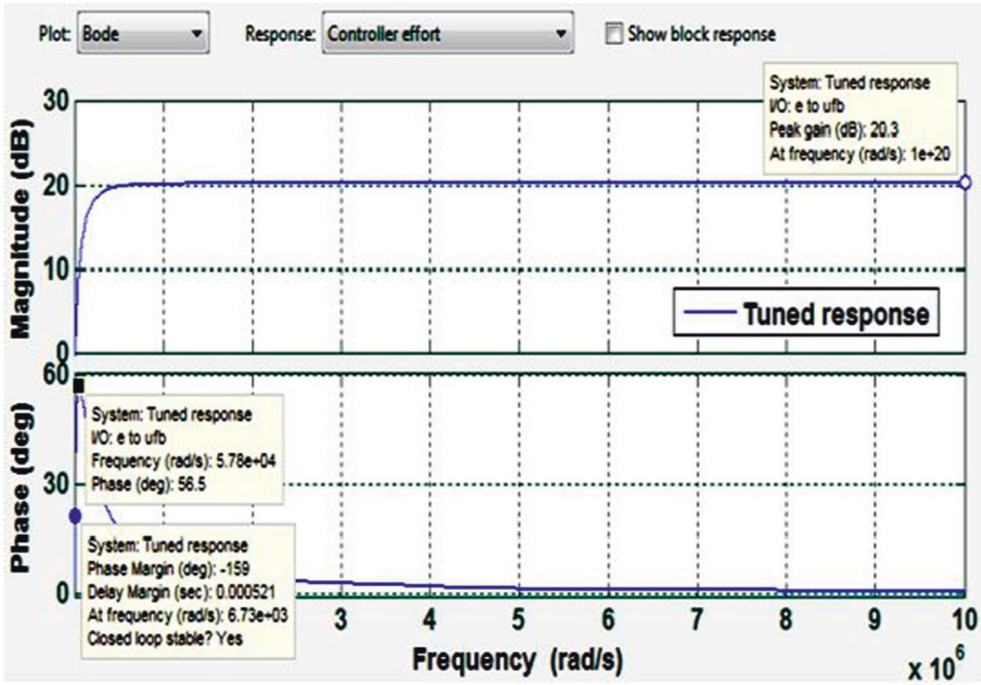

Figure 11: Response of the Bode plot for effort of controller at Kp = 10.3 and Ki = 19174.

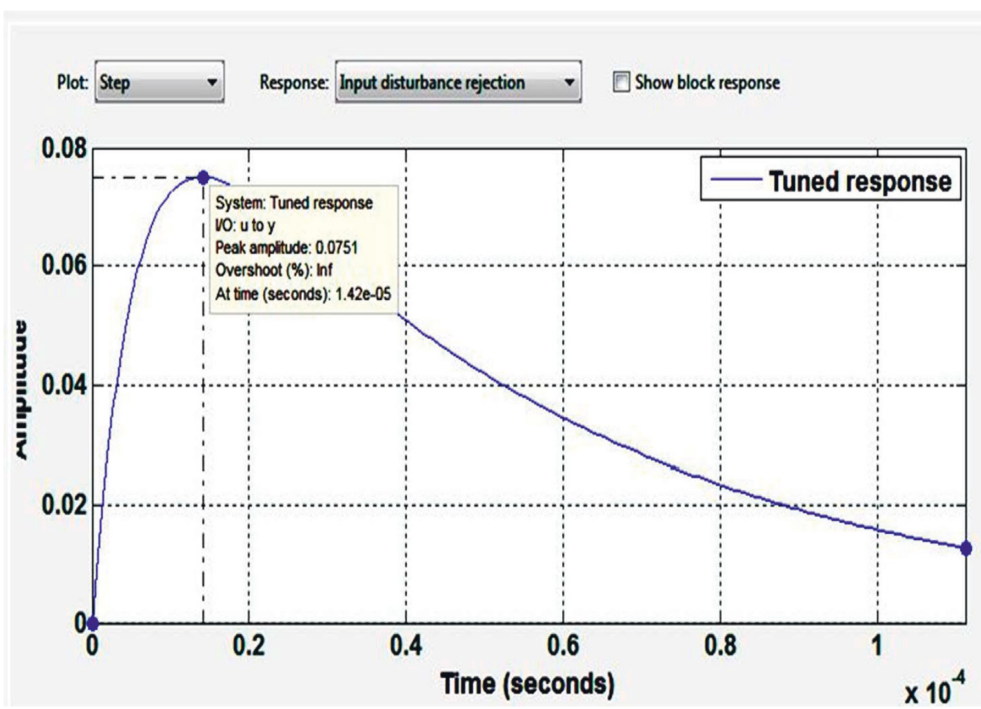

Figure 12: Step response for input disturbance rejection at Kp = 10.3 and Ki = 19174.

outperforms both the P and PI controllers in terms of performance.

2.3. Determining the Settings of the PI Controller. Tuning or enhancing the efficiency of the whole device is the key target of every controller, and the proposed PI controller is as follows:

$$T(s)\left(K_p + \frac{K_i}{s}\right). \tag{3}$$

Almost all Kp and Ki constants of the PI controller are chosen on the basis of checking the various values corresponding to their performance quality on a trial basis. In addition, by reducing the peak overshoot, the PI controller easily decreases the steady state error and increases the

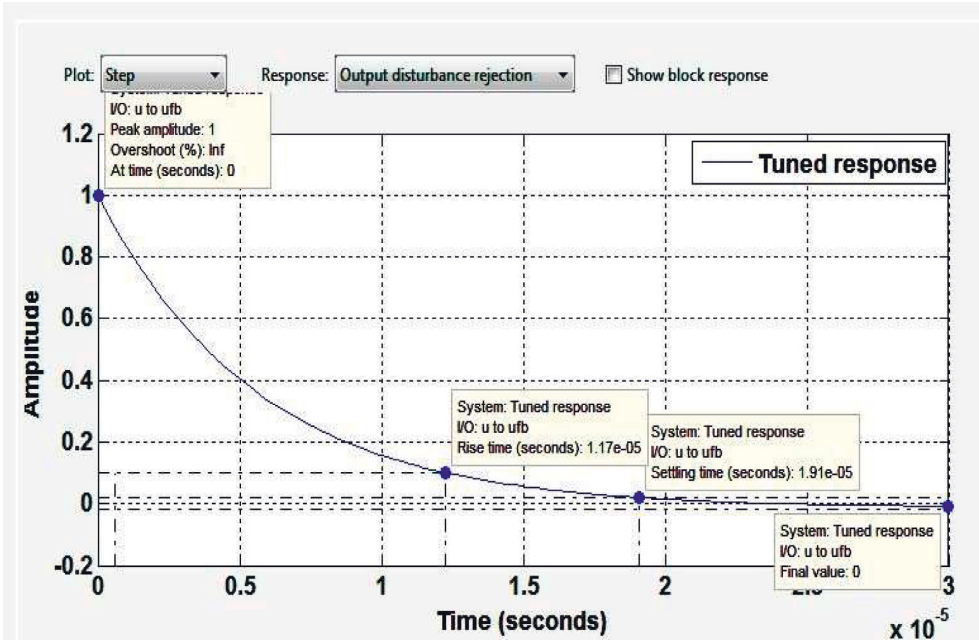

Figure 13: Step response for output disturbance rejection at Kp = 10.3 and Ki = 19174.

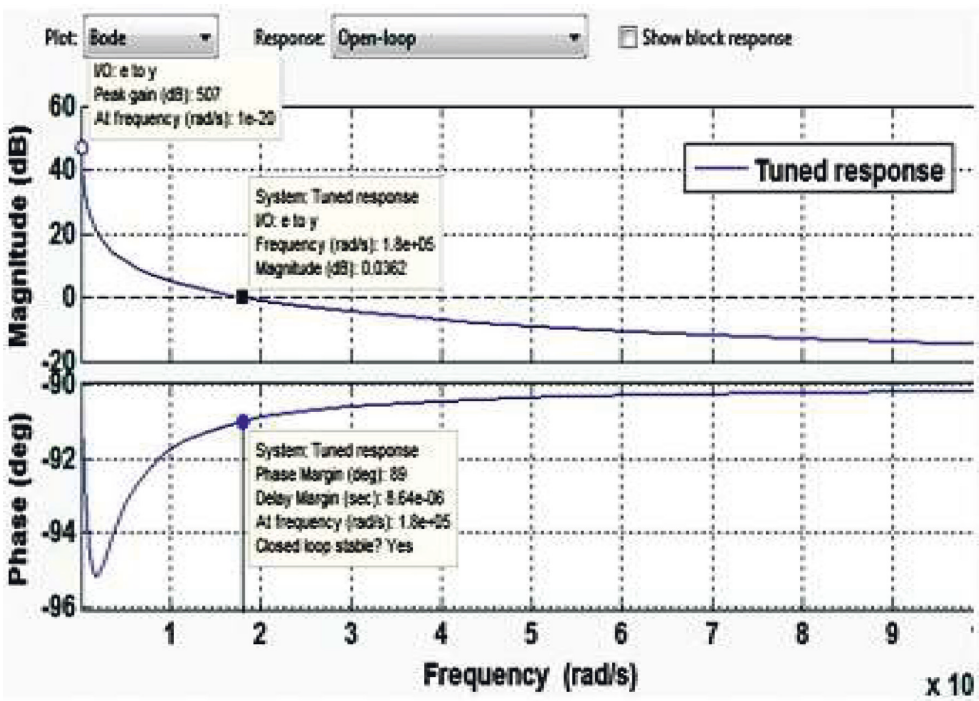

Figure 14: Open loop response of the Bode plot at Kp = 10.3 and Ki = 19174.

system's performance. From the output of the current controller reduction gain block, the closed-loop switch is then obtained.

As seen in Figure 4, the modeled controller was implemented in the proposed boost multilevel inverter of fifteen stages.

As per the load impedance rating, the Kp and Ki values are determined. 0.013008 is the proportional Kp controller, and 36 is the Ki. Depending on the impedance of the load, all values are tuned. [23].

3. Simulation and Hardware Results with the PI Controller

The simulation of the fifteen-level boost cascaded multilevel inverter with a PI controller was introduced in this segment

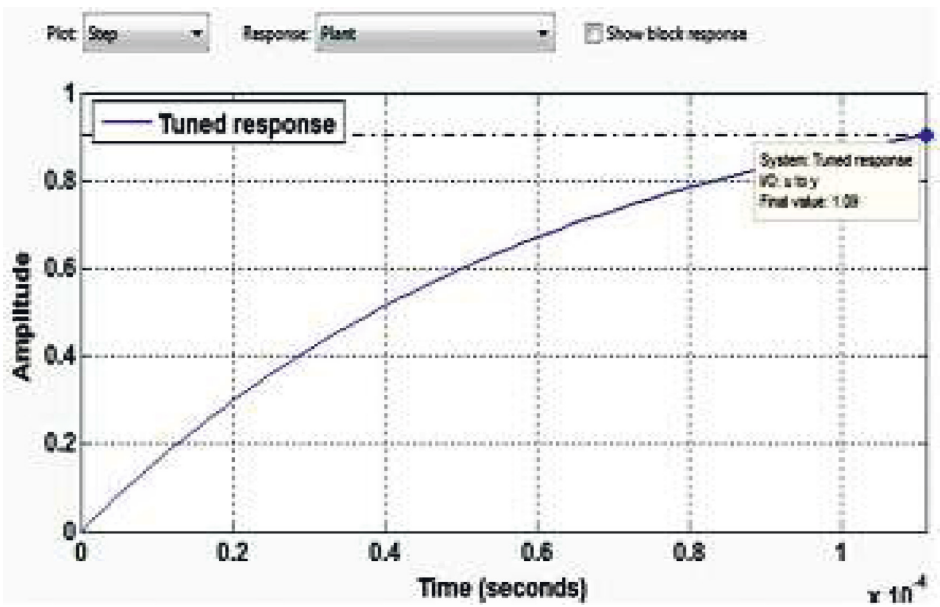

Figure 15: Response plant step at Kp = 10.3 and Ki = 19174.

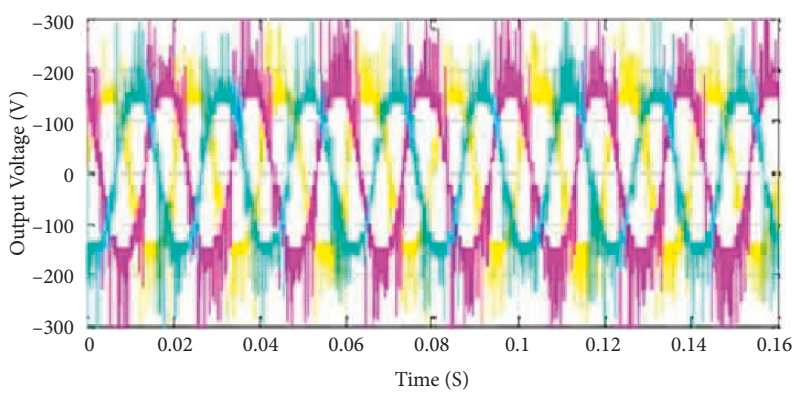

(a)

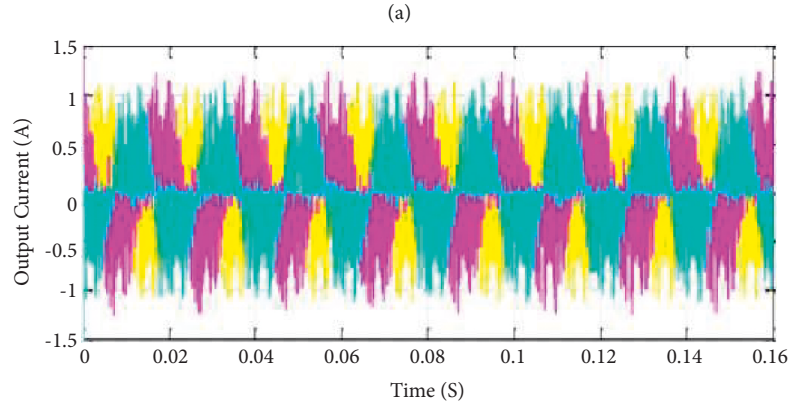

(b)

Figure 16: Output waveform of three phases (a) voltage and (b) current.

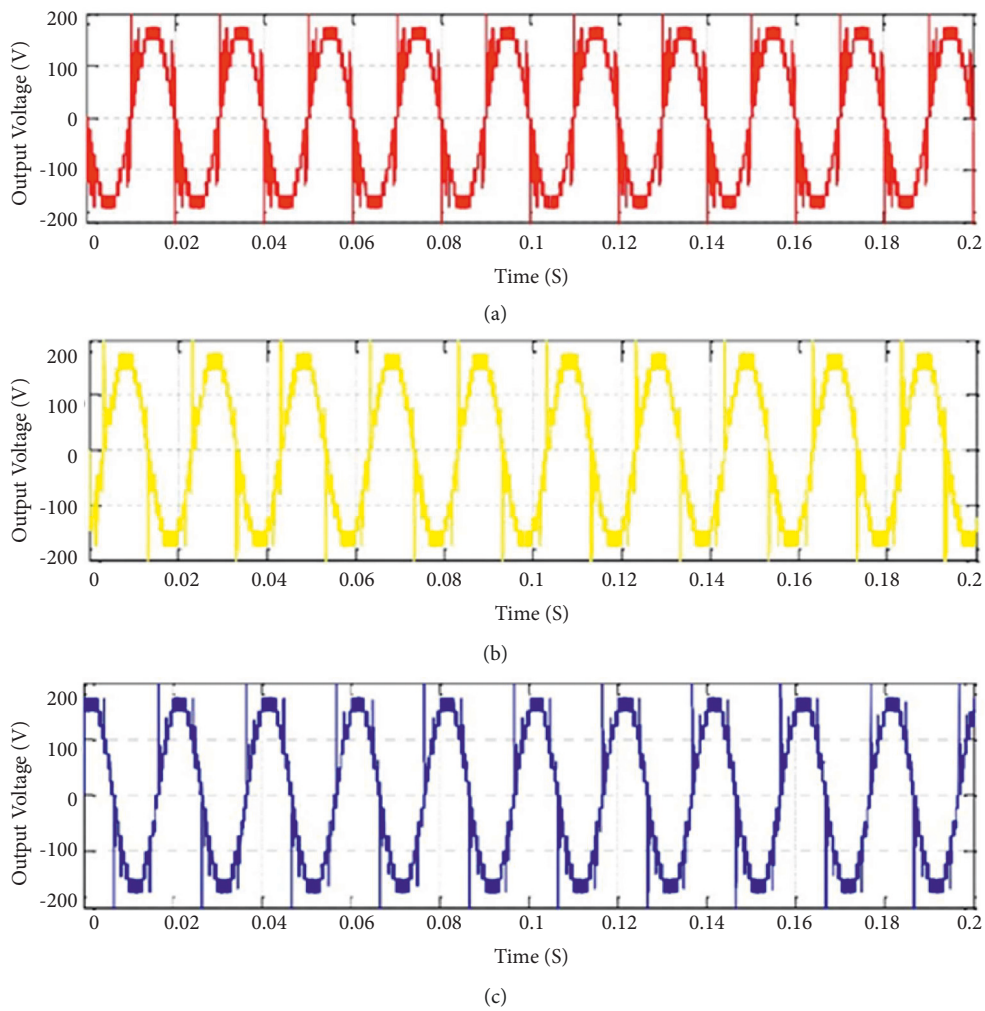

Figure 17: Phase output waveform of three phases (a) phase 'a', (b) phase 'b', and (c) phase 'c'.

and the software component in FPGA was experimentally updated. [2].

3.1. Simulation Results. Figure 5 displays the Simulink diagram of the fifteen-level boost cascaded multilevel inverter with feedback and the PI controller.

In addition, the abc to dq, PI controller input and dq to abc transition blocks are used in this method. As seen in Figure 6, the output voltage and current component are converted into dq to regulate the actual component and to remove the complex component.

The input from the mathematical modeling of previous parts with the PI controller block was created, as seen in Figure 7. The current and voltage of the output load were compared with the comparison by converting the dq part.

From the unbalanced load voltage, the neutral line voltage and current were calculated and removed from the dq portion. In Figure 7, the calculated the value of Kp is 0.013008 and the value of Ki is 36; values are given in the PI controller block.

As shown in Figure 6, the tuned value of the feedback unit has been given to the dq input to the abc transformation block. The input was assigned to the regulated output voltage component and this can be inserted or subtracted depending on the load output. The gating signal was produced by comparison with the multicarrier signal with the changed relation. In Figures 8–15, the virtual output voltage and current waveforms with voltage harmonics continuum are displayed.

The virtual feedback system, three-phase output and current, phase output voltage, phase output current, and phase output voltage THD range of the planned fifteen-level boost cascaded multilevel inverter with the PI controller are seen in Figures 16–18. The Kp = 0.013008 and Ki = 36 for the PI controller were determined for the unbalanced nonlinear form of the proposed inverter configuration in this converter. In the PI controller, autotuning was allowed to change the value of Kp and Ki based on the feedback system's closed-loop response.

By comparing the previous and current tuned value of Kp and Ki, the output of the closed-loop feedback controller system to decrease harmonics and unbalanced between phase voltages was obtained. A stable system and lower rise time, peak overshoot, and settling time are needed for the target of the closed-loop PI controller system. The reference

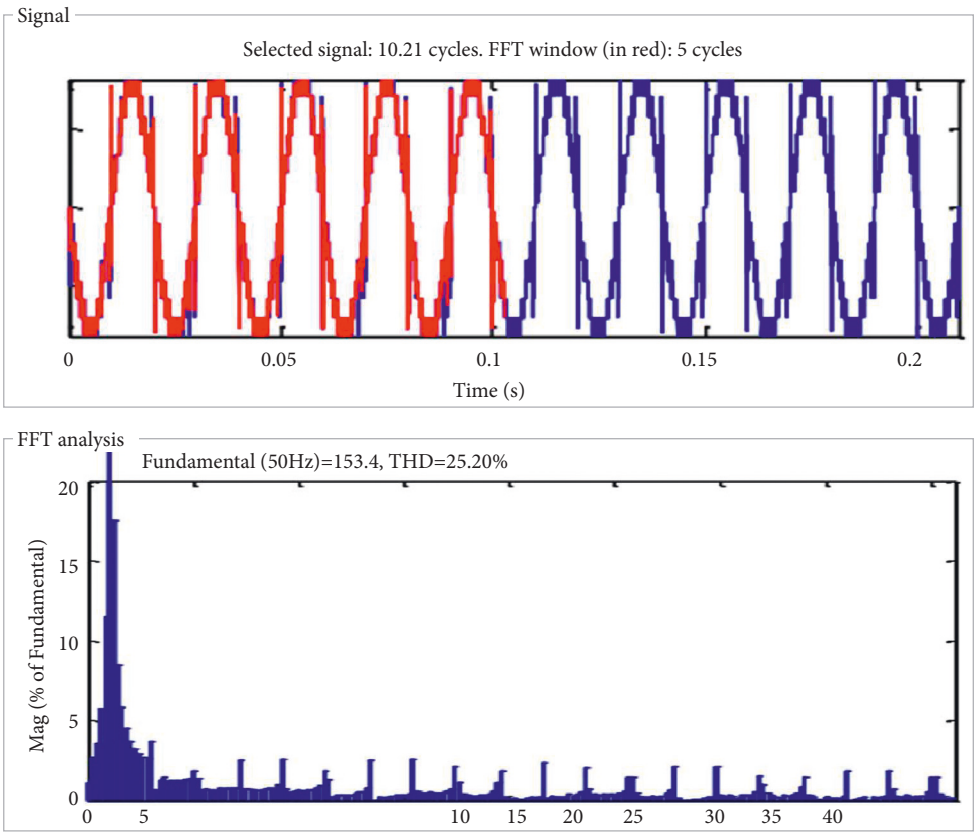

(a)

Figure 18: Continued.

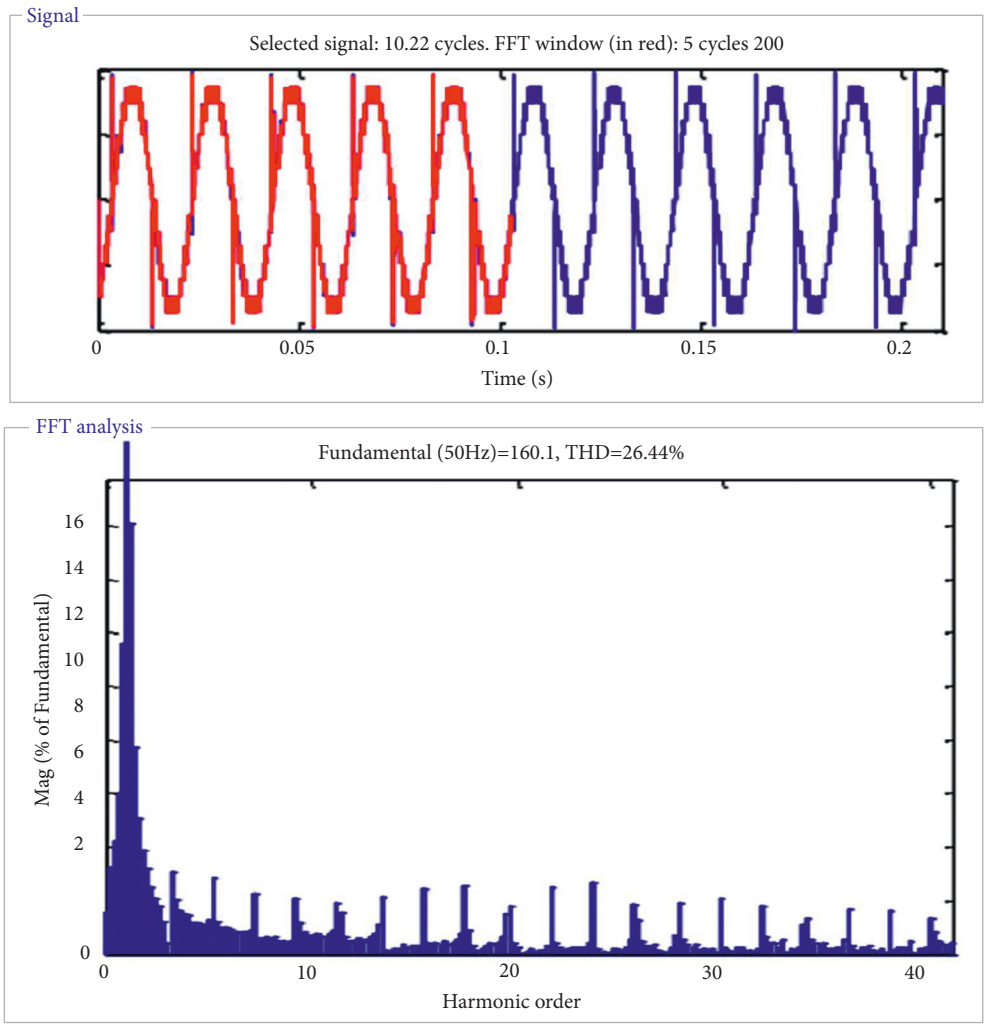

(b)

Figure 18: Continued.

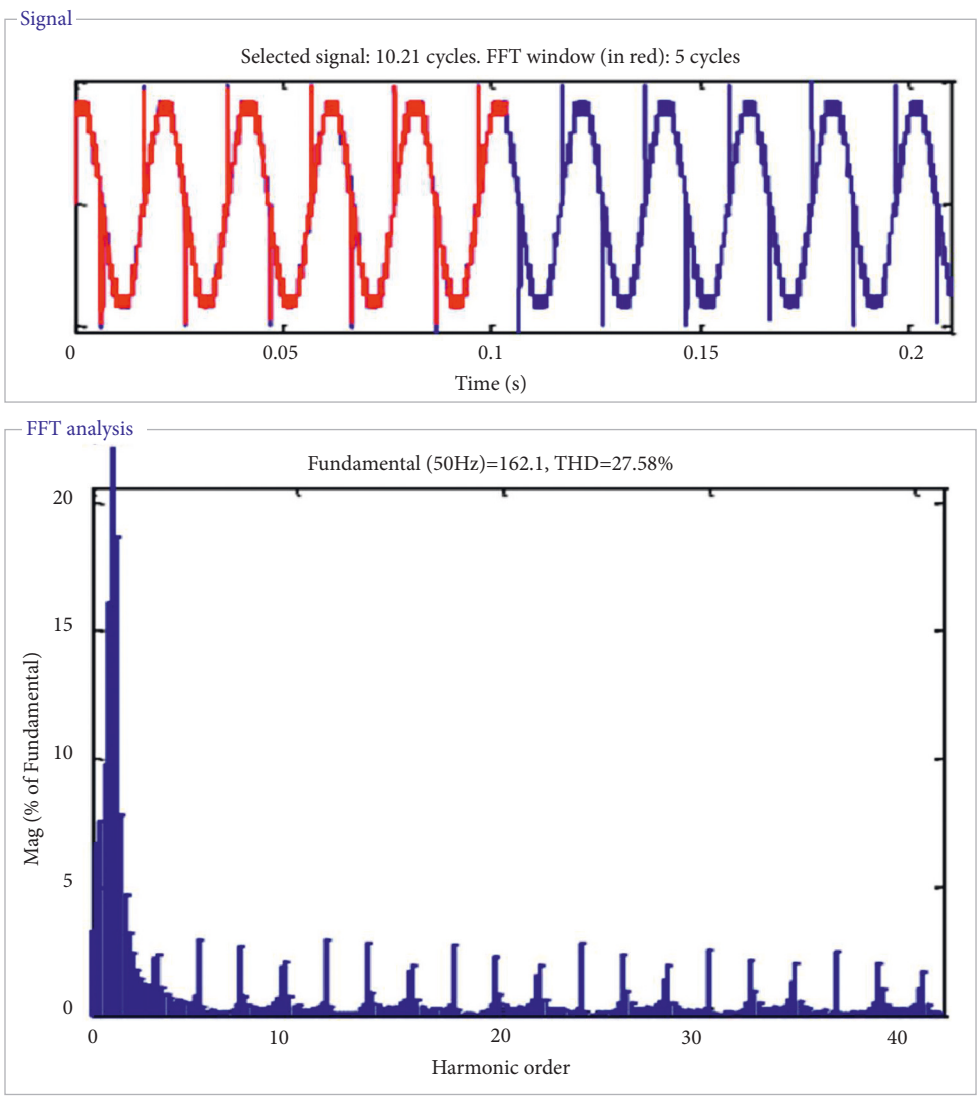

(c)

Figure 18: Harmonic analysis of phase output voltage phase (a) phase 'a', (b) phase 'b', (c) phase 'c'.

was tracked in Figure 8 with Kp = −12.9134 from −0.40133 and Ki −233865.3511 from −11065.9585. The rise time was fairly reduced from 0.000198 sec to 1.67e-05 sec and the settle time was also reduced from 0.000573 sec to 8.92e-05 secs. The reference tracking peak value is 3.74 percent, which is reduced by 5.38 percent. The tuned system reference tracking peak overshoot was reduced by 3.74 percent from 5.38 percent in this respect. Even though the overshoot and settling time were significantly reduced, the peak value is 1.04 from 1.05.

After this, Kp = 10.3256 and Ki = 19174.3203 were adjusted, and as seen in Figure 9, this provided a strong phase response. The reference tracking phase margin of the Bode plot is 171 and the lag margin is 0.000101 sec at the 29700 rad/sec frequency. Figure 10 shows the reference tracking phase margin of the Bode plot. The peak gain of the controller action is −20.3 db at a 1x sec frequency and the phase margin is −159 at 6730 rad/sec with a corresponding 0.000521 sec delay margin as seen in Figure 12. For any controller loop, the rejection of the input and output disturbance is sufficient to minimize the gap between the output to input ratio or to achieve the same as the output relation.

At 142 msec, the input interference of this peak amplitude system is 0.0751. The time of the production disruption raise is 117 msec and 191 msec is the settling time. The observation of input and output disturbance rejection from graph Figures 9–14 Kp = 10.3256 and Ki = 19174.3203 is accomplished with the shortest settling time to reduce the gap between the reference and output.

The output obtained via the inverter at the PI controller Kp = 10.3256 and Ki = 19174.3203 is explained in the following figures from Figures 17 and 18. Figures 17(a) and 17(b) are the three-phase output voltage and the waveform of the current. As opposed to control methods, the output voltage distortions were minimized. However, the output voltage involves major distortions in the quantity and has

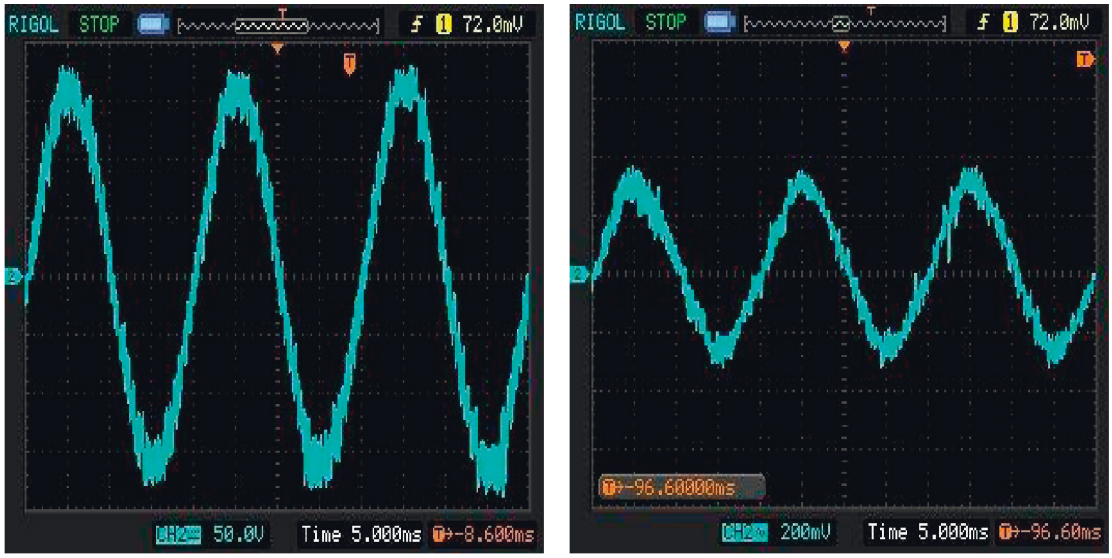

(a) (b)

Figure 19: Output waveform for phase 'a' (a) voltage and (b) current.

(a) (b)

Figure 20: Output waveform for phase 'b' (a) voltage and (b) current.

not been completely minimized in the waveform. The distortion in the output voltage waveform and the peak value is 163 volts, as seen in Figure 17(a).

Similarly, because of inductive reactance load and step "a", "b", and "c" are 0.96 Amps, 0.83 Amps, and 0.61 Amps, respectively, the output current harmonics were decreased in considerable amounts in Figure 17(b). Because of the nonlinear unbalanced load present, these loads smooth the current waveform and decrease the current harmonics.

Phases *a*, *b*, and *c* have a peak output voltage of 157.3 volts, 161.5 volts, and 150.7 volts are 25.2 percent, 26.44 percent, and 27.58 percent, respectively, in Figures 18(a)–18(c) and their equivalent output voltage proportion of gross harmonics distortion. The simple output voltage was increased and the harmonic portion was substantially reduced relative to the fifteen-level asymmetrical cascaded multilevel inverter without the controller. 153.4 volts, 160.1 volts, and 162.1 volts in phases "a", "b", and "c", respectively, are the first output voltages. In the inverter output phase terminals, the harmonic portion is due to the presence of neutral current or unbalanced voltage and current.

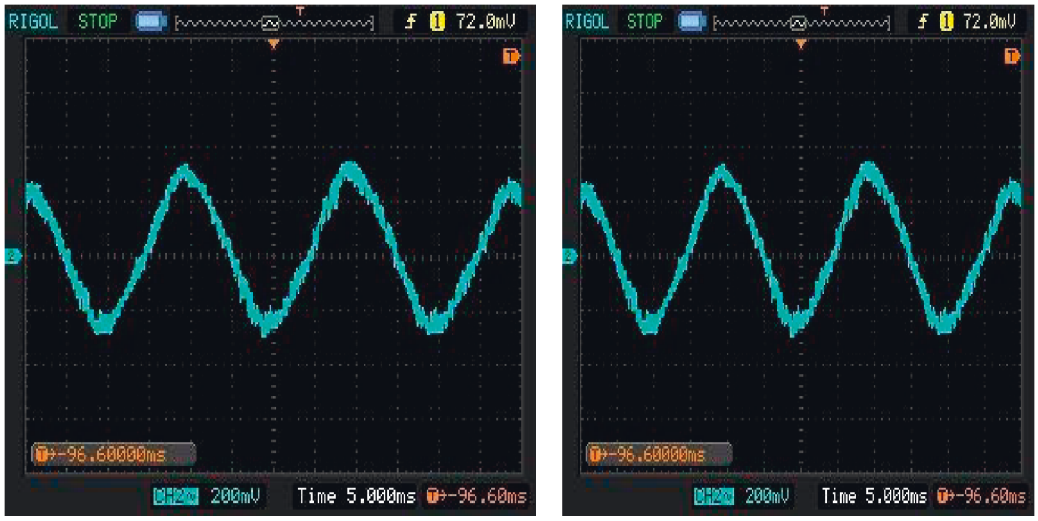

(a) (b)

Figure 21: Output waveform for phase 'c' (a) voltage and (b) current.

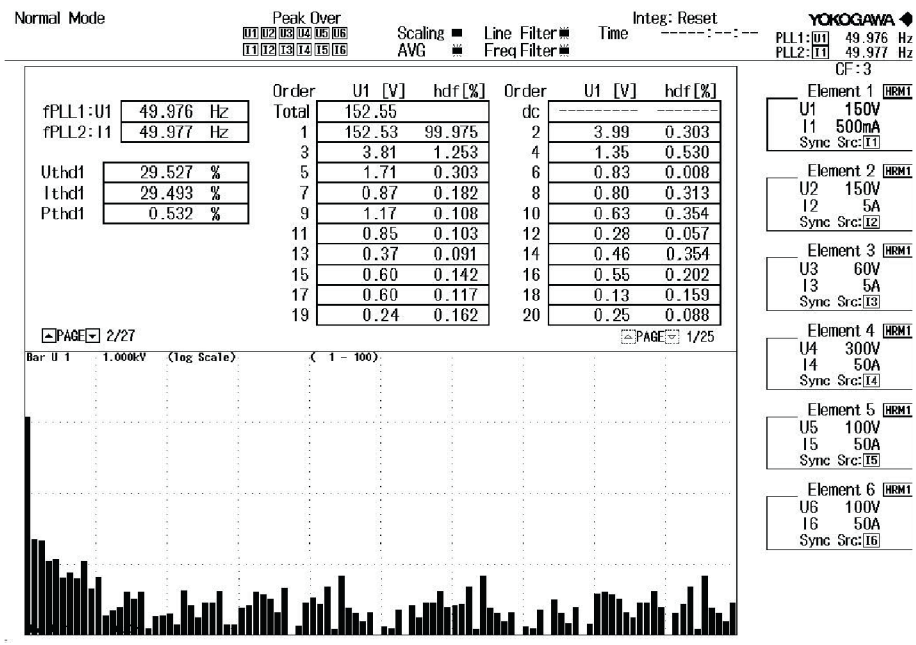

Figure 22: THD spectrum analysis of the phase output voltage.

3.2. Hardware Results. The simulated effects of the fifteen-level boost cascaded multilevel inverter with the PI controller were conducted experimentally to validate designed DC source parameters, nonlinear unbalanced load, and carrier frequency and inverter configuration with the same value.

In Figures 19–21, the inverter hardware phase output was given and the maximum output voltage of the inverter phase "a", "b", and "c" are 152 V, 157 V, and 160 V, respectively. Similarly, in Figures 19(a) and 21(a), the inverter is 0.76 amps, 0.9 amps, and 0.65 amps, respectively. The output voltages of an inverter are distortions that are smaller than those without the output voltage waveform controller, as seen in Figure 19(a). As seen in Figure 20(a), the simple output voltage of the inverter is increased to 152.55 volts. In Figure 22, the output voltage even and odd harmonic component magnitudes are shown, and in the same Figure 22, the estimated component range bar map up to the hundred orders is also presented. The effects of the simulated and hardware configuration are similar to significance, and this suggested scheme provided improved the performance compared to the experimental results without the technique of the controller. In the hardware performance, the THD was lowered by 29.527 percent, and as seen in Figure 22, the unbalanced phase voltage was also increased relative to the previous device. The proposed system did not generate less

than the normal THD value and allowed increased output in switching systems.

4. Conclusion

In this segment, with the lower count of power semiconductor switches and other supporting circuits, the three phase fifteen stage asymmetrical cascaded multilevel inverter with the PI controller was modeled. The output of the PI controller inverter due to unbalanced nonlinear loads has a higher percentage of harmonics. In order to restrict the harmonics and track the output as close as a comparison, PI controller feedback was introduced for this purpose. In order to regulate the voltage and the reference for generating the switching pulses of the inverter PWM, the inner current loops and outer voltage loops were planned. The line impedances are eliminated by cross-coupling the feed-forward loop of imaginary components. In simulation with nonlinear unbalanced loads, the built components are verified. The PI controller's simulated results minimized the steady-state error, peak overshoot, and settling time. In contrast with the open-loop operation of the proposed inverter, the non-linear unbalanced output voltage difference, and the harmonics were minimized. Around the same time, the proposed system did not yield lower THDs and did not conform to the THD limit norm.

Data Availability

The data used to support the findings of this study are included within the article.

Conflicts of Interest

The authors declare that they have no conflicts of interest.

References

[1] S. S. Lee, Y. Yang, Y. P. Siwakoti, and K.-B. Lee, "A novel boost cascaded multilevel inverter," *IEEE Transactions on Industrial Electronics*, vol. 68, no. 9, pp. 8072–8080, 2021.

[2] R. Ravindran, C. R. Sathiasamuel, P. Ramasamy, and K. Balasubramanian, "MSVM-based hybrid energy-fed quasi-Z-source cascaded H-bridge inverter for grid-connected system," *Int Trans Electr Energ Syst*, vol. 31, no. 12, Article ID e13139, 2021.

[3] Yu Liu, H. Hong, and A. Q. Huang, "Real-time algorithm for minimizing THD in multilevel inverters with unequal or varying voltage steps under staircase modulation," *IEEE Transactions on Industrial Electronics*, vol. 56, no. 6, pp. 2249–2258, 2009.

[4] R. Ramkumar, M. V. Kumar, and D. Sivamani, "Fuzzy logic based soft switched active clamped boost converter charging strategy for electric vehicles," in *Proceedings of the 2020 4th International Conference on Electronics, Communication and Aerospace Technology (ICECA)*, pp. 1334–1339, Coimbatore, India, November 2020.

[5] A. Ajami, M. R. J. Oskuee, M. T. Khosroshahi, and A. Mokhberdoran, "Cascade-multi-cell multilevel converter with reduced number of switches," *IET Power Electronics*, vol. 7, no. 3, pp. 552–558, 2014.

[6] R. S. Alishah, D. Nazarpour, S. H. Hosseini, and M. Sabahi, "-voltage levels," *IET Power Electronics*, vol. 7, no. 1, pp. 96–104, 2014.

[7] I. Colak, E. Kabalci, and R. Bayindir, "Review of multilevel voltage source inverter topologies and control schemes," *Energy Conversion and Management*, vol. 52, no. 2, pp. 1114–1128, 2011.

[8] E. E. Espinosa, J. R. Espinoza, P. E. Melin et al., "A new modulation method for a 13-level asymmetric inverter toward minimum THD," *IEEE Transactions on Industry Applications*, vol. 50, no. 3, pp. 1924–1933, 2014.

[9] A.-V. Ho and T.-W. Chun, "Topology and modulation scheme for three-phase three-level modified Z-source neutral-point-clamped inverter," *IEEE Transactions on Power Electronics*, vol. 34, no. 11, pp. 11014–11025, 2019.

[10] A. Hota, S. Jain, and V. Agarwal, "An improved three-phase five-level inverter topology with reduced number of switching power devices," *IEEE Transactions on Industrial Electronics*, vol. 65, no. 4, pp. 3296–3305, 2018.

[11] A. Masaoud, H. W. Ping, S. Mekhilef, and A. Taallah, "-level inverter," *IET Power Electronics*, vol. 7, no. 12, pp. 3052–3061, 2014.

[12] Y. Yu, G. Konstantinou, B. Hredzak, and V. G. Agelidis, "Power balance optimization of cascaded H-bridge multilevel converters for large-scale photovoltaic integration," *IEEE Transactions on Power Electronics*, vol. 31, no. 2, pp. 1108–1120, 2016.

[13] Y. Nakagawa and H. Koizumi, "A boost-type nine-level switched capacitor inverter," *IEEE Transactions on Power Electronics*, vol. 34, no. 7, pp. 6522–6532, 2019.

[14] J. Liao, K. Corzine, and M. Ferdowsi, "A new control method for single-dc-source cascaded H-bridge multilevel converters using phase-shift modulation," in *Proceedings of the 2008 Twenty-Third Annual IEEE Applied Power Electronics Conference and Exposition*, pp. 886–890, Austin, TX, February 2008.

[15] H. Abu-Rub, J. Holtz, J. Rodriguez, and G. Baoming, "Medium-voltage multilevel converters-state of the art, challenges, and requirements in industrial applications," *IEEE Transactions on Industrial Electronics*, vol. 57, no. 8, pp. 2581–2596, 2010.

[16] E. Villanueva, P. Correa, J. Rodriguez, and M. Pacas, "Control of a single-phase cascaded h-bridge multilevel inverter for grid-connected photovoltaic systems," *IEEE Transactions on Industrial Electronics*, vol. 56, no. 11, pp. 4399–4406, 2009.

[17] M. R. Gharib, "Comparison of robust optimal QFT controller with TFC and MFC controller in a multi-input multi-output system," *Reports in Mechanical Engineering*, vol. 1, no. 1, pp. 151–161, 2020.

[18] V. Dertimanis, E. Chatzi, and S. Masri, "On the active vibration control of nonlinear uncertain Structures," *Journal of Applied and Computational Mechanics*, vol. 7, pp. 1183–1197, 2021.

[19] L. Wang, Q. H. Wu, and W. Tang, "Novel cascaded switched-diode multilevel inverter for renewable energy integration," *IEEE Transactions on Energy Conversion*, vol. 32, no. 4, pp. 1574–1582, 2017.

[20] G. Xu, D. Chen, and A. Qu, "Simple boost modified space vector modulation strategy for three-phase quasi-z-source inverter," in *Proceedings of the IECON 2020 The 46th Annual Conference of the IEEE Industrial Electronics Society*, pp. 5365–5370, Singapore, October 2020.

[21] M. Mohseni and S. M. Islam, "A new vector-based hysteresis current control scheme for three-phase PWM voltage-source

inverters," *IEEE Transactions on Power Electronics*, vol. 25, no. 9, pp. 2299–2309, 2010.

[22] Y. He, Y. Xu, and J. Chen, "New space vector modulation strategies to reduce inductor current ripple of z-source inverter," *IEEE Transactions on Power Electronics*, vol. 33, no. 3, pp. 2643–2654, 2018.

[23] J. Pereda and J. Dixon, "Cascaded multilevel converters: Optimal asymmetries and floating capacitor control," *IEEE Transactions on Industrial Electronics*, vol. 60, no. 11, pp. 4784–4793, 2013.

[24] M. R. V. Goutham and M. V. G. Rao, "Control of a three-phase cascaded h-bridge multilevel inverter for stand-alone PV system," *International Journal of Modern Engineering Research*, vol. 2, no. 2, pp. 278–282, 2012.

Hindawi
Mathematical Problems in Engineering
Volume 2022, Article ID 2401261, 8 pages
https://doi.org/10.1155/2022/2401261

Review Article

A Bridgeless LUO Converter with Glowworm Swarm Optimized Tuned PI Controller for Electrical Applications

M. Sivaramkrishnan,[1] M. Siva Ramkumar,[2] Siva Subramanian S,[1] and Nyagong Santino David Ladu[3]

[1]*Department of EEE, Karpagam College of Engineering, Tamil Nadu, India*
[2]*Department of EEE, Karpagam Academy of Higher Education, Coimbatore, Tamil Nadu, India*
[3]*Department of Mathematics and Physics, Rumbek University of Science and Technology, South Sudan*

Correspondence should be addressed to Nyagong Santino David Ladu; nyagongsantino19@gmail.com

Received 24 March 2022; Revised 17 April 2022; Accepted 22 April 2022; Published 17 May 2022

Academic Editor: Abu Zaharin Ahmad

The synchronous reluctance motor (Sync-RM) is known for its higher reliability, faster dynamic response, higher efficiency, higher speed range, higher power density, and higher torque per ampere. Consequently, the scope of research into emerging Sync-RMs drive system has been extended. For different kinds of mechanical and electrical applications, motors are important components of any machine or tool. There are several types of motors available for various kinds of industrial applications, but the benefits of Sync-RM in medium- and low-power applications have eventually been very efficient compared to other motor types, regarding the factors such as high flux density per unit volume, high efficiency, requirements of low maintenance, and low electromagnetic obstruction. This research proposed a Sync-RM drive fed by a bridgeless LUO converter (BLLC) using the Glowworm Swarm Optimization (GSO) tuned proportional integral (PI) controller. High competence, higher power density, and a small structure of the motor drive are delivered by the PI-tuned converter. The output voltages are related to the Sync-RM motor of the proposed converter. Due to its minimum effort and modest development, the Sync-RM here is chosen for the drive. The proposed Sync-RM drive framework based on the LUO converter was evaluated by simulation using the Matlab/Simulink tool.

1. Introduction

The term "Synchronous Reluctance Motor" implies a synchronous speed of rotation. In variable speed applications, it is a significant match to the induction motor. The Sync-RM is absolutely free of magnets and their problems with operation [1]. It is economical to manufacture and can run at extremely high speeds and higher temperatures than motors with a permanent magnet (PM). Its power factor and performance, however, are not as high as those of a PM motor and the requirement for the converter kVA is higher. It can work from basically normal PWM AC inverters and has a lower ripple of torque [2]. The synchronous PM motor functions as a Sync-RM; the magnets are left out or demagnetized; that is, there is no field winding or permanent magnet on the rotor for the Sync-RM. There are salient poles in the rotor, but there are flat, scattered poles in the stator. Low cost, robust, and high efficient (ideally no rotor loss) Sync-RMs are capable of working at very high speeds at higher temperatures than PM motors [3].

For low-power equipment such as IEC 61000-3-2, the PFC converter offers the power factor based on power quality requirements. In addition, the new formation decreases the THD input current that improves the present correction factor [4]. To operate the PFC converters, continuous conduction mode (CCM), critical conduction mode (CRM), and discontinuous conduction mode (DCM) are the three working modes explored. Low input current surge and decreased electromagnetic interference (EMI) are given by the consistent inductor current in CCM. As the inductor current remains constant in the switching time frame, electromagnetic interference encounters hard switching [5, 6].

The LUO converter is widely utilized due to the voltage contains inherent qualities such as lift, ultra-lift, and super-lift, which are all useful in the conversion process. For example, the super-lift converter was considered to be remarkable since the voltage switch gain is larger than that of the other converters. This proposed structure was hence taken by the single-phase power source, which was followed by a filter, and a BLLC, which transforms it into a Sync-RM motor drive. The BLLC is regarded as the precontroller with the in-built power factors that is used in conjunction with the DICM (discontinuous inductor current mode). Controlling the speed of the Sync-RM motor to a substantial extent can be accomplished by varying the DC link voltage of the proposed LUO converter. The Sync-RM is powered by direct current derived from a BLLC, which serves as a PFC rectifier and was sustained by the single-phase alternating current. There are two components to the proposed PFC BLLC. This converter was divided into the operations between supply voltage's negative and positive half-cycles, as well as the complete switching cycles.

PFC converters achieve zero power switch current and, for the diode, zero current in CRM operation. Although the negative label related to CRM is the switching frequency fluctuating through a broad range, resulting in a decrease in efficiency and complexity in the outline of the electromagnetic field (EMF) channel [6], the transformation techniques are easily established in the end, and there are many divisions for DC-DC converters. Since the voltage has its intrinsic qualities such as the ultra-lift, super-lift, and lift, an LUO converter is commonly used. The super-lift LUO converter was remarkably dependent, among other things, on the fact that the gain of the voltage switch was high [7, 8]. In the electronic circuit strategy, the voltage lift (VL) method is widely used.

The super-lift (SL) technique, along with enhancing the transformation mechanism, was more efficient than the VL system. For controlling the stator windings sequence, Sync-RM requires energy converters. Generally, at each point, Sync-RM converters have two switches. These Sync-RM current waveforms are very flexible and compulsive controls [9]. Additionally, the circuit of the converter contains a passive low-pass LC filter. An alteration in the DPF (distortion power factor) is given by the LC passive filters, as the design of the filter capacitor was created to provide the appropriate phase to switch to PFC. In the meantime, without considering the supply-side details, this passive filter also for the switching harmonic provides low impedance.

2. Related Works

Due to the high output power, low cost, and durability in different industry applications, Sync-RMs has received a lot of attention [9]. Sync-RM may replace the induction, switched reluctance, and permanent magnet motors that are most widely used. In the performance, torque, and power density, Sync-RM has been shown to outperform similarly dimensioned induction motors. Due to the inclination of the salient rotor poles to harmonize them with the synchronously rotating field produced by the stator, the motor-driven torque was generated by reluctance. The magnets were left out of the rotor in this motor, or they were demagnetized. There are salient poles in the rotor of a Sync-RM, but neither field windings nor PMs.

The Sync-RM is based on the reluctance torque principle. A spatial sinusoidal distributed magneto-motive force (MMF) was produced by the stator windings. Because of the configuration that generated a nonisotropic magnetic reluctance that interacted with the stator MMF [1], the rotor saliency generated the rotor torque. Cage less and line-start were the main types of Sync-RMs. The other two kinds were radial type and axial type, depending on the magnetization (when the stator winding was energized). The brushless DC motor drive, which was supplied by a BLLC power-factor-correction (PFC) converter, was controlled by a single voltage sensor, which also controlled the BLDC motor speed and PFC on the alternating current supply[5, 6].The Sync-RM's output depends primarily on the magnetizing inductance values of the d and q-axis. Sync-RM's saliency ratio determined the power factor, parameter variance sensitivity, and field-weakening efficiency of the motor. In particular, about half of the saliency ratio was the ideal constant-power speed range. Hence, for achieving a 4:1 stable power range, theoretically, the saliency rate of at least 8 was needed [3]. A technique based on finite element simulation of the magnetic field was used to improve the Sync-RM architecture [2]. Based on the cascaded field-oriented vector control (FOC), the classical Sync-RM control technique was proposed. The Sync-RM exhibited substantial nonlinearity in magnetic saturation despite numerous advantages, rendering its power-optimal and ideally sensor less FOC complicated [10].

If the source was acquired from single-phase or three-phase AC transmission, the source current presents rich harmonics. Comprehensive research was made and continues to enhance the generated torque efficiency and source current's efficiency when power was used from the AC supply [11]. Analysis in specific primary direction would analyze the different potential of utilizing new design tools, such as the analysis of finite elements or the use of various other software tools for the electromagnetic design, which can result in enhanced torque development abilities with minimum torque ripple [12]. The pole face structuring was also addressed a potential technique to increase the efficiency of torque. The other line of research was to discover the options of new circuit topologies to drive the Sync-RM, and this line of research has also delivered substantial several topological changes that typically occur with the form of accessible sources such as DC sources from rectifiers, renewable sources such as solar panels, sources of fuel cells, and batteries [10].The Sync-RM could be tried with uncontrolled and controlled rectifiers trailed with the DC-DC converter of a general kind or latest converters such as SEPIC, CUK, or LUO. Another alternative was the matrix converter if the source was a multiphase form AC. The development of different control schemes was the other direction of research [7].

For convenience, the PI speed controller parameters and the initial EKF covariance matrix value were tuned off using

PSO (particle swarm optimization) in [12]. Newly built prototypes of Sync-RMs provide an alternative to the reference induction motors shown in [13]. Since rotor losses are reduced, Sync-RM has slight high efficiency over IM. Low-power variables were the key downside of Sync-RM. There was no need for field excitation at zero torque in this motor; hence, the losses of electromagnetic spinning were removed. Demagnetization was not a concern; Sync-RMs were, therefore, generally more efficient than permanent magnet motors.

Using multipurpose feature, a smart controller for speed regulation of the BLDC drive system was presented in [14]. It was decided to employ a fractional order PID controller based on a modified LUO converter in order to eliminate the torque ripples and manage the BLDC motor speed in this case. With the hybrid technique, the researchers were able to synthesize an improved LUO converter that was on the basis of ANFIS as well as elephant herding optimization. To begin, the optimization technique was examined in order to determine the error function. ANFIS controllers are also efficient since they are built using a method that is systematic in its tracking of error function to deliver the greatest possible gain values optimal. The control method used to decrease harmonics and torque ripples was successful.

The use of a bridgeless power factors adjusted LUO converter allows the switched reluctance motor to be driven directly from the utility alternating current supply. It was, therefore, appropriate for a wide range of home applications due to this. The usage of a sliding mode controller helps to improve the control over speed management. For achieving the appropriate speed, the front-end BLLC and the drive systems could both be controlled. Various configurations of the modulation index and duty cycle are possible, allowing the system to be versatile in order to fulfil different demands while maintaining a low steady-state error rate [15].

A hybrid renewable energy source that was incorporated into the grid was proposed in [16]. The LUO converter, which was controlled by an optimized PI controller, was employed to maintain a steady DC link voltage. The voltage was raised with the help of a LUO converter, and the raised voltage was regulated by an optimized PI controller, which was implemented. The optimization process was carried out with the support of the ABC optimization. Because of this optimization approach, it was possible to keep the power fluctuation in a steady-state mode. It was a straightforward and dependable approach for doing optimization effectively.

3. Proposed Methodology

The proposed Sync-RM drive system based on the BLLC block diagram is shown in Figure 1. After the filter, a single-phase supply then adopts this proposed model, and BLLC converts to a Sync-RM motor drive. The BLLC converter was held to be an in-built power factor precontroller for DICM (discontinuous inductor current mode) operation. The Sync-RM motor's speed is significantly controlled by switching the DC link voltage of the proposed LUO converter.

The Sync-RM is operated by DC power attracted from a BLLC converter used from AC single-phase utility power supply as a PFC rectifier. In the following sections, the delicate elements of the BLLC-based PFC rectifier are presented.

3.1. PFC BLLC Converter. The PFC BLLC was divided into two parts that integrate the task into the supply voltage's negative and positive half-cycles and the complete switching period. The circuit diagram of the proposed BL-LUO Converter is shown in Figure 2.

3.2. Operation Modes in BLLC Converter. The PFC function of the BLLC switch between the supply voltage's positive half-cycle and the complete switching time is shown in Figures 3–5.

3.2.1. Mode I. As shown in Figure 6, the inductor on the input side (i_{Li1}) saves energy according to the current passage (i_{Li}) through it, and (i_{Li1}) is the inductor when the switch SW_1 is triggered. In addition, at the direct current side capacitor (C_d) and an output side inductor (L_{o1}), the energy contained in a transition capacitor (C1) was transformed. The median transverse capacitor (V_{c1}) voltage, therefore, minimizes when the DC interface voltage (V_{dc}) and the output inductance (i_{Lo1}) current are extended.

3.2.2. Mode II. As shown in Figure 7, the inductor at input side (L_{i1}) switches its energy to the capacitor (C_1) over diode D_{p1} when SW_1 has been switched off. The current i_{Li1} decreases until it reaches 0, while the voltage increases across over the centre of the middle capacitor (V_{C1}). C_d provides the load with the energy required. Therefore, in this method of operation, DC link voltage V_{dc} decreases.

3.2.3. Mode III. As it is seen in Figure 8, in the input inductor (L_{i1}), no energy was left, i.e., the i_{Li1}current ends at 0 and enters the DCM operation. The capacitor C_a and the output inductance (L_{o1}) were released; thus, when DC voltage link V_{dc} increase in this task appears in the fig, the V_{C1} voltage current of $i_{Lo1}$are decreased. When the SW_1 switch has been returned, the task is repeated.

Similarly, to achieve the desired operation, the supply voltage's negative half-cycle L_{i2} and L_{o2} of the inductor, intermediate D_{n1}, and capacitor diodeC_2 were conducted.

3.3. Zeigler Nicholas Approach for PI Controller Tuning. The initial technique of tuning the PI controller by Zeigler Nicholas (ZN) is additionally called as the method of the reaction curve. Both the elements a and *b* are obtained from the reaction curve obtained, and from these both elements and by utilizing an empirical law, Ki and Kp values are obtained. The Sync-RM speed is an operating voltage function for given load torque, and the DC link operating voltage could be controlled by regulating the duty cycle

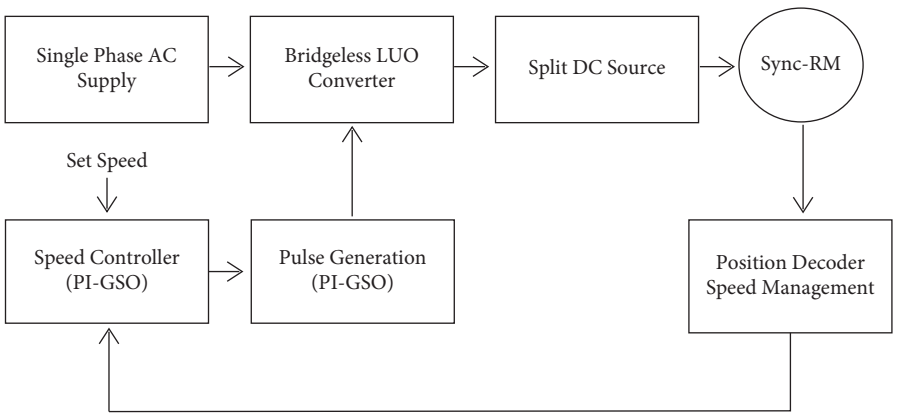

Figure 1: Proposed work schematic diagram of BLLC converter.

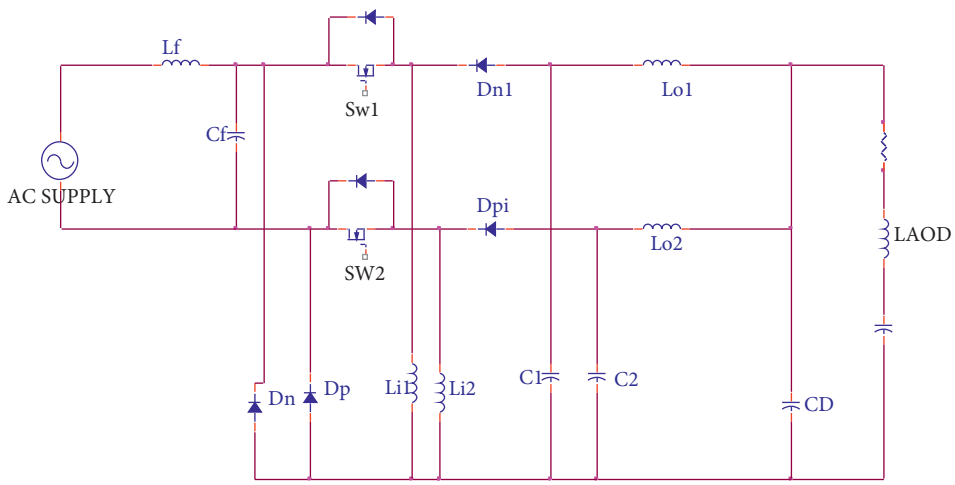

Figure 2: Proposed power factor correction using BL-Luo converter: circuit diagram.

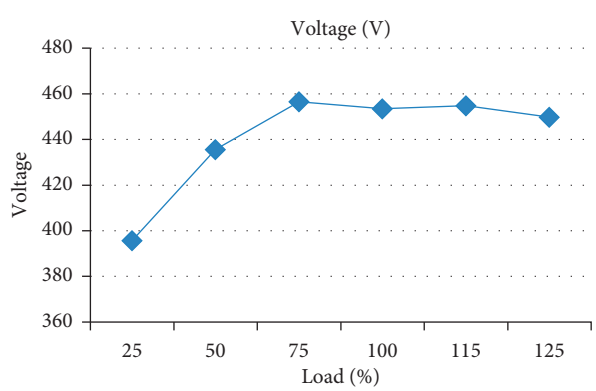

Figure 3: Voltage vs. load.

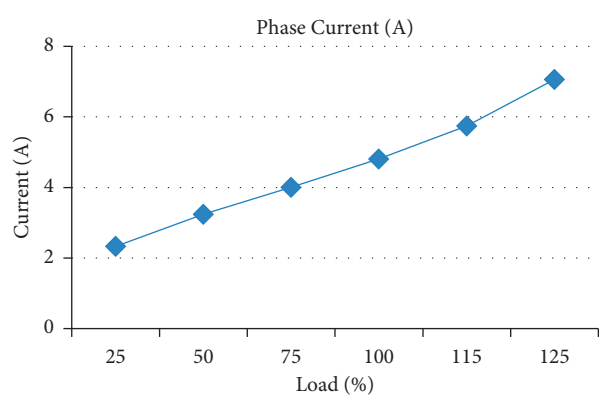

Figure 4: Phase current vs. load.

utilized in the PWM drive system to consecutively energize Sync-RM phases [17].

The DC link voltage hence turns out as the regulated variable, and the manipulated variable turns out as the duty cycle. A transfer function (TF) was obtained to outline the reaction curve among the duty cycle and DC link voltage. In (1), the TF of the approximate model PFC-LUO converter was presented. It estimates the TF among the duty cycle and the voltage of the DC link:

$$\text{DC link Voltage} = 1.746e^{05}s + 4.542e^{08}. \quad (1)$$

To obtain the reaction curve, the transfer function is used. With the change of step from 0 to 0.5, the reaction curve was acquired by adding a step input.

The ZN tuning approach is a conventional method, where the reaction was initially drawn. The curve has a concave section accompanied by a convex section, starting

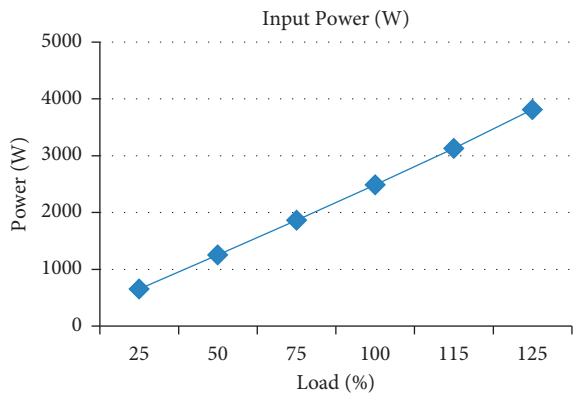

Figure 5: Input power vs. load.

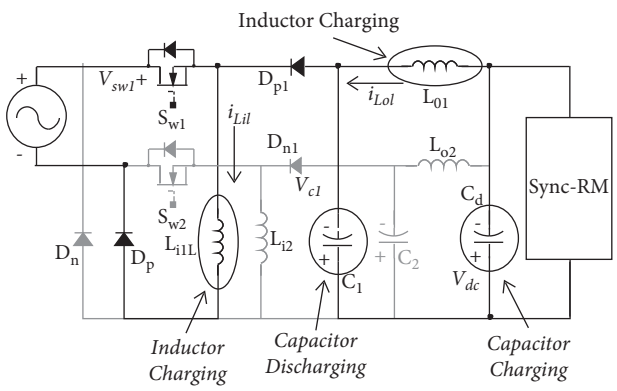

Figure 6: Mode I operation.

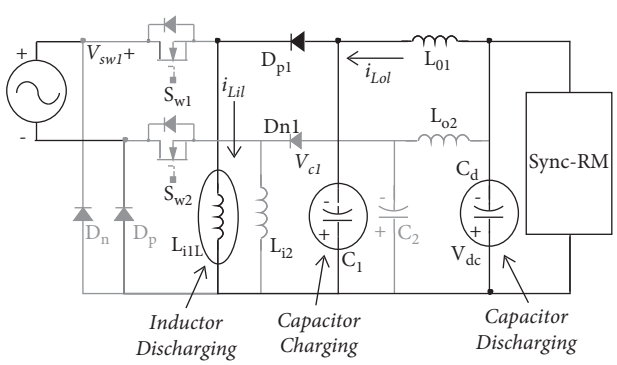

Figure 7: Mode II operation.

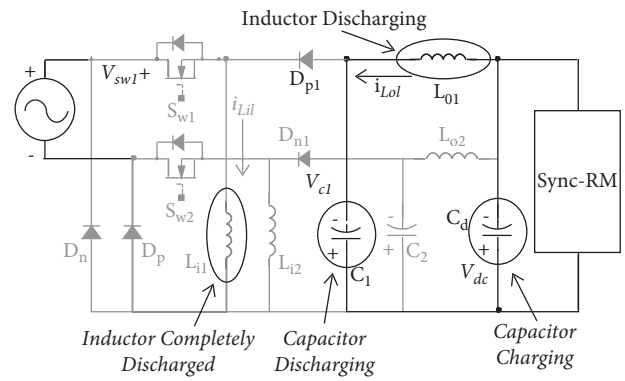

Figure 8: Mode III operation.

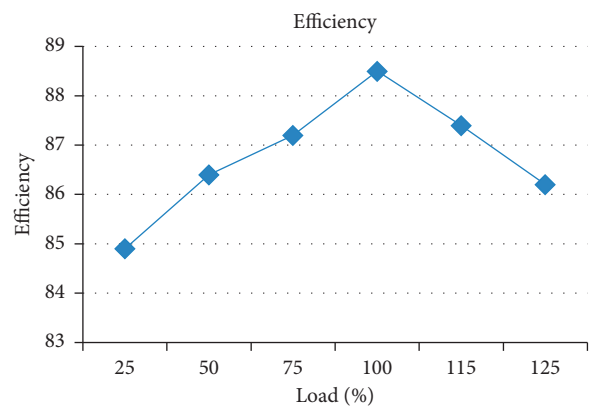

Figure 9: Efficiency vs. load.

from the origin. In the reaction curve, the transition point from the concave section to the convex section is called the point of inflection. By extending the steady-state level according to Figure 9, the acquired values for Ki and Kp and a tangent were plotted through the inflection point, and this tangent obstructs the y-axis and x-axis and the line plotted to the y-axis.

3.4. GSO-Based PI Controller Tuning. By the idea of glowworms foraging or courtship behavior, which glows to attract companions, the GSO algorithm was developed. In GSO, every glowworm has a particular amount of luciferin that defines the intensity of the luminance [18]. Glowworms operate using an algorithm that causes them to seek out their brightest neighbor. Using just local data, the swarm may be separated into several subgroups that intersect via various optimums to a multimodal function, which is the result of these activities. GSO consists of four main stages: distribution, luciferin update, movement, and neighborhood range update. Controlling the performance index is the primary goal of this basic PI tuning approach. For example, the integral square error (ISE) was the objective function's output index that is framed to minimize the ISE. Each of the glowworms solution vectors will be modified at the end of each iteration [19–21].

3.5. Glowworm Distribute Stage. Randomly dispersed n glowworms are placed at various points in the search space. Every glowworm carries the same quantity of luciferin.

3.5.1. Luciferin Update Stage. The update process for luciferin is according to the objective function's value and the past level of individual luciferin. The luciferin update rule is

$$l_g(i) = (1-\rho)l_{g-1}(i-1) + \gamma H\left(x_g(i)\right), \tag{2}$$

where l_g(i) represents at the ith iteration the luciferin value of glowworm g, γ,and ρ, H(xg(i)) is the objective function's

Table 1: Evaluation of kp and ki.

Tuning technique	Gain parameters	
	Kp	Ki
ZN technique	0.1	1.3
PSO technique	0.106	1.38
GSO technique	0.125	1.44

value at the position of the glowworm g, and L(xg(i)) is the luciferin enhancement factor and decay.

3.5.2. Glowworm Movement Stage. During the movement stage, each glowworm follows a probabilistic path to a neighbor with a higher brightness than its own. The chance of a glowworm g travelling to a neighbor h is calculated as follows:

$$p_{gh}(i) = \frac{\left(l_h(i) - l_g(i)\right)}{\sum_{j \in N_g(i)}\left(l_j(i) - l_g(i)\right)}, \quad (3)$$

where $h \in N_g(i)$; N_g(i) is a set that could be verified by

$$h \in N_g(i), N_g(i) = \left\{h: d_{gh}(i) < r_d^g(i); l_g(i) < l_h(i)\right\}, \quad (4)$$

where d_{gh}(i) represents the Euclidean distance within glowworm g and h at the iteration of i and $r_d^g(i)$ represents the variable neighborhood range at the iteration of i related to glowworm g. Then, the movement model for the glowworm is

$$x_g(i+1) = x_g(i) + si * \left(\frac{x_h(i) - x_g(i)}{x_h(i) - x_g(i)}\right), \quad (5)$$

Where $x_g(i)\ \epsilon R^m$ is the glowworm g location at the ith iteration in the m-dimensional real space R^m, $x_h(i) - x_g(i)$ indicates the operator of the Euclidean norm, and si(>0) is the step's size.

3.5.3. Neighborhood Range Update Stage. In the following equation, each glowworm's neighborhood domain is given, considering r_0 as the first neighborhood domain for each glowworm:

$$r_d^g(i+1) = \min\left\{r_s, \max\left\{0, r_d^g(i) + \beta\left(n_i - N_g(i)\right)\right\}\right\}, \quad (6)$$

where β is a constant, n_i is a parameter of control for the number of neighborhoods, r_s represents a glowworm's sensory radius, and N_g(i) represents neighborhoods set [22–28].

The two random numbers are utilized along with this simple GSO algorithm. In Table 1, the ki and kp values obtained from the ZN and the GSO technique were estimated.

4. Results and Discussion

For this section, the simulation based on MATLAB SIMULINK and the setup was designed around a Sync-RM of 2.2 kW (4 pole) motor.

Table 2: Performance analysis of Sync-RM.

Parameters	25%	50%	75%	100%	115%	125%
Voltage (V)	395.7	435.6	456.5	453.4	454.8	449.7
Input_Power (W)	652	1255	1862	2485	3129	3814
Phase_Current (A)	2.33	3.24	4.01	4.81	5.75	7.06
Torque (Nm)	3.48	7.01	10.12	14.07	17.53	21.08
Speed (rpm)	1500	1500	1500	1500	1500	1500
Output power (W)	551.3	1104	1645	2206	2756	3302
Efficiency	84.9	86.4	87.2	88.5	87.4	86.2

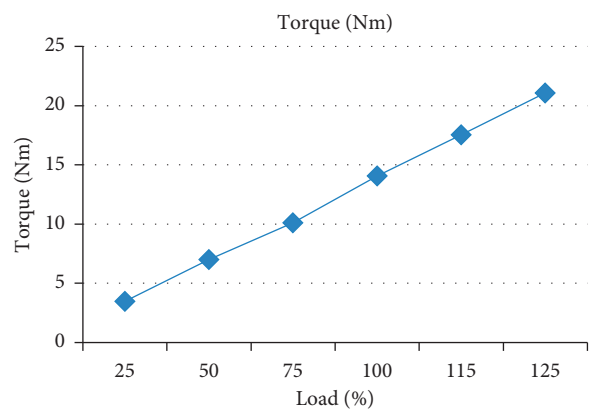

Figure 10: Torque vs. load.

Variable frequency drives are used in the model. The variable AC power source is fed to the inverter. During the measurement, the inverter's input voltage is set. In the inverter's operational menu, the power and rotational speed are adjusted to the suitable rated outcome. The inverter controls the motor's output power and speed. Two power analyzers are employed in the prototype system for measurements. One is among the varying AC supply and inverter, while the other is among the motor and inverter. A direct calculation of electrical output of the converter, based on the motor's input power and the output mechanical power of its shaft, is used to estimate Sync-RM efficiency. The output torque of the motor was determined using a torque sensor. The IEC 60034-2-3 loads test is used to base the computation. At regulated speeds of 1, 25, 1, 15 and 1, 0, 75 and 0, 50, and 25 percent of the rated load, six normal operating points are carried out according to the rules. For each load, we monitor the input control, load torque, stator total current, phase-phase voltage, and speed. Table 2 displays the results of the load test.

The measurements of the parameters included both input and output measurements. These measurements are calculated at different load levels, with load level varying from 25% to 125%. Based on the load level, there is variation

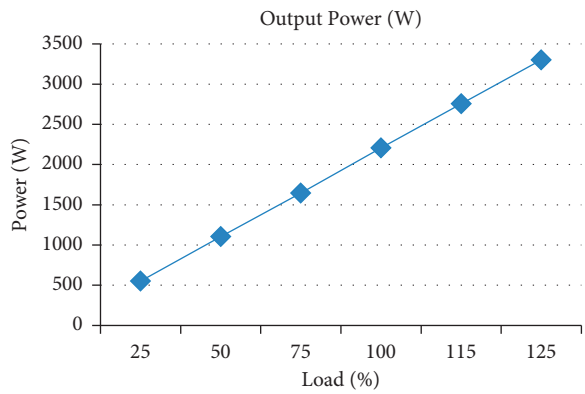

Figure 11: Output power vs. load.

in the performance of the Sync-RM. The voltage increases constantly while the load increases; the voltage reaches to its maximum level of 449.7 V when the load is given at 125%. The phase current reaches from 2.33 A to 7.06 A. The input power was measured in watts; it varies from 652 W to 3814 W based on the load level given from 25% to 125%. The torque was measured using the sensor which ranges between 3.48 Nm and 21.08 Nm based on different load levels. The speed of the motor is measured at each load level, where the speed is set at constant speed of 1500 Rpm at each load. The output power was measured in watts, where it varies from 551W to 3302W. The efficiency obtained was varied for 84.9% to 88.5% (refer Figures 3–11).

5. Conclusion

To drive the 2.2 kW Sync-RM with a split DC power source, a novel PFC BLLC was developed in this research. Utilizing a Zeigler [29] Nicholas approach and GSO-based tuned PI controller, the Sync-RM speed regulation was carried out, which [30] controls the BLLC's duty cycles and controls DC link voltage. Correlated with a standard rectifier-based drive for the Sync-RM, the primary current extracted from the AC single-phase supply showed enhanced quality of power. Using the MATLAB SIMULINK tool and experimental verification, the proposed concept was simulated and validated. The proposed GSO-based PI tuned method compared to the ZN method and PSO provided better results. Stator current and phase-phase voltage were evaluated in addition to input control and output torque during the performance evaluation.

Data Availability

No data were used to support this study.

Consent

Not Applicable.

Conflicts of Interest

The authors declare that there is no conflicts of interest.

Authors' Contributions

Dr. M. Sivaramkrishnan and. Dr. M. Siva Ramkumar are responsible for data collection and validation. Author Siva Subramanian S. is responsible for surveys and content writing and proof reading. Author Nyagong Santino David Ladu is responsible for algorithm design, development, and proofreading.

References

[1] B. L. Mbula and s. Chowdhury, "Performance improvement of synchronous reluctance motor: a review," in *Proceedings of the IEEE PES Power Africa*, pp. 402–406, Accra, Ghana, June 2017.

[2] A. V. Zakharov, S. I. Malafeev, and A. L. Dudulin, "Synchronous reluctance motor: design and experimental research," in *Proceedings of the International Conference on Electrical Power Drive Systems*, pp. 1–4, Novocherkassk, Russia, October 2018.

[3] L. Haataja and L. Pyrhonen, "Permanent magnet assisted synchronous reluctance motor: an alternative motor in variable speed drives," in *Energy Efficiency in Motor Driven Systems*, F. Parasiliti and P. Bertoldi, Eds., pp. 101–110, Springer, Berlin, Germany, 2003.

[4] Y. Li, Y. Yang, Z. Zhu, and W. Qiang, "A feed forward compensation design in critical conduction mode boost power factor correction for low-power low total harmonic distortion," *Journal of Semiconductors*, vol. 33, no. 3, 035007 pages, 2012.

[5] B. Singh, V. Bist, A. Chandra, and K. Al-Haddad, "Power quality improvement in PFC bridgeless-Luo converter fed BLDC motor drive," in *Proceedings of the IEEE Industry Applications Society Annual Meeting, Lake Buena Vista*, pp. 1–8, Lake Buena Vista, FL, USA, October 2013.

[6] B. Singh, V. Bist, A. Chandra, and K. Al-Haddad, "Power factor correction in bridgeless-Luo converter fed BLDC motor drive," *IEEE Transactions on Industry Applications*, vol. 51, no. 2, pp. 1179–1188, 2015.

[7] V. R. Kota and B. N. Kommula, "A modified bridgeless Luo converter for simultaneous torque ripple minimization and power factor correction in BLDC motors," *Journal of Engineering Technology*, vol. 6, pp. 71–81, 2018.

[8] M. Vishvanath and R. Balamurugan, "Bidirectional Luo converter fed switched reluctance motor," *TELKOMNIKA Indonesian Journal of Electrical Engineering*, vol. 12, no. 12, pp. 8120–8125, 2014.

[9] S. H. Hwang, J. M. Kim, H. V. Khang, and J. W. Ahn, "Parameter identification of a synchronous reluctance motor by using a synchronous PI current regulator at a standstill," *Journal of Power Electronics*, vol. 10, no. 5, pp. 491–497, 2010.

[10] Z. Mynar, P. Vaclavek, and P. Blaha, "Synchronous reluctance motor parameter and state estimation using extended kalman filter and current derivative measurement," *IEEE Transactions on Industrial Electronics*, vol. 68, no. 3, pp. 1972–1981, 2021.

[11] J. Soltani and H. A. Zarchi, "Robust control of encoderless synchronous reluctance motor drives based on adaptive backstepping and input-output feedback linearization techniques," *International Journal of Electrical and Electronics Engineering*, vol. 43, no. 1, pp. 11–22, 2011.

[12] A. Farhan, M. Abdelrahem, A. Saleh, A. Shaltout, and R. Kennel, "Simplified sensorless current predictive control of synchronous reluctance motor using online parameter estimation," *Energies*, vol. 13, no. 2, p. 492, 2020.

[13] N. G. Ozcelik, U. E. Dogru, M. Imeryuz, and L. T. Ergene, "Synchronous reluctance motor vs. Induction motor at low-power industrial applications: design and comparison," *Energies*, vol. 12, no. 11, pp. 2190–2220, 2019.

[14] M. Dasari, A. S. Reddy, and M. V. Kumar, "Modified Luo converters based FOPID controllers for torque ripple minimizations in BLDC drive systems," *Journal of Ambient Intelligence and Humanized Computing*, vol. 32, pp. 1–18, 2022.

[15] R. K. Selvi and R. S. M. Malar, "Different strategies of sliding modes controllers for speed controls of power factors corrected Luo converter fed switched reluctance motor," *Journal of Electrical Engineering*, vol. 21, no. 2, pp. 170–177, 2021.

[16] L. Anbarasu, R. Subramanian, and V. V. Karthikeyan, "Renewable energy based smart microgrid system using artificial bee colony algorithm optimized PI controller and efficient Luo converter," *Dynamic Systems and Applications*, vol. 30, no. 8, pp. 1362–1383, 2021.

[17] M. Yaich and M. Ghariani, "A novel technique for tuning PI-controller in switched reluctance motor drive for transportation systems," *International Journal of Electrical and Computer Engineering*, vol. 8, no. 6, pp. 4272–4281, 2018.

[18] T. Kalaiselvi, P. Nagaraja, and Z. A. Basith, "A review on glowworm swarm optimization," *International Journal of Information Technology*, vol. 3, no. 2, pp. 49–56, 2017.

[19] R. Kalaiselvi and R. Suja Mani Malar, "A bridgeless Luo converter based speed control of switched reluctance motor using particle swarm optimization (Pso) tuned proportional integral (Pi) controller," *Microprocessors and Microsystems*, vol. 75, Article ID 103039, 2020.

[20] Z. Li and X. Huang, "Glowworm swarm optimization and its application to blind signal separation," *Mathematical Problems in Engineering*, vol. 2016, Article ID 5481602, 8 pages, 2016.

[21] T. Zhonghua and Z. Yongquan, "Swarm optimization algorithms for uninhabited combat air vehicles paths planning," *Journal of Intelligent Systems*, vol. 24, no. 1, pp. 69–83, 2014.

[22] P. Anitha and B. Kaarthick, "Oppositional based Laplacian grey wolf optimization algorithm with SVM for data mining in intrusion detection system," *Journal of Ambient Intelligence and Humanized Computing*, vol. 12, no. 3, pp. 3589–3600, 2019, https://doi.org/10.1007/s12652-019-01606-6.

[23] T. Anitha, P. L. G. Charlyn, and P. M. Surendra, "A proficient adaptive K-means based brain tumor segmentation and detection using deep learning scheme with PSO," *J Comput Sci Intell Technol*, vol. 1, no. 3, pp. 09–14, 2020.

[24] S. Manimurugan, A. Q. Majdi, M. Mohmmed, C. Narmatha, and R. Varatharajan, "Intrusion detection in networks using crow search optimization algorithm with adaptive neuro-fuzzy inference system," *Microprocessors and Microsystems*, vol. 79, Article ID 103261, 2020.

[25] M. Mustafa, R. Eltayeb Ahmed, and S. Mustafa Eljack, "Hybrid convolutional neural network with PSO based severe dengue prognosis method in human genome data," *J Comput Sci Intell Technol*, vol. 1, no. 1, pp. 22–28, 2020.

[26] C. Narmatha, S. M. Eljack, A. A. R. M. Tuka, S. Manimurugan, and M. Mustafa, "A hybrid fuzzy brain-storm optimization algorithm for the classification of brain tumor MRI images," *Journal of Ambient Intelligence and Humanized Computing*, vol. 12, pp. 1–9, 2020, https://doi.org/10.1007/s12652-020-02470-5.

[27] P. M. Surendra and S. Manimurugan, "A new modified recurrent extreme learning with PSO machine based on feature fusion with CNN deep features for breast cancer detection," *J Comput Sci Intell Technol*, vol. 1, no. 3, pp. 15–21, 2020.

[28] R. Thavasimuthu, K. P. Sridhar, S. Manimurugan, and S. Deepa, "Recent innovations in soft computing applications," *Current Signal Transduction Therapy*, vol. 14, no. 2, pp. 129-130, 2019.

[29] A. Farhan, M. Abdelrahem, A. Saleh, A. Shaltout, and R. Kennel, "Simplified sensorless current predictive control of synchronous reluctance motor using online parameter estimation," *Energies*, vol. 13, no. 2, pp. 492–518, 2020.

[30] H. Heidari, A. Rassõlkin, A. Kallaste et al., "A review of synchronous reluctance motor-drive advancements," *Sustainability*, vol. 13, no. 2, pp. 729–737, 2021.

Hindawi
Mathematical Problems in Engineering
Volume 2022, Article ID 1984595, 15 pages
https://doi.org/10.1155/2022/1984595

Research Article

Equivalent Circuit Analysis of Linear Phase-Shifting Transformer with End Effect

Mei Wu, Jinghong Zhao, Guoqiang Guo, and Yiyong Xiong

School of Electrical Engineering, Naval University of Engineering, Wuhan, Hubei 430033, China

Correspondence should be addressed to Jinghong Zhao; zhaojinghong@163.com

Received 14 September 2021; Revised 21 January 2022; Accepted 29 January 2022; Published 10 May 2022

Academic Editor: Albert Alexander Stonier

The linear phase-shifting transformers (LPSTs) are a new type of transformers with a structure similar to a linear motor that can be used in multiplex technology. A reasonable equivalent circuit is the premise of control research. Based on one-dimensional electromagnetic field analysis of the LPST, we reference the theory of linear motor and propose an equivalent circuit model of the LPST. The LPSTs, which are a phase-shifting transformers based on linear motor structure, are affected by end effects. The end effects affect the mutual inductance and secondary resistance of the LPST, which is modified by four correction coefficients. This paper calculates the four correction coefficients, inductance, and resistance of the LPST and then proposes a single-phase T-type equivalent circuit model considering end effects. Using the analytical model, the output voltages under the three working conditions are calculated and analyzed, and the accuracy is verified by comparison with results obtained by the finite element method. Finally, the accuracy of the analytical method is further verified by experiments under two working conditions, which indicates that the equivalent model is credible and useful for control research of multi-inverter system based on the LPST.

1. Introduction

Multiple superposed technology can effectively reduce voltage harmonics, reduce pollution to the power grid, improve output voltage waves, and improve output performance. Phase-shifting transformers are essential devices of multiphase equipment, so it is of great significance to design and research them. Linear phase-shifting transformers (LPSTs) are a new type of transformers that can be used in multi-rectifier and multi-inverter systems [1]. In addition to realizing the traditional phase-shifting functions of conventional transformers, the LPSTs offer numerous advantages, such as the capability of realizing arbitrary phase angle shifts, easy adjustment of the magnetic field in the air gap, suitability for high-power settings, and relatively simple structure, which makes LPSTs easy to modularize and expand.

A multi-inverter system based on the LPST is proposed in this paper, which combines multi-overlapping technology with LPSTs. The performances of the LPST directly affect the stability of the whole system in multi-inverter system, so the research of ontology characteristics and control methods must be paid attention to. Because the LPST is similar to linear motor in structure and principle and is also affected by end effect, the characteristic analysis of the LPST is more complicated than that of circular transformer [2], which is mainly based on the following reasons: (1) the magnetic circuit is disconnected, and the mutual inductances of three-phase windings are asymmetric; (2) the end effects cause the distortion of air gap magnetic field; (3) the distribution of the windings is asymmetric [3–5].

In order to research the adjustable multi-inverter system with low switching frequency and good dynamic performance, it is very significant to propose an equivalent circuit of the LPST. However, few domestic and overseas scholars propose a reasonable equivalent circuit to study the characteristics of the LPSTs. In addition, because its structure is not exactly the same as linear motor and rotary motor, there is no equivalent circuit model that can be directly used for the LPST. In order to derive the equivalent circuit of the LPST, based on its structural characteristics (the air gap is very small, and both the secondary side and the primary side

are fixed), some research about linear motors and rotary motors can be referred to. In the procedures of the field analytical theories, the quasi-1D and 2D methods are a practical way to analyze the characteristics of the linear induction motor (LIM), which can consider both the skin effect and end effect [6]. Nonaka and Yoshida [7] proposed a series of accurate models based on the space harmonic method considering the end effects and obtained more accurate calculated results. Lv et al. [8, 9] proposed various transverse m.m.f. models in the end-region. Compared with the space harmonic method, the results calculated by these models were more accurate and were validated by the experimental measurements. Bolton [10] proposed a model considering that the LIM worked with an asymmetric secondary sheet. However, an equivalent circuit for the LPSTs is difficult to derive by the sophisticated space harmonic method. Lipo and Nondahl [11] proposed an equivalent circuit based on the winding function method, and the air gap flux in the LIM was divided into various components. Despite the model being able to analyze the steady-state, transient-state, and dynamic characteristics of the LPSTs, the winding function theory is achieved by some approximate hypotheses neglecting end effects. Kim and Kwon [12] proposed an equivalent model for the LIM developed by the finite element method (FEM) considering skin effect and magnetic saturation. The circuital approach was greatly useful for both the analysis and synthesis of the LIMs, and its performance could easily be obtained from the steady-state equivalent circuit with the end effects. However, it is a challenge to put the model by FEM into the LPST design and control. Gieras et al. [13] proposed the linear induction motor (LIM) analysis model based on the consideration of the end effect, skin effect, and eddy current of the secondary plate. Kang and Nam [14] proposed the *dq*-axis model neglecting the half-filled slot and the saturation of magnetic circuit and only considering the influence of the secondary eddy current on the air gap flux linkage the transverse end effect. The above two models can meet the control requirements to a certain extent, but the algorithm is very rough. Nozaki [15] proposed the equivalent model of motor by considering longitudinal end effect and skin effect and analyzed the magnetic flux density traveling wave of LIM by Fourier's pole expansion method and finite element method (FEM). This model has a wide range of applications, but the whole operation and programming process is very complex, so many equations need to be solved iteratively. It is difficult to derive the equivalent circuit of the LPSTs by the above methods. Zare-Bazghaleh et al. [16–18] proposed an equivalent circuit basically derived from the T-model circuit, and its parameters were obtained from field theories.

For simplifying the algebra and lowering the computation load of vector controller in practical engineering, Duncan [19] put forward an intelligible equivalent circuit for LIMs by using the rotary-motor model as a basis through inheriting merely the T-type circuit without any field theories. The rotary-motor model was modified to account for the so-called "end effect" and was used to predict output thrust, vertical forces, and couples. Further improvements [20, 21] were mostly based on Duncan's model. Xu et al. [22, 23] optimized the previous model by using the relation of equal field-circuit complex power and presented a novel equivalent circuit considering the end effects. The results calculated by the equivalent circuit were validated by the experimental measurements. The solution formulas of fictitious primary symmetrical phase potential, secondary current, secondary resistance, secondary leakage reactance, and excitation reactance were derived.

The special structure of the LPST means that its performance is different from these of above-mentioned motors. Considering the structural characteristics of the LPSTs, based on the analytical model (AM) of linear motors, the AM of the LPSTs is established in this paper. The correction coefficients related to the end effects are introduced to modify the results of the AM. Finally, the inverter system based on the AM is proposed. The accuracy of the proposed AM is verified by comparison of the results obtained with those obtained by the FEM.

The research focuses on the modeling and optimization analysis of the mathematical model of the system in this paper. It is organized as follows. The basic working principle of the LPST inverter system is described in Section 2 in detail. In Section 3, the derivations on how to get four correction coefficients related to the end effects are indicated by the relation of equal field-circuit complex power. The magnetic density of the air gap is analyzed. Based on 1D flux density equations, the per-phase T-model equivalent circuit of the LPST is derived. Then, two axis equivalent circuits are deduced based on the per-phase equations so as to study the LPST dynamic performance. The simulation and experimental verifications of the multi-inverter system based on the LPST are given in Section 4 and Section 5, respectively. Finally, this paper is summarized in Section 6.

2. Basic Working Principle of the LPSTS Inverter System

The working principle of the LPSTs is similar to that of LIMs. Figure 1 indicates a schematic diagram of the structure of the LPSTs. The length of the primary core is equal to that of secondary core of the LPSTs. Both the primary side and secondary side are fixed. The primary and secondary cores are embedded with $3N$ phase windings. The flexible selection of the phase-shifting angle can be realized by changing the value of N. There is an adjustable air gap between the iron cores. Therefore, the LPSTs can be equivalent to a linear motor with a slip rate of 1, which can be widely used in multi-inverter systems [24].

In order to better illustrate the basic principles, an LPST used in multi-inverter is selected as an example. The primary side of the LPST is embedded with 4 sets of 3-phase windings. The phase difference between the adjacent windings is 15°. The secondary side of the transformer is embedded with a group of 3-phase windings, which are connected by star mode. The four sets of three-phase six-step waves output by the inverter circuit, which are different from each other by 120 electrical angles, are connected to the 12-phase winding of the primary side of the LPSTs. The traveling wave magnetic field is generated in the air gap, and a set

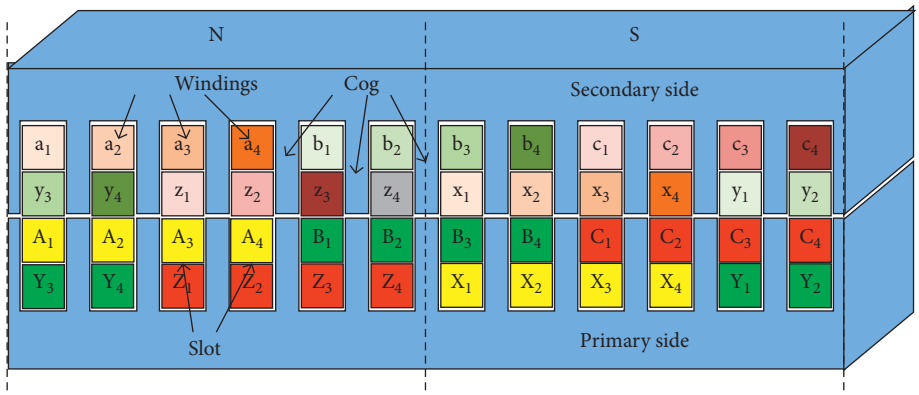

Figure 1: Schematic diagram of the structure of the LPSTs.

of three-phase alternating currents which are similar to sinusoidal waves is induced from the windings of the secondary side [25]. Figure 2 describes the spatial phase relation of the primary 12-phase winding. The multi-inverter system based on the LPSTs is shown in Figure 3.

3. Mathematical Modeling with End Effects

3.1. Single-Phase T-Equivalent Circuit End Effect. Both the primary windings and the secondary windings are treated as 12 phases, and the single-phase T-equivalent circuit is obtained. Then, a set of three-phase output voltage can be synthesized by matrix transformation of the 12-phase output voltage of the secondary side. The LPSTs are affected by the end effect that exists in linear motors due to the openings at both ends of the physical structure. Therefore, the influence of the end effect must be considered in the modeling.

For the convenience of the modeling, the following assumptions are made [26]: (1) the magnetic potential produced by the currents in the primary windings is replaced by the surface current layer, and only its fundamental component is considered; (2) the influence of the cogging effect is considered by the air gap coefficient; (3) the various field quantities vary with time according to the sinusoidal wave.

3.2. Mathematical Analysis of Longitudinal End Effect. According to the physical structure of the LPST, the two-dimensional AM of the LPST with the longitudinal end effect can be obtained. After simplification, it can be shown as Figure 4.

The equivalent current layer on the primary side of the LPST can be expressed as follows:

$$\dot{J}_1 = J_1 \exp[j(\omega_e t - kx)],$$
$$J_1 = \frac{\sqrt{2} m_1 W_1 k_{w1}}{p\tau} I_1. \tag{1}$$

Here, J_1 is the amplitude of primary traveling wave current layer, m_1 is the number of phases in the primary winding, $k = \pi/\tau$, ω_e is the angular velocity of the primary current, p is the polar pairs of the primary side, k_{w1} is the primary winding coefficient, W_1 is the number of coil turns per phase on the primary side, and I_1 is the effective value of primary phase current.

Along the path of the rectangle in Figure 4, this yields the following equation:

$$\frac{g_e}{\mu_0} \frac{\partial \dot{B}_{3y}}{\partial x} = \dot{J}_1 + \dot{J}_2, \tag{2}$$

where $\dot{J}_2$ is the complex form of the equivalent traveling wave current layer in region 2, $\dot{B}_{3y}$ is the component of the magnetic flux density in region 3 on the y-coordinate, and ge is equivalent air gap.

Since the current contains only z-component, the vector magnetic potential also contains only z-component. This yields the following equation:

$$\dot{B}_{3y} = -\frac{\partial \dot{A}_{3z}}{\partial x}, \tag{3}$$

$$\dot{E}_{3z} = -\frac{\partial \dot{A}_{3z}}{\partial t}. \tag{4}$$

Substituting (4) into Maxwell's equations yields the following equation:

$$\dot{J}_2 = -\sigma_e \frac{\partial \dot{A}_{3z}}{\partial t}, \tag{5}$$

where σ_e is the surface conductivity of the secondary conductor and conforms to the formula $\sigma_e = \sigma d$. The primary current changes as the function $(\exp(j\omega_e t))$ of time yields the following equation:

$$\begin{aligned} \dot{A}_{3z} &= A_{3z}(x,t) \\ &= A_z(x)\exp(j\omega_e t). \end{aligned} \tag{6}$$

Substituting (4), (5), and (6), into (2) yields the following equation:

$$\frac{g_e}{\mu_0} \frac{d^2 \dot{A}_{3z}}{dx^2} - j\omega_e \sigma_e \dot{A}_{3z} = -J_1 \exp(-jkx). \tag{7}$$

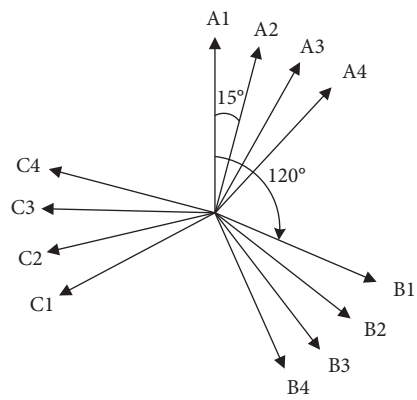

Figure 2: Phase position of 12-phase windings.

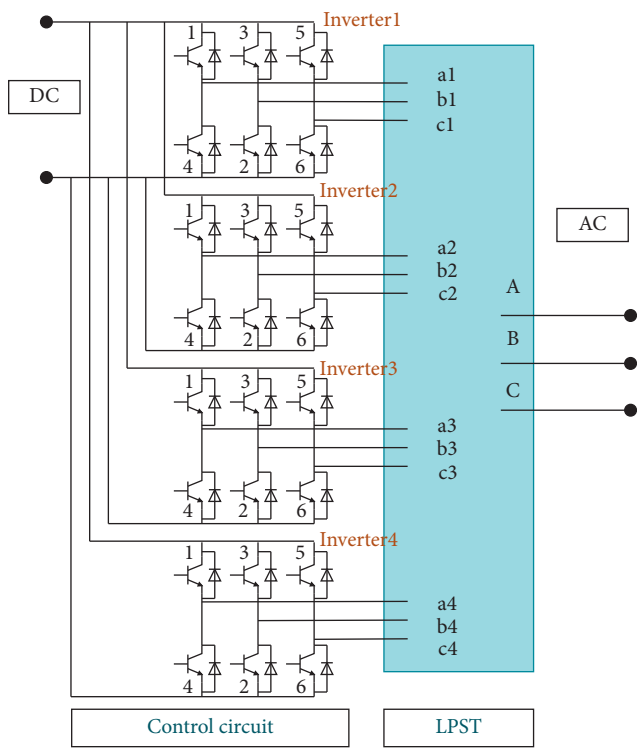

Figure 3: Principle chart of multi-inverter system based on the LPSTs.

The general solution of (7) is obtained as follows:

$$A_z = c_s \exp(-jkx) + c_1 \exp\left[-\left(\frac{1}{\alpha_1} + j\frac{\pi}{\tau_e}\right)x\right] + c_1' \exp\left[\left(\frac{1}{\alpha_1} + j\frac{\pi}{\tau_e}\right)x\right], \tag{8}$$

$$\dot{A}_{3z} = c_s \exp[j(\omega_e t - kx)] + c_1 \exp\left(-\frac{x}{\alpha_1}\right)\exp\left[j\left(\omega_e t - \frac{\pi}{\tau_e}x\right)\right] + c_1' \exp\left(\frac{x}{\alpha_1}\right)\exp\left[j\left(\omega_e t + \frac{\pi}{\tau_e}x\right)\right]. \tag{9}$$

Here, $c_1 c_1'$ is the undetermined coefficient, $\alpha_1 = 1/\sqrt{2}\omega_e\sigma_e$, and $\tau_e = 2\sqrt{2}\pi g_e/\mu_0$.

Equation (9) is related to the sinusoidal magnetic dense traveling wave, the incoming magnetic dense traveling wave,

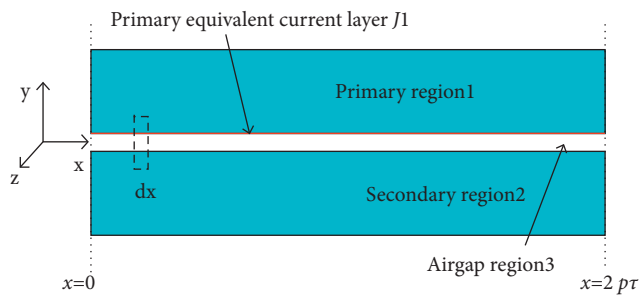

FIGURE 4: A two-dimensional physical model diagram of the simplified LPST.

and the outgoing magnetic dense traveling wave. The third term $c_1' = 0$ is generally ignored, and other coefficients can be obtained by boundary conditions. The results are shown as follows:

$$c_s = \frac{\mu_0 J_1}{k^2 g_e (1 + jG)},$$
$$c_1 = \frac{-jkc_s}{(1/\alpha_1 + j\pi/\tau_e)}. \tag{10}$$

Here, G is the quality factor.

$$G = \frac{2\mu_0 \sigma_e f \tau^2}{\pi g_e}. \tag{11}$$

In combination with equations (4), (5), (6), and (9), the following equations can be obtained:

$$\dot{B}_{3y} = jkc_s \exp[j(\omega_e t - kx)] + \left(\frac{1}{\alpha_1} + \frac{\pi}{\tau_e}\right) c_1 \exp\left(-\frac{x}{\alpha_1}\right) \exp\left[j\left(\omega_e t - \frac{\pi}{\tau_e} x\right)\right],$$
$$\dot{B}_{3y} = B_s \left\{\exp[j(\omega_e t - kx + \delta_s)] - \exp\left(-\frac{x}{\alpha_1}\right) \exp[j(\omega_e t - kx)]\right\}. \tag{12}$$

Here, $B_s = jkc_s \exp(-j\delta_s) = \mathrm{GJ}_1/\delta_s V_s \sqrt{1 + G^2}$.

$$\dot{E}_{3z} = -j\omega_e \left\{c_s \exp[j(\omega_e t - kx)] + c_1 \exp\left(-\frac{x}{\alpha_1}\right) \exp\left[j\left(\omega_e t - \frac{\pi}{\tau_e} x\right)\right]\right\},$$
$$j_2 = -j\sigma_s \omega_e \left\{c_s \exp[j(\omega_e t - kx)] + c_1 \exp\left(-\frac{x}{\alpha_1}\right) \exp\left[j\left(\omega_e t - \frac{\pi}{\tau_e} x\right)\right]\right\}. \tag{13}$$

According to Poynting's theorem, considering that the resistance loss, electric field energy, and magnetic field energy in the current layer are all 0, the total complex power is equal to the complex power per unit length in the z-direction multiplied by the length in the z-direction. The total complex power transmitted from the primary windings to the secondary windings and the air gap is shown as follows:

$$\begin{aligned}
S_{23} &= \int_{-a_1}^{a_1} \int_0^{p\tau} 0.5[-j_1^* E_{3z}] \mathrm{d}x\mathrm{d}z \\
&= J_1 B_m a_1 V_s \left\{2p\tau \cos \delta_s - N_L \left[\alpha_1^{-1} \exp\left(-\frac{2p\tau}{\alpha_1}\right) \sin(\delta_s - \beta + 2S_L p\tau)\right.\right. \\
&\quad \left.\left. + S_L \exp\left(-\frac{2p\tau}{\alpha_1}\right) \cos(\delta_s - \beta + S_L p\tau) - \alpha_1^{-1} \sin(\delta_s - \beta) - S_L \cos(\delta_s - \beta)\right]\right\} \\
&\quad + jJ_1 B_m a_1 V_s \left\{2p\tau \sin \delta_s - N_L \left[\alpha_1^{-1} \exp\left(-\frac{2p\tau}{\alpha_1}\right) \cos(\delta_s - \beta + 2S_L p\tau)\right.\right. \\
&\quad \left.\left. + S_L \exp\left(-\frac{2p\tau}{\alpha_1}\right) \sin(\delta_s - \beta + S_L p\tau) + \alpha_1^{-1} \cos(\delta_s - \beta) - S_L \sin(\delta_s - \beta)\right]\right\} = P_2 + jQ_3.
\end{aligned} \tag{14}$$

Here,

$$\delta_s = \tan^{-1}\left(\frac{1}{G}\right),$$
$$\beta = \tan^{-1}\left(\frac{\pi\alpha_1}{\tau_e}\right),$$
$$S_L = k - \frac{\pi}{\tau_e}, \tag{15}$$
$$M_L = \left(\alpha_1^{-1}\right)^2 + S_L^2,$$
$$N_L = \frac{\alpha_1 \pi \tau_e}{M_L \tau \sqrt{\tau_e^2 + (\pi\alpha_1)^2}}.$$

P_2 is the active power transferred to the secondary and Q_3 is the reactive power transferred to the air gap. Then, the effective value of the primary phase current can be calculated as follows:

$$I_1 = \frac{p\tau J_1}{\sqrt{2} m_1 W_1 k_{w1}}. \tag{16}$$

In (16), m_1 is the number of phases, W_1 is the number of serial turns per phase of the primary winding, and k_{w1} is the coefficient of the primary winding.

The primary air gap electromotive force is assumed to be $\dot{E}_{\mathrm{m}}(s)$, and according to the equal relationship of the complex power, the following equation can be obtained:

$$-m_1 \dot{I}_s \dot{E}_m(s) = P_2 + jQ_3. \tag{17}$$

Substituting (14) and (16) into (17), $\dot{E}_m(s)$ can be obtained as follows:

$$\begin{aligned}
-\dot{E}_m = {} & \frac{\sqrt{2} W_1 k_{w1} a_1 V_s B_s}{p\tau} \Bigg\{ 2p\tau \cos\delta_s - N_L \Bigg[\alpha_1^{-1} \exp\left(-\frac{2p\tau}{\alpha_1}\right) \sin(\delta_s - \beta + 2S_L p\tau) \\
& + S_L \exp\left(-\frac{2p\tau}{\alpha_1}\right) \cos(\delta_s - \beta + S_L p\tau) - \alpha_1^{-1} \sin(\delta_s - \beta) - S_L \cos(\delta_s - \beta) \Bigg] \Bigg\} \\
& + j \frac{\sqrt{2} W_1 k_{w1} a_1 V_s B_s}{p\tau} \Bigg\{ 2p\tau \sin\delta_s - N_L \Bigg[-\alpha_1^{-1} \exp\left(-\frac{2p\tau}{\alpha_1}\right) \cos(\delta_s - \beta + 2S_L p\tau) \\
& + S_L \exp\left(-\frac{2p\tau}{\alpha_1}\right) \sin(\delta_s - \beta + 2S_L p\tau) + \alpha_1^{-1} \cos(\delta_s - \beta) - S_L \sin(\delta_s - \beta) \Bigg] \Bigg\}.
\end{aligned} \tag{18}$$

It is further deduced that when only the longitudinal end effect is considered, the secondary resistance and excitation reactance of each phase reduced to the primary can be obtained as follows:

$$\begin{aligned}
R_r(s) &= \frac{m_1 \left|\dot{E}_m(s)\right|^2}{P_2} \\
&= \frac{2a_1 m_1 (W_1 k_{w1})^2}{\sigma_e p\tau} \frac{G}{p\tau\sqrt{1+G^2}} \frac{C_1^2 + C_2^2}{C_1}.
\end{aligned} \tag{19}$$

$$\begin{aligned}
X_m(s) &= \frac{m_1 \left|\dot{E}_m(s)\right|^2}{Q_3} \\
&= \frac{2a_1 m_1 (W_1 k_{w1})^2}{g_e p\tau} \frac{G}{p\tau\sqrt{1+G^2}} \frac{C_1^2 + C_2^2}{C_2}.
\end{aligned} \tag{20}$$

The coefficient expressions in (19) and (20) are shown as follows:

$$C_1 = 2p\tau\cos\delta_s - N_L\left[\alpha_1^{-1}\exp\left(-\frac{2p\tau}{\alpha_1}\right)\sin(\delta_s-\beta+2S_Lp\tau) + S_L\exp\left(-\frac{2p\tau}{\alpha_1}\right)\cos(\delta_s-\beta+2S_Lp\tau) - \alpha_1^{-1}\sin(\delta_s-\beta) - S_L\cos(\delta_s-\beta)\right],$$
$$C_2 = 2p\tau\sin\delta_s - N_L\left[-\alpha_1^{-1}\exp\left(-\frac{2p\tau}{\alpha_1}\right)\cos(\delta_s-\beta+2S_Lp\tau) + S_L\exp\left(-\frac{2p\tau}{\alpha_1}\right)\sin(\delta_s-\beta+2S_Lp\tau) + \alpha_1^{-1}\cos(\delta_s-\beta) - S_L\sin(\delta_s-\beta)\right]. \quad (21)$$

The expressions of the secondary resistance and excitation reactance of each phase of the LPST are shown as follows:

$$r_r = \frac{4a_1m_1(W_1k_{w1})^2}{\sigma_e p\tau}, \quad (22)$$

$$\begin{aligned} x_m &= r_rG \\ &= \frac{4m_1\mu_0a_1V_s(W_1k_{w1})^2}{\pi g_e p} \\ &= \frac{8a_1m_1\mu_0f\tau(W_1k_{w1})^2}{\pi g_e p}, \end{aligned} \quad (23)$$

$$\begin{aligned} R_m(s) &= K_r'r_r, \\ X_m &= K_x'x_m. \end{aligned} \quad (24)$$

Comparing (19), (20) and (22), (23), it is known that the secondary resistance and excitation reactance of the LPSTs are affected by the longitudinal end effect, which can be modified by the coefficients $K_r'(s)$ and $K_x'(s)$, as shown in the following equations:

$$K_r'(s) = \frac{G}{2p\tau\sqrt{1+G^2}}\frac{C_1^2+C_2^2}{C_1}. \quad (25)$$

$$K_x'(s) = \frac{1}{2p\tau\sqrt{1+G^2}}\frac{C_1^2+C_2^2}{C_2}. \quad (26)$$

3.3. Mathematical Analysis of Transverse End Effect. Following the rectangular ring path in Figure 5, Maxwell's equations can be obtained as follows.

$$\frac{g_e}{\mu_0}\frac{\partial \dot{B}_{1y}}{\partial z} = -\dot{J}_{1x}. \quad (27)$$

In the longitudinal section, the following equation can be obtained:

$$\frac{g_e}{\mu_0}\frac{\partial \dot{B}_{1y}}{\partial x} = \dot{J}_{1z} - \dot{J}_1. \quad (28)$$

In (28), $\dot{J}_{1x}$ and $\dot{J}_{1z}$ are the x and y components of the secondary conductor line current density in region 1, and $\dot{B}_{1y}$ is the y component of the air gap magnetic density. Taking the curl of (27), the following equation can be obtained:

$$\frac{\partial^2\dot{B}_{1y}}{\partial x^2} + \frac{\partial^2\dot{B}_{1y}}{\partial z^2} - \frac{\mu_0\sigma_e}{g_e}\frac{\partial\dot{B}_{1y}}{\partial t} = -\frac{\mu_0\sigma_e}{g_e}\frac{\partial\dot{J}_1}{\partial x}. \quad (29)$$

Assuming $\dot{B}_{1y} = B_{1y}(x,z,t) = B(z)\exp[j(\omega_e t - kx)]$, substituting it into yields the full solution as follows:

$$B_{1y}(x,z,t) = \left(B_T\cosh\alpha z - j\frac{\mu_0}{kg_e}J_1R^2\right)\exp[j(\omega_e t - kx)], \quad (30)$$

where $R^2 = 1/1 + jG$, $\alpha^2 = k^2 + j\omega_e\mu_0\sigma_e/g_e$, and B_T is the undetermined coefficient, which can be obtained by the boundary conditions and the current continuity theorem.

$$B_T = -jJ_1\frac{\mu_0}{kg_e}\frac{1-R^2}{\cosh a_1\alpha}\lambda. \quad (31)$$

In addition,

$$\lambda = \frac{1}{1 + 1/R\tanh(a_1\alpha)\tanh k(c_2 - a_1)}. \quad (32)$$

Because $c_2 = a_1$ and $\lambda = 1$, according to (30) and (31), we can obtain

$$B_{1y}(x,z,t) = -j\frac{\mu_0}{kg_e}J_1R^2\left(1 + \frac{1-R^2}{R^2}\frac{\cosh\alpha z}{\cosh\alpha a_1}\right) \cdot \exp[j(\omega_e t - kx)]. \quad (33)$$

The magnetic flux of each pole is supposed to be $\phi(t)$, which can be expressed as follows:

$$\begin{aligned} \dot{\phi} &= \int_0^\tau\int_{-a_1}^{a_1} B_{1y}(x,z,t)\mathrm{d}z\mathrm{d}x \\ &= -\frac{4\mu_0\tau}{\pi g_e}J_1R^2\left(a_1 + \frac{1-R^2}{R^2}\frac{1}{\alpha}\tanh\alpha a_1\right)\exp(j\omega_e t). \end{aligned} \quad (34)$$

The instantaneous value of the excitation potential of each phase of the primary can be obtained as follows:

$$\begin{aligned} \dot{e}_m &= \int_0^\tau\int_{-a_1}^{a_1} B_{1y}(x,z,t)\mathrm{d}z\mathrm{d}x \\ &= -W_1k_{w1}\frac{\mathrm{d}}{\mathrm{d}t}[\dot{\phi}] \\ &= -\sqrt{2}\dot{E}_m(s)\exp(j\omega_e t). \end{aligned} \quad (35)$$

Here,

$$-\dot{E}_m(s) = \frac{4\sqrt{2}\mu_0fW_1k_{w1}a_1\tau^2}{\pi g_e}J_1\left\{j\left[R^2 + (1-R^2)\frac{1}{a_1\alpha}\tanh a_1\alpha\right]\right\}. \quad (36)$$

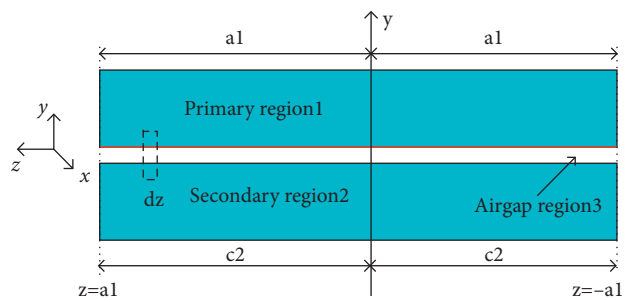

Figure 5: The two-dimensional simplified physical model diagram of LPST considering the transverse end effect.

The power transmitted from the primary to the air gap and the secondary is shown as follows:

$$\begin{aligned} &-m_1\dot{I}_s\dot{E}_m(s) \\ &= P_2 + jQ_3 \\ &= \frac{2\mu_0 a_1 f p \tau^3}{\pi g_e} J_1 \\ &\left\{\mathrm{Re}\left(j\left[R^2 + \left(1+R^2\right)\frac{1}{a_1\alpha}\tanh a_1\alpha\right]\right) + j\mathrm{Im}\left(j\left[R^2 + \left(1+R^2\right)\frac{1}{a_1\alpha}\tanh a_1\alpha\right]\right)\right\}. \end{aligned} \tag{37}$$

According to the equal power of the complex quantity, the secondary resistance and excitation reactance of each phase reduced to the primary can be calculated as follows:

$$\begin{aligned} R_r(s) &= \frac{m_1\left|\dot{E}_m(s)\right|^2}{P_2} \\ &= \frac{8\mu_0 f \tau a_1 m_1 (W_1 k_{w1})^2}{\pi g_e p}\frac{\left\{\mathrm{Re}^2[T] + \mathrm{Im}^2[T]\right\}}{\mathrm{Re}[T]} \\ X_m(s) &= \frac{m_1\left|\dot{E}_m(s)\right|^2}{Q_3} \\ &= \frac{8\mu_0 f \tau a_1 m_1 (W_1 k_{w1})^2}{\pi g_e p}\frac{\left\{\mathrm{Re}^2[T] + \mathrm{Im}^2[T]\right\}.}{\mathrm{Im}[T]} \end{aligned} \tag{38}$$

Similarly, the correction coefficient of the transverse end effect of the secondary resistance and the magnetizing inductance are assumed to be $C_r(s)$ and $C_x(s)$, which can be expressed as follows:

$$\begin{aligned} C_r(s) &= \frac{G\left\{\mathrm{Re}^2[T] + \mathrm{Im}^2[T]\right\}}{\mathrm{Re}[T]}, \\ C_x(s) &= \frac{\left\{\mathrm{Re}^2[T] + \mathrm{Im}^2[T]\right\}}{\mathrm{Im}[T]}. \end{aligned} \tag{39}$$

Here,

$$T = j\left[R^2 + \left(1-R^2\right)\frac{1}{a_1\alpha}\tanh a_1\alpha\right]. \tag{40}$$

According to the above analysis, the T-type equivalent circuit of LPST with end effects can be obtained, as shown in Figure 6.

3.4. Transformer Mathematical Modeling. The LPSTs can be regarded as a linear motor with a slip rate of 1, and its basic structure is similar to that of a linear motor. The voltage equations of the four groups of three-phase windings on the primary side of the LPSTs are shown as follows:

$$\begin{cases} \mathbf{U}_1 = \mathbf{R}_1\mathbf{I}_1 + \dfrac{\mathrm{d}\psi_1}{\mathrm{d}t}, \\ \psi_1 = \mathbf{L}_{11}\mathbf{I}_1 + \mathbf{L}_{12}\mathbf{I}_2. \end{cases} \tag{41}$$

In (41), $\mathbf{U}_1$ is the primary-side input voltage vector. $\mathbf{R}_1$ is the primary-side winding resistance matrix. $\mathbf{I}_1$ is the primary-side current matrix. ψ_1 is the primary-side flux matrix of the LPSTs. $\mathbf{L}_{11}$ is the primary-side inductance matrix. $\mathbf{L}_{12}$ is the primary-side and the mutual inductance matrix on the secondary side. $\mathbf{I}_2$ is the current matrix on the secondary side.

$$\begin{aligned}
\mathbf{U}_1 &= \left[U_{s1} \;\; U_{s2} \;\; \cdots \;\; U_{s12} \right]^T, \\
\mathbf{R}_1 &= \mathrm{diag}\left[r_s \;\; r_s \;\; \cdots \;\; r_s \right], \\
\mathbf{I}_1 &= \left[I_{s1} \;\; I_{s2} \;\; \cdots \;\; I_{s12} \right]^T, \\
\mathbf{L}_{11} &= \begin{bmatrix} L_{s1s1} & L_{s1s2} & \cdots & L_{s1s12} \\ L_{s2s1} & L_{s2s2} & \cdots & L_{s2s12} \\ \vdots & \vdots & \ddots & \vdots \\ L_{s12s1} & L_{s12s2} & \cdots & L_{s12s12} \end{bmatrix} + L_{1\sigma} I_{12\times 12}, \\
\mathbf{L}_{12} &= \begin{bmatrix} L_{s1r1} & L_{s1r2} & L_{s1r3} \\ \vdots & \vdots & \vdots \\ L_{s12r1} & L_{s12r2} & L_{s12r3} \end{bmatrix}.
\end{aligned} \tag{42}$$

Since the primary side and the secondary side of the LPSTs are fixed, the inductance matrix of the primary side and the secondary side does not change with time. Substituting the flux linkage expression into the primary voltage equation yields the following equation:

$$\mathbf{U}_1 = \mathbf{R}_1 \mathbf{I}_1 + \mathbf{L}_{11} \frac{\mathrm{d}\mathbf{I}_1}{\mathrm{d}t} + K'_x C_x \mathbf{L}_{12} \frac{\mathrm{d}\mathbf{I}_2}{\mathrm{d}t}. \tag{43}$$

The secondary windings of the LPSTs are connected to a three-phase symmetrical load, the load impedance of each phase is $Z_l = r_l + j\omega L_l$, and the output voltage equation on the secondary side is shown as follows.

$$\begin{cases} K'_r C_r \mathbf{U}_2 = K'_r C_r \mathbf{R}_2 \mathbf{I}_2 + \dfrac{\mathrm{d}\psi_2}{\mathrm{d}t}, \\ \psi_2 = \mathbf{L}_{22} \mathbf{I}_2 + K'_x C_x \mathbf{L}_{21} \mathbf{I}_1. \end{cases} \tag{44}$$

$\boldsymbol{R}_2$ is the secondary-side winding resistance matrix, $\boldsymbol{R}_1$ is the load resistance matrix, $\boldsymbol{L}_1$ is the load inductance matrix, $\boldsymbol{L}_{21}$ is the secondary-side and primary-side mutual inductance matrix, and $\boldsymbol{L}_{22}$ is the secondary-side inductance matrix.

Here,

$$\begin{aligned}
\mathbf{R}_2 &= \mathrm{diag}\left[r_r \;\; r_r \;\; r_r \right], \\
\mathbf{R}_l &= \mathrm{diag}\left[r_l \;\; r_l \;\; r_l \right], \\
\mathbf{L}_l &= \mathrm{diag}\left[L_l \;\; L_l \;\; L_l \right], \\
\mathbf{L}_{21} &= \mathbf{L}_{12}^T, \\
\mathbf{L}_{22} &= \begin{bmatrix} L_{r1r1} & L_{r1r2} & L_{r1r3} \\ L_{r2r1} & L_{r2r2} & L_{r2r3} \\ L_{r3r1} & L_{r3r2} & L_{r3r3} \end{bmatrix} + L_{2\sigma} I_{3\times 3}.
\end{aligned} \tag{45}$$

4. Simulation Analysis and Comparison

In order to verify the accuracy of the analytical model (AM), the main parameters of the LPST which can be used for multi-rectification are listed in Table 1. There are twelve-phase windings on the primary side, and there are three-phase windings on the secondary side. The FEM is established as shown in Figure 7.

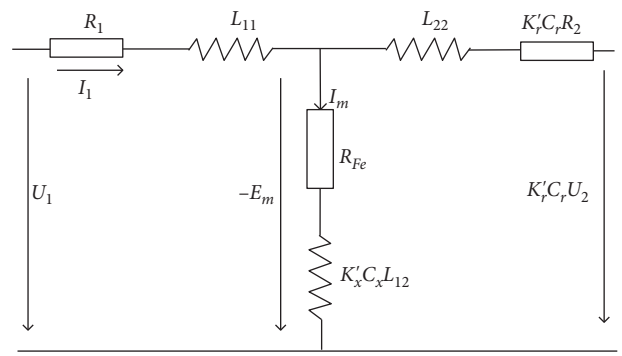

Figure 6: T-type equivalent circuit considering end effects.

Table 1: Main parameters of the model.

Parameter setting	Numeric value
Rated capacity SN (kVA)	1
Number of primary phases	12
Number of secondary phases	3
Primary turns	210
Secondary turns	210
Number of pole pairs	1
Core length L (mm)	216
Core height H (mm)	40
Core stack thickness D (mm)	100
Slot pitch b_s (mm)	6
Slot width (mm)	12
Slot depth (mm)	25
Air gap length g (mm)	0.3
Inverter input voltage (V)	100
The rated output voltage (V)	220

The AM is used to obtain the output voltage waveform and FFT analysis under three different working conditions, as shown in Figures 8–13.

Figures 8–13 show the analysis of three-phase voltage and A-phase FFT of output on the secondary side of the LPST under different load conditions. Table 2 shows the main performance indexes changing rules with load. Analysis shows the following:

(1) When there is no load, the inverter output is 24 step waves, and the harmonic content is 9.42%. Under rated load, the output voltage waveform of the inverter system is very close to the sine wave, and the harmonic content of the output voltage is 1.38%, which meets the requirement of less than 5% in the national standard. The harmonic content of the output voltage increases with the decrease of the load and reaches the maximum at no load. Because the winding material is perceptual, when the current flows through the winding, the role of partial voltage have been filtered.

(2) At rated load, the efficiency is 92.3%. In other load conditions, the efficiency (EF) of the inverter system based on the LPST is above 90%, which meets the design requirements. The greater the load, the

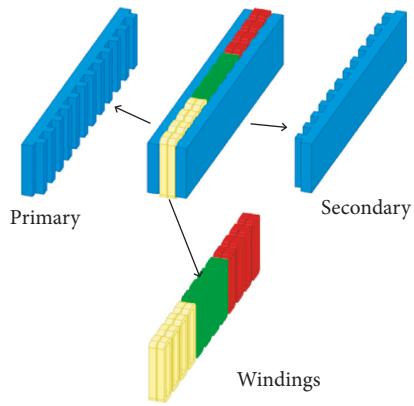

Figure 7: Diagram of model structure associated with the finite element method (FEM).

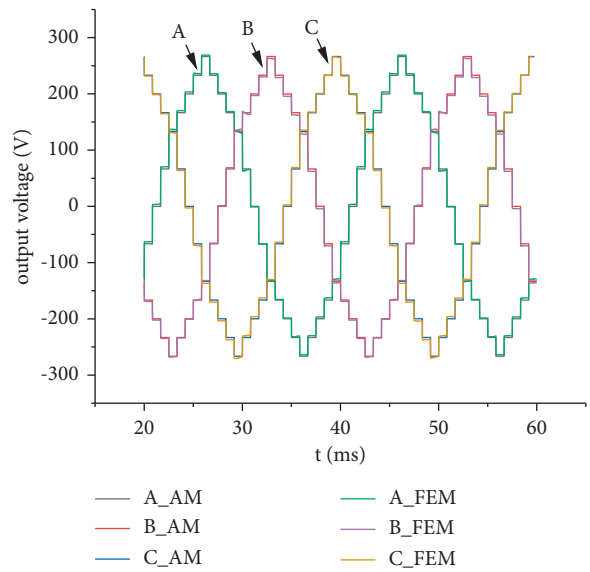

Figure 8: Output three-phase voltage waveform at no load.

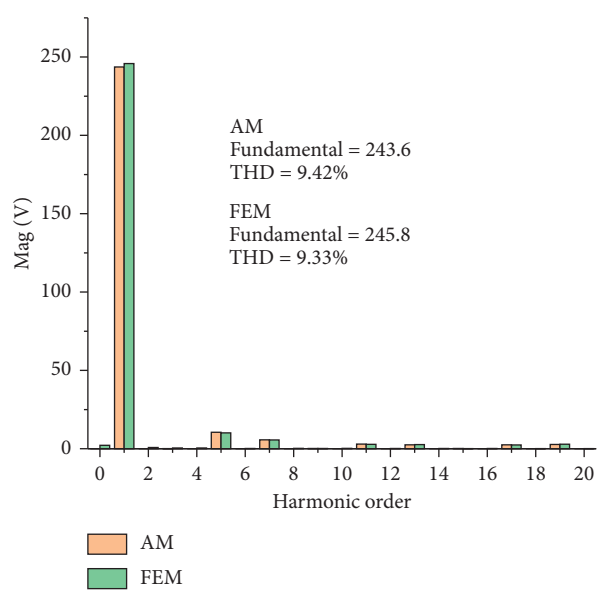

Figure 9: Output A-phase voltage harmonic analysis at no load.

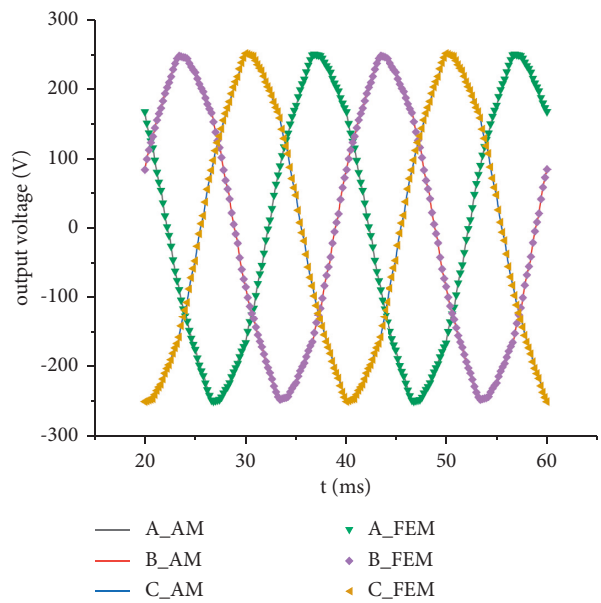

Figure 10: Three-phase voltage waveform output at 50% load.

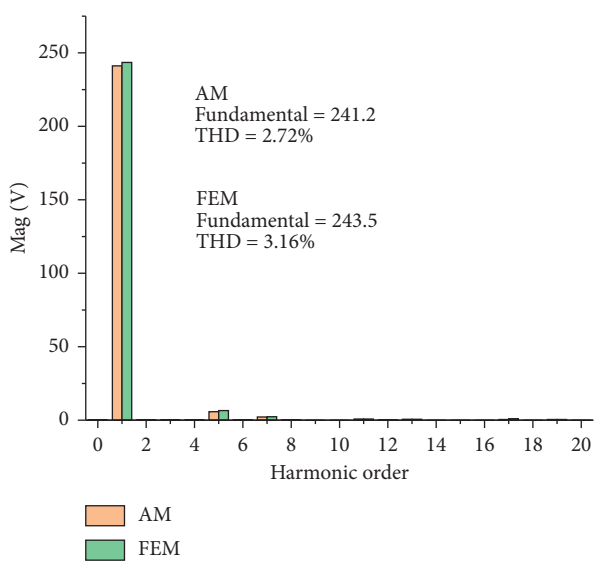

Figure 11: Output A-phase voltage harmonic analysis at 50% load.

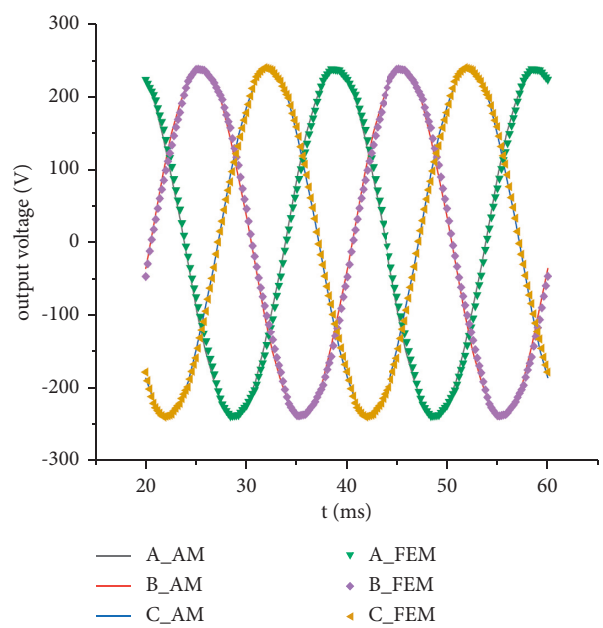

Figure 12: Output three-phase voltage waveform at rated load.

greater the current, and the stronger the filtering effect of the LPST.

(3) Three-phase imbalance factor (IF) increases the loss of the transformer and causes zero sequence current to be too large and local metal parts temperature to rise. Under different loads, the IF of the output voltage of the secondary windings of the LPST is much less than 2%, which meets the national standard.

(4) In the harmonic analysis diagram, the A-phase voltage mainly contains 5th and 7th harmonics. The output voltages under three different load conditions are compared with the FEM results, and the amplitude error is extremely small within 2%, which proves the accuracy of the AM.

5. Experiment

According to the proposed multi-inverter system based on LPST above, we have fabricated a prototype of multi-inverter system as shown in Figure 14.

The LPST is on the far right of Figure 14. To modify the wiring method, the terminal of each coil winding on the left side of the LPST is connected to the pillar terminal to facilitate wiring and to modify the wiring method. The control circuit is on the far left.

The results show the following: (1) From Figures 15–18, the harmonic content of A-phase at 50% load is 5.45%, and

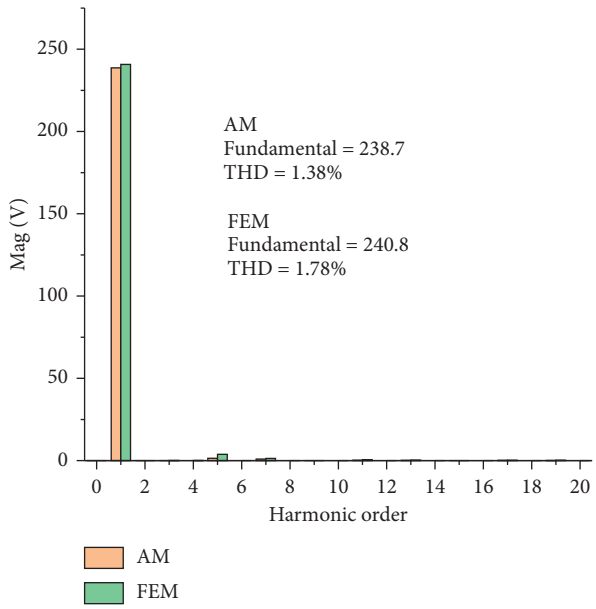

Figure 13: Output A-phase voltage harmonic analysis at rated load. The main performance indexes obtained from the analytical model and the FEM are shown in Table 2.

Table 2: Performance analysis of the phase-shifting transformer under different load conditions.

AM load (%)	*THD (%)*	*Fundamental*	*IF*	*EF (%)*
100	1.38	238.7	0	92.3
50	2.72	241.2	0	92.7
0	9.42	243.6	0	—
FEM load (%)	*THD (%)*	*Fundamental*	*IF (%)*	*EF (%)*
100	1.78	240.8	0.26	91.8
50	3.16	243.5	0.16	92.6
0	9.33	245.8	0.12	—

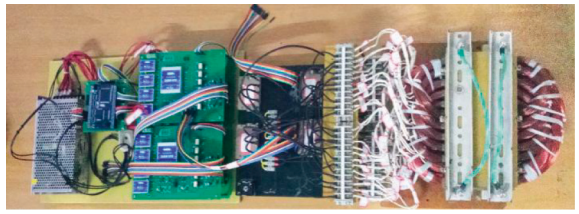

Figure 14: Multi-inverter system based on the LPST experimental platform.

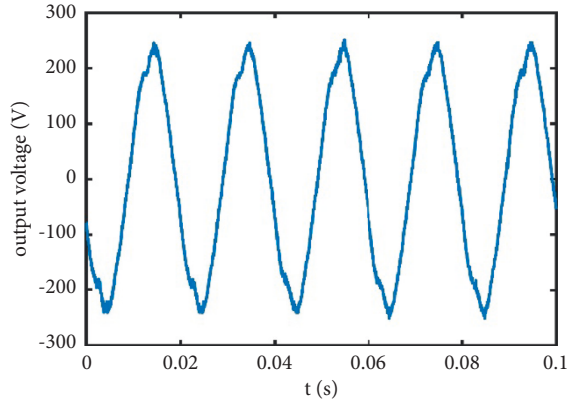

Figure 15: Experimental diagram of output A-phase voltage at 50% load.

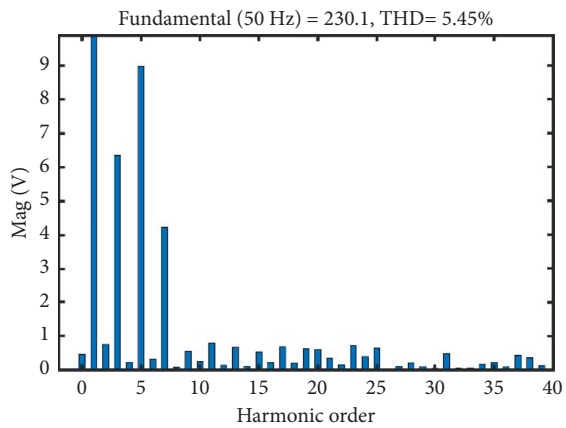

Figure 16: Output A-phase voltage harmonic analysis diagram at 50% load.

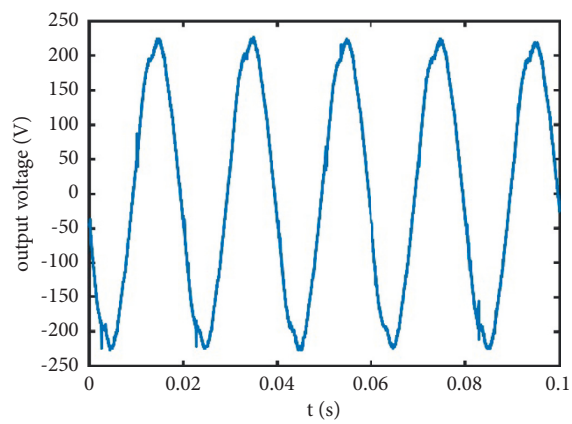

Figure 17: Experimental diagram of output A-phase voltage at rated load.

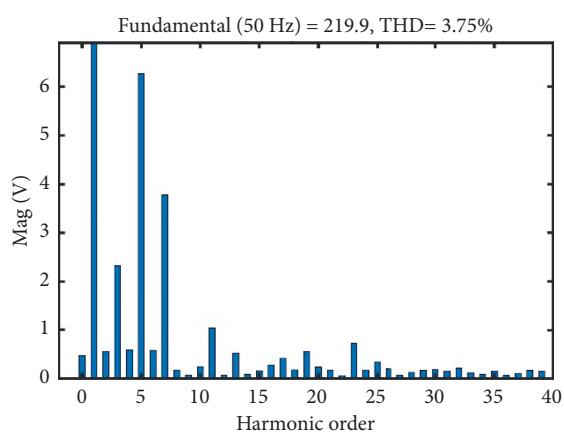

Figure 18: Experimental diagram of output A-phase voltage at rated load.

that of A-phase at rated load is 3.75%, which are larger than the results of the AM on the equal conditions. Due to the processing level, it is difficult for the air gap to be very small, and it is difficult for the primary and secondary sides to be symmetrical, which makes the experimental value slightly larger. (2) From Figures 9, 11, and 13, when the AM and FEM are performed, the A-phase output voltage harmonics are mainly concentrated at 5th and 7th times, while the even harmonics and the multiple harmonics of 3 are very few and can be neglected. As shown in Figures 16 and 18, the 3rd, 5th, and 7th harmonics are more significant, and the even harmonics are also more obvious. This is due to the fact that it is difficult to achieve absolute uniformity of the iron core during the manufacture of the LPST, and the asymmetry of

the three-phase windings is more obvious. At the same time, the LPST is close to saturation, which leads to even harmonics and multiple harmonics of 3.

6. Conclusion

In this paper, the equivalent circuit of the LPSTs was derived by considering the influence of the end effect on the mutual inductance and the secondary-side circuit. The following conclusions can be drawn:

(1) The proposed equivalent circuit of the LPST was derived based on the 1D air gap flux density equation, and four coefficients were got to describe the influence on the mutual inductance and secondary resistance brought by the longitudinal and transversal end effects. These coefficients had clear physical meanings so as to understand the end effects. Hence, it was convenient to study the performance of the LPST.

(2) The FEM was carried out. The results in three different working conditions showed that the error between the AM and the FEM was less than 2%. The accuracy of the AM was verified by comparison with the results obtained by the FEM.

(3) A small prototype was made, and experimental research was carried out. The experimental results were analyzed in detail. The amplitude of the output voltage obtained by AM was higher than the experimental results, which is explained in detail in Section 5. The accuracy of the AM was far verified by comparison with the experimental results.

As a result, we believe that the equivalent circuit model proposed in this paper can be used to analyze the characteristics and control of LPSTs.

Data Availability

The data used to support the findings of this study are included within the article.

Conflicts of Interest

The authors declare that they have no conflicts of interest.

References

[1] G. Guo, J. Zhao, M. Wu, and Y. Xiong, "Design of linear phase shift transformer and analytical calculation of no-load electromagnetic field," *Journal of Physics: Conference Series*, vol. 1802, no. 3, Article ID 032085, 2021.

[2] T. Wang, F. Fang, X. Jiang, K. Wang, L. Yang, and X. Jiang, "Performance and design analysis on round-shaped transformers applied in rectifier systems," *IEEE Transactions on Industrial Electronics*, vol. 64, no. 2, pp. 948–955, 2017.

[3] G. Lv, Z. Liu, and S. Sun, "Analysis of torques in single-side linear induction motor with transverse asymmetry for linear metro," *IEEE Transactions on energ*, vol. 31, pp. 165–173, 2016.

[4] L. Gang, Z. Liu, and S. Sun, "Electromagnetism calculation of single-sided linear induction motor with transverse asymmetry using finite-element method," *Electric Power Applications Iet.*vol. 10, no. 1, pp. 63–73, 2015.

[5] J. Xu, W. Ma, J Lu, Z. L. Sun, Y. X. Zhang, and J. Rao, "Analysis of air gap magnetic field distribution and mutual inductance asymmetry of segmentally-supplied linear induction motor," *Proceedings of the CSEE*, vol. 31, no. 15, pp. 61–68, 2011.

[6] S. Yamamura, *Theory of Linear Induction Motors*, Tokyo Univ. Press, Tokyo, Japan, 1978.

[7] S. Nonaka and K. Yoshida, "Analysis of linear induction motors using a space harmonic technique," in *Transport without wheels*, pp. 187–216, Elek Science, London, England, 1977.

[8] L. Zhiming, S. Shouguang, and L. Gang, *IET Electric Power Applications*, vol. 10, no. 1, pp. 1–8, 2016.

[9] G. Lv, D. Zeng, and T. Zhou, "Influences on performance in 3D analysis of linear induction motors with different transverse m.m.f. models in winding end," *IET Electric Power Applications*, vol. 11, no. 8, pp. 1424–1431, 2017.

[10] H. Bolton, "Forces in induction motors with laterally asymmetric sheet secondaries," *Proceedings of the Institution of Electrical Engineers*, vol. 117, no. 12, pp. 2241–2248, 1970.

[11] T. A. Lipo and T. A. Nondahl, "Pole by Pole d-q model of a linear induction machine," *IEEE trans. Power app. Syst*, vol. 2, pp. 629–642, 1979.

[12] D. K. Kim and B. I. Kwon, "A novel equivalent circuit model of linear induction motor based on finite element analysis and its coupling with external circuits," in *Proceedings of the 2006 IEEE International Magnetics Conference (INTERMAG)*, pp. 3407–3409, San Diego, CaliforniaUSA, May 2006.

[13] J. Gieras, G. Dawson, and A. Eastham, "Performance calculation for single-sided linear induction motors with a double-layer reaction rail under constant current excitation," *IEEE Transactions on Magnetics*, vol. 22, no. 1, pp. 54–62, 1986.

[14] G. Kang and K. Nam, "Field-oriented control scheme for linear induction motor with the end effect," *IEE Proceedings - Electric Power Applications*, vol. 152, no. 6, pp. 1565–1572, 2005.

[15] Y. Nozaki, "Analysis of linear induction motors for HSST and linear metro using finite difference method, presented at LDIA2005 meeting," 2005, https://koseki.t.utokyo.ac.jp/static/b6f8cbb069f96c155a7c565a18f14030/1QiyWYdBCqc57GhdduDSNefznxfH5LOc.pdf.

[16] A. Zare-Bazghaleh, M. R. Naghashan, and A. Khodadoost, "Derivation of equivalent circuit parameters for single-sided linear induction motors," *IEEE Transactions on Plasma Science*, vol. 43, no. 10, pp. 3637–3644, 2015.

[17] E. Amiri and E. A. Mendrela, "A novel equivalent circuit model of linear induction motors considering static and dynamic end effects," *IEEE trans. Magn*, vol. 50, no. 3, Article ID 8200409, 2014.

[18] S. Nonaka, "Investigation of equivalent circuit quantities and equations for calculation of characteristics of single-sided linear induction motors," *trans. IEEJ*, vol. 115, no. 3, pp. 223–232, 1996.

[19] J. Duncan, "Linear induction motor-equivalent-circuit model," *IEE Proceedings B Electric Power Applications*, vol. 130, no. 1, pp. 51–57, 1983.

[20] A. Shiri and A. Shoulaie, "Design optimization and analysis of single-sided linear induction motor, considering all phenomena," *IEEE Transactions on Energy Conversion*, vol. 27, no. 2, pp. 516–525, 2012.

[21] K. Woronowicz and A. Safaee, "A novel linear induction motor equivalent-circuit with optimized end effect model," in

Proceedings of the Canadian Journal of Electrical and Computer Engineering, pp. 34–41, IEEE, Dearborn, MI, USA, July 2004.

[22] Y. Xu, J. G. Zhu, and Y. Zhang, "Equivalent circuits for single-sided linear induction motors," *IEEE Transactions on Industry Applications*, vol. 46, no. 6, pp. 2410–2423, 2010.

[23] X. Wei, Yongchang, and Yaohua, "An improved equivalent circuit model of a single-sided linear induction motor," *IEEE Transactions on Vehicular Technology*, vol. 59, no. 5, pp. 2277–2289, 2010.

[24] Z. Zhang, J. Zhao, M. A. Yuanzheng, and X. Hao, "Analytical modeling of inverter system of linear phase shift transformer," *Journal of electrical engineering*, vol. 14, no. 3, pp. 54–60, 2019.

[25] J. Zhao, H. Xu, P. Sun, Y. Z. Ma, and L. Wang, "Analysis of two types of longitudinal side effects of linear phase shifter transformer," *Transactions of China Electrotechnical Society*, vol. 36, no. 5, pp. 984–995, 2021.

[26] *Theory and Electromagnetic Design Methods of Linear Induction Motors*, Science Press Co., Beijing, China, 1 edition, 2006.

Hindawi
Mathematical Problems in Engineering
Volume 2022, Article ID 3917775, 12 pages
https://doi.org/10.1155/2022/3917775

Research Article

Low Voltage Ride through Enhancement Using Grey Wolf Optimizer to Reduce Overshoot Current in the Grid-Connected PV System

N. Jaalam, A.Z. Ahmad, A. M. A. Khalid, R. Abdullah, N. M. Saad, S. A. Ghani, and L. N. Muhammad

Faculty of Electrical & Electronics Engineering, University of Malaysia Pahang, 26600 Pekan, Malaysia

Correspondence should be addressed to N. Jaalam; zila@ump.edu.my

Received 5 November 2021; Revised 17 March 2022; Accepted 30 March 2022; Published 6 May 2022

Academic Editor: Amin Jajarmi

In today's world, the DG should not be disconnected in the event of a power outage but should instead remain linked to the grid and supported by reactive power. This can be accomplished by implementing the low voltage ride through (LVRT) with a proportional integral (PI) controller. As a result, the voltage profile can be enhanced. The PI controller, on the other hand, has drawbacks in that setting the gain takes a long time and results in an overshoot current on the grid, which could trigger the protection relay. To address this issue, this paper proposes employing a grey-wolf optimizer (GWO) to enhance the LVRT in a 5 MW three-phase grid-connected PV system. A MATLAB simulation was carried out then under a three-phase fault and load disturbance to verify the efficiency. It is found that, even with a 70% voltage sag, the PV system can remain connected to the electrical grid while minimising overshoot current on the grid side.

1. Introduction

The grid-connected PV system often experiences balance and unbalance voltage sags that are caused by short circuits and the connection of large loads. According to IEEE 1547, if a voltage sag occurs at the point of common coupling (PCC) during a grid fault, the grid must be disconnected immediately to preserve the power converters, and the inverter should not actively participate in voltage/var regulation, especially at low levels of PV penetration. However, with the high penetration of solar PV generators into the grid, stability issues may arise on the grid side if there is a disconnection of the PV plant during the fault. Furthermore, if the disconnection is repeated, the component lifetime will be negatively impacted, and the reconnection of the PV plant to the utility grid will necessitate substantial start-up costs [1]. Therefore, the inverter should stay connected to the grid within a permissible time and inject some reactive power to support the grid during voltage sags [1, 2]. This new requirement which is known as a LVRT, is an important practise in grid-connected PV systems nowadays to prevent long-term voltage instability that may lead to power outages [3]. Malaysia's LVRT limitation curve is depicted in Figure 1. If the voltage decrement value for the particular time range is above the red line, the distributed generation (DG) should stay connected to the grid while maintaining normal operation. However, if the voltage decrement value is less than the red line, the DG can be disconnected right away to avoid more serious damage, and this is the exact time for the anti-islanding to happen.

LVRT can be divided into 2 categories: either by adding external devices such as energy storage systems or supercapacitors [4], flexible alternating current transmission system (FACTS) devices [5], and braking chopper, or by modifying the internal inverter controller as shown in Figure 2. The latter method is getting massive attention now as it does not require any external device, so it will be cheaper and simpler. It is based on a control algorithm that can be

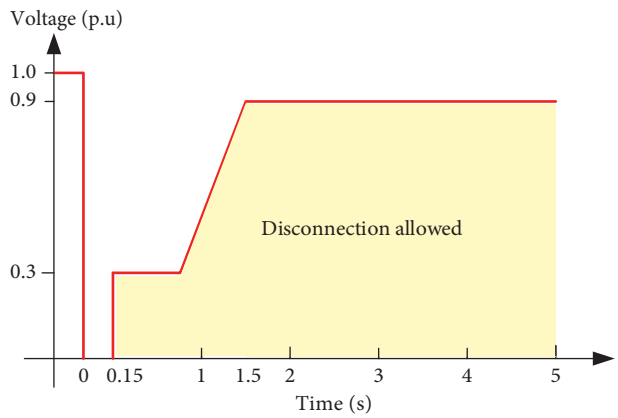

Figure 1: The LVRT limiting curve of Malaysia.

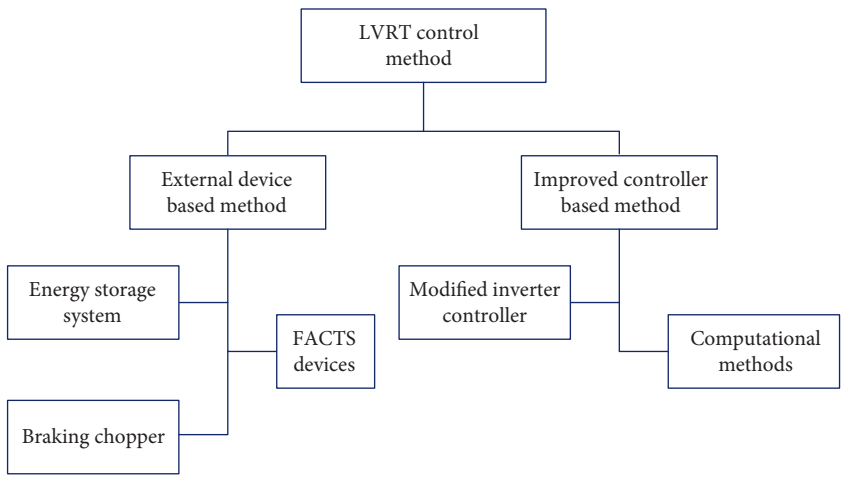

Figure 2: LVRT control method.

utilised using proportional integral (PI), proportional-resonant (PR), droop control, fuzzy logic controller, and particle swarm optimization (PSO) [6–10].

In the previous study, the inverter controller was successfully modified internally to provide reactive power into the grid during weak grid conditions using a PI controller [3, 11]. The PI controller has wide application in the industry due to its simplicity and effectiveness and does not need a more sophisticated approach [12]. However, in the power system industry, the rise of renewable energy penetration into the grid has brought uncertainty about the effectiveness of the PI controller [13]. The use of the PI controller will lead to an overshoot current on the grid side that can have a negative impact on the stability and operation of the power system. The PI controller tuning process also takes a long time because of the trial-and-error method used and does not produce good performance when it operates in a wide range of conditions [13, 14].

Thus, a metaheuristic algorithm that has already been well-known over the last two decades has now gained more interest in enhancing the LVRT strategy. It is a popular choice for obtaining accurate parameters as it is a simple, flexible, robust, and derivation-free mechanism [15]. Authors in [5] use neural networks (NNs) to detect grid faults in a grid-connected PV system. When a voltage sag is detected, a finite control set model predictive control (FCS-MPC) will provide reactive power support to enhance the LVRT capability. A probabilistic wavelet fuzzy neural network (PWFNN) and a Takagi–Sugeno–Kang probabilistic fuzzy neural network (TSKPFNN) were presented in [16, 17] to accommodate the LVRT requirement for power balance during various grid fault situations. It consists of a 6-layer feedforward neural network which consists of an input layer, membership layer, probabilistic layer, TSK-type fuzzy interference mechanism layer, rule layer, and output layer, all of which require an online learning algorithm. Both simulation and experimental results of this research have confirmed that this approach is able to stabilise the voltage under grid disturbance. However, the drawback of this approach lies in the complexity of the controller in confronting the uncertainties of the PV system. Meanwhile, a study on neurofuzzy controllers has been presented in [18] to enhance the LVRT. It is found that the proposed controller is effective in providing the required reactive power, but the output current at the PCC side is not present. Thus, it is not clear whether the overshoot current is present or not.

In this study, the PI controller will be tuned by GWO (GWO-PI) to compute the value of the proportional and

integral gain. The GWO algorithm was chosen as it is simple and can be easily programmed with speedy convergence [19]. The main objectives of the study are first to provide the required reactive power during the fault disturbance and second, to reduce the overshoot current in the grid-connected photovoltaic system. Based on Tenaga Nasional Berhad (TNB) distribution system parameters, a simulation model of a 5 MW PV system which is connected to a 33 kV grid will be developed using MATLAB/Simulink, as shown in Figure 3. A balanced three-phase fault with a load disturbance will be applied to see how well the proposed method works.

2. Methodology

This section will present the strategies applied to achieve the objectives of the study which can be divided into two parts: PV modelling and controller design.

2.1. PV Modelling. A single diode model, as shown in Figure 4, is used for PV modelling due to its simplicity and accuracy for power system analysis [18]. For more accurate results, series resistance R_s and shunt resistance R_{sh} can be added. However, the R_{sh} value is normally very large. Therefore, it is always neglected to reduce complexity.

By applying Kirchhoff's law, the mathematical equation for this model is given by (1) where I_{ph} represents the photocurrent, I_D is a diode current, and I_{PV} is the output current of the PV cell. The parameters of the system used in this study are listed in Table 1 which is based on the Suntech Power STP270-24/V_b solar PV module.

$$I_{\mathrm{pv}} = I_{\mathrm{ph}} - I_D. \tag{1}$$

From Table 1, one single Suntech Power STP270-24/Vb module can only generate 270 W. Hence, the PV module needs to be connected in parallel and series configurations to increase its current and voltage, respectively. When PV cells are joined in series, the voltage increases, whereas when PV cells are connected in parallel, the current increases. 28 series modules with 665 parallel strings are used to create a 5 MW PV system, as shown in the following calculation:

28 series module x $I_{\mathrm{mp}} = 215.88$ A

665 parallel strings x $V_{\mathrm{mp}} = 665 \times 35 = 23275$ V

$215.88\ \mathrm{A} \times 23275\ \mathrm{V} = 5.02\ \mathrm{MW}$

2.2. Controller Design. The LVRT requirement specifies that when the voltage sag happens, the PV-DG should stay connected to the grid for a certain period of time, and at the same time, reactive current injection (RPI) should be provided to improve the voltage profile. For the successful implementation of the LVRT in faulty-mode operation, two major steps must be considered: the fault detection method and RPI. A fast and accurate fault detection method is crucial as it will determine the efficiency of the proposed LVRT system. In a weak grid condition, the system must be able to switch from normal operation to faulty-mode operation immediately for the LVRT with the RPI controller to take place. Figure 5 shows a flow chart of the system where the

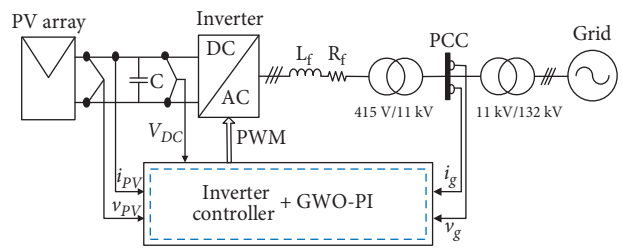

Figure 3: Basic structure of grid-connected PV system.

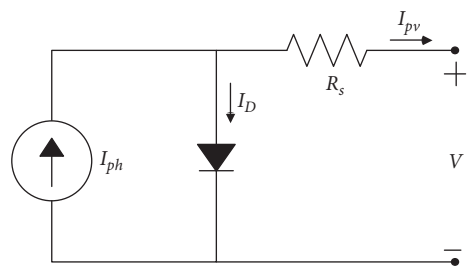

Figure 4: A simplified PV equivalent circuit with R_s only.

Table 1: PV model parameters.

Parameters	Values
Nominal peak power, P_m (W)	270
Nominal current, I_{mp} (A)	7.71
Nominal voltage, V_{mp} (V)	35
Short circuit current, I_{sC} (A)	8.2
Short circuit voltage, V_{sC} (A)	44.5
Series resistor, R_s (Ω)	0.32
Coefficient, K_i (%/K)	0.06
Total number of cells in series, N_s	72
Total number of cell in parallel, N_p	1

grid voltage, v_g will be continuously monitored to check whether it is still in the permissible range or not. If v_g is less than the normal grid voltage, $v_{gn,}$ two conditions must be checked, whether it is in the permissible range for more than 0.6 s or not. If so, the inverter must be disconnected from the grid immediately. Otherwise, the reactive power must be injected using GWO-PI to improve and stabilise the voltage profile. So, the PV inverter does not have to be disconnected from the grid to keep working.

To regulate the reactive power, a conventional method employing a PI controller can be used as shown in Figure 6 where the reactive current reference i_q^* is given by (2). However, it is very time consuming to determine the right value for the proportional gain (K_p) and integral gain (K_i). In addition, it always takes a long time to restore to its steady-state value after any fault clearance due to the error accumulation in the integral part of the PI controller, and sometimes overshoot current may occur [20].

$$i_q^* = K_p e + K_i \int e(t)\mathrm{d}t. \tag{2}$$

Therefore, to overcome this problem, a GWO-PI technique that imitates the leadership hierarchy and hunting mechanism of grey wolves is proposed. It is a meta-heuristic

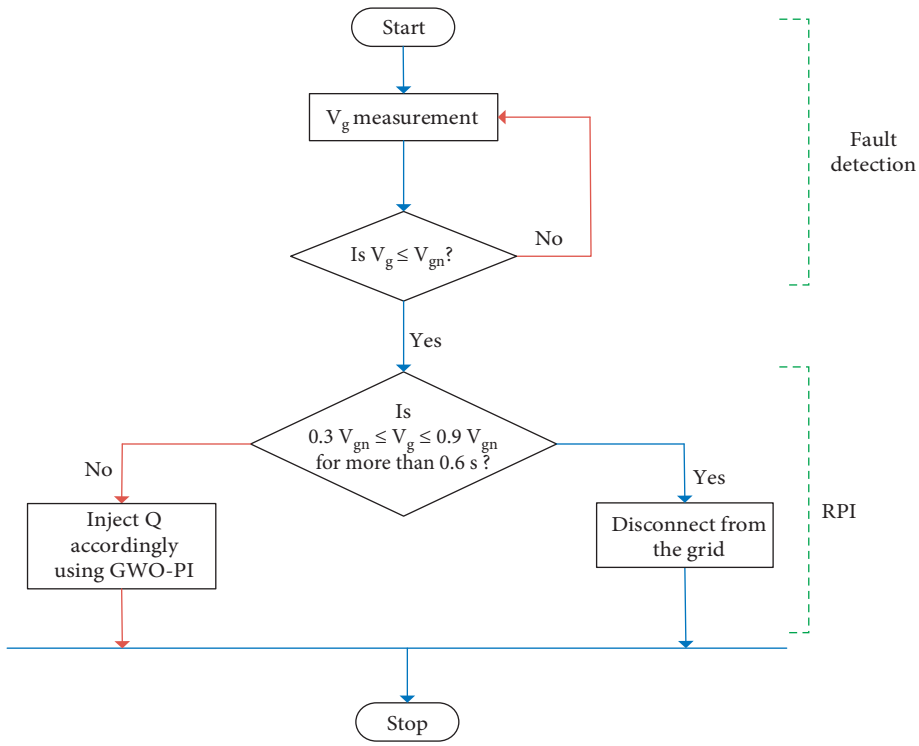

Figure 5: Flow chart of the proposed LVRT using GWO-PI.

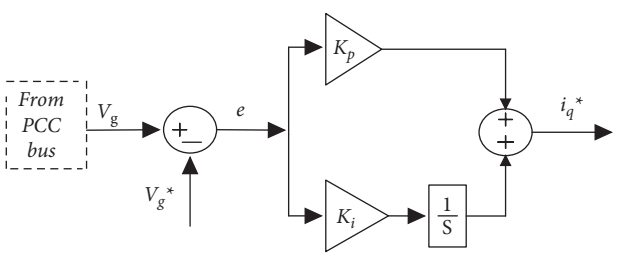

Figure 6: PI-based controller block diagram.

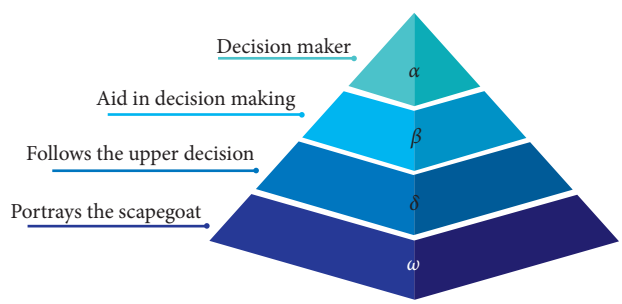

Figure 7: Social hierarchy of grey wolves.

algorithm that was introduced by Muro et al. and Mirjalili et al. [15, 21]. The grey wolf is an apex predator that is at the top of the food chain. Usually, five to twelve grey wolves would live together in a group. Figure 7 depicts the social hierarchy of the grey wolves. Alpha is the leader who makes the decisions about hunting, sleeping space, and other matters. Alpha is supported by beta to aid in decision making. Alpha will be replaced by beta if alpha is ill or dead. Omega is the lowest-ranking character, and he plays the role of a scapegoat. Delta follows the decisions of alpha and beta but is more dominant than omega. In the GWO algorithm, alpha is the fittest solution, beta is the second-best solution, while delta is the third best solution. Figure 8 shows the hunting behaviour of the grey wolves, and the three main stages of wolf hunting are as follows:

(i) Tracking, chasing, and approaching the prey

(ii) Pursuing, encircling, and harassing the prey until it stops moving

(iii) Attack towards the prey

For the fitness function, the integral time absolute error (ITAE) as in (3) is used to gain the controller parameters. In the MATLAB editor, the GWO code is executed while considering the fitness function, number of iterations, number of variables, and particles. Meanwhile, the ITAE value that was calculated in Simulink will be sent to the workspace where the GWO is employed. The optimised PI parameters are obtained after the GWO algorithm completes its iteration which will determine the character of the system. Figure 9 shows the GWO-PI controller feedback control system while Figure 10 depicts the flow chart of the algorithm.

$$\text{ITAE} = ft|\epsilon|\mathrm{d}t. \tag{3}$$

To provide reactive current $i^*_{q\text{new}}$ to the grid, the algorithm shown in (4) is used. The reference grid voltage v_g^* will be first compared with the measured grid voltage v_g. The error difference e produced by v_g and v_g^* will be utilised by the GWO to compute the proportional gain (Kp) and integral

Figure 8: Hunting behaviour of grey wolves: (a) Chasing, approaching, and tracking prey. (b–d) Pursuing, harassing, and encircling. (e) Stationary situation and attack [21].

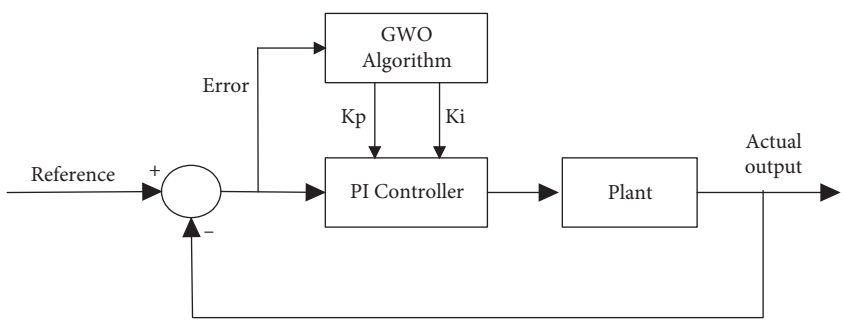

Figure 9: GWO-PI controller block diagram.

gain (Ki) with the maximum reactive current i^*_{qmax} defined by equation (5). The upper boundary is set to 40 and 5000 for the Kp and Ki while both lower boundaries are set to 0.

$$i^*_{q\,\text{new}} = \begin{bmatrix} 0, & \text{case } a\text{: } v_g > 0.9v_{gn}, \\ 2 - 2\dfrac{V_g}{V_{gn}}, & \text{case } b\text{: } 0.9v_{gn} \geq v_g \geq 0.3v_{gn}, \\ 1, & \text{case } c\text{: } v_g \leq 0.3v_{gn}, \end{bmatrix}, \tag{4}$$

$$i^*_{q\,\max} = \sqrt{i_n^2 - i_d^{*\,2}}. \tag{5}$$

The mathematical modelling of the GWO can be outlined as follows:

(i) Social hierarchy: for GWO, alpha (α) is considered the fittest solution, followed by beta (β) and delta (δ) as the second and third best solutions, respectively.

(ii) Encircling the prey: the encircling of prey can be expressed in the following equations:

$$\begin{aligned} \vec{D} &= \vec{C} \cdot \vec{X}(t) - \vec{X}(t), \\ \vec{X}(t+1) &= \vec{X}(t) - \vec{A} \cdot \vec{D}, \end{aligned} \tag{6}$$

(i) where $\vec{A}$ and $\vec{C}$ represent coefficient vectors, t is the current iteration, $\vec{X}$ is the position vector of the grey wolf, and $(X \cdot \vec{P})$ is the position vector of the prey. Meanwhile, $\vec{A}$ and $\vec{C}$ are vectors that can be calculated by using the following equations:

$$\begin{aligned} \vec{A} &= 2\vec{a} \cdot \vec{r}_1 - \vec{a}, \\ \vec{C} &= 2 \cdot \vec{r}. \end{aligned} \tag{7}$$

(iii) Hunting: the hunting is led by α, β, and δ ability to detect prey and encircle them. The other

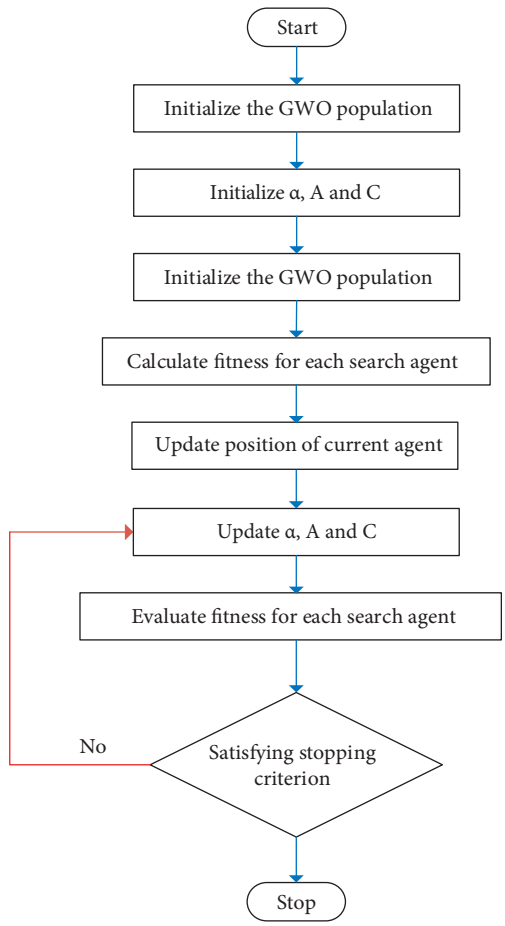

Figure 10: Flow chart of GWO.

search agents will update their positions according to the position of the best search agent. The following equations express this behaviour:

$$\vec{D}_{a\{3,8} = \vec{C}_{1,3}\vec{X}_{a\{3,8} - \vec{X},$$

$$\vec{X}_{1,3} = \vec{X}_{a,\{3,8} - \vec{A}_{1,3}\vec{D}_{a,\{3.8}, \quad (8)$$

$$\vec{X}(t+1) = \frac{\vec{X}_1 + \vec{X} + \vec{X}_3}{3}.$$

(iv) Attacking the prey: the grey wolves will attack the prey when there are halts in the movement of the prey. For every iteration, α decreased from 2 to 0.

(v) Searching for prey: the exploration of the GWO algorithm is formulated based on the positions of α, β, and δ wolves. The wolves diverge during the search for prey and then converge to attack the prey.

3. Results

Two case studies were performed using MATLAB Simulink to validate the effectiveness of the proposed control strategy: one with a 20% voltage drop and the other with a 30% voltage drop, both with a balanced three-phase fault and load disturbances. With a 0.5 MW load connected, the fault occurred between 3.5 and 3.65 s in both situations. During 4.5 s to 5 s, another 0.1 MW load is applied.

3.1. 20% Voltage Drop. For the 20% voltage drop case, the number of iterations is 30, with the number of search agents set to 5. The convergence curve for this simulation is shown in Figure 11, with the best optimal value of the objective function obtained by the GWO being 0.014546. When the optimization is completed, the best solution gained by GWO is 40 and 3188.5158, which is the optimised value for K_p and K_i. Figure 12 shows the voltage profile comparison between systems with GWO-PI, PI only, and without RPI (NO RPI). Under normal conditions, the reactive current, $i_q = 0$, because there is no reactive power being injected, as shown in Figure 13. Therefore, the voltage dropped to 189.82 V when the fault happened at 3.5 s which accounted for more than 20% of the nominal value. The voltage dropped further when the load was connected at 4.5 s. With PI and GWO-PI based controllers, the voltage has successfully increased to 239.6 V as both controllers were able to inject the desired reactive power and have completely reduced the voltage drop to zero, thus grid disconnection can be avoided. However, the PI controller has a high overshoot voltage, but the GWO-PI

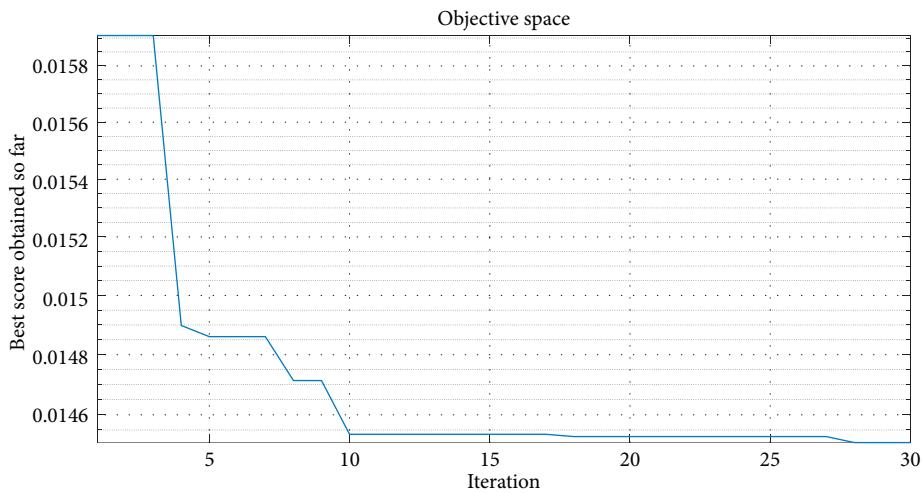

Figure 11: Convergence curve at 20% voltage drop.

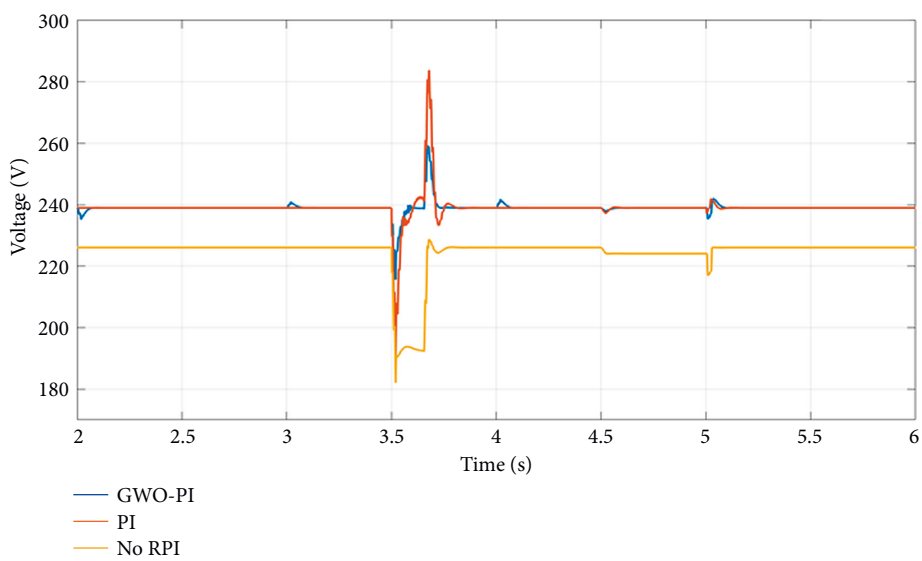

Figure 12: Voltage profile comparison at 20% voltage drop.

manages to reduce it by 8%. Meanwhile, Figure 14 shows the active and reactive power of the GWO-PI controller. When the fault occurs at 3.5 s, the reactive power increases significantly while the active power tries to maintain its power generation since the voltage drop is not severe. Table 2 summarises the performance of all controllers.

3.2. 30% Voltage Drop. For the second case, the number of iterations set is also 30. The number of search agents is 5. Figure 15 shows the convergence curve for this case where the best optimal value of the objective function found by GWO is 0.014509. After the optimization stopped, the best solution obtained by GWO was 40 and 4076.8579 which is the optimised value for K_p and K_i. Figure 16 illustrates the voltage profile comparison between GWO-PI, PI, and NO RPI. Without the RPI controller, the voltage drops by 30% to 168 V. With the PI and GWO-PI controllers, the reactive power can be injected accordingly as shown in Figure 17. Therefore, the voltage profile was improved as the voltage drop decrement has been reduced by at least 15%. The voltage significantly increased to 203.73 V for the PI and 238.03 V for the GWO-PI. Using GWO-PI, not only the highest value of reactive power can be injected, but it also shows the fastest settling time compared to the PI controller, as summarised in Table 3. During the fault condition, the

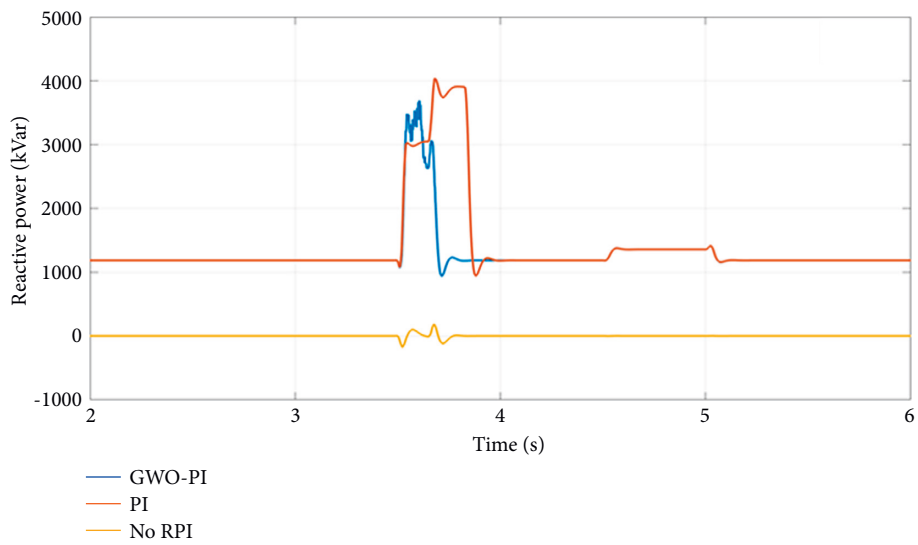

Figure 13: Reactive power comparison at 20% voltage drop.

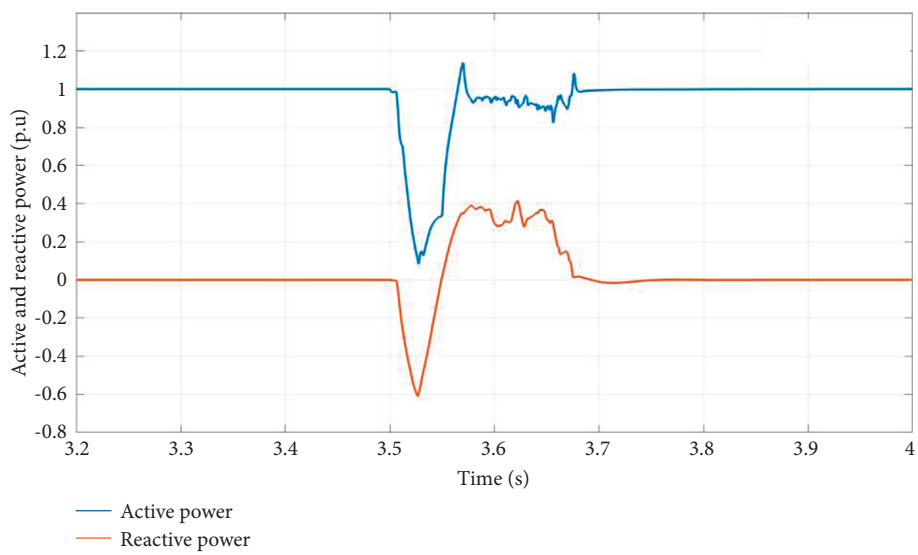

Figure 14: Active and reactive power for the GWO-PI controller.

Table 2: Controller performance comparison at 20% voltage drop.

	NO RPI	PI	GWO-PI
Voltage during fault (V)	189.82	239	239
Percentage of voltage drop (%)	20.91	0	0
Reactive power (kVar)	0	3763.54	3421.52
Overshoot voltage (%)	-	17.92	7.5

supply of active power should be limited to give sufficient room for the inverter to provide maximum reactive power as shown in Figure 18. Meanwhile, Figure 19 shows the grid or PCC current and voltage (phase A) under a 30% voltage drop with the PI controller. It can be seen that the current and voltage are not in phase when the fault occurs, and a high overshoot current is also noticeable. However, the GWO-PI controller was able to reduce this overshoot by

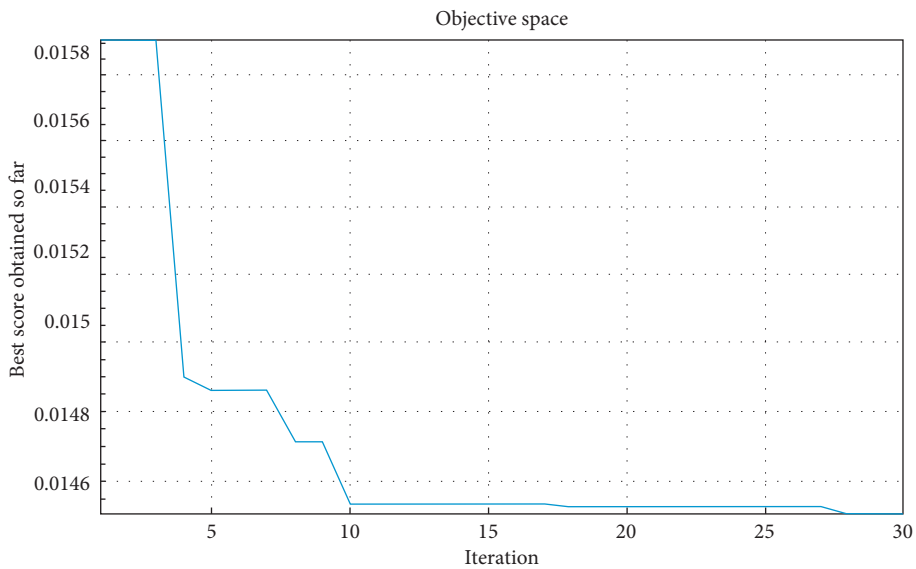

Figure 15: Convergence curve of the GWO.

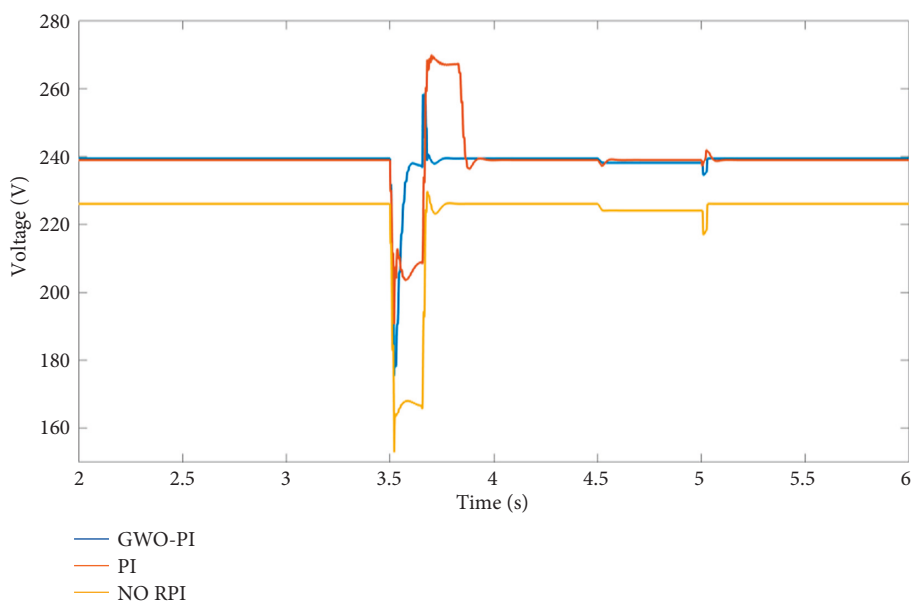

Figure 16: Voltage profile comparison at 30% voltage drop.

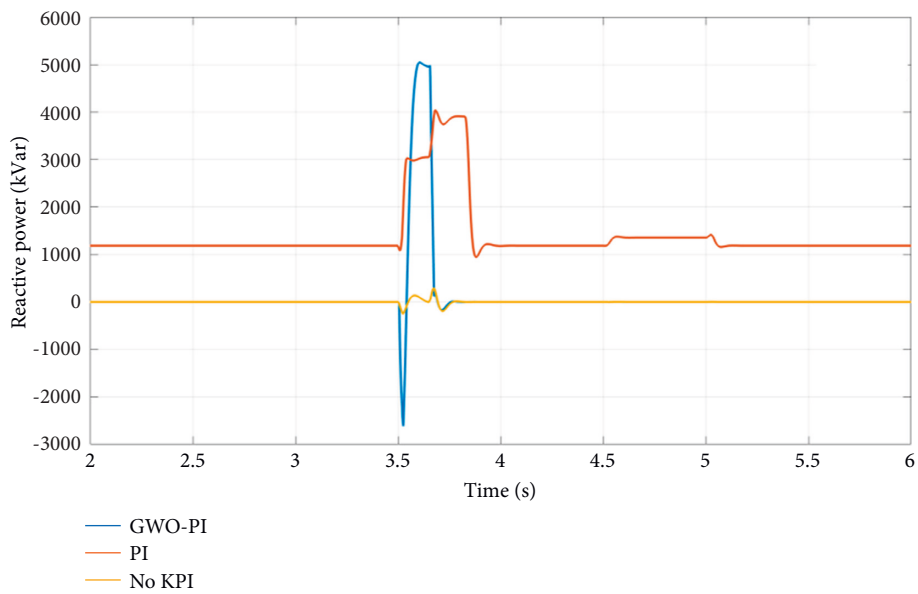

Figure 17: Reactive power comparison at 30% voltage drop.

Table 3: Controller performance comparison at 30% voltage drop.

	NO RPI	PI	GWO-PI
Voltage during fault (V)	168.01	203.73	238.03
Percentage of voltage drop (%)	30	15.4	0.83
Reactive power (kVar)	0	3763.18	4987.61
Voltage settling time (s)	-	0.29	0.13
Overshoot current	-	4.8	0.5

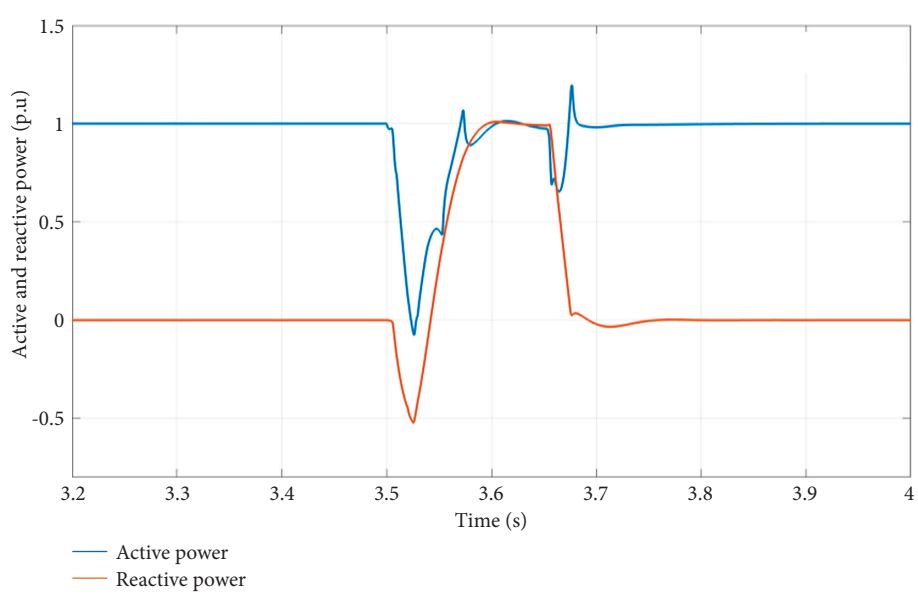

Figure 18: Active and reactive power of the GWO-PI controller.

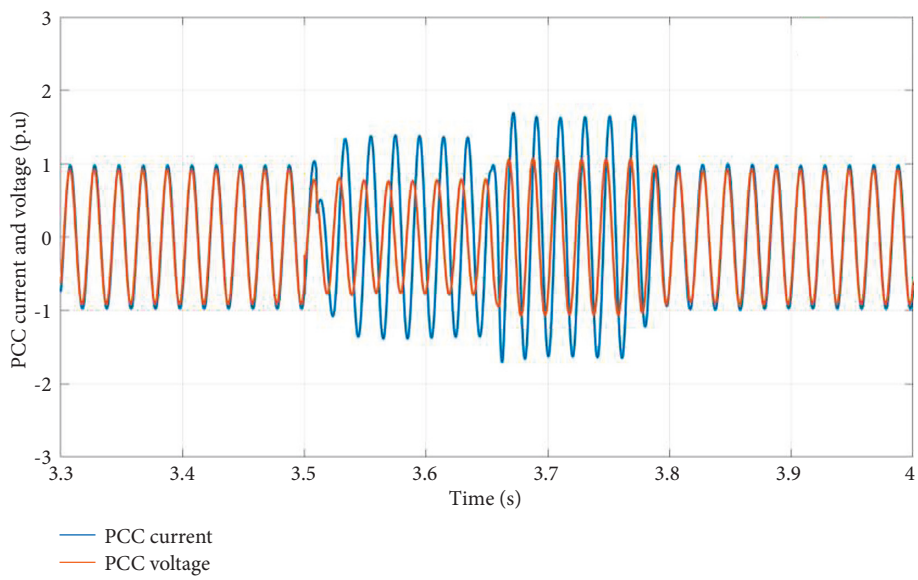

Figure 19: PCC current and voltage with PI controller.

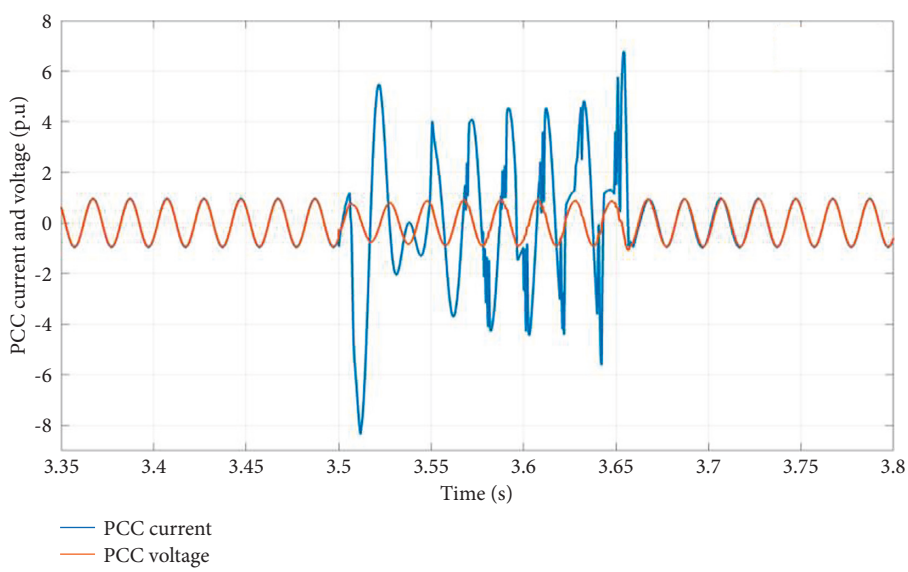

Figure 20: PCC current and voltage with GWO-PI controller.

approximately 4%, as illustrated in Figure 20. Table 3 summarises the performance of all controllers under 30% voltage sag.

4. Conclusion

This paper presents a new control strategy for the LVRT enhancement of the three-phase grid-connected PV system using the GWO-PI controller. The MATLAB simulation is used to assess the system's performance under a balanced three-phase fault and load disturbance. In a nutshell, it is found that the GWO-PI approach is more efficient than the PI controller. Even though both controllers are effective in compensating the desired reactive power during weak conditions, especially under 70% voltage sag, the GWO-PI controller managed to minimise the overshoot current. Besides, it can also significantly reduce the time it takes to tune the PI parameters. Even so, the proposed controller needs to be tested in more severe weak grid situations in the future including those caused by asymmetrical faults.

Data Availability

The GWO coding used to support the findings of this study are available from the corresponding author upon request.

Conflicts of Interest

The authors declare that they have no conflicts of interest.

Acknowledgments

The authors would like to thank the Ministry of Higher Education and the University of Malaysia Pahang for providing financial support under an internal research grant (Grant Number: RDU200329).

References

[1] N. Gira and A. K. Dahiya, "Solar PV-BES in distribution system with novel technique for DC voltage regulation," *Engineering Science and Technology, an International Journal*, vol. 23, no. 5, pp. 1058–1067, 2020.

[2] N. Hamrouni, S. Younsi, and M. Jraidi, "A flexible active and reactive power control strategy of a LV grid connected PV system," *Energy Procedia*, vol. 162, pp. 325–338, 2019.

[3] N. Jaalam, N. A. Rahim, A. H. A. Bakar, and B. M. Eid, "Strategy to enhance the low-voltage ride-through in photovoltaic system during multi-mode transition," *Solar Energy*, vol. 153, pp. 744–754, 2017.

[4] I. Hamdan, A. Maghraby, and O. Noureldeen, "Stability improvement and control of grid-connected photovoltaic system during faults using supercapacitor," *SN Applied Sciences*, vol. 1, no. 12, pp. 1–19, 2019.

[5] M. A. Khan, A. Haque, V. S. B. Kurukuru, and S. Mekhilef, "Advanced control strategy with voltage sag classification for single-phase grid-connected photovoltaic system," *IEEE Journal of Emerging and Selected Topics in Industrial Electronics*, vol. 3, no. 2, pp. 258–269, 2022.

[6] M. Mirhosseini, J. Pou, and V. G. Agelidis, "Single-stage inverter-based grid-connected photovoltaic power plant with ride-through capability over different types of grid faults," *IECON 2013 - 39th Annual Conference of the IEEE Industrial Electronics Society*, vol. 1, pp. 8008–8013, 2013.

[7] M. Mirhosseini, J. Pou, and V. G. Agelidis, "Single- and two-stage inverter-based grid-connected photovoltaic power plants with ride-through capability under grid faults," *IEEE Transactions on Sustainable Energy*, vol. 6, no. 3, pp. 1150–1159, 2015.

[8] F. Yang, L. Yang, and X. Ma, "An advanced control strategy of PV system for low-voltage ride-through capability enhancement," *Solar Energy*, vol. 109, pp. 24–35, 2014.

[9] M. M. Hasaneen, M. A. L. Badr, and A. M. Atallah, "Control of active/reactive power and low-voltage ride through for 40 kW three-phase grid-connected single-stage PV system," *CIRED - Open Access Proceedings Journal*, vol. 2017, no. 1, pp. 1655–1659, 2017.

[10] O. Noureldeen, I. Hamdan, and B. Hassanin, "Design of advanced artificial intelligence protection technique based on low voltage ride-through grid code for large-scale wind farm generators: a case study in Egypt," *SN Applied Sciences*, vol. 1, no. 6, pp. 1–19, 2019.

[11] Y. Yang, H. Wang, and F. Blaabjerg, "Reactive power injection strategies for single-phase photovoltaic systems considering grid requirements," in *Proceedings of the 2014 IEEE Applied Power Electronics Conference and Exposition - APEC 2014*, pp. 371–378, Fort Worth, TX, USA, March 2014.

[12] F. Khavari, A. Badri, and A. Zangeneh, "Energy management in multi-microgrids considering point of common coupling constraint," *International Journal of Electrical Power & Energy Systems*, vol. 115, no. 2020, Article ID 105465, 2020.

[13] W. Liu, Y. Zheng, Q. Chen, and D. Geng, "An adaptive CGPC based anti-windup PI controller with stability constraints for the intermittent power penetrated system," *International Journal of Electrical Power & Energy Systems*, vol. 130, Article ID 106922, 2021.

[14] Z. Ahmad and S. N. Singh, "An improved single phase transformerless inverter topology for grid connected PV system with reduce leakage current and reactive power capability," *Solar Energy*, vol. 157, pp. 133–146, 2017.

[15] S. Mirjalili, S. M. Mirjalili, and A. Lewis, "Grey wolf optimizer," *Advances in Engineering Software*, vol. 69, pp. 46–61, 2014.

[16] F.-J. Lin, K.-C. Lu, and T.-H. Ke, "Probabilistic wavelet fuzzy neural network based reactive power control for grid-connected three-phase PV system during grid faults," *Renewable Energy*, vol. 92, pp. 437–449, 2016.

[17] F.-J. Lin, K.-C. Lu, T.-H. Ke, B.-H. Yang, and Y.-R. Chang, "Reactive power control of three-phase grid-connected PV system during grid faults using Takagi-Sugeno Kang probabilistic fuzzy neural network control," *IEEE Transactions on Industrial Electronics*, vol. 62, no. 9, pp. 5516–5528, 2015.

[18] N. Jaalam, A. M. A. Haidar, N. L. Ramli, N. L. Ismail, and A. S. M. Sulaiman, "A neuro-fuzzy approach for stator resistance estimation of induction motor," in *ProceeInECCE 2011 - International Conference on Electrical, Control and Computer Engineering*, pp. 394–398, Kuantan, Malaysia, June 2011.

[19] S. Padhy, S. Panda, and S. Mahapatra, "A modified GWO technique based cascade PI-PD controller for AGC of power systems in presence of plug in electric vehicles," *Engineering Science and Technology, an International Journal*, vol. 20, no. 2, pp. 427–442, 2017.

[20] N. H. Saad, A. A. El-Sattar, and A. E.-A. M. Mansour, "Improved particle swarm optimization for photovoltaic system connected to the grid with low voltage ride through capability," *Renewable Energy*, vol. 85, pp. 181–194, 2016.

[21] C. Muro, R. Escobedo, L. Spector, and R. P. Coppinger, "Wolf-pack (*Canis lupus*) hunting strategies emerge from simple rules in computational simulations," *Behavioural Processes*, vol. 88, no. 3, pp. 192–197, 2011.

Hindawi
Mathematical Problems in Engineering
Volume 2022, Article ID 9083307, 13 pages
https://doi.org/10.1155/2022/9083307

Research Article

An Efficient Energy Management Scheme for an Islanded DC Microgrid with Hybrid VRFB System

S. Hameed,[1] **I. Prabhakar Reddy**,[2] **V Ganesh**,[1] **and Aruna rai Vadde**[3]

[1]*Department of Electrical and Electronics Engineering, Jawaharlal Nehru Technological University, Anantapur, India*
[2]*Department of Electrical and Electronics Engineering, NBKR Institute of Science and Technology, Andhra Pradesh, India*
[3]*Department of Electrical and Computer Engineering, Debre Tabor University, Debre Tabor, Ethiopia*

Correspondence should be addressed to Aruna rai Vadde; dr.rai@dtu.edu.et

Received 22 February 2022; Revised 11 March 2022; Accepted 21 March 2022; Published 14 April 2022

Academic Editor: Albert Alexander Stonier

This paper presents an efficient energy management scheme for an islanded DC microgrid included with vanadium redox flow battery (VRFB) with supercapacitor based hybrid energy storage system for a 3-phase variable load profile. The analysed islanded DC microgrid system is composed with sources such as lithium-ion batteries, fuel cell, supercapacitors, and vanadium redox flow battery (VRFB), along with involved DC/DC (buck, boost, and bidirectional) and DC/DC converters. In this paper, an adaptive proportional plus integral (PI) control based energy management scheme is implemented. The main theme on which the performance of this system is analysed is the state of charge of energy storage devices (VRFB, supercapacitor, and Li-ion battery) and the overall efficiency of system. The voltage spikes due to sudden change in load have been regulated by using supercapacitor and Li-ion battery with VRFB. To minimize the fuel consumption, an adaptive proportional plus integral control strategy is being used. In this paper the modelling and simulations are carried out by using MATLAB/SIMULINK software to demonstrate minimizing the effect of load fluctuations with the help of supercapacitor and batteries by synchronizing it to the DC microgrid.

1. Introduction

In the modern world, when the conventional sources of energy are on the verge of their extinction and the pollution levels associated with their extensive use, it has become a serious issue. It is time we switch to the nonconventional ways at a much faster rate. In present scenario, power plants are used to generate electricity and some renewable energy sources such as wind energy and solar energy at their initial stages. The main problem associated with solar energy sources is less efficient power generation, and with wind energy, the rapid fluctuation in power generation becomes the main issue. To reduce the stress on power plants for energy requirements, microgrids have become an important alternative. They are capable of extracting power from the grids and also deliver power to the grid, if and when needed. A type of microgrid which can be used as an affordable source for isolated places is an islanded DC microgrid. They are able to extract and deliver power as per the load requirements on their own, without the aid of external grid. In this paper, an energy management scheme has been proposed for the islanded DC microgrid with VRFB as the main source for the hybrid system.

In a previous paper [1], an energy management scheme with fuel cell as the main scheme has been proposed. Fuel cells though being a very useful energy source have a significant disadvantage regarding their input. The inputs of the fuel cell are hydrogen and oxygen. Although they are easily available, their pumping into the fuel cell can become an issue. To overcome this problem, we have come up with a solution to use vanadium redox flow battery as the main supply source. Another disadvantage with fuel cells is that it cannot be recharged from the DC bus unlike Li-ion and VRFBs.

In this article, VRFBs are being used as the main source to supply power to the load, with supercapacitors (which smoothens the voltage spikes at transience) and Li-ion batteries. The vanadium redox flow battery is a type of

rechargeable battery which uses vanadium ions at different oxidation states and stores chemical potential energy by the help of oxidation-reduction process. It makes use of ability of vanadium to exist in solution in four different oxidation states. The advantages associated with vanadium redox flow battery are its durability to handle more than 15,000 cycles with a charge/discharge efficiency of 75–80 per cent and energy density of 25 Wh/Kg. In addition to this, an important advantage is its cheap capital cost. It can be inferred from previous researches that for grid application it has a cost range from 745 to 825 dollars KW/h which is half of the Li-ion battery cost. VRFBs can be used to withstand a Depth of Discharge (DOD) of around 90 percent and more. In this article, Li-ion battery stores extra energy of DC grid by the help of DC/DC buck converters.

Vanadium redox flow battery has poor response in transient conditions. To overcome this issue, its synchronization with various energy storing elements like Li-ion batteries, supercapacitors, and fuel cell is required.

Different energy management schemes (EMS) have been reported in previous papers. Some of them are as follows:

(i) State control scheme

(ii) Indistinct (fuzzy) logic strategy

(iii) Adaptive P and I control strategy

(iv) Decoupling of frequency and indistinct (fuzzy) logic

(v) Minimization of consumption strategy

The details regarding these strategies are explained in [1]. It is to be understood that the capability of the designer regarding the knowledge of various components determines the performance of the applied scheme. In this paper, adaptive proportional and integral (PI) control strategy has been discussed [1]. This strategy is mainly based on the parameter controls like SOCs of batteries, supercapacitor, and DC bus voltage. This paper deals with the adaptive P and I control strategy using VRFB as the main source along with fuel cell, supercapacitors, and Li-ion battery and is connected and synchronized with the DC microgrid. VRFB is arising as another option in contrast to ESS batteries applied to inexhaustible power age frameworks to take care of ecological and asset exhaustion issues. Right now, lithium batteries are predominantly utilized in ESS; however there is an issue that a fire mishap might happen and the life expectancy is restricted. VRFB enjoys the benefit of being reasonable for enormous limit frameworks since it has a more extended life expectancy than lithium batteries and has a limit relative to amount of electrolyte. Nonetheless, there is an impediment in that it is hard to appraise the limit because of the working qualities. Vanadium redox stream battery (VRFB) has attracted a lot of thoughts since it can truly handle the unpredictable issue of supportable power age. Regardless, the low energy thickness of VRFBs prompts massive cost, which will genuinely restrict the improvement in the field of energy storing. VRFB stream field plan and stream rate upgrade is a suitable strategy for additional creating battery execution without enormous improvement costs. This overview summarizes the basic issues of VRFB improvement, depicting the working guideline, electrochemical reaction connection, and system model of VRFB. The course of stream field plan and stream rate improvement is inspected, and the battery credits and estimations for evaluating VRFB execution are summarized. The point of convergence of the assessment is the systems for stream field plan and stream rate smoothing out and the expansive relationship of battery execution between different stream field plans. Composing assessment shows that reasonable stream field arrangement can deal with the consistency of electrolyte, further foster battery credits and estimations, and in this way work on the overall execution of VRFB and reduce the cost. In this paper, Section 2 deals with the architecture of hybrid power module, Section 3 describes component modelling, Section 4 explains the EM scheme used, and Section 5 provides simulation and experimental results.

2. Architecture of Hybrid Power Module

The architecture of hybrid power is modelled based on the requirements of energy and power for fluctuating load conditions, when the system is connected to an islanded DC microgrid. The VRFB system is used to meet the average load demand of the system, whereas the batteries (Li-ion, fuel cell) and supercapacitor are designed to help the VRFB during peak demands of continuous and transient nature, respectively. The analysis in detail regarding the selection of design and its features are not covered in this paper but can be referred from [2]. As shown in Figure 1, the VRFB of 52.6 KW (46.2 Vdc) along with a battery system which contain four battery packs (12.8 V, 40 Ah) is combined with 6-NESSCAP supercapacitor module (48.6 V, 88 F). The FC (fuel cell) power module of 12.45 KW having PEM assists VRFB. The energy of VRFB, fuel cell, and batteries are controlled through their associated DC/DC converters with the help of National Instrument Embedded Controller (NI PXI-8108). In PI controller strategy DC/DC converter uses output voltage and maximum input/output current as a reference, the battery operating system (BOS) is then used to prevent battery from overcharging, overtemperature, and overdischarge. Batteries are attached with DC bus through DC/DC converter, and in case of VRFB, a bidirectional converter is used, which helps in charging and discharging of VRFB. A resistor is also used which protects supercapacitor from overvoltage and is termed as protecting resistor.

The main elements of the hybrid power module are as follows.

(i) The vanadium redox flow battery system: It is a 52.6 KW, 46.2 Vdc with built-in two separate columns separated by a Proton Exchange Membrane (PEM). The VRFB has an in-built controller which assists the main controller.

(ii) The FC power module: A 12.45 KW 60–30 Vdc PEM system provided with liquid cooling, built-in auxiliary components which include air blower, filter, hydrogen recirculation pumps, pressure regulator, fans, and pumps for cooling is used. The

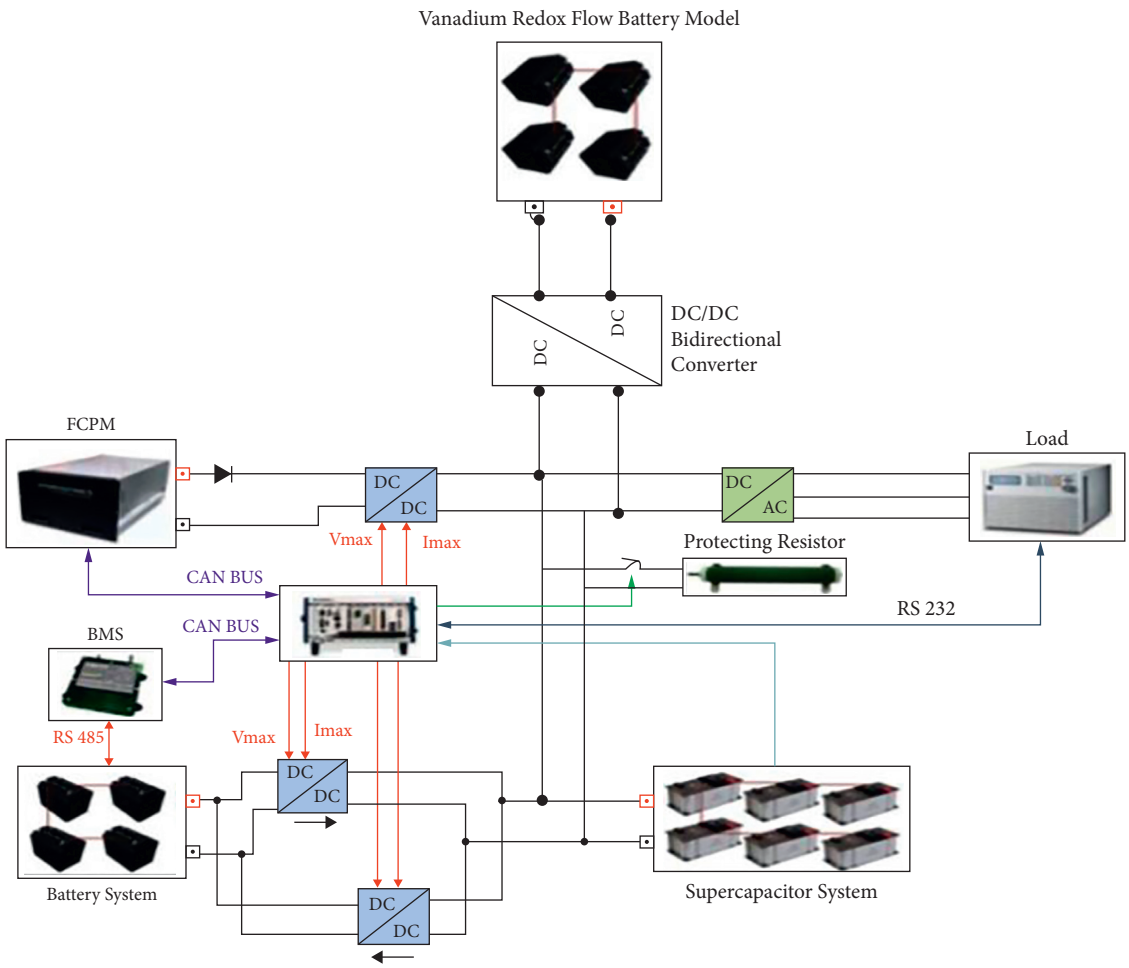

Figure 1: EM scheme for a VRFB hybrid power module.

fuel cell is equipped with its own controller for connecting to the main one.

(iii) The battery system: 4 Li-ion batteries are connected in series (12.5 KW 60–30 Vdc). Cell-to-cell balancing is provided through controllers (connected internally) to eliminate stress on individual battery and divide it uniformly to the whole battery system. This controller is then connected to the overall BMS.

(iv) The supercapacitor system: 6 supercapacitors are connected in series (48.2 V, 88 Farads) and then connections are made to a controller internally to eliminate stress on individual supercapacitor.

(v) The FC converter system: It has five DC/DC boost converters connected in parallel with 40–64 V DC input and 270 V (adjustable 243–297 V), 9.2 A DC output. Here the balancing is made possible through active current sharing.

(vi) The Li-ion converter system: Two converters, one DC/DC boost [with 40–58.2 V as DC input and 270 V, 7 A DC output] converter (for discharging of batteries) is connected in parallel with another DC/DC buck [with (243–297 V) as DC input and 48 V, 20 A DC output] converter (for charging).

(vii) The VRFB bidirectional converter system: It is used for both charging and discharging of VRFB, it acts like buck converter when charging and boost at the time of discharging (with 46.2 V as DC input and 270 V, 19 A DC output).

(viii) The inverter system: 3 DC/AC isolated converters are connected here in parallel (configuration: DC in of 160–320 V and AC output of 200 V, 400 Hz, and 5 KVA). Protection for overvoltage, short circuit, and overload is made. The output voltage of converter is then regulated to keep total harmonic distortion within three percent.

(ix) The programmable DC/AC load: Six 4.5 KW, 45 A, 350 V loads are used which can be programmed electronically.

(x) Sensor and signals conditioning: Voltage and current sensors are used at input and output of all the converters. Individual device temperature can be controlled through their controllers or thermistors.

3. Component Modelling

The study of the energy management system for an islanded DC microgrid requires that each subsystem is properly modelled with accuracy. This leads to a better understanding of the system, which allows for an effective design of the EMS. This section now describes the modelling approach of each individual component.

3.1. Vanadium Redox Flow Battery Model. Two electrolytic half-cells connected by a membrane that selectively exchanges the ions constitute the VRFB. Pumps connected inside electrolytic tanks provide corresponding ions to the respective electrolytic tanks. The V (5+) and V (4+) ions are stored as electrolytes in the positive half-compartment. The V(3+) and V(2+) ions are present as electrolytes in the negative half-compartment. At the time of discharge, in the positive half-cell, VO2(+) gets converted to VO(2+) ion and in the negative half-cell an electron is liberated from V(2+) to provide V(3+). Reverse reactions take place during charging. Open circuit voltage lies between 1 and 1.6 V. The chemical reactions for charging and discharging are not used in modelling. However, modelling is explained in this section with the help of suitable formulae and Figure 2.

For the VRFB shown, the equation for various parameters can be evaluated as follows:

$$h_{\text{delVs}} = K_{\text{cont}}\left(1 + \frac{V_S^2}{2g}\left(1 - A_{\text{pipe}}\right)^2\right), \tag{1}$$

where Kcont is a constant, V_s is the flow velocity, g is acceleration due to gravity, hdelVs is the enthalpy change due to flow velocity, and Apipe is area of pipes.

$$h_m = K\frac{V_S^2}{2g}, \tag{2}$$

where K is a constant and h_m is the enthalpy change of medium.

$$h_f = 0.316\frac{l}{d}\frac{V_S^2}{2g}, \tag{3}$$

where l and d are dimensions of the container (length and depth), and h_f is the enthalpy of flow of electrolytes.

Now, change in pressure of pipes can be formulated as

$$\text{del.}p_{\text{pipes}} = \left[r_o g\left(h_{\text{delVs}} + h_f + h_m\right)\right]. \tag{4}$$

P.pump is then evaluated as

$$P_{\cdot\text{pump}} = \frac{K_i}{Q}\text{del.}p_{\text{system}}, \tag{5}$$

where Q is the rate of flow of electrolyte, K_i is a constant, and

$$\text{del.}p_{\text{system}} = \text{del.}p_{\text{stack}} + \text{del.}p_{\text{pipes}}, \tag{6}$$

and cell voltage can then be calculated as

$$V_{\text{cell}} = V_{eq} + \frac{2RT}{F}\ln\frac{\text{SOC}}{1 - \text{SOC}}. \tag{7}$$

So, stack voltage comes out to be

$$V_{\text{stack}} = n * V_{\text{cell}}, \tag{8}$$

where N is the number of cells.

Various equations for the given parameters are extracted from [3].

3.2. Fuel Cell Model. Among the various types of fuel cells, PEM fuel cells have gained best response for their operation at low temperature and also because of their fast response time. Fuel cells are one of the most important components for a hybrid power system owing to their inputs which are oxygen and hydrogen, and their output, i.e., water. The modelling of this system is done in SIMULINK using MATLAB functions and the overall model is also available in Simulink Library Browser, as fuel cell stack model. The control circuit in Figure 3 is controlled by the output of blocks B and C which are E_{oc}, i_o, and A. For given values of P_{fuel}, V_{fuel}, Pair, and V_{air}, the above three parameters are determined for a detailed fuel cell stack model by the formulae given in [3].

However, for a simplified fuel cell stack model, the main formula are as follows.

From open circuit voltage E_{oc}, if output voltage is to be determined, then activation losses (owing to kinetics of reactions) and charge transport losses (resistive and diffusion) are to be subtracted to obtain the actual output power, which is

$$V = E_{\text{OC}} - V_{\text{act}} - V_r, \tag{9}$$

with

$$V_{act} = S_t \ln\left(\frac{i_{fc}}{i_o}\right) * \left(\frac{1}{(ST_d/3)} + 1\right),$$
$$V_r = r_{\text{ohm}} * i_{fc}, \tag{10}$$

where S_t is Tafel slope (in V), given by

$$S_t = \frac{RT}{z\alpha F}. \tag{11}$$

α is the charge transfer coefficient. Here, io is the exchanging current (in As), rohm is the cell and diffusion total resistance (in ohms), T_d is settling time required by cell for a current step. Here, it is considered that the cell voltage would have a delay approximately the same as time constant because of sudden change in cell current. So, Tds = 1 second. The stack voltage of a fuel cell when a number of fuel cells are connected is given as the product of individual fuel cell voltage and the number of cells, i.e.,

$$V_{fc} = N_1 * V. \tag{12}$$

Here number of cells is given as N_1.

3.3. Battery Model. Li-ion batteries are considered in this paper owing to their high energy density and highest efficiency (almost 100 percent) compared to other battery

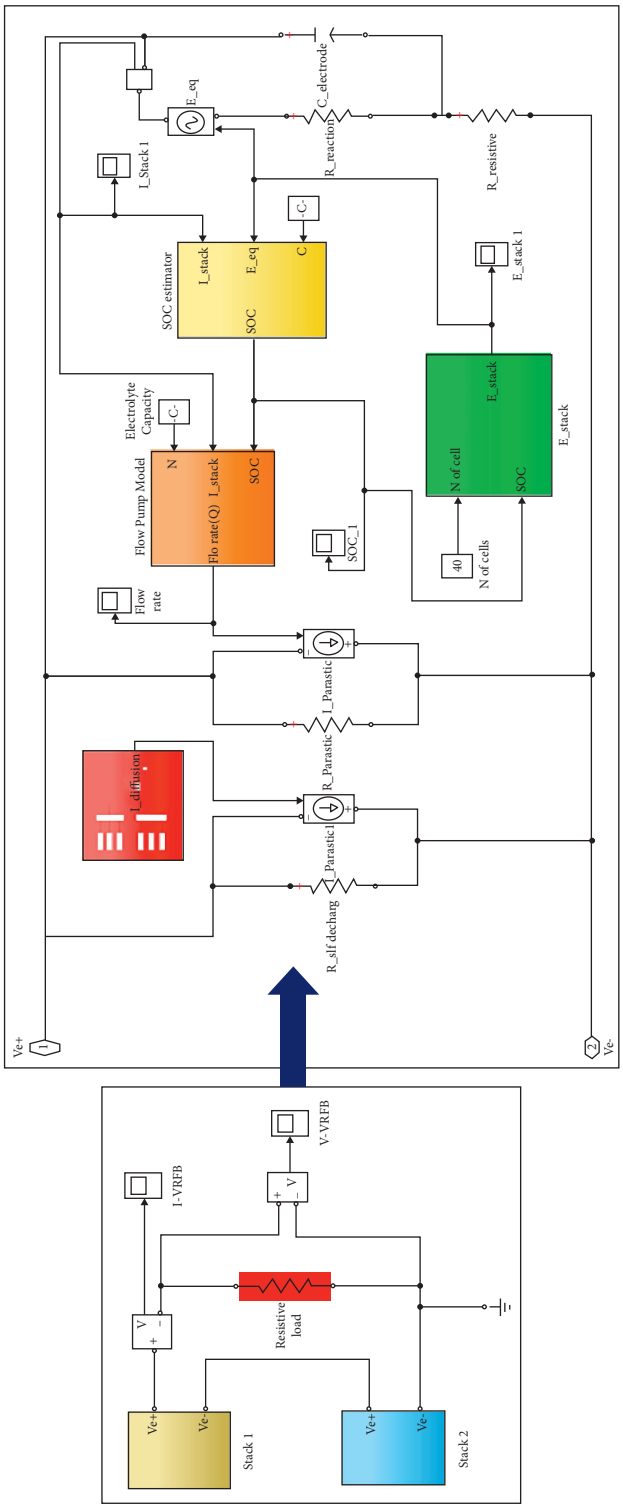

Figure 2: Vanadium Redox Flow Battery simulation model.

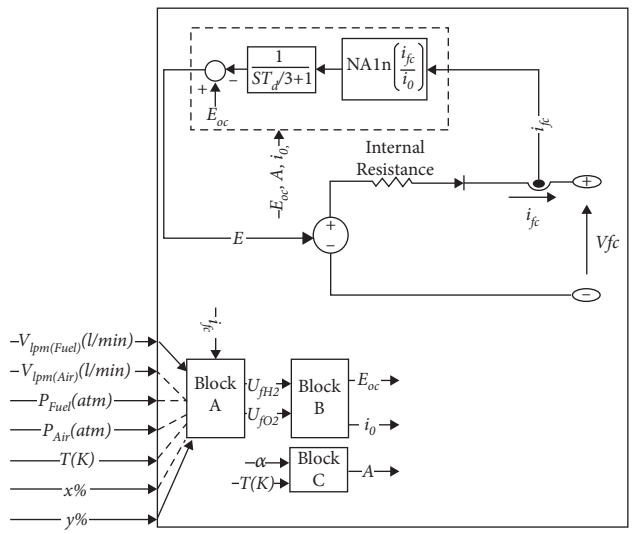

Figure 3: Fuel cell stack model is reproduced from Njoya M et al. 2013.

sources such as Lead Acid (85 percent) and sodium-sulfur (89 percent). The model discussed is available in MATLAB Simulink Library Browser as shown in Figure 4. Shepherd curve fitting method is used where an additional term is added [10]. This enables better representation of the effect of battery SOC on its performance. For stable simulation, battery current is filtered before use, which accounts for polarization resistance. Model parameters can be derived from the data sheet.

The main equations for a Li-ion battery are discussed here.

The V_{batt} is given by

$$V_{batt} = E_0 - K_a \frac{q}{q - It} It - R_b I - A_b \exp(-C * It) - K \frac{q}{q - It} I *, \tag{13}$$

where

(i) E_o = constant battery voltage (in volts)
(ii) K_a = constant of polarization (in V/Ah)
(iii) q = charge capacity (ampere hour)
(iv) $I *$ = battery current filtered (in As)
(v) It = battery charge actual (in Ah)
(vi) A_b = exponential constant (in V)
(vii) C = inverse exponential time constant (in Ah-1)
(viii) R_b = internal R of batt. (in ohms)

The term $K_a(q/q - It) *$ It from (12) is polarized voltage, and the term $K_a(q/q -$ It) is the polarized resistance PolR [11].

The battery voltage increases suddenly when fully charged and this behaviour leads to modification of polarization resistance as follows:

$$\text{Pol}\, R = K_a \left(\frac{q}{It - 0.1q} \right). \tag{14}$$

3.4. Super Capacitor Model. Supercapacitors structures are similar to conventional electrolytic capacitors. Additionally, it has a property to store or release more energy in small instances of time due to their high capacitance [12]. Owing to this property, it is used here to operate in transient state for voltage regulation. SC compensates for high frequency component of fast changing power peaks and also compensates for the uncompensated battery power (due to slow dynamics of battery) as shown in Figure 5. The supercapacitors model presented here is made in MATLAB using MATLAB function block and is based on the Stern model, which combines the Helmholtz and Gouy-chapman models [4]. The capacitance of an SC cell is expressed as

$$C = \frac{1}{(1/C_H) + (1/C_{GC})}, \tag{15}$$

with

$$C_H = \frac{N_C e e_0 A_i}{d},$$
$$C_{GC} = \frac{F q_C}{2 N_C RT} \sinh\left(\frac{q_c}{(N^C)^2 A_i (8RTee_0 c)^{0.5}} \right), \tag{16}$$

where C_H = Helmholtz capacitance (in F), CGC = Gouy-Chapman capacitance (in F), N_c = Number of electrode layers, e = Permittivity value (in F/m) of the electrolytic material used, e_o = Permittivity value (in farads per meter) of free space, A_i = Interfacial area between the electrode and electrolytes (in meter-square), d = radius of molecules (in m), q_c = electric charge of each cell (in Coulomb), and c = Molar concentrations (in moles per meter cube).

For a supercapacitor module, with N_s cells in series and N_p cells in parallel, the total capacitance is given as

$$C_T = \frac{N_P}{N_S} C. \tag{17}$$

When V_{sc} is measured by taking into account the losses (due to resistance), it comes out as

$$V_{\text{SC}} = \frac{Q_T}{C_T} - R_{\text{SC}} i_{\text{sc}}, \tag{18}$$

with

$$Q_T = N_P Q_C = \int i_{\text{sc}} \mathrm{d}t, \tag{19}$$

where Q_T = Total electric charge (in coulombs), R_{SC} = Total SC resistance (in ohms), and i_{SC} = SC module current (in amperes).

3.5. DC-DC Converter Model. The VRFB, FC power module, and battery system are connected to load through DC/DC converters and DC/AC converter as shown in Figures 6 and 7. DC/DC converters are used for voltage conversion in the case of charging and discharging. In the case of fuel cell, we use boost converter, and Li-ion battery has both buck (charge converter) and boost (discharge converter)

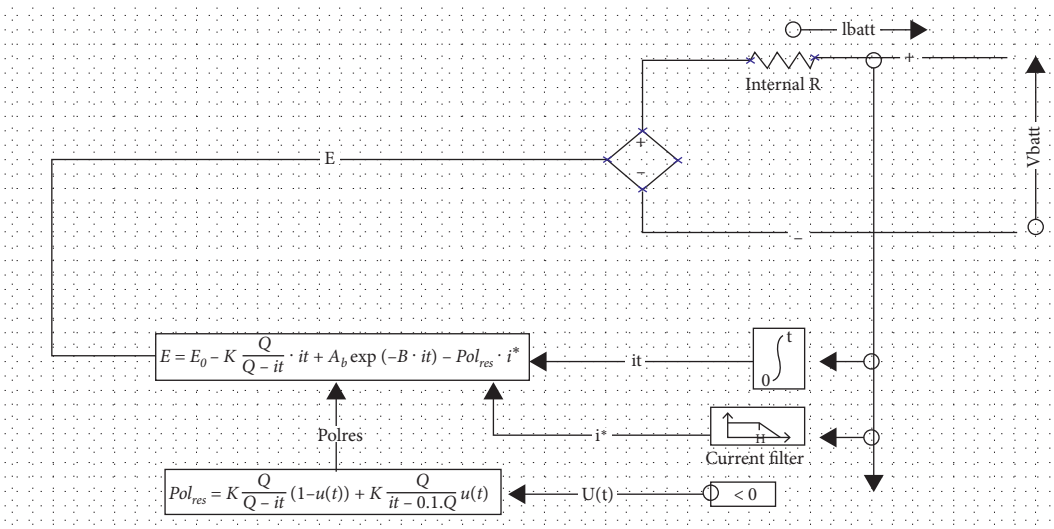

Figure 4: Li-ion battery model.

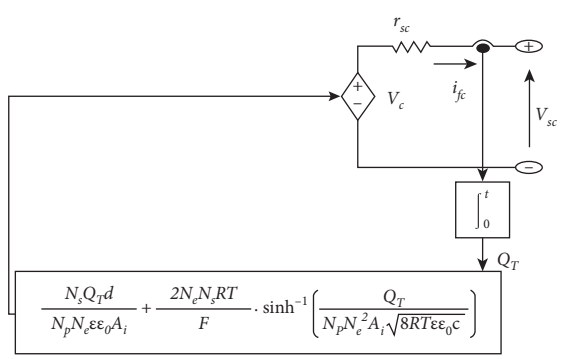

Figure 5: Supercapacitor model.

converter [13]. The VRFB system has a DC/DC bidirectional converter.

Here DC/DC converters are operating in switching mode, which are mainly used for design purpose. In this paper by the help of PI controller and filters we generate duty signals (pulse width modulated signals) by comparing DC bus voltages and reference voltages; these signals are further used to operate the switch of converters [14].

3.6. DC/AC Converter Model. The DC/AC converter model is represented in the same way as in the DC/DC converter models, i.e., through average value models as shown in Figures 8 and 9. As most of the loads are AC in nature, here, the obtained output of the system is converted into AC to feed the load demand [15]. A reference voltage signal is used to generate controlled voltage source signal and the input current is generated from output power and DC bus voltage.

3.7. Load Profile. For experimental purpose, we have 3-phase AC electronically programmable load. Here load current is obtained by three-phase apparent power (in KVA), the nominal line voltage, and its power factor [16].

3.8. EM Scheme. The EMS is used to ensure the following:

(i) minimization of voltage spikes
(ii) low consumption of hydrogen fuel
(iii) enhancing efficiency of system
(iv) minimum variation in battery/VRFB/super-capacitor SOC
(v) higher durability
(vi) in this paper we are using adaptive P and I control minal line voltage, and its power strategy
(vii) adaptive P and I control strategy

Adaptive P and I controller are used to control the SOC level of batteries. It modifies the error between reference SOC and obtained SOC with the help of PI controller and saturator blocks. If SOC level is above reference and at the same point VRFB power is below the required value, then PI controller allows battery to

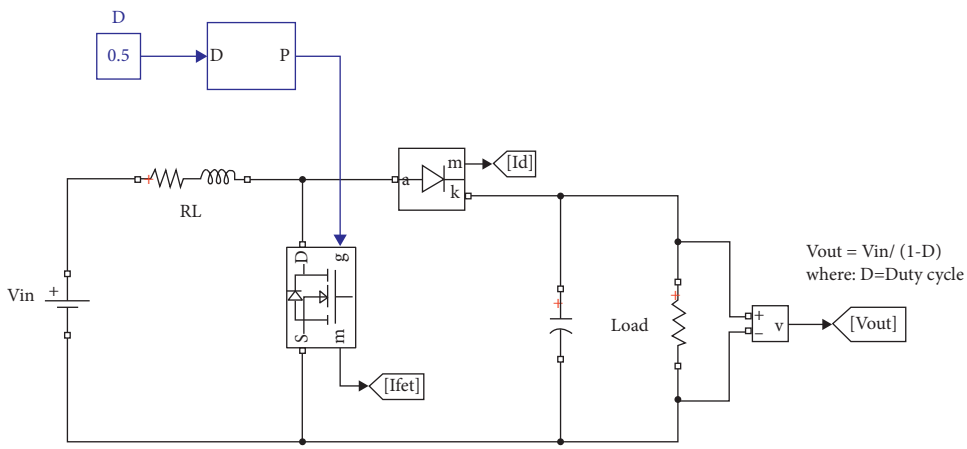

Figure 6: Boost converter model.

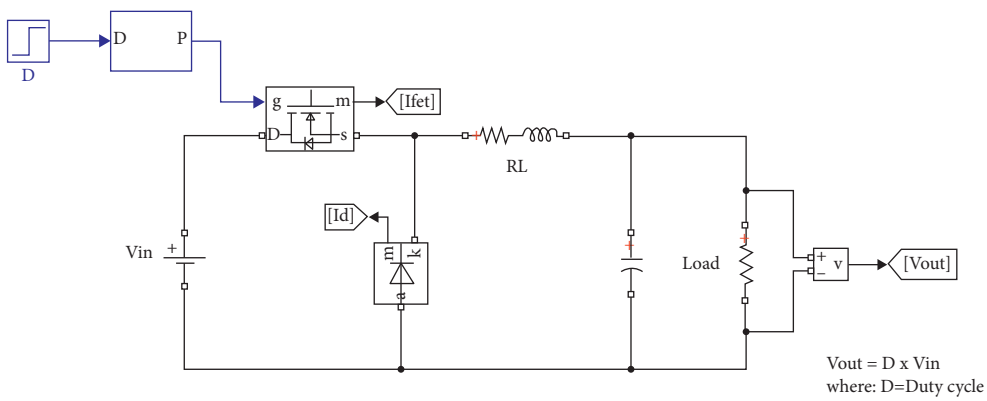

Figure 7: Buck converter model.

provide its full power to DC buses [5]. If SOC is below reference then controller generates duty for its charging; in this case VRFB provides power to load. Adaptive P + I controller energy management can be implemented easily as compared to others.

4. Simulation and Experimental Results

In order to understand the performance of the hybrid power system and control, a simple islanded DC microgrid network as shown in Figure 1 is simulated using MATLAB/SIMULINK software. In this paper adaptive P and I controller are used to control the SOC level of batteries. There are a lot of investigations proposing microgrids for country charge applications in creating nations. For instance, creators talked about the past and current practices to further develop energy access, as well as advancing country charge utilizing microgrids in China, India [17]. The system has been tested with various conditions and its results have been plotted in Figures 10–12 showing the gate pulse waveforms for buck and boost converter. The DC microgrid system with buck/boost converter along with conventional and adaptive PI controller hardware results for SOC of the battery is shown in Figures 13(a)–13(e). The converter output voltage waveform is shown in Figure 14.

The DC-DC buck converter is displayed in MATLAB/SIMULINK with the reproduction result of the converter. The simulation output shows that the planned DC-DC buck convertor controls and lessens the input voltage. The simulation parameters are as shown in Table 1.

Most batteries are intended to work in the condition of charge scope of 20–90%. Subsequently, the methodology in the regulator will check assuming that the batteries are in the scope of 20–90%. Other than that, the battery regulator is relying upon the power age and burden interest. In the event that the power produced is higher than the required load power and the battery is at a low SOC underneath 90% the battery will be charged [6]. Nonetheless, on the off chance that the heap power is higher than the created power load shedding ought to be thought about to safeguard the wellbeing of the battery [7]. Likewise, in the event that the produced power is more noteworthy than the power load and SOC is in the scope of 20% to 90% the battery will be charged except if the battery ought to be released [18].

AC microgrids require more parts, and the outcomes acquired in this study are unique. As a result of the expected inverters, there will be extra power misfortunes that lead to an alternate PV and battery estimating to adjust the stock and the interest [8]. As overreleasing the battery routinely will cause its time span of usability to

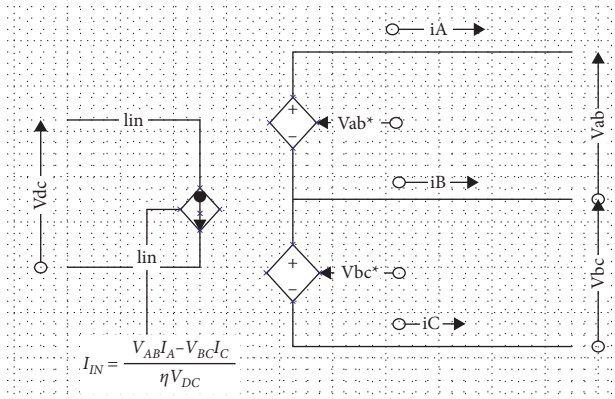

Figure 8: DC/AC converter model.

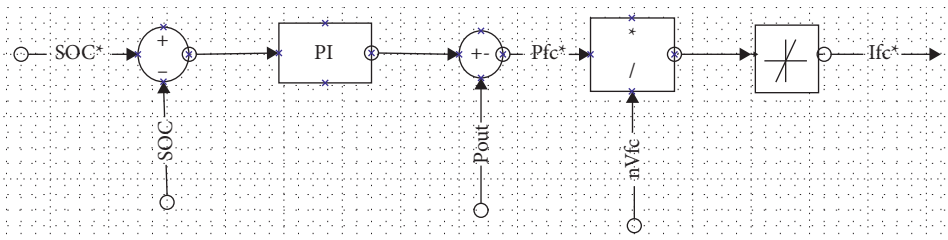

Figure 9: Adaptive $P+\mathrm{I}$ control strategy.

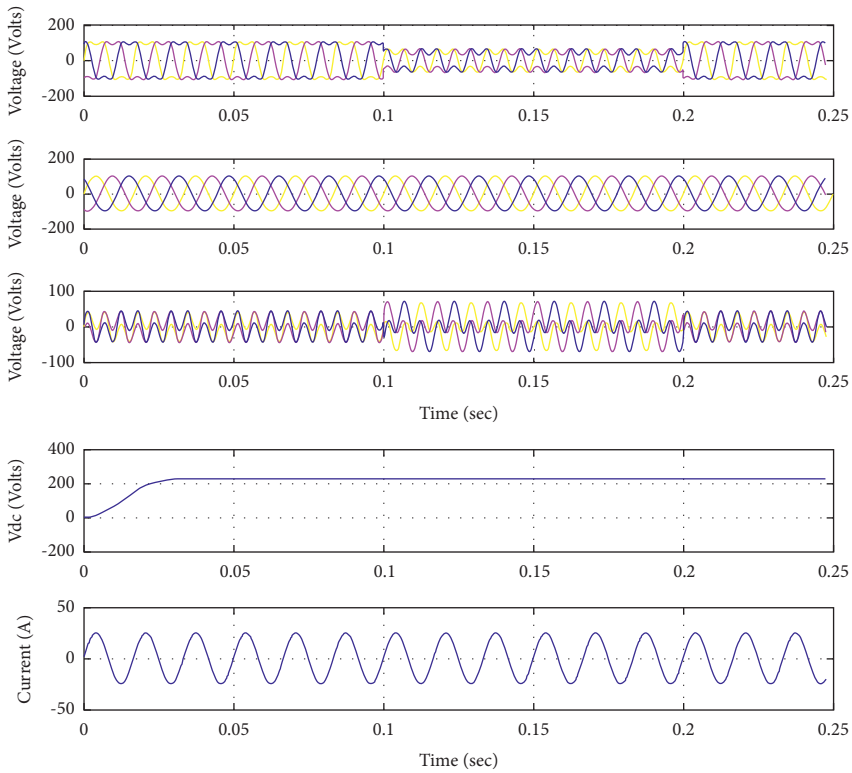

Figure 10: DC voltage and its compensation current in simulation.

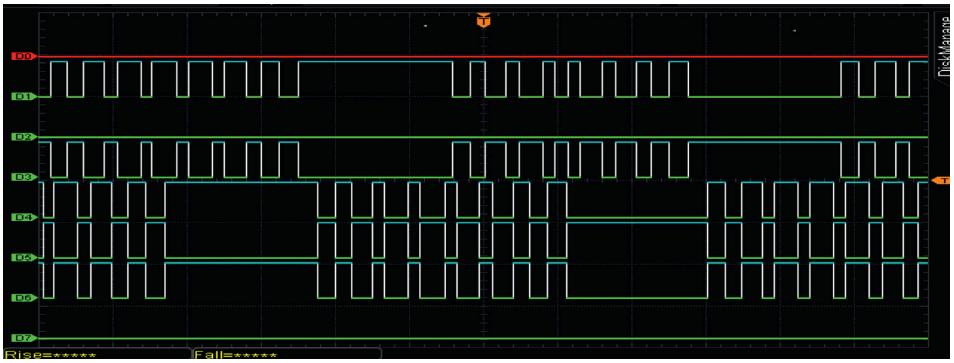

Figure 11: Buck converter gate pulse.

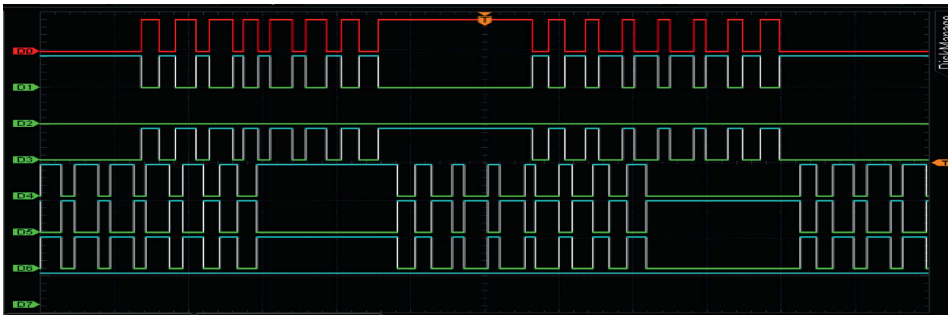

Figure 12: Boost converter gate pulse.

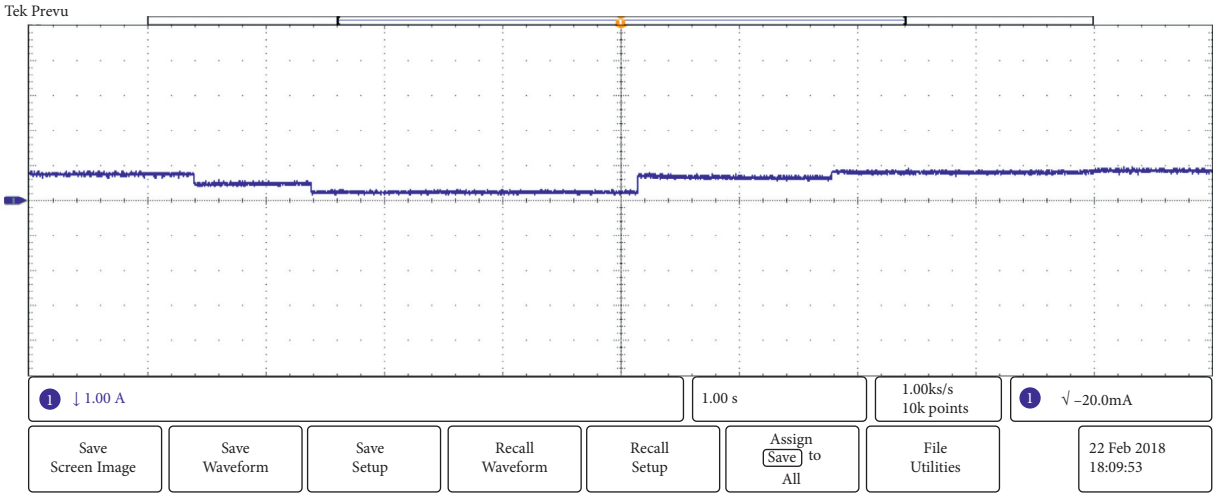

(a)

Figure 13: Continued.

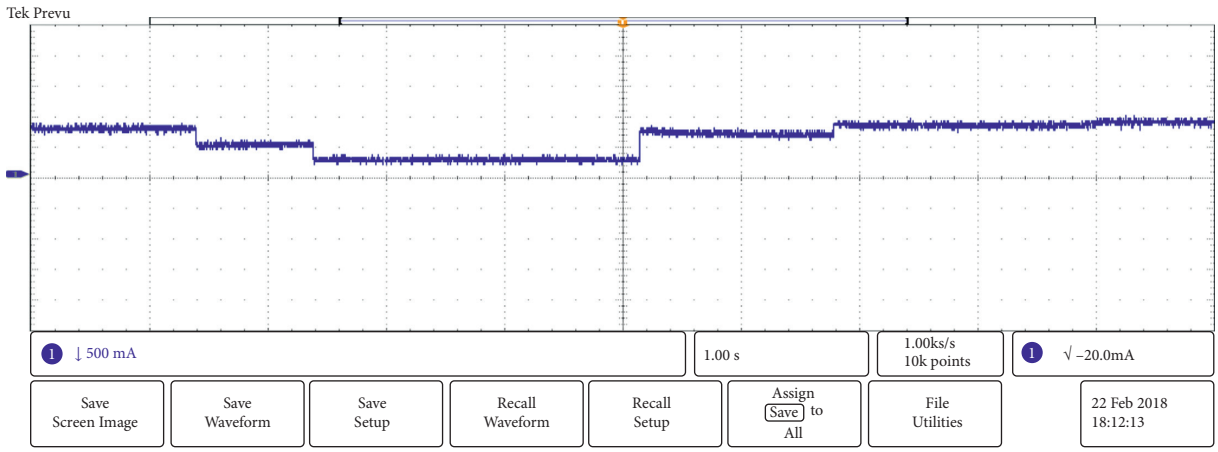

(b)

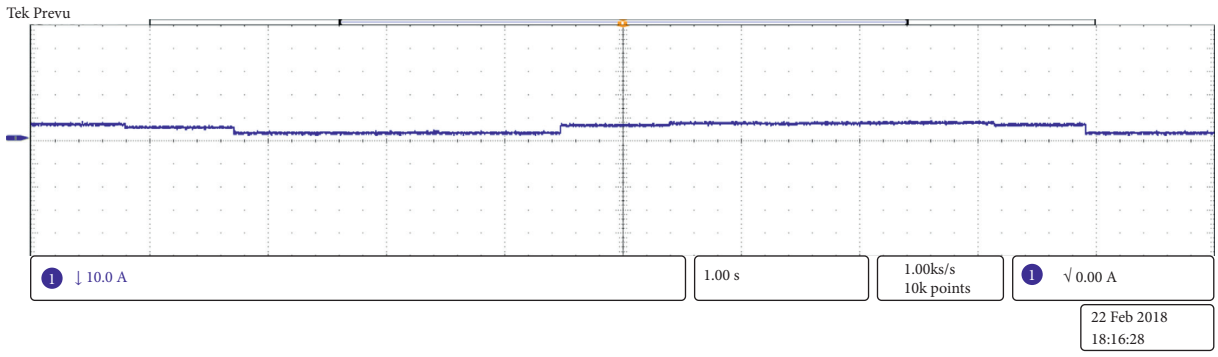

(c)

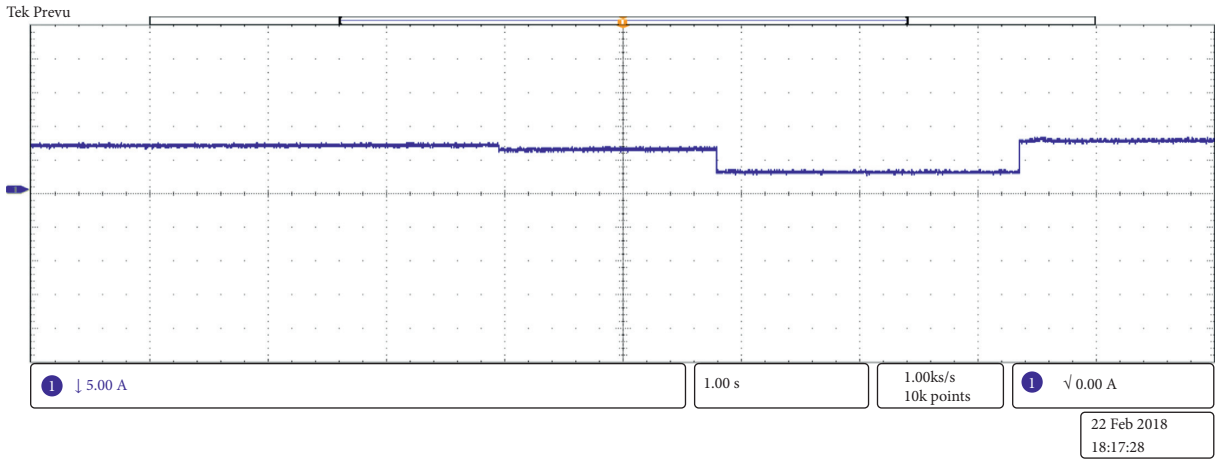

(d)

Figure 13: Continued.

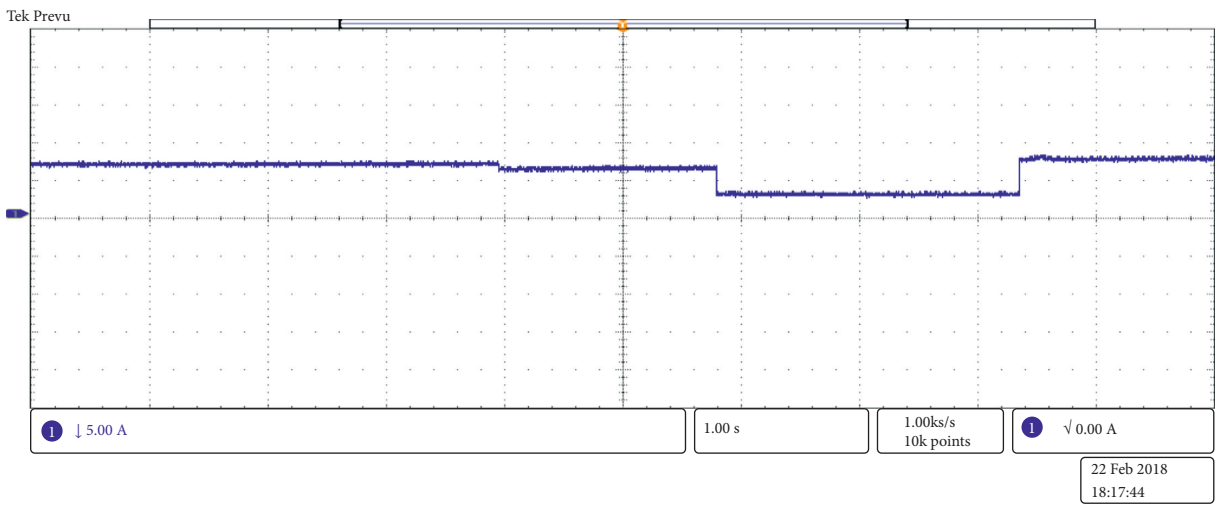

(e)

Figure 13: Islanded DC microgrid network with PI controller and adaptive PI controller investigated with SOC level of batteries. (a) Charge control with conventional control scheme. (b) Charge control with conventional control scheme and buck converter. (c) Charge control with conventional control scheme and boost converter. (d) Charge control with adaptive PI controller. (e) Charge control with adaptive PI controller and buck converter.

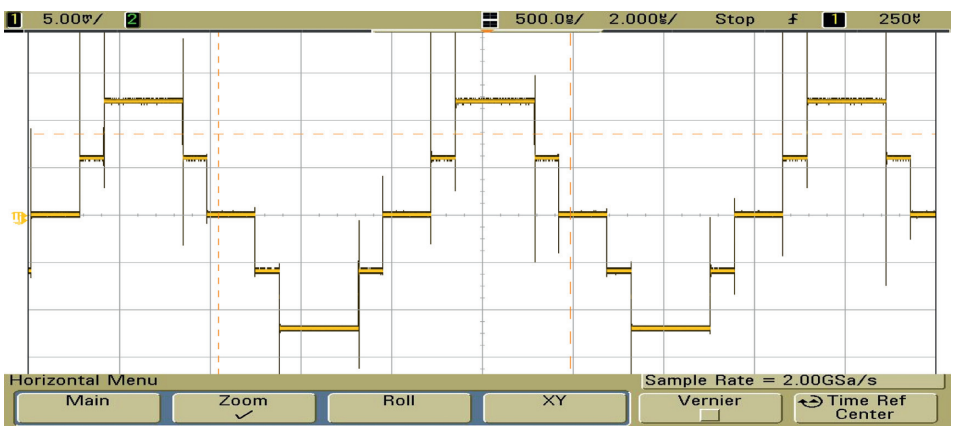

Figure 14: Output voltage waveform obtained from converter.

Table 1: Simulation parameters of DC grid are reproduced from Beykverdi et al. 2016.

Parameter	Symbol	Value
Dc bus voltage	V_{dc}	230 V
Low threshold DC voltage	V_L	212 V
High threshold DC voltage	V_H	235 V
Battery capacity	C_{bat}	50 Ah
Initial SOC	SOC	65%
Maximum SOC	SOC_{max}	90%
Minimum SOC	SOC_{min}	20%

abbreviate, the power device may be actuated when certain conditions are met. Charge regulators are vital in BIPV frameworks to keep batteries from being harmed by cheating and overreleasing by controlling the current stream from and to the batteries [9]. They can likewise safeguard the machines that are associated with the batteries in BIPV frameworks. Most batteries can scarcely recuperate in the wake of cheating and overreleasing, so the work of regulators in BIPV frameworks can delay the assistance life of the batteries.

5. Conclusions

An energy management scheme for an islanded DC microgrid with VRFB hybrid system has been presented. The hybrid system is modelled and validation is provided through experiments. The voltage spikes due to sudden change in load have been regulated by using supercapacitor and Li-ion battery integrated with VRFB. To reduce fuel consumption, adaptive P and I control strategy is used. Vanadium redox stream battery (VRFB) frameworks are the most evolved among stream batteries in light of their dynamic species staying in arrangement consistently during charge/release cycling, their high reversibility, and their somewhat enormous power yield. Be that as it may, the capital expense of these frameworks stays very high for profound market entrance. To meet the proposed cost targets, ongoing examinations have featured the utilization of natural dynamic materials in strong state natural batteries, in which energy is put away inside the cell, principally as an extreme polymer.

Data Availability

The required data can be obtained from the corresponding author upon request.

Conflicts of Interest

The authors declare that they have no conflicts of interest.

References

[1] S. N. Motapan, L.-A. Dessaint, and K. Al-Haddad, "A comparative study of energy management schemes for a fuel-cell hybrid emergency power system of a more-electric aircraft," *IEEE Transactions on Industrial Electronics*, vol. 61, no. 3, 2014.

[2] P. Thounthong and S. Rael, "The benefits of hybridisation," *IEEE Ind. Electron Mag.*vol. 3, no. 3, pp. 25–37, 2009.

[3] W. Wei Jiang and B. Fahimi, "Active current sharing and source management in fuel cell-battery hybrid power system," *IEEE Transactions on Industrial Electronics*, vol. 57, no. 2, pp. 752–761, 2010.

[4] K. B. Oldham, "A Gouy-Chapman-Stern model of the double layer at a (metal)/(ionic liquid) interface," *Journal of Electroanalytical Chemistry*, vol. 613, no. 2, pp. 131–138, 2008.

[5] G. Peter and S. Bin Iderus, "Design of enhanced energy meter using GSM prepaid system and protective relays," *Materials Today Proceedings*, vol. 39, pp. 582–589, 2021.

[6] N.-G. Lim, H.-W. Song, H.-H. Jung, and S. Lee, "A study on capacity estimation of VRFB system using cumulated charge," *The Transactions of the Korean Institute of Electrical Engineers*, vol. 70, no. 9, pp. 1304–1311, 2021.

[7] Z. Huang, A. Mu, L. Wu, and H. Wang, "Vanadium redox flow batteries: flow field design and flow rate optimization," *Journal of Energy Storage*, vol. 45, Article ID 103526, 2022.

[8] P. Geno Peter and M. Rajaram, "An enhanced Z-source inverter topology-based permanent magnet brushless DC motor drive speed control," *International Journal of Electronics*, vol. 102, no. 8, pp. 1289–1305, 2015.

[9] M. Boselli, F. Cavrini, V. Colombo et al., "High-Speed and schlieren imaging of a low power inductively coupled plasma source for potential biomedical applications," *IEEE Transactions on Plasma Science*, vol. 42, no. 10, pp. 2748-2749, 2014.

[10] C.-T. Liu, K.-Y. Cheng, Z.-H. Lin, C.-J. Wu, J.-Y. Wu, and J.-S. Wu, "Effect of ground and floating electrode on a helium-based plasma jet and its applications in sterilization and ceramic surface treatment," *IEEE Transactions on Plasma Science*, vol. 44, no. 12, pp. 3196–3200, 2016.

[11] S. Wu, Y. Cao, and X. Lu, "The state of the art of applications of atmospheric-pressure nonequilibrium plasma jets in dentistry," *IEEE Transactions on Plasma Science*, vol. 44, no. 2, pp. 134–151, 2016.

[12] G. Peter and A. Sherine, "Induced over voltage test on transformers using enhanced Z-source inverter based circuit," *Journal of Electrical Engineering*, vol. 68, no. 5, pp. 378–383, 2017.

[13] J. Florian, N. Merbahi, G. Wattieaux, J.-M. Plewa, and M. Yousfi, "Comparative studies of double dielectric barrier discharge and microwave argon plasma jets at atmospheric pressure for biomedical applications," *IEEE Transactions on Plasma Science*, vol. 43, no. 9, pp. 3332–3338, 2015.

[14] Y.-J. Kim, S. Jin, G.-H. Han et al., "Plasma apparatuses for biomedical applications," *IEEE Transactions on Plasma Science*, vol. 43, no. 4, pp. 944–950, 2015.

[15] K. H. Becker, B. B. Godfrey, E. E. Kunhardt et al., "Robert barker memorial session: leadership in plasma science and applications," *IEEE Transactions on Plasma Science*, vol. 43, no. 4, pp. 914–936, April 2015.

[16] G. Peter, K. Praghash, A. Sherine, and V. Ganji, "A combined PWM and AEM-based AC voltage controller for resistive loads," *Mathematical Problems in Engineering*, vol. 2022, 11 pages, Article ID 9246050, 2022.

[17] G. Peter, A. Sherine, and S. B. Iderus, "Enhanced Z-source inverter-based voltage frequency generator to conduct induced over voltage test on power transformers," *International Journal of Power Electronics*, vol. 12, no. 4, p. 493, 2020.

[18] X. Lu and A. Fridman, "Guest editorial the second special issue on atmospheric pressure plasma jets and their applications," *IEEE Transactions on Plasma Science*, vol. 43, no. 3, pp. 701-702, 2015.

Hindawi
Mathematical Problems in Engineering
Volume 2022, Article ID 5845249, 11 pages
https://doi.org/10.1155/2022/5845249

Research Article

Tournament Selected Glowworm Swarm Optimization Based Measurement of Selective Harmonic Elimination in Multilevel Inverter for Enhancing Output Voltage and Current

Udayakumar Chandran,[1] **Sathiyasekar Kumarasamy**,[2] **Ravi Samikannu**,[3] **Rajamani M. P. E.**,[4] **Vinoth Krishnamoorthy**,[5] **and Srinivasan Murugesan**[6]

[1]*Department of Electrical and Electronics Engineering, J.K.K. Nattraja College of Engineering and Technology, Namakkal, India*
[2]*Department of Electronics and Communication Engineering, Prathyusha Engineering College, Chennai, India*
[3]*Department of Electrical Computer and Telecommunications Engineering, Botswana International University of Science and Technology, Palapye, Botswana*
[4]*Department of Electrical and Electronics Engineering, National Engineering College, Kovilpatti, Tamil Nadu, India*
[5]*Department of Electrical and Electronics Engineering, Vel Tech Rangarajan Dr Sagunthala R&D Institute of Science and Technology, Chennai, India*
[6]*Department of Electrical and Electronics Engineering, Kongu Engineering College, Perundurai, Tamil Nadu, India*

Correspondence should be addressed to Udayakumar Chandran; cudayakumareee@gmail.com

Received 5 November 2021; Revised 22 January 2022; Accepted 4 March 2022; Published 30 March 2022

Academic Editor: Mohammad Yaghoub Abdollahzadeh Jamalabadi

In modern days Multi Level Inverters (MLIs) in the power industry receive a large interest. The MLIs with multilevel structures produces higher-power, higher-voltage inverters. Selective Harmonic Elimination (SHE) has become a popular one. It has been utilized widely studied during the past several decades for multilevel inverters as it has many merits like lesser switching losses and lesser Total Harmonic Distortion (THD). However, many researchers have failed to reduce the selective harmonic elimination time consumption and improve efficiency. A novel Tournament Selected Glowworm Swarm Optimization-Based Selective Harmonic Elimination (TSGWSO-SHE) approach is proposed in this paper for addressing these problems. The major aim of the TSGWSO-SHE approach is selecting optimal switching angles for removing the lower order harmonics. In the TSGWSO-SHE technique, initially, multilevel-inverters are created, and the modulation index is measured. Based on the modulation index, Switching Angles (SAs) are determined. Then several switching angles are initialized randomly. The objective function is determined for every switching angle. Using it detects and chooses the neighbouring switching angle with higher brightness by tournament selection and move to it. Lastly, the switching angle updates its position and finds the optimal switching angle. In this way, an optimal SA is selected during the process of selective harmonic eradication in MLI with higher efficiency and minimal time consumption. The efficiency of TSGWSO-SHE technique is simulated using parameters such as time of SHE, SHE efficiency and THD. Results prove that the proposed TSGWSO-SHE technique provides better SHE performance as compared to the existing studies. Experimental results demonstrate that the TSGWSO-SHE technique reduces the THD and SHE time by 46% and 33%, and the efficiency of selective harmonic elimination is increased by 13% compared to existing methods.

1. Introduction

Multilevel inverters employ average and higher voltage utilization. Use of SHE for voltage waveform by multilevel inverters has been studied broadly in the last decade. By harmonic eradication of the cascaded H-bridge MLI, the SHE Pulse Width Modulation (PWM) method depends on hybrid Asynchronous PSO-Newton–Raphson (APSO-NR) algorithm was explained [1]. However, SHE time is not reduced by using the APSO-NR algorithm. To choose harmonic eradication in a single-phase seven-level inverter by minimum switches, a novel ant colony optimization

algorithm is presented in [2]. The algorithm is formulated in two phases. At the initial phase, ant colony optimization is carried out. In the second phase, the primary guess of the Newton–Raphson algorithm which is the solution attained from ACO is employed, but ant colony optimization does not reduce total harmonic distortion.

Similarly Bacterial Foraging Algorithm (BFA) is introduced in [3] to switch angles in the PWM inverter. The voltage harmonic elimination by output voltage regulation problem is addressed by optimization performance. However, the efficiency of the selective harmonic elimination is not improved. Artificial Neural Network (ANN) based solution was attained in [4] for determining angles and creating PWM signals. ANN generates optimum switching angels for each modulation index, but the output voltage is not improved.

The artificial Bee colony optimization is developed in [5] to solve the nonlinear equation of SHE with an extreme direct power resource. However, the computational complexity is not reduced. Likewise, a selective harmonic elimination system is introduced in [6] by using fuzzy logic to eradicate the higher magnitude harmonics by frequencies near the basic frequency of single-phase inverters in output voltage. However, selective harmonics elimination is not done efficiently using a selective harmonic elimination system.

An Imperialist Competitive Algorithm (ICA) also is introduced in [7] to eradicate undesired harmonics. DC-DC converter is employed for enhancing the SHE task. The algorithm designed reduces many harmonics where the entire harmonics output voltage is less. However, the output current is not improved using ICA. A novel SHE modulation method is presented in [8] to obtain multiple solutions to eliminate particular harmonics in modulation indices via changed NR and pattern generation methods, but the time of selective harmonic elimination is not reduced.

Similarly, a new DC-link balancing approach is introduced in [9] for a 7-level inverter fed by utilizing the photovoltaic scheme. The redundant state procedure is linked by SHE-PWM rather than the Space Vector (SV)-PWM. But the efficiency of selective harmonic elimination is not improved by using DC-link balancing method. The performance of the modular cascaded multilevel inverter dependent on Shunt Hybrid Active Power Filter (SHAPF) performance is studied in [10] to react power allowance and SHE below the deformed/uneven voltage grid condition within the average voltage levels, but time consumption is not minimized to exploit SHAPF.

In the existing techniques there are some issues identified such as higher time consumption for selective harmonic elimination, nonselection of the optimal switching angle, higher computational complexity, higher switching losses, lesser efficiency of selective harmonic elimination and higher THD rate. To address these issues, the proposed TSGWSO depends on the SHE approaches.

The contribution of the paper is given as follows.

(i) The main aim of the TSGWSO-SHE technique is to select optimal switching angles where the basic part is at the preferred value and to eradicate the lower order harmonics for improving output voltage and current in the multilevel inverter.

(ii) TSGWSO-SHE technique uses a tournament-selected glowworm swarm optimization algorithm for reducing harmonic distortion by eliminating the lower order harmonics. The Modulation Index (MI) is determined and SAs are computed. The number of glowworms, i.e., SAs, is considered arbitrarily. The OF is estimated for every glowworm. It identifies and chooses the neighboring glowworm with higher brightness through Tournament Selection (TS) and shift to it. The glowworm restores its position and analyses the excellent one.

(iii) Thus, the optimal SA is identified to choose harmonic removal in a multilevel inverter to improve the performance of output voltage and current.

This paper is structured as follows. Section 2 presents works related to optimization techniques designed to choose selective harmonic removal in the multilevel inverter. Section 3 describes the proposed technique. In Section 4, comparative performance analysis is presented. Section 5 concludes the study.

2. Literature Survey

A harmony search on optimization is designed in [11] with the help of Artificial Neural Networks (ANNs) on the new 21-level inverter topology. Its dependents on the music improvisation process, but the THD is not minimized using harmony search optimization. A cascaded H-Bridge multilevel inverter concept is introduced in [12], where switching angles are independent of the basic voltage. Polynomial term computes the relationship among switching angles and DC voltages, but the optimization technique is not used for discovering the optimal switching angle.

A Generalized Hopfield Neural Network (GHNN) dependent on SHE PWM was implemented in [13] for one phase inverter. It is introduced to remove fifth, seventh, eleventh and thirteenth order of harmonic, but the output current is not improved. MLI with a lesser amount of switches was introduced in [14] for system cost minimization. The nonlinear SHE equation is optimized through Genetic Algorithm (GA) software.

One phase 9-level cascaded H-Bridge MLI using FLC, and P&O is introduced in [15] for Photo Voltaic (PV) power generation, but lower-order harmonics are not eliminated efficiently. A novel altered Cascaded H-bridge (CHB) MLI by using SHE technique and passive LC filters is introduced in [16] for the enhancement of output voltage waveform. With SHE, a PWM technique is employed to handle the basic harmonic and to remove lower order harmonics in CHB multilevel inverter. However, the execution time is not minimized by the modified CHB multilevel inverter.

In the same way, a cuckoo evolutionary optimization method is introduced in [17] to eradicate the unwanted harmonics in multilevel inverters by using equivalent DC

origin. SHE is an effective technique for attaining basic parts and removing selection harmonics, but the computational time using this cuckoo evolutionary optimization is higher. A new variant of SO that depends on the SHE approach is introduced in [18] to lessen harmonics in MLI. Nevertheless, it does not reduce the time of selective harmonic elimination.

A two-phase adaptive algorithm is introduced in [19] for generating real-time optimal switching angles in the multilevel inverters. An optimal switching angle is computed offline by using a Real Coded Genetic Algorithm (RCGA), but selective harmonic elimination is not done efficiently. Likewise, a novel 5-level MLI using switch count is introduced in [20] for the standalone PV system. Firefly-Assisted Genetic Algorithm (FAGA) dependent on the SHE approach is introduced to minimize the harmonics, but the THD is not reduced for 5-level MLI. An optimized switching angle was introduced in [21] to take away unnecessary harmonics which comprise a low order value in the cascaded H-Bridge MLI. However, the convergence rate is not higher. Selective harmonic elimination is done in [22] with the help of PWM to eradicate the low-level harmonics. However, the optimized transition points on the time axis minimize the unwanted low-order harmonics. Further, MLI topologies are introduced in [23] to for application in dc-ac power transformation and thereby to get better power quality.

3. Proposed Methodology

Multilevel inverters are employed in power utilization for acquiring small total THD in average or higher voltage levels. The SHE method is essential in power electronic applications. It is a modulation technique used for attaining suitable switching instants to eliminate the small order harmonics. In it switch moments are identified through the preferred magnitude of basic and harmonics concealed. Different techniques are utilized for the multilevel inverter for attaining the low THD for enhancing the output voltage and current, but THD is not minimized by employing the existing methods. To address these problems, TSGWSO-SHE approach is introduced. The aim of the TSGWSO-SHE technique is used to identify optimal switching angles where the basic part is at the preferred value and to take away the harmonics which include a lower order. The architecture of the TSGWSO-SHE Technique is given in Figure 1.

Figure 1 explains the flow of the TSGWSO-SHE technique. In using TSGWSO-SHE technique, multilevel inverters are designed. Then the MI is determined and switching angles are computed. The number of glowworms is initialized randomly. Additionally, the Objective Function (OF) is calculated for every glowworm. In addition, it identifies and selects the neighboring glowworm with higher brightness by using tournament selection and shifting to into. Then the glowworm upgrades its point to finds the excellent one. In this way, selective harmonic elimination is carried out in a multilevel inverter for output voltage with current enhancement.

3.1. Multilevel Inverter. The power electronic device with a higher potential to convert the DC power into AC power is termed as an inverter. The inverters drive the lightning load when the grid gets powered off. With technological advancements, inverters are employed in motor drives, Uninterrupted Power Supply (UPS), and power system utilization. A multilevel inverter creates the smooth sinusoidal waveform by DC voltage levels as input. Multilevel inverters develop into an attractive region in industrial utilization for higher power and voltage ranges. They are associated with sustainable energy sources for different higher power utilization.

MLIs are developing one as more approved beside single level inverter in the high-power utilization. By employing DC voltage levels, the multilevel output is combined. The switches are connected in sequences in multilevel inverters that permit the process at higher voltage level. Multilevel inverters present a huge improvement of harmonic decrease in output waveform, lacking the switching frequency or lessening the inverter output current. They are employed different industrial utilization like motor drives, sustainable energy, power conditioners, active filters, Flexible AC Transmission System (FACTS), higher voltage direct current lines, and so on.

Multilevel inverters obtain large awareness in both academy and industry. They are optimal solutions for attaining superior voltages by enhancing the harmonic spectrum. The multilevel inverter is an electronic power scheme that combines the output voltage with different DC voltages. The main aim of a multilevel inverter is to generate staircase output voltage with the existing DC current origin. The standard of the output current is enhanced by improving the quantity of energy levels.

MLIs are the collection of power semiconductors and capacitor power resources that generate voltages with stepped waveforms. By enhancing the number of stages in the inverter, output currents are introduced process with lesser harmonic distortions. A MLIs includes many metrics over a two-stage inverter that exploits the higher switching rate of PWM. The key characteristics of MLI are given as below.

3.1.1. Low dv/dt Stress. MLI creates the output voltages by lesser alteration to minimize the low dv/dt stresses.

3.1.2. Common-Mode (CM) Voltage. MLI creates less CM voltage. The anxiety in the comportments of the motor linked with the multi-level motor drive decreases.

3.1.3. Input Power. MLI collects the input power with low bias.

3.1.4. Switching Frequency. MLI involves the basic frequency and higher switching frequency PWM. Switching frequency is a smaller switch frequency using lesser switching loss with superior performance.

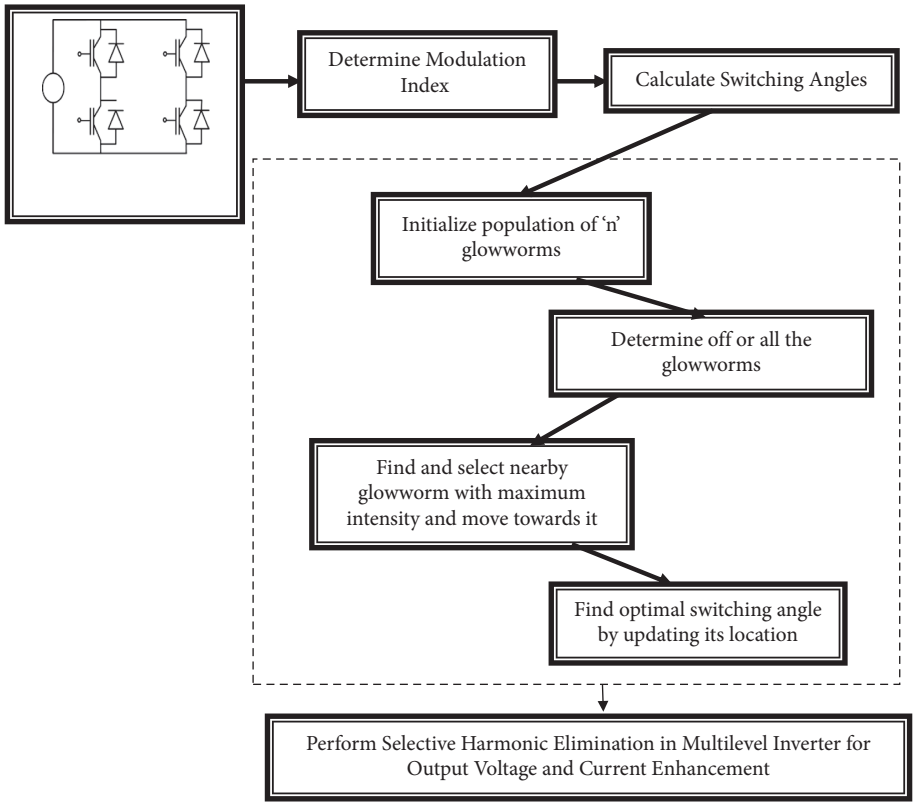

Figure 1: Architecture of TSGWSO-SHE technique.

A Seven Level Inverter comprises 12 switches and a series of switches. The output voltage waveforms of a multilevel inverter include an amount of level voltages. When the number of levels gets increased, the output of the THD gets reduced. The output waveform of seven-level inverters is shown in Figure 2.

The output waveform is examined in THD and is represented as

$$\mathrm{THD}\,(\%) = \left[\left(\frac{1}{a_1^2}\sum_{n=5}^{\infty} a_n^2\right)^{1/2}\right] * 100. \tag{1}$$

Equation (1), the THD is calculated. THD is the amount used to classify harmonic contents in the output concerning the basic. It is a nonlinear transcendental mathematical statement.

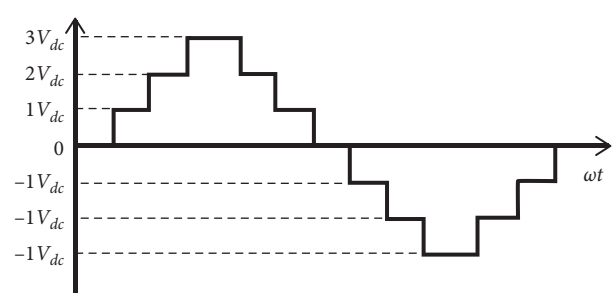

Figure 2: Output Waveform for seven-level inverter.

3.2. Tournament Selected Glowworm Swarm Optimization (TSGWSO). The TSGWSO-SHE technique is a type of swarm intelligence development technique that depends on the behaviour of glowworm. The glowworms behaviour patterns modify the strength of Lucifer in release and glow at the diverse powers. The TSGWSO algorithm agents are considered as glowworms i.e., switching angles that transmit the luciferin's luminescence. Each glowworm exploits the luciferin i.e., neutral basis to transmit data from the current place to the closets. The glowworms get involve in the intense luciferin surrounding. They depend upon the variable neighborhood to identify and select the neighbors by using tournament selection. After selecting the neighbors, it performs the actions.

Every glowwormem plays a tournament selection technique for selecting the surrounding with high luciferin value and moves into it. It comprises the dynamic result gap with the luciferin higher apart and space within the dynamic result area. The glowworm updates its places to glowworm within the dynamic result area and the decision space radius. TSGWSO algorithm consists of the two key ideas:

(i) The agents glow to the intensities proportional for the objective task optimization. Glowworms of brighter intensities get attracted by glowworms of lesser intensity.

(ii) TSGWSO algorithm involves the dynamic decision range where the distant glowworm effect is discounted while the glowworms have enough closest places.

In the TSGWSO-SHE technique, all glowworm include the limited-result area cleared by radial sensor choice. All glowworms find their closest place in the limited result area and get involved by the brighter glow of extra glowworms by neighborhood set. Limited-result area volume is unstable, which gets influenced by their closest places. When closest places have a lower thickness, the limited-result area increases to find and select their closest place. If not, the limited-result area is minimized. At last, the action of glowworms leads to the gathering of optimal solutions. TSGWSO algorithm performs the following process to find excellent glowworms.

3.2.1. Deployment of Glowworm Phase. The glowworms i.e. switching angles are scattered in the objective gap in this part. All the glowworm include the identical size of luciferin.

The glowworm location and every glowworm launches the parallel luciferin rate based on function rate through the primary iteration. A rate get changed regularly with the function rate in the existing position. Each glowworm loads to the preceding luciferin stage during the luciferin update phase. A luciferin quantity depends upon the calculated rate in the sensed form. The fraction of luciferin rate is removed for imitating decay in luciferin by time. Each glowworm changes the luciferin rate constant by employing objective function rate in the current position. This luciferin update rule can be formulated as

$$LE_i(T) = (1-\rho) * LE_i(T-1) + \gamma * OF_i(T), \tag{2}$$

$$OF_i(T) = \min_{\delta_i}\left\{\left(\frac{100 * (V_1{}^* - V_1)}{V_1{}^*}\right)^4 + \sum_{i=2}^{S}\frac{1}{h_s}\left(50 * \frac{V_{h_s}}{V_1}\right)^2\right\}. \tag{3}$$

In equation (2), "ρ" represents the luciferin decay steady. "γ" denotes luciferin's increasing fraction. "$LE_i(T-1)$" symbolizes the previous luciferin level for glowworm."$OF_i(T)$" denotes the objective task rate in glowworm. "i^{th}" is the position in the time instant "T".

3.2.2. Movement-phase. Every glowworm takes result with tournament mechanism to move the adjacent by luciferin rate superior to own. TS is employed for determining the best glowworm using the objective function. Manhattan Distance (MD) is calculated based on the current and the neighboring glowworm positions. It is given by

$$\text{Manhattan distance} = \sqrt{\sum_{i,j=1}^{n}\left(g_j - g_i\right)^2}. \tag{4}$$

In equation (4), where "g_i" denotes the current position of glowworm and "g_j" represents the neighboring glowworm position. When the distance is lesser, it has a higher fitness value. Tournament selection is a method used for randomly choosing glowworms from a population with higher fitness. For every tournament, the winner is selected with the best fitness. The glowworm selection is used to create successive generations. By applying the selection approach, the fitness of each glowworm is calculated. The selection of each glowworm is carried out with probability and it is formulated as,

$$P = \frac{F_i}{\sum_{j=1}^{n} F_j}. \tag{5}$$

Equation (5), the tournament selection Probability (P) of every glowworm and F_i represent the average fitness of the population in j^{th} glowworm. When the population generation changes, fitness value and selection probability get varied. The first appropriate glowworm from the tournament is chosen with the probability and the next appropriate glowworm selection probability is computed as

$$P * (1-P). \tag{6}$$

The third best glowworm with the probability is chosen as

$$P * (1-P)^2. \tag{7}$$

Correspondingly, the entire best glowworm is chosen along with the selection probability. When the size of the tournament is high, weak glowworm comprises the lesser possibility for tournament selection. After selection, the glowworm has involved at neighbors that glow brighter. For each glowworm, the chance of moving for a neighbor "q"can be represented as

$$\begin{aligned} N_i(t) &= \left\{q\colon D_{iq}(T) < R_d{}^i(T)\right\}, LE_i(T) \\ &= LE_q(T), \end{aligned} \tag{8}$$

$$\rho_{iq}(T) = \frac{LE_q(T) - LE_i(T)}{\sum_{k\varepsilon N_i(T)} LE_q(T) - LE_i(T)}. \tag{9}$$

Equations (8) and (9), "T" point outs the index value of time. "$D_{iq}(T)$" shows the Euclidian gap among glowworms "i" with "q" to the time "T". "$LE_q(T)$"illustrates luciferin stage by the glowworm "q" in time instant "T". "$R_d^i(T)$" signifies uneven local-result variety by glowworm 'i' in the period 'T'. "R" symbolizes the range of radial in luciferin sensor. Each glowworm updates its location by

$$X_i(T+1) = X_i(T) + S_s\left(\frac{X_q(T) - X_i(T)}{X_q(T) - X_i(T)}\right). \tag{10}$$

In equation (10), "S_s" denotes the step size and "$|X_q(T) - X_i(T)|$" indicates Euclidean utilizes glowworms.

Local decision range update rule:- To conclude the position of glowworms that depends upon local detail, it is measured as a strong function in the radial sensor choice. The glowworm's dynamic decision space is based on the decision space in the existing radius and connected sensor of luciferin of radial range. The dynamic glowworm of decision space radius is represented by

$$R_d^{\,i}(T+1) = \min\left\{R, \max\left\{0, R_d^{\,i}(T) + \beta N_T - \left|N_i(T)\right|\right\}\right\}. \quad (11)$$

Equation (11), "β" represents a constant parameter. "N_t" illustrates the clear threshold parameter. Thus, the best glowworm is identified using the TSGWSO algorithm efficiently. The step-by-step process of the TSGWSO algorithm is explained in Algorithm 1.

The Algorithm 1 describes the step-by-step process of TSGWSO to choose the best SA with lower time complexity. In the TSGWSO algorithm, agents are considered as SAs. Each glowworm computes objective function and transmits its current position information to the neighbors. The neighboring location is identified using the tournament selection process. The brighter objective function neighbors with lesser objective function nodes are attracted. The probabilistic concepts for moving to the neighbor with a higher OF are decided by each glowworm. The switching angle is updated by position and it the avoids THD of multilevel inverters to eliminate selective harmonic by selecting the optimal switching angle. In this manner, selective harmonic elimination time is reduced using the TSGWSO algorithm.

4. Simulation Settings

The experimental settings of the proposed TSGWSO-SHE technique and the two existing methods, namely asynchronous PSO-Newton-Raphson algorithm [1] and ACO-based hybrid algorithm [2] are carried out using MATLAB/Simulink environment. To evaluate the performance of the technique, the metrics like elimination time of THD and efficiency of selective harmonic elimination are used. The same amount of switching angles are achievd by the 7-level multi-level inverter, three SHE equations must address the issues. The fundamental voltage and the remaining two remove the order of 5th and 7th harmonic components generated by one switching angle. In the attained solution, the value of arbitrary modulation index varies from 0 to 1. The simulation parameters are shown in Table 1.

4.1. Simulation Result Analysis of Total Harmonic Distortion. The HD determines the harmonic deformation of the signal by taking the ratio for summation of the power amplitude of all the harmonic components to the power of basic frequency computed by THD rate. It is measured in percentage (%) and computed as,

$$\text{THD}(\%) = \left[\frac{1}{V_1}\sum_{n=5,7}^{\infty}\sqrt{\left(V_n^{\,2}\right)}\right] * 100. \quad (12)$$

In equation (12), "V_n" symbolizes the amplitude of the harmonic n^{th} order and "V_1" signifies the amplitude of basic frequency. When the THD is lesser, the method is more effective.

Table 2 depicts the simulation measurement of the THD using the three methods like TSGWSO-SHE Technique, asynchronous PSO-Newton-Raphson algorithm and ACO based hybrid algorithm. The Table 2 shows that the THD of TSGWSO-SHE is lesser than the other two existing methods. The graphical representation of THD is given in Figure 3.

Figure 3 explains the total harmonic distortion result versus the varied number of modulation index ranges. The Figure 3 gives the modulation index in the "X-axis" and the total harmonic distortion is considered "Y-axis." In Figure 3, the blue colour symbolizes the total harmonic distortion in TSGWSO-SHE technique, the red colour describes the total harmonic distortion in APSO-NR algorithm and the green colour describes the total harmonic distortion of Asynchronous PSO-Newton-Raphson Algorithm [1] and ACO based hybrid algorithm [2]. The total harmonic distortion of the TSGWSO-SHE technique is lesser due to the use of the tournament-selected glowworm swarm optimization algorithm. The current location information to the neighbors is transmitted, and each glowworm's objective function is computed. The neighboring location is identified using the tournament selection process. The neighbors with brighter objective function get attracted by lesser objective function nodes. To move the neighbor with a higher objective function, each glowworm decided by the probabilistic mechanism. The optimal glowworms are chosen for the elimination of selective harmonic to avoid the total harmonic distortion of multilevel inverters and to update the glowworm's position.

For simulation, the proposed TSGWSO-SHE technique gets ten dissimilar modulation index values and thereby minimize the THD. When the modulation index is 0.5, the total harmonic distortion of the TSGWSO-SHE technique is 8%, while total harmonic distortion of asynchronous PSO-Newton-Raphson algorithm and ACO-based hybrid algorithm is 12% and 15% respectively. The total harmonic distortion of the TSGWSO-SHE technique is reduced by 40% and 52% compared to the existing asynchronous PSO-Newton-Raphson algorithm [1] and ACO based hybrid algorithm respectively [2].

4.2. Impact of Selective Harmonic Elimination Time. The complexity m is measured as time. The Selective Harmonic Elimination Time (SHET) is the time taken for eliminating the selective harmonics to improve the output voltage results. SHET refers to a variation between the beginning time and the finishing time of the selective harmonic elimination process in a multilevel inverter. It is measured in milliseconds (ms) and given by,

$$\text{SHET} = \textit{e}\text{nding time} - \text{starting time of SHE}. \quad (13)$$

```
\\ Tournament Selected Glowworm Swarm Optimization Algorithm
Input: Number of SAs
Output: Find Optimal SA for SHE
Step 1: Begin
Step 2: For each SA
Step 3: Evaluate OF
Step 4: Determine the probability of movement
Step 5: if (Neighbor SA > current SA) then
Step 6: Movement takes place to neighboring
Step 7: Neighboring SA is identified by the tournament selection
Step 8: else
Step 9: No movement occurs
Step 10: End if
Step 11: updates location of SA
Step 12: End for
Step 13: Select the optimal SA for selective harmonic elimination
Step 14: End
```

Algorithm 1: Tournament Selected Glowworm Swarm Optimization Algorithm.

Table 1: List of simulation factors.

Parameters	Values
DC sources	100 V each
Switching rate	50 Hz
Basic frequency	50 Hz
Iteration count	200
Population initialization	$0 \le \alpha_1 < \alpha_2 < \alpha_3 \le \pi/2$
Modulation index	$0 \le M \le 1$
Difference between switching angles	10^{-15}

Table 2: Comparison of total harmonic distortion (%).

Modulation index (M)	Total harmonic distortion (%)		
	TSGWSO-SHE technique	APSO-NR algorithm	ACO based hybrid algorithm
0.1	21	28	32
0.2	18	24	25
0.3	15	18	20
0.4	11	15	19
0.5	8	12	15
0.6	6	10	14
0.7	4	8	11
0.8	5	11	15
0.9	3	9	12
1.0	2	6	9

Equation (13), the selective harmonic elimination time is determined. When the selective harmonic elimination time is lesser, the technique is more effective.

Table 3 explains the performance results of SHET using the proposed TSGWSO-SHE Technique and the existing Asynchronous PSO-Newton-Raphson algorithm and ACO-based hybrid algorithm with respect to various modulation index values. Table 3 makes clear that the SHET of the proposed TSGWSO-SHE is very minimal compared to the other state-of-the-art methods. The graphical results of SHET using the three methods shown in Table 3.

Figure 4 explains the results of selective harmonic elimination time results for various modulation indexes ranging from 0.1 to 1. In it the modulation index is considered as the "X-axis, SHET is given as the "Y-axis. From Figure 4, the blue colour symbolizes the selective harmonic elimination time in the TSGWSO-SHE technique, the red colour represents as selective harmonic elimination time in the APSO-NR algorithm, green colour indicate selective harmonic elimination time in the asynchronous PSO-Newton-Raphson algorithm [1] and ACO depends on the hybrid algorithm [2]. The selective harmonic removal time of the TSGWSO-SHE technique is lesser due to the tournament-selected glowworm swarm optimization algorithm. The information about the current location to neighbors has been transmitted and then the objective function of every glowworm is calculated. The brighter objective function neighbors are attracted in

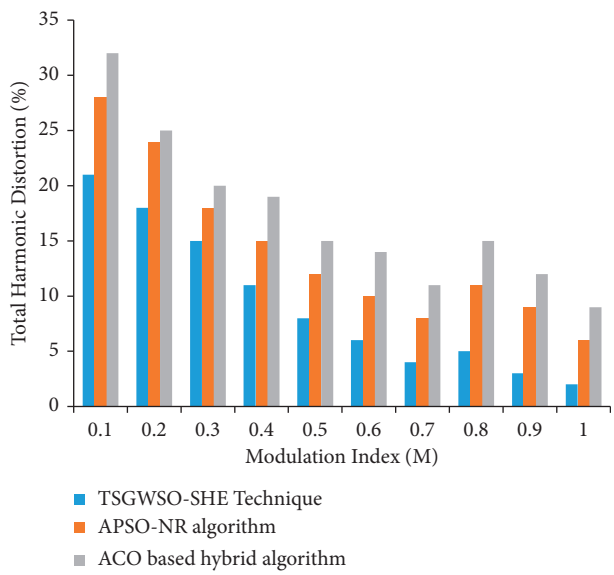

Figure 3: Result of total harmonic distortion.

Table 3: Comparison of selective harmonic elimination time.

Modulation index (M)	Selective harmonic elimination time (ms)		
	TSGWSO-SHE technique	APSO-NR algorithm	ACO based hybrid algorithm
0.1	36	55	61
0.2	39	59	64
0.3	42	63	67
0.4	40	60	65
0.5	38	57	62
0.6	37	54	57
0.7	41	58	60
0.8	45	62	65
0.9	48	65	69
1.0	52	68	73

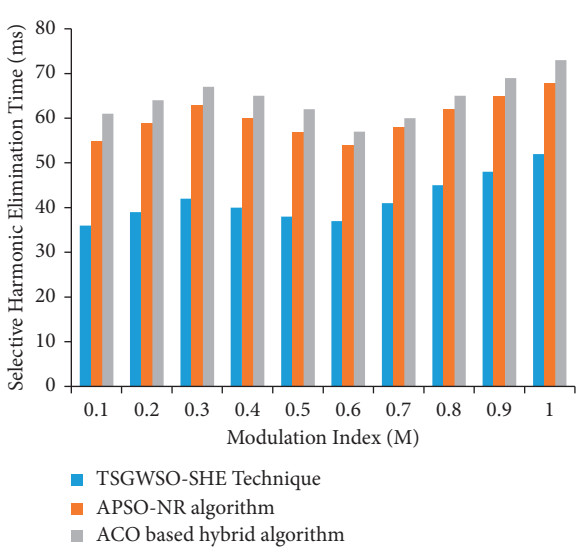

Figure 4: Measure of selective harmonic elimination time.

lesser objective function nodes. To move the neighbor with a high objective function, decisions are taken by each glowworm. The optimal glowworms are chosen for the elimination of selective harmonic to avoid the total harmonic distortion of multilevel inverters and to update the glowworm's position.

During simulation, the proposed TSGWSO-SHE technique takes ten different modulation index values as input to minimize the SHET. While getting the modulation index of 0.2 as input, the selective harmonic elimination time of the TSGWSO-SHE technique is 39 ms while the selective harmonic elimination time of the asynchronous PSO-Newton-Raphson algorithm and the ACO based hybrid algorithm is 59 ms and 64 ms, respectively. The SHET of the TSGWSO-SHE technique is lessened by 31% as compared to the traditional PSO-Newton-Raphson algorithm [1] and 35% as compared to the ACO based hybrid algorithm [2].

4.3. Impact of Selective Harmonic Elimination Efficiency. The Selective Harmonic Elimination Efficiency (SHEE) is described as the rate of eliminating the selective harmonics accurately for increasing the performance of the output voltage. It is measured in percentage (%). When the efficiency of the selective harmonic elimination is higher, the technique is said to be more effective.

Table 4: Comparison of the efficiency of Selective Harmonic Elimination Efficiency.

Modulation index (M)	Selective harmonic elimination efficiency (%)		
	TSGWSO-SHE technique	APSO-NR algorithm	ACO based hybrid algorithm
0.1	90	83	77
0.2	93	85	79
0.3	92	82	76
0.4	93	83	79
0.5	95	85	82
0.6	97	88	85
0.7	94	86	83
0.8	95	87	86
0.9	93	85	84
1.0	97	90	87

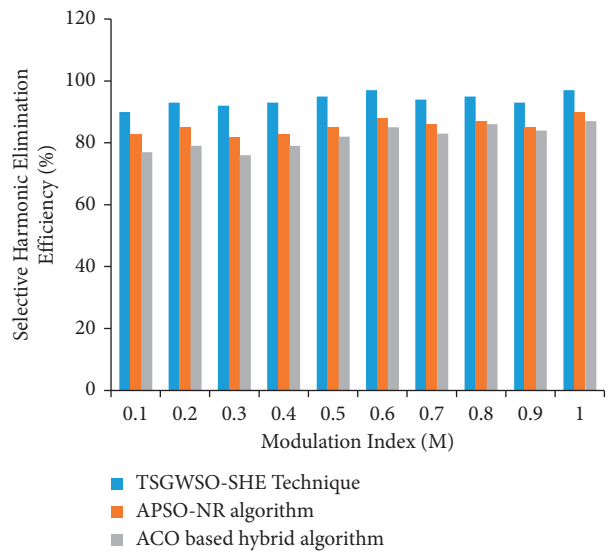

Figure 5: Measure of Selective harmonic Elimination Efficiency.

Table 4 explains the efficiency of the selective harmonic elimination of three different techniques, namely TSGWSO-SHE technique, Asynchronous PSO-Newton-Raphson algorithm, and ACO based hybrid algorithm based on the diverse modulation index values that are taken as the input. It shows that the SHEE of the proposed TSGWSO-SHE is higher than the other two conventional techniques. The result of SHEE is presented in Figure 5.

Figure 5 describes the results of the efficiency selective harmonic elimination with respect to different modulation index ranges. It shows that the modulation index is considered in the "X"-axis and the selective harmonic elimination efficiency is given in the "Y"-axis. In Figure 5, the blue colour represents the efficiency of selective harmonic elimination of the TSGWSO-SHE technique where the red colour and green colour line denote the selective harmonic elimination efficiency of the asynchronous PSO-Newton-Raphson algorithm [1] and ACO depends on the hybrid algorithm [2]. The elimination of selective harmonic efficiency of the TSGWSO-SHE technique is higher with the tournament-selected glowworm swarm optimization algorithm. The objective function of every glowworm is calculated. The brighter objective function neighbors get attracted by lesser objective function nodes. To move the neighbor with a higher objective function, each glowworm is decided by using probabilistic mechanism. The optimal glowworms are chosen for the elimination of selective harmonic for avoiding the total harmonic distortion of multilevel inverters and for updating the position of the glowworm. In this manner, the efficiency of selective harmonic elimination gets improved.

In the present study, the proposed TSGWSO-SHE technique considers ten different modulation indexes during the simulation evaluation process to improve the SHEE. While considering the modulation index value of 0.9, the efficiency of the selective harmonic elimination of TSGWSO-SHE technique is 93% while that of the Asynchronous PSO-Newton-Raphson algorithm and ACO based hybrid algorithm is 85% and 84% respectively. The SHEE of the proposed TSGWSO-SHE technique gets decreased by 10% and 15% as compared to the conventional asynchronous PSO-Newton-Raphson algorithm [1] and ACO based hybrid algorithm [2].

Table 5 shows the comparative result of Total Harmonic Distortion, Selective Harmonic Elimination Time, Selective Harmonic Elimination Efficiency using the proposed and the existing methods. The proposed TSGWSO-SHE technique reduces the Total Harmonic

Table 5: Overall comparison of the existing techniques with the proposed technique.

Parameters	TSGWSO-SHE technique (%)	APSO-NR algorithm (%)	ACO based hybrid algorithm (%)
Total harmonic distortion (%)	9	14	17
Selective harmonic elimination time	42	60	64
Selective harmonic elimination efficiency	94	85	82

Distortion by 9%, Selective Harmonic Elimination Time by 42% and the Selective Harmonic Elimination Efficiency is enhanced by 94%.

5. Conclusion

In this paper, an efficient TSGWSO-SHE method is designed for the multilevel inverter. In the TSGWSO-SHE technique, multilevel inverters are designed, and the modulation index is calculated. Then the, switching angles are computed. The number of SAs is initialized and the objective function is determined for every SA. It detects and selects the neighboring switching angle with higher brightness by tournament selection. Finally, the switching angle updates its position and identifies the optimal switching angle. In this way, an optimal SA is selected during the selective harmonic elimination process in a multilevel inverter for output voltage and current enhancement with improved efficiency and lower amount of time consumption. The effectiveness of the TSGWSO-SHE technique is analyzed by using the parameters such as THD, SHDE and SHDT. The proposed TSGWSO-SHE technique presents the improved performance of selective harmonic distortion in multilevel inverters. The simulation results demonstrate that the TSGWSO-SHE technique presents better results with reduced SHDE and higher SHDE for output voltage as compared to the existing works.

Data Availability

The data will be provided based on the request.

Conflicts of Interest

The authors declare that they have no conflicts of interest.

References

[1] M. Ahmed Memon, S. Mekhilef, and M. Mubin, "Selective harmonic elimination in multilevel inverter using hybrid APSO algorithm," *IET Power Electronics*, vol. 11, no. 10, pp. 1673–1680, 2018.

[2] S. D. Patil and S. G. Kadwane, "Hybrid optimization algorithm applied for selective harmonic elimination in multilevel inverter with reduced switch topology," *Microsystem Technologies*, vol. 24, no. 8, pp. 3409–3415, 2018.

[3] T. Sudhakar Babu, K. Priya, D. Maheswaran, K. Sathish Kumar, and N. Rajasekar, "Selective voltage harmonic elimination in PWM inverter using bacterial foraging algorithm," *Swarm and Evolutionary Computation*, vol. 20, pp. 74–81, 2015.

[4] E. Deniz and Z. Aydogmus, "Implementation of ANN-based selective harmonic elimination PWM using hybrid genetic algorithm-based optimization," *Measurement, Elsevier*, vol. 85, pp. 32–42, 2016.

[5] S. Y. M Mousavi, M. ZabihiLaharami, A. NiknamKumle, and S. H. Fathi, "Application of ABC algorithm for selective harmonic elimination switching pattern of cascade multilevel inverter with unequal DC sources," *International Transactions on Electrical Energy System*, Wiley Online Publication, vol. 28, no. 4, , pp. 1–14, 2018.

[6] Z. BalaDuranay and H. Guldemir, "Fuzzy logic based selective harmonic elimination for single phase inverters," *Advances in Science, Technology and Engineering Systems Journal*, vol. 3, no. 3, pp. 161–167, 2018.

[7] A. Ali, M. R. JannatiOskuee, and A. OllahMokhberdoran, "Implementation of novel technique for selective harmonic elimination in multilevel inverters based on ICA," *Advances in Power Electronics*, vol. 2013, pp. 1–10, 2013.

[8] M. Al-Hitmi, S. Ahmad, A. Iqbal, S. Padmanaban, and I. Ashraf, "Selective harmonic elimination in a wide modulation range using modified Newton–Raphson and pattern generation methods for a multilevel inverter," *Energies*, vol. 11, no. 2, pp. 1–16, 2018.

[9] K. Imarazene and E. M. Berkouk, "Selective harmonics elimination PWM with self-balancing DC-link in photovoltaic 7-level inverter," *Turkish Journal of Electrical Engineering and Computer Sciences*, vol. 24, no. 5, pp. 3999–4014, 2016.

[10] T. Demirdelen, R. I. Kayaalp, and M. Tumay, "A modular cascaded multilevel inverter based Shunt hybrid active power filter for selective harmonic and reactive power compensation under distorted/unbalanced grid voltage conditions," *Engineering, Technology & Applied Science Research*, vol. 6, no. 5, pp. 1133–1138, 2016.

[11] F. Chabni and H. Mhamed, "ANN-based SHEPWM using a harmony search on a new multilevel inverter topology," *Turkish Journal of Electrical Engineering and Computer Sciences*, vol. 25, pp. 4867–4879, 2017.

[12] H. Firouzkouhi, "Control of cascaded H-bridge multilevel inverter based on optimum regulation of switching angles, and the FPGA implementation," *European Journal of Electrical and Computer Engineering*, vol. 3, no. 1, pp. 1–5, 2019.

[13] P. A. Ghonge and P. L. Agiwale, "GHNN based selective harmonic elimination implementation for single phase inverter," *International Journal of Engineering Research and Technology*, vol. 8, no. 2, pp. 64–69, 2019.

[14] H. Karaca and E. Bektas, "Selective harmonic elimination using genetic algorithm for multilevel inverter with reduced number of power switches," *Engineering Letters*, vol. 24, no. 2, pp. 138–143, 2016.

[15] Y. Gopal, D. Birla, and M. Lalwani, "Selected harmonic elimination for cascaded multilevel inverter based on photovoltaic with fuzzy logic control maximum power point tracking technique," *Technologies*, vol. 6, no. 3, pp. 1–17, 2018.

[16] R. T. FaycalChabni, L. Abdelhak and M. Bounadja, New modified CHB multilevel inverter topology with elimination of lower and higher order harmonics," *Journal for Control, Measurement, Electronics, Computing and Communications*, vol. 59, no. 1, pp. 1–10, 2018.

[17] A. Ali, B. Mohammadzadeh, and M. R. JannatiOskuee, "Utilizing the cuckoo optimization algorithm for selective harmonic elimination strategy in the cascaded multilevel inverter," *ECTI Transactions on Electrical Engineering, Electronics, and Communications*, vol. 12, no. 1, pp. 7–15, 2014.

[18] Y. Gopal, K. P. Panda, D. Birla, and M. Lalwani, "Swarm optimization-based modified selective harmonic elimination PWM technique application in symmetrical H-bridge type multilevel inverters," *Engineering, Technology & Applied Science Research*, vol. 9, no. 1, pp. 3836–3845, 2019.

[19] I. A. Adeyemo, J. A. Ojo, and D. O. Babajide, "Artificial intelligence approach to real-time selective harmonic elimination in voltage source multilevel inverter," *International Journal of Soft Computing and Engineering*, vol. 8, no. 4, pp. 7–13, 2018.

[20] P. Sen, P. Ranjan Bana, and K. Prasad Panda, "Firefly assisted genetic algorithm for selective harmonic elimination in PV interfacing reduced switch multilevel inverter," *International Journal of Renewable Energy Resources*, vol. 9, no. 1, pp. 32–43, 2019.

[21] M. Ahmed Memon and M. D. Siddique, "Asynchronous particle swarm OptimizationGenetic algorithm (APSO-GA) based selective harmonic elimination in a cascaded H-bridge multilevel inverter," *IEEE Transactions on Industrial Electronics*, vol. 69, no. 2, pp. 1477–1487, 2022.

[22] M. Ahmed Memona, S. Mekhilefa, M. Mubina, and M. Aamir, "Selective harmonic elimination in inverters using bio-inspired intelligent algorithms for renewable energy conversion applications: a review," *Renewable and Sustainable Energy Reviews*, vol. 82, no. 3, pp. 2235–2253, 2021.

[23] M. D. Siddique, M. Saad, and P. Sanjeevikumar, "Single phase step-up switched-capacitor based multilevel inverter topology with SHEPWM," *IEEE Transactions on Industry Applications*, vol. 57, no. 3, pp. 3107–3119, 2021.

Hindawi
Mathematical Problems in Engineering
Volume 2022, Article ID 9540033, 12 pages
https://doi.org/10.1155/2022/9540033

Research Article

Elderly People Activity Recognition in Smart Grid Monitoring Environment

Anusha Ganesan,[1] **Anand Paul**,[1] **and HyunCheol Seo**[2]

[1]*School of Computer Science and Engineering Kyungpook National University, Daegu 41566, Republic of Korea*
[2]*School of Architectural, Civil, Environmental and Energy Engineering, Kyungpook National University, Daegu, Republic of Korea*

Correspondence should be addressed to HyunCheol Seo; charles@knu.ac.kr

Received 3 February 2022; Accepted 7 March 2022; Published 22 March 2022

Academic Editor: Ravi Samikannu

Elderly people activity recognition has become a vital necessity in many countries, because most of the elderly people live alone and are vulnerable. Thus, more research to advance in the monitoring systems used to recognize the activities of elderly people is required. Many researchers have proposed different monitoring systems for activity recognition using wired and wireless wearable sensing devices. However, the activity classification accuracy achieved so far should be improved to meet the challenges of more precise activity monitoring. Our study proposes a smart Human Activity Recognition system architecture utilizing an open source dataset generated by wireless, batteryless sensors used by 14 healthy aged persons and unsupervised and supervised machine learning algorithms. In this paper, we also propose using a smart grid for checking regularly the wearable sensing device operational status to address the well-known reliability challenges of these devices, such as wireless charging and data trustworthiness. As the data from the sensing device is very noisy, we employ the K-means++ clustering to identify outliers and use advanced ensemble classification techniques, such as the stacking classifier for which a meta model built using the random forest algorithm gave better results than all other base models considered. We also employ a bagging classifier, which is an ensemble meta-estimator fitting the prediction outputs of the base classifiers and aggregating them to produce the ensemble output. The best classification accuracy of 99.81 was achieved by the stacking classifier in training and 99.78% in testing, respectively. Comparisons for finding the best model were conducted using the recall, F1 score, and precision values.

1. Introduction

Several countries in the world currently have a vast elderly population. This situation entails additional challenges in providing quality healthcare services and facilities for this demographic. Elderly people require more physical and psychological support and assistance. Most of the elderly people currently live on their own as their children work in the different geographic locations. This leads to a lesser likelihood of children taking care of their parents. This makes the elderly parents very vulnerable to risks with no immediate assistance available. However, this problem can be mitigated with the technological advancements in activity monitoring systems for elderly people. Data required by these systems are acquired by wearable sensing devices and then analyzed to understand and forecast the individual's health condition and required support. These monitoring systems are referred to as Human Activity Recognition (HAR) systems. HAR systems play important roles in several domains such as healthcare, security, and smart environment deployment [1]. The operation of these systems involves five major steps, which are illustrated in Figure 1 for four basic activities such as sleeping, walking, standing, and sitting.

However, to successfully implement these steps, appropriate devices and sensors are required to ensure the efficiency of the entire system. Hence, the development of such system relies on wireless networks, machine learning (ML), data processing, and classification methods. A HAR system can detect and monitor the activities as well as the hazards that can affect the elderly people. Since the devices

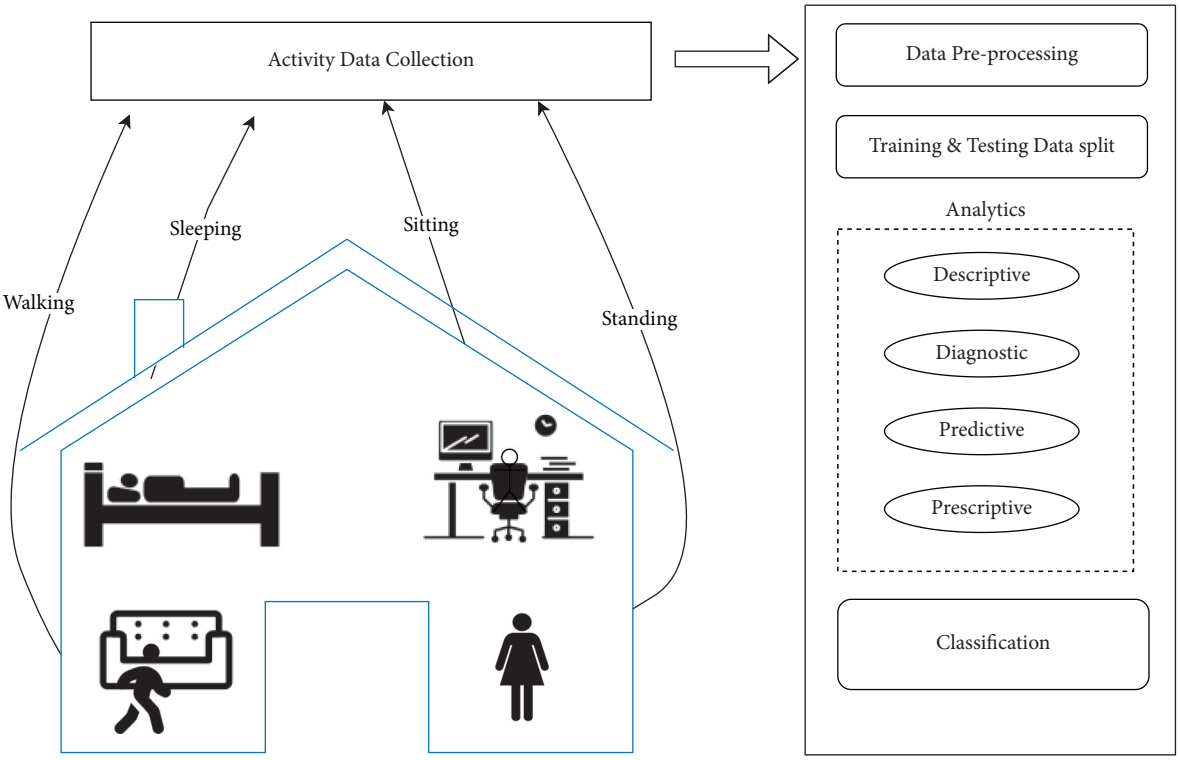

Figure 1: Overview of HAR system operation.

connected to users can generate huge amounts of data while monitoring their activities, ML algorithms can help to discover the patterns in the activity logs and make necessary predictions of future trends to assist in adequately supporting elderly persons.

The HAR systems can be considered as a type of Cyber-Physical Systems (CPSs). A CPS is an integrated ensemble of hardware and software components that can run a given process effectively and safely. Nowadays in Smart Homes (SHs), CPSs effectively perform the following tasks:

(1)Monitoring human activities

(2)Learning inhabitant preferences or needs

(3)Providing the required assistance for activity determination, localization, and scheduling

Thus, the HAR systems adopting machine or deep learning offer very efficient health and safety monitoring method, especially for the elderly people. In these systems, data are collected by sensors, wearable devices, and cameras, and transmitted using wireless networks, to be later analyzed to detect the activity changes, behavioral patterns, social interactions, and sleep patterns [2–4]. These types of systems can even help in assessing several health risk factors such as depression, loneliness, and fall risk, as well as unexpected changes in behavior of healthy people. Many researchers have implemented various CPSs for these purposes. Mohsen et al. [5] proposed a TensorFlow-based model for classifying human activities. However, deep learning models require substantial computation power. Hence, other approaches using ML algorithms with good classification and prediction accuracy have been proposed. Staab et al. [6] examined the performance of several supervised learning algorithms for classifying daily activities of dementia patients using data collected by smartwatches. In another article, Ullrich et al. [7] demonstrated the detection of Parkinson's disease from inertial sensor data using unsupervised standardized gait tests. Although developing more accurate monitoring models to recognize human activities and detect problems using HAR systems or CPSs is challenging, these challenges must be overcome to enhance the effectiveness of the HAR systems. The existing literature works indicates that HAR systems can be generally based on either sensors or computer vision. In the latter, the system gathers data in form of images or videos with cameras deployed in the monitored environment. Alrashdi et al. [8] proposed a Markov recognition model using maximum entropy utilizing depth camera data. However, their method may infringe on user's privacy as cameras capture their every motion in videos or images. Hence, the methods which use wearable sensors to gather data are efficient and are strongly preferred. Therefore, in this study we used a dataset gathered using sensors worn by healthy elderly people.

This study proposes a smart HAR system that also tracks the wearable sensing device operational status in addition to the activity data log gathered by the wearable sensors. Because the monitoring process relies exclusively on the data collected by the sensors, checking the sensing device operational state is essential to achieve accurate activity monitoring. Therefore, we propose using a smart grid (SG) in a smart environmental setup to monitor the wearable sensor operational status and report either correctly working

or faults such as faulty, short circuited, good working, or device dead. So, to create a SG monitoring system in a smart environment, we can deploy phasor measurement units (PMUs). These are high speed sensors which can measure voltage and current phasors of the power system with an accuracy in the order of one microsecond [9, 10]. A PMU can help to understand the power status of the device to which it is connected. Using the data collected from PMUs, we can also identify the condition of wearable sensors in a wireless network. However, this study proposes the including such SG elements for sensor state monitoring with a future long-term goal of implementing them. Thus, this study aims to design a smart environment for the proposed system and focuses on developing better computational model for the HAR system. As mentioned earlier, a monitoring system for elderly people must be accurate to predict the required assistance and make prompt decisions to implement necessary actions. In our study, we used the data gathered from 14 healthy elderly people using a batteryless wearable sensing device placed at the sternum level and transmitted via a RFID reader antenna [11–13, 14]. The approach we propose starts with preprocessing of the noisy sensor data. So we use the K-means ++ algorithm to form clusters of data points corresponding to predefined activities, which leaves remaining spurious data in separate, distinct clusters. As the clustering algorithm is used prior to building the classifier, the recognition accuracy is significantly improved and identification of abnormal activity data becomes easier and quicker. The classification model takes the clusters obtained in the previous step as its input. We adopted the ensemble ML algorithms such as the stacking and bagging classifiers at this stage. By analyzing the classification results, we obtain information about the person's activity or the monitoring device condition. Based on the detection outcome, an appropriate alert will be triggered to notify the care taker.

In summary, the key contributions of this paper are as follows:

(i) Design of a smart HAR system for elderly people physical activity recognition

(ii) Proposal for using a SG monitoring system to track the wearable device operational status to enhance the reliability of the entire system

(iii) Evaluation of the efficiencies of the numerical models using ensemble ML algorithms utilizing statistical metrics such as recall, F1 score, and precision values of training and testing accuracies

The rest of the paper is organized as follows. We first provide a short overview of the literature on existing activity recognition systems. In Materials and Methods, we present the materials and methods used to design our proposed system. This section also describes the dataset used in our study. The next section is Proposed Smart HAR System where we explain the design of our system. The experimental setup and results are described and discussed in Results and Discussion. Finally, we conclude the paper with an overview of the future research directions for the development of the proposed system.

2. Literature Survey

This section contains a brief survey of literature works about the HAR system and wearable sensing systems. The review covers the earlier and more recent studies in recognition, classification, and monitoring the human activity patterns. During the current COVID-19 pandemic, many individuals are quarantined in designated places or isolated at home; thus there is an increased need to monitor their physical activities. In this context, Tan et al. [15] used smartphone sensor data and proposed an ensemble learning algorithm comprising a convolutional neural network (CNN) stacked on a gated recurrent unit and deep neural network. Similarly, using smartphone-based accelerometer sensor data, Prasad et al. [16] used a CNN to recognize the six basic human activities of jogging, sitting, standing, and walking up and down the stairs. In fact, in recent years, there have been many studies using the smartphone-based sensor data for activity recognition. In 2020, Sarwar et al. [17] proposed a double-layer approach called physical activity recognition having complex interclass variations (PARCIV). The authors used the smartphone semantic data in their study. Chen et al. [18] analyzed smartphone-based sensor data for HAR using the maximum full a posteriori algorithm. On the other hand, some researchers used the Global Positioning System (GPS) tracking feature available in almost every smartphone along with the sensor data for monitoring the physical activities within indoor and outdoor environments. Selected efforts related to using GPS data for activity recognition are mentioned herein. Wannenburg and Malekian [19] made a prediction model using the kNN and kStar algorithms to recognize the physical activities. Wan and Lin [20] used GPS data collected by a smartphone to classify the human activity patterns utilizing fuzzy logic and aggregation approach. Wu et al. [21] used smartphone motion sensors and kNN classifier to classify physical activities. Kelishomi et al. [22] presented a model for the recognition of the environment type, such as indoor or outdoor, based on the activity data collected using a smartphone. Nan et al. [23] presented a deep learning-based model for elderly people activity recognition using a pocket-worn smartphone. The model was built using a CNN with Long Short-Term Memory algorithm.

Although there have been several studies on recognizing the physical activities using smartphone sensor data, the drawback of such data is that they are likely to have more variation due to dynamic movement of the devices. This can affect the accuracy while monitoring the physical activities of elderly people. However, the CPSs can assist in monitoring of the human activities with wearable sensors and in improving the accuracy of physical activity recognition. The studies reviewed below give an indication of the potential applications and benefits of CPSs for developing efficient monitoring systems for activity recognition. Amarasinghe et al. [24] proposed a framework for data-driven status monitoring of CPS which utilized an additional CPS testbed apart from the key components of the status monitoring system, such as data acquisition, state identification and estimation, cyber-physical status monitoring, and warning generation. The CPS testbed

included a microgrid simulator and cyber network that connected the grid to its controller. The experimental results demonstrated that such a framework can be useful for extracting the relationships between the data features and for highly accurate monitoring of patients or elderly people. Pereda et al. [25] adopted a CPS to perform daily activities in a SH with the help of robots. The paper argued that CPSs can also be used to perform a wide range of activities that makes life easier. Bocicor et al. [26] presented a CPS-based system for indoor ambient monitoring for assisted living, equipped with recognition, monitoring, and alerting features. Bergweiler [27] designed a CPS model for an assistance system based on virtual digit object memories. These types of systems are typically adopted for commercial purposes such as manufacturing of spare parts for automobile and quality assurance for consumer products.

Among the demographics targeted for monitoring their physical activities, the elderly people are a very important group because of the support they may require. There are some studies in which models have been proposed for monitoring their daily activities and selected medical problems, and issuing alerts to the caregivers or hospitals, or healthcare specialists [28]. Lim et al. [29] designed an interactive CPS for assisting elderly people and individuals with disabilities by reminding them about the sequence of their activities and in supporting their daily routine using a smart agent. In the early 2000's, Ohta et al. [30] developed a health monitoring system for elderly people living alone. The monitoring system adopted infrared sensors placed in every room. This early publication demonstrates the need to monitor elderly people health. Chernbumroong et al. [31] proposed an activity recognition and classification model for elderly people. They collected data using wrist worn sensors. However, their classification was at most only 90% accurate. To alleviate the problem, the authors suggested to combine temperature data with acceleration. In a later review paper, Wang et al. [32] presented a detailed account of the wearable sensing technologies for elderly persons to accurately recognize and track their indoor activities and detect their health condition promptly. This review paper is useful for determining which wearable sensors may be suitable for designing a highly accurate HAR system.

It is also necessary to overview the existing HAR algorithms to select an appropriate one for building our model. Sriwichian and Muangprathub [33] adopted different deep learning and ML algorithms for elderly people activity recognition using the R program and compared their results to determine the best performing model (an artificial neural network). Papagiannaki et al. [34] proposed an activity recognition model for aged people using ML algorithms SVM, CNN3 classifiers, etc. While the authors admitted that the accuracy of their model might be lower than that of other approaches, they claimed that low accuracy was because of a single sensor placed at the sternum, and the age of the population from whom the data were collected. However, our own experimental results indicate that better classification results can be achieved even for a single sensor and elder people. We succeeded in developing a more accurate recognition model by applying clustering and ensemble models to the data. The following section explains the benefits of the methods used in the proposed model along with the materials required.

3. Materials and Methods

This section provides a description of the materials and methods used to design the proposed model.

3.1. Computational Environment. Simulations were executed in the Python environment and Python environment integrated with sklearn libraries for ensemble model libraries to create the classification models and evaluate them using statistical metrics.

3.2. Dataset Description. The dataset used in this study was generated by monitoring 14 healthy elderly people, aged within 66 to 86 in two clinical rooms, while they performed the broadly defined activities using a batteryless, wearable sensor attached to their clothing at the sternum level. Room 1 and Room 2 had four and three RFID reader antennas, respectively, for collecting of activity data. The dataset consisted of 9 features listed in Table 1. There were 75,128 observations in the dataset and 4 classes of the activity labels: (1) sitting on the bed (16,406 instances), (2) sitting on the chair (4,911 instances), (3) lying on the bed (51,520 instances), and (4) ambulating (walking or standing within the room) (2,291 instances). The entire dataset was randomly divided in an 80:20 ratio for the training and testing sets. Hence, the training set had 60,102 samples and the testing set had 15,026 samples, respectively.

3.3. Methods. In this section, firstly, we present a description of the HAR system working and then explain the methods used for designing the proposed system.

3.4. HAR System. HAR systems are typical representatives of pattern recognition systems [35]. They work in two stages: (1) training and (2) recognition. In fact, both stages consist of almost identical steps. The training stage involves gathering prior knowledge of the activities which must be recognized. The recognition stage uses the information collected in the training stage to accurately recognize those activities. In other words, the second stage strongly depends on the success of the first stage. The training stage includes steps such as data collection, feature selection, and learning from the selected features. Data can be collected from different types of sensors employed by the system. However, data are often noisy and must be preprocessed to clean them before further analyses. This preprocessing occurs during the feature selection process. In the feature selection process, the collected data can be classified into structural and statistical features. Structural features are those which indicate correlations between data points. Statistical features are those resulting from the application of statistical methods directly to the data or after they have been transformed, and include the mean, variance, and others. The most widely used

Table 1: Dataset features.

Feature number	Description
1	Time in seconds
2	Frontal axis acceleration
3	Vertical axis acceleration
4	Lateral axis acceleration
5	ID of sensor reading antenna
6	Received signal strength indicator (RSSI)
7	Phase
8	Frequency
9	Activity label

transformations are the Fourier and wavelet transforms. Following feature selection, the learning process is executed as the final step in the training phase of a HAR system. In this step, a recognition model is trained from the data gathered by sensors. Several algorithms can be used for creating a best-fit model for recognition. All these three steps are again performed in the recognition stage. At the conclusion of the recognition stage, the most accurate, fastest, and resource-efficient recognition model is chosen. We propose a smart HAR system with the most accurate recognition model for elderly people activity monitoring and prompt assistance. To enhance the effectiveness and reliability of the HAR system in smart environments, we use a SG monitoring system in the proposed system.

3.5. Smart Grid Monitoring System. SGs are electrical power grids, which can be employed for advanced networking, instantaneous monitoring, and controlling to save energy, reducing costs, and enhancing security, interoperability, and reliability [36]. SGs can automatically and spontaneously react to changes in the grid environment. However, they require specific smart sensors to provide real-time monitoring information and status. These sensors are used to measure several physical parameters of the environment and the devices connected to that environment, including energy storage, transmission connectivity, and power generation. Examples of such sensors are PMUs, voltage transformers, current transformers, smart meters, temperature sensors, gas sensors, accelerometers, humidity sensors, and network cameras. However, the sensors must meet certain requirements to be able to perform their intended tasks with efficiency. For instance, the intelligent capabilities required for these sensors are self-identification, self-calibration, self-diagnostics, self-awareness, and localization. Using these sensors, a SG monitoring system can be designed. Such systems monitor the operations of the network and its devices in real time [37]. These systems also aim at lowering the energy consumption and enhancing life quality by saving time and reducing failure rates and stress. The other advantages of SG monitoring systems include monitoring the operational status of the physical devices in the network, providing greater reliability, and increasing the sustainability of the data transmission through clean and energy efficient resources. The core ability of the SG is the ability to communicate the status of the system from the sensors used. Figure 2 shows a schematic diagram of a wireless SG monitoring system. The SG monitoring system is active when the sensor module present in each SG node collects the voltage and current data from the device connected to it. These data are then sent over the Internet to a server for storage, from where they can be accessed remotely on smart phones. However, data must be interrogated to extract the relevant information about the state of devices connected to the SG system.

Therefore, we propose including this SG monitoring system in the smart environment equipped with specific sensors, such as PMUs, that can support the active monitoring of the system status and obtain the operational data of devices connected to the system. However, only when the quality of the data from a smart environment is enhanced can the end users experience the full benefit of the wearable device. Thus, we employ a clustering technique, the K-means++ algorithm, for data cleaning.

3.6. Clustering. Clustering is an unsupervised technique in which unlabeled input data are divided into groups called clusters based on a certain user-defined criterion. It is a data mining technique, as it partitions the data into clusters based on similarities or patterns common within each cluster. Therefore, data cleaning and outlier removal can be performed by generating a prototype of the data from a clustering algorithm. Many researchers [38, 39] used clustering algorithms for data cleaning to enhance data quality. In our study, we adopted the K-means++ clustering algorithm for data prototyping after removing duplicates from the dataset, which enhanced clustering performance as discussed in the results section. K-means ++ algorithm is much similar to the K-means algorithm; however, it works smarter because of the steps followed during the centroid initialization. In the result section, we explain about the algorithmic steps followed by K-means ++ to select the centroids. So, in this section, we describe the mathematics behind the K-means ++ algorithm for clustering. Like K-means clustering, K-means ++ algorithm also uses the centroids to create the clusters. A centroid of m datapoints on an X-Y plane is another point having its own x and y coordinates such that it is a geometric center of the m points. So we have to create K clusters for the given data points based on their Euclidean distance from their centroid. For m data points and K = number of clusters, the centroid initialization is the first step. In K-means ++ algorithm, only one centroid is randomly selected from one of the datapoints. Then, for every datapoint x in a set of datapoints given by S, it calculates the distance between every datapoint x and the centroid chosen c using Euclidean distance formula:

$$d(x,c) = \sqrt{\sum_{i=1}^{n} (c - x_i)^2}. \quad (1)$$

The next cluster centroid is chosen with this distance calculated by selecting the datapoint which is at maximum distance from the first centroid. However, the subsequent centroids are identified with the distance calculated between the datapoint x and the nearest selected centroids. And the weighted probability distribution is used to select the cluster

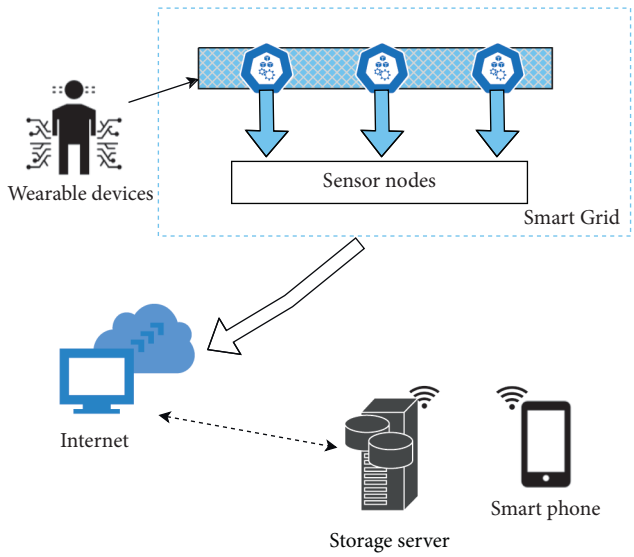

Figure 2: Schematic diagram of SG monitoring system.

where the datapoint is farthest to the first cluster center till the required K centroids have been chosen. Using the centroids chosen, the K-means ++ algorithm performs the grouping of the datapoints with the least Euclidean distance between the datapoint and nearest centroid.

The flowchart shown in Figure 3 provides an overall flow of the adopted data processing process, which is one of the main steps of the proposed system. After the duplicate data were identified and removed, data prototyping was performed using the K-means ++ clustering algorithm with the initial cluster assumption as the activity labels defined in the dataset. The data with essential similarity was clustered based on the activity label, whereas the data with no required similarity were considered outliers or noise and not assigned to any of the clean clusters.

At the end of this process, we created clean clusters to be used for further classification. In this paper, we used the ensemble classification as it has proven itself to be more accurate than the traditional classification models. The next subsection details the benefits of the ensemble techniques and their working principle.

3.7. Ensemble Classification. Ensemble classification is carried out using the ensemble learning concept. One of the major tasks of any artificial intelligence algorithm is to create an adequate model using a given dataset. The process of generating such a model using the available data is called learning, whereas the learned model is referred to as the hypothesis. The learning algorithms that construct a set of classifiers and then classify the new data points by considering jointly their individual predictions are called the ensemble learning algorithms. The ensemble methods have been demonstrated to create more accurate models than their individual constituent classifiers [40–44]. The ensemble methods are known for their capability to boost weak learned models. Generally, other learning algorithms which give a single hypothesis face the following three types of fundamental problems:

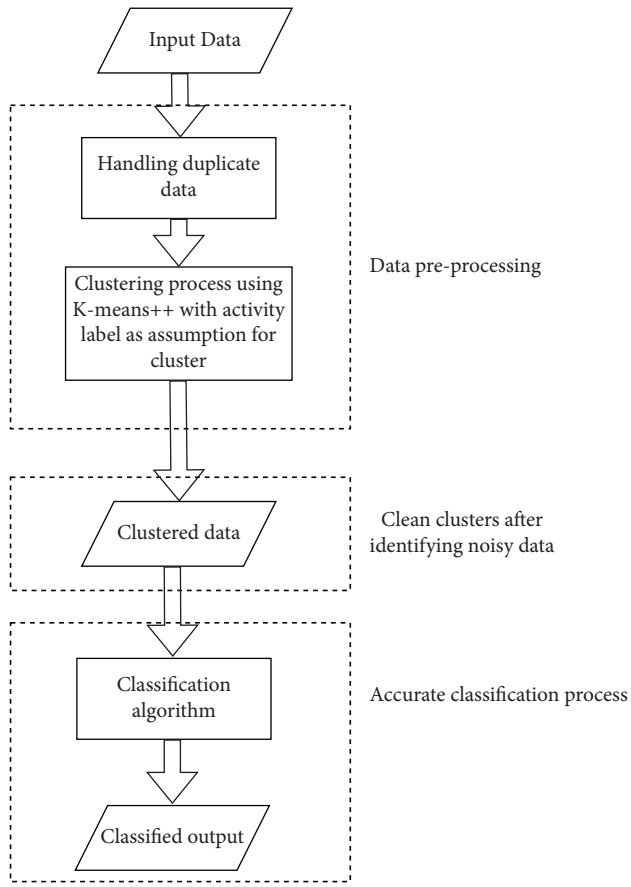

Figure 3: Flowchart of data processing.

(1) Statistical problems
(2) Computational problems
(3) Representation problems

The most common statistical problem faced by other algorithms is high variance, the computational problems are related to the computational variance and time, and the representation problem is related to high bias. The ensemble methods help reducing the bias, variance, and computation time. Therefore, we have adopted several ensemble classification methods for creating our recognition model, which resulted in a higher accuracy of activity recognition. In our experimental study, we considered advanced ensemble techniques, such as the stacking and bagging classifiers. Stacking is an ensemble ML algorithm that learns how to perfectly combine the predictions from several well-performing ML models. Its architecture comprises two or more base models (level-0 models) and a meta-model (level-1 model) which combines the predictions of the base models. The output of the base models is used as an input to the meta-model, which can be the probabilities or class labels for data classification. The training dataset for the meta-model is mostly prepared using a K-fold cross-validation of the base models. Therefore, stacking is often used to improve the modelling performance in different applications, including health monitoring and predictions [45, 46]. The other ensemble method, bagging, is an ensemble meta-estimator which fits the base classifiers on random subsets of the entire dataset and then

aggregates the individual predictions to form the final prediction. This meta-classifier can be used to reduce the variance of a black-box estimation methods, such as neural networks or gradient boost methods, by using randomly selected data for establishing separate prediction models and forming their ensemble output. The bagging classifiers have been found to be very effective in various applications [47, 48]. Therefore, we have created stacking and bagging classifier models using various meta-level classifiers and evaluated their performance using several statistical classification metrics. We found that the stacking classifier with the random forest (RF) as the meta-model performed the best as the activity recognition model in our proposed system. An illustration of a stacking ensemble algorithm is given in Figure 4. As shown in the figure, the original dataset is fed as input to the first level learners, which are the base classifier models. Using the outputs of these base models, a new dataset is generated for the second-level learner, which is the meta-classifier model. The aim is to train the base models using the original data and generate new data for training the meta-model so that the risk of overfitting can be avoided. When the same data is used to train the base and meta-models, there can be a high risk of overfitting. Hence, the instances used for generating the new dataset should be excluded from the training data used for the base models, and cross-validation is also recommended.

Therefore, in our experiment, we performed the K-fold cross-validation to train the models. In order to explain this in detail, we consider that given dataset $D = \{(x_1, y_1), \ldots, (x_n, y_n)\}$ are randomly split into k equal parts approximately, $D_1, D_2, \ldots, D_k$. D_j and $D_{(-j)} = \{D \backslash D_j\}$ are defined as testing and training sets for the jth fold. Then, suppose M learning algorithms are given; the output of the first-level learning algorithm $h_m^{(-j)}$ is obtained by invoking the mth learning algorithm on $D_{(-j)}$. Then, for every element x_i in D_j, a variable z_{im} is defined to store the output $h_m^{(-j)}$ for every x_i. So, at the end of this cross-validation process, the new dataset for the meta level learning algorithm is generated from the M individual learners as

$$D\prime = \{(z_{i1}, \ldots, z_{iM}, y_i)\}_{i=1}^{n}. \tag{2}$$

And the resulting output function from the meta level learner is given as h'.

4. Statistical Evaluation Metrics

4.1. Accuracy. Accuracy shows how often the classifier makes correct predictions. It is defined as the ratio of the number of correct predictions to the total number of predictions:

$$\text{accuracy} = \frac{\text{true positive} + \text{true negative}}{\text{true positive} + \text{true negative} + \text{false positive} + \text{false negative}} \times 100\%. \tag{3}$$

However, a very high model accuracy does not always identify the best model; thus metrics such as precision and recall need to be used to judge the model quality in more detail.

4.2. Precision. Precision is a useful indicator when the cost of false positives is high. It is a measure of how accurately the model detects the actual positives compared to the total predicted positives:

$$\text{precision} = \frac{\text{true positive}}{\text{true positive} + \text{false positive}}. \tag{4}$$

4.3. Recall. A false negative is an occurrence classified as a negative rather than as an actual positive. Recall is the ratio of actual positives to the sum of actual positives and false negatives:

$$\text{recall} = \frac{\text{true positive}}{\text{true positive} + \text{false negative}}. \tag{5}$$

5. Proposed Smart HAR System

The detailed structure of proposed smart HAR system is shown in Figure 5. The system performs the following five major processes:

(1) Data collection
(2) Setting up a smart environment
(3) Data management
(4) Computational modelling
(5) Activity recognition or alert notification

5.1. Data Collection. This process is concerned with the generation of the data from the users of the smart HAR system. The data is collected by the wearable sensors. In our study, we used the data gathered from elderly people using wearable batteryless sensor devices because our aim was to propose this smart system for elderly people who need immediate assistance in emergency situations. However, setting up a smarter environment ensures the efficiency of this process and the overall quality of this proposed system which is dependent entirely on the data collected.

5.2. Setting Up a Smart Environment. In this process, a smart environment for data collection from the wearable sensing devices, monitoring and issuing alerts to care takers, is set up. Here, we deployed a SG monitoring system with appropriate sensors, such as PMUs, to monitor the device operational status and the system data transmission status. An activity data log is collected using RFID reader antennas, which is used for recognizing the physical activities. However, use of appropriate sensors and wireless networks assists

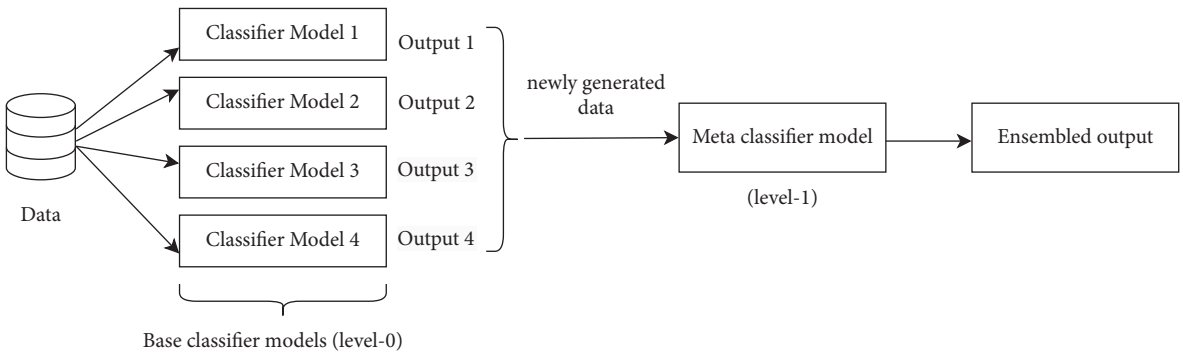

Figure 4: Stacking ensemble classifier model.

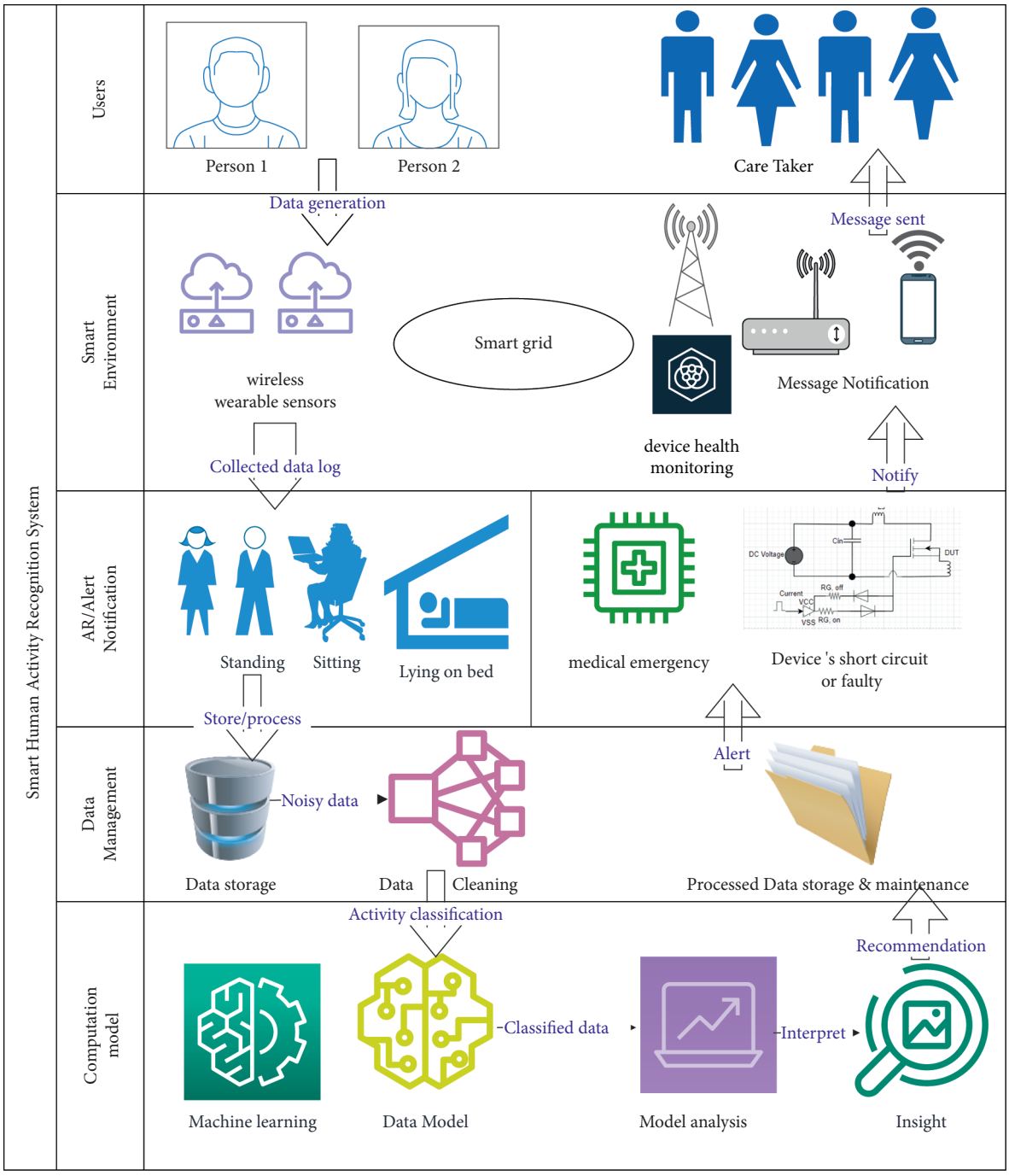

Figure 5: Proposed smart HAR system.

in accurate monitoring the physical activities and recording a proper log of data in the cloud or on servers. But, the raw sensor data is likely very noisy; the data management process must also include data cleaning.

5.3. Data Management. There are three main tasks involved in the data management process. Firstly, the data which is collected have to be properly stored for future retrieval. Then, the collected data are likely to require transformation into a suitable format for creating a more accurate recognition model. Later, there is an increased likelihood of noise in the sensor-based data; therefore we have to perform data cleaning. In our study, we used data clustering for data cleaning as it is very efficient. In our experiment, we considered four activities typically performed by elderly people who live alone in their homes. We selected an appropriate dataset and applied the K-means++ clustering algorithm to group the data for these four activities. The clustering algorithm produced four clean clusters, which were fed as inputs into the activity classification model as a part of the HAR system training. Once the model is adequately trained using the ensemble classification method, it can be tested to recognize all the activity data that is generated from the sensors during the HAR system recognition stage. This process also takes care of the management of processed data.

5.4. Computational Modelling. In this process, the clustered output is fed to the ensemble classification model so that it can learn and formulate a hypothesis about the activities to be recognized during the training phase and ensure that those activities are accurately identified during the recognition phase. In our study, we used the stacking and bagging classifiers as the ensemble algorithms. We designed these models using four base models, including the logistic regression (LR), support vector machine (SVM), RF, and decision tree (DT) classifiers, and modified the meta-classifier or evaluation classification model using the outputs of the base models. However, the obtained models must be compared and evaluated to find the best one.

Hence, we compared the models using several statistical metrics. So, whenever there is abnormal activity identified by the model, the corresponding classification results are visualized. And, based on the classification result, the alert notification process is initiated.

5.5. Activity Recognition or Alert Notification. The activity recognition or alert notification is carried out based on the output of the computation model. As mentioned above, we included the SG system for monitoring the sensing device status separate from the sensing system gathering the activity data. Hence, the data collected from the smart environment also include the data related to the condition status of the monitoring devices. Therefore, the classification model can also be trained to classify the condition of the sensors, but this functionality will only be implemented in the future. This device status can be classified as working correctly, faulty, short-circuited, or no power. Thus, the alert notification is triggered not only in a medical emergency but also when the device operational status is deviating from correct working. Hence, the entire proposed HAR system for monitoring the elderly people physical activities is more reliable by monitoring the wearable sensing devices as well.

6. Results and Discussion

Using the publicly available dataset taken from the UCI repository, we performed an experiment using our proposed system with the hardware and software specifications listed in Table 2. We started the experiment with data cleaning using the K-means++ clustering algorithm for the four labeled activity classes (sitting on the bed, sitting in the chair, lying on the bed, and ambulating (walking and standing in the room)). An important feature of the K-means++ algorithm is intelligent initialization of centroids that produce better clusters. The steps to find such centroids are as follows:

(1) Select a random centroid point from the given dataset

(2) For each instance "i" in the dataset, find the distance x from that instance "i" to the closest, earlier chosen centroid

(3) Select the subsequent centroid from the dataset with the termination goal that the probability of selecting a point as centroid corresponds to the distance from the closest, recently selected centroid

(4) Repeat Steps 2 and 3 until we find the K centroid points

The output of the K-means ++ clustering algorithm is shown in Figure 6. It produced four distinct clusters of activity labels based on the features such as acceleration, phase, and frequency selected from the given dataset. We used the elbow method to find the optimal number of clusters. The optimal k value for clustering all data samples was determined to be 4.

Next, a classification model was created using the clustered output, which supported improving the accuracy of the recognition results. We used ensemble classification techniques, including stacking and bagging classifiers. The models were created with base models including LR, SVM, RF, and DT classifiers. In this way, we created the following ensemble classification models: stacking-LR (S-LR), stacking-RF (S-RF), stacking-DC (S-DC), bagging-LR (BAG-LR), bagging-RF (BAG-RF), and bagging-DC (BAG-DC). These models were evaluated using several statistical metrics to identify the best classification model for the proposed system. Figures 7 and 8 show comparisons of training and testing accuracies from all the constructed models, from which we determined that the stacking model with RF performed much better than the remaining models.

However, in concluding which classification model is the best, we cannot restrict ourselves exclusively to the accuracy achieved by the models. Therefore, metrics such as precision, recall, and F1 score were also determined for both training and testing stage. These values are listed in Table 3. Higher

Table 2: Experimental setup.

Component	Specifications
Processor	Intel(R)Core (TM) i7-3770
Hard disk	Seagate 1 TB
GPU	NVIDIA GeForce GTX 750
SSD	256 GB
Memory	10240 MB DDR3 1333 MHz
Operating system	Windows 10 professional
Computational software	Python 3.7
Interface	PyCharm

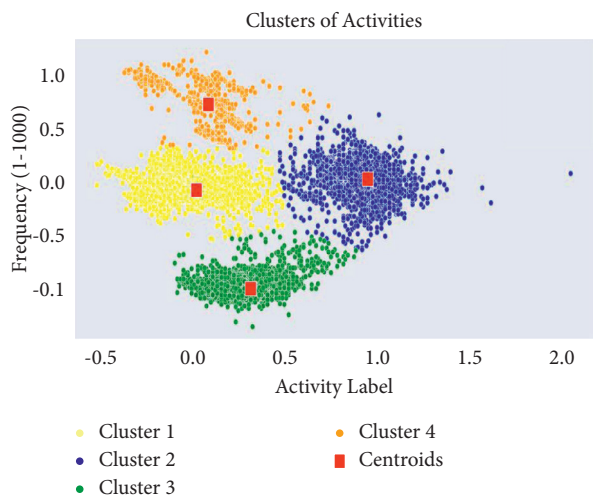

Figure 6: Clustering output produced by K-means++ algorithm.

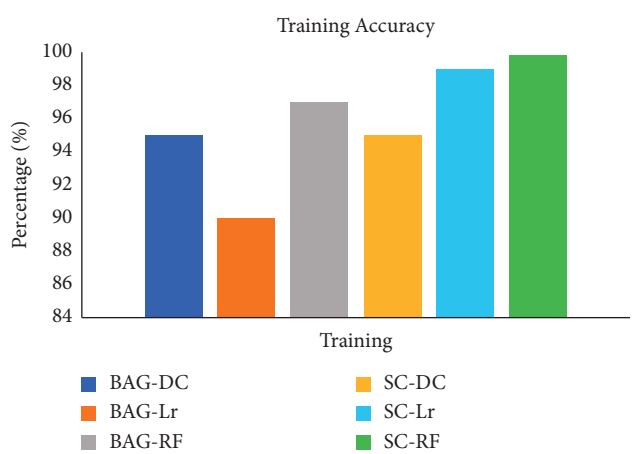

Figure 7: Comparison of model accuracy on training data.

values of precision, recall, and F1 score indicate better classification results.

From the values listed in Table 3, we concluded that both stacking and bagging classifiers produced recognition models with good accuracies when RF was used as the meta-model. However, when all the metrics are compared, the stacking-RF model performed much better than the bagging-RF classifier. Thus, we have determined experimentally the best classification model to recognize the activities from the data recorded by the sensors. As a part of the future research, we will implement the monitoring the smart wearable devices to track their operational status and the associated classification model will be developed.

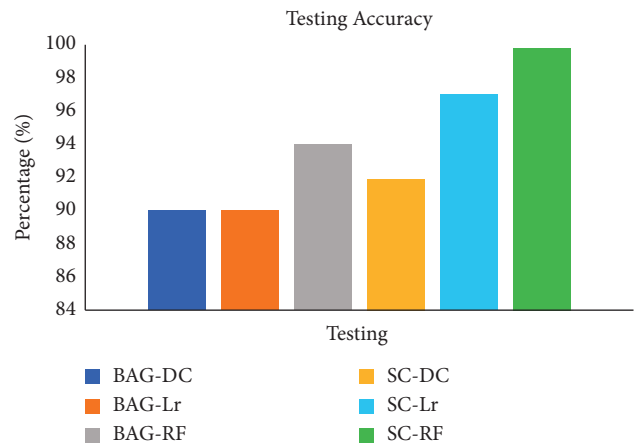

Figure 8: Comparison of model accuracy on testing data.

Table 3: Comparison of classification metrics for different models.

Model	Training			Testing		
	Precision	Recall	F1 score	Precision	Recall	F1 score
BAG-DC	0.975	0.972	0.973	0.949	0.943	0.946
BAG-Lr	0.947	0.941	0.944	0.947	0.941	0.944
BAG-RF	0.986	0.982	0.984	0.970	0.967	0.969
SC-DC	0.975	0.973	0.974	0.951	0.963	0.957
SC-Lr	0.995	0.995	0.995	0.990	0.980	0.985
SC-RF	0.999	0.996	0.999	0.999	0.999	0.999

7. Conclusions

In this paper, we proposed a smart HAR system to identify the physical activities performed by elderly people and a SG monitoring system to track the wearable sensing device operational status for ensuring the data quality and sensing device as well as entire system reliability. A major challenge in the development of the HAR system was the creation of a more accurate activity recognition model. In this study, we used a combination of clustering and ensemble classification algorithms to increase the efficiency of the recognition model and provide accurate classification of predefined and abnormal activities, so that elderly people can be assisted promptly in emergencies.

Data Availability

The numeric data supporting this analysis are from previously reported studies and datasets, which have been cited.

Conflicts of Interest

The authors declare that there are no conflicts of interest regarding the publication of this paper.

Acknowledgments

This research was supported by the National Research Foundation of Korea Grant funded by Korean Government (MSIP, South Korea) Number: 2020R1C1C1007127.

References

[1] J. Muangprathub, A. Sriwichian, A. Wanichsombat, S. Kajornkasirat, P. Nillaor, and V. Boonjing, "A novel elderly tracking system using machine learning to classify signals from mobile and wearable sensors," *International Journal of Environmental Research and Public Health*, vol. 18, pp. 12652–23, 2021.

[2] D. Bouchabou, S. M. Nguyen, C. Lohr, B. Leduc, and I. Kanellos, "A survey of human activity recognition in smart homes based on iot sensors algorithms: taxonomies, challenges, and opportunities with deep learning," *Sensors*, vol. 21, no. 18, pp. 6037–18, 2021.

[3] R. Kolkar and V. Geetha, "Human activity recognition in smart home using deep learning techniques," in *Proceedings of the 2021 13th International Conference on Information & Communication Technology and System (ICTS) 2021*, pp. 230–234, Surabaya, Indonesia, October 2021.

[4] H. D. Mehr and H. Polat, "Human activity recognition in smart home with deep learning approach," in *Proceedings of the 2019 7th International Istanbul Smart Grids and Cities Congress and Fair (ICSG)*, pp. 149–153, Istanbul, Turkey, April 2019.

[5] S. Mohsen, A. Elkaseer, and S. G. Scholz, "Industry 4.0-oriented deep learning models for human activity recognition," *IEEE Access*, vol. 9, pp. 150508–150521, 2021.

[6] S. Staab, J. Luderschmidt, and L. Martin, "Recognition of usual similar activities of dementia patients via smartwatches using supervised learning," in *Proceedings of the 2021 IEEE International Conference on Progress in Informatics and Computing (PIC)*, pp. 397–402, Shanghai, China, December 2021.

[7] M. Ullrich, A. Mucke, A. Kuderle et al., "Detection of unsupervised standardized gait tests from real-world inertial sensor data in Parkinson's disease," *IEEE Transactions on Neural Systems and Rehabilitation Engineering*, vol. 29, pp. 2103–2111, 2021.

[8] I. Alrashdi, M. H. Siddiqi, Y. Alhwaiti, M. Alruwaili, and M. Azad, "Maximum entropy Markov model for human activity recognition using depth camera," *IEEE Access*, vol. 9, pp. 160635–160645, 2021.

[9] H. Manoharan, Y. Teekaraman, I. Kirpichnikova, R. Kuppusamy, S. Nikolovski, and H. R. Baghaee, "Smart grid monitoring by wireless sensors using binary logistic regression," *Energies*, vol. 13, no. 15, p. 3974, 2020.

[10] L. J. Awalin and M. K. Rahmat, "A recent development of monitoring devices on smart grid," in *Proceedings of the E3S Web of Conferences*, vol. 186, pp. 02004–02008, OSAKA, Japan, March 2020.

[11] R. L. Shinmoto Torres, R. Visvanathan, D. Abbott, K. D. Hill, and D. C. Ranasinghe, "A battery-less and wireless wearable sensor system for identifying bed and chair exits in a pilot trial in hospitalized older people," *PLoS One*, vol. 12, no. 10, pp. e0185670–25, 2017.

[12] R. Shinmoto Torres, R. Visvanathan, S. Hoskins, A. Van den Hengel, and D. Ranasinghe, "Effectiveness of a batteryless and wireless wearable sensor system for identifying bed and chair exits in healthy older people," *Sensors*, vol. 16, no. 4, pp. 546–4, 2016.

[13] R. L. Shinmoto Torres, D. C. Ranasinghe, Q. Qinfeng Shi, and A. P. Sample, "Sensor enabled wearable RFID technology for mitigating the risk of falls near beds," in *Proceedings of the 2013 IEEE International Conference on RFID (RFID) 2013*, pp. 191–198, Johor Bahru, Malaysia, September 2013.

[14] "UCI activity recognition with healthy older people using a batteryless wearable sensor Data Set," 2017, https://archive.ics.uci.edu/ml/datasets/Activity+recognition+with+healthy+older+people+using+a+batteryless+wearable+sensor.

[15] T.-H. Tan, J.-Y. Wu, S.-H. Liu, and M. Gochoo, "Human activity recognition using an ensemble learning algorithm with smartphone sensor data," *Electronics*, vol. 11, no. 3, pp. 322–417, 2022.

[16] A. Prasad, A. K. Tyagi, M. M. Althobaiti, A. Almulihi, R. F. Mansour, and A. M. Mahmoud, "Human activity recognition using cell phone-based accelerometer and convolutional neural network," *Applied Sciences*, vol. 11, no. 24, pp. 12099–24, 2021.

[17] M. Usman Sarwar, A. Rehman Javed, F. Kulsoom, S. Khan, U. Tariq, and A. Kashif Bashir, "PARCIV: recognizing physical activities having complex interclass variations using semantic data of smartphone," *Software: Practice and Experience*, vol. 51, no. 3, pp. 532–549, 2021.

[18] Z. Chen, C. Jiang, S. Xiang, J. Ding, M. Wu, and X. Li, "Smartphone sensor-based human activity recognition using feature fusion and maximum full a posteriori," *IEEE Transactions on Instrumentation and Measurement*, vol. 69, no. 7, pp. 3992–4001, 2020.

[19] J. Wannenburg and R. Malekian, "Physical activity recognition from smartphone accelerometer data for user context awareness sensing," *IEEE Transactions on Systems, Man, and Cybernetics: Systems*, vol. 47, no. 12, pp. 3142–3149, 2017.

[20] A. Approach, "Classifying human activity patterns from smartphone collected," vol. 20, no. 6, pp. 869–886, 2017.

[21] W. Wu, S. Dasgupta, E. E. Ramirez, C. Peterson, and G. J. Norman, "Classification accuracies of physical activities using smartphone motion sensors," *Journal of Medical Internet Research*, vol. 14, no. 5, pp. e130–9, 2012.

[22] A. Esmaeili Kelishomi, A. H. S. Garmabaki, M. Bahaghighat, and J. Dong, "Mobile user indoor-outdoor detection through physical daily activities," *Sensors*, vol. 19, no. 3, pp. 511–3, 2019.

[23] Y. Nan, N. H. Lovell, S. J. Redmond, K. Wang, K. Delbaere, and K. S. van Schooten, "Deep learning for activity recognition in older people using a pocket-worn smartphone," *Sensors*, vol. 20, no. 24, pp. 7195–7214, 2020.

[24] K. Amarasinghe, C. Wickramasinghe, D. Marino, C. Rieger, and M. Manicl, "Framework for data driven health monitoring of cyber-physical systems," *2018 Resilience Week (RWS)*, vol. 2018, pp. 25–30, 2018.

[25] C. Pereyda, N. Raghunath, B. Minor, G. Wilson, M. Schmitter-Edgecombe, and D. J. Cook, "Cyber-physical support of daily activities," *ACM Transactions on Cyber-Physical Systems*, vol. 4, no. 2, pp. 1–24, 2020.

[26] M. I. Bocicor, D. C. Frau, I.-C. Draghici et al., "Cyber-physical system for assisted living and home monitoring," in *Proceedings of the 2017 13th IEEE International Conference on Intelligent Computer Communication and Processing (ICCP) 2017*, pp. 487–493, Cluj-Napoca, Romania, September 2017.

[27] S. Bergweiler, "Intelligent manufacturing based on self-monitoring cyber-physical systems," in *Proceedings of the Ninth International Conference of Mobile Ubiquitous*

Computer System Service Technology, pp. 108–113, İstanbul, Turkey, July 2015.

[28] A. Ganesan, A. Paul, G. Nagabushnam, and M. J. J. Gul, "Human-in-the-Loop predictive analytics using statistical learning," *Journal of Healthcare Engineering*, vol. 2021, pp. 1–14, 2021.

[29] S. Lim, L. Chung, O. Han, and J.-H. Kim, "An interactive cyber-physical system (CPS) for people with disability and frail elderly people," in *Proceedings of the 5th International Confernece on Ubiquitous Information Management and Communication-ICUIMC'11 2011*, Seoul Korea, February 2011.

[30] S. Ohta, H. Nakamoto, Y. Shinagawa, and T. Tanikawa, "A health monitoring system for elderly people living alone," *Journal of Telemedicine and Telecare*, vol. 8, no. 3, pp. 151–156, 2002.

[31] S. Chernbumroong, S. Cang, A. Atkins, and H. Yu, "Elderly activities recognition and classification for applications in assisted living," *Expert Systems with Applications*, vol. 40, no. 5, pp. 1662–1674, 2013.

[32] Z. Wang, Z. Yang, and T. Dong, "A review of wearable technologies for elderly care that can accurately track indoor position, recognize physical activities and monitor vital signs in real time," *Sensors*, vol. 17, no. 2, p. 341, 2017.

[33] A. Sriwichian and J. Muangprathub, "Comparison of algorithm selection to analyze elderly activity recognition based on sensor data using r program," in *Proceedings of the 2019 16th International Conference on Electrical Engineering/Electronics, Computer, Telecommunications and Information Technology (ECTI-CON) 2019*, pp. 377–380, Pattaya, Thailand, July 2019.

[34] A. Papagiannaki, E. Zacharaki, G. Kalouris et al., "Recognizing physical activity of older people from wearable sensors and inconsistent data," *Sensors*, vol. 19, no. 4, pp. 880–919, 2019.

[35] D. Castro, W. Coral, C. Rodriguez, J. Cabra, and J. Colorado, "Wearable-based human activity recognition using an IoT Approach," *Journal of Sensor and Actuator Networks*, vol. 6, no. 4, pp. 28–4, 2017.

[36] E. Y. Song, G. J. Fitzpatrick, and K. B. Lee, "Smart sensors and standard-based interoperability in smart grids," *IEEE Sensors Journal*, vol. 17, no. 23, pp. 7723–7730, 2017.

[37] G. Luca, M. Benedetta, F. Nardecchia, F. Bisegna, and G. Chiara, "Home smart grid device for energy saves and failure monitoring," in *Proceedings of the 2015 IEEE 15th International Conference on Environment and Electrical Engineering (EEEIC) 2015*, pp. 671–676, Rome, Italy, June 2015.

[38] S. Joshi, T. Usha, and S. Ata, "Data cleaning using clustering based data mining technique," vol. 4, no. 2, pp. 2–5, 2015.

[39] W. Hu, A. Zaveri, H. Qiu, and M. Dumontier, "Cleaning by clustering: methodology for addressing data quality issues in biomedical metadata," *BMC Bioinformatics*, vol. 18, no. 1, pp. 1–13, 2017.

[40] P. Yildirim and V. Radevski, "Comparative analysis of ensemble learning methods for signal classification," pp. 1–4, 2018.

[41] P. Lohumi, S. Garg, T. P. Singh, and M. Gopal, "Ensemble learning classification for medical diagnosis," in *Proceedings of the 2020 5th International Conference on Computing, Communication and Security (ICCCS) 2020*, Patna, India, October 2020.

[42] B. J. Kim, "Ensemble methods applied to classification problem," *Int. J. Internet, Broadcast*, vol. 11, no. 1, pp. 47–53, 2019.

[43] E. A. Alshdaifat, M. Al-hassan, and A. Aloqaily, "Effective heterogeneous ensemble classification: an alternative approach for selecting base classifiers," *ICT Express*, vol. 7, no. 3, pp. 342–349, 2021.

[44] N. A. B. S. Noor, I. Elamvazuthi, and N. Yahya, "Classification of diabetes mellitus using ensemble algorithms," in *Proceedings of the 2020 8th International Conference on Intelligent and Advanced Systems (ICIAS)*, pp. 1–6, Kuala Lumpur, Malaysia, July 2021.

[45] V. O. Khilwani, V. Gondaliya, S. Patel, J. Hemnani, B. Gandhi, and S. K. Bharti, "Diabetes prediction, using stacking classifier," in *Proceedings of the 2021 International Conference on Artificial Intelligence and Machine Vision (AIMV)*, pp. 1–6, Gandhinagar, India, September 2021.

[46] P. Ri, A. U. Berliana, and A. Bustamam, "Implementation of stacking ensemble learning for classification of COVID-19 using image dataset CT scan and lung x-ray," in *Proceedings of the 2020 3rd International Conference on Information and Communications Technology (ICOIACT)*, pp. 148–152, Yogyakarta, Indonesia, November 2021.

[47] M. S. Bin Alam, M. J. A. Patwary, and M. Hassan, "Birth mode prediction using bagging ensemble classifier: a case study of Bangladesh," in *Proceedings of the 2021 International Conference on Information and Communication Technology for Sustainable Development (ICICT4SD) 2021*, pp. 95–99, Bangladesh, Dhaka, February 2021.

[48] X. Li, T. Shi, P. Li, and W. Zhou, "Application of bagging ensemble classifier based on genetic algorithm in the text classification of railway fault hazards," in *Proceedings of the 2019 2nd International Conference on Artificial Intelligence and Big Data (ICAIBD) 2019*, pp. 286–290, Chengdu, China, May 2019.

Hindawi
Mathematical Problems in Engineering
Volume 2022, Article ID 9365214, 9 pages
https://doi.org/10.1155/2022/9365214

Research Article

Electric Vehicle Usage Pattern Analysis Using Nonnegative Matrix Factorization in Renewable EV-Smart Charging Grid Environment

Anandkumar Balasubramaniam,[1] Thirunavukarasu Balasubramaniam,[2] Anand Paul,[1] and HyunCheol Seo[3]

[1]*School of Computer Science & Engineering, Kyungpook National University, Daegu, Republic of Korea*
[2]*School of Computer Science and Centre for Data Science, Queensland University of Technology, Brisbane, Australia*
[3]*School of Architectural, Civil, Environmental and Energy Engineering, Kyungpook National University, Daegu, Republic of Korea*

Correspondence should be addressed to HyunCheol Seo; charles@knu.ac.kr

Received 28 January 2022; Accepted 7 March 2022; Published 22 March 2022

Academic Editor: Ravi Samikannu

The global utilization of electric vehicles (EVs) is exponentially increasing due to the increased availability of cost-efficient EVs and infrastructure managements for the EVs. In spite of the increasing usage of EVs, the problem of EV usage patterns' analysis and implementing sustainable infrastructure for the EV transportation is still under development. In addition to this, there is a challenging problem of long waiting hours in traffic signals. This study deals with these problems by proposing an architecture that includes EV usage pattern analysis using nonnegative matrix factorization (NMF) technique and renewable solar-powered wireless smart charging grid to effectively utilize or mitigate the long traffic signal waiting hours. The insights from the EV usage patterns are analyzed and presented showing the importance of usage pattern analysis alongside to the presented architecture of renewable solar-powered wireless EV-smart charging grid. These implementations improvise the usage of the EVs and enhancing the transportation experience, which in turn leads to the development of sustainable smart transportation.

1. Introduction

Intelligent transportation system (ITS) is one of the emerging research topics due to its latest advancements and technological developments [1–3]. There are various aspects in improvising ITS by means of implementing efficient traffic management systems, congestion and collision control mechanism, sustainable transportation, etc., [4, 5]. Sustainability is one of the important factors that need to be considered in this current scenario as it acts as the bridge between the efficient usage of advanced technological developments and pollution-free environmental welfares [6, 7]. This leads to the balanced usage of technology while maintaining the eco-friendly environment for the welfare of human life.

EVs [8] are a part of technological developments in ITS that favors sustainable transportation [9–11], especially in the field of ITS. Nowadays, the global usage of the EVs is exponentially increasing as well as there is an increase in the installation of various types of EV charging station/grids [12]. Figure 1 shows the statistics of the worldwide usage of the EVs from the year 2016 to 2020 [13]. According to these statistics, there is an exponential increase in the worldwide usage of the EVs in comparison to the previous years, i.e., only 1.2 million EVs in 2016, whereas nearly 6.8 million EVs are in movement in 2020.

Despite these developments, the problem of longer waiting time in traffic signals is also increasing in parallel [14–16]. Many people including passengers and taxi drivers are wasting time during long waiting hours in many traffic signals. Considering this problem of long traffic signal waiting hours, we propose the concept of utilizing those long waiting time for powering up the EVs using the EV charging grids installed underneath the roadway. To effectively

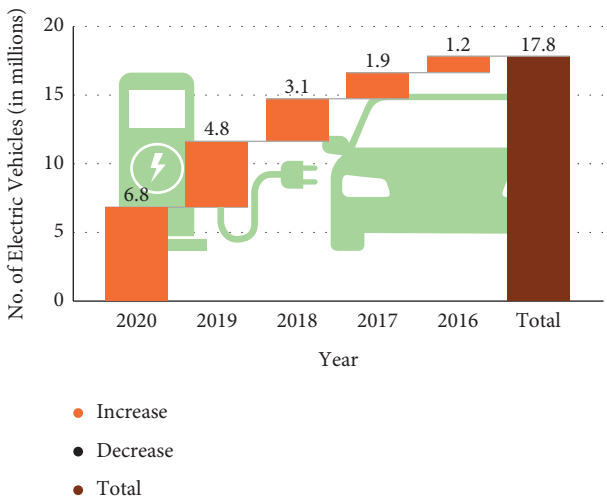

Figure 1: Worldwide usage of the EVs from 2016 to 2020.

implement the above, understanding the usage patterns of the EVs is much more important so that efficient usage of EV charging grid lines can be implemented accordingly.

Eliciting the usage patterns of the EVs helps to understand the complete usage of the EV charging patterns, car appliances usage, and number of passengers utilizing the EVs. To elicit the patterns, we apply NMF, a dimensionality reduction technique [17–20] on the EV usage dataset from the smart-grid smart-city (SGSC) project [21, 22]. This analysis helps to identify the EV usage patterns by the passengers and business people involved in the SGSC project. These usage patterns not only help in understanding various aspects such as understanding the charging patterns and appliance usage patterns but also help for efficient charging of the EVs from the grid installed underneath the road during the long waiting hours in traffic signals.

The rest of the paper is organized as follows. Section 2 contains related works. Section 3 contains the proposed architecture that includes performing EV usage pattern analysis using NMF technique and renewable solar-powered wireless smart charging grid to effectively utilize or mitigate the long traffic signal waiting hours. Section 4 contains EV pattern elicitation that incorporates dataset description, dataset representation, NMF for EV usage pattern and analysis of EV usage data, and understanding the usage patterns. Section 5 contains renewable solar-powered wireless EV-smart charging in relation to the obtained EV usage patterns during long traffic signal waiting time. Section 6 concludes the study.

2. Related Works

As usage of the EVs is exponentially increasing, the importance of eliciting the usage patterns is much needed for effective implementation of various user benefitable traffic enhancement measures. In one of the recent works, the authors proposed the methodology to carry out the driving pattern analysis in the Nordic region [23]. Their analysis is more likely to be concentrated only on the driving patterns of the vehicles on the weekdays and weekends in the Nordic region. In another research work, the authors presented the study on the various factors that affect the intention of the consumer to use the EVs in Malaysia [24]. Their study is focused on providing the directions for the various policymakers and automotive manufacturers. However, these existing works did not focus on providing the architecture that facilitates the behavioral analysis and sustainable characteristics of the EV usage. In another research work, the authors presented the report on impact analysis of EV integration on the component and system levels [25]. Their work mainly focused on the EV load distribution. However, in order to effectively perform the load distribution, it is important to analyse the EV usage patterns. Authors of another recent work investigated the impact of ambient temperature to increase the EV energy consumption during cold weather conditions [26]. The outcome of their study reveals the efficient utilization of the EVs in the urban regions based on the ambient temperature. However, irrespective of the ambient temperature, efficient infrastructure is needed to encourage the usage of the EVs in the roadways for balancing the sustainable environment. In another research work, authors performed the sensitivity analysis on EVs and its impact on low-voltage distribution systems [27]. In this work, the authors analyzed the impacts of modeling of the load of EVs influencing flows and voltages in the grid using transformer and line loadings, and highest sensitivities are observed for the vehicles in the grid. However, people's charging behavior plays minor roles. In order to overcome the above-mentioned challenges, in this study, we performed the EV usage pattern elicitation and analysis using one of the dimensionality reduction techniques such as NMF to thoroughly analyze the EV usage patterns and people's charging and other behaviors and proposed the architecture of renewable solar-powered wireless smart charging grid in relation to the usage pattern analysis to improve the usage of EVs with the thought of achieving the sustainable smart transportation.

3. Proposed Architecture

The proposed architecture is shown in Figure 2, which includes EV usage pattern analysis using NMF technique and renewable solar-powered wireless smart charging grid to effectively utilize or mitigate the long traffic signal waiting hours. The architecture begins with the data processing layer in which preprocessing on the EV usage data is performed. Following the data processing layer, matrix generation and normalization are performed on the normalization layer. Once the matrix is normalized, NMF is performed on the normalized data matrix in the dimensionality reduction layer. Based on the NMF outputs, the similar data points are clustered and different patterns are analyzed in the pattern analysis layer. The analyzed patterns and the pattern insights are sent to the control hub of the traffic control monitoring center to perform various traffic control measures related to the EV based on the pattern analysis. Application of the solar-powered wireless EV-smart charging is elaborated in Figure 2.

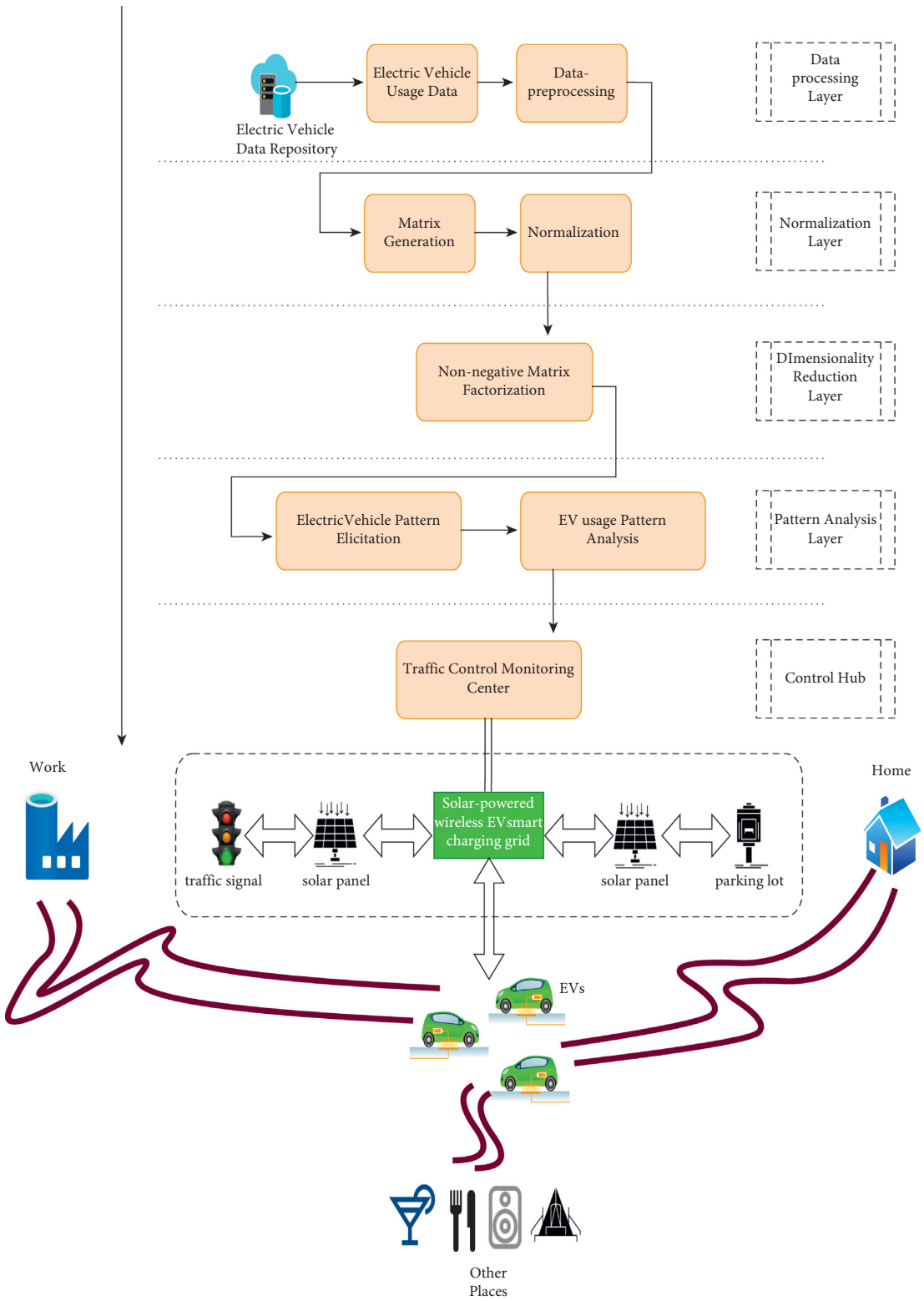

Figure 2: Proposed architecture of renewable EV charging during traffic signal waiting time based on EV usage patterns.

4. EV Pattern Elicitation

4.1. Dataset. The analysis is performed on the dataset which is downloaded from the data repository in the Australian Government's Department of Industry, Science, Energy, and Resources data archive. The dataset includes the usage of the EV by households and businesses in which the EV usage data is a part of the smart-grid smart-city (SGSC) project [21]. This project involves the trial of 20 Mitsubishi iMiEV cars of the 2010 model and the trips' details including the usage of

car appliances such as headlamp, air-conditioning, and state of the battery charge during beginning and end of each trip. The entire data were collected during the period of August 2011 to May 2013.

4.2. Dataset Representation. The EV dataset that records the overall vehicle trips alongside to the record of trip duration, state of charging during start and end of the trip, average velocity, AC 'On' duration, headlamp 'On' duration, distance travelled from source to destination, and number of passengers occupied on the EV. Let us consider $\mathbf{X} \in \mathbb{R}^{\mathbf{M}\times\mathbf{N}}$ is the data matrix consisting of the above records. This matrix can be factorized into two lower-dimensional factor matrices, say, $\mathbf{U} \in \mathbb{R}^{\mathbf{M}\times\mathbf{r}}$ and $\mathbf{V} \in \mathbb{R}^{\mathbf{N}\times\mathbf{r}}$ using nonnegative matrix factorization technique. Equation (1) represents the factorization of the matrix:

$$\begin{aligned} X &\approx UV^T \\ s.t,\ U &\geq 0 \text{ and } V \geq 0, \end{aligned} \tag{1}$$

whereas,

$$U \in \mathbb{R}^{M\times r}, \tag{1a}$$

$$V \in \mathbb{R}^{N\times r}. \tag{1b}$$

4.3. Nonnegative Matrix Factorization (NMF). In this scenario of EV data, trip-feature matrix $X \in \mathbb{R}^{M\times N}$ is the representation of the count of the vehicle trips with respect to the feature records. M is the total number of trips by the EV, i.e., 26150 trips, and N is the feature records, i.e., 8 features ranging from trip duration, state of charging during start and end of the trip, average velocity, AC 'On' duration, headlamp 'On' duration, distance travelled from source to destination, and number of passengers occupied by the vehicle. Implementation of NMF on this dataset is much useful in separately extracting the usage patterns by the representation of lower-dimensional factor matrices U (trips × patterns) and V (features × patterns). As defined in Equations 1(a) and 1(b), "r" distinctive patterns can be obtained from X matrix during the factorization process based on the rank "r." Optimization problem is formulated, in Equation (2), which is the minimization problem with Euclidean distance as the cost function:

$$\min_{U\geq 0, V\geq 0} f(U, V) = X - UV^{T2}. \tag{2}$$

The cost function as defined in Equation (2) is a nonconvex optimization problem that can be solved using factorization algorithms such as alternating least squares (ALS), multiplicative update (MU) rule, and stochastic gradient descent. In this study, we used MU rule to solve Equation (2). Due to the nonconvex nature, we must fix U to learn V and fix V to learn U. The NMF starts with randomly initialized values for the factor matrices U and V. The MU rules will then be applied to update the factor matrices using gradient calculation. The MU rules will take the following form:

$$U \leftarrow U - \mu_U.\nabla_U f(U, V), \tag{3a}$$

$$V \leftarrow V - \mu_V.\nabla_V f(U, V), \tag{3b}$$

where μ_U and μ_V indicate the learning rates for updating U and V, respectively, and $\nabla_U f(U, V)$ and $\nabla_V f(U, V)$ represent the gradients (derivatives) of $f(U, V)$ with respect to U and V, respectively.

By substituting the derivatives of U and V in Equations 3(a) and 3(b), the MU rules will become

$$\begin{aligned} U &\leftarrow U - \mu_U.\left(XV - UVV^T\right), \\ V &\leftarrow V - \mu_V.\left(U^T X - U^T UV\right). \end{aligned} \tag{4}$$

The simplest form of update rule avoids subtractions by defining the learning rates μ_U and μ_V as (U/UVV^T) and $(V^T/U^T UV)$. In this form, the positive component and negative component of the derivatives are used as numerator and denominator, respectively:

$$\begin{aligned} U &\leftarrow U.\frac{XV}{UVV^T}, \\ V &\leftarrow V.\frac{U^T X}{U^T UV}. \end{aligned} \tag{5}$$

4.4. Evaluation Measures. As Equation (2) is a nonconvex optimization problem, the choice of "r" is not straightforward. Therefore, the rank "r" in Equations 1(a) and 1(b) is determined using the various evaluation measures such as within-cluster dispersion and between-cluster dispersion. Based on the abovementioned evaluation measures, optimal rank is determined on the clusters and data points, whereas cluster is nothing but patterns. The determination of within-cluster dispersion and between-cluster dispersion is to prove that the clusters are well separated from the other data points and clusters as well as the data points are grouped together within the cluster, respectively. Figure 3 shows the rank evaluation measures for the EV dataset, whereas 1e6 in Figure 3(b) represents the unit of Y-axis in exponential notation (1e6 is equivalent of 1 million). Equations (6) and (7) show the within-cluster dispersion and between-cluster dispersion, respectively:where B_d and W_d are between-cluster and within-cluster dispersions, S shows the set of data, clusters are represented as g, and the set of points in the cluster are represented as C_g. c_g and c_s are the center of cluster and center of data, respectively, while n_g indicates the number of points in the cluster.

$$W_d = \sum_{g=1}^{m} \sum_{x\in C_g} \left(x - c_g\right)\left(x - c_g\right)^T, \tag{6}$$

$$B_d = \sum_{g=1}^{m} n_g\left(c_g - c_S\right)\left(c_g - c_S\right)^T. \tag{7}$$

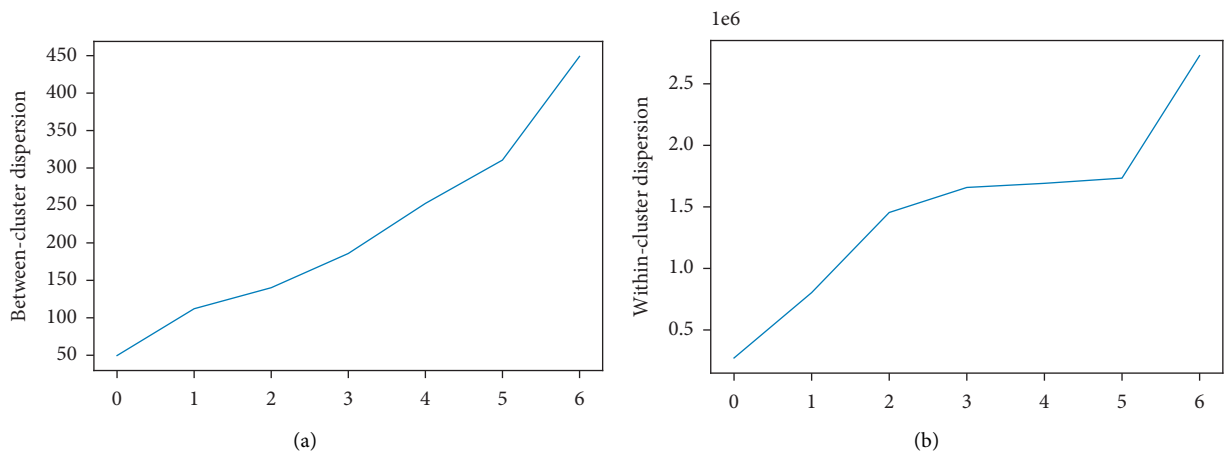

Figure 3: Rank evaluation measures: (a) between-cluster dispersion; (b) within-cluster dispersion.

4.5. Analysis on EV Data. Elicitation of patterns from the EV usage data helps to understand the EV usage patterns based on the various features including trip duration, state of charging during start and end of the trip, average velocity, AC 'On' duration, headlamp 'On' duration, distance travelled from source to destination, and number of passengers occupied by the vehicle.

Figure 4 shows the heatmap representation of the EV usage patterns based on various features. The heatmap representation shows that there are 7 different patterns such as P1 to P7, on the EV usage data with corresponding feature representations. If we consider pattern P1, trip duration has more dominance in comparison to other features. In pattern P2, passenger occupancy is more. In pattern P3, there is no dominance of trip duration and passenger occupancy; however, distance travelled shows its dominance in P3 pattern. Likewise, pattern P4 shows average velocity is dominating than other features. Pattern P5 is quite interesting as this shows the dominance of AC Power-On duration compared to others. Also, the state of charge during the end of the trip is dominating in the P6 pattern while there are no moderate changes in the P7 pattern.

The above pattern analysis is very difficult to obtain from the initial preanalysis of the dataset. Here comes the usage of NMF technique in eliciting these latent pattern behaviors in the EV usage dataset.

4.6. Understanding the EV Usage Patterns Based on Source/Destination. As discussed in Section 4.5, it is important to analysis the impact of the pattern variations based on the source and destination of the EV. Figure 5 shows the pattern analysis of the EV trips based on the origin (source) of the trip. In Figure 5, X-axis shows the representation of cluster IDs, which are the patterns ranging from P1 to P7, and Y-axis shows the count of the total number of trips by the EV based on the source such as home, work, or other locations.

The analysis on Figure 5 shows that patterns P1 and P6 have the huge impact based on the EV trip origin, whereas there is a moderate impact of patterns P3 and P7. On considering pattern P6, it is very clear pattern P6 is more concentrated to the other places as the origin of the trip such that the usage of the EV from other places to either home or work is preferred. This applies to almost all the patters ranging from P1, P2, P3, and P7, whereas only moderate usage of the EVs travelling from home to work or other locations.

Figure 6 shows the pattern analysis of the EV trips based on the trip end, i.e., destination. As discussed in Figure 5, patterns P1 and P6 have more records of the EV usage based on the trip destination. As similar to the trip source, the usage of the EV from either home or work to other places is more preferred. However, pattern P7 is quite different such that the usage of vehicle is more preferred to home as the destination irrespective of the trip origin which is either from work or other places. From the analysis based on Figure 4, Figure 5, and Figure 6, pattern P6 is more dominating in which the EV users are travelling from home/work to other places and vice versa. Also, on considering the heatmap representation in Figure 4, pattern P6 is corresponding to the high dominance of state of charge of EV during trip end.

5. Renewable Solar-Powered Wireless EV Charging during Traffic Signal Waiting Time

One of the problems identified from the analysis of the EV usage patterns is that a greater number of EV travelling from home/work to other places or vice versa are undergoing the charging pattern during the end of most of the trips. This can be addressed using the proposed architecture in which the solar-powered wireless EV charging grid installed underneath the roadway nearby to the traffic signal areas provides the electric power needed to the EV during long traffic signal waiting time. The power to the smart grid is obtained using the solar panels installed alongside to the roadways. However, the length of the solar-powered wireless EV-smart charging grid varies according to the respective landscape of the regions.

Application of the solar-powered wireless EV-smart charging is elaborated in Figure 7, which shows the schematic representation of the implementation of the solar-

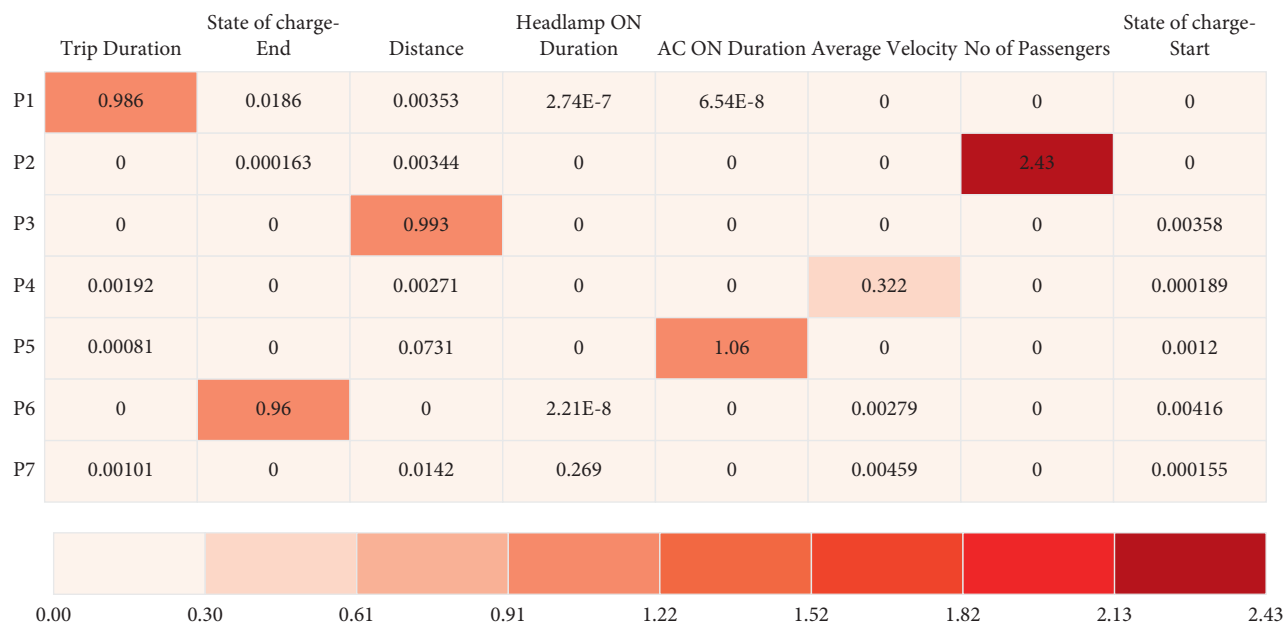

Figure 4: Heatmap representation of EV usage patterns based on various features.

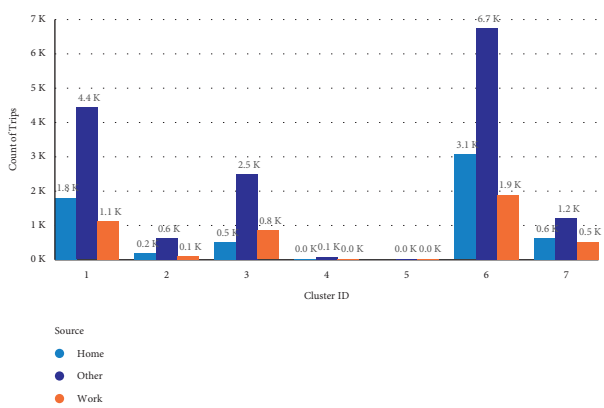

Figure 5: Pattern analysis of EV trips based on trip origin (source).

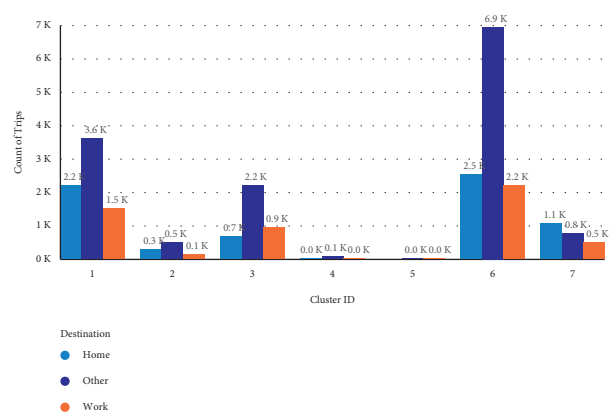

Figure 6: Pattern analysis of EV trips based on trip end (destination).

powered wireless EV-smart charging grids installed underneath the roadway of the traffic signal areas where there is a long waiting time due to the heavy traffic scenarios. By this implementation, it is very easy to tackle the problem of state of charge of the EV during trip end from the dataset analyzed in this study while utilizing the renewable resources as the power source for efficiently powering up the smart grid (Figure 7).

Alongside to the above analysis, additional dataset [28, 29] consisting of 24 hours traffic signal volume data recorded on traffic signals in various places of Victoria is analyzed.

Traffic signal volume data are recorded by utilizing the detectors and installed into the road surface, which is activated once the vehicle passes over it. The detector sends the pulse signal to the traffic signal in this manner. The analysis is conducted on the quarter Q1 of 2020 traffic signal volume count data to get the insights of traffic signal volume data. Figure 8 shows the pie-chart representation of the total traffic signal volume counts data recorded during the Q1 of 2020, i.e., traffic signal volume count data from January to April 2020. The representation shows that nearly 20 billion of vehicles crossed the traffic signals per month in the Q1 of 2020.

Figure 9 shows the graphical representation of traffic signal volume counts recorded on the respective regions of Victoria location, whereas BBN, Blackburn, BEN, Bendigo, BRI, Brighton, CA1, Carlton 1, CA2, Carlton 2, CRN, Croydon, DIO, Dialin/Dialout, DON, Doncaster, ES2, Essendon 2, ESS, Essendon, FR2, Frankston 2, FRA, Frankston, FT1, Footscray 1, FT2, Footscray 2, FT3, Footscray 3, GE2, Geelong2, GEE, Geelong, GLI, Glen Iris, GR2, Greensborough 2, GRE, Greensborough, KEW, Kew, MC1, Melbourne City 1, MC2, Melbourne City 2, MC3, Melbourne City 3, MEN, Mentone, MNP, Moonee Ponds, PR2, Preston 2, PRS, Preston, SK1, St Kilda 1, SK2, St Kilda 2, SP2, Springvale 2, SPR, Springvale, VI2, regional Victoria 2, VIC,

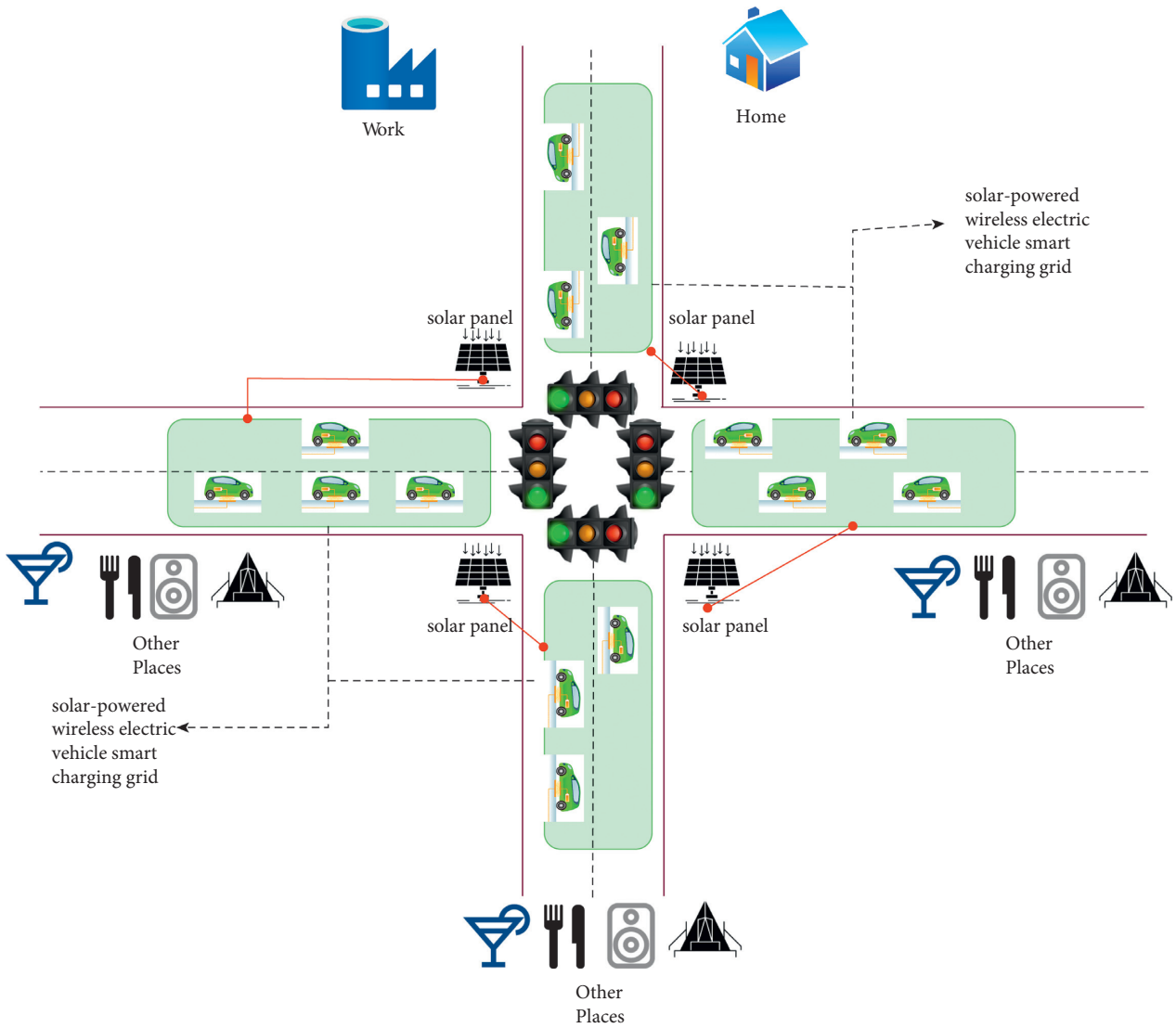

Figure 7: Schematic representation of solar-powered wireless EV-smart charging grid.

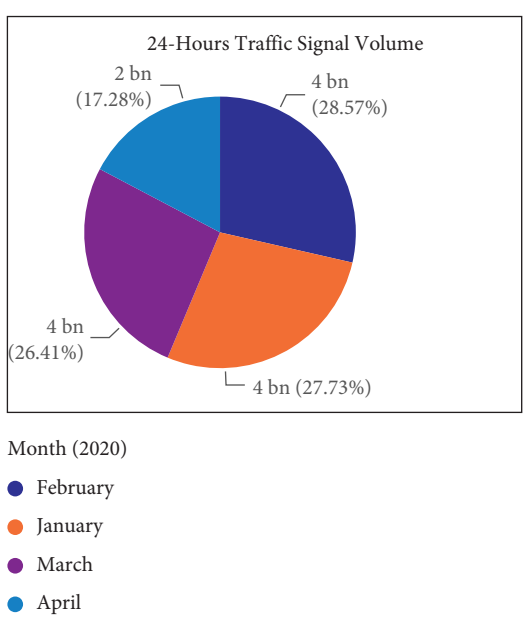

Figure 8: Pie-chart representation of 24-hours traffic signal volume data.

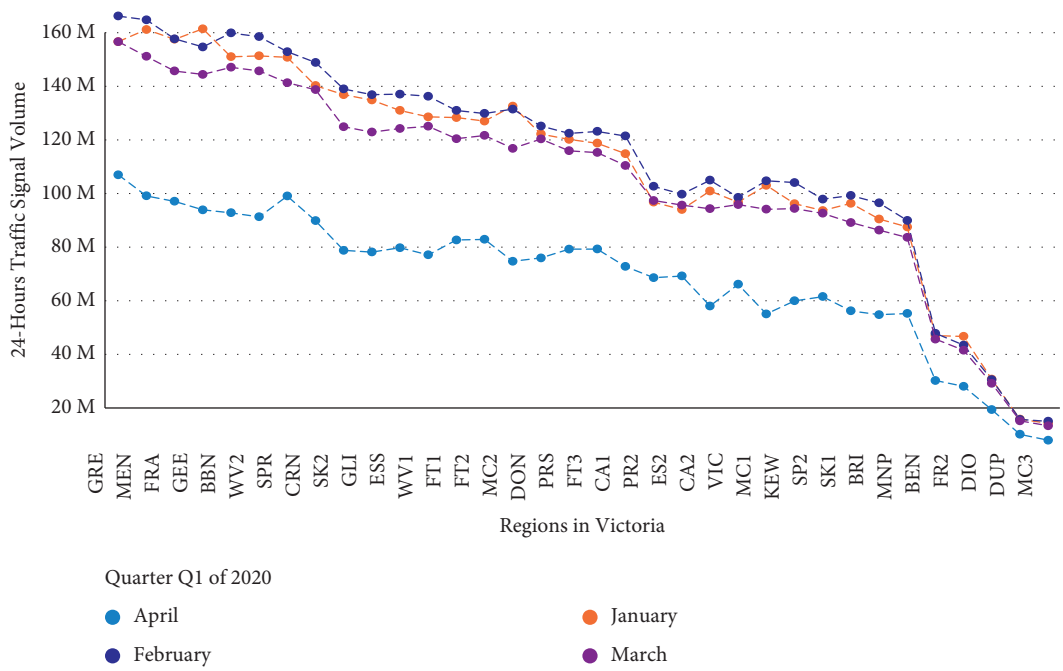

Figure 9: Twenty-four hours' traffic signal volume data by regions in Victoria during Q1 of 2020.

regional Victoria, WV1, Waverly 1, and WV2, Waverly 2. This analysis shows that passengers are spending long times on traffic signals based on the traffic signal volume records. In Figure 9, except few regions of Victoria, almost all the regions are experiencing a greater number of traffic signal volumes, which leads to long waiting hours in the traffic signals. The similar pattern can be expected on the EV usage as the growth of the EV usage is exponentially increasing. The proposed architecture of implementation of the solar-powered wireless EV-smart charging grids installed underneath the roadway of the traffic signal areas can be efficiently utilized on these kinds of use cases based on the historical traffic signal volume records alongside to the initial analysis of the EV usage patterns. In this manner, the proposed architecture improves urban planning. Initial installation cost of the wireless solar-powered EV charging smart grids may seem to be challenging; however, the overall usage is very effective which leads to the efficient utilization of the traffic signal waiting time and improves the passenger's or driver's overall transportation experience.

6. Conclusion

This study analyses the usage patterns of the EV trips that were recorded on the smart-grid smart-city EV trial data project which utilizes 20 EVs used by households and businesses. Also, the importance of NMF to elicit the latent usage patterns of the EV trips from the outputs of NMF is discussed. Alongside to this pattern analysis, impact of the pattern variations based on the EV's source and destination is analyzed to have a clear picture on how the variation in the patterns impacting the overall mobility. In addition, we proposed the architecture that explains the usage of implementing solar-powered wireless EV-smart charging grid installed underneath the roadway of the traffic signal area to mitigate the problems in traffic signal long waiting time in relation to the obtained usage patterns. This implementation also helps to encourage the use of a greater number of EVs in the near future which leads to the development of efficient and sustainable transportation to the mankind.

Data Availability

The datasets used in the study are openly available to the readers. Readers can access EV usage data and traffic signal volume count data used in this paper at https://data.gov.au/data/dataset/smart-grid-smart-city-electric-vehicle-trial-data and https://discover.data.vic.gov.au/dataset/traffic-signal-volume-data.

Conflicts of Interest

The authors declare that there are no conflicts of interest regarding the publication of this paper.

Acknowledgments

This research was supported by the National Research Foundation of Korea. Grant was funded by Korean Government (MSIP, South Korea) (no. 2020R1C1C1007127).

References

[1] C. Liu and L. Ke, "Cloud assisted Internet of things intelligent transportation system and the traffic control system in the smart city," *Journal of Control and Decision*, 2022.

[2] A. Lamssaggad, N. Benamar, A. S. Hafid, and M. Msahli, "A survey on the current security landscape of intelligent transportation systems," *IEEE Access*, vol. 9, pp. 9180–9208, 2021.

[3] A. Mohandu and M. Kubendiran, "Survey on big data techniques in intelligent transportation system (ITS)," *Materials Today Proceedings*, vol. 47, pp. 8–17, 2021.

[4] A. Balasubramaniam, A. Paul, W.-H. Hong, H. C. Seo, and J. H. Kim, "Comparative analysis of intelligent transportation systems for sustainable environment in Smart Cities," *Sustainability*, vol. 9, no. 7, pp. 1–12, 2017.

[5] A. Balasubramaniam, M. J. J. Gul, V. G. Menon, and A. Paul, "Blockchain for intelligent transport system," *IETE Technical Review*, vol. 38, no. 4, pp. 438–449, 2020.

[6] E. Stawiarska and P. Sobczak, "The impact of intelligent transportation system implementations on the sustainable growth of passenger transport in EU regions," *Sustainability*, vol. 10, no. 5, Article ID 1318, 2018.

[7] R. De la Torre, C. G. Corlu, J. Faulin, B. S. Onggo, and A. A. Juan, "Simulation, optimization, and machine learning in sustainable transportation systems: models and applications," *Sustainability*, vol. 13, no. 3, Article ID 1551, 2021.

[8] A. M. Farid, A. Viswanath, R. Al-Junaibi, D. Allan, and T. J. T. Van der Wardt, "Electric vehicle integration into road transportation, intelligent transportation, and electric power systems: an abu dhabi case study," *Smart Cities*, vol. 4, no. 3, pp. 1039–1057, 2021.

[9] Z. Bi, T. Kan, C. C. Mi, Y. Zhang, Z. Zhao, and G. A. Keoleian, "A review of wireless power transfer for electric vehicles: prospects to enhance sustainable mobility," *Applied Energy*, vol. 179, pp. 413–425, 2016.

[10] A. Poullikkas, "Sustainable options for electric vehicle technologies," *Renewable and Sustainable Energy Reviews*, vol. 41, pp. 1277–1287, 2015.

[11] S. Mehar, S. Zeadally, G. Remy, and S. M. Senouci, "Sustainable transportation management system for a fleet of electric vehicles," *IEEE Transactions on Intelligent Transportation Systems*, vol. 16, no. 3, pp. 1401–1414, 2015.

[12] S. Deb, K. Kalita, and P. Mahanta, "Review of impact of electric vehicle charging station on the power grid," in *Proceedings of the IEEE International Conference on Technological Advancements in Power and Energy: Exploring Energy Solutions for an Intelligent Power Grid, TAP Energy*, vol. 1, IEEE, Kollam, India, June 2018.

[13] "Worldwide number of electric cars. statista," 2022, https://www.statista.com/statistics/270603/worldwide-number-of-hybrid-and-electric-vehicles-since-2009/ accessed on.

[14] S. Neelakandan, M. A. Berlin, S. Tripathi, V. B. Devi, I. Bhardwaj, and N. Arulkumar, "IoT-based traffic prediction and traffic signal control system for smart city," *Soft Computing*, vol. 25, no. 18, 2021.

[15] K.-F. Chu, A. Y. S. Lam, and V. O. K. Li, "Traffic signal control using end-to-end off-policy deep reinforcement learning," *IEEE Transactions on Intelligent Transportation Systems*, pp. 1–12, 2021.

[16] S. Ghanadbashi and F. Golpayegani, "An ontology-based intelligent traffic signal control model," in *Proceedings of the IEEE Conference on Intelligent Transportation Systems, ITSC*, Indianapolis, IN, USA, October 2021.

[17] J. Vendrow, J. Haddock, E. Rebrova, and D. Needell, "On a guided nonnegative matrix factorization," in *Proceedings of the IEEE International Conference on Acoustics, Speech and Signal Processing*, IEEE, Toronto, Canada, May 2021.

[18] A. Balasubramaniam, T. Balasubramaniam, R. Jeyaraj, A. Paul, and R. Nayak, "Nonnegative matrix factorization to understand spatio-temporal traffic pattern variations during COVID-19: a case study, Communications in Computer and Information Science," in *Data Mining. AusDM Communications in Computer and Information Science*, Y. Xu, Ed., vol. 1504, pp. 223–234, Springer, Berlin, Germany, 2021.

[19] T. Balasubramaniam, R. Nayak, K. Luong, and M. A. Bashar, "Identifying Covid-19 misinformation tweets and learning their spatio-temporal topic dynamics using Nonnegative Coupled Matrix Tensor Factorization," *Social Network Analysis and Mining*, vol. 11, no. 1, p. 57, 2021.

[20] A. Balasubramaniam, A. Paul, and F. Afghah, "Combined dense urban traffic surveillance and principal component analysis for intelligent transportation systems," in *Proceedings of the IEEE Region 10 Annual International Conference, TENCON*, Kochi, India, December 2019.

[21] "Smart-grid smart-city electric vehicle trial data - dataset - data.gov.au," 2022, https://data.gov.au/data/dataset/smart-grid-smart-city-electric-vehicle-trial-data accessed on.

[22] "Smart-grid smart-city electric vehicle trial data - electric vehicle trial data dictionary - data.gov.au," 2022, https://data.gov.au/data/dataset/smart-grid-smart-city-electric-vehicle-trial-data/resource/b8adbdda-b4f2-4f1b-895d-f585477200af accessed on.

[23] Z. Liu, Q. Wu, L. Christensen, A. Rautiainen, and Y. Xue, "Driving pattern analysis of Nordic region based on National Travel Surveys for electric vehicle integration," *Journal of Modern Power Systems and Clean Energy*, vol. 3, no. 2, pp. 180–189, 2015.

[24] S. Asadi, M. Nilashi, M. Iranmanesh et al., "Drivers and barriers of electric vehicle usage in Malaysia: a DEMATEL approach," *Resources, Conservation and Recycling*, vol. 177, Article ID 10, 2021.

[25] S. Rahman, I. A. Khan, A. A. Khan, A. Mallik, and M. F. Nadeem, "Comprehensive review & impact analysis of integrating projected electric vehicle charging load to the existing low voltage distribution system," *Renewable and Sustainable Energy Reviews*, vol. 153, Article ID 111756, 2022.

[26] Y. Al-Wreikat, C. Serrano, and J. R. Sodré, "Effects of ambient temperature and trip characteristics on the energy consumption of an electric vehicle," *Energy*, vol. 238, Article ID 122028, 2022.

[27] J. Stiasny, T. Zufferey, G. Pareschi, D. Toffanin, G. Hug, and K. Boulouchos, "Sensitivity analysis of electric vehicle impact on low-voltage distribution grids," *Electric Power Systems Research*, vol. 191, Article ID 106696, 2020.

[28] "Traffic signal volume data - dataset - victorian government data directory," 08 Feb. 2022, https://discover.data.vic.gov.au/dataset/traffic-signal-volume-data accessed on.

[29] "Metadata capture & discovery tool," 08 Feb. 2022, http://data.vicroads.vic.gov.au/Metadata/Traffic_Signal_Volume_Data.html accessed on.

Hindawi
Mathematical Problems in Engineering
Volume 2022, Article ID 7739945, 13 pages
https://doi.org/10.1155/2022/7739945

Research Article

Multithreaded Multiswarm Model for Intelligent Economic Prosumer Load Dispatch for Battery Supported DC Microgrid

C. R. Sarin,[1] **Geetha Mani**,[1] **Albert Alexander Stonier**,[2] **M. Arivarasu**,[3] **Ravi Samikannu**,[4] **and Srinivasan Murugesan**[2]

[1]*School of Electrical Engineering, Vellore Institute of Technology, Vellore, Tamil Nadu, India*
[2]*Department of Electrical and Electronics Engineering, Kongu Engineering College, Perundurai, Tamil Nadu, India*
[3]*Centre for Innovative Manufacturing and Research, Vellore Institute of Technology, Vellore, Tamil Nadu, India*
[4]*Department of Electrical Computer and Telecommunications Engineering, Botswana International University of Science and Technology, Palapye, Botswana*

Correspondence should be addressed to Geetha Mani; geetha.mani@vit.ac.in

Received 30 October 2021; Revised 2 February 2022; Accepted 16 February 2022; Published 21 March 2022

Academic Editor: Alessandro Lo Schiavo

Economic load dispatch should be given special care even when the primary responsibility of any demand response model is to provide a consistent supply to the load. Demand can be satisfied by the utility grid as well as self-sustaining user sources. If a user generates excess power after meeting demand, the user can pool it and transfer it to the grid or neighboring consumers. This is referred to as the prosumer model, in which the user serves as both a producer and a consumer. Furthermore, some of the surplus power may be stored in energy storage devices. A sophisticated mathematical model is required to estimate how much power should be generated, pooled, pulled from the grid, gathered from close users, supplied to nearby customers, and so on. This paper tries to present a smart economic load dispatch model for a demand response system that combines a multithreaded swarm model with a reward-based reinforcement system to assure optimal source selection and power flow management. To identify the optimum cost-effective power sharing model among a user, the grid, and neighboring users, the system uses particle swarm optimization (PSO) and artificial bee colony (ABC) optimization. Both models have benefits and drawbacks, and not all models work well with all data input. Using two models at the same time consumes a significant amount of time and computational power. As a consequence, for each data input, an upper bound confidante (UBC) model is used in parallel to select the best economical swarm model based on a semisupervised reinforcement model. A weighted Boruvka's algorithm based on transmission line cost and transmission loss is being used to construct an optimum economic power sharing model, which is backed by swarm models. The efficiency of each model is evaluated using the same data for both models, and error analysis is performed. It was discovered that each model performs differently for various data, and creating a reinforced multithreaded model helps to increase accuracy, reduce computing time, and improve efficiency.

1. Introduction

1.1. Background. In addition to delivering a consistent and high-quality supply, every power system model must be prepared to satisfy demand while expending the least amount of operational and capital resources. The task described above is termed as economical load dispatch [1]. Economic load dispatch is an inventory management technology in which the system chooses discrete combination energy sources from all accessible sources to achieve the lowest possible costs [2]. These challenges must be investigated in grid-connected microgrid models that comprise a diverse set of distributed energy sources (DESs) [3]. Depending on their socio-techno-economic restrictions, any residential, industrial, or commercial operator could utilize different energy sources [4]. Each source will have its own set of operating costs, capital expenditures, start-up delay, integration complexity, power-generating capacity, efficiency, pollution scale, operational lifetime, consumption time, dependability, and stability, to name a few [5]. Some

characteristics improve responsiveness, while others reduce system quality, performance, and economy. All these factors should be addressed by an intelligent demand response system without sacrificing steady supply to demand [6, 7]. In traditional systems, electricity flows unidirectional from a main source to the load. However, if the system supports DES, even though the user is generally a load point, it may occasionally function as a source point. When a user's power output exceeds demand, the energy can be pooled and sold to the grid. As a result, a diverse set of sources and loads will be dispersed over the microgrid, with heterogeneous multidirectional power flow between them [8, 9]. In order to make a combinatorial optimal decision among all of these attributes, a sophisticated mathematical model is necessary [10]. The DRS aims to identify the optimal solution by evaluating the fitness of these attributes by emphasizing positive features while minimizing negative traits within a reasonable range of alternatives.

1.2. Literature Review. Wen et al. examined the state of DES research in three areas: applications, assessments, and regional support measures [11]. They also analyzed the current status of DES approaches focusing on a number of variables such as energy, environment, society, and economy. The prior study offers information on the factors that impact DES. Tolmasquim et al. investigated electrical distributor techniques in the context of distributed energy resources, including SWOT assessments for internal and external electricity distributors in the DES distribution scenario [12]. This research examines the advantages and disadvantages of DES in detail. Wolsink focused on the sociopolitical layer for societal acceptance of DES, which combines high DES dispersion in intelligent microgrids to produce polycentricity rather than hierarchy [13]. This research contributes to the qualitative modeling of DRS based on the influence of consumer interactions on power systems. After determining the qualitative and quantitative properties of distributed energy sources, demand response models based on these inputs are established. McIlwaine et al. examined global electrical market trends, which include a majority of DES, as well as a global evaluation of energy storage, with a focus on power quality services at the distribution level [14]. Ehsan and Yang discussed active distribution network planning as well as distribution network planning in general [15]. Iqbal et al. used a nonlinear programming technique to model a DC microgrid system with peer-to-peer sharing, which allows users to share surplus energy from distributed energy resources with minimal system losses, including distribution and conversion losses, in comparison to the traditional factory-warehouse transportation method [16]. Zeng et al. presented a state-of-charge (SoC) dynamic balancing control approach for DES in DC microgrids that takes into account energy storage capacity disparity to achieve SoC balancing [17]. The aforementioned publications provide information on demand response strategies. The next step is to figure out how to put this concept into action.

Ramadhani et al. reviewed the most up-to-date load flow methodologies for DES in great detail, including recommendations for the best modeling methodology for distribution networks with PV generating and EV charging [18]. Ullah et al. investigated the advantages and disadvantages of various integration approaches centered on interconnection challenges and opportunities for DC microgrids [19]. Holari et al. constructed a hybrid AC/DC microgrid system with variable demand and unknown characteristics in order to provide a coordinated performance strategy for power electronic converters in grid-connected and islanding operational scenarios for hybrid microgrid power management [20]. Liaquat et al. examines into a multitude of dispatch challenges as well as the nature of the objective functions in consideration. The study also includes recommendations on demand management problems as well as the underlying constraints associated with each optimization function [21]. Luna et al. showcased an energy management system for coordinating distributed household prosumer activities [22]. Zia et al. proposed a case study for a standalone marine microgrid system as well as a paradigm for smart demand management [23]. Ali et al. offered "The Day Ahead Shifting" approach for cost and peak load optimization on the demand side [24]. Iqbal et al. outlines an effective home energy management system for residential clients in research, which allows them to properly organize demand-responsive appliances in the context of local solar and energy storage systems [25]. Bhamidi and Sivasubramani presented the framework for a two-stage optimization model for smart home renewable energy resources and battery integration, as well as the association of prosumer-based energy management [26].

The two preceding articles provide technical information for developing a load flow analysis within a DC microgrid. The next phase is to provide a framework for power management optimization. Mbuwir et al. optimized the power exchange between a microgrid and utility grid using the Jacobi-alternating direction multiplier approach, which assists in congestion management by breaking down the optimization problem into subproblems that are addressed locally and in parallel using fitted Q iteration [27]. Gunantara conducted a thorough examination of multiobjective optimization methods and applications [28]. Molzahn et al. focused research on distributed algorithms and their applications in optimized power system control [29]. Fan et al. provided a thorough and realistic assessment of recent developments in bioinspired algorithms, bioinspired swarm intelligence algorithms, bioinspired ecological algorithms, and multiobjective bioinspired algorithms [30]. The above three publications provide guidance for the application of bioinspired swarm intelligence in power system challenges. Chaudhari utilized ant colony optimization (ACO), particle swarm optimization (PSO), artificial bee colony (ABC), firefly algorithm (FA), and genetic algorithm (GA) to solve the travelling salesman problem, and provided an overview of the performance of the various algorithms using some standard benchmarks [31]. Shareef and Srinivasa Rao shown the combination of two swarming algorithms, ABC and FA, to improve the

performance, and this hybrid algorithm is to regulate variables that are adjusted to get the best outcomes [32].

1.3. Motivation. The responsibility of a demand management system is to ensure uninterrupted power supply to the load while also taking into account heterogeneous social-techno-economic conditions. Distributed energy sources of diverse capacity, its type, and manufacturer are used in modern microgrid models. Furthermore, different sources may experience a delay in integrating with the grid due to technological hurdles, and they have a temporal limitation on how long they may be used. Each source will produce varying levels of pollution and have varying environmental implications. Due to the operational characteristics of the sources and coupling transience, the system will encounter certain dynamic disturbances that will influence the power quality. Every source needs a certain amount of upfront investment as well as ongoing operational costs. The operational and capital investment in the electric grid has a substantial influence as well. The impact of these sources on the overall quality of the power system is assessed using a variety of socio-techno-economic factors. As a result, DRS cannot expect the sources to behave in the homogeneous way when modeling demand responses.

Because energy networks are typically designed to stave off peak demand, the aggregate capacity of installed sources is always substantially greater than the average demand. In the significant majority of situations, only a modest portion of the total installed capacity sources is required to fulfill demand. As previously stated, the DRS need to use sophisticated mathematical techniques to select the best sources from among all those accessible. Transmission line characteristics, particularly transmission loss and transmission cost, should be given further consideration when constructing an optimal load flow analysis. In addition to the fundamental qualities, a prosumer model may be layered on top of the previously stated models. A prosumer is a person who consumes as well as generates energy. Extra energy generated by a user can be pooled and shared with other users or the grid. When energy is pulled from the nearest accessible source, transmission loss is reduced, resulting in a more cost-effective and energy-efficient system. Hence, the DRS should be built to handle all of these aspects and make the best combinatorial decision possible between the socio-techno-economic factors mentioned above.

The most adaptable approach for dealing with such a challenge is to combine bioinspired algorithms with a range of mathematical techniques. As previously stated, this paper supports the use of multiple optimization models in parallel threads. This research employs the artificial bee colony (ABC) and particle swarm optimization (PSO) methods. Every method will have its own set of benefits and drawbacks. PSO is significantly more profitable when there are multiple local optimum models to choose from, the global best is less desirable, or convergence is delayed. PSO, on the other hand, may fail if the preliminary parameters are mistakenly inputted or if there is a high-dimensional search space. The ABC has several advantages, including fast convergence, cognitive speed, and flexibility, but it can also lead to premature convergence or erroneous global best selection. As a result, deciding on the optimal strategy is a complex process and a reward-penalty ranking system-assisted reinforcement learning model that may be used to distinguish between the techniques. Each optimization strategy is assessed using reinforcement learning based on the reward - penalty contributions of each source/component. The upper confidence bound method is used to rank components with a balanced exploration-exploitation ratio.

1.4. Contributions. The main objective of this paper is to present a smart economic load dispatch model for a demand response system that combines a multithreaded swarm model with a reward-based reinforcement model to assure optimal source selection and power flow management. The swarm models employed in the study are PSO and ABC, which run in parallel and independently. The swarm model is used in two phases in two applications: economic modeling and optimum source allocation. The benefits and limitations of each model vary, as do the computer processing power and time. Different optimization techniques may demonstrate varying efficiency for different factors and operating ranges. Itis a waste of time and computing resources to run all of the models. Hence, only one model is chosen at a time using a semisupervised reinforcement learning approach. An upper confidence bound (UCB) is used to rate each approach in a reward-penalty scenario. Each method is evaluated after each outcome computation, and the data are submitted to UCB. Time and iterations are used as performance criteria to evaluate the models. The last phase comprises a weighted Boruvka model for optimal power flow analysis. The boundaries, constraints, and equalities will be built using the prosumer microgrid model, which will include the following features:

(1) A consumer may only use the main utility grid to meet their needs

(2) A user may be separated from the utility grid if they are capable of satisfying their own demand using their own resources. Swarm models will aid in the choice of the appropriate providers from all available sources in such scenarios.

(3) Users with the ability to generate more energy than their demand can trade it to the utility grid or nearby users. Adding more power to the grid through a prosumer model has numerous benefits. There are three options for prosumers.

   (a) The user can sell their excess power to the grid in exchange for a monetary reward for each unit they provide. Swarm models can be used to create a monetization scheme as well as trade of ratio.

   (b) There is also a supplement option, in which the user can pool additional energy into the grid or other users and then take it back whenever they need it for free or at a modest compensatory cost.

Both a monetization and a trading strategy can be created using swarm models.

(c) Many users may have batteries installed in order to store energy for future usage. The surplus energy may be used to charge the battery or pool to the grid. Even though the user has more power, if it is more cost effective, the user can utilize electricity from the grid while conserving his own. Swarm models are used to assess how much power is shared and to simulate the economics of sharing.

The swarm model will aid in source selection as well as the trading ratio between consumers and producers, depending on socio-techno-economic limitations.

2. Adaptive Multiswarm Economic Demand Response Model

This study aims to develop an intelligent demand response model based on a multithreaded swarm model and an exploitation-exploration model. Figure 1 shows a block diagram of the entire model. The architecture of the system is divided into two segments. The first layer has two elements. One is an edge computing hardware model that comprises an energy monitoring circuit to track energy consumption and generation. As an energy monitoring circuit, a potential divider supported a ZMPT101B DC voltage sensor and a MAX471 based current sensor that are combined with an MKL25Z128VLK4 MCU. The second element is a centralized data processing unit (CDPU) made up of a 1 GHz BCM2835 single-core CPU with 512 MB RAM that serves as the system's central hub and is linked to the edge controller through WPWAN. For ease of implementation, the data are acquired from a real-time environment, but the load scheduling is carried out by manual switching. The system will keep track of each user's energy output and consumption. The data are transmitted to a central database for further analysis. The second layer is the software layer, which contains all of the mathematical models as well as their code. The second layer is made possible by the CDPU itself. Multiple swarm models, UBC, and Boruvka analysis are used in the software layer at various phases. The entire presentation is divided into four blocks. UBC will be able to operate only if there are enough readily available inputs for modeling. As a consequence, the system will only use UBC after the first six iterations as indicated in the previous paragraph.

Computational Block I - Power system models: the power system constraints, limits, and objective function are all set up in this block. There are four subblocks in this block. For an ith user, P_L^i is the load demand, P_{SG}^i is the solar generation, P_B^i is the battery supply, P_{DG}^i is the generation from diesel generator, P_W^i is the generation from wind, P_{MS}^i is the generation from miscellaneous units, P_{UG}^i is the ith user consumption from utility grid, and P_X^j is the generation from j^{th} user so that j can be varied for each user except $j = i$, and x is the type of source. To begin, the system makes certain that the total supply constantly exceeds the load. To do this, four options are available.

Sub-block I Case I: as seen in equation (1), all power is drawn from the user's own sources if they are sufficient. If the user's demand is not met by their own sources, the main grid delivers all of the power, as shown in equation (2).

$$P_L^i \leq \left(P_{SG}^i + P_B^i + P_{DG}^i + P_W^i + P_{MG}^i\right), \tag{1}$$

$$P_L^i \leq \left(P_{UG}^i\right). \tag{2}$$

Sub-block I Case II: as previously stated, under some circumstances, some energy is pulled from the utility grid and some from local sources linked to the utility grid. The percentage share of each source is calculated using a swarm optimization approach based on economic and transmission network factors. The swarm approach attempts to reduce total power sharing while lowering overall costs. Equations (3)–(5) provide the boundaries and constraints for power sharing where W represents the weight of each source, while C represents the cost of each share.

$$P_L^i \leq \left(W_{SG} * P_{SG}^i + W_B * P_B^i + W_{DG} * P_{DG}^i + W_W * P_W^i + W_{MG} * P_{MG}^i + W_{UG} * P_{UG}^i + W_X * P_X^{I+N}\right), \tag{3}$$

$$\left(C_{SG} + C_B + C_{DG} + C_W + C_{MG} + C_{UG} + C_X^{I..N}\right) \Rightarrow \text{Min}, \tag{4}$$

$$P_L^i - \left(W_{SG} * P_{SG}^i + W_B * P_B^i + W_{DG} * P_{DG}^i + W_W * P_W^i + W_{MG} * P_{MG}^i + W_{UG} * P_{UG}^i + W_X * P_X^{I+N}\right) \Rightarrow \text{Min}. \tag{5}$$

Sub-block III Case III: even though a user is self-sufficient, if electricity is available at a reduced cost from the utility grid or nearby sources, the user may utilize it. This may also be used to store lower-cost grid energy or current power production from the user to the battery for later use when prices rise. The boundaries and constraints for power sharing are defined by equations (6)–(8) where W_{Ext} and W_{User} represent the grid and user power contributions, respectively, whereas C_{Ext} and C_{User} reflect the cost constraints of both the grid and the user.

$$P_L^i < \left(W_{Ext} * P_{Ext}^i + W_{\text{User}} * P_{\text{User}}^i\right), \tag{6}$$

$$C_{Ext} + C_{\text{User}} \Rightarrow \text{Min}, \tag{7}$$

$$P_L^i - \left(W_{Ext} * P_{Ext}^i + W_{\text{User}} * P_{\text{User}}^i\right) \Rightarrow \text{Min}. \tag{8}$$

Sub-Block IV Case IV: the user can offer their excess power to the grid/nearby users in return for a monetary benefit for each unit provided. Equations (9)–(12)

illustrate trading strategies and proportions based on technological and economic aspects. The system will seek to maintain user contribution weights X_i as low as possible, while keeping the user revenue Z_{OUT} as high as possible and the cost of power acquired from the grid, Z_{IN} as low as possible.

$$P_L^i < \left(X_{\mathrm{User}} * P_{\mathrm{User}}^i\right), \tag{9}$$

$$\begin{aligned} Z_{\mathrm{Out}} &\Rightarrow \mathrm{Max}, Z_{\mathrm{Intake}}, \\ &\Rightarrow \mathrm{Min}, \left(Z_{\mathrm{Out}} + Z_{\mathrm{Intake}}\right) \Rightarrow \mathrm{Min}, \end{aligned} \tag{10}$$

$$P_L^i - \left(X_{\mathrm{User}} * P_{\mathrm{User}}^i\right) \Rightarrow \mathrm{Min}, \tag{11}$$

$$\left(X_{\mathrm{Out}} * P_{\mathrm{out}}^i\right) \Rightarrow \mathrm{Max}, \tag{12}$$

whereas P_{out} determines the power pooled and P_{user} is local power drawn. Even though the system maximizes the cost of income to users, it will always try to reduce overall cost.

Computational Block II - Optimization: mathematical models of optimization systems are included in this section. Even when the identical data are fed into both swarm models, PSO and ABC, outcomes will differ. As a result, each block is considered as a separate sub-chapter, with only one chosen for implementation based on its performance.

Sub-block I PSO: the first input vector is set to the overall population. Optimization issues are now defined by suitable equality constraints, inequality constraints, and boundary problems. The cost function, loss factor, and objective function for each of the earlier cases have now been established. Using the aforementioned criteria, the fitness of each particle in terms of velocity and position is now evaluated. New values of the global best (G_{Best}) and local best (L_{Best}) are tested for each cycle. This approach is continued until the exit iteration criteria or the lowest cost are satisfied. The $\mathrm{G}_{\mathrm{Best}}$ is utilized as the output.

Sub-block II ABC: initially, input variables are specified in terms of the general population. As explained in the prior section, optimization problems are now given with proper constraints, boundary problems, and objective functions. The next two steps entail the creation of employer and out-looker bees, followed by a fitness evaluation based on food sampling at each level. Each cycle, new values for the global best (G_{Best}), and local best (L_{Best}) are evaluated. This process is repeated by new scout bees until the conditions for the lowest cost or exit iteration are met. The G_{Best} is taken as the output.

To begin, the system will use ABC and PSO to calculate the exchange of ratios between sources. The next phase will result in the optimum source combination based on economic factors. Based on this data, power flow analysis is performed using Boruvka load flow analysis.

Computational Block III - Optimal Power Flow: initially, each user's linkages to neighbors and the grid, as well as the grid architecture, are identified. Each transmission station is now weighted (K) based on maximum capacity and transmission line cost. Equation (13) explains the power equation, where U is the voltage and Y is the transmission line impedance.

$$P_i = K_{ij} * U_i \sum_{i,j}^{N} Y_{ij} * U_j. \tag{13}$$

The method is now repeated until the least loss path is identified by selecting the lightest weighted node for a user. This procedure is repeated until a user is connected to at least one other user or grid. The following step is to utilize UCB to determine the best swarm model.

Computational Block IV - UCB: after a number of iterations, this block is utilized to identify the best swarm optimization model. This is split down into sections.

Sub-block I: The models receive a credit or penalty based on the number of times their divergence between real and planned is less than 5%.

Sub-block II: we compute the average reward R_i, maximum range N, deviation delta, and the machine's confidence interval up to n rounds at a time, and range r_i is found as shown in equations (14) and (15)

$$r_i(n) = R_i \frac{(n)}{N_i}(n), \tag{14}$$

$$\Delta_i = \sqrt{r_i}. \tag{15}$$

Sub-block III: the machine with the maximum UCB is selected:

$$\left[r_i(n) - \Delta_i r_i(n) + \Delta_i\right] \Rightarrow \mathrm{SEL}. \tag{16}$$

3. Results and Discussions

A simulation framework is created to put the notion into action. A proteus design suite simulation is used to generate sample data. Some of the sample information comes from the real world and is fed into the simulation. Figure 2 shows a distribution system consisting of 20 homes each of whom is connected to one or more of their neighbors. Each user is connected to a battery, a solar photovoltaic (SPV), a diesel generator (DG), a microwind source (MWG), and different miscellaneous sources (MS) such as a natural gas turbine. There is also a direct or indirect link to the main grid (MG). The sample status of connected sources for a set of users is shown in Table 1. Each source has a maximum capacity of 1 kW.

As such, each user will have access to a variety of sources, and each user may connect to one or more sources at the same time. Analysis is performed based on this data. Table 2

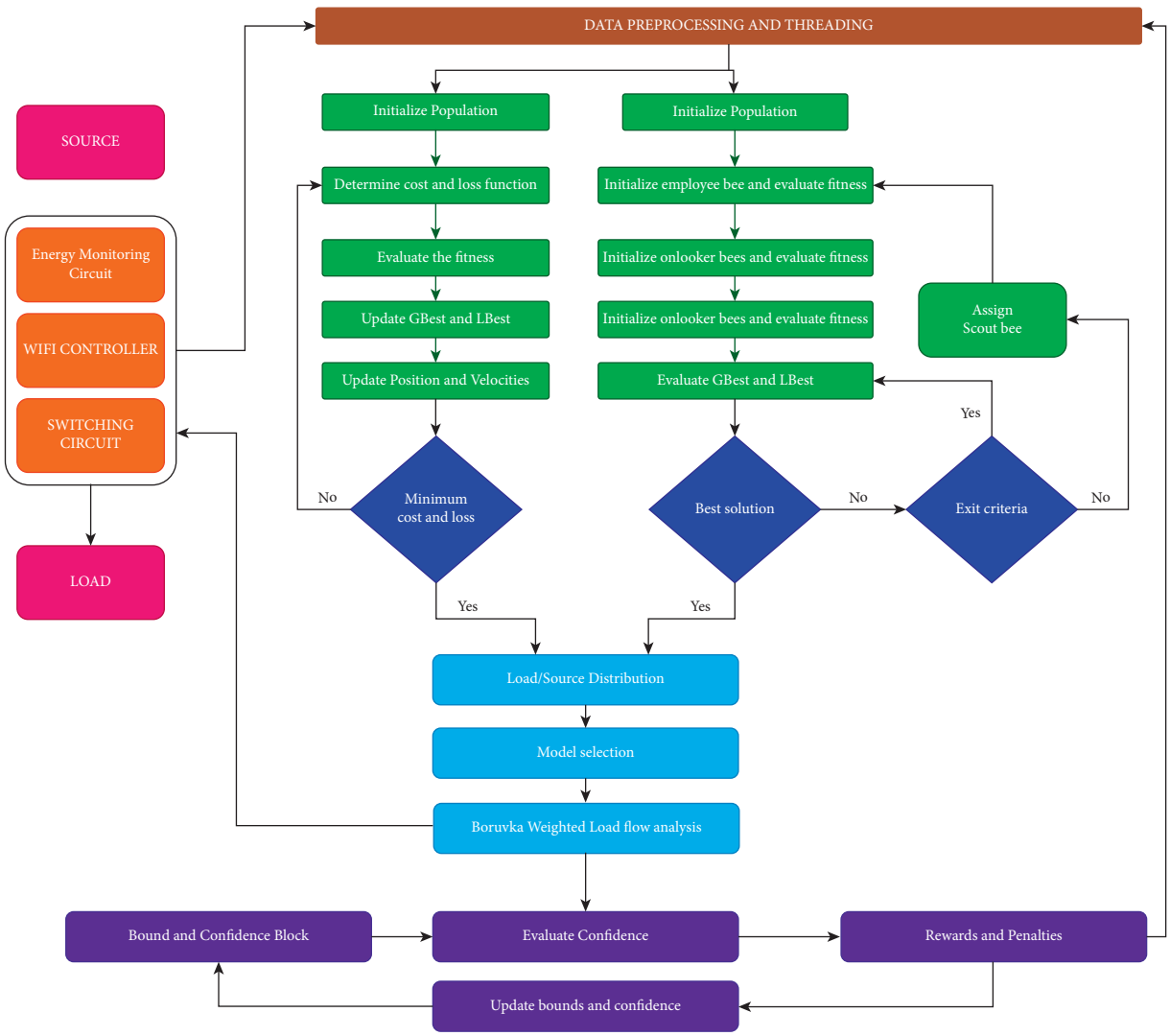

Figure 1: Architecture of multiswarm model for an intelligent economic load dispatch.

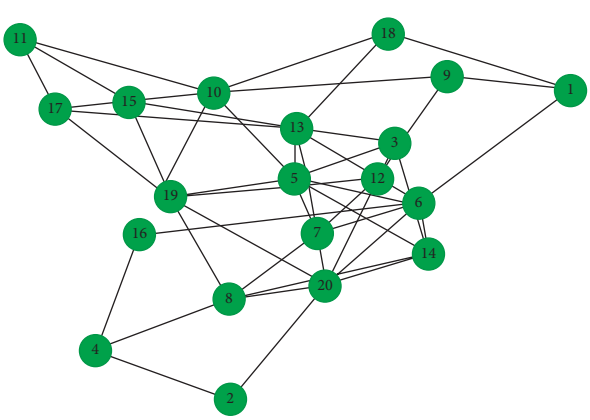

Figure 2: Sample grid used for simulation.

Table 1: Sample source connection status of 10 users.

Users	Battery	SG	DG	MWG	MG
1	No	No	Yes	No	Yes
2	Yes	Yes	No	Yes	No
3	Yes	Yes	Yes	No	No
4	Yes	No	Yes	No	Yes
5	No	No	No	No	Yes
6	Yes	Yes	No	No	Yes
7	No	No	No	No	Yes
8	Yes	No	No	No	No
9	Yes	No	No	Yes	Yes
10	No	Yes	Yes	Yes	No

Note. *Yes: source is connected; No: source is not connected.

displays the example source generation status of five users whose load is smaller than the production capacity. Table 3 displays the example source generation status of five users whose load exceeds production capacity.

The next step is to calculate transmission line factors. Each transmission line has its own transmission loss, which is denoted by a per unit value ranging from 0 to 1. Table 4 shows the sample transmission line per unit loss for three different sample consumers across five different interconnections.

Table 2: Sample source generation status of 5 users - demand less than generation.

Users	Battery (Watts)	SG (Watts)	DG (Watts)	MWG (Watts)	MS (Watts)	Load (Watts)
1	0	16	257	0	44	321.18
2	0	0	889	0	0	908.82
3	228	710	0	844	12	1850.91
4	700	0	523	0	0	1263.81
5	155	0	827	562	902	2500.02

Table 3: Sample source generation status of 5 users - demand greater than generation.

Users	Battery (Watts)	SG (Watts)	DG (Watts)	MWG (Watts)	MS (Watts)	Load (Watts)
1	0	0	334	573	342	1279
2	0	747	0	151	0	1385
3	0	14	476	0	0	1203.84
4	0	105	637	0	0	1556.1
5	732	761	0	681	0	1878.24

Table 4: Transmission loss parameters between nodes.

Node	Transmission loss
1 to 12	0.154
1 to 14	0.486
1 to 17	0.193
2 to 7	0.989
3 to 18	0.906

The next step is to design the cost factor for transmission between the users. For the transmission between user, for each side, the cost of transmission will be different. This is due to the fact that a user may sell energy at a separate price while purchasing energy at a different price. Bidirectional cost variations for five transmission elements are shown in Table 5. Table 6 depicts the cost of pooling as determined by each user over a 24-hour period, whereas Table 7 depicts the individual cost factor split of five users during a defined time period. As a result, each user (HG), node, and grid (MG) will have a unique price indexing, and the system will have to select the optimal economic model from among all potential ones.

In the following stage, the optimization method must be implemented. The first step is to establish how much power will be pulled from the grid and how much from local users. This was done first for ABC and then for PSO. UBC will use this information later to choose the best approaches. For preliminary purposes, the load is adjusted from no load to full load. For home grid (HG) and main grid (MG), the performance of each approach across these values is determined by calculation time and iterations. Table 8 depicts the performance analysis of the swarm models as the load step varies for 100 W. It has been discovered that when it comes to low load, PSO has demonstrated the best performance; thus, G_{Best} is a suitable choice, whereas lower load may utilize ABC. However, this is not always the case; thus, a UCB is used at this stage to select the best model.

The number of iterations has an effect on the computations as well. As a result, the influence of iterations is discovered in the following step. Figure 3 shows the effects of iterations in terms of RMSE, whereas Figure 4 shows the consequences of iterations in terms of time. It should be emphasized that as the number of iterations rises, so does the accuracy. However, this is not a linear deviation, and if required, an early stop is possible, as inaccuracy beyond a certain number of repetitions is less effective. When it comes to iterations and time, though, it resembles a stepped linear curve.

After assessing the impact of iterations and time, the exit criteria were defined. As shown in Table 9, after 100 iterations of the PSO technique, the optimal solution shifts from local to global best. Hence, it is set as the exit point.

At this point, a comparison of PSO and ABC solution convergence might be considered. As previously stated, the optimal output is typically achieved in fewer than 200 iterations. Different techniques will indicate different fitness convergence in distinct ranges. As previously stated, ABC has a superior impact over PSO in a number of scenarios. This does not imply, however, that ABC is always the better choice. Figure 5 depicts the comparison of PSO and ABC solution convergence for three different cases for both methods.

So, once the cost functions and source status have been determined, the following step is to select a trading ratio between users and grid. The fixed cost (FC) and operating cost (OC) for both the home grid and the main grid, as well as the transmission line cost, have all been specified. It is expressed in a scale of 0 to 1. The cost of pooling is determined by the user and the main grid. After meeting his own needs, the user will constantly seek to contribute as much energy to the grid as feasible. The user will also make an effort to reduce supply while boosting cost. Table 10 depicts trade pooling for five users. The same procedure will be followed for nearby houses that will be replaced by the utility grid if the cost exceeds the grid's cost. Table 11 depicts grid pooling among individual houses while also taking transmission line characteristics into consideration.

Once the trade of ratio and percentage share of each user has been determined, the following stage is to locate the best sources. In most situations, the system will be built to satisfy peak demand, but because peak load occurs only for a

Table 5: Cost factors of transmission system between nodes.

Flow A	Cost	Flow B	Cost
1 to 12	0.202	12 to 1	0.323
1 to 14	0.709	14 to 1	0.554
1 to 17	0.054	17 to 2	0.302
2 to 7	0.604	7 to 3	0.96
3 to 18	0.199	18 to 4	0.175

Table 6: Cost of pooling of 5 users for a day.

Time	User 1	User 2	User 3	User 4	User 5
0–4	0.456	0.332	0.674	0.294	0.764
4–8	0.489	0.49	0.968	0.54	0.476
8–12	0.782	0.776	0.656	0.617	0.906
12–16	0.471	0.475	0.808	0.316	0.336
16–20	0.723	0.172	0.435	0.755	0.606
20–24	0.45	0.374	0.569	0.136	0.786

Table 7: Cost of pooling divisions of 5 users.

Users	Fixed cost	Operating cost	Transmission cost
User 1	0.054	0.141	0.251
User 2	0.02	0.219	0.092
User 3	0.112	0.163	0.029
User 4	0.027	0.14	0.373
User 5	0.17	0.171	0.232

Table 8: Compassion of ABC and PSO for a full load range.

Time	Load (W)	PSO				ABC				Best
		HG (W)	MG (W)	Time (m/s)	Total (W)	HG (W)	MG (W)	Time (m/s)	Total (W)	
1	10	6.72	6.96	531	13.68	12.33	0	88.25	12.33	ABC
2	20	14.77	9.21	522	23.98	18.07	3.19	74.66	21.26	ABC
3	25	20.25	10.72	314	30.97	24.42	4.11	75.03	28.53	ABC
4	40	26.67	14.56	307	41.23	41.05	2.53	80.6	43.58	PSO
5	50	39.9	14.22	314	54.12	45.23	8.72	86.4	53.95	ABC
6	60	37.29	30.26	310	67.55	52.51	9.71	90.7	62.22	ABC
7	75	50.25	26.25	314	76.5	64.95	18.88	86.8	83.83	PSO
8	90	57.71	41.37	317	99.08	57.34	36.95	82.3	94.29	ABC
9	100	69.45	38.76	310	108.21	64.12	45.61	87	109.73	PSO

Note. *HG: home grid; MG: main grid.

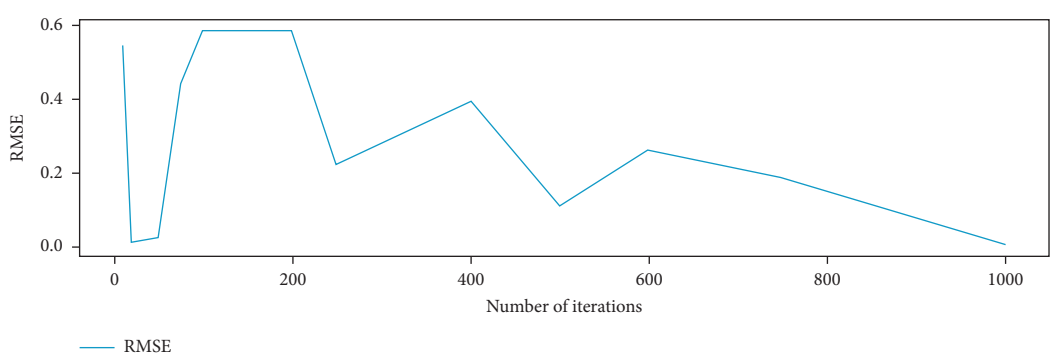

Figure 3: Effects of iterations in RMSE.

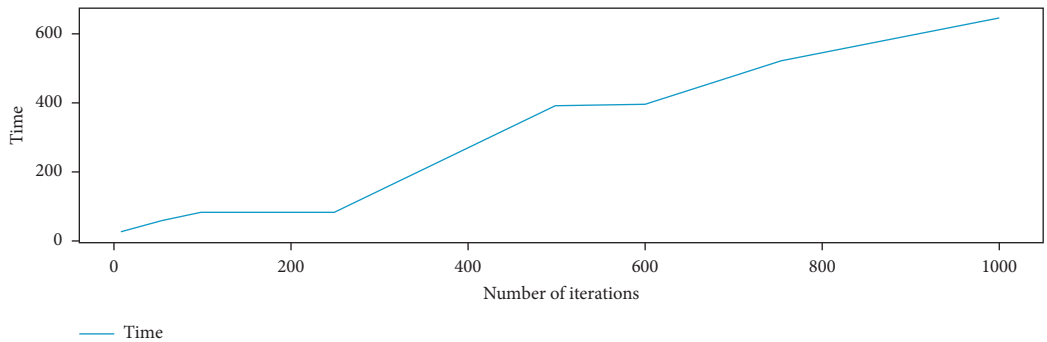

Figure 4: Effects of iterations in time.

Table 9: Drift from L_{Best} to G_{Best} for PSO.

Iterations	L_{Best}	G_{Best}
10	59.21	59.21
20	50.68	59.21
30	86.84	86.84
40	78.36	86.84
50	69.97	86.84
60	68.73	86.84
70	58.97	86.84
80	25.35	86.84
90	97.18	97.18
100	90.99	97.18

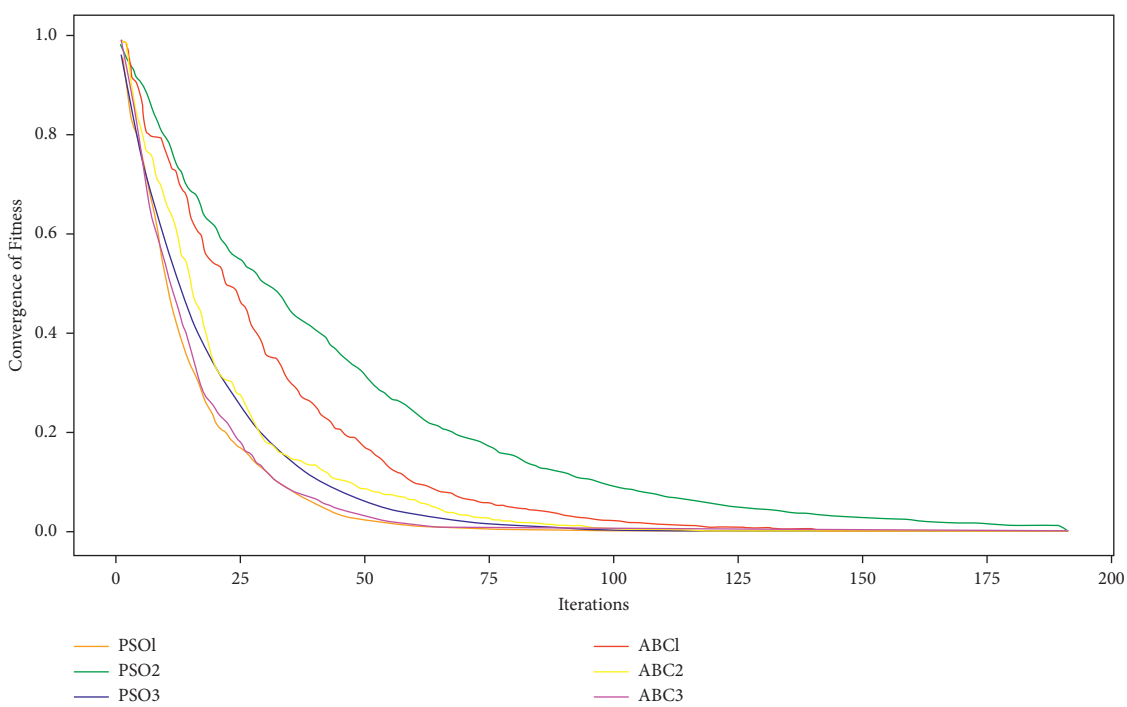

Figure 5: Comparison of PSO and ABC solution convergence.

portion of the day, alternative source combinations will be available to meet the need. Both PSO and ABC are being used at this time. Implementation involves two phases: bounding and nonbounding paradigms.

As long as power generation is fixed, boundary models are employed to calculate power. Solar and wind energy are unreliable, and additional power must be obtained through a grid connection as necessary. In this situation, an

Table 10: Grid pooling decision making with only main grid.

Users	Cost factors					Forecasted power (W)		Demand (W)	
	HG		TF	MG		MG	HG	Actual demand	Pooled power
	FC	OC		FC	OC				
User 1	0.98	0.82	0.41	0.80	0.20	52.78	85.8	145.49	138.58
User 2	0.84	0.90	0.98	0.26	0.56	61.99	99.88	171.58	161.87
User 3	0.68	0.54	0.10	0.37	0.28	51.99	90.16	170.23	142.15
User 4	0.74	0.40	0.02	0.41	0.51	65.34	51.28	125.94	116.62
User 5	0.76	0.54	0.31	0.31	0.74	39.92	85.37	137.81	125.29

Table 11: Grid pooling decision making with nearby users.

Users	Cost factors					Forecasted power (W)		Demand(W)	
	HG		TF	MG		MG	HG	Load	Pooled
	FC	OC		FC	OC				
User 1	0.744	0.475	0.649	1	0.516	0	61	67.1	61
User 2	0.737	0.133	0.193	0.729	0.991	45.65	87.67	136.11	133.32
User 3	0.743	0.54	0.557	0.054	0.817	100	18	114.35	118
User 4	0.384	0.005	0.06	0.977	0.325	81.67	67.88	160.61	149.55
User 5	0.269	0.68	0.298	0.031	0.505	100	59.75	160.54	159.75

Table 12: Source selection using PSO.

	Battery (WH)	SG (W)	DG (W)	MWG (W)	MS (W)	Total generation (W)	Total load (W)
User 1							
Generation	0	641	910	0	146	1697	1000
Cost factor	0.259	0.55	0.707	0.264	0.733	After optimization	
Final selection	0	0	910	0	146	1056	1000
User 2							
Generation	788	665	734	463	640	3290	2000
Cost factor	0.806	0.111	0.876	0.047	0.795	After optimization	
Final selection	788	0	734	0	640	2162	2000
User 3							
Generation	405	565	552	432	194	2148	1700
Cost factor	0.334	0.279	0.718	0.963	0.28	After optimization	
Final selection	405	565	552	0	194	1716	1700

*MS: miscellaneous sources.

Table 13: Comparison of PSO and ABC.

PSO	Battery 1 (WH)	Battery 2 (WH)	SG 1 (W)	SG 2 (W)	DG 1 (W)	DG 2 (W)	MWG 1 (W)	MWG 2 (W)	MS 1 (W)	MS 2 (W)	Total
	966	15	384	443	699	922	188	388	395	795	5195
	Total demand							2408.66 W			
	155.23	0.009	54.528	0	13.84	0	10.22	93.97	68.53	105.7	Demand 2456
	Time							257 millisecond			
ABC	Battery 1 (WH)	Battery 2 (WH)	SG 1 (W)	SG 2 (W)	DG 1 (W)	DG 2 (W)	Wind 1 (W)	Wind 2 (W)	MS 1 (W)	MS 2 (W)	Total
	966	15	384	443	699	922	188	388	395	795	5195
	Total demand							2729.0612 W			
	0	0	384	7.30	0	922	188	367.39	231.50	628.84	Demand 2456
	Time							167 millisecond			

*MS: miscellaneous sources.

Table 14: Selected nodes and transmission line factors.

From	To	TF
0	8	0.7
1	4	0.2
2	6	0.9
2	5	0.5
3	7	0.9
4	7	0.6
5	1	0.4
5	3	0.3
6	5	0.8
6	7	0.8
6	10	0.1
7	1	1
7	9	0.6
8	10	0.2
9	4	0.5
10	1	0.5

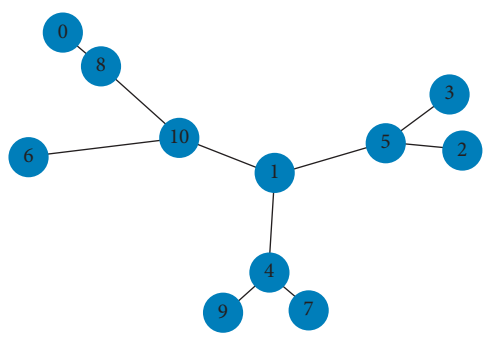

Figure 6: Optimal power flow between nodes.

Table 15: Selected nodes and transmission line factors.

ABC		PSO	
Rewards	Penalties	Rewards	Penalties
0.41	0.92	0.18	0.1
0.88	0.79	0.45	0.35
0.21	0.69	0.03	0.23
0.84	0.76	0.69	0.12
0.55	0.28	0.32	0.58
0.28	0.82	0.1	0.9
0.98	0.57	0.96	0.5
0.65	0.83	0.34	0.46

unbounded model is employed. Source selection using PSO is shown in Table 12. Table 13 compares the efficacy of PSO and ABC when it comes to selecting sources.

When the source optimization is complete, the power flow analysis is carried out using the specified sources and transmission line factors. Table 14 provides the nodes and transmission line factors that were chosen, whereas Figure 6 depicts the optimum power flow between sources.

The UBC is now being used to determine the optimal optimization model for the next iteration. UBC is used to assess each model's output in terms of both time and accuracy. As a result, the system will continually evaluate the results of each model. Whenever a new value arrives for execution, the UBC will choose the best model based on the incentives and penalties from previous stages. Table 15 shows example of each model's rewards and penalties,

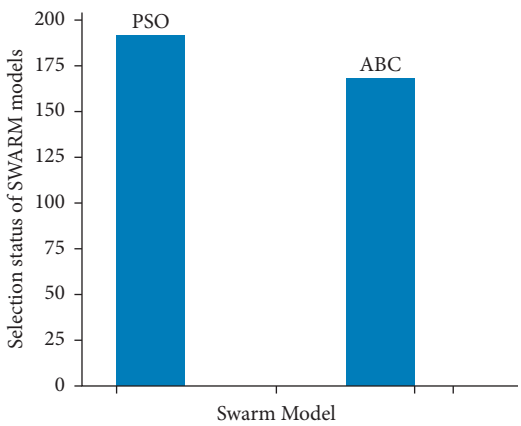

Figure 7: UBC selection of the swarm model.

and Figure 7 provides 360-instances of selections of the swarm model.

4. Conclusion

This work developed a smart economic load dispatch model for a demand response system by combining a multi-threaded swarm model with reward-based reinforcement learning. Particle swarm optimization and artificial bee colony (ABC) optimization methods were used to analyze users, the grid, and neighboring users in order to determine the most cost-effective power sharing model. An upper bound confident (UBC) model is used as a semisupervised reinforcement model for each input data point to choose the best swarm model. The weighted Boruvka's Algorithm is used to determine the optimal power flow depending on transmission line costs and transmission losses. Each model's efficiency is assessed using the identical data for both models, and an error analysis is carried out. RMSE is used to verify the effectiveness of the findings. When it comes to economic trade calculations, ABC is proven to have an advantage over PSO in the majority of cases. PSO is still more accurate for optimal power sharing. A multithreaded model with improved accuracy, processing time, and efficiency was constructed supported by UBC.

Data Availability

The grid data used to support the findings of this study are available from the corresponding author upon request.

Conflicts of Interest

The authors declare that they have no conflicts of interest.

Acknowledgments

The authors acknowledge and thank the Department of Science and Technology (Government of India) for sanctioning the research grant for the project titled "Design and Development of Solar Photovoltaic Assisted Microgrid Architecture with Improved Performance Parameters Intended for Rural Areas" (Ref. No. DST/TMD/CERI/RES/2020/32 (G) dated (03.06.2021) under TMD - W&CE scheme for completing this work.

References

[1] D. Rwegasira, I. B. Dhaou, A. Anagnostou et al., "A framework for load shedding and demand response in DC microgrid using multi agent system," in *Proceedings of the 2017 21st Conference of Open Innovations Association (FRUCT)*, November, 2017.

[2] X. Lu, K. Zhou, X. Zhang, and S. Yang, "A systematic review of supply and demand side optimal load scheduling in a smart grid environment," *Journal of Cleaner Production*, vol. 203, pp. 757–768, 2018.

[3] Y. Wang, Y. Huang, Y. Wang et al., "Energy management of smart micro-grid with response loads and distributed generation considering demand response," *Journal of Cleaner Production*, vol. 197, pp. 1069–1083, 2018.

[4] N. Good, K. A. Ellis, and P. Mancarella, "Demand response and the smart grid: review, analysis and classification of socio-techno-economic barriers and enablers," *Renewable and Sustainable Energy Reviews*, vol. 72, pp. 57–72, 2017.

[5] H. E. Li and L. Ü. Hongfang, "Research on optimal dispatching of multi-microgrid considering economy," *Power Generation Technology*, vol. 39, no. 5, pp. 397–404, 2018.

[6] Q.-V. Pham, M. Liyanage, N. Deepa et al., "Deep Learning for Intelligent Demand Response and Smart Grids: A Comprehensive Survey," 2021.

[7] Z. Zhao and A. L. Liu, "Intelligent demand response for electricity consumers: a multi-armed bandit game approach," in *Proceedings of the 2017 19th International Conference on Intelligent System Application to Power Systems (ISAP)*, September, 2017.

[8] B. Spasova, D. Kawamoto, and Y. Takefuji, "Energy exchange strategy for local energy markets with heterogenous renewable sources," in *Proceedings of the 2018 IEEE International Conference on Environment and Electrical Engineering and 2018 IEEE Industrial and Commercial Power Systems Europe (EEEIC/I&CPS Europe)*, June, 2018.

[9] Z. Li, M. Shahidehpour, A. Alabdulwahab, and Y. Al-Turki, "Valuation of distributed energy resources in active distribution networks," *The Electricity Journal*, vol. 32, no. 4, pp. 27–36, 2019.

[10] M. H. Amrollahi and S. M. T. Bathaee, "Techno-economic optimization of hybrid photovoltaic/wind generation together with energy storage system in a stand-alone micro-grid subjected to demand response," *Applied Energy*, vol. 202, pp. 66–77, 2017.

[11] Q. Wen, G. Liu, Z. Rao, and S. Liao, "Applications, evaluations and supportive strategies of distributed energy systems: a review," *Energy and Buildings*, vol. 225, Article ID 110314, 2020.

[12] M. T. Tolmasquim, P. M. A. Senra, A. R. Gouvêa, A. O. Pereira, A. C. Alves, and M. Moszkowicz, "Strategies of electricity distributors in the context of distributed energy resources diffusion," *Environmental Impact Assessment Review*, vol. 84, Article ID 106429, 2020.

[13] M. Wolsink, "Distributed energy systems as common goods: socio-political acceptance of renewables in intelligent microgrids," *Renewable and Sustainable Energy Reviews*, vol. 127, Article ID 109841, 2020.

[14] N. McIlwaine, A. M. Foley, D. J. Morrow et al., "A state-of-the-art techno-economic review of distributed and embedded

energy storage for energy systems," *Energy*, vol. 229, Article ID 120461, 2021.

[15] A. Ehsan and Q. Yang, "State-of-the-art techniques for modelling of uncertainties in active distribution network planning: a review," *Applied Energy*, vol. 239, pp. 1509–1523, 2019.

[16] S. Iqbal, M. Nasir, M. F. Zia, K. Riaz, H. Sajjad, and H. A. Khan, "A novel approach for system loss minimization in a peer-to-peer energy sharing community DC microgrid," *International Journal of Electrical Power & Energy Systems*, vol. 129, Article ID 106775, 2021.

[17] Y. Zeng, Q. Zhang, Y. Liu et al., "State-of-charge dynamic balancing strategy for distributed energy storage system in DC shipboard microgrid," *International Journal of Electrical Power & Energy Systems*, vol. 133, Article ID 107094, 2021.

[18] U. H. Ramadhani, M. Shepero, J. Munkhammar, J. Widén, and N. Etherden, "Review of probabilistic load flow approaches for power distribution systems with photovoltaic generation and electric vehicle charging," *International Journal of Electrical Power & Energy Systems*, vol. 120, Article ID 106003, 2020.

[19] S. Ullah, A. M. A. Haidar, P. Hoole, H. Zen, and T. Ahfock, "The current state of Distributed Renewable Generation, challenges of interconnection and opportunities for energy conversion based DC microgrids," *Journal of Cleaner Production*, vol. 273, Article ID 122777, 2020.

[20] Y.T. Holari, A. T. Seyed, and M. Mehrasa, "Power management using robust control strategy in hybrid microgrid for both grid-connected and islanding modes," *Journal of Energy Storage*, vol. 39, Article ID 102600, 2021.

[21] S. Liaquat, M. F. Zia, and M. Benbouzid, "Modeling and formulation of optimization problems for optimal scheduling of multi-generation and hybrid energy systems: review and recommendations," *Electronics*, vol. 10, no. 14, p. 1688, 2021.

[22] A. C. Luna, N. L. Diaz, M. Graells, J. C. Vasquez, and J. M. Guerrero, "Cooperative energy management for a cluster of households prosumers," *IEEE Transactions on Consumer Electronics*, vol. 62, no. 3, pp. 235–242, 2016.

[23] M. F. Zia, E. Elbouchikhi, and M. E. H. Benbouzid, "An energy management system for hybrid energy sources-based standalone marine microgrid," *IOP Conference Series: earth and Environmental Science*, vol. 322, no. 1, 2019.

[24] M. Ali, M. Fahad Zia, and M. Waqas Sundhu, "Demand side management proposed algorithm for cost and peak load optimization," in *Proceedings of the 2016 4th International Istanbul Smart Grid Congress and Fair (ICSG)*, April, 2016.

[25] M. M. Iqbal, M. F. Zia, K. Beddiar, and M. Benbouzid, "Optimal scheduling of grid transactive home demand responsive appliances using polar bear optimization algorithm," *IEEE Access*, vol. 8, Article ID 222285, 2020.

[26] L. Bhamidi and S. Sivasubramani, "Optimal sizing of smart home renewable energy resources and battery under prosumer-based energy management," *IEEE Systems Journal*, vol. 15, no. 1, pp. 105–113, 2020.

[27] B. V. Mbuwir, F. Spiessens, and G. Deconinck, "Distributed optimization for scheduling energy flows in community microgrids," *Electric Power Systems Research*, vol. 187, Article ID 106479, 2020.

[28] N. Gunantara, "A review of multi-objective optimization: methods and its applications," *Cogent Engineering*, vol. 5, no. 1, Article ID 1502242, 2018.

[29] D. K. Molzahn, F. Dorfler, H. Sandberg et al., "A survey of distributed optimization and control algorithms for electric power systems," *IEEE Transactions on Smart Grid*, vol. 8, no. 6, pp. 2941–2962, 2017.

[30] X. Fan, W. Sayers, S. Zhang, Z. Han, L. Ren, and H. Chizari, "Review and classification of bio-inspired algorithms and their applications," *Journal of Bionics Engineering*, vol. 17, no. 3, pp. 611–631, 2020.

[31] K. Chaudhari and A. Thakkar, "Travelling salesman problem: an empirical comparison between ACO, PSO, ABC, FA and GA," in *Emerging Research in Computing, Information, Communication and Applications*, pp. 397–405, Springer, Cham, Singapore, 2019.

[32] S. M. Shareef and R. Srinivasa Rao, "Optimal reactive power dispatch under unbalanced conditions using hybrid swarm intelligence," *Computers & Electrical Engineering*, vol. 69, pp. 183–193, 2018.

Hindawi
Mathematical Problems in Engineering
Volume 2022, Article ID 9246050, 11 pages
https://doi.org/10.1155/2022/9246050

Research Article

A Combined PWM and AEM-Based AC Voltage Controller for Resistive Loads

Geno Peter,[1] **K. Praghash**,[2] **Anli Sherine**,[3] **and Vivekananda Ganji**[4]

[1]*CRISD, School of Engineering and Technology, University of Technology Sarawak, Sibu, Malaysia*
[2]*Department of Electronics and Communication Engineering, Koneru Lakshmaiah Education Foundation, Guntur, India*
[3]*School of Computing and Creative Media, University of Technology Sarawak, Sibu, Malaysia*
[4]*Department of Electrical and Computer Engineering, Debre Tabor University, Debre Tabor, Ethiopia*

Correspondence should be addressed to Vivekananda Ganji; drvivek@bhu.edu.et

Received 7 January 2022; Accepted 20 January 2022; Published 14 February 2022

Academic Editor: Albert Alexander Stonier

AC voltage controller using PWM technique integrated with equal area digital modulation technique and connected to resistive loads is discussed in this paper. The proposed technique reduces the harmonics in the lower order significantly and improves the power factor compared to the existing conventional line commutated voltage controllers. The voltage and current waveforms are smoothened; therefore, a sinusoidal nature is achieved. The power factor is considerably improved at the low output voltage range when compared to existing methods. The capabilities of the proposed technique are computed mathematically and simulation results are compared with the existing methods.

1. Introduction

The voltage and current waveforms delivered to the customer should satisfy the different international standards, thereby ensuring quality power to different domestic and industrial applications. Conventional outage management practices in the distribution system are tedious and complex due to long time taken in locating the fault. Emerging smart technologies and various cloud services offered could be utilized and integrated into the power industry to enhance the overall process, especially in the fault monitoring and normalizing fields in the distribution system. The voltage waveform may experience a sag, swell, surges, and harmonics which causes the sinusoidal waveform to be distorted. AC voltage controllers with line frequency control are commonly used as it does not require any sophisticated commutation circuit for switching and stable control. It is used in various applications such as heater room control, induction motor starting, fan, and pump speed control [1]. The output voltage control is obtained by controlling the switching phase. Though line commutated AC voltage controllers are economic in design, it suffers from low power factor, thereby creating harmonics in the input current waveform [2]. Phase angle control (PAC) method has a poor input power factor, and the power flow is not continuous even for resistive loads. This method when used for electric drive speed control causes pulsating torque and harmonics on the input frequency. The power factor of such controllers is generally very low when the output voltage is decreased which is at a higher firing angle [3]. Force commutated AC voltage converters show a significant improvement in terms of efficiency as the input power factor is improved and the harmonics have reduced very significantly [4]. When compared to PAC method, control methods such as symmetric angle control (SAC) employing forced commutation produce better results in the form of reduced THD and improved PF during in AC-AC conversion. Using a new technique called area equalization method reduction in THD, complete elimination of lower order harmonics and power factor improvement can be achieved [5].

For the proposed technique, Matlab-Simulink Real-Time Target Windows (RTW) provided by Math Works Inc., is used for half-wave symmetry, multiple pulses, and direct PWM technique wherein several pulses per half cycle (m) are

generated under the integrated development environment [6]. Continuously variable output voltage is obtained by squaring off the actual output voltage with the target output voltage by using these pulses. For different values of m, the chopped output voltage waveform is analyzed for its harmonic content. For evaluation, the SAC method has been considered, and while doing so, the harmonics profile is found to be improved with the proposed digital strategy for certain values of m. The filtering requirements are reduced to a minimum as higher-order harmonics are pushed away from the fundamental frequency towards the sampling frequency for the entire output voltage range. Thus, improvement of THD and improved power factor at high-frequency chopping mode (more m) facilitate easy filtration at a lower cost [7].

In a power electronic circuit if the switches operate in a discontinuous fashion resulting in the generation of harmonics, lagging power factor occurs on the input side of the converter when the firing angle is delayed. The development in the power electronics design technology has paved the way to improve the efficiency of the converters by reducing the switching losses and the harmonics. AC line commutated controllers can be operated in chopped mode, hence providing a better output voltage control. The output voltage of the converter can be controlled by the duty cycle of the controlled switches as the output and input voltages are chopped into segments. Sinusoidal output voltage and current are obtained when using the PWM technique as the power factor is improved and the harmonics at lower order are reduced considerably. In electric drives, switching control method is used which heats up the induction motor due to the switching losses and harmonics present [8]. The power quality issue can occur when the renewable energy sources deliver power to the grid. Insulated gate bipolar junction transistor (IGBT)-based pulse with modulation technique is used to improve the power quality [14]. PWM techniques are used to eliminate the harmonics of lower order so that the output voltage and current waveform get improved. PWM technique can be implemented in power electronics converters using a square wave, sampled wave, and sinusoidal wave, and the designer makes the choice [15].

In the proposed method, the PWM technique is enhanced using the equal area criteria method. The actual output is made equal as the sampling time for both the output voltage and the pulse area is the same. The switching pulses are generated by the control circuit irrespective of the technique used to control the converter operation [16]. The simulated proposed method results are compared with the existing methods, and the main goal is to reduce the total harmonic distorting using the enhanced method. The power factor is considerably improved at the low output voltage range when compared to symmetric angle control (SAC) method using this technique.

1.1. Digital Control Strategies for AC Voltage Controllers

1.1.1. Symmetrical Angle Control. The single-phase circuit bidirectional topology of an AC voltage regulator is shown in Figure 1. It consists of a pair of metal oxide semiconductor field-effect transistors (MOSFET) connected in parallel and a diode in series so that the reverse voltage can be blocked [9]. Bidirectional power transfer prevents the problem of DC input current, and the topology dictates the use of blocking the voltage in either direction by the switches and controlling the reverse and forward conduction of the current.

Both S1 and S2 are forward biased during positive and negative half-cycles and made to conduct for the same conduction angle (δ), from $(\pi/2 - \delta/2)$ to $(\pi/2 + \delta/2)$ and $(3\pi/2 - \delta/2)$ to $(3\pi/2 + \delta/2)$, respectively, and the concept of the SAC method is shown in Figure 2.

The conceptual diagram of the SAC method for half-sine wave is shown, and the firing angle is chosen at a particular value so that it has to provide a maximum conduction period, so that the load can get maximum load voltage with reduced harmonics, thus enhancing continuous conduction mode over a long period of time. The input voltage and output voltage waveforms along with gating signals are shown in Figure 3.

If $V_s = \sqrt{2}V_s \sin \omega t$is the input voltage, and the pulse widths for S1 and S2 are equal, the output voltage RMS value is calculated as

$$V_0 = \left[\frac{2}{\pi}\int_{\pi-\delta/2}^{\pi+\delta/2} V_m^2 \sin^2 \omega t \; d(\omega t)\right]^{1/2}, \tag{1}$$

$$V_0 = \frac{V_m}{\sqrt{2}}\left[\frac{1}{\pi}(\delta + \sin \delta)\right]^{1/2} \text{Volts.} \tag{2}$$

Thus, by varying δ from π to 0, the RMS output voltage can be varied from RMS input voltage V_s to 0.

2. Proposed Area Equalization Method

In the SAC method, the lower order harmonics are dominant and the THD increases with δ, as it is varied from π to 0 and is high for the minimum output voltage [10].

The AEM is a direct PWM strategy suitable for single-phase AC voltage regulators. In this method, switching is done in such a way that the integrated area of the target output voltage waveform over the carrier interval is the same as the integrated area of the actual output voltage waveform, i. e., each area or pulse in the actual output waveform for a duration is equated to the region under the sampled target waveform for the same duration and hence the name area equalization method (AEM) [11]. The concept of the proposed AEM is illustrated in Figure 4. To equate the target output voltage with the actual output voltage, the area under the target output voltage is also divided into the same number of samples (m) per half-cycle as in the actual output.

The lower and upper limits for any sample in AEM lie between $((k-1)\pi/m + X_{oi} - \delta_k/2)$ and $((k-1)\pi/m + X_{oi} + \delta_k/2)$, and the conceptual diagram shown in Figure 4 explains the AEM concept. As pointed out earlier, AEM is a direct PWM method and the pulse width (δk) is determined by equating the two regions shown in Figure 4.

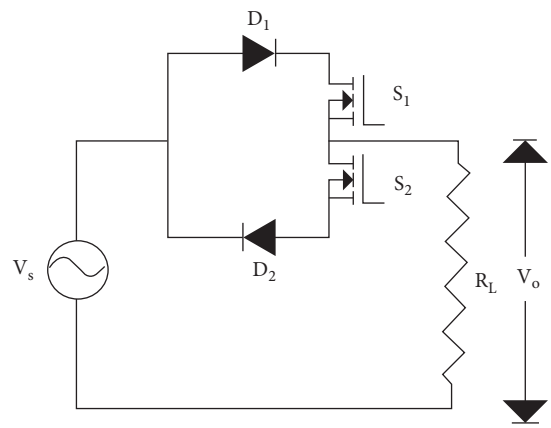

Figure 1: Single-phase AC voltage regulator power circuit.

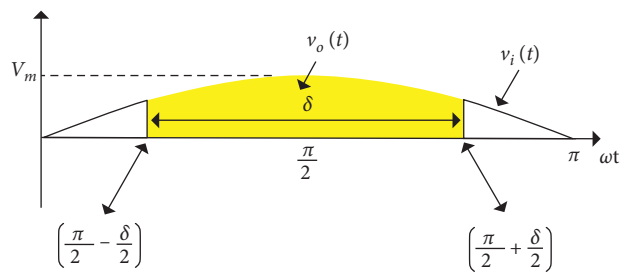

Figure 2: Conceptual diagram for the SAC method.

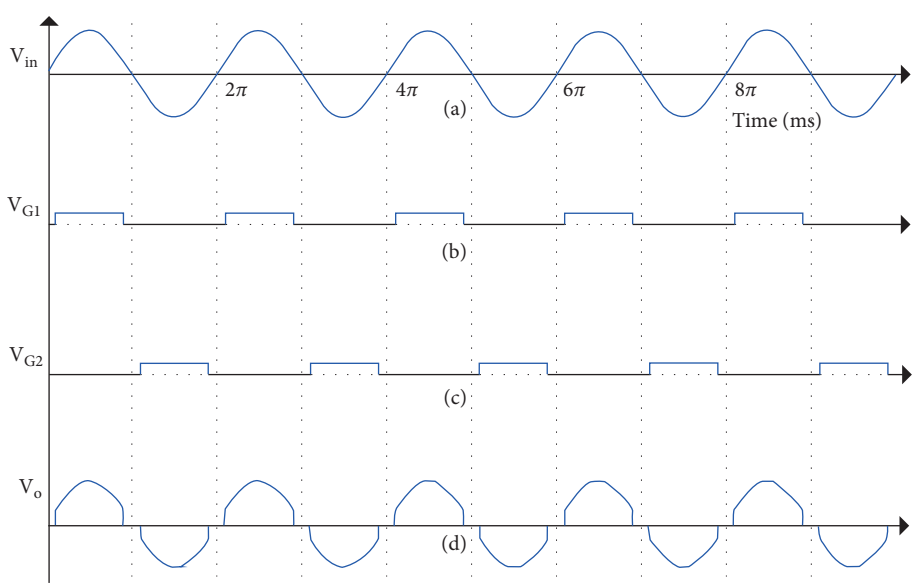

Figure 3: SAC method. (a) Input voltage waveform. (b) and (c) gating signals for S1 and S2. (d) Output voltage waveform.

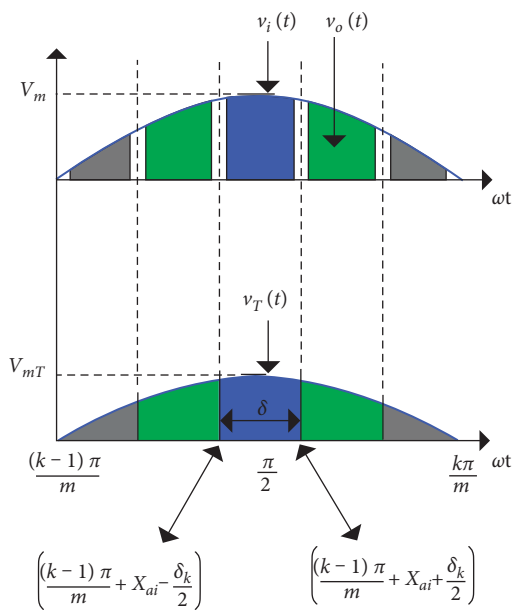

Figure 4: Area equalization method (AEM).

$$A_k = V_{mT}\left[\cos\left(\frac{(k-1)\pi}{m}\right) - \cos\left(\frac{k\pi}{m}\right)\right], \tag{3}$$

where A_k is the area of the kth sample of the target voltage, V_{mT} is the maximum value of the target voltage, m is the number of samples per half cycle, and k is the kth sample; $k = 1,2,3, \ldots\ldots\ldots n$.

$$A_{ko} = \int_{((k-1)\pi/m+Xoi-\delta_k/2)}^{((k-1)\pi/m+Xoi+\delta_k/2)} V_m \sin\,\omega t\; d(\omega t), \tag{4}$$

where A_{ko} is the area of the kth sample in the actual output, V_{m} is the value of the maximum input voltage, and ∂ is the conduction angle.

$$\begin{gathered}
A_{ko} = 2V_m\left[\sin(k-0.5)\frac{\pi}{m}\sin\left(\frac{\delta_k}{2}\right)\right], \\
A_k = A_{\text{outputk}}, \\
V_{mT}\left[\cos\left(\frac{(k-1)\pi}{m}\right) - \cos\left(\frac{k\pi}{m}\right)\right] = 2V_m\left[\sin(k-0.5)\frac{\pi}{m}\sin\left(\frac{\delta_k}{2}\right)\right], \\
\frac{\delta_k}{2} = \sin^{-1}\left[\frac{V_{mT}[\cos((k-1)\pi/m) - \cos(k\pi/m)]}{2V_m\sin(k-0.5)\pi/m}\right].
\end{gathered} \tag{5}$$

The value of δ_{k} obtained from (5) decides the pulse positioning to satisfy the AEM concept.

The value of the fundamental target output voltage is

$$\begin{gathered}
V_0 = \left[\frac{1}{\pi}\int_0^{\pi} V_m^2 \sin^2 x\mathrm{d}x\right]^{1/2} \\
V_0 = \left(\sum_{k=1}^{m}\left(\frac{V_m^2}{2\pi}\left[\delta_k - \frac{1}{2}\left\{\sin\left[2\left(\frac{(k-1)\pi}{m} + Xoi + \frac{\delta_k}{2}\right)\right] - \sin\left[2\left(\frac{(k-1)\pi}{m} + Xoi - \frac{\delta_k}{2}\right)\right]\right\}\right]\right)\right)^{1/2}.
\end{gathered} \tag{6}$$

The output voltage and input current contain harmonics and need Fourier analysis to decide the magnitude of the fundamental THD and the individual harmonic distortion. The analysis is carried out in the same way as it is done for the SAC method. The theoretical Fourier analysis removes the harmonics at higher order completely, and therefore, the power factor correction gets improved significantly and the harmonic distortion is reduced [12]. Figures 5–7 show the input voltage waveform, gate current pattern, and the output voltage measured at the load terminals.

The PWM technique for AC voltage controllers is completely different as the input voltage waveform is sliced numerously in each cycle while switching the converter. The DC voltage and the carrier wave which is triangular in nature are compared to get the switching signal. It is seen that the switching of the converter occurs at the point of interaction. The main frequency must be less than the converter switching frequency. Duty cycle of any converter is the ratio of the ON times to the completion of the switching cycle. The Simulink analysis for the proposed method is shown as follows.

3. Simulink and Harmonic Analysis for SAC

3.1. SAC Simulink Methodology. Using Matlab 7.1-Simulink platform, the AC voltage regulator shown in Figure 1 employing the SAC method is simulated.

The input voltage is 230 V, 50 Hz, and the load resistance is RL = 110 Ω. Figure 3 shows the sample output voltage and input current waveforms along with their harmonic spectrum for $\delta = 15.66$ corresponding to a low output voltage of 40 V. A sample output of 40 V is chosen as the idea to study and describe the power quality and the PF in the low output voltage range [13].

Similarly, the sample output voltage and input current waveforms along with their harmonic spectrum for $\delta = 55$ are shown in Figure 8 corresponding to a low output voltage of 130 V.

As the load is resistive, the output voltage and current at the input side are in phase as well as the harmonics at lower order are dominant as shown in Figure 9, in the spectrum for $\delta = 15.66$. The lower order harmonics are relatively less dominant for $\delta = 55$ as shown in Figure 10. The harmonics at lower order is presiding in both the output voltage and input current waveforms which is objectionable, particularly at reduced output voltage levels [11, 12]. The SAC output voltage is as shown in Figure 11.

Table 1 compares the theoretical and simulation results of the SAC method in terms of the fundamental RMS voltage. The target fundamental RMS voltage is 40 V with $\delta = 15.66$ and the theoretical value of the fundamental voltage calculated using equations stands at 39.7718 V while the simulation yields 40.1 V. While the fundamental voltage h1 is calculated as % of target voltage, the individual harmonics h_{a3} to h_{a25} are calculated as the % of fundamental voltage (h_{a1}) using equations (4) and (6). The lower order harmonics are thus found to be dominant as seen in Table 1. Simulation results also substantiate the theoretical predictions. The multiples of the fundamental frequency are called voltage or current harmonics. The first harmonic is the fundamental component of the sinusoidal waveform. It is the base frequency on which periodically the waveform is built. Harmonics are caused because of the nonlinear loads, and the load which draws current proportional to the voltage fed from the input does not cause much implication to the power quality as the impedance is constant during the sinusoidal cycle.

4. Simulink and Harmonic Analysis for AEM

The power circuit model shown in Figure 1 is simulated again using Matlab-Simulink with the AEM concept applied to it. As seen in Figures 12(a) and 12(b), the proposed AEM provides a better power quality spectrum and relatively improved PF at reduced output voltage levels, the same target output voltage of 40 V with $\delta = 31.18$ for AEM is chosen for the sake of comparison. AEM is one of the PWM methods, and we consider $m = 10$ as the pulses per half cycle for our analysis. The simulated output voltage and input current waveforms are as shown in Figures 5–7, respectively.

It is evident from the spectrum that, the fundamental component is maintained at 100%, and the lower order harmonics ranging from h_3 to h_{17} are completely eliminated while h_{19} and h_{21} are dominant around. Still better results are obtained for higher voltages and such results are clearly shown in Figures 13(a) and 13(b). Table 2 describes the variation of harmonic order voltage content as the percentage of target fundamental output voltage of 40 V.

5. Comparative Analysis of SAC and AEM

The distortion factor of individual harmonics as a percentage of the fundamental voltage also proves that the proposed AEM is superior to the SAC method as the harmonics h_3 to h_{17} and h_{23} and h_{25} are only a fraction of the fundamental voltage. Though h_{19} and h_{21} are dominant, the filtering requirements are less as they are pushed far away from the fundamental frequency.

Total harmonic reduction places a vital role in improving power factors. However, the decrease in THD will increase the overall performance of the power factor for SAC and AEM as shown in Table 3. The comparative harmonic distortion factor for SAC and AEM is shown in Table 4.

The variations in PF with the input current for the SAC method and AEM with $m = 11$ are shown in Figure 14. It is evident that the more the value of m is, the better the PF will be, especially at the low output voltage range. From Figure 15, it is evident that the power factor varies with "m".

Figure 16 shows the variation in THD with the fundamental target output voltage. This discloses that the SAC method has rich lower order harmonics and poor THD whereas the proposed AEM not only reduces the THD but also completely gets rid of the harmonics at lower order at the low target output voltage range for increasing samples m as evident from Figure 17 [13]. It is clear that in the SAC method, the lower order harmonics are leading and dominant and the individual harmonic numbers are progressively decreasing whereas the harmonics of lower order are

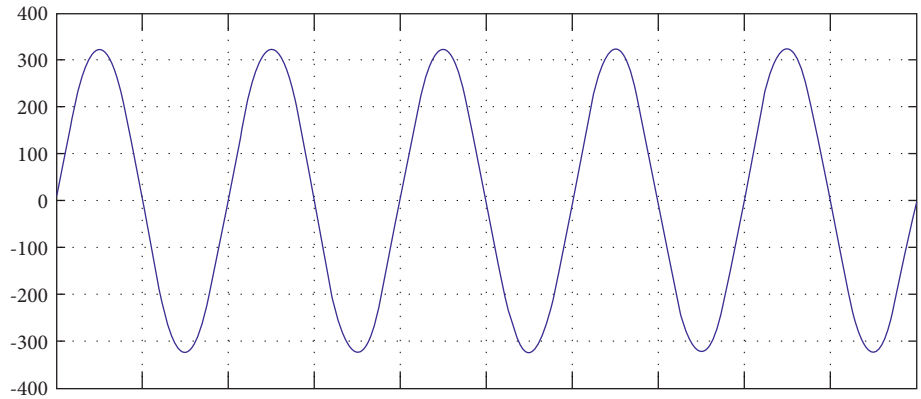

Figure 5: Input voltage waveform.

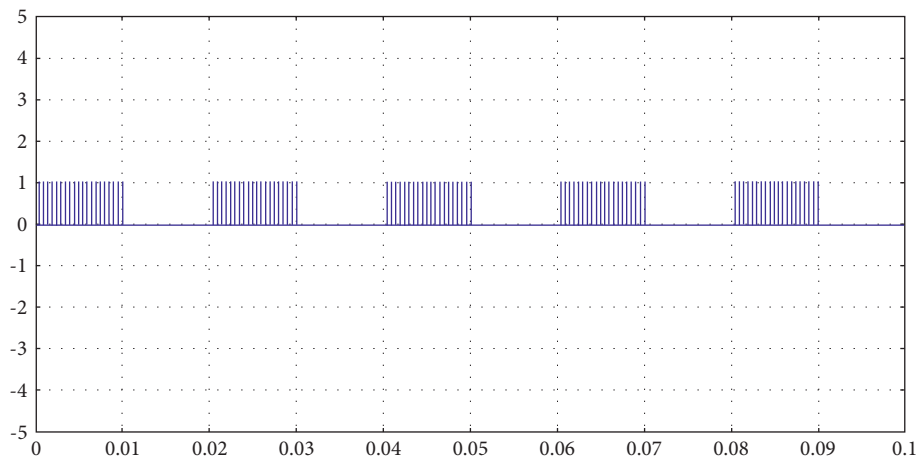

Figure 6: Input gate pulse pattern.

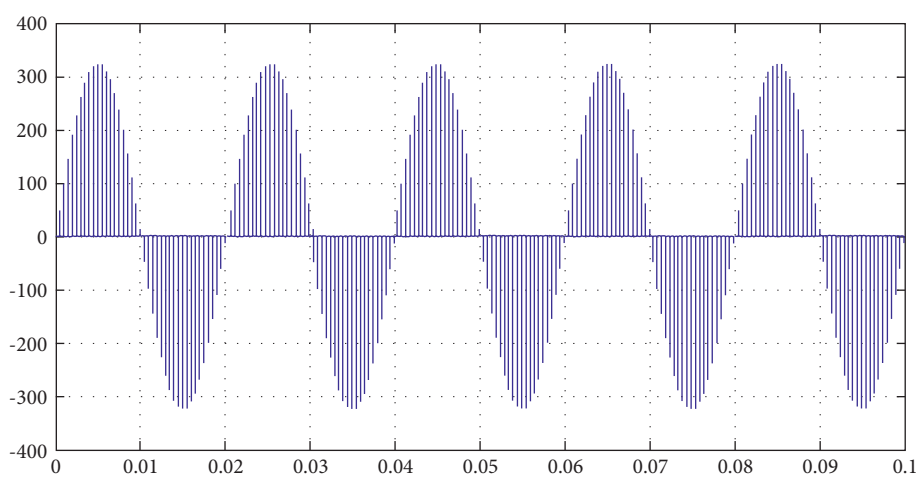

Figure 7: Output voltage at load terminals.

absolutely absent in AEM. At the same time, harmonics h_{19} and h_{21} are dominant only around, and hence, they can be filtered out using a low pass filter.

Figure 18 substantiates the concept that the increasing value of m decides the placement of dominant harmonics in the high-frequency band for minimum filter requirements.

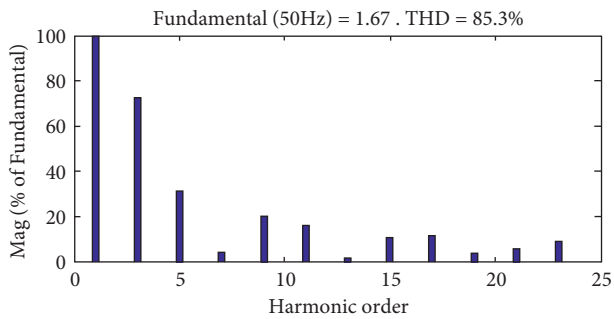

Figure 8: Harmonic spectrum for $\delta = 55$.

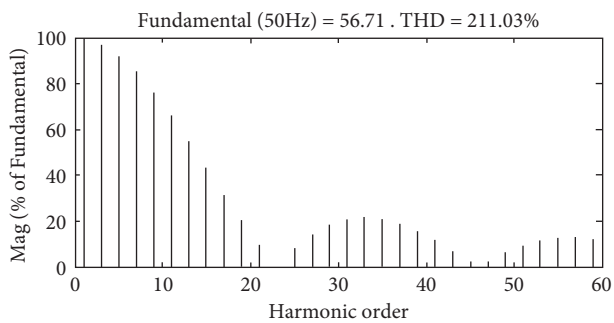

Figure 9: Harmonic spectrum for $\delta = 15.66$.

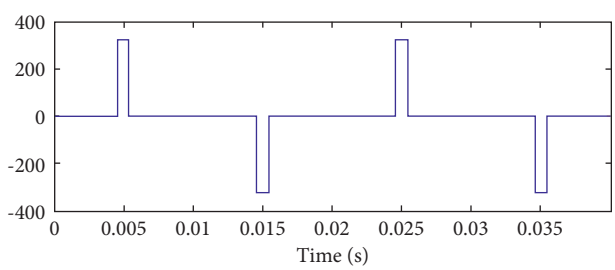

Figure 10: Input current for SAC.

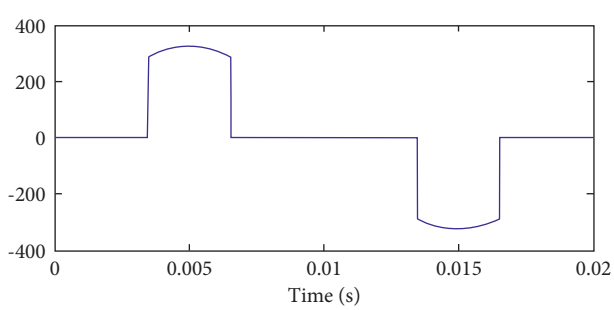

Figure 11: SAC output voltage.

Table 1: Comparison of individual harmonics as % of the fundamental voltage.

Harmonic order	Fundamental RMS output voltage	
	Theoretical	Simulation
h_{a1}	**39.7718(100%)**	**40.1(100%)**
h_{a3}	97.53152	96.31464
h_{a5}	96.26102	91.53594
h_{a7}	85.7326	84.64122
h_{a9}	76.92234	75.94786
h_{a11}	66.65723	65.80855
h_{a13}	55.37655	54.66411
h_{a15}	43.554	42.99067
h_{a17}	31.67204	31.24671
h_{a19}	20.19883	19.90832
h_{a21}	9.557332	9.416334
h_{a23}	0.140099	0.1058
h_{a25}	7.778001	7.705878

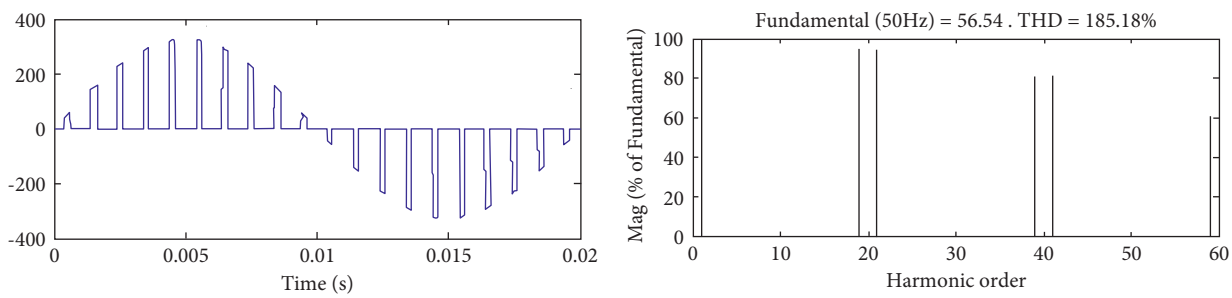

(a) (b)

Figure 12: (a, b) AEM output voltage and harmonic spectrum for $\delta = 31.18$.

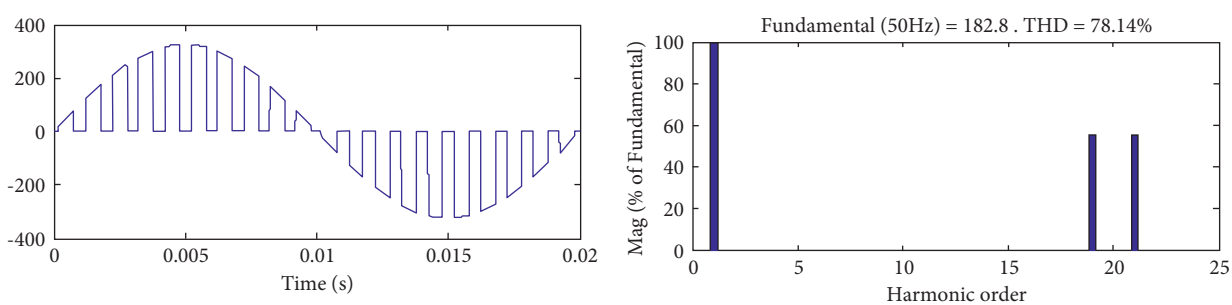

(a) (b)

Figure 13: (a, b) Output voltage and harmonic spectrum for $\delta = 101.454$.

Table 2: Comparison of individual harmonics as % of the fundamental voltage.

Harmonic order	Fundamental RMS output voltage	
	Theoretical	Simulation
h_1	**39.8411(100%)**	**39.98(100%)**
h_3	0	0.15918
h_5	0	0.035373
h_7	0	0.035373
h_9	0	0.141493
h_{11}	0	0.106118
h_{13}	0	0.070745
h_{15}	0	0.053059
h_{17}	0	0.15918
h_{19}	95.13678	93.95075
h_{21}	95.13678	94.00383
h_{23}	0	0.141493
h_{25}	0	0.053059

Table 3: Comparison between SAC and AEM in terms of power factor.

Target output voltage	SAC		AEM	
	THD	PF	THD	PF
20	302.52	0.313854	208.22	0.432922
40	211.03	0.428220	185.18	0.475159
60	164.39	0.519706	154.3	0.54386
80	133.88	0.598429	126.12	0.621295
100	112.39	0.664727	105.27	0.688726
120	93.91	0.728955	88.35	0.749411
130	86.36	0.756837	81.14	0.776532
140	78.81	0.785407	74.09	0.803496
160	64.76	0.839363	61.12	0.853248
180	51.66	0.88845	47.69	0.902612
200	37.64	0.935898	30.39	0.956793
210	29.92	0.958037	20.35	0.979916

Table 4: Comparison of SAC and AEM in terms of harmonic distortion factor.

Harmonic order	SAC THD	AEM THD
h_3	96.31464	0.15918
h_5	91.53594	0.035373
h_7	84.64122	0.035373
h_9	75.94786	0.141493
h_{11}	65.80855	0.106118
h_{13}	54.66411	0.070745
h_{15}	42.99067	0.053059
h_{17}	31.24671	0.15918
h_{19}	19.90832	93.95075
h_{21}	9.416334	94.00383
h_{23}	0.1058	0.141493
h_{25}	7.705878	0.053059

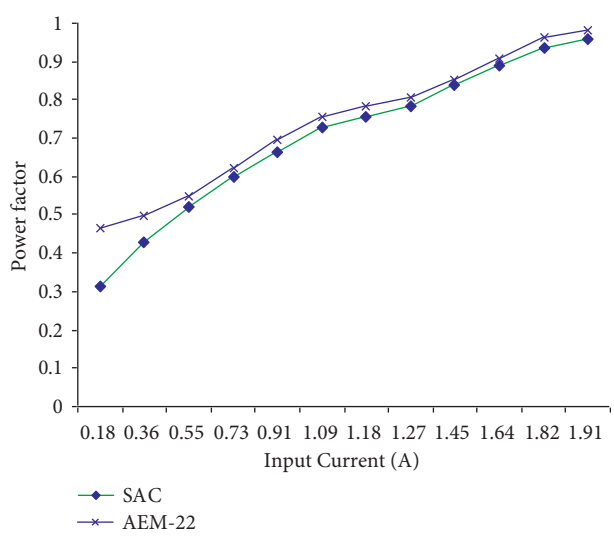

Figure 14: Variation of power factor with the input current.

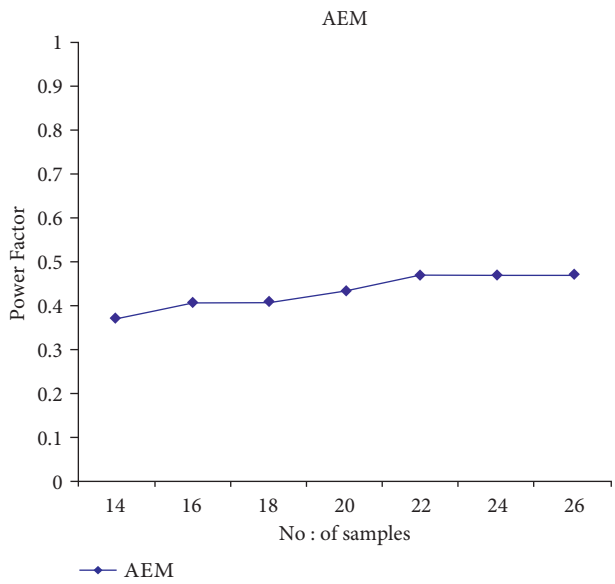

Figure 15: Variation of power factor with "m".

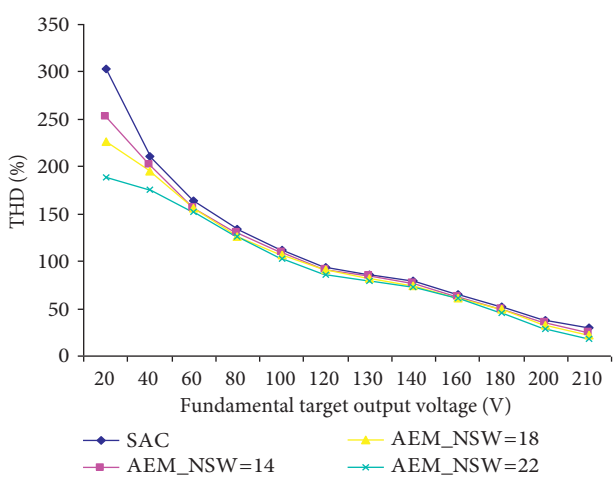

Figure 16: Variation of THD with the fundamental target output voltage.

6. Conclusion

The conventional forced commutated SAC method suggested fails to improve the power factor. It is seen that the total harmonic distortion is high at low output voltage. AEM employing the forced commutation technique improves the input PF considerably and improves the harmonic spectrum. The proposed method provides good AC power control. The output voltage fundamental component and the duty cycle of the control circuit are flatly linear; hence, a good linear voltage control is seen. The lower order harmonic components, which increase the filter size and cost, have been drastically reduced, besides having contributed to an enhancement in input power factor and THD.

Data Availability

The data used to support the findings of this research are available from the corresponding author upon request.

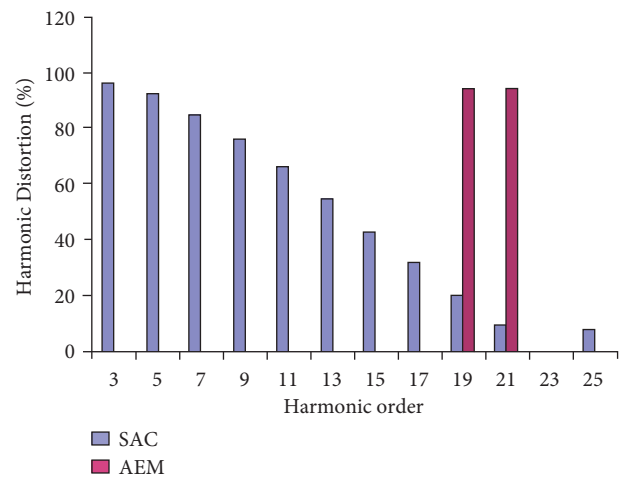

Figure 17: Comparison of individual harmonics order for a target output of 40 V.

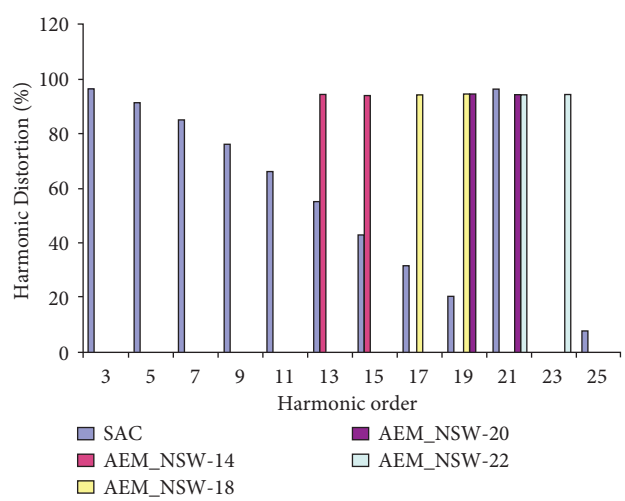

Figure 18: Variation in the individual harmonic order with increasing "m".

Conflicts of Interest

The authors declare that they have no conflicts of interest.

References

[1] S. Williamson, "Reduction of the voltage and current harmonics introduced by a single- phase triac ac controller," *Instrumentation*, vol. 28, no. 4, 1981.

[2] E. El-Bidweihy, "Power factor of ac controllers for inductive loads," *IEEE Transactions on Industrial Electronics and Control Instrumentation*, vol. 27, no. 3, 1980.

[3] M.-Ho Park, "An improved PWM technique for ac choppers," *IEEE Transactions on Power Electronics*, vol. 4, no. 4, pp. 496–405, 1989.

[4] Do-H. Jang, "A new APWM technique with harmonic elimination and power factor control in AC choppers," in *Proceedings of International IEEE conference*, pp. 252–258, San Diego, CA, USA, November 1992.

[5] K. E. Addoweesh, "Microprocessor based harmonic elimination in chopper type ac voltage regulators," *IEEE Transactions on Power Electronics*, vol. 5, pp. 191–200, 1990.

[6] F. Swift, "A new Walsh domain technique of harmonic elimination and voltage control in pulse-width modulated inverters," *IEEE Transactions on Power Electronics*, vol. 8, no. 2, pp. 170–185, 1993.

[7] T. Kato, "Sequential homotopy –based computation of multiple solutions for selected harmonic elimination in PWM inverters," *IEEE Transactions on Circuits and Systems -1: Fundamental Theory and Applications*, vol. 46, pp. 586–593, 1999.

[8] P. N. Enjeti, "Programmed PWM techniques to eliminate harmonics: a critical evaluation," *IEEE Transactions on Industry Applications*, vol. 26, pp. 302–316, 1990.

[9] H. S. Patel, "Generalized harmonic elimination and voltage control in thyristors inverters: part I—harmonic elimination," *IEEE Transactions on Industry Applications*, vol. 9, pp. 310–317, 1973.

[10] H. S. Patel, "Generalized harmonic elimination and vol tage control in thyristors inverters: part II—voltage control technique," *IEEE Transactions on Industry Applications*, vol. 10, pp. 666–673, 1974.

[11] R. Corapsiz, H. Kahveci, and M. F. Çorapsiz, "Design and Implementation of Single-phase AC Voltage Controller with Phase Triggering Control," in *3rd International Conference on Advanced Engineering Technologies*, Bayburt, September 2019.

[12] A.. Altintas, "A study on power quality improvement in PWM controlled AC voltage controller," *Süleyman Demirel Üniversitesi Fen Bilimleri Enstitüsü Dergisi*.vol. 12, 2009.

[13] F. M. Serra, L. M. Fernández, O. D. Montoya, W. G. González, and J. C. Hernández, "Nonlinear voltage control for three-phase DC-AC converters in hybrid systems: an application of the PI-PBC method," *Electronics*, vol. 9, no. 5, p. 847, 2020.

[14] Md. R. Islam, Md Uddin, Md Uddin, I. Ahmed, and Md. M. Hasan, *A Model of Voltage Stabilization Using PWM Inverter at the Load End*, , pp. 154–159, IEEE, 2020.

[15] A. Viswas, C. Santhanam, and Y. Kashyap, "A single phase modular multilevel inverter based on controlled DC-cells under two SPWM techniques for renewable energy applications," in *International Conference -RARE 2020 Inverter and PWM Control Technique suitable for Renewable Energy Applications*, vol. 1, pp. 117–122, 2020.

[16] Prajakta Kasulakar, Chetan Dethe, Paras Patil, and Pratik Murkute, "Single phase inverter using pwm technique," *International Journal of Engineering Applied Sciences and Technology*, vol. 04, pp. 225–230, 2020.

Hindawi
Mathematical Problems in Engineering
Volume 2022, Article ID 7129610, 11 pages
https://doi.org/10.1155/2022/7129610

Research Article

Design and Implementation of Automatic Water Spraying System for Solar Photovoltaic Module

L. Ashok Kumar,[1] V. Indragandhi,[2] Yuvaraja Teekaraman,[3] Ramya Kuppusamy,[4] and Arun Radhakrishnan[5]

[1]*Department of Electrical and Electronics Engineering, PSG College of Technology, Coimbatore 641004, India*
[2]*School of Electrical Engineering, Vellore Institute of Technology, Vellore 632014, India*
[3]*Department of Electronic and Electrical Engineering, The University of Sheffield, Sheffield S1 3JD, UK*
[4]*Department of Electrical and Electronics Engineering, Sri Sairam College of Engineering, Bangalore 562106, India*
[5]*Department of Electrical & Computer Engineering, Jimma Institute of Technology, Jimma University, Jimma, Ethiopia*

Correspondence should be addressed to Yuvaraja Teekaraman; yuvarajastr@ieee.org and Arun Radhakrishnan; arun.radhakriahnan@ju.edu.et

Received 2 October 2021; Revised 13 November 2021; Accepted 27 December 2021; Published 17 January 2022

Academic Editor: Abu Zaharin Ahmad

Photovoltaic (PV) cell has a characteristic of decrease in power beyond a certain temperature. This decrease in power is due to a drop in the open circuit cell voltage. This decreases the efficiency of the PV cell. The objective of this research is to increase the efficiency of PV cells by reducing the PV cell temperature and reflection loss. The cell temperature and reflection loss can be reduced by spraying water over the PV cells. On spraying water over the USP36, 24V PV module, the power is found to be increased. The test result shows a 1V to 2V increase in voltage, with an efficiency increment of 1% to 1.27%. The test results of USP37 show the voltage increase of 1.2 V to 2.1 V in the PV module voltage. Due to the increase in voltage, efficiency increment of 1.29% is observed. The efficiency of USP36 with water spraying is more than the efficiency of USP37 without water spraying. In the PV power systems, an average increase in efficiency of 0.5% is observed.

1. Introduction

The operation of a water pumping system needs a power source. Overall, when an AC power supply is available from the nearby power grid, the AC power system is economical and requires minimum maintenance. However, water sources are spread over many miles of land in rural areas, and power lines are scarce. It is also prohibitively costly to install a modern transmission line and a transformer at the site. In such places, windmills have historically been installed; however, many of them are now inactive due to inadequate maintenance and aging. Most stand-alone water pumping systems today use internal combustion engines. There are compact and easy to mount programs. However, they do have some big drawbacks, such as they need regular refueling and repair site visits, and in addition, diesel fuel is often costly and not readily accessible in rural areas of many developed countries. Fossil fuel consumption also has an environmental effect, particularly the carbon dioxide (CO_2) release into the atmosphere. By implementing clean energy systems, which are now cost-competitive with fossil fuels in some instances, CO_2 emissions can be significantly reduced. Carbon dioxide emissions in 2010 and 2020, by select country (in million metric tons), is shown in Figure 1. A very attractive idea is the use of green energies for water pumping systems. In particular, for applications needing less than 10 kW, where grid energy is not possible, and where internal combustion engines are costly to run, PV systems are incredibly efficient and are mostly preferred because they provide the lowest cost of the life cycle. PV is a desirable economic option if the water supply is 1/3 mile or more away from the power line [1].

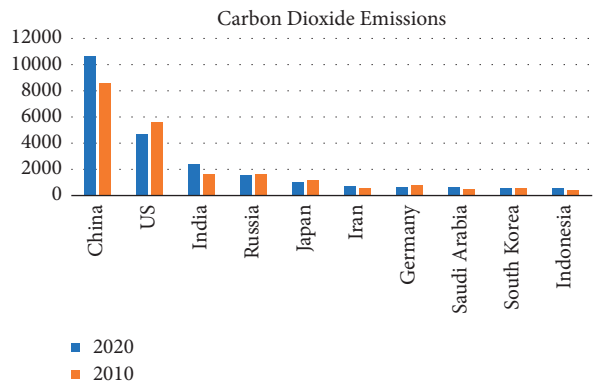

Figure 1: Global CO_2 emissions in 2010–2020.

The removal of heat from the front surface into the water spray over the cells that absorb the heat produced by the cells during the day will minimize the loss of productivity due to the increased temperature of PV arrays. Spraying water over the cells has been shown to increase the average performance of PV cells, subsystem efficiency, and overall efficiency by 3.26%, 1.40% and 1.35%, respectively. The overall productivity of PV cells in normal conditions is 13.5%. Measurements of the modules' short circuit current, almost independent of temperature, showed that the water spray increased the optical output by 1.8%. Reducing the temperature of the cell and lack of reflection will also decrease the threshold radiation during the hot days of the starting motor pump torque and contributes to an increase in the early morning consumer requirement [2, 3].

2. Literature Work

The operation of a separately excited, series, and shunt motor is investigated and concluded that a separately excited motor coupled to a centrifugal pump was the most suitable for a solar cell generator. They conclude that after comparison, the DC motor has the advantage of higher utilization of PV power, and direct coupling between the DC motor and the PV generator reduces the cost of the system [4–7].

Jafar [8] suggested a very simple but precise method to model the PV water pumping system, which, given the head and irradiance, is applied to the solar star 1000 pumping system to arrive at a model that calculates the volume flow rate. When used to power water pumps, PV does not need any storage batteries, which means significant cost savings and contributes to a device that is efficient and needs less maintenance [9, 10].

Langridge et al. [11] indicated that an improvement in overall system performance would decrease the size of the PV array and hence the expense of the capital system, which is largely driven by the cost of the PV array. A PV pumping system using a DC brushless motor has been developed. This paper outlines the system's operation and the creation of array part models and the brushless DC engine. Simulation results are included as well as subsequent test results for the entire system. Through a variety of loads and working conditions for 4×1 and 4×2 array setups, efficiencies of between 30 and 50 percent for the system (excluding the array) have been obtained [12–14].

This method only uses the knowledge available from the suppliers of the PV module and pump motor. From monthly averages of horizontal radiation and ambient temperatures, the weather data is "generated" using well-known weather data statistics. Based on hourly weather info, the system forecasts the monthly pumped water within 6 percent of TRNSYS predictions. The use of a single average monthly day has been seen to forecast monthly pumped water at low average monthly radiation levels and to predict monthly pumped water at moderate radiation levels and above. The use of a single monthly average day provides a fair calculation of monthly pumped water only at high radiation levels [15, 16].

A method of the electrical yield through water flow over the front of PV panels is suggested. Numerous ideas have been suggested to minimize reflection. Still, most of them have drawbacks such as the anti-reflective coatings are not durable, and structured surfaces are pricey, dust collection, and are hard to clean. In addition to helping to maintain clear surface, water reduces reflection by 2–3.6 percent, reduces cell temperatures by up to 22°C, and can return a 10.3 percent surplus; even after accounting for the electricity required to operate the pump, a net benefit of 8–9 percent can be obtained [17, 18].

A. Moussi. et al. [19] with enhanced performance, a permanent magnet brushless DC motor PV pumping system was developed. According to this proposal, where insolation differs far from the nominal value and where the machine was sized, the efficiency of a photovoltaic pumping system based on an induction engine is degraded. The findings of the simulation indicate that the suggested solution achieves an improvement in both the regular pump quantity and pump efficiency. The generator voltage control law, however, leads to a less costly and non-complex application. The arrangement of MPPT control does not always lead to maximum efficiency of the system. For optimum usage of PV water pumping systems, proper sizing of system components is important [20]. Combining a battery bank and a water tank is the most cost-effective way to address the irrigation difficulties that arise during dry weather. The

PVWPS is yet to be explored in locations of the Arctic where solar radiation is very high at certain times of the year. Weather conditions, high atmospheric transparency, clean air, and radiation reflection from ice and ice may all help the photoelectric modules work more efficiently. These locations, however, are sparsely populated and hard to reach [21–23].

This literature study helps to understand the problems in the performance of photovoltaic cells and solutions to increase the performance. It is incurred from the study that at increased temperatures, i.e., beyond 45°C, the power output from the PV cells decreases. This is due to the basic characteristic of PV cells. The loss of power is reduced by reducing the PV cell temperature. Water spraying over the cells will reduce the temperature and helps to increase power and efficiency.

3. Methodology

Loss of efficiency due to a raised temperature of PV cells can be reduced by heat removal from the PV cell front surface by spraying water over the cells, which absorbs the heat from the cells. The temperature of the PV cell is measured using the LM35 temperature sensor, and the output is fed into the control unit. The control unit includes a microcontroller that compares the measured temperature with the reference temperature and controls the MOSFET switch.

If the measured temperature is more than the reference temperature, then the microcontroller produces the pulse width modulation (PWM) signal to trigger the MOSFET. The MOSFET acts as a switch between the solenoid valve and the power supply. A solenoid valve is placed between the water tank and the spraying unit. Water spraying includes flexible PVC tubes with appropriate holes for water flow. The change in voltage before and after spraying water is measured using a voltage sensor and is displayed in the LCD. The temperature variation is also displayed in LCD (Figure 2).

4. Experimental Setup

This chapter deals with the experimental setup of the project work, including the temperature measurement, control unit, and water spraying unit.

The circuit of the control system is shown in Figure 3. The LCD is interfaced with the microcontroller to display the measured temperature and voltage. A PIC microcontroller is provided with the reset circuit, which includes two Schmitt triggers 7414. A 12 MHz crystal oscillator is connected to the PIC microcontroller. A Darlington amplifier configuration using two BC547 transistors is used to amplify the PWM signals from the microcontroller. The IRF250 MOSFET is connected between the solenoid valve and the power supply.

Figure 4 depicts the basic components of a solenoid valve. The valve shown in the picture is a normally-closed direct-acting valve. This type of solenoid valve has the simplest and easy-to-understand principle of operation. The media controlled by the solenoid valve enters the valve through the inlet port. The media must flow through the orifice before continuing into the outlet port. The orifice is closed and opened by the plunger.

The valve pictured above is a normally-closed solenoid valve. Normally closed valves use a spring that presses the plunger tip against the opening of the orifice. The sealing material at the tip of the plunger keeps the media from entering the orifice until the plunger is lifted up by an electromagnetic field created by the coil.

The LM35 temperature sensor is fixed on the backside of the PV module. It is kept back to prevent the sensor from getting wet due to the water sprayed over the cells. The temperature at the backside of PV cell is 2°C more as compared to that of the front side of the cell. The control unit includes a voltage sensor, MOSFET switch control, and LCD. The output voltage from a single PV module is given to the voltage sensor for measurement and display. PIC16F877 microcontroller controls the MOSFET switch according to the output from the temperature sensor. The MOSFET switch is connected between the 12 V power supply and solenoid valve.

Figure 5 shows the water spraying unit of the experimental setup in which solenoid valve and flexible tubes of 5 mm diameter are included. Uniform holes at equal distances in the tubes are made for water flow. LM35 measures the temperature and the output is fed to the microcontroller. The microcontroller compares the measured temperature with a reference value. If the measured temperature value is greater than the reference value, then the microcontroller produces a PWM signal, and the MOSFET gets energized. If the MOSFET switch is closed, a 12 V supply is applied across the solenoid valve. Energizing the solenoid opens the valve, and thereby water flows over the cells, which is shown in Figure 6. The sun's radiation is measured using the pyranometer, and the temperature of the PV cell is measured by an IR thermometer while the experiment is conducted manually. Then the temperature is measured using an LM35 temperature sensor, and the water spraying is performed automatically by the controller unit.

5. Results and Discussion

This section deals with the results of experiments conducted in various PV modules and its discussion. In this paper, experiments are conducted with different PV modules at various temperature ranges. USP36, USP37, a flexible panel, and USP10 are the PV modules with which experiments are conducted at different periods. Various parameters, including voltage, current, temperature, time, and solar radiation, are measured during the experimentation. The experiment is conducted with and without water spraying over the cells.

5.1. Experimental Results of USP36 PV Module. A single USP36 PV module is used for experimentation. This PV module has already completed a lifetime of 10 years. It is tested with and without water spraying throughout the day at regular time intervals. A 16 Ω resistive heating element is used as a load for this experiment.

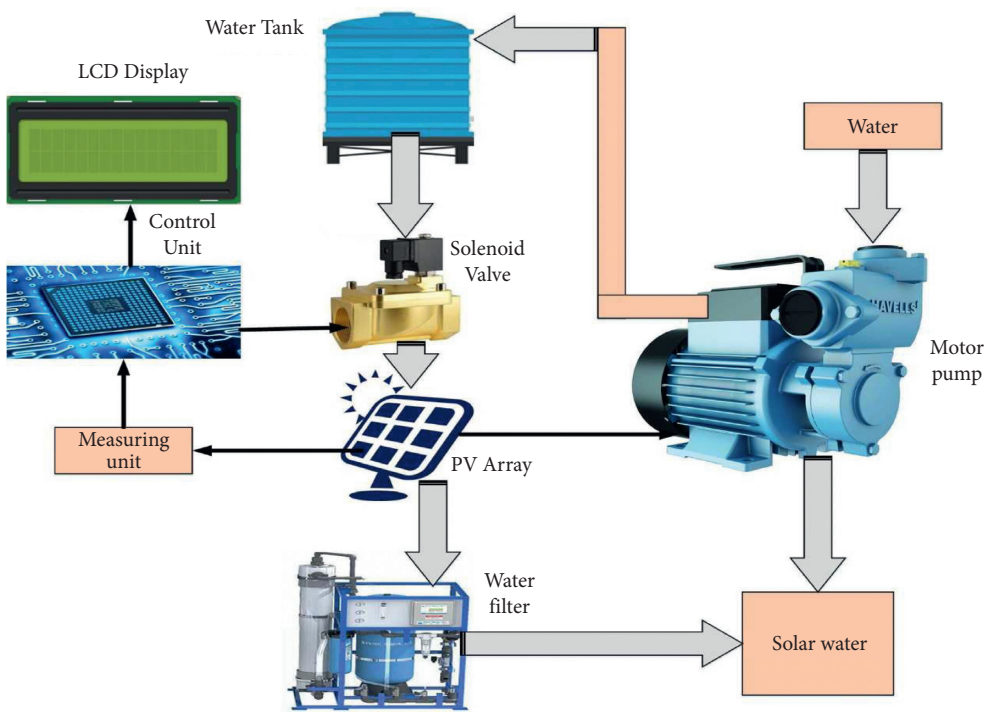

Figure 2: Proposed block diagram.

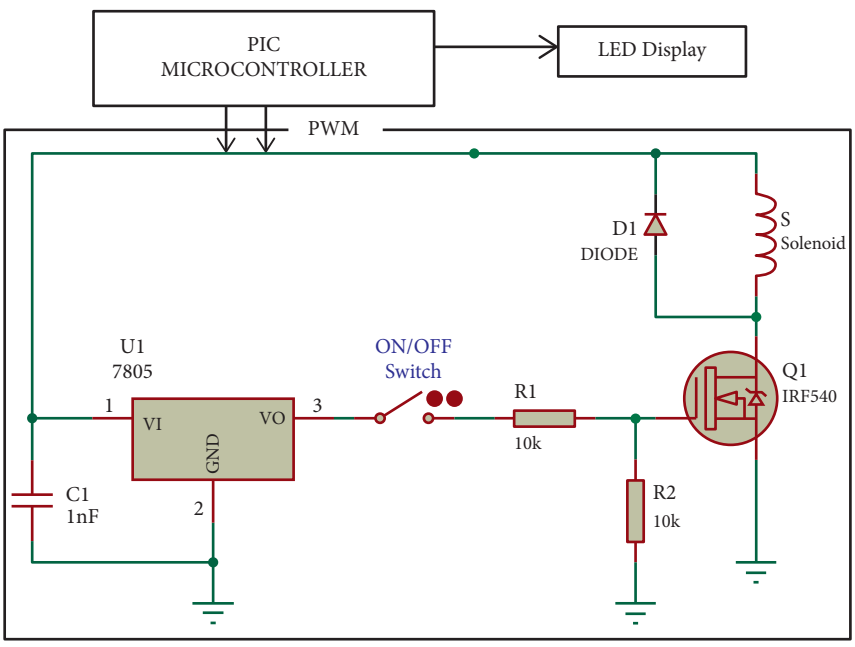

Figure 3: Control circuit.

The experiment was conducted on a 36W PV panel. From the results, it is clear that the voltage and current values after water spraying vary with respect to solar radiation. It shows that from 12.00 pm to 01.00 pm, the cell temperature is 50°C to 60°C, at which the voltage drops. There is a gradual increase in voltage from 8 am to 12.00 pm, after then the voltage drops due to increased cell temperature. After 01.00 pm again, the voltage increases gradually and decreases towards evening with respect to solar radiation. The voltage increases with the increase in solar radiation unless the temperature exceeds 45°C. The current increases gradually with a rise in solar radiation, and there are small changes with the increase in temperature, which is negligible when compared with the voltage variation. At increased temperature, spraying water over the cells increases the cell voltage, and the current decreases slightly.

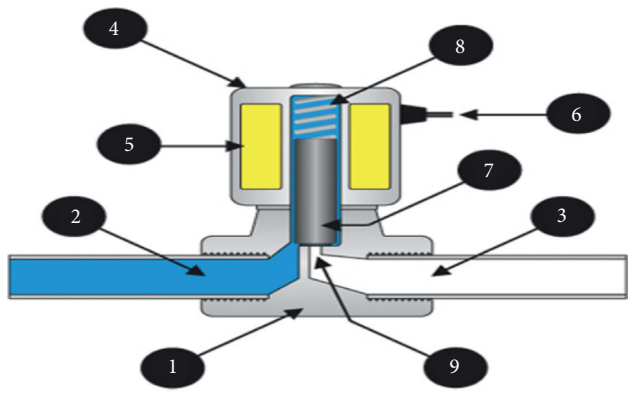

1. Valve Body
2. Inlet Port
3. Outlet Port
4. Coil / Solenoid
5. Coil Windings
6. Lead Wires
7. Plunger
8. Spring
9. Orifice

Figure 4: Solenoid valve.

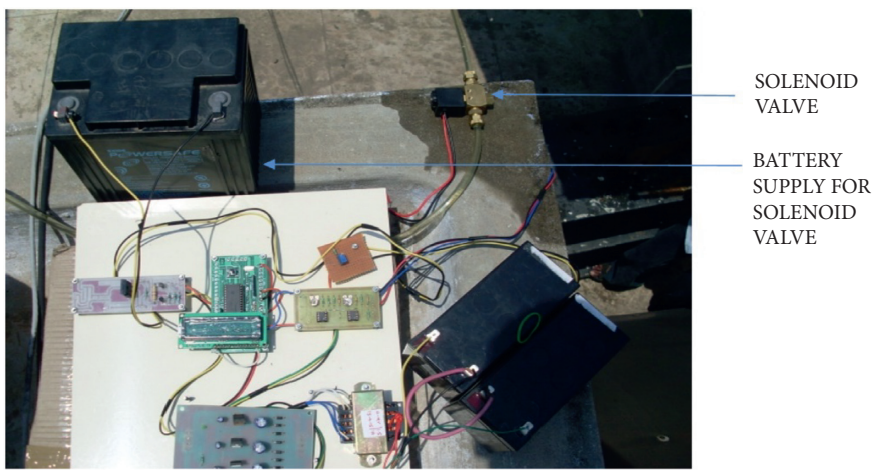

Figure 5: Experimental setup.

The increase in voltage is significantly more, while a decrease in the current is very small. Voltage increment is in the range of 1.5 V to 2.0 V approximately, and the current variation is in the range of 0.01 A to 0.03 A.

The tabulated experimental results are plotted in the graph, and the variations are compared. Figure 7 shows the voltage output from the PV panel with and without spraying water over the cells. On comparing the voltage output with and without spraying water, it is found that an average of 1V is increased by spraying water.

The current output from the panel with and without water spraying is shown in Figure 8. Though current is dependent on the temperature, there is a small increase in the valve on reducing temperature.

The power output from the PV module before and after spraying water is shown in Figure 9. A maximum of 4 W increase in power is found at 12.30 pm after spraying water. Figure 10 shows the comparison of the efficiency of the PV module with and without water spraying. It shows that there is an average increase of 1% efficiency with a maximum increase of 1.5% efficiency after spraying water.

Figure 11 shows the comparison of PV cell temperature before and after spraying water. On comparing, a maximum of around 20°C temperature decrease is found. An average of around 10°C temperature decrease is obtained.

5.2. Experimental Results of USP37 PV Module. A newly bought USP37 PV module has been experimented with this project to compare the output with that of the old USP36 PV module. It is tested with and without water spraying throughout the day at regular time intervals. A 16 Ω resistive heating element is used as a load for this experiment.

The experiment was conducted on a 37W PV panel. From the results, it is clear that the voltage and current values after water spraying vary with respect to solar radiation. There is a gradual increase in voltage from 8 am to 12.00 pm; after then, the voltage drops due to increased cell temperature. After 01.00 pm, again the voltage increases gradually and decreases towards evening with respect to solar radiation. It shows that from 12.00 pm to 01.00 pm, the cell temperature is 50°C to 60°C, at which the voltage drops.

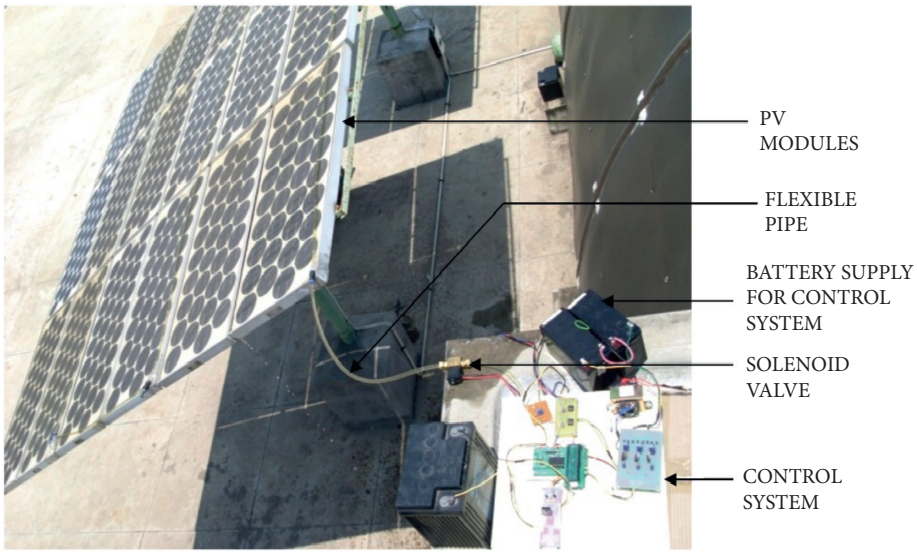

Figure 6: Water spraying setup.

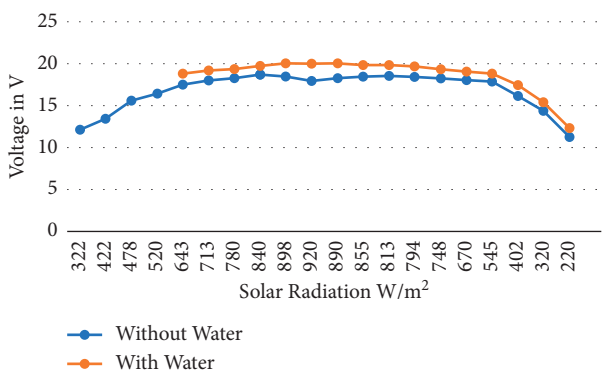

Figure 7: Voltage comparison of USP36 with and without water spray.

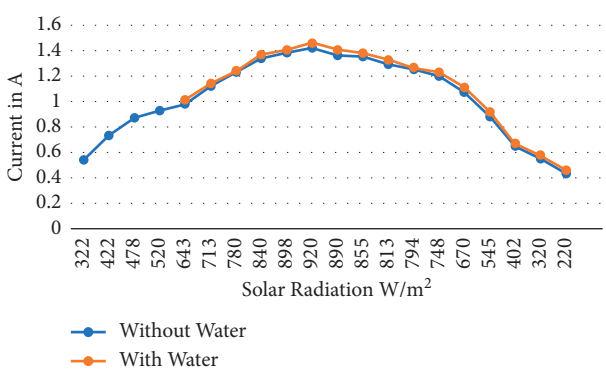

Figure 8: Current comparison of USP36 with and without water spray.

The voltage increases with the increase in solar radiation unless the temperature exceeds a certain limit. The current increases gradually with the rise in solar radiation, and there are small changes with the increase in temperature. At increased temperature, spraying water over the cells increases the cell voltage, and the current decreases slightly. The increase in voltage is significantly more, while a decrease in the current is very small.

The tabulated experimental results are plotted in the graph, and the variations are compared. Figure 12 shows the voltage output from the PV panel with and without spraying water over the cells. On comparing the voltage output with

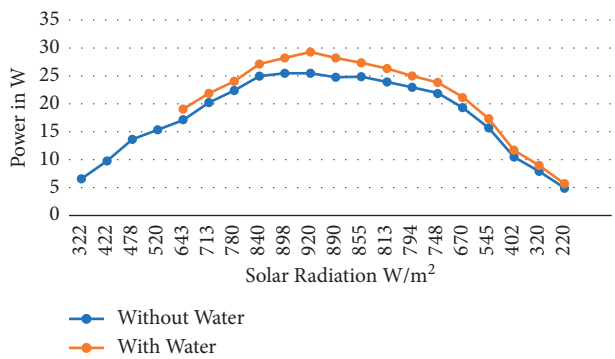

Figure 9: Power comparison of USP36 with and without water spray.

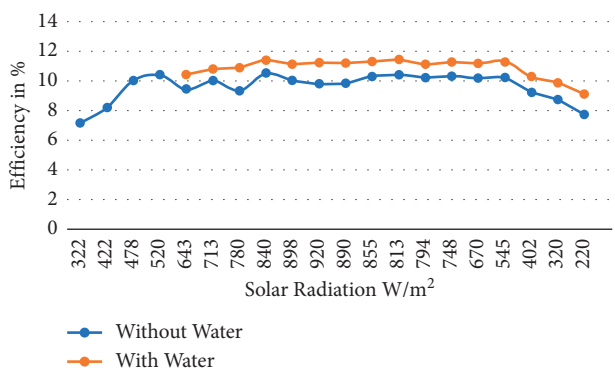

Figure 10: Efficiency comparison of USP36 with and without water spray.

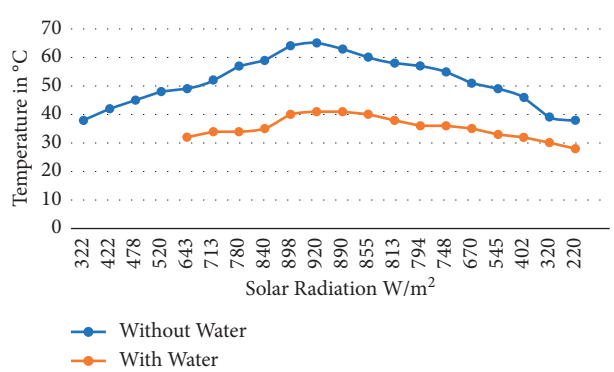

Figure 11: Comparison of the temperature of USP36 with and without water spray.

and without spraying water, it is found that an average of 1V is increased by spraying water.

The current output from the panel with and without water spraying is shown in Figure 13. Though the current is dependent on the temperature, there is a small increase in the valve on reducing temperature.

The power output from the PV module before and after spraying water is shown in Figure 14. A maximum of 4W increase in power is found at 12.30 pm after spraying water. Figure 15 shows the comparison of the efficiency of the PV module with and without water spraying. It shows that there is an average increase of 1% efficiency with a maximum increase of 1.5% efficiency after spraying water.

Figure 16 shows the comparison of the PV cell temperature before and after spraying water. On comparing, a maximum of around 20°C temperature decrease is found. An average of around 10°C temperature decrease is obtained.

Figure 17 shows the comparison of efficiencies of USP36 and USP37 PV modules with and without water spraying. It is clear from the graph that the efficiency of the USP36 PV module with water spraying is more than the efficiency of the USP37 PV module without water spraying.

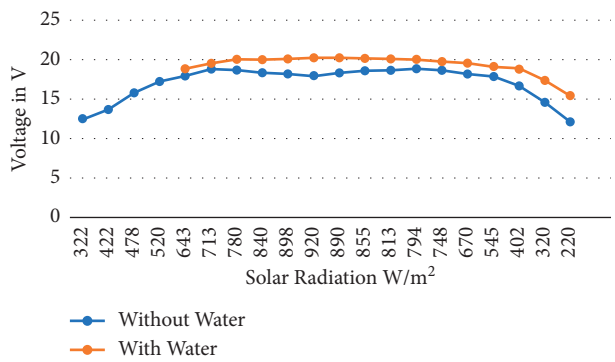

Figure 12: Voltage comparison of USP37 with and without water spray.

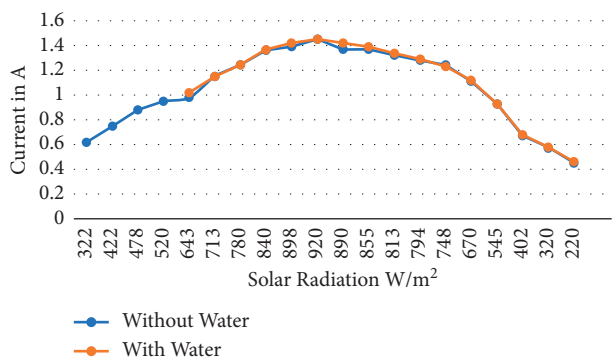

Figure 13: Current comparison of USP37 with and without water spray.

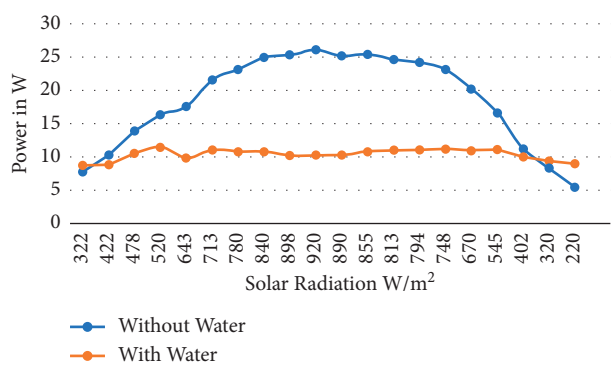

Figure 14: Power comparison of USP37 with and without water spray.

5.3. Experimental Results of PV System. The experiment is conducted on a PV system with 26 USP36 PV modules. A 1 HP DC motor is connected as a load which drives the centrifugal pump to pump up the water. The tabulated experimental results are plotted in the graph, and the variations are compared. Figure 18 shows the voltage output from the PV system with and without spraying water over the cells. On comparing the voltage output with and without pouring water, it is found that an average of 0.8 V is increased by rushing water.

The current output from the PV system with and without water spraying is shown in Figure 19. Though the current is dependent on the temperature, there is a small increase in the valve on reducing temperature.

The power output from the PV system before and after spraying water is shown in Figure 20. A maximum of 34W increase in power is found at 12.30 pm after spraying water. Figure 21 shows the comparison of the efficiency of the PV system with and without water spraying. It shows that there is an average increase of 0.5% efficiency with a maximum increase of 1.0% efficiency after spraying water.

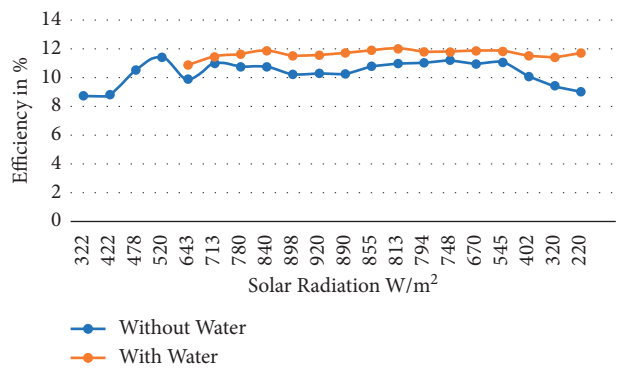

Figure 15: Efficiency comparison of USP37 with and without water spray.

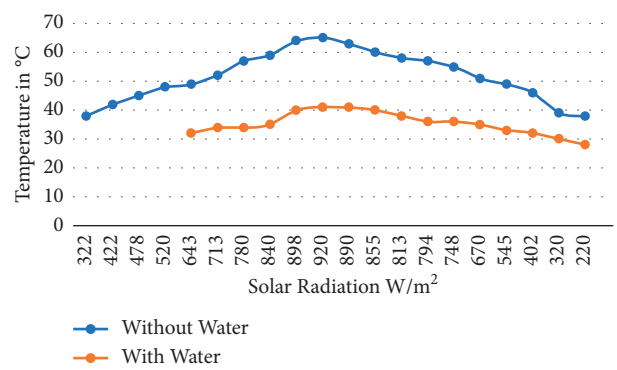

Figure 16: Temperature comparison of USP37 with and without water spray.

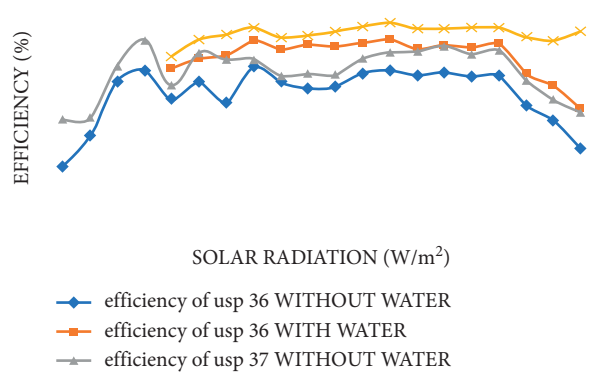

Figure 17: Comparison of efficiencies of USP36 and USP37 with and without water spraying.

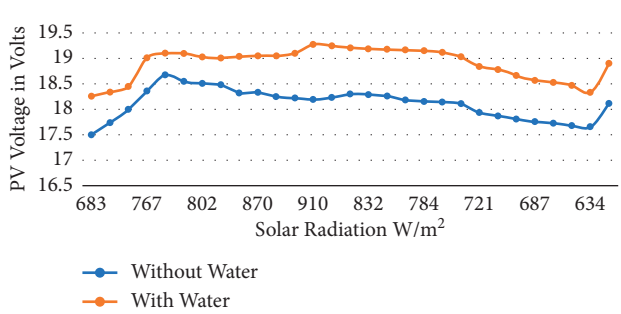

Figure 18: Voltage comparison of PV system with and without water spray.

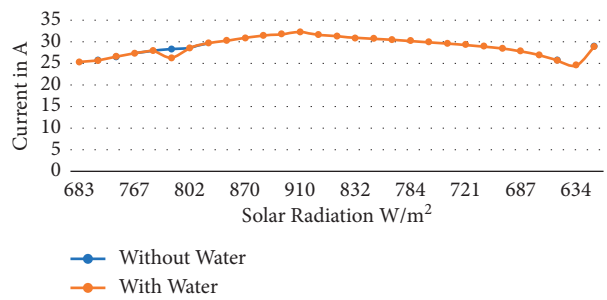

Figure 19: Current comparison of PV system with and without water spray.

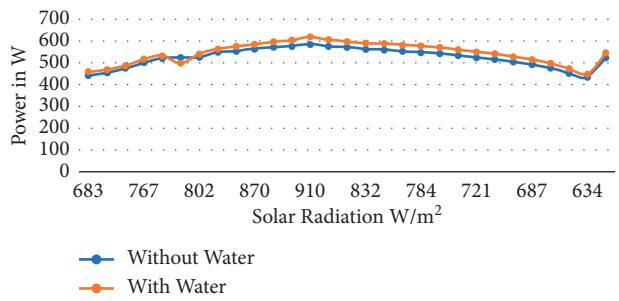

Figure 20: Power comparison of PV system with and without water spray.

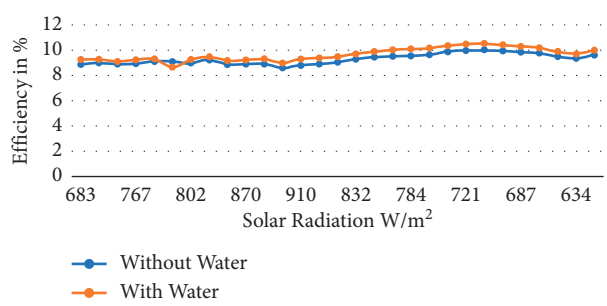

Figure 21: Efficiency comparison of PV system with and without water spray.

6. Conclusion

In this research, loss of efficiency due to the temperature rise in PV arrays is reduced by spraying water over the cells. The efficiency of the USP36 PV module with water spraying is more than the efficiency of the USP37 PV module without water spraying. It is found that spraying water over the photovoltaic cells enormously improves the PV system efficiency by around 0.5%. Thus the efficiency increase in the PV system increases the water pumping system efficiency. The approximate calculation reveals that 15.6 liters/day of water is sprayed over the entire PV modules at temperatures beyond 45°C. Due to this, water gets heated, and its temperature rises to an average of 30°C. The water with increased temperature is fed into the solar water heating system, which improves the water heating system performance. In the future, the proposed methodology can be used for the domestic PV power system with an integrated water heating system.

Data Availability

The data used to support the findings of this study are available from the corresponding author upon request.

Conflicts of Interest

The authors declare that they have no conflicts of interest.

References

[1] D. H. Muhsen, T. Khatib, and H. T. Haider, "A feasibility and load sensitivity analysis of photovoltaic water pumping system with battery and diesel generator," *Energy Conversion and Management*, vol. 148, pp. 287–304, 2017.

[2] R. Rawat, S. C. Kaushik, and R. Lamba, "A review on modeling, design methodology and size optimization of photovoltaic based water pumping, standalone and grid connected system," *Renewable and Sustainable Energy Reviews*, vol. 57, pp. 1506–1519, 2016.

[3] Y. Imene, A. Ahmad, A. Sernac, and F. Tadeoc, "Sensitivity analysis for photovoltaic water pumping systems: energetic and economic studies," *Energy Conversion and Management*, vol. 135, pp. 402–415, 2017.

[4] A. M. Zaki and M. N. Eskander, "Matching of photovolatic motor-pump systems for maximum efficiency operation," *Renewable Energy*, vol. 7, no. 3, pp. 279–288, 1996.

[5] W. H. Kazeza, S. P. Chowdhury, and L. J. Ngoma, "Optimization of a solar based water pumping system using a high step up inverter," in *Proceedings of the International Conference on Renewable Power Generation (RPG 2015)*, pp. 1–6, Beijing, China, October 2015.

[6] G. Biji, "Modelling and simulation of PV based pumping system for maximum efficiency," in *Proceedings of the 2012 International Conference on Power, Signals, Controls and Computation*, pp. 1–6, Thrissur, India, January 2012.

[7] A. Moussi and A. Torki, "An improved efficiency Permanent Magnet brushless DC motor PV pumping system," *LARHYSS 144 Journal*, vol. 1, 2002.

[8] M. Jafar, "A model for small-scale photovoltaic solar water pumping," *Renewable Energy*, vol. 19, no. 1-2, pp. 85–90, 2000.

[9] S. M. A. Ibrahim, H. H. El-Ghetany, and A. G. M. Shabak, "Comprehensive design tool for sizing solar water pumping system in Egypt," *Applied Solar Energy*, vol. 56, no. 1, pp. 18–29, 2020.

[10] A. Al-Badi, H. Yousef, T. Al Mahmoudi, M. Al-Shammaki, A. Al-Abri, and A. Al-Hinai, "Sizing and modelling of photovoltaic water pumping system," *International Journal of Sustainable Energy*, vol. 37, no. 5, pp. 415–427, 2017.

[11] D. Langridge, W. Lawrance, and B. Wichert, "Development of a photo-voltaic pumping system using a brushless d.c. motor and helical rotor pump," *Solar Energy*, vol. 56, no. 2, pp. 151–160, 1996.

[12] R. Nisha and K. G. Sheela, "Review of pv fed water pumping systems using BLDC motor," *Materials Today Proceedings*, vol. 24, no. 3, pp. 1874–1881, 2020.

[13] R. Kumar and B. Singh, "BLDC motor driven water pump fed by solar photovoltaic array using boost converter," in *Proceedings of the 2015 Annual IEEE India Conference (INDICON)*, pp. 1–6, New Delhi, India, December 2015.

[14] B. Singh and R. Kumar, "A simple BLDC motor drive for solar PV array fed water pumping system," *IET Power Electronics*, vol. 9, no. 7, 2016.

[15] B. Singh, U. Sharma, and S. Kumar, "Standalone photovoltaic water pumping system using induction motor drive with reduced sensors," *IEEE Transactions on Industry Applications*, vol. 54, no. 4, 2018.

[16] R. Chinthamalla, S. Padmanaban, R. Karampuri, S. Jain, A. H. Ertas, and V. Fedak, "A solar PV water pumping solution using a three-level cascaded inverter connected induction motor drive," *Engineering Science and Technology, an International Journal*, vol. 19, no. 4, pp. 1731–1741, 2016.

[17] P. Choudhary, R. K. Srivastava, and S. De, "Solar powered induction motor-based water pumping system: a review of components, parameters and control methodologies," in *Proceedings of the Conference: 2017 4th IEEE Uttar Pradesh Section International conference on Electrical, Computer and Electronics (UPCON)*, Mathura, India, October 2017.

[18] P. Dwivedi, K. Sudhakar, A. Soni, E. Solomin, and I. Kirpichnikova, "Advanced cooling techniques of PV modules: a state of art," *Case Studies in Thermal Engineering*, vol. 21, Article ID 100674, 2020.

[19] K. Benlarbi, L. Mokrani, and M. S. Nait-Said, "A fuzzy global efficiency optimization of a photovoltaic water pumping system," *Solar Energy*, vol. 77, no. 2, pp. 203–216, 2004.

[20] A. Betka and A. Moussi, "Performance optimization of a photovoltaic induction motor pumping system," *Renewable Energy*, vol. 29, no. 14, pp. 2167–2181, 2004.

[21] S. Biswas and M. T. Iqbal, "Dynamic modelling of a solar water pumping system with energy storage," *Journal of Solar Energy*, vol. 2018, Article ID 8471715, 12 pages, 2018.

[22] O. V. Shepovalova, A. T. Belenov, and S. V. Chirkov, "Review of photovoltaic water pumping system research," *Energy Reports*, vol. 6, no. S6, pp. 306–324, 2020.

[23] M. Das and R. Mandal, "A comparative performance analysis of direct, with battery, supercapacitor, and battery-supercapacitor enabled photovoltaic water pumping systems using centrifugal pump," *Solar Energy*, vol. 171, pp. 302–309, 2018.

Hindawi
Mathematical Problems in Engineering
Volume 2022, Article ID 2447299, 9 pages
https://doi.org/10.1155/2022/2447299

Research Article

SSNN-Based Energy Management Strategy in Grid Connected System for Load Scheduling and Load Sharing

Yuvaraja Teekaraman,[1] **K. A. Ramesh Kumar**,[1] **Ramya Kuppusamy**,[1] **and Amruth Ramesh Thelkar**[2]

[1]*Department of Energy Science (Formerly Energy Studies), Periyar University, Salem City 636011, India*
[2]*Faculty of Electrical & Computer Engineering, Jimma Institute of Technology, Jimma University, Jimma, Ethiopia*

Correspondence should be addressed to Yuvaraja Teekaraman; yuvarajastr@gmail.com and Amruth Ramesh Thelkar; amruth.rt@gmail.com

Received 25 October 2021; Revised 22 November 2021; Accepted 10 December 2021; Published 10 January 2022

Academic Editor: Ravi Samikannu

The proposed research work focused on energy management strategy (EMS) in a grid connected system working in islanding mode with the connected renewable energy resources and battery storage system. The energy management strategy developed provides a balancing operation at its output by utilizing perfect load sharing strategy. The EMS technique using smart superficial neural network (SSNN) is simulated, and numerical analyses are presented to validate the effectiveness of the centralized energy management strategy in a grid connected islanded system. A SSNN prediction model is unified to forecast the associated household load demand, PV generation system under various time horizons (including the disaster condition), EV availability, and status on EV section and distance. SSNN is one the most reliable forecasting methods in many of the applications. The developed system is also accounted for degradation battery model and its associated cost. The incorporation of energy management strategy (EMS) reduces the amount of energy drawn from the grid connected system when compared with the other optimized systems.

1. Introduction

Energy storage and management play a vital role in the installation of the smart grid system as they increase the stability, resiliency, and efficiency of the grid connected system. In today's scenario, generating power using renewable energy resources needs to be balanced dynamically with the dynamic changing load. The smart grid operator has limited resources and techniques to maintain stability in the present changing atmospheric condition and load profiles.

The power conversion system plays a prominent role in the grid connected renewable energy resource system. The most challenging phenomenon in the power distribution system is the loss occurring in the conversion system. The power conversion system is utilized when the power is required to transfer it from source to load; else the process manages to store the energy in the connected storage system [1]. Genetic algorithm is used for better system optimization, and it has gained importance in reducing the cost of electricity [1]. In integrating the energy storage system with the power generation system, an effective operating point on storage capacity needs to be considered. Reinforcement learning is incorporated in battery sizing and real-time EMS [2].

Electric traction is the most prominent area for implementing the energy storage and energy management technique.

Model predictive control algorithm was utilized in railway control activity to improve the system efficiency and to reduce the operating cost of the system [3]. The integration of RES like solar, wind, geothermal, and biomass with the grid addresses many issues towards environmental pollution and energy scarcity [4]. Decentralized control strategy architecture is used for better energy management. The uncertainties in the RES connected system [5] are handled by modeling the EMS at the level of individual grid

and in turn can be configured for multistage systems. Energy storage in the grid connected system provides larger benefits. The modeling of BESS along with BMS in [6] is categorized based on time scale. The study made by the authors in [6] investigates the benefits of energy storage during power generation, distribution, and power transmission. Due to energy crisis, RES is integrated with the present conventional sources system.

The integrated grid allows the customer to use the load. The HEMS installed at home server collects all the data pertaining to load usage, analyzes the collected data, and develops the control strategy for reducing the cost of electricity [7]. The control strategy in [8] compares the grid connected system with centralized and decentralized control strategies. Implementing the CCS and DCS provides output comparative statement in terms of battery life cycle, cost of electric energy, and battery size determination. Existing energy management techniques discussed in [9] examine the effect of system level energy reduction strategy in accordance with the energy consumption of RTS which uses duplication for fault tolerance. The comparative analysis gives a key note to the researcher for deciding the most appropriate energy storage and management strategy for particular application. The energy management strategies installed in the grid connected system [10] ensure complete system stability and economic level of operation. The multiagent HEMS (MAHEMS) includes the feature of both CCS and DCS. Therefore, the MAHEMS is developed as 3 levels of EMS framework that provides both local and autonomous level of coordinated energy control in centralized grid operation. With the development of smart grid, energy transition happens from passive energy consumers to an active smart grid supplier [11]. The integration of RES in [12] plays a vital role in future energy system. The use of RES as integrated resources reduces CO_2 emission with the high-level penetration of RES in various transmission system operators. Grid with an integrated RES with energy storage and curtailable load and non-curtailable load provides low-voltage distribution system (LVDS). Smart grid is a novel approach that clusters the small distributed generators. The variable power generation, load profiles, and energy cluster parameters are compared with decision tree approach under different battery energy storage conditions. The universal energy storage and management strategy in [13] produce result as reduction in energy saving as compared with the traditional approach. The present available PHEV in [14] is being connected with battery as single energy storage system. The battery has limited power density due to its inherent chemical characteristics, which affects the performance of the PHEV system. The objective focused in [14] minimizes the usage of electricity in EV and increases the lifetime of the battery. The control strategy as two-level structure for the integrated hybrid standalone system is discussed in [15]. Due to continuous change in atmosphere, the uncertainties occurring in RES are handled by the two-level control strategy and provide perfect energy management, power regulation, and load scheduling operation and control.

2. System Architecture

The grid connected system can be operated either by centralized control strategy (CCS) or by means of decentralized control strategy (DCS). In the case of decentralized control strategy (DCS), individual customer pertaining to the load usage will deal all sort of energy transactions directly with the grid, whereas it is not in the case of centralized control strategy (CCS). The fishbone diagram of centralized control strategy is shown in Figure 1. The centralized strategy shown in Figure 1 is the aggregator which is responsible to make energy transactions between the grid and various loads (EV system, household loads, and industrial loads). The grid support services are provided by the individual customer in DCS and the aggregator in CCS. The fishbone shown in Figure 1 acts as an aggregator which groups all the agents connected in a power system and acts as a single object in energy markets/grid operator services. The fishbone as aggregator performs demand response operation, monitors various connected loads, and controls system equipment, energy generation, and storage sources. The developed fishbone model for CCS reduces the electric tariff for an individual customer and shared stakeholders and prepares an augmented schedule for charging/discharging of EV and connected stationary battery based on the most prominent time of power generation by the PV system. The fishbone connected to the CCS completely owns and manages the connected PV source, fuel cell power module, and the battery connected system.

The EV system owners send their augmented schedule preferences for charging/discharging of EV to the aggregator. The fishbone as aggregator is a place for predicting the power required to handle the connected load profiles based on the weather condition. The weather condition and the time horizon (short term, midterm, and long term) develop a series of dataset in solar PV generation. The status of the system components under various time horizons is shown in Table 1. Based on this historical time series datasets, the aggregator is having the access to towards the connected loads, EV charging and discharging station, connected PV source, grid connected power station, and the battery storage system.

3. Energy Management Proposed Flow Model

The energy management strategy's process flow model comprises the (i) optimization model, (ii) prediction model, (iii) battery operation model, and (iv) validation model. The function hold by each of the process flow model is represented in Figure 2. The proposed EM strategy bifurcates its operation in terms of load sharing and managing by scheduling the process of charging/discharging in daily basis and governs the energy supply and demand to reduce the tariff rate. The proposed EMS model analyzes the connected load, connected PV resources, and required power for EV charging/discharging station based on time horizon. The fishbone aggregator model analyzes all the required loads that are connected to the interconnected system and communicates the charging/discharging schedule of EV

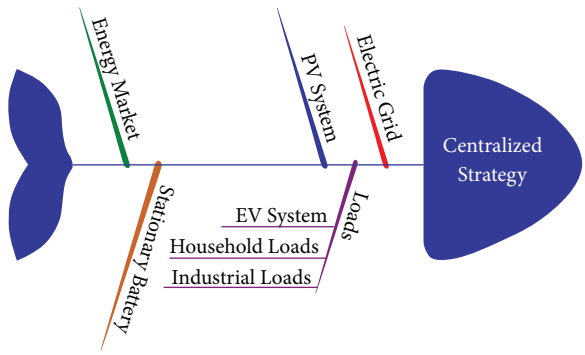

Figure 1: Fishbone aggregator architecture diagram of centralized strategy.

based on the mixed-integer linear programming (MILP) model subjected to grid constraints. The load predictions for the day are predicted and given as input to optimization model in order to formulate the optimum schedule of charging/discharging required for the EV station and other connected battery storage systems.

$$\mathscr{F}_t^{loads} = \sum_{j=1}^{n} \mathfrak{L}_j f\left[\mathscr{W}_{0j} + \sum_{i=1}^{x} \mathscr{W}_{ij} \mathscr{F}_{t-1}^{loads}\right] + \mathfrak{R}_t + \mathfrak{L}_0, \quad (1)$$

4. Energy Prediction Model

A smart superficial neural network (SSNN) prediction model is incorporated to predict the connected household load demand, PV generation system from different time horizons, EV availability, and status on EV section and distance. SSNN is one the most reliable forecasting methods in many of the applications. A commonly used backpropagation algorithm (BPA) is utilized in feed-forward mode. The forecasted value in terms of connected household load demand and PV generation system from different time horizons can be expressed as follows:

where equation (1) refers to the forecasted value of the demand with reference to connected load and the power availability in PV generation system. The forecasted value is calculated using SSNN, in which the weight function and the bias variable decide the amount of load to be handled in the connected system.

$\mathscr{F}_t^{loads}$-Forecasted value in terms of connected household load demand and PV generation system, $\mathfrak{L}_j$ and $\mathscr{W}_{ij}$-Weights from the layer, n-Number of hidden layers in SSNN model, $\mathfrak{L}_0$ and $\mathscr{W}_{0j}$-Bias terms of SSNN model, Loads $\in \mathscr{L}_t$ $\mathscr{K}_t$-$\mathscr{L}_t$: household loads and $\mathscr{K}_t$: PV generation system, t-Time.

The next parameter in the prediction model is EV availability. The existing antique time series data for EV travel pattern are utilized to extract probability distribution function (PDF) for categorizing the EV availability with reference to travel distance and range efficiencies. The EV availability for charging and discharging is represented in terms of binary definition as "0" when EV is "not available" and "1" when EV is "available." The EV availability as a function of time "t" and day "d" of the week is expressed as in equation (2) subjected to varying atmospheric temperature. The flow diagram showing the EV availability status is shown in Figure 3.

$$\mathbb{EV}_t = f\left(t \| \mathbb{S}_{EV,t}, \mathbb{P}_{EV,t}\right) = \binom{\mathbb{S}_{EV,t}}{\mathbb{P}_{EV,t}} \mathbb{P}_{EV,t}\left(1 - \mathbb{P}_{EV,t}\right)^{\left(\mathbb{S}_{EV,t} - t\right)}, \quad (2)$$

where $\mathbb{EV}_t$ represents the EV availability w.r.t time, $\mathbb{S}_{EV,t}$ represents the number of scenarios available in EV w.r.t time, and $\mathbb{P}_{EV,t}$ represents the PDF of EV scenarios.

The algorithm to find the EV availability status is shown below. The value given in the EV availability status algorithm is calculated as a function of time, day of the week at varying temperature as given in equation (2). At $t = 12$ noon, the EV availability is measured in terms of insolation. The available insolation at 12 noon is 1000. From $t = 8$ am to $t < 12$ noon, the insolation measured is 650, and it is applied in equation (2), and the obtained EV status is 3 and 2, depending on the variation occurring due to atmospheric condition. For $t > 12$ noon, the insolation measured varies from 700 to 990 and the obtained EV status is 4 and 2 (Algorithm 1).

5. Battery Operation Mathematical Modeling

The state of charge (SOC) and the state of health (SOH) define the battery life. The SOC on EV at any time t is modeled by using equation (3) based on SOC on EV at time $t = t - 1$, charging/discharging efficiency on EV battery, charging/discharging power on EV, and maximum EV battery capacity. By specification, each battery has its own maximum and minimum SOC. Based on the specification according to equation (4), the modeled system considers its upper and lower limits of battery SOC and its distance travelled when EV is away from the substation so as to improve the effectiveness of battery SOH.

$$\mathrm{SOC}_t^{\mathrm{EV}} = \mathrm{SOC}_{t-1}^{\mathrm{EV}} + \frac{\eta_{\mathrm{EVC}} \mathbb{P}_{\mathrm{EVC},t} \mathbb{A}_t \mathscr{F} t}{\mathbb{AH}_{EV,\max}} - \frac{\mathbb{P}_{EV\ d,t} \mathbb{A}_t \mathscr{F} t}{\eta_{EV\ d} \mathbb{AH}_{EV,\max}}, \quad \leftrightarrow \mathbb{A}_t = 1,\ t \in T, \quad (3)$$

where SOC_t^{EV} represents the state of charge on EV battery at time "t," η_{EVC} represents the charging efficiency on EV battery, $\eta_{EV\ d}$ represents the discharging efficiency on EV battery, SOC_{t-1}^{EV} represents the state of charge on EV battery at time "$t-1$," $\mathbb{P}_{EVC,t}$ represents the maximum EV battery charging power (kW), $\mathbb{P}_{EV\ d,t}$ represents the maximum EV battery discharging power (kW), $\mathbb{A}_t$ represents the availability matrix, $\mathbb{AH}_{EV,\max}$ represents the maximum battery

Table 1: Connected system status under various time horizons.

Scenario	Status of PV system	Stationary battery usage	Gas turbine system	Thermal storage system	Cost minimization	Maximum CO_2 emissions
Short-term horizon	No	No	No	No	Yes	No
Midterm horizon	Yes	Yes	Yes	No	Yes	No
Long-term horizon	Yes	Yes (discounted)	Yes	Yes	Yes	No

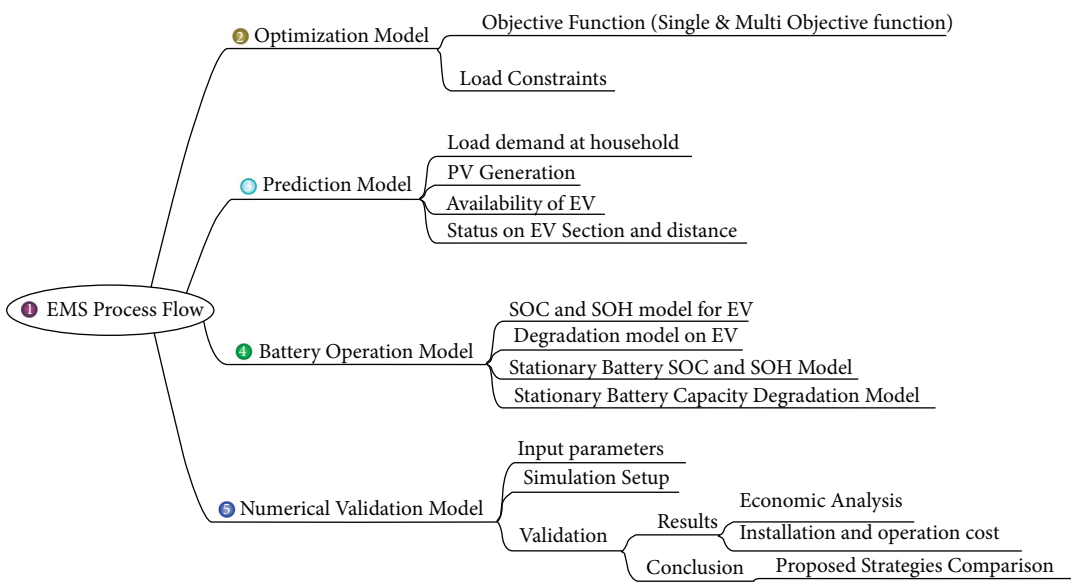

Figure 2: Energy management strategy process flow.

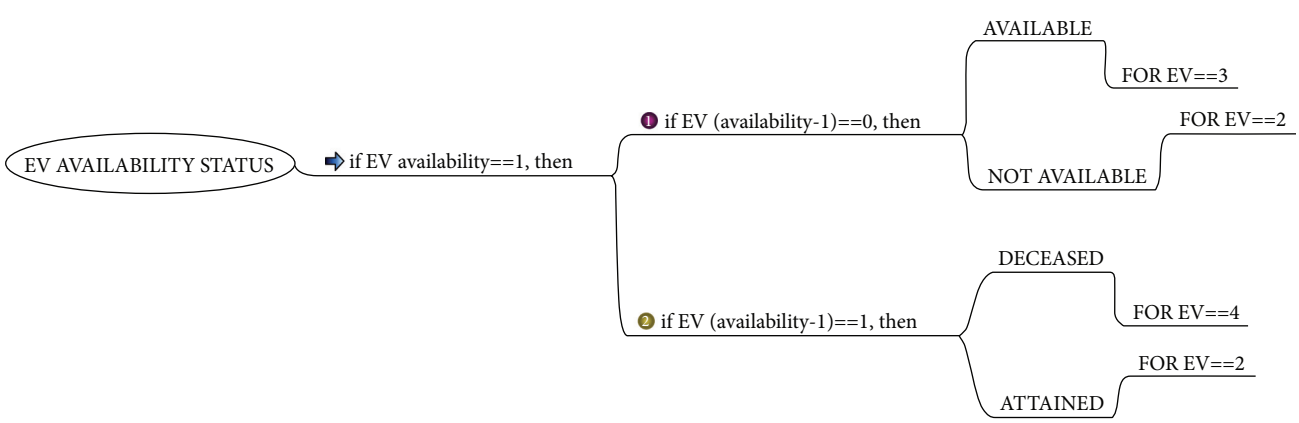

Figure 3: Flow diagram of EV availability status.

capacity in ampere hour, η_{EV} represents the efficiency on EV battery (KWh/km), and d_{EV} represents the distance travelled by EV.

$$\mathrm{SOC}_t^{EV} = \mathrm{SOC}_{t-1}^{EV} - \frac{\eta_{EV} d_{EV}}{\mathbb{AH}_{EV,\max}}, \quad \leftrightarrow \mathbb{A}_t = 0,\ t \in T. \tag{4}$$

The degradation phenomenon in EV battery is observed in rechargeable batteries that reduce the lifetime of the battery over the specific period of time. This in turn increases the operating cost. Therefore, while modeling the battery degradation model, cost should be taken into account along with all the services.

6. Optimization Model

The main objective of developing the optimization model is to minimize the electric tariff. The process flow optimization model is shown in Figure 4, and the objective function is

```
for t ∈ T,  perform
if EV availability EV_t = 1, then
if EV (availability-1) EV_{t-1} = 0, then
EV Status = 3
Else
EV Status = 2 endif
else
if EV (availability-1) EV_{t-1} = 1, then
EV Status = 4 else
EV Status = 2 endif
endif
endfor
```

Algorithm 1: EV availability status algorithm.

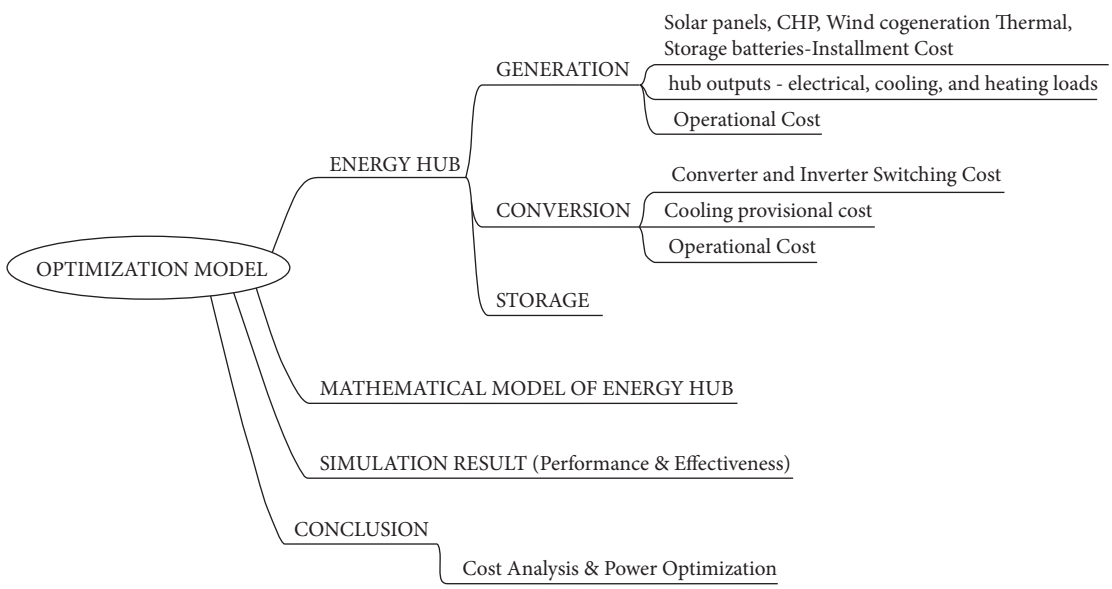

Figure 4: Process flow optimization model.

developed based on energy purchased, energy sold, and the degradation cost.

The expected operating cost of the asset is expressed as follows:

$$\text{OC} = \text{energy purchased} + \text{energy sold} + \text{degradation cost},$$

$$OC = \sum_{t\in T} (\alpha P_t \Delta t)\$_p + (\beta P_t \Delta t)\$_S + \left(\$_d^{EV} + \$_d^B\right), \tag{5}$$

where P_t is the power flow to and from grid at any time "t," α and β are binary variables for power drawn and power supplied to or from the grid, $\$_p$ is the purchased energy tariff, and $\$_S$ is the energy sold tariff. Table 2 presents the binary variable constraints and their status. Energy is purchased to the grid, when $\alpha = 1$ and $\beta = 0$; under this condition, the power drawn from the grid is positive. Energy is sold from the grid, when $\alpha = 0$ and $\beta = 1$; under this condition, the power drawn from the grid is negative.

Table 2: Binary variable constraints and their status.

	PCC status	α	β
Energy purchase	Power drawn from the grid is positive	1	0
Energy sold	Power drawn from the grid is negative	0	1

7. Simulation Setup and Test Results

The proposed strategy is developed for the given system configuration as shown in Table 3, using MATLAB, and its simulation set of energy management system with hybrid sources is as shown in Figure 5. The PV source is connected to the grid connected system PCC point via the energy storage systems like fuel cell, battery, and supercapacitor. The system is operated at discrete time interval with an operating switching frequency of 10 KHz. The energy management system (EMS) controls the power of the entire energy source devices through reference signals.

Table 3: System configuration.

Parameter	System rating
Solar panel	Polycrystalline solar panel
Number of solar panels connected	70 nos.
Total number of stationary battery units	10 nos.
Battery AH	5 AH
Household load capacity	6 kW

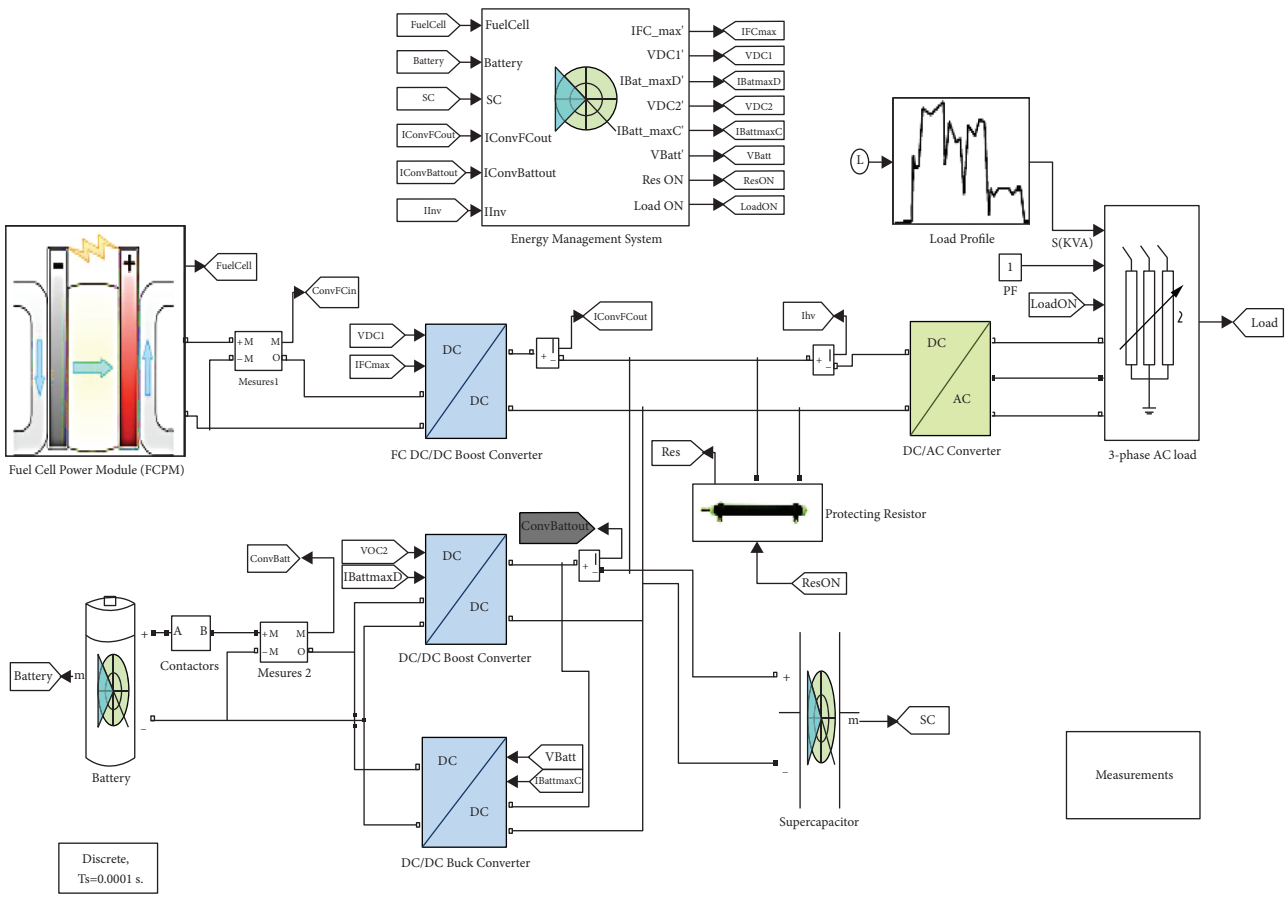

Figure 5: Simulation of grid connected system with its energy storage.

The subsystem of energy system modeling is shown in Figure 6 which provides the state machine control strategy. The simulation of the grid connected islanding mode network uses the ANN prediction model to generate the household load and the details of solar PV generation. The nntool in MATLAB is utilized to develop feed-forward backpropagation algorithm. It comprises the input layer (time of the day), hidden layer (load schedule), output layer (power gets distributed to the load according to the required schedule). The hidden layer neuron is assigned with the membership function of tansig (hyperbolic tangential sigmoidal), and the output layer is assigned with purelin (pure linear function) membership function. The SSNN showing the details of the attributes towards the input layer, hidden layer, and output layer is shown in Figure 6. The prediction model developed uses the three-layer network and is trained by the Levenberg–Marquardt algorithm (LMA). LMA is one of the most prominent algorithms as it is operative in categorizing the least convex objective function. The integration of the steepest descent method and the Gauss–Newton quadratic convergence method makes it possible in categorizing the least convex objective function. Increasing the power availability in the system makes perfect system load forecast schedule.

Load scheduling is done based on power generation in the integrated grid system. Figure 7 shows the PV system inclination angle analysis using fuzzy ANN. As shown in Figure 7, the amount of solar irradiance falling on the solar PV system is increased when the tilt angle is at 10.1°. During this period of time, the amount of power generation is more. Based on this sample, the PV dataset is taken and analyzed as shown in Figure 8.

Since the irradiance is not constant throughout the day, power generation will not be constant. To supply constant

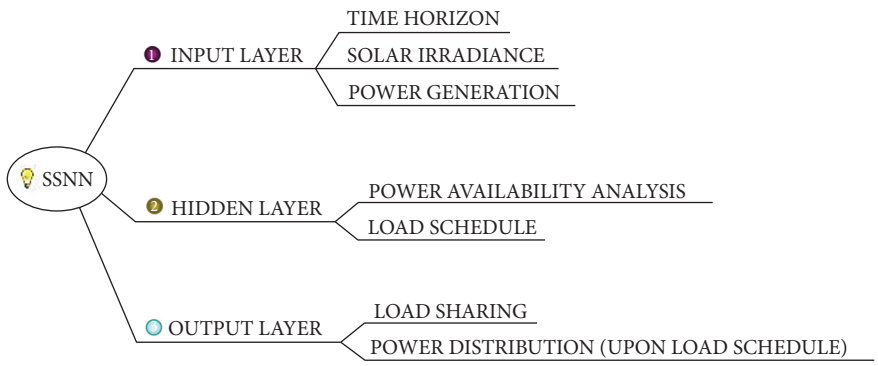

Figure 6: Smart superficial neural network attributes.

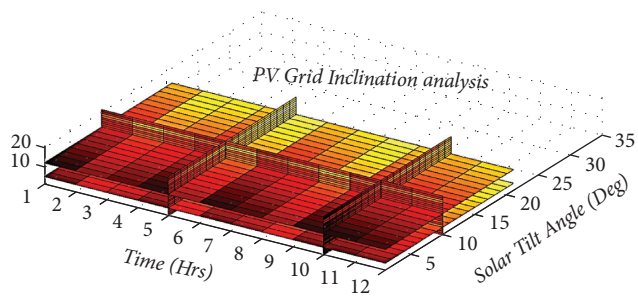

Figure 7: PV grid inclination analysis.

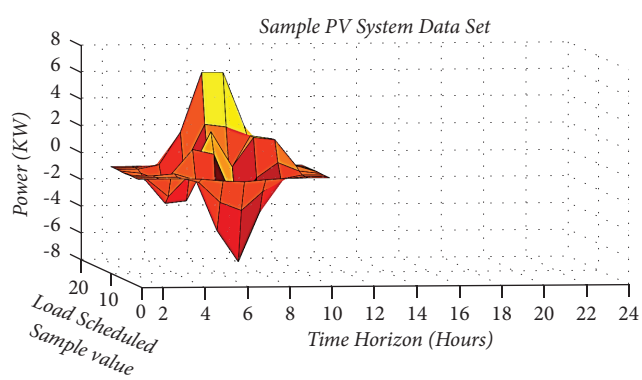

Figure 8: Sample PV dataset.

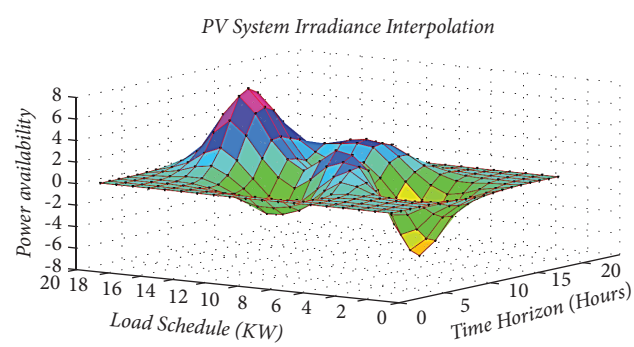

Figure 9: PV system interpolation towards load schedule.

power to the load, energy storage system is incorporated. Since the insolation is varied in nature based on time horizon, the designed model is considered to fall under nonlinear system analysis and outstrips using gradient descent and conjugate gradient methods. Based on sample PV system data, 10 neurons were initiated in the hidden layer and later the number of neurons in the hidden layer is increased depending upon the load schedule. The interpolation of the PV system towards the forecasted load schedule is shown in Figure 9. Peak power availability and its utilization towards EV and stationary system load demand are shown in Figure 9.

The sample dataset shown in Figure 8 is utilized by the prediction model. The sample dataset is subclassified as training set, validating set, and testing set, in which 70% of data are considered as training set and remaining 30% are considered as validating and testing sets.

The output shown in Figure 10 shows SOC of V2G service that regulates the frequency on the interconnected grid system on 24-hour basic. The V2G service has two main functions which control the charging on to the connected battery and use the available power to regulate the grid.

Figure 10 shows the battery SOC status at 5 different profiles.

Profile #1: Figure 10(a) shows the status of battery charging status. During this stage, the battery gets charged to a maximum value of 95%. Most of the time, the battery is connected to the system resources and gets charged to a maximum value.

Profile #2: as shown in Figure 10(b), the battery is in the charging state but is no longer used to supply load. In

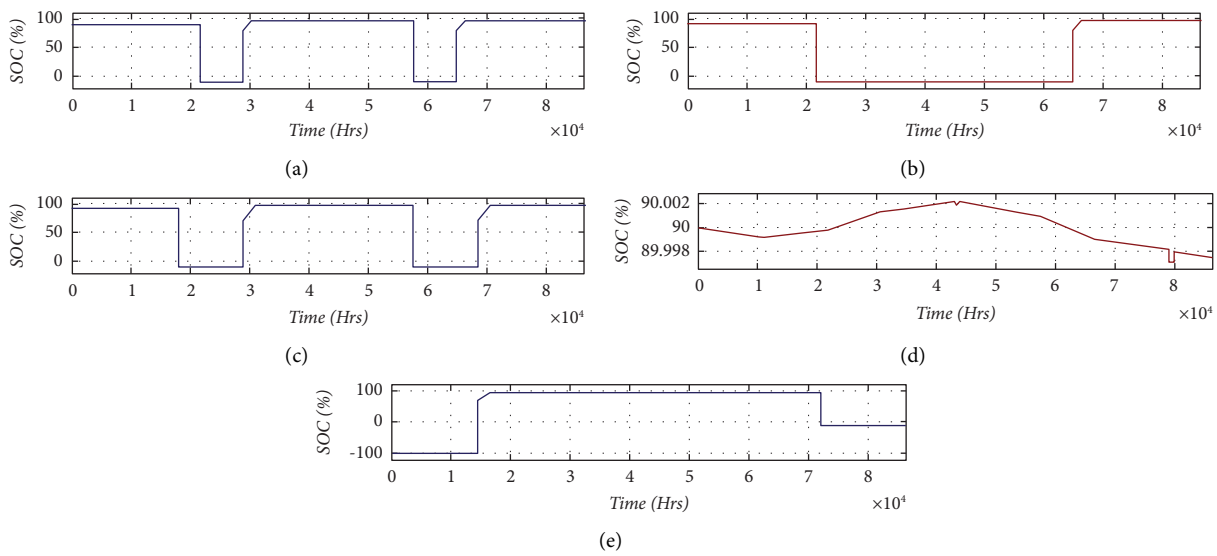

Figure 10: Battery SOC status at various profiles.

this condition, the PV system charges the battery but does not supply power to load. From $t = 2$ to $t = 6.5$, the battery power is drained and the SOC value is approximately 0%. Again from $t = 6.5$, the battery starts to charge from the source.

Profile #3: as shown in Figure 10(c), the battery is connected, but there is no possibility to charge.

Profile #4: as shown in Figure 10(d), the battery is in the ideal state. During this condition, the range of SOC varies between 89.998 and 90.002%.

Profile #5: as shown in Figure 10(e), during night time, the solar PV system does not deliver any power, and at that moment, the battery connected in the system supplies power to the charging EV station.

8. Conclusion

A centralized energy management strategy is proposed in this paper for EV system charging and discharging strategy, so as to reduce the tariff rate. The prediction models were investigated using SSNN to predict the availability of solar power at various time horizons. Based on the availability of power, the load forecasting schedule is proposed for EV charging/discharging and the stationary battery storage system. The SSNN-based EMS strategy is designed based on weight adjustment, where in the simulation process, 70% of data are considered as training set and the remaining 30% are considered as validating and testing sets. The weight adjustment finds the exact EV availability status at different atmospheric conditions as EV Status = 4 & 2 for EV (availability-1) $\mathbb{EV}_{t-1} = 1$ and EV status = 3 & 2 for EV (availability-1) $\mathbb{EV}_{t-1} = 0$. The status of power drawn is given in equation (5) when $\alpha = 1$ and $\beta = 0$; under this condition, the power drawn from the grid is positive. Energy is sold from the grid, when $\alpha = 0$ and $\beta = 1$, and under this condition, the power drawn from the grid is negative. The modeling and simulation test results indicate that the designed CEMS is more effective in terms of reducing the tariff rate and load sharing. The relevance of the proposed work provides better V2G service and supplies high-quality power to the scheduled EV load and stationary load. As future enhancement, atmospheric disaster can be considered and big data analysis can be incorporated to further enhance the system security with effective load sharing in the grid connected smart system. The role of big data analysis in optimization techniques can be applied to reduce the uncertainty caused by the connected renewable energy resources. The power generation by nondispatchable energy conversion technologies is highly variable and unpredictable; that leads to the technology of developing and planning for an optimized operation tool in order to maximize the economy with sustained performance.

Nomenclature

EMS:	Energy management strategy
CCS:	Centralized control strategy
DCS:	Decentralized control strategy
DBM:	Degradation battery model
MILP:	Mixed-integer linear programming
SSNN:	Smart superficial neural network
PDF:	Probability distribution function
SOC:	State of charge
SOH:	State of health
PCC:	Point of common coupling
ANN:	Artificial neural network
LMA:	Levenberg–Marquardt algorithm
V2G:	Vehicle-to-grid
RTS:	Real-time system
RES:	Renewable energy source
HEMS:	Hybrid energy management system
MAHEMS:	Multiagent hybrid energy management system
LVDS:	Low-voltage distribution system.

Data Availability

The data used to support the findings of this study are available from the corresponding author upon request.

Conflicts of Interest

The authors declare that they have no conflicts of interest.

References

[1] S. Gangatharan, M. Rengasamy, R. M. Elavarasan, N. Das, E. Hossain, and V. M. Sundaram, "A novel battery supported energy management system for the effective handling of feeble power in hybrid microgrid environment," *IEEE Access*, vol. 8, pp. 217391–217415, 2020.

[2] J. Nunez Forestieri and M. Farasat, "Integrative sizing/real-time energy management of a hybrid supercapacitor/undersea energy storage system for grid integration of wave energy conversion systems," *IEEE Journal of Emerging and Selected Topics in Power Electronics*, vol. 8, no. 4, pp. 3798–3810, Dec. 2020.

[3] H. Novak, V. Vasak, and M. Vašak, "Hierarchical model predictive control for coordinated electric railway traction system energy management," *IEEE Transactions on Intelligent Transportation Systems*, vol. 20, no. 7, pp. 2715–2727, July 2019.

[4] R. H. Byrne, T. A. Nguyen, D. A. Copp, B. R. Chalamala, and I. Gyuk, "Energy management and optimization methods for grid energy storage systems," *IEEE Access*, vol. 6, pp. 13231–13260, 2018.

[5] B. Zhao, X. Wang, D. Lin et al., "Energy management of multiple microgrids based on a system of systems architecture," *IEEE Transactions on Power Systems*, vol. 33, no. 6, pp. 6410–6421, 2018.

[6] M. T. Lawder, B. Suthar, P. W. C. Northrop et al., "Battery energy storage system (BESS) and battery management system (BMS) for grid-scale Applications," *Proceedings of the IEEE*, vol. 102, no. 6, pp. 1014–1030, June 2014.

[7] J. Han, C.-s. Choi, W.-k. Park, I. Lee, and S.-h. Kim, "Smart home energy management system including renewable energy based on ZigBee and PLC," *IEEE Transactions on Consumer Electronics*, vol. 60, no. 2, pp. 198–202, May 2014.

[8] T. Kovaltchouk, A. Blavette, J. Aubry, H. B. Ahmed, and B. Multon, "Comparison between centralized and decentralized storage energy management for direct wave energy converter farm," *IEEE Transactions on Energy Conversion*, vol. 31, no. 3, pp. 1051–1058, Sept. 2016.

[9] S. Aminzadeh and A. Ejlali, "A comparative study of system-level energy management methods for fault-tolerant hard real-time systems," *IEEE Transactions on Computers*, vol. 60, no. 9, pp. 1288–1299, 2011.

[10] M. Mao, P. Jin, N. D. Hatziargyriou, and L. Chang, "Multi-agent-based hybrid energy management system for microgrids," *IEEE Transactions on Sustainable Energy*, vol. 5, no. 3, p. 1, July 2014.

[11] C. Molitor, S. Gross, J. Zeitz, and A. Monti, "MESCOS-A m system c for city district energy systems," *IEEE Transactions on Industrial Informatics*, vol. 10, no. 4, pp. 2247–2256, 2014.

[12] G. K. Venayagamoorthy, R. K. Sharma, P. K. Gautam, and A. Ahmadi, "Dynamic energy management system for a smart microgrid," *IEEE Transactions on Neural Networks and Learning Systems*, vol. 27, no. 8, pp. 1643–1656, Aug. 2016.

[13] N. Nishikawa, M. Nakano, and M. Kitsuregawa, "Application sensitive energy management framework for storage systems," *IEEE Transactions on Knowledge and Data Engineering*, vol. 27, no. 9, pp. 2335–2348, 1 Sept. 2015.

[14] C. Zheng, W. Li, and Q. Liang, "An energy management strategy of hybrid energy storage systems for electric vehicle applications," *IEEE Transactions on Sustainable Energy*, vol. 9, no. 4, pp. 1880–1888, Oct. 2018.

[15] A. M. O. Haruni, M. Negnevitsky, M. E. Haque, and A. Gargoom, "A novel operation and control strategy for a standalone hybrid renewable power system," *IEEE Transactions on Sustainable Energy*, vol. 4, no. 2, pp. 402–413, April 2013.

Hindawi
Mathematical Problems in Engineering
Volume 2021, Article ID 7629414, 10 pages
https://doi.org/10.1155/2021/7629414

Research Article

Dynamic Equivalent Modeling of Wind Farm Based on Dominant Variable Hierarchical Clustering Algorithm

Wenbo Jiang[1,2] **and Mingyue Zhong**[1,2]

[1]*School of Electrical Engineering and Electronic Information, Xihua University, Chengdu 610039, China*
[2]*Sichuan Provincial Key Laboratory of Signal and Information Processing, Xihua University, Chengdu 610039, China*

Correspondence should be addressed to Wenbo Jiang; caswenbojiang@gmail.com

Received 23 September 2021; Accepted 9 November 2021; Published 29 November 2021

Academic Editor: Albert Alexander Stonier

The actual operating state of the wind turbine group is influenced by the wake effect and control mode; however, the current models cannot describe the actual operating state very well. A dynamic equivalent modeling method for a doubly fed wind power generator is proposed on the basis of ensuring the accurate description of the wind turbine group. As the clustering index, dominant variables are used in the hierarchical clustering algorithm, which are extracted by principal component analysis. Three dynamic equivalent models of 24 wind turbines are established using PSCAD software platform, which use 13 state variables, wind speed, and dominant variables as clustering indexes, respectively. Furthermore, the active power and reactive power output curves of wind farm are simulated in the case of the three-phase short-circuit fault on the system side or wind speed fluctuation, respectively. The simulation results demonstrate that it is reasonable and effective to extract slip ratio and wind turbine torque as clustering index, and the maximal relative error between the dominant variable equivalent model and 13-state-variable model is only 9.9%, which is greatly lower than that of the wind speed model, K-means clustering model, neural network model, and support vector machine model. This model is easy to implement and has wider application prospect, especially for characteristics analysis of large-scale wind farm connected to power grid.

1. Introduction

Wind power generation is one of the most important renewable energies, which has attracted more and more attention from most of the countries for its mature technology and low cost in recent years [1]. However, wind energy has characteristics of random, intermittent, and instability. It is very difficult to study the operational characteristics of power grid with large-scale wind farm interconnection [2–4]. Therefore, it is necessary to establish an effective model of wind farm, which should be as close as possible to the actual operating state of wind farm. Literature [5] proposed a method of reduced-order model computation for planning grid connection of a large-scale wind farm, and the effectiveness of the proposed method is demonstrated and evaluated by an illustrative simple example wind farm and an example large-scale wind farm with 200 WTGs (wind turbine generators). Literature [6] used the integrating field measurement method to characterize the monthly wind speed and wind direction distributions and investigate the wind characteristics in turbine wakes. The research work shows that good agreement is obtained for both mean wind speed and turbulence intensity, which also verifies the possibility of combining actual field measurements and high-fidelity simulations to describe the characterization of utility-scale wind farms. Literature [7] studied large-eddy simulations of coherent structures within and above different wind farm configurations in a neutral atmospheric boundary layer (ABL) using proper orthogonal decomposition (POD) to improve understanding of the flow structures in both physical and spectral space. The research work indicates that wind farm dynamics in the ABL are very complex. Literature [8] proposed a simplified floating offshore wind turbine model, which is applicable for the real-

time simulation of large-scale floating offshore wind farms. The real-time results of offshore wind farms show the feasibility of the proposed turbine models for the real-time model of large-scale offshore wind farms.

Generally speaking, the wind farm model can be divided into detailed models and equivalent models, where the detailed model is difficult to solve, does not have good adaptability to parameter changes, takes a lot of work to modify, and requires high computer performance [9,10]. Therefore, most of the current research studies choose the equivalent model to describe the wind farm.

The equivalent model can be further divided into single-machine equivalence and multi-machine equivalence, where the single-machine equivalent model uses a large-capacity wind turbine to replace the whole wind farm for reducing the complexity of the simulation system and improving the speed of calculation, and the multi-machine equivalent model divides the whole wind farm into many groups according to one or more indexes and then uses a wind turbine to replace the wind farm within the same group.

Literatures [11–14] proposed the single-machine equivalent model of wind farm, but the characteristics of wind turbines change greatly based on actual applications. Literature [15] proposed a systematic and simple method to model large-scale induction machine-based wind farms by a single WTG that contains an equivalent mechanical wind turbine and an equivalent electrical generator. The research results shows that the proposed method is adequately accurate in both transients and steady-state responses and it can be readily used for modeling large-scale wind farms to reduce the overall computational burden of the system. In a sense, the single-machine equivalent model is not accurate enough.

Literatures [16–18] proposed the earlier research results on multi-machine equivalent models of wind farm, where the wind farm is mainly grouped according to the geographic location. This classification method needs a regular arrangement of wind turbines and does not have good adaptability. To overcome the above shortcoming, literatures [19–29] proposed some novel classification methods, which are more close to the actual operating state of wind turbines. Yan et al. [19] sorted the wind farm using the support vector machine (SVM) under the consideration of similar wind speed and the wake effect of the wind farm. This method cannot accurately characterize the actual operating state of wind farm, which will lead to large algorithm errors. Literatures [20–22] sorted the wind farm by clustering algorithm, which is based on the measured data of all the wind turbines, the wind speed model, and the steady-state model of wind farm. However, this method does not consider dynamic characteristics of wind turbines. The clustering index of [23–25] was the dominant variable during the operation, and the dominant variables were extracted by the feature analysis method. However, the influence of disturbance location and type on the operation characteristics of wind turbines has not been considered by the characteristic roots. Literatures [3, 5, 26, 27] sorted the wind farm considering 13 state variables of wind turbines during the operation. Literature [28] presented a method to develop computationally efficient dynamic model of a wind farm suitable for large disturbance simulation. The method based on a trajectory piecewise linear (TPWL) approximation uses single and multiple training trajectory to develop a nonlinear reduced-order model (ROM). Simulation results demonstrated the effectiveness of the model in capturing dynamic behavior of wind farm following large disturbances. But this kind of classification method has the disadvantages of redundant data, high calculation complexity, low applicability, etc.

There are still some shortcomings in the above classification methods, such as large error, incomplete consideration of actual operating state, complicated calculation and low applicability, and so on. More importantly, the large-scale wind farm has the characteristics of multi-time-scale and strong nonlinearity on the time axis. With the increase of wind farm's scale, the shortcomings of existing modeling methods are more obvious. To overcome the above shortcomings, the multi-machine dynamic equivalent modeling of wind farm based on dominant variables hierarchical clustering algorithm is proposed in this paper. The essence of principal component analysis is a mathematical transformation method, which transforms a given set of related variables into another set of irrelevant variables by linear transformation. These new variables are arranged in descending order of variance. During the process of mathematical transformation, the total variance of variables should always remain unchanged, and the first variable has the largest variance, which is called the first principal component. The second variable has the second largest variance and is independent of the first variable, which is called the second principle component. Then, the third and the fourth variables are obtained in the same method. Compared with other parameter analysis methods (correlation analysis, feature analysis, factor analysis, and so on), principal component analysis can not only retain as much information as possible about the original variables but also achieve the goal of dimensionality reduction, thus reducing the computational complexity and the cost of the algorithm. Meanwhile, compared with other classification methods (support vector machine, neural network, density clustering, grid clustering, and so on), the hierarchical clustering method does not need to determine the number of classifications and has high classification efficiency, which is especially suitable for the classification of large data.

The specific research steps in this paper are as follows. Firstly, the 13 state variables of the wind turbines during actual operation are calculated. Secondly, the dominant variables are extracted from 13 state variables by principal component analysis. Then, the wind farm is clustered by hierarchical clustering algorithm, where the dominant variables are used as clustering index. Furthermore, three dynamic equivalent models of 24 wind turbines are established using PSCAD software, which use 13 state variables, wind speed, and dominant variables as clustering indexes, respectively. Finally, the active power and reactive power output curves of wind farm are simulated in the case of the three-phase short-circuit fault on the system side or wind speed fluctuation, respectively. The simulation results verify the effectiveness of dominant variables and the advantages of this proposed model.

2. Mathematical Model of Doubly Fed Induction Generator

At present, the doubly fed induction generator (DFIG) is most widely used in wind farms all over the world. Its mathematical model mainly includes wind turbine module, induction motor module, transmission system module, back-to-back converter system control module, boost transformer module, R-L series components, etc. Some important modules will be described below [29–32].

2.1. Wind Turbine Module. The relationship between active power of the doubly fed induction generator and wind energy captured by wind turbines can be expressed as follows:

$$p_e = \frac{1}{2C_p \rho A v^3}, \tag{1}$$

where p_e is the active power of the generator, C_p is the utilization coefficient of wind energy, ρ is the air density, A is the sweeping area of the blade, and v is the input wind speed endured by the wind turbine.

In the case of a given wind speed, the captured wind power of the wind turbine mainly depends on the C_p, which is the function of the pitch angle (β) and tip speed ratio (λ).

$$\lambda = \frac{R\omega_r}{v}, \tag{2}$$

where ω_r is the rotating speed of the wind turbine, which can be obtained from the power characteristic curve under the known active power of the generator (p_e).

The characteristic curve of wind energy utilization coefficient is shown in Figure 1.

For variable-pitch wind turbines, the wind power of the impeller can be controlled by changing the pitch angle (β). Usually, the wind energy utilization factor (C_p) of the wind turbines reaches the maximum value when $\beta = 0$.

2.2. Induction Motor Module. In DQ coordinate, the flux-linkage equation and voltage equation of the doubly fed induction generator can be obtained from the characteristics of induction motor [23–25], which can be expressed as follows:

$$\begin{cases} \psi_{\mathrm{d}s} = -L_{ss} I_{ds} + L_m I_{dr}, \\ \psi_{\mathrm{q}s} = -L_{ss} I_{qs} + L_m I_{qr}, \\ \psi_{\mathrm{d}r} = L_{rr} I_{dr} - L_m I_{ds}, \\ \psi_{\mathrm{q}r} = L_{rr} I_{qr} - L_m I_{qs}, \end{cases} \tag{3}$$

$$\begin{cases} U_{\mathrm{d}s} = -R_s I_{ds} + \dfrac{\mathrm{d}\psi_{ds}}{\mathrm{d}t} - \psi_{qs}, \\ U_{\mathrm{q}s} = -R_s I_{qs} + \dfrac{\mathrm{d}\psi_{qs}}{\mathrm{d}t} + \psi_{ds}, \\ U_{\mathrm{d}r} = R_r I_{dr} + \dfrac{\mathrm{d}\psi_{dr}}{\mathrm{d}t} - S\psi_{qs}, \\ U_{\mathrm{q}r} = R_r I_{qr} + \dfrac{\mathrm{d}\psi_{qr}}{\mathrm{d}t} + S\psi_{ds}, \end{cases} \tag{4}$$

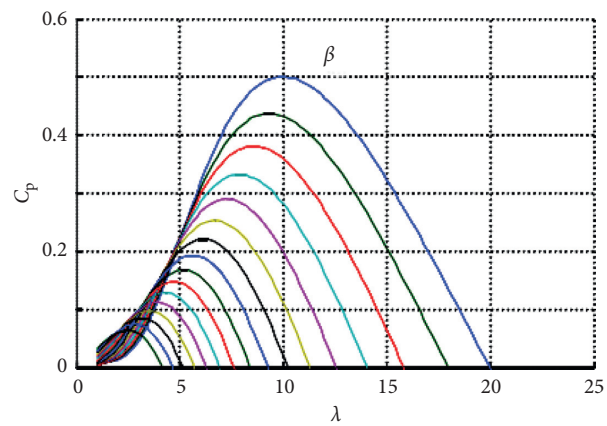

Figure 1: The characteristic curve of wind energy utilization coefficient.

where ψ and U represent flux linkage and the voltage, respectively; the subscripts d and q represent the direct-axis component and the quadrature-axis component, respectively; the subscripts s and r represent the stator and the rotor, respectively; L_{ss} and L_{rr} represent the self-inductance of the stator winding and rotor winding, respectively; L_m represents the mutual inductance between stator and rotor; R represents the resistance; and S represents the slip ratio.

2.3. Transmission System Module. By incorporating the inertia of gearbox into the inertia of generator rotor, a two-mass model of transmission device can be obtained [33], which can be expressed as follows:

$$\begin{cases} \dfrac{\mathrm{d}T_t}{\mathrm{d}t} = \dfrac{1}{T_d}(T_m - T_t), \\ \dfrac{\mathrm{d}S}{\mathrm{d}t} = \dfrac{1}{T_j}(T_e - T_t), \end{cases} \tag{5}$$

where T_{m} represents the wind turbine torque, T_t represents rotor mechanical torque, T_e represents the electromagnetic torque, and T_d and T_j represent the inertia time constant of the transmission system and the generator, respectively.

The electromagnetic power is the output power of the stator, and the expression of the electromagnetic torque (T_e) can be deduced from the electromagnetic power, which can be expressed as follows:

$$T_e = L_m\left(I_{dr} I_{qs} - I_{ds} I_{qr}\right). \tag{6}$$

2.4. Converter Control System Module. The rotor of the doubly fed induction motor is connected to the power grid through back-to-back converter. Active power and reactive power of the generator consist of stator side and rotor side, where P_s and Q_s represent the active power and reactive power on stator side, while P_r and Q_r represent the active power and reactive power on rotor side [29–32]. In the steady-state process, the stator copper consumption is

neglected, the differential component is 0, and the direct-axis component of the stator voltage is 0. Combining with the stator side active power expression, the active power and reactive power expression of the stator side can be obtained, which can be expressed as follows:

$$\begin{cases} P_s = U_s I_{qs}, \\ Q_s = -U_s I_{ds}. \end{cases} \tag{7}$$

From the above formula, it can be seen that under the DQ coordinate, assuming that the direction of the stator flux linkage is consistent with that of the generator, the active power and reactive power of the stator of the doubly fed induction generator can be decoupled by adjusting the direct-axis component and quadrature-axis component, respectively.

When the stator flux-linkage orientation is used, the stator flux linkage coincides with the synchronous rotating coordinate system on the direct axis, and the quadrature-axis flux-linkage component is zero. Combining with the stator flux-linkage equation, the relationship between stator current and rotor current can be obtained, which can be expressed as follows:

$$\begin{cases} I_{ds} = \dfrac{U_s}{L_{ss}} - \dfrac{I_{dr} L_m}{L_{ss}}, \\ I_{qs} = -\dfrac{I_{qr} L_m}{L_{ss}}. \end{cases} \tag{8}$$

The relationship between the rotor voltage and the rotor current can be obtained from the aforementioned simultaneous flux-linkage equation and the stator-rotor voltage equation.

$$\begin{cases} U_{dr} = R_s I_{ds} - S\left(L_{rr} - \dfrac{(L_m)^2}{L_{ss}}\right) I_{qr}, \\ U_{qr} = R_s I_{qr} - S\left(L_{rr} - \dfrac{(L_m)^2}{L_{ss}}\right) I_{dr} + S\dfrac{U_s L_m}{L_{ss}}, \end{cases} \tag{9}$$

where R represents the resistance and S represents the slip ratio.

The relationship between the rotor voltage and the stator current is established based on formulas (8) and (9). The control of active power and reactive power on the stator side can be realized by controlling the rotor voltage by the control system.

2.5. Transient Model. When using the pulse width modulation (PWM) converter, the power factor of the PWM converter can be controlled to be close to 1.0. That is to say, the active power of the doubly fed wind turbine is approximately equal to the reactive power, which can be expressed as

$$\begin{cases} P_e = (1 - s) P_s, \\ Q_e = Q_s. \end{cases} \tag{10}$$

If the wind turbine works under the status of constant power factor, it can be expressed as

$$\frac{Q_s}{P_s} = C, \quad (C \text{ is a constant}). \tag{11}$$

The relationship between the power of the doubly fed wind turbine and the active power on the stator side can be obtained by equations (3)–(11), which can be expressed as

$$\begin{cases} P_e = \dfrac{R_r (L_{ss})^2}{(L_m)^2 (U_s)^2}\left(1 + C^2\right)(P_s)^2 + \left(1 - S + \dfrac{2CL_{ss}R_r}{(L_m)^2}\right) P_s, \\ Q_e = CP_s. \end{cases} \tag{12}$$

If the flux linkage of the stator is neglected, the rotor transient model can be expressed as

$$\begin{cases} \dfrac{\mathrm{d}E_d'}{\mathrm{d}t} = -\dfrac{R_r}{L_{rr}}\left(E_d' - \omega_s I_{qs}\dfrac{(L_m)^2}{L_{ss}}\right) + S\omega_s E_q' - \omega_s U_{qr}', \\ \dfrac{\mathrm{d}E_q'}{\mathrm{d}t} = -\dfrac{R_r}{L_{rr}}\left(E_q' + \omega_s I_{ds}\dfrac{(L_m)^2}{L_{ss}}\right) + S\omega_s E_d' + \omega_s U_{dr}'. \end{cases} \tag{13}$$

From the above detailed deduction and analysis, one can see that these 13 state variables (slip ratio S (no unit, just a ratio), pitch angle β (unit: 0), wind turbine torque T_{m} (unit: N·m), rotor mechanical torque T_t (unit: N·m), electromagnetic torque T_e (unit: N·m), stator direct-axis current I_{ds} (unit: A), stator quadrature-axis current I_{qs} (unit: A), rotor direct-axis current I_{dr} (unit: A), rotor quadrature-axis current I_{qr} (unit: A), rotor direct-axis voltage U_{dr} (unit: V), rotor quadrature-axis voltage U_{qr} (unit: V), direct-axis transient potential E_d (unit: V), and quadrature-axis transient potential E_q (unit: V)) can describe the actual operation process of DFIGs. When some special faults or wind speed disturbances occur, the control system of DFIGs can be controlled according to the initial values and the variations of these 13 state variables, whose initial values can be used to describe the initial operating state of DFIGs.

3. Dominant Variable Hierarchical Clustering Algorithm

Based on the theoretical analysis and formula deduction in Section 2, 13 state variables of wind turbines during operation can be calculated only under the consideration of few parameters, such as wind speed, power factors, nameplate parameters and power characteristic curves of the wind turbines, and so on.

In practical application, the analysis and calculation of 13 state variables will be difficult for huge computational complexity, especially for large-scale wind farm. Therefore, this paper extracts the dominant variables using principal component analysis and considers them as clustering indexes, which can effectively reduce the computational

complexity. This method can not only reduce the data dimension but also ensure the information completeness, so it has better performance than analyzing the original data of wind farm [34–38].

The detailed modeling process can be expressed as follows:

(i) Step 1: according to the mathematical model of doubly fed wind turbines, 13 complete state variables representing the actual operation state of wind turbines are calculated.

(ii) Step 2: based on the principal component analysis method, the dominant variables representing the main oscillation characteristics of the 13 complete state variables are extracted.

(iii) Step 3: considering dominant variables as clustering index, the wind farm of doubly fed wind turbines are clustered by hierarchical clustering algorithm, where the hierarchical clustering algorithm includes the following steps:

Step 3.1: each sample point is defined as a class.
Step 3.2: calculate the distance between sample points within different classes using Euclidean distance formula.
Step 3.3: according to the above distance, the two classes with the shortest distance are merged into one class.
Step 3.4: the distance between the merged class and other classes is recalculated using Euclidean distance formula.
Step 3.5: repeat the step 3.3.
Step 3.6: the algorithm ends until all samples are merged into one class.

(iv) Step 4: according to the clustering results of dominant variables, wind farm is divided into several groups.

(v) Step 5: according to the partition results, the equivalent model of wind farm is constructed.

4. Simulations

4.1. Simulation Tool. PSCAD is an electromagnetic simulation software platform, which has been widely used in many research fields. It can use the time-domain analysis method to solve the complete power system, and the operation results are very accurate. It also has an abundant component library and complex control modules, allowing users to flexibly establish circuit models for simulation analysis, such as inverter, transformer, rectifier, wind source, wind governor, wind turbine component, synchronous generator component, speed control component, and so on. In addition, it also provides a large number of simulation cases for learning. Therefore, PSCAD software platform is especially suitable for model establishment and performance analysis of large-scale wind farm.

4.2. Initial Parameters. A wind farm model with 24 DFIGs is established using PSCAD software platform. The terminal voltage of wind turbine is 690 V, which is boosted to 33 KV by one-machine one-variable connection. Every 4 transformers are connected by overhead lines to public connection points, and then one boost transformer is connected to the infinite bus system.

Actually, the initial wind speed data of 24 wind turbines have a great influence on the calculation cost of the algorithm. Literature [26] uses a K-means clustering algorithm to sort the wind farm, which is one of the state-of-the-art clustering methods. Meanwhile, the wake effect and topographic differences have also been considered in this literature, and the initial wind speed data of each wind turbine have been set as different values. To compare and quantitatively analyze the advantages and disadvantages of hierarchical clustering algorithm and K-means clustering algorithm, we use the same initial wind speed data as literature [26], as shown in Table 1, where all the data retain one significant digit after decimal point.

The 13 state variables of 24 DFIGs are calculated according to initial wind speed data in Table 1 and equations (1)–(13) described in Section 2, and the calculation results are shown in Table 2, where all the data retain two significant digits after decimal point.

Because the transient time constant of motor stator is very small, I_{ds} is ignored because its value is close to 0. Meanwhile, to obtain maximal value of wind energy utilization factor (C_p) of wind turbines, the pitch angle (β) should be equal to 0. Moreover, assuming that the wind speed is a fixed value, principal component analysis is carried out based on the above 13 state variables of 24 wind turbines. In general, according to the algorithm rules of principal component analysis, these variables can be considered as dominant variables as long as they can explain or express more than 85% variance. The analysis results are shown in Table 3.

As shown in Table 3, 94.331% variance can be expressed or explained by extracting only two factors, such as slip rate (S) and wind turbine torque (T_m). It demonstrates that these two variables can represent the actual operating state of wind turbines, so slip rate (S) and wind turbine torque (T_m) are regarded as dominant variables.

4.3. Numerical Simulations. To verify the effectiveness of dominant variables, three clustering trees are obtained using hierarchical clustering algorithm, where 13 state variables, dominant variables, and wind speed are regarded as clustering indexes, respectively. Figure 2 shows three clustering trees.

References [3, 26, 27] indicate that it is most reasonable to divide 24 wind turbines into four groups. According to Figure 2, the clustering results can be obtained, as shown in Table 4.

Figures 2(a), 2(b), and 2(c) correspond to (a), (b), and (c) in Table 4, respectively. From (a) and (b) in Table 4, one can see that clustering results are consistent when the 13 state variables and dominant variables are regarded as clustering indexes, respectively. From (a) and (c) in Table 4, one can see that the clustering results are quite different when the 13

Table 1: Initial wind speed data of 24 wind turbines.

No	1	2	3	4	5	6	7	8
Initial wind speed (m/s)	10.6	9.7	8.7	7.7	10.6	9.7	8.7	7.7
No	9	10	11	12	13	14	15	16
Initial wind speed (m/s)	10.3	9.3	8.2	6.9	10.3	9.3	8.2	6.9
No	17	18	19	20	21	22	23	24
Initial wind speed (m/s)	8.2	6.9	8.2	6.9	10.3	9.3	8.2	6.9

Table 2: Calculation results of 13 state variables of 24 wind turbines.

No	S	β	T_m	T_t	T_e	I_{ds}	I_{qs}	I_{dr}	I_{qr}	U_{dr}	U_{qr}	E_d	E_q
1	−0.20	0	0.72	0.72	0.72	0	0.67	0.59	−0.70	−0.02	−0.23	0.14	1.08
2	−0.20	0	0.58	0.58	0.58	0	0.54	0.59	−0.57	−0.02	−0.23	0.11	1.08
3	−0.20	0	0.44	0.44	0.44	0	0.41	0.59	−0.43	−0.01	−0.23	0.09	1.08
4	−0.11	0	0.33	0.33	0.33	0	0.31	0.59	−0.32	0.00	−0.13	0.06	1.08
5	−0.20	0	0.72	0.72	0.72	0	0.67	0.59	−0.70	−0.02	−0.23	0.14	1.08
6	−0.20	0	0.58	0.58	0.58	0	0.54	0.59	−0.57	−0.02	−0.23	0.11	1.08
7	−0.20	0	0.44	0.44	0.44	0	0.41	0.59	−0.43	−0.01	−0.23	0.09	1.08
8	−0.11	0	0.33	0.33	0.33	0	0.31	0.59	−0.32	0.00	−0.13	0.06	1.08
9	−0.20	0	0.68	0.68	0.68	0	0.63	0.59	−0.67	−0.02	−0.23	0.13	1.08
10	−0.20	0	0.53	0.53	0.53	0	0.49	0.59	−0.52	−0.02	−0.23	0.10	1.08
11	−1.97	0	0.38	0.38	0.38	0	0.35	0.59	−0.38	−0.01	−0.23	0.07	1.08
12	−0.01	0	0.27	0.27	0.27	0	0.25	0.59	−0.27	0.00	−0.01	0.05	1.08
13	−0.20	0	0.68	0.68	0.68	0	0.63	0.59	−0.67	−0.02	−0.23	0.13	1.08
14	−0.20	0	0.53	0.53	0.53	0	0.49	0.59	−0.52	−0.02	−0.23	0.10	1.08
15	−0.19	0	0.38	0.38	0.38	0	0.35	0.59	−0.38	−0.01	−0.23	0.07	1.08
16	−0.01	0	0.27	0.27	0.27	0	0.25	0.59	−0.27	0.00	−0.12	0.05	1.08
17	−0.20	0	0.68	0.68	0.68	0	0.63	0.59	−0.67	−0.02	−0.23	0.13	1.08
18	−0.20	0	0.53	0.53	0.53	0	0.49	0.59	−0.52	−0.02	−0.23	0.10	1.08
19	−1.96	0	0.38	0.38	0.38	0	0.35	0.59	−0.38	−0.01	−0.23	0.07	1.08
20	−0.01	0	0.27	0.27	0.27	0	0.25	0.59	−0.27	0.00	−0.12	0.05	1.08
21	−0.20	0	0.68	0.68	0.68	0	0.63	0.59	−0.67	−0.02	−0.23	0.13	1.08
22	−0.20	0	0.53	0.53	0.53	0	0.49	0.59	−0.52	−0.02	−0.23	0.10	1.08
23	−0.19	0	0.38	0.38	0.38	0	0.35	0.59	−0.38	−0.01	−0.23	0.07	1.08
24	−0.01	0	0.27	0.27	0.27	0	0.25	0.59	−0.27	0.00	−0.12	0.05	1.08

Table 3: Results of principal component analysis.

Components	Variances (%)	Total (%)
S	82.918	82.918
T_m	11.413	94.331
T_t	3.224	97.555
T_e	2.309	99.864
I_{qs}	0.130	99.994
I_{dr}	0.006	100
I_{qr}	3.281×10^{-6}	100
U_{dr}	3.332×10^{-8}	100
U_{qr}	1.309×10^{-24}	100
E_d	1.008×10^{-25}	100
E_q	2.131×10^{-26}	100

state variables and wind speed are regarded as clustering indexes, respectively. Therefore, it is proved that it is effective and feasible to extract dominant variables as clustering indexes by principal component analysis.

Based on the above results, three models are established using PSCAD software platform, which use 13 state variables, dominant variables, and wind speed as clustering indexes, respectively. In order to compare the advantages and disadvantages of the above three models, the active power and reactive power output curves of wind farm are simulated in the case of the three-phase short-circuit fault on the system side or wind speed fluctuation, respectively. Because the exact data of large-scale wind farm are not readily available in real time, we set the wind speed of each wind turbine as a non-zero constant value, and the values of each wind turbine are not exactly equal during simulation process, and the detailed value is shown in Table 1. Therefore, the active power and reactive power output curves of wind farm are continuous but relatively flat, where the X-axis is running time of wind turbine (unit: s). Meanwhile, the faults or wind speed fluctuations are superimposed when the wind turbine is running, not stationary. If this method is applied to real measurements, just only reset the initial wind speed data of each wind turbine and change the wind speed from a constant value to a variable value during the actual operating process. This method is also valid, but the computational cost will be largely increased. Moreover, the output curve is no longer so flat but fluctuates a lot.

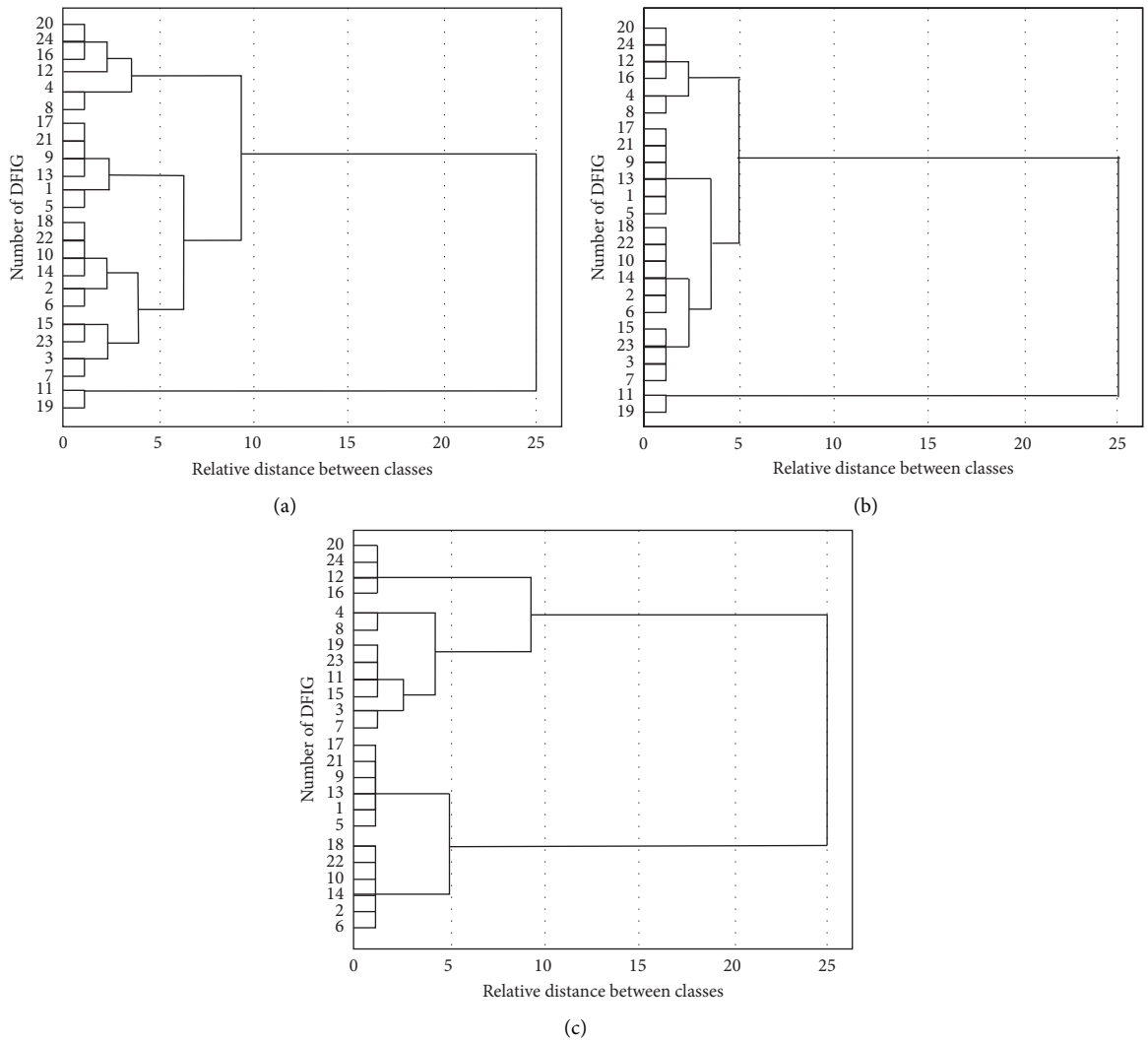

Figure 2: Clustering tree graphs under different indexes. (a) Clustering result using 13 state variables as clustering indexes. (b) Clustering result using dominant variables as clustering indexes. (c) Clustering result using wind speed as clustering index.

Table 4: Clustering results of 4-group wind turbines under different indexes.

(a) 13 state variables	
Equivalent unit number	Clustering results
1	1, 5, 9, 13, 17, 21
2	2, 3, 6, 7, 10, 14, 15, 18, 22, 23
3	4, 8, 12, 16, 20, 24
4	11, 19
(b) Dominant variables	
1	1, 5, 9, 13, 17, 21
2	2, 3, 6, 7, 10, 14, 15, 18, 22, 23
3	4, 8, 12, 16, 20, 24
4	11, 19
(c) Wind speed	
1	1, 5, 9, 13, 17, 21
2	2, 6, 10, 14, 18, 22
3	3, 4, 7, 8, 11, 15, 19, 23
4	12, 16, 20, 24

It is worth mentioning that only a part of the curves with faults or wind speed fluctuations is captured to show the differences among three models, while the curves in other periods are not captured.

4.4. Three-Phase Short-Circuit Fault on System Side. The simulation curve from the beginning stage to the stable stage is not captured. When the simulation curve reaches a stable state and lasts for 14 seconds, a man-made three-phase short-circuit fault is imposed to the system side, which lasts for 0.2 seconds. After 14.2 seconds, the output curve is relatively stable and there is no abnormal change. Hence, we only capture the curves for a period of time around 14 seconds. Within this period of time, the active power and reactive power output curves of wind farm are shown in Figure 3.

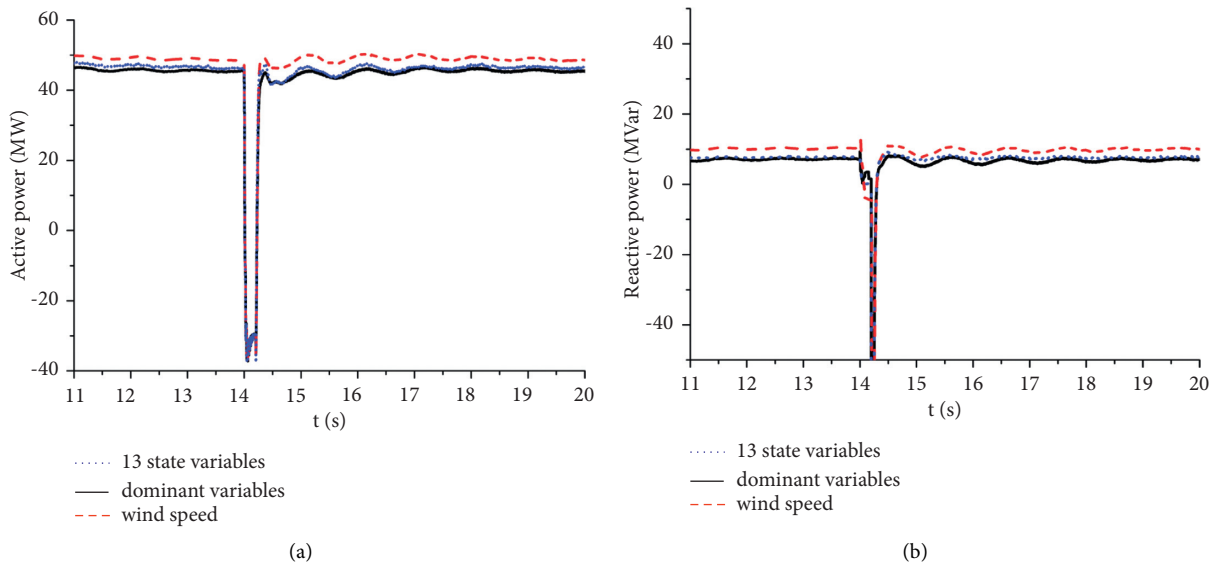

Figure 3: The output curve of wind farm in case of the three-phase short-circuit fault on system side. (a) Active power curve of three models. (b) Reactive power curve of three models. Blue line, black line, and red line represent 13 state variables, dominant variables, and wind speed, respectively.

From Figure 3, one can see that the active curve and reactive curve of dominant variables almost coincide with that of 13 state variables, which demonstrates that it is reasonable to extract the dominant variables using dominant variable hierarchical clustering algorithm proposed in this paper. The dominant variable can represent actual operating state of wind turbines in wind farm in the case of the three-phase short-circuit fault on system side. On the contrary, there is a large error between wind speed curve and 13-state-variable curve, which demonstrates that it is inappropriate to only take the wind speed as the clustering index.

4.5. Wind Speed Fluctuation. The simulation curve from the beginning stage to the stable stage is not captured. When the simulation curve reaches a stable state and lasts for 14 seconds, a man-made gust fluctuation is imposed, which lasts for 2 seconds and the maximum wind speed is 6 m/s. Because of the short lag and persistence effect of wind speed fluctuation, the curve is relatively stable after 20 seconds. Hence, we only capture the curves from 11 seconds to 20 seconds. Within this period of time, the active power and reactive power output curves of wind farm are shown in Figure 4.

From Figure 4, one can see that the active curve and reactive curve of dominant variables almost coincide with that of 13 state variables, which demonstrates that it is reasonable to extract the dominant variables using dominant variable hierarchical clustering algorithm proposed in this paper. The dominant variable can represent actual operating state of wind turbines in wind farm even in the case of wind speed fluctuation. On the contrary, there is a large error between wind speed curve and 13-state-variable curve, which demonstrates that it is inappropriate to only take the wind speed as the clustering index.

4.6. Results and Discussion. From Figures 3 and 4, the following conclusions can be drawn:

(1) In the case of the three-phase short-circuit fault on system side or wind speed fluctuation, the maximal relative errors of output power curve of wind farm between the wind speed model and 13-state-variable model and between the dominant variable equivalent model and 13-state-variable model are 50.14% and 9.9%, respectively.

(2) Reference [19] indicates that the maximal relative error of output curve of wind farm between the neural network model and 13-state-variable model is 12.1% and between the support vector machine model and 13-state-variable model is 11.4%, respectively. Reference [33] indicates that the maximal relative error of output power curve of wind farm between the K-means clustering model and 13-state-variable model is 18.06%.

(3) Compared with the wind speed model, K-means clustering model, neural network model, and support vector machine model, the maximal relative error of the dominant variable equivalent model is the smallest, which demonstrates that this model is more accurate and much closer to the actual operating state of wind farm.

(4) The dominant variable can also represent actual operating state of wind turbines in wind farm, even in the case of the three-phase short-circuit fault on system side or wind speed fluctuation. Therefore, it is reasonable to extract slip rate (S) and wind turbine torque (T_m) as dominant variables from 13 variables, and it is also reasonable to classify 24 wind turbines using hierarchical clustering algorithm.

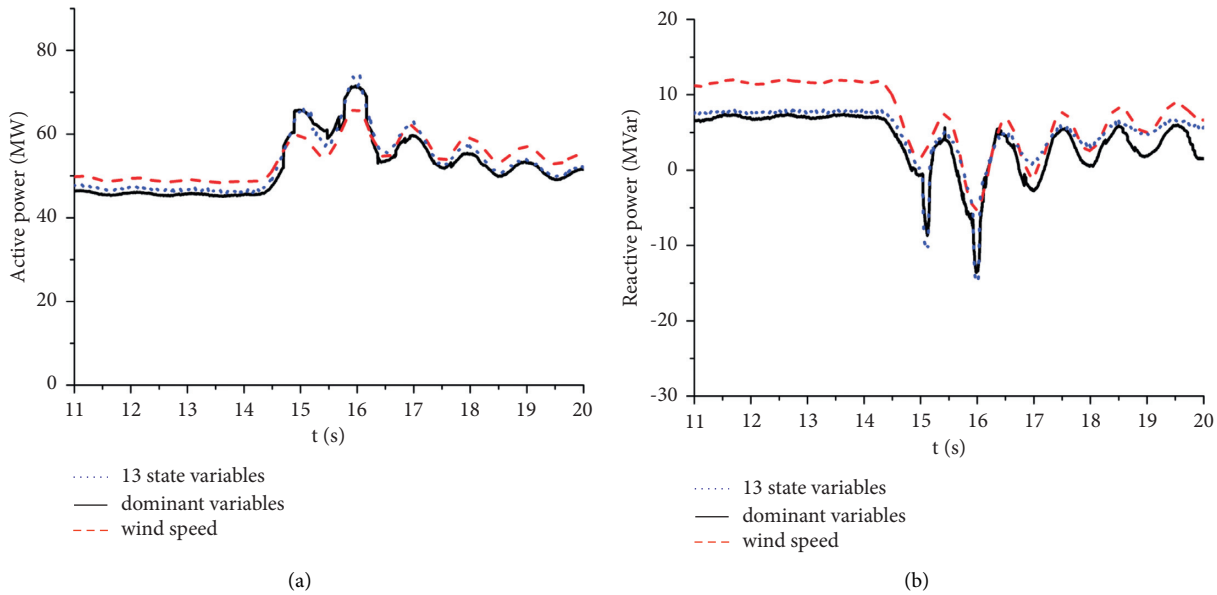

Figure 4: The output curve of wind farm in case of wind speed fluctuation. (a) Active power curve of three models. (b) Reactive power curve of three models. Blue line, black line, and red line represent 13 state variables, dominant variables, and wind speed, respectively.

5. Conclusions

In this paper, the mathematical model of the doubly fed induction generator is established under the consideration of the actual industrial applications of large-scale wind farm, and 13 state variables which can represent the dynamic operation process of wind turbines are calculated. The principal component analysis is proposed to extract dominant variables from 13 state variables, which can be used as clustering index. Then, three equivalent models are established, which use 13 state variables, dominant variables, and wind speed as clustering indexes, respectively. In order to compare the advantages and disadvantages of the above three models, the active power and reactive power output curves of wind farm are simulated in the case of the three-phase short-circuit fault on the system side or wind speed fluctuation, respectively. The simulation results demonstrate the following conclusions. (1) It is reasonable and effective to extract dominant variables by principal component analysis. (2) The dominant variable equivalent model has higher accuracy than the wind speed model, K-means clustering model, neural network model, and support vector machine model. (3) When the scale of wind farm increases, the advantage of this model will be more obvious. (4) The research result is especially suitable for characteristics analysis of large-scale wind farm connected to power grid. The question of how to conduct the systematic experimental research on large-scale wind farm, establish a better model to be as close to the actual operation state of large-scale wind farm as possible, and quantify and evaluate the errors between various equivalent models, complete models, and actual large-scale wind farm will be focus of future research work.

Data Availability

The data supporting the findings of this study are included within the article.

Conflicts of Interest

The authors declare that they have no conflicts of interest.

Acknowledgments

This study was supported by Sichuan Provincial Academic and Technical Leader Training Plan and Xihua Scholars Training Plan of Xihua University. Wenbo Jiang would like to acknowledge the Overseas Training Plan of Xihua University (09/2014–09/2015, University of Michigan, Ann Arbor, US).

References

[1] V. Nelson, *Introduction to Renewable Energy*, CRC Press, Boca Raton, FL, USA, 2010.

[2] M. A. Chowdhury, W. X. Shen, N. Hosseinzadeh, and H. R. Pota, "A novel aggregated DFIG wind farm model using mechanical torque compensating factor," *Energy Conversion and Management*, vol. 67, no. 3, pp. 265–274, 2013.

[3] J. Zou, C. Peng, Y. Yan, H. Zheng, and Y. Li, "A survey of dynamic equivalent modeling for wind farm," *Renewable and Sustainable Energy Reviews*, vol. 40, no. 12, pp. 956–963, 2014.

[4] M. A. Chowdhury, W. Shen, N. Hosseinzadeh, and H. R. Pota, "Transient stability of power system integrated with doubly fed induction generator wind farms," *IET Renewable Power Generation*, vol. 9, no. 2, pp. 184–194, 2015.

[5] W. Du, W. Dong, and H. Wang, "A method of reduced-order modal computation for planning grid connection of a large-scale wind farm," *IEEE Transactions on Sustainable Energy*, vol. 11, no. 3, pp. 1185–1198, 2019.

[6] X. Yang, C. Milliren, M. Kistner et al., "High-fidelity simulations and field measurements for characterizing wind fields in a utility-scale wind farm," *Applied Energy*, vol. 281, no. 1-17, Article ID 116115, 2021.

[7] M. Zhang and R. J. A. M. Stevens, "Characterizing the coherent structures within and above large wind farms," *Boundary-Layer Meteorology*, vol. 174, no. 1, pp. 61–80, 2020.

[8] T.-D. Pham, M.-C. Dinh, H.-M. Kim, and T.-T. Nguyen, "Simplified floating wind turbine for real-time simulation of large-scale floating offshore wind farms," *Energies*, vol. 14, no. 15, pp. 1–18, Article ID 4571, 2021.

[9] S. K. Salman and A. L. J. Teo, "Windmill modeling consideration and factors influencing the stability of a grid-connected wind power-based embedded generator," *IEEE Transactions on Power Systems*, vol. 18, no. 2, pp. 763–802, 2003.

[10] Z. Chen, J. M. Guerrero, and F. Blaabjerg, "A review of the state of the art of power electronics for wind turbines," *IEEE Transactions on Power Electronics*, vol. 24, no. 8, pp. 1859–1875, 2009.

[11] A. S. Dobakhshari and M. Fotuhi-Firuzabad, "A reliability model of large wind farms for power system Adequacy studies," *IEEE Transactions on Energy Conversion*, vol. 24, no. 3, pp. 792–801, 2009.

[12] J. Brochu, C. Larose, and R. Gagnon, "Validation of single- and multiple-machine equivalents for modeling wind power plants," *IEEE Transactions on Energy Conversion*, vol. 26, no. 2, pp. 532–541, 2011.

[13] M. J. Mercado-Vargas, D. Gómez-Lorente, O. Rabaza, and E. Alameda-Hernandez, "Aggregated models of permanent magnet synchronous generators wind farms," *Renewable Energy*, vol. 83, no. 11, pp. 1287–1298, 2015.

[14] W. Li, P. Chao, X. Liang, D. Xu, and X. Jin, "An improved single-machine equivalent method of wind power plants by calibrating power recovery behaviors," *IEEE Transactions on Power Systems*, vol. 33, no. 4, pp. 4371–4381, 2018.

[15] N. Shabanikia, A. A. Nia, A. Tabesh, and S. A. Khajehoddin, "Weighted dynamic aggregation modeling of induction machine-based wind farms," *IEEE Transactions on Sustainable Energy*, vol. 12, no. 3, pp. 1604–1614, 2021.

[16] V. Akhmatov and H. Knudsen, "An aggregate model of a grid-connected, large-scale, offshore wind farm for power stability investigations-importance of windmill mechanical system," *International Journal of Electrical Power & Energy Systems*, vol. 24, no. 9, pp. 709–717, 2002.

[17] D. J. Trudnowski, A. Gentile, J. M. Khan, and E. M. Petritz, "Fixed-speed wind-generator and wind-park modeling for transient stability studies," *IEEE Transactions on Power Systems*, vol. 19, no. 4, pp. 1911–1917, 2004.

[18] L. M. Fernández, J. R. Saenz, and F. Jurado, "Dynamic models of wind farms with fixed speed wind turbines," *Renewable Energy*, vol. 31, no. 8, pp. 1203–1230, 2006.

[19] J. Yan, Y. Liu, S. Han, and M. Qiu, "Wind power grouping forecasts and its uncertainty analysis using optimized relevance vector machine," *Renewable and Sustainable Energy Reviews*, vol. 27, pp. 613–621, 2013.

[20] J. Liu, M. Zhu, Z. Lin, and S. Chen, "A dynamic clustering model of wind farm based on the operation data," *Journal of Renewable and Sustainable Energy*, vol. 7, no. 4, Article ID 043111, 2015.

[21] G. Xia, L. Zhou, J. M. Freedman, S. Baidya Roy, R. A. Harris, and M. Charles Cervarich, "A case study of effects of atmospheric boundary layer turbulence, wind speed, and stability on wind farm induced temperature changes using observations from a field campaign," *Climate Dynamics*, vol. 46, no. 7-8, pp. 2179–2196, 2016.

[22] D. C. Fabrizio, V. Alfredo, and V. Domenico, "Adaptive wind generation modeling by fuzzy clustering of experimental data," *Electronics*, vol. 7, no. 4, pp. 1–16, 2018.

[23] Z. H. Zhang, J. H. Li, and P. Zhuge, "Failure analysis of large-scale wind power structure under simulated typhoon," *Mathematical Problems in Engineering*, vol. 2014, no. 7, pp. 1–10, Article ID 486524, 2014.

[24] X. Cheng, W. J. Lee, M. Sahni, Y. Cheng, and L. K. Lee, "Dynamic equivalent model development to improve the operation efficiency of wind farm," *IEEE Transactions on Industry Applications*, vol. 52, no. 4, pp. 1–9, 2016.

[25] P. Wang, Z. Zhang, Q. Huang, N. Wang, X. Zhang, and W.-J. Lee, "Improved wind farm aggregated modeling method for large-scale power system stability studies," *IEEE Transactions on Power Systems*, vol. 33, no. 6, pp. 6332–6342, 2018.

[26] S. Y. Chen, C. Wang, and H. Shen, "Dynamic equivalence for wind farms based on clustering algorithm," *Proceedings of the Csee*, vol. 32, no. 4, pp. 11–19, 2012.

[27] L. Lin and X. Pan, "Wind turbine grouping based on semi-supervised split-hierarchical spectral clustering algorithm for wind farm," *Electric Power Automation Equipment*, vol. 35, no. 2, pp. 8–14, 2015.

[28] H. R. Ali, L. P. Kunjumuhammed, B. C. Pal, K. Vershinin, and A. G. Adamczyk, "A trajectory piecewise-linear approach to nonlinear model order reduction of wind farms," *IEEE Transactions on Sustainable Energy*, vol. 11, no. 2, pp. 894–905, 2019.

[29] S. Muller, M. Deicke, and R. W. De Doncker, "Doubly fed induction generator systems for wind turbines," *IEEE Industry Applications Magazine*, vol. 8, no. 3, pp. 26–33, 2002.

[30] J. B. Ekanayake, L. Holdsworth, X. G. XueGuang Wu, and N. Jenkins, "Dynamic modeling of doubly fed induction generator wind turbines," *IEEE Transactions on Power Systems*, vol. 18, no. 2, pp. 803–809, 2003.

[31] L. L. Fan and Z. X. Miao, *Modeling and Analysis of Doubly Fed Induction Generator Wind Energy Systems*, Academic Press, Cambridge, MA, USA, 2015.

[32] M. Ahmad, *Operation and Control of Renewable Energy Systems*, Wiley Press, Hoboken, NJ, USA, 2017.

[33] J. Zou, C. Peng, H. Xu, and Y. Yan, "A fuzzy clustering algorithm-based dynamic equivalent modeling method for wind farm with DFIG," *IEEE Transactions on Energy Conversion*, vol. 30, no. 4, pp. 1329–1337, 2015.

[34] J. B. Daniel and J. O. Mark, "A study of power principal component analysis applied spatially distributed," *IEEE Transactions onPower Systems*, vol. 26, no. 4, pp. 2084–2092, 2011.

[35] L. Li, Z. Yan, D. H. Feng, and D. Han, "Discussion on intelligent technology evaluation of electrical power grid based on principal component analysis and production function," *Automation of Electric Power Systems*, vol. 38, no. 11, pp. 56–61 +73, 2014.

[36] G. Fu, P. Hall, and N. J. Miles, "Performance evaluation for composites based on recycled polypropylene using principal component analysis and cluster analysis," *Journal of Cleaner Production*, vol. 115, no. 3, pp. 343–353, 2016.

[37] Y. Wang, D. Xie, X. Wang, and Y. Zhang, "Prediction of wind turbine-grid interaction based on a principal component analysis-long short term memory model," *Energies*, vol. 11, no. 11, pp. 1–19, Article ID 3221, 2018.

[38] G. Melendez-Melendez, D. Cruz-Paz, D. Cruz-Paz, J. A. Carrasco-Ochoa, and J. F. Martínez-Trinidad, "An improved algorithm for partial clustering," *Expert Systems with Applications*, vol. 121, no. 5, pp. 282–291, 2019.